Experimental Investigation to Compare the Cyclic Response of A500 and A1085 HSS Braces

Will Bergendahl

A thesis

submitted in partial fulfillment of the

requirements for the degree of

Master of Science in Civil Engineering

University of Washington

2021

Reading Committee:

Jeffrey W. Berman

Dawn E. Lehman

Charles W. Roeder

Program Authorized to Offer Degree:

Civil and Environmental Engineering

University of Washington

Abstract

Experimental Investigation to Compare the Cyclic Response of A500 and A1085 HSS Braces

Will Bergendahl

Co-Chairs of the Supervisory Committee:

Professor Jeffrey W. Berman
Civil and Environmental Engineering

Professor Dawn E. Lehman
Civil and Environmental Engineering

HSS are often used as bracing members in special concentrically braced frames (SCBFs) in areas of high seismicity. These systems efficiently resist seismic forces through the stable and ductile inelastic yielding and buckling of braces. However, the current requirements for braces in SCBFs have reduced their practicality and usage in recent years, in particular due to the stringent local slenderness requirements for ductile members and the R_y factor. Traditionally, ASTM A500 HSS sections are used in SCBFs. However, AISC 341 now permits the use of ASTM A1085 HSS sections. The ASTM A1085 specification requires tighter control over the material and geometric properties of HSS, allowing for more efficient designs, i.e. the same section has a smaller local slenderness ratio for an A1085 HSS section than an A500 HSS section. Additionally, the R_y factor for A1085 members is smaller than that of A500 members, thus reducing the brace force demands used to design the remaining components of the SCBF. Previous research has indicated an increase in ductility associated with the use of A1085 HSS in braced frames, which could make SCBFs with A1085 braces a more commonly used seismic force resisting system.

The objective of this research is to investigate the behavior of A1085 square HSS members subjected to inelastic cyclic loading and compare their structural response to that of conventional A500 HSS members. A test frame was designed and constructed to accommodate testing, with a maximum specimen length of 20 feet. Two hydraulic actuators acting in parallel were used to apply forces up to 1000 kips in tension and 650 kips in compression, with a displacement range of $\pm$10 inches. Ten different square HSS shapes were tested in both A500 and A1085 steel using the same symmetric quasi-static displacement history. Study parameters such as brace local and global slenderness ratios, steel type, and steel producer were investigated in this research. The local slenderness ratios of the test specimens ranged from 9 to 25.7, and the global slenderness ratios ranged from 60 to 127.

The results of this experimental program indicate that the seismic performance of both the A500 and A1085 HSS members depends considerably on the local and global slenderness ratios, as expected. The performance of the A500 and A1085 HSS sections were evaluated based on their strength, deformability, and energy dissipation capacity. Material testing revealed some differences in strength and toughness between the HSS members from different steel producers. Minor differences in structural response between the pairs of A500 and A1085 HSS sections were observed through component testing, but no significant differences in deformability or energy dissipation capacity between the types of steel were observed across the entire test series. Brace damage in the form of local deformations and striations typically developed at similar levels of axial deformation in the A500 and A1085 HSS sections. Plots of brace deformation range prior to fracture and energy dissipation capacity showed that the A500 and A1085 HSS sections exhibited similar seismic performance across a wide range of width-to-thickness and global slenderness ratios. This may be a result of the similarities in the measured material and geometric properties of the different types of steel. Additionally, the symmetric displacement history used in this test series does not replicate the typical displacement demands on a brace in a braced-frame. It is well established that low-cycle fatigue depends on the applied displacement history. Therefore, the next phase of the research will investigate the impact of the tube producer as well as the displacement history on structural response.

TABLE OF CONTENTS

LIST OF FIGURES

LIST OF TABLES

Acknowledgements

I would first like to acknowledge my three advisors, Professors Dawn Lehman, Jeffrey Berman, and Charles Roeder, for giving me the opportunity to join this project and providing me with funding for this research. I would also like to acknowledge Professor Andrew Sen of Marquette University, who provided valuable insight throughout my time working on this project. I'd like to thank them for their guidance and support in the design and construction of the test frame and specimens, and throughout the testing program and writing of this thesis. They spent many hours reading and revising this thesis, and provided helpful feedback and suggestions for its improvement.

I would also like to extend my gratitude to everyone who helped me in the lab. I would like to thank Vince Chaijaroen, the lab manager, for his support during the year I was working in the lab. His knowledge and experience was a valuable resource, and he not only taught me everything I needed to know about working in the lab, but made it a fun and enjoyable place to work during a difficult year. I would also like to thank Joe Kaldestad for joining this project and providing indispensable support throughout the construction and testing phases of this project. Without his tireless effort and knack for solving problems it would not have been possible to complete this project. I would also like to thank fellow grad students Spencer Lindsley, Austin Anderson, Michelle Chang, Danielle Voytko, and Kristinn Hlíðar for their help during my time working in the lab. I am incredibly grateful to Doug Lindblad for welding all of my specimens and for being available on short notice. Thank you to all of my friends and classmates at UW that made my time as a grad student more enjoyable.

Thank you to the American Institute of Steel Construction, the Steel Tube Institute, Atlas Tube, Nucor Tubular Products, Searing Industries, and Maruichi American Corporation for providing funding, materials, and support for this project.

Most importantly, I would like to thank my family and friends for their love, support, and encouragement from across the country.

Chapter 1. INTRODUCTION

1.1 BACKGROUND

HSS members are commonly used as bracing members in braced frame systems, such as concentrically braced frames (CBFs), which form vertical trusses to provide increased stiffness and resist lateral loads. In areas of high seismicity, special concentrically braced frames (SCBFs) are often used as seismic force resisting systems. SCBFs are designed to exhibit stable and ductile behavior to maximize drift capacity when subjected to severe seismic loading. ASTM A500 hollow structural sections (HSS) have been used as braces in CBFs since the 1970s. The ASTM A1085 specification, released in 2013, provides an alternative to the conventional ASTM A500 specification for HSS used in steel structures. The A1085 specification presents a number of potential benefits over the A500 specification, including more stringent control over material and geometric properties of the sections. These tighter tolerances allow for more economical and efficient designs using A1085 HSS. Previous research at the University of Washington on SCBFs has indicated that braced frames using A1085 HSS braces may exhibit greater ductility than those using A500 HSS braces. However, systematic experimental testing of A1085 HSS members is required to fully characterize their inelastic response and seismic performance.

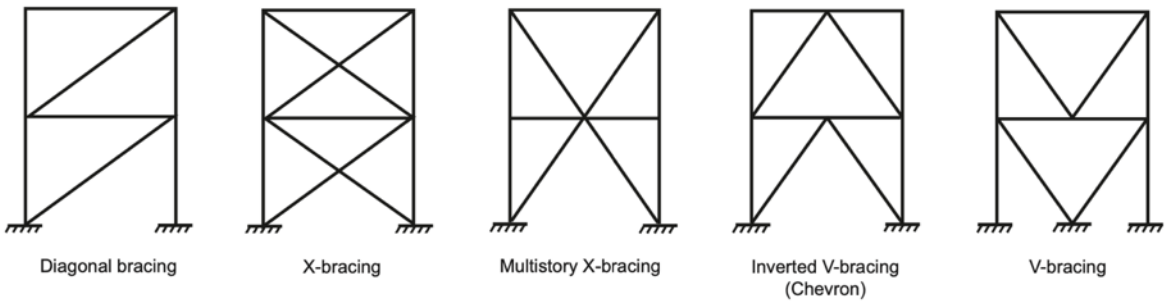

Figure 1.1. Concentrically Braced Frame Configurations (Sabelli et al., 2013)

SCBFs are designed to withstand significant inelastic deformations primarily through the buckling and yielding of the diagonal brace members, and are often used in low-rise buildings in areas of high seismic demand. (Sabelli et al., 2013) When subjected to seismic loading, the braces in SCBFs are designed to dissipate energy through inelastic buckling and yielding. As the

braces buckle under compressive displacements, local deformations develop at the center of the brace. Under increased displacements, this damage becomes more severe and eventually leads to brace fracture. This results in a significant loss of strength and stiffness to the braced frame system, leaving the structure vulnerable to collapse.

Brace fracture typically occurs in tension shortly after the initiation of local deformations at the plastic hinge region of the brace. Therefore, delays in the development of these deformations are associated with increased brace fracture life and deformability. The deformability of HSS braces has been shown to depend significantly on the local compactness ratio (b/t) and global slenderness ratio (KL/r) of the brace. The local compactness and global slenderness ratios of bracing members have an effect on the initiation and severity of damage to the center of the brace. Generally, more locally compact and globally slender braces exhibit greater deformability prior to brace fracture. However, less globally slender braces are able to resist greater compressive forces and dissipate more energy in compression, but are also more susceptible to early brace fracture.

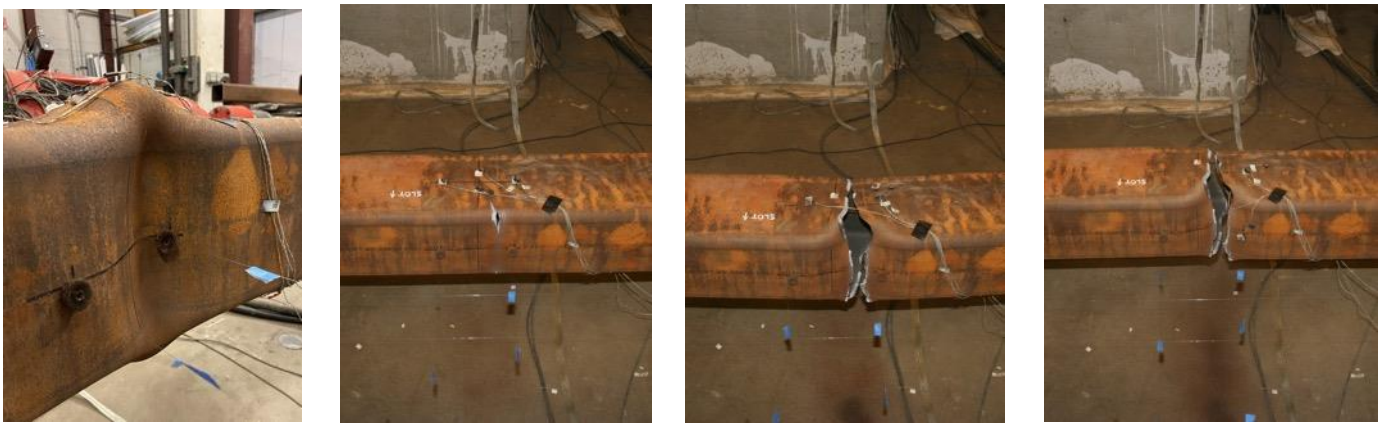

Figure 1.2. Progression of Brace Deformation and Damage at Center

SCBFs have become less frequently used in regions of high seismicity, where buckling-restrained braced frames (BRBFs) and special moment resisting frames (SMRFs) are becoming more common. To some extent, this is a result of the local slenderness requirements for A500 HSS braces and the relatively large yield overstrength factor, R_y, associated with A500 HSS members. These factors reduce the efficiency of SCBFs using A500 HSS braces. However, increased ductility in SCBFs using A1085 HSS braces would make SCBFs a more competitive

choice in regions of high seismicity. Several other advantages associated with the tighter material and geometric tolerances of A1085 HSS are shown in the tables below. Larger A1085 HSS members meet the AISC 341 local compactness limits for highly and moderately ductile members, as shown below in Table 1.1. The current highly ductile b/t limits for A500 braces restrict the maximum HSS size to 10x10x3/8, while highly ductile A1085 members up to 14x14 are permitted. Using larger braces in braced frames makes it possible to reduce the number of braced bays in a structure, which can be beneficial from a financial and architectural perspective.

Table 1.1. Width-to-thickness limits for HSS with different steels

HSS Steel	F_y **(ksi)**	R_y	**AISC 341-16 *b/t* Limits**	
			Moderately Ductile $(0.76\sqrt{E/R_yF_y})$	**Highly Ductile** $(0.65\sqrt{E/R_yF_y})$
A500 Gr. B	46	1.4	16.1	13.8
A500 Gr. C	50	1.3	16.1	13.7
A1085	50	1.25	16.4	14.0

Table 1.2 provides a summary of the material and geometric requirements for the ASTM A1085 and A500 specifications. The A1085 specification provides tighter control over the wall thickness of HSS members. A 10% tolerance in wall thickness is permitted by the A500 standard, allowing steel tube manufacturers to produce A500 HSS with walls significantly thinner than the nominal thickness. This is reflected in the 7% reduction in the nominal wall thickness used in calculations involving A500 HSS. (AISC, 2010) However, the A1085 standard significantly reduces this tolerance, allowing only a 5% tolerance in wall thickness. Therefore, the 7% reduction is not required when designing structures with A1085 HSS members, which improves the efficiency of designs.

The ASTM A1085 specification also establishes a maximum yield stress of 70 ksi for HSS members, while the A500 specification provides only a minimum value for yield stress. Therefore, the allowable variation in the strength of A1085 HSS members is reduced, which allows for more efficient designs. Additionally, the A1085 specification requires tighter control

over the corner radius of HSS members. The A1085 specification maintains the same upper limit on corner radius, but also introduces a minimum corner radius for rectangular HSS members. By introducing a minimum corner radius, the A1085 specification is designed to prevent HSS members from being produced with excessively tight corners, which can cause cracking. A minimum toughness criteria is also introduced for HSS members in the A1085 specification, which requires a Charpy V-Notch test value of 25 ft-lbs at 40° F. The effects of these geometric and material requirements on specimen performance will be analyzed in this thesis.

Table 1.2. Comparison of Geometric and Material Requirements

Property	**ASTM A500 Gr. B**	**ASTM A500 Gr. C**	**ASTM A1085**
Yield Stress	46 ksi (min)	50 ksi (min)	50 ksi (min) 70 ksi (max)
Yield Strength Ratio	1.4	1.3	1.25
Tensile Stress	58 ksi (min)	62 ksi (min)	65 ksi (min)
Wall Thickness Limits	-10%	-10%	-5%
Mass Tolerance	N/A	N/A	-3.5%
Corner Radii	$r < 3t$	$r < 3t$	$t < 0.4$" : $1.6t < r < 3t$ $t > 0.4$" : $1.8t < r < 3t$
CVN Toughness	N/A	N/A	25 lb-ft at 40° F

This thesis will examine the differences between A500 and A1085 HSS members through a series of experiments conducted using a large scale test frame at the University of Washington Structural Research Lab (UW SRL). This test frame was designed and built at the UW SRL, and has a capacity of 1000 kips in tension and 700 kips in compression. The test frame can accommodate various size HSS specimens, and is capable of applying displacement of ±10 inches to test members. A variety of square HSS sections were studied through full scale experiments as well as material testing at the UW SRL. HSS members with a wide range of b/t and KL/r ratios were selected for testing, since it has been shown that the ductility of HSS members is strongly related to these factors. The HSS selected for component testing include

members both meeting and exceeding the current b/t limits, and were provided by several different steel producers. This research is necessary to evaluate the inelastic cyclic response of A1085 and A500 HSS members. The structural response, geometric properties, and material properties of the A1085 and A500 HSS members from different producers will be analyzed in this thesis. The behavior and performance of A1085 and A500 HSS members under cyclic loads must be systematically investigated and compared to characterize any potential advantages of using A1085 HSS braces in lateral force resisting systems.

Figure 1.3. View of Test Frame During Testing

1.2 RESEARCH OBJECTIVES

The goals of this research project are to compare the engineering performance of A500 and A1085 HSS through an experimental testing program. The research objectives described in this thesis are as follows:

- Compare the structural response of A500 and A1085 HSS subjected to cyclic loading through component testing

- Investigate the effects of local slenderness and global slenderness on brace behavior
- Examine the material and geometric properties of A500 and A1085 HSS through material testing and evaluation of tube sections
- Evaluate the performance-based engineering tools used to model the inelastic response of HSS braces

1.3 DOCUMENT OVERVIEW

To address the objectives and goals of this research project in a clear and organized manner, this document is broken up into an additional six chapters.

Chapter 2 includes background information for this project, including a discussion of the A1085 specification and requirements for SCBFs. This chapter also includes a review of literature describing the previous experimental research on the inelastic response of steel HSS under cyclic loading.

Chapter 3 describes the design of the test frame used in this research project, and also provides a thorough description of the specimens tested in this experimental program. Additionally, the instrumentation and testing procedure is presented in this chapter.

In Chapter 4, results and observations from the tests are discussed. The performance and behavior of the test specimens are described in this chapter based on the observations and quantitative data collected during the tests.

Chapter 5 describes the processing and analysis of the data collected during testing. In this chapter, test specimen performance is analyzed and compared between the A1085 and A500 HSS. The effects of local slenderness, global slenderness, steel type, and steel producer are evaluated.

Chapter 6 presents an evaluation of the performance-based engineering tools used in practice to model the inelastic behavior and capacity of HSS braces in braced frames.

Chapter 7 summarizes the objectives and results of the research project, and presents conclusions as well as recommendations for future work.

Chapter 2. LITERATURE REVIEW

2.1 INTRODUCTION

In this chapter, background context and justification for this project is presented through a review of previous research. Section 2.2 discusses the design requirements for braces used in SCBFs, as well as the evolution of these requirements over the past several decades.

The experimental setup, results, and conclusions of previous research projects studying the behavior and performance of HSS members are described in Section 2.3. The test setup used in this research project was heavily influenced by the experimental designs of these previous projects. Additionally, the methods used to compare the performance of different HSS members are discussed in this section. Several of these techniques were used in this project to evaluate the differences in brace behavior between the A500 and A1085 HSS members. This previous research demonstrates the need for the systematic testing program of A500 and A1085 tubes presented in this thesis.

2.2 DESIGN REQUIREMENTS FOR BRACES IN SCBFS

Bracing members in modern SCBFs are designed to provide adequate inelastic deformation capacity during seismic events. The intent of current design requirements for braces in SCBFs is to ensure that the braces are capable of withstanding buckling in compression and yielding in tension such that significant story deformations can be achieved prior to brace fracture. This allows for stable inelastic behavior under large seismic loads, where the braces are designed as fuses in the system. In this capacity-based design approach, damage due to cyclic seismic loading is concentrated in the brace rather than other components such as beams, columns, and connections. These other members are designed based on the expected tensile and compressive forces that may develop in the brace, ensuring that the structure remains stable as seismic loads are applied. By designing braces to withstand significant inelastic buckling and yielding demands, the braces effectively dissipate seismic energy and help ensure ductile

behavior in SCBFs when combined with framing members and end connections designed based on the expected brace capacity.

Prior to the introduction of the capacity-based design approach in the 1988 Uniform Building Code, braced frame components were designed to resist the expected seismic loads (ICBO, 1988). Braced frames designed following this approach are expected to be more susceptible to damage during seismic events. This approach does not ensure ductile behavior in braced frames, which can result in the premature failure of structural members. The connections, beams, and columns were not designed based on the expected strength of the brace, which could result in unpredictable failure modes of these members prior to the buckling and yielding of the brace. If these components fail before the brace is able to dissipate energy through inelastic deformation, the seismic-force-resisting system can be especially vulnerable in seismically active areas. Additionally, there were no design requirements for the compactness or slenderness of the brace, or any rotation and clearance requirements for the end connections of braces. Table 2.1 below shows the evolution of brace and end connection requirements in braced frames over the past several decades.

Table 2.1 Brace Requirements in Braced Frames (Hsiao, 2012)

Component	**Non-Seismic CBFs** (R = 3)	**OCBFs** (R = 3.25)	**Current SCBFs** (R = 6)
Brace Global Slenderness	No limit	$KL/r < 4\sqrt{E/F_Y} \approx 100$	KL/r < 200
Brace Local Slenderness	No limit	Compactness ratio < λ_{md}	Compactness ratio < λ_{hd}
Net Section	Design for factored loads	Design for factored loads	Design for $R_yF_yA_g$ of brace
Brace Connection Design	Design for factored loads	Design for minimum of $R_yF_yA_g$ of brace or amplified seismic load	Design for $R_yF_yA_g$ and $1.1R_yP_n$ of brace & permit end rotation of brace

Design requirements for braced frames in seismic regions were introduced to ensure that these systems would perform in a ductile manner when subjected to earthquake loads. In modern SCBFs, there are a number of requirements for braces that are intended to produce ductile

behavior. As discussed in Chapter 1, the seismic performance of braces largely depends on brace local compactness and global slenderness. The connections and surrounding framing members must be capable of developing the expected brace forces to generate ductile frame behavior. Experimental research on steel bracing members subjected to inelastic cyclic loads has shown that local buckling deformations and brace fracture occur at lower drift demands in less compact braces, and the severity of these local deformations is inversely proportional to the slenderness ratio (Gugerli, 1982). These early studies indicated a need for the introduction of compactness criteria in bracing members to prevent premature fracture and ensure that braced frames perform effectively under seismic loading.

The current brace compactness limits shown in Table 1.1. were developed based on research showing that braces exceeding these limits are unlikely to sustain the drifts imposed during large earthquakes (Fell et al., 2009). The limits for highly and moderately ductile members are based on the expected yield stress, R_yF_y , of the member. Both A500 and A1085 HSS have a nominal yield strength of 50 ksi. Since the value for R_y in the A1085 HSS specification is lower than that of A500 HSS (1.25 instead of 1.3), the b/t limits for seismically compact sections are effectively higher for A1085 HSS.

The increased cross-sectional compactness limits for A1085 HSS, combined with the tighter wall thickness tolerance, allows for larger and less compact A1085 HSS members to be used in SCBFs. In this experimental program, the 6x6x3/8 and 8x8x1/2 A1085 test specimens meet the AISC width-to-thickness criteria for highly ductile members, while the A500 specimens of the same size only meet the requirements for moderately ductile members. Additionally, the 6x6x5/16 and 7x7x3/8 A1085 test specimens meet the requirements for moderately ductile members, while the A500 sections of the same size are not categorized as moderately ductile members. The largest A500 section that meets the AISC requirements for highly ductile members is the 10x10x5/8 section, while A1085 HSS up to 14x14x7/8 meet the criteria for highly ductile members. Using larger braces in SCBFs can reduce the number of braced bays required in structures, which can reduce costs and enhance the architectural characteristics.

A brace global slenderness limit of 200 is also required by the current AISC Seismic Provisions. Although the brace inelastic deformation capacity generally increases with greater brace slenderness, this limit is intended to prevent unwanted dynamic effects that are associated with very slender braces (AISC, 2016). Additionally, the compressive load capacity is

significantly reduced in very slender braces. SCBFs are often designed such that the lateral load is distributed between the tensile and compressive braces, which is not possible when very slender braces are used.

Current SCBFs are typically designed to allow for rotations at the brace end connections as the bracing member buckles laterally under compressive loads. The brace end connections are permitted to be designed as fully restrained moment connections, with the connections designed based on the expected strength of the connected beam or column. (AISC, 2016) In practice, most braces in SCBFs are designed to allow for rotation at their end connections. The gusset plates connecting the brace to the framing members must be capable of forming plastic hinges to allow for this rotation. As mentioned above, the end connections, along with the beams and columns, are now required to be designed based on the tensile and compressive strength of the brace, rather than the expected seismic forces. The introduction of these detailing requirements increases the inelastic deformation capacity of SCBFs, improving their performance as a seismic-force-resisting system.

2.3 Cyclic Testing and Behavior of Steel Bracing Members

2.3.1 *Effect of Beam Yielding on Chevron Braced Frames (Roeder et al., 2019)*

In this experimental program, six single-story chevron braced frames were tested at the UW SRL to investigate the effect of beam strength on the seismic performance of braced frames. The goal of this research was to study the effects of reducing the strength of beams in SCBFs on the ductility and behavior when subjected to seismic loading. Finite element models were developed to further investigate the effects of beam yielding on seismic performance, which were validated based on the experimental results of this research project. In all six chevron braced frames tested in this project, a pair of 4x4x5/16 HSS were used as bracing members. These braces met the AISC width-to-thickness limits for highly ductile members, and had a length of about 143”. The geometry of the chevron braced frame test specimens are shown below in Figure 2.1, along with the layout of the test frame. The specimens were subjected to an identical, symmetric loading protocol with increasing cyclic displacements. Although the focus

of this project was on the effect of the yielding beam on seismic performance, this review will focus on the bracing members used in the experiments. In five of the frames tested, the braces were A1085 HSS, and only one specimen used A500 HSS braces. A500 HSS braces were used in Chevron 5, which had an identical configuration to Chevron 3, except for the type of steel used in the bracing members. This makes it possible to evaluate the effects of steel type on the performance of the braced frame. The Chevron 3 and Chevron 5 test specimens both used W14x38 beams, which had a strength of about 35% of the AISC 2016 requirements for SCBFs.

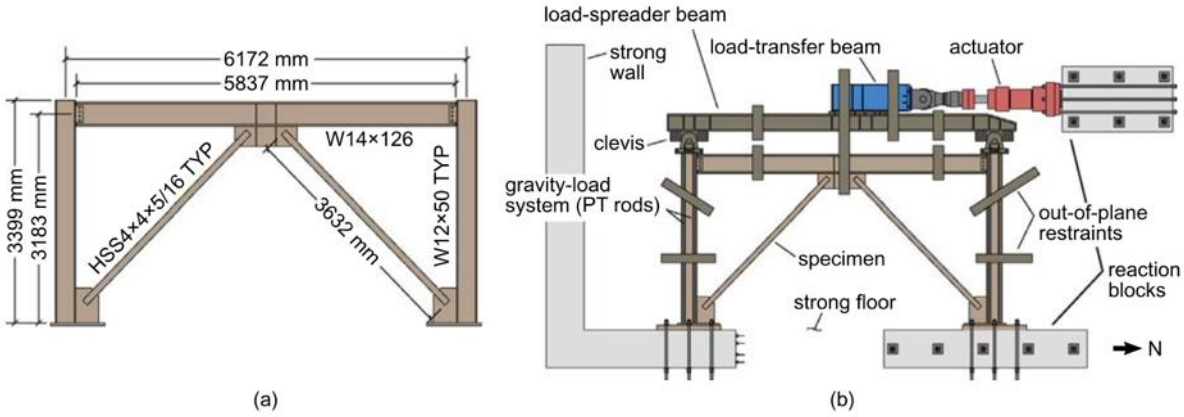

Figure 2.1. Chevron Braced Frame Geometry (a) and Test Frame Layout (b)

Findings

This experimental program indicated that chevron braced frames with yielding beams achieved greater story drifts prior to brace fracture than braced frames without yielding beams. Increased drift capacity was observed in braced frames with greater beam yielding, suggesting that the AISC requirements for the strength of beams in SCBFs were excessively high. Additionally, the downward deflection of beams in chevron configurations results in an increase in compressive brace deformation, but reduced the tensile deformations. This has been shown to increase the drift capacity of chevron SCBFs compared with other braced frame configurations.

The findings most relevant to this thesis were related to the performance of Chevron 3 (using A1085 HSS braces) and Chevron 5 (using A500 HSS braces). These braced frames were identical aside from the type of steel used in the bracing members, and were subjected to the same cyclic displacement protocol. The hysteretic behavior of these braced frames are shown below in Figure 2.2. Chevron 3, with A1085 HSS braces, reached a maximum drift range of

7.2% prior to brace fracture. Both the north and south braces fractured during the ±3.6% drift cycles, and reached an out-of-plane buckling deflection of 19.6". Chevron 5, with A500 HSS braces, achieved a drift range of 6.6% prior to brace fracture. The north brace fractured at a story drift of -3.0%, while the south brace fractured at +3.6% drift. Therefore, the braced frame with A1085 HSS braces reached a drift range about 9% greater than that of the braced frame with A500 HSS, indicating a modest increase in deformability associated with the A1085 HSS braces. Both braced frames reached similar levels of lateral resistance, showing no significant difference in strength associated with the different brace types.

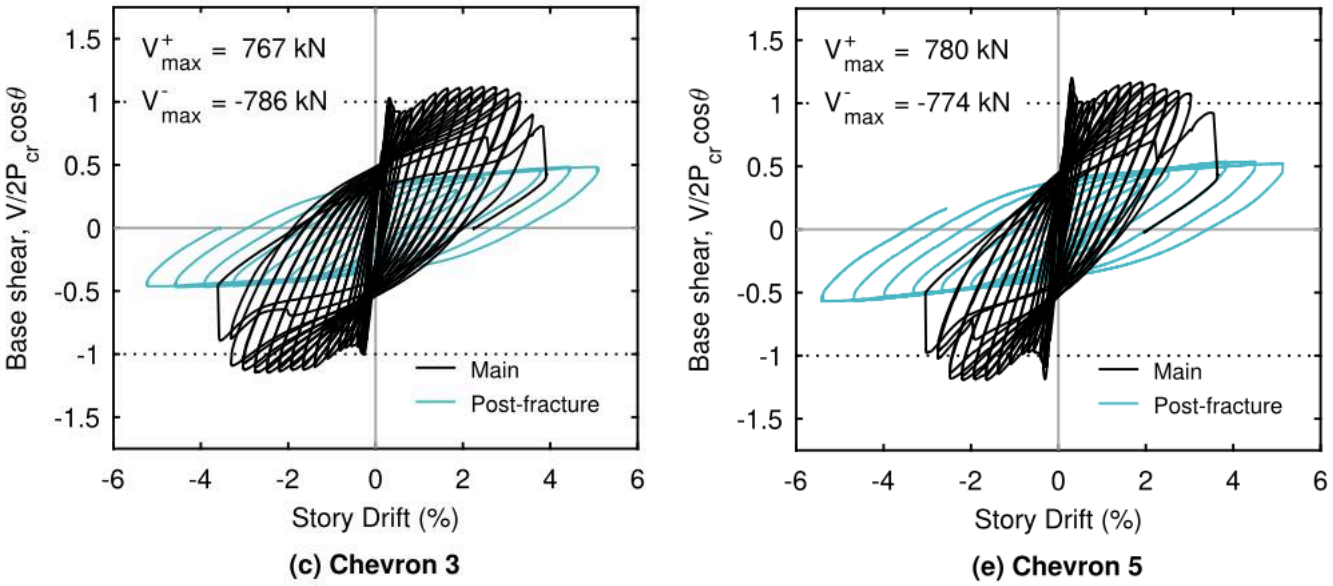

Figure 2.2. Hysteretic Behavior of Chevron 3 (A1085) and Chevron 5 (A500)

Commentary

The increase in deformability exhibited by the braced frame using A1085 HSS braces provided motivation for the experimental program presented in this thesis. Relatively few tests on A1085 HSS have been performed in previous research projects, making it necessary to examine and compare the behavior of A500 and A1085 HSS through component testing. Although the results of this project indicate a relationship between the steel type of bracing members and deformation capacity, only one pair of similar braced frames with bracing members using different types of steel was tested in this experimental program. Thus, it is

difficult to draw any conclusions regarding the effect of steel type on the deformation capacity of HSS braces.

Most full-scale component tests of square HSS members predate the introduction of the ASTM A1085 specification in 2013. Therefore, there is a significant lack of data regarding the performance of A1085 HSS members. In a separate research project, A1085 HSS members were used in the testing of two full-scale, two-story concentrically braced frames. (Bradley et al., 2017) These tests were performed to investigate and compare the cyclic performance of an ordinary concentrically braced frame (OCBF) and a concentrically braced frame designed without seismic detailing. However, it is difficult to compare the performance of these A1085 braces to A500 braces tested in previous research, since brace performance has been shown to depend significantly on displacement protocol. Additionally, 5x5x3/8 A1085 HSS were used as bracing members in the testing of a three-story chevron SCBF tested at the National Center for Research on Earthquake Engineering (NCREE) Laboratory in Taipei, Taiwan. (Roeder et al., 2020) Again, it is difficult to evaluate the performance of the A1085 braces used in this experiment due to the effects of displacement protocol and brace configuration on specimen performance. Therefore, the experimental program described in this thesis is intended to provide additional data regarding the seismic performance of A1085 HSS relative to A500 HSS.

2.3.2 *Inelastic Seismic Response of Steel Bracing Members (Tremblay, 2002)*

This paper presents a review of previous experimental research on the behavior of steel bracing members subjected to seismic loading. The aim of this study was to gain a better understanding of the inelastic response of bracing members, and to create equations to model the seismic performance of such members. The results of these previous studies are used to develop recommendations for appropriate design values for the actual buckling strength, maximum tensile force, and reduced post-buckling compressive capacity of steel bracing members. Additionally, data from previous tests was used to examine the lateral deformation and fracture life of rectangular HSS members, and an equation was developed to predict the ductility of these braces. This paper describes the general behavior of steel components under increasing applied cyclic displacements.

Seventy-six (76) test specimens, including 38 rectangular HSS (RHS) from 9 separate experimental programs are included in this study. All of the ASTM A500 RHS members discussed in this study were tested as part of experimental programs at the University of Michigan. (Gugerli, 1982; Lee, 1988; Liu, 1987) In all of these tests, the displacement protocols were compression dominated to represent the expected demands on braces in chevron braced frame configurations. These specimens represent a fairly comprehensive review of steel bracing members and include components with various cross-sectional shapes and lengths, a wide range of compactness and slenderness ratios, and different applied loading histories. These early tests on A500 RHS components were critical for understanding the behavior of RHS members subjected to cyclic inelastic displacements. The focus of this review will be on the RHS members included in this study.

Findings

In the 38 RHS members included in this study, brace fracture occurred following the development of local deformation at the mid-span of the brace. High strains developed at the plastic hinge location when the brace was in compression, and cracks first developed in the corners of the member due to the effects of cold-working reducing the fracture strain of the corners. These cracks propagated through the cross section once the specimens were loaded in tension, which eventually leads to fracture. It was found that the development of local buckling behavior was influenced by the compactness of the cross section to a large extent, and also by the global slenderness and applied loading history. Generally, braces with a low width-to-thickness ratio exhibited greater ductility, although in less slender members the local buckling was more severe despite the greater compactness of the cross section. This was a result of the increased compressive strains that developed in the plastic hinge regions of less slender members.

The damage level at the point of brace fracture was determined based on the accumulated damage in the test specimen, which was then related to the brace compactness and slenderness. However, the actual amount of inelastic strain prior to fracture was difficult to determine and led to poor correlation. A simpler approach based on the total ductility at the point of brace fracture was implemented, which was related to the global slenderness ratio of the test specimen. This

approach yielded better results and may be more useful for design purposes, since it depends only on the maximum expected ductility rather than the expected seismic loading history. Figure 2.3 below shows the results of the 38 RHS members included in this study. The study indicated that a symmetrical loading history may be less critical for brace fracture than a compression dominated history, although the sample size in the study was relatively small. This figure also shows that the width-to-thickness ratio limits are more critical for less slender braces, and that minimum global slenderness requirements could lead to improved ductility. However, the braces with large b/t ratios were generally less slender, and more research is required to determine the behavior of thin-walled slender sections and thick-walled non-slender sections. A simple equation to predict the peak ductility of RHS bracing was proposed based on the results of this review, where a = 2.4 and b = 8.3:

$$\mu_f = a + \lambda b$$

In this equation, and in Figure 2.3 below, the slenderness parameter λ is defined as follows:

$$\lambda = \frac{KL}{r}\sqrt{\frac{F_y}{\pi^2 \, \mathrm{E}}}$$

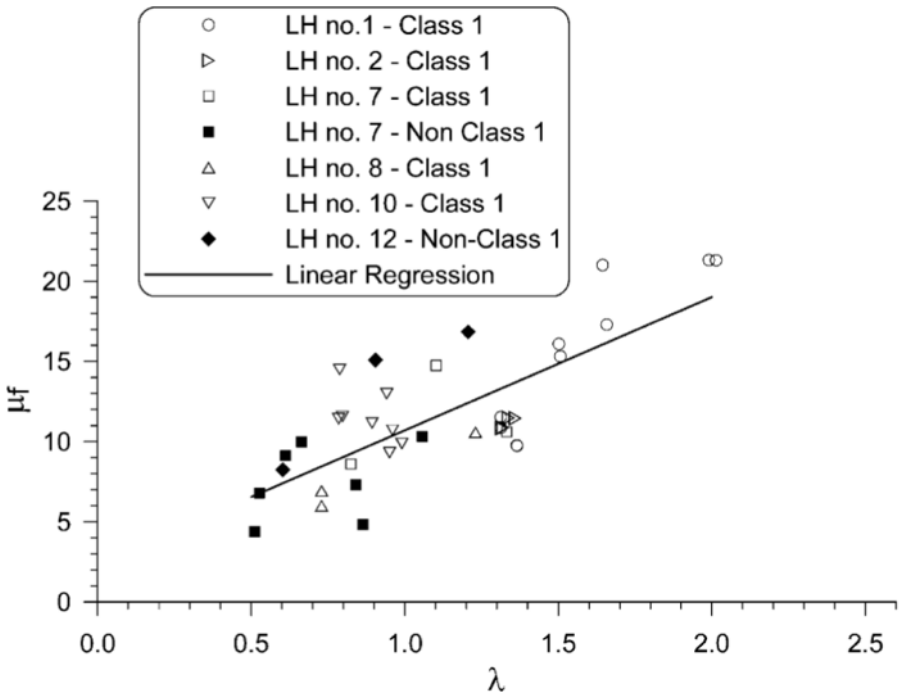

Figure 2.3. Peak Ductility at Fracture for RHS Bracing Members

Commentary

This paper presents a fairly comprehensive review of the behavior of A500 RHS members subjected to inelastic cyclic displacements. The proposed equations to model the behavior and performance of steel braces in braced frames may be useful in practice, but are not especially relevant to this project. However, the examination of the deformation capacity and fracture life of RHS bracing members presents interesting findings that relate to this thesis. The observation that the fracture life of bracing members is largely dependent on brace slenderness and, to a lesser extent, brace compactness suggests that current design requirements based on brace compactness may not be sufficient to ensure adequate deformation capacity in stocky, cross-sectionally compact braces. Additionally, the suggestion that brace width-to-thickness limits should be more stringent for less slender members, and that a minimum slenderness requirement should be specified are noteworthy but require additional research. Globally slender braces with thin walls, as well as thick-walled non-slender braces must be tested to fully characterize the behavior of such sections. This review did not include an analysis of the energy dissipation capacity of steel bracing members, which may have provided greater insight into the relationships between brace compactness and slenderness as they relate to seismic performance.

As discussed above, many A500 RHS components have been tested in various experimental programs over the past several decades. The seismic performance of such specimens has been characterized based on the results of these tests. However, there is a serious lack of data available regarding the inelastic response of A1085 RHS members. The experimental program described in this thesis is intended to provide a comparison of A500 and A1085 sections across a wide range of b/t and KL/r ratios. This testing is necessary to evaluate differences in seismic performance and behavior between the different types of steel.

2.3.3 *Behaviour of Square Hollow Structural Steel Braces with End Connections Under Reversed Cyclic Axial Loading (Shaback and Brown, 2003)*

A series of nine square HSS members were tested at the M.A. Ward Civil Engineering Laboratories at the University of Calgary. The hysteretic behavior of the sections was analyzed to increase the amount of data available on the behavior of these members. Parameters such as brace slenderness, compactness, and end connection type were evaluated in these tests to determine their effects on the ductility and seismic performance of square HSS members. The hysteretic behavior, out-of-plane deflections, compressive capacity degradation, energy dissipation, and fracture life of these specimens were studied in this paper. All 9 of the specimens were designed to meet slenderness and width-to-thickness requirements at the time of testing. The global slenderness ratios ranged from about 52 to 66, while the width-to-thickness ratios ranged from 8.9 to 15.1. The braces were tested in a test rig using two hydraulic actuators in parallel. The test setup described in Chapter 3 used at the UW SRL is comparable to the test frame shown below. Quasi-static cycles of reversing axial loads were applied to the specimens, with the displacement amplitudes increasing throughout the test. However, the loading sequence was not symmetric and the braces were subjected to greater compressive than tensile axial displacements in later cycles.

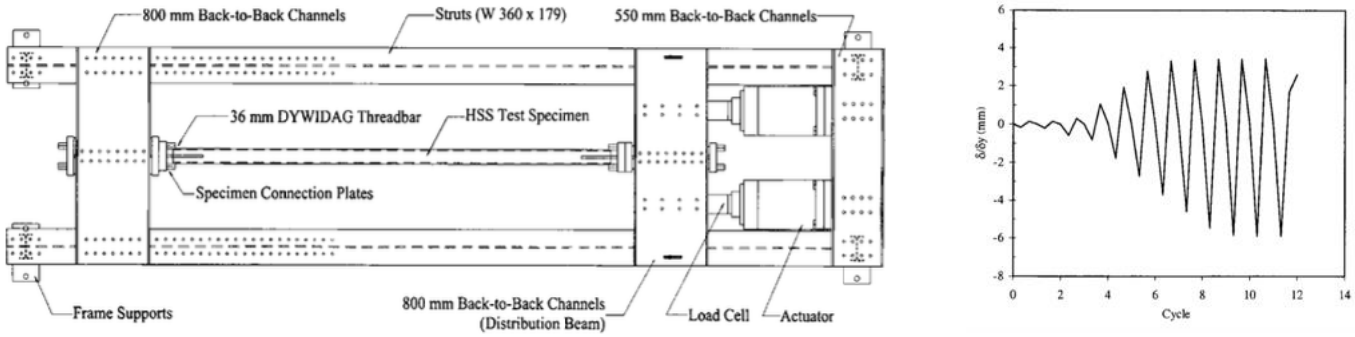

Figure 2.4. Test Frame and Loading Sequence

Findings

The initial compressive resistance and compressive strength degradation behavior of the 9 HSS members was compared to the suggested values from CAN/CSA-S16-01 and AISC. It

was found that the experimental results for initial compressive strength were consistent with the predicted values, but the predicted values for strength degradation were non-conservative. The compressive capacity of the specimens continued to decrease under larger compressive displacements, which may have been caused by the non-symmetric loading sequence. In the later, inelastic cycles of the loading protocol used in this experimental program, shown in Figure 2.4 above, the applied tensile displacements remained relatively constant while the compressive displacements continued to increase. This compression biased loading protocol is representative of the axial brace displacements in chevron configured braced frames with yielding beams. As a result of the applied displacement protocol, the braces did not fully straighten in tension before being put into compression. This initial lateral displacement, or eccentricity, in the brace resulted in a reduced compressive capacity during later cycles.

As discussed previously, the actual loading histories can have a significant impact on the deformation capacity of steel HSS members. All of the specimens in this program were subjected to similar displacement protocols, but it is not clear what affect the applied displacement history had on the deformation capacity of the braces. Brace ductility and resistance to early fracture were evaluated and were compared to several models used to predict brace fracture. The equations used in these models include parameters such as the effective slenderness ratio, width-to-thickness ratio, breadth to depth ratio, and yield strength. These equations are shown below, along with a plot showing a comparison of the predicted and experimental results.

$$\Delta_f = C_s \frac{(350/F_y)^{-3.5}}{[(b-2t)/t]^{1.2}} \left(\frac{4(b/d)-0.5}{5}\right)^{0.55} (70)^2 \quad \text{for } \frac{KL}{r} < 70$$

$$\Delta_f = C_s \frac{(350/F_y)^{-3.5}}{[(b-2t)/t]^{1.2}} \left(\frac{4(b/d)-0.5}{5}\right)^{0.55} \left(\frac{KL}{r}\right)^2 \quad \text{for } \frac{KL}{r} \geq 70$$

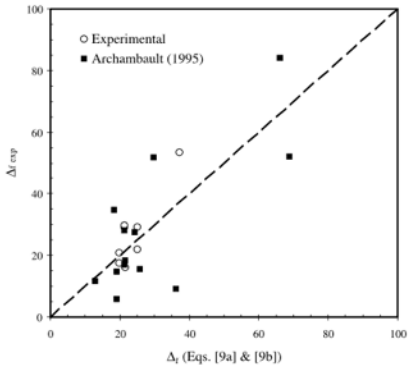

Figure 2.5. Predicted and Experimental Fracture Life

The hysteretic behavior of the test specimens was used to determine the energy dissipation capacity of the square HSS members. The force-displacement behavior shows that

stockier members perform better in compression and are capable of dissipating more energy, shown by the fuller hysteretic loops compared to the more slender members. Less stiffness degradation was also observed in members with smaller slenderness ratios. Additionally, the data shows that members with lower b/t ratios exhibit local buckling behavior at larger displacements. As a result of the delay in damage to the brace, the more cross-sectionally compact specimens survived more displacement cycles and fractured at larger displacements. The width-to-thickness ratio was found to have the greatest effect on the fracture life of square HSS members, although global slenderness and yield strength were also observed to have an effect on brace deformation capacity. The energy-dissipation capacity of the test specimens is shown below in Figure 2.6, which shows that in general, less-slender specimens exhibit more efficient energy dissipation behavior. These specimens had greater compressive strength than the more globally slender specimens, and thus were able to dissipate more energy in compression. It was found that global slenderness has the greatest influence on energy dissipation efficiency, rather than brace compactness, since the b/t ratio has a lesser effect on the hysteretic behavior of the specimen. However, the figure below also shows that more globally slender test specimens fractured at later cycles than the stockier members. Although more globally slender specimens dissipate energy less efficiently, their overall energy dissipation capacity may exceed that of the stockier specimens due to their increased deformation capacity.

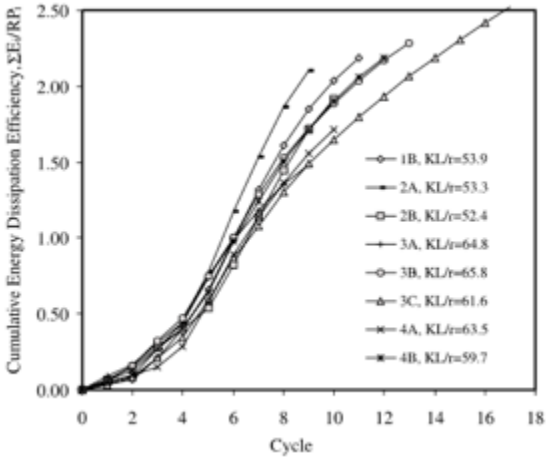

Figure 2.6. Comparison of Energy Dissipation Capacity

Commentary

The compressive strength degradation behavior observed in the 9 test specimens is likely caused by the non-symmetrical loading protocol, resulting in an initial out-of-straightness that led to a significant reduction in compressive strength. Additionally, although more refined equations to predict the fracture life of square HSS members are presented in this paper, the equations are still only somewhat accurate. These equations were fit to this set of data, and the mean value for the ratio of predicted to experimental fracture life is 1.0, with a 0.36 standard deviation. Compared with previous, similar models of the deformation capacity of braces, the proposed equations result in a 50% reduction in standard deviation. However, this amount of variation between the measured and predicted behavior indicates that some of the factors that affect fracture life are not fully captured by these equations. This test program included only 9 HSS components, and additional testing could prove to be useful in establishing a clearer link between brace fracture life and hysteretic behavior and factors such as brace compactness, slenderness, and material properties. All of the square HSS were selected to meet the requirements for bracing members in braced frames, which limited the range of slenderness and compactness ratios of the test specimens. Additionally, compression biased displacement protocols were applied to all specimens, which may have affected the measured fracture life. Alternative displacement protocols should be study to analyze their impact on brace deformation capacity. Testing of specimens with properties that do not meet the required values could provide additional information showing the relationship between brace compactness and slenderness and the seismic behavior of square HSS members.

2.3.4 *Inelastic Cyclic Testing of Large Size Steel Bracing Members (Tremblay, 2008)*

The behavior of 34 steel bracing members subjected to quasi-static cyclic loading was studied in this project, which was carried out at the Hydro-Quebec Structural Engineering Lab at Ecole Polytechnique of Montreal. The test specimens included square HSS, circular tubing, and W shape members, although only the tests on the square HSS are relevant to this thesis. Prior to the test series presented in this paper, most tests on HSS braces were performed on sections

smaller than those commonly used in practice. Therefore, this experimental program sought to generate data for large bracing members to develop a better understanding of the effects of brace slenderness and cross-sectional compactness on the fracture life of HSS bracing members used in practice. These larger sections were less slender and may be more susceptible to premature fracture under seismic loads. A total of 19 ASTM A500 RHS braces were tested, and the test specimens included members with width-to-thickness ratios less than, equal to, and greater than the limits required by design codes for ductile members. Additionally, these specimens were designed with slenderness ratios between 40 and 60, which is representative of stocky members used in design that may be susceptible to premature fracture.

In this experimental program, the test specimen geometry was based on a brace in an X-bracing configuration at an angle of 35°. This assumed braced frame geometry was used to develop the displacement protocol, but HSS components rather than full story frames were tested in this study. The displacement history was developed based on this assumed brace configuration and consists of two symmetric sequences. The displacement protocol and assumed braced frame geometry are shown in Figure 2.7. In the first sequence, the displacements were based on the seismic demand associated with the 2% in 50 years seismic hazard level in Vancouver, BC. Next, two smaller cycles were followed by cycles of increasing amplitude that represent the seismic demands associated with large earthquakes in areas of high seismicity. End connections designed to result in both in-plane and out-of-plane buckling were used in this test series. The individual brace components were tested in a 12 MN vertical load frame.

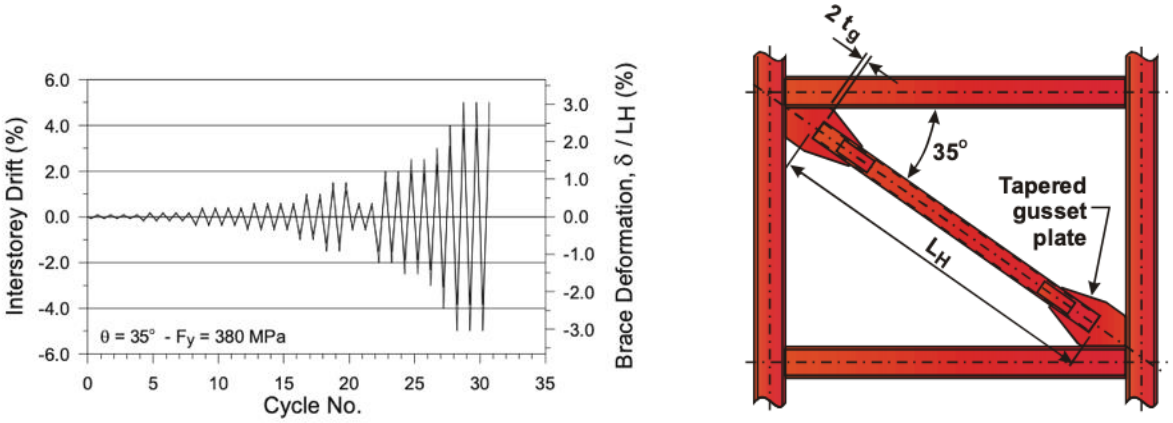

Figure 2.7. Loading Protocol and Assumed Brace Geometry

Findings

As observed in previous research, the bracing members subjected to cyclic displacements of increasing amplitude experienced several cycles of yielding in tension and global buckling in compression prior to the development of local deformations at the mid-span plastic hinge. This resulted in increased local strains at the center of the specimen leading to the fracture of the brace in tension. One of the RHS members (RHS 4) that was tested barely complied with CSA-S16 compactness limits and had a slenderness ratio of 40, but fractured at an interstory drift of only 1.0%. A similar member (RHS 2) had a similar slenderness ratio to RHS 4, but the wall thickness was slightly greater resulting in a b/t ratio of about 75% of the code limit. This specimen fractured at an interstory drift of 1.5%. Another specimen, RHS 19, was designed with the same reduced compactness ratio as RHS 2, but a global slenderness ratio of 60, and fractured at an interstory drift of 2.0%. These tests of large HSS bracing members indicate that local buckling behavior and brace fracture occur at larger drifts in specimens with more compact cross sections and greater global slenderness ratios. Additionally, these tests revealed that stocky HSS braces that comply with code requirements may not sustain the expected seismic demands for braced frames. Stocky braces used in braced frames are susceptible to premature fracture, and may not provide braced frames with sufficient ductility to withstand moderate to severe seismic events.

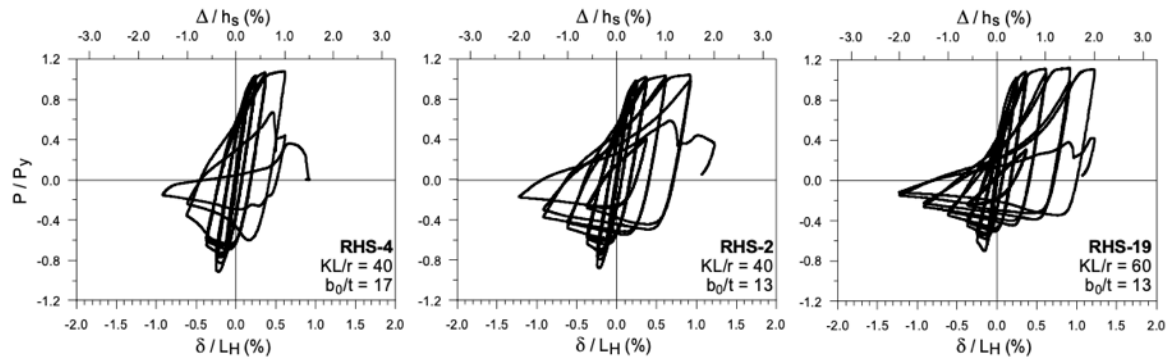

Figure 2.8. Comparison of RHS Seismic Performance

Commentary

This series of tests provides essential experimental data on the behavior of large-scale steel members subjected to inelastic cyclic loads. The steel components tested in previous experimental programs were generally smaller than those commonly used in practice, and

therefore the data generated by this study may be more applicable to existing structures. Although the results from this study show that stocky, code-compliant members may not provide adequate levels of ductility, further testing of large square tubular sections is necessary to fully evaluate the effects of brace cross sectional compactness and global slenderness on performance. The current AISC code requirements for braced frames do not include a minimum global slenderness ratio for bracing members, and thus it is critical to test stocky members with seismically compact cross-sections.

2.3.5 *Experimental Investigation of Inelastic Cyclic Buckling and Fracture of Steel Braces (Fell et al., 2009)*

A total of 18 steel bracing members with varying cross section shapes and sizes were tested in this experimental program to evaluate their inelastic behavior and seismic performance. The effects of brace compactness, slenderness, cross-section shape, fill, and loading history and rate were studied in this experimental program. The goal of this study was to gain a better understanding of the inelastic buckling and yielding behavior of steel bracing members, and to evaluate the design standards for OCBFs and SCBFs. In this testing program, seven square HSS specimens, eight pipe specimens, and three WF specimens were tested, and the results and analysis of the five hollow, square HSS specimens will be presented in this review. These specimens were 4x4x1/4 and 4x4x3/8 HSS members, which are smaller than any of the specimens tested at the UW SRL. All braces were about 117.5" in length, and the width-to-thickness and brace slenderness ratios for all of the square HSS specimens were within the AISC 341-10 limits. Four specimens were subjected to a standard, symmetric cyclic loading protocol with displacements of increasing amplitudes. The other hollow square HSS specimen was subjected to a protocol representing a compression dominated near-field ground motion. These loading protocols were developed based on an assumed drift ratio of 0.2% at brace buckling and a 4% drift ratio at the maximum considered earthquake. These drift demands were converted to the applied axial displacements based on assumed brace angle of 45^{o} in a chevron configuration.

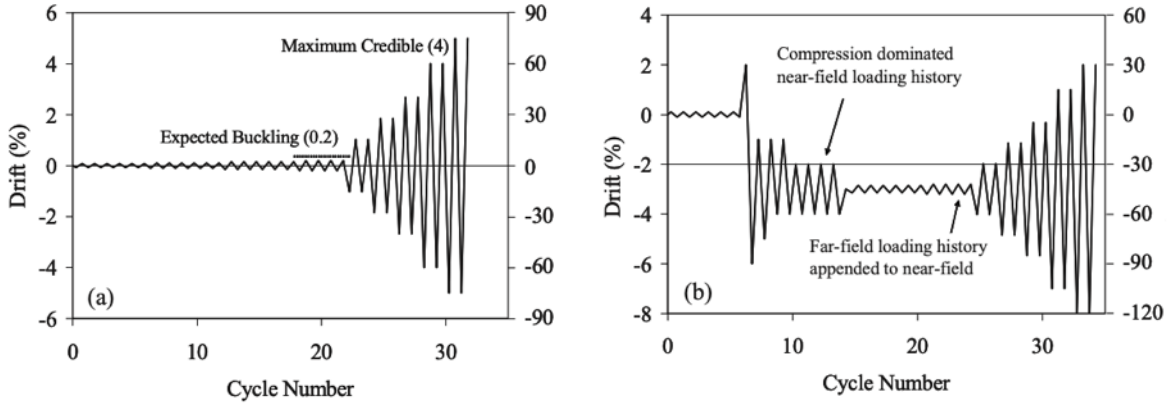

(a) (b)

Figure 2.9. Loading Protocol: Standard (a) and Compression Dominated (b)

Findings

The progression of brace behavior and damage leading up to the point of fracture generally followed the sequence observed in previous research, although in several cases HSS members without net section reinforcement fractured at the ends of the brace prior to the development of local buckling at the mid-span plastic hinge. Typically, as the displacement amplitudes increased, local deformations developed at the center of the brace in compression. These high localized strains led to the initiation of tearing at the corners of the brace in subsequent tensile displacements, which propagated across the entire cross section resulting in brace fracture. It was found that the standard, symmetric cyclic loading protocol was more damaging to the braces than the compression dominated loading protocol developed to simulate near-field ground motions. However, only one of the five hollow HSS specimens was subjected to this compression dominated loading protocol.

In the figures below, the maximum compressive or tensile drifts prior to the initiation of brace fracture are shown as the fracture drift. The effect of width-to-thickness ratio on brace fracture and energy dissipation capacity is shown in Figure 2.11 below. The horizontal lines at 2% and 4% drift represent assumed minimum and design drift capacities of SCBFs. The results show that although all HSS specimens were within the AISC compactness limits, not all sections reached a drift of at least 4% prior to fracture. Previous work has indicated that during large

earthquakes, the imposed drift demands may exceed 4%. HSS1 specimens fractured at an average drift of 2.9%, suggesting that the design requirements for braces in SCBFs are non-conservative. The author suggests that a reduction to 3/4 of the compactness limit would ensure that braces achieve a 4% drift capacity, although all but one of the specimens survived a drift of at least 2%.

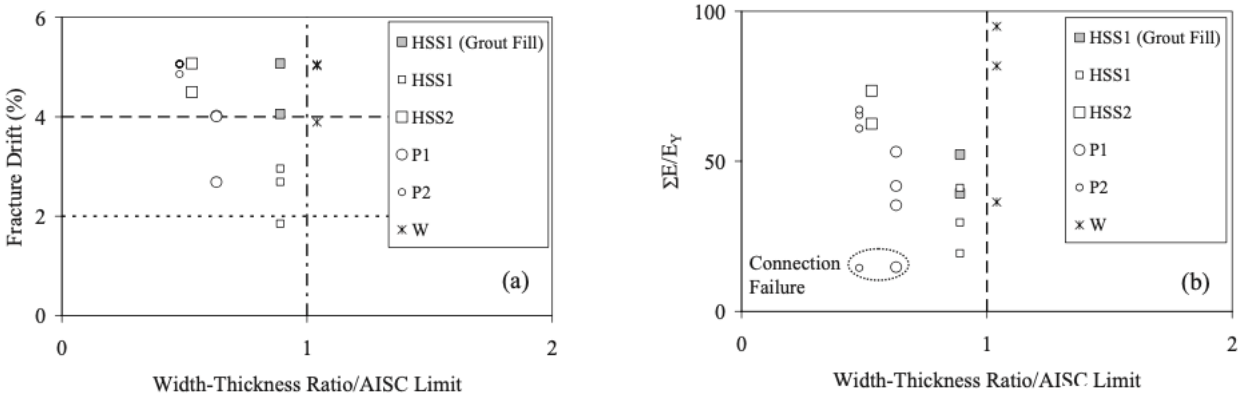

Figure 2.10. Effect of Local Compactness on Fracture Drift and Energy Dissipation

The data from this experimental program also showed a slight increase in ductility and energy dissipation capacity with greater global slenderness, as shown in Figure 2.11. However, there was less variation in the global slenderness than brace compactness of the HSS specimens, and therefore it is difficult to establish a clear relationship between global slenderness and seismic performance from this data.

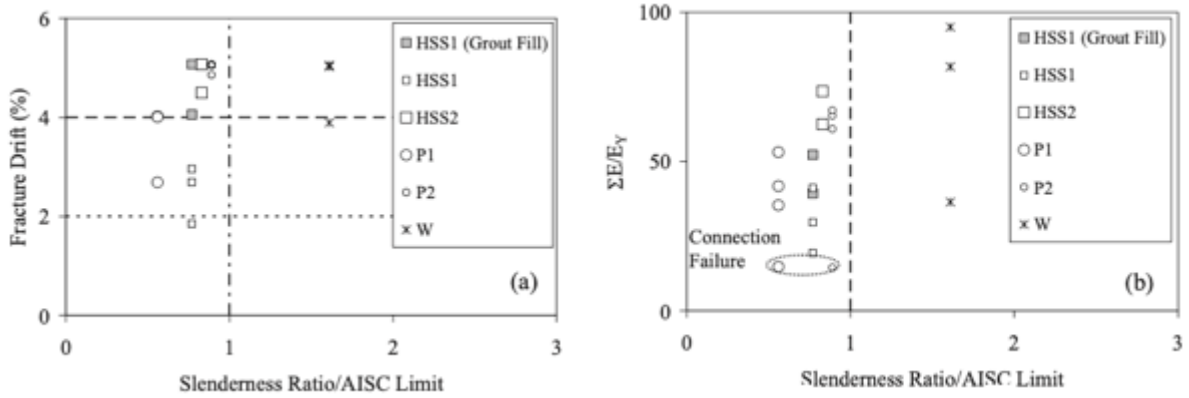

Figure 2.11. Effect of Global Slenderness on Fracture Drift and Energy Dissipation

In general, these tests show that braces with more compact cross sections and greater global slenderness exhibit improved fracture ductility, although cross sectional compactness was shown to have the largest impact. It was suggested by the author that the width-to-thickness limits should be reduced to 90% of the AISC 341-05 limits.

Commentary

AISC-341-05 provides a width-to-thickness limit for highly ductile members of $0.64 \cdot \sqrt{\frac{E}{F_y}}$ for HSS used as diagonal braces. The above research indicated that this limit may not be satisfactory, since several HSS test specimens meeting this criteria fractured at an approximate story drift significantly below 4%. These HSS members had a global slenderness ratio of 77, which is not especially low for bracing members. Therefore, the relatively early fracture observed in these specimens is not likely to be a result of excessive stockiness, which has been observed in previous research. As a result of this research project and others, in 2010 the width-to-thickness limits for highly ductile HSS bracing members in the AISC Seismic Provisions were adjusted to $0.55 \cdot \sqrt{\frac{E}{F_y}}$, which is about 90% of the previous limit and matches the suggestions provided in this paper. Since 2010, these limits have been slightly modified to account for the expected yield strength of the bracing member, and in AISC 341-16 this limit is provided as $0.65 \cdot \sqrt{\frac{E}{R_y F_y}}$. For A500 Grade B HSS members, this modification does not change the width-to-thickness limits, which remain as 13.8 for highly ductile members. The introduction of the overstrength factor R_y in the width-to-thickness limit equation, which is 1.4 for A500 Grade B HSS members, is balanced out by increasing the coefficient from 0.55 to 0.65. However, this change does result in an increase in the width-to-thickness limits for A1085 HSS members, which have a minimum yield stress of 50 ksi and an overstrength factor of 1.25. Therefore, A1085 HSS members with width-to-thickness ratios up to 14 are classified as highly ductile members according to AISC 341-16. This change, along with the tighter control over wall thickness required by the ASTM A1085 specification, allows for larger and less compact A1085 HSS members to be used in SCBFs.

2.4 SUMMARY OF FINDINGS

Previous research projects investigating the inelastic response of A500 HSS have established a clear relationship between seismic performance and properties such as brace local and global slenderness. Additionally, factors such as the displacement protocol used during testing, braced frame configuration, and brace end condition have been shown to affect the behavior of HSS members. Globally slender braces with compact cross sections generally exhibited greater deformation capacity prior to brace fracture. Currently, braces in SCBFs are must meet the AISC width-to-thickness limits for highly ductile members, but there is no minimum global slenderness requirement. Previous research indicates that stocky, cross-sectionally compact HSS members may not achieve adequate deformation prior to fracture. However, further research is necessary to characterize the behavior of stocky, locally compact sections and globally slender members with thin walls. Additionally, very little research has focused on the behavior of A1085 HSS members in comparison with A500 HSS. Full-scale component tests of A500 and A1085 HSS members must be performed to realize the effects of the tighter geometric tolerances and material property requirements associated with the A1085 specification. In this thesis, square HSS members with a wide range of b/t and KL/r ratios will be tested in both A500 and A1085 HSS to characterize the differences in structural response between the types of steel. The results of this experimental program will have implications for the design requirements of SCBFs using A1085 HSS as bracing member.

Chapter 3. TEST SETUP AND SPECIMEN DESIGN

3.1 INTRODUCTION

The purpose of this chapter is to describe the design of the test setup and specimens used in this experimental program. Twenty square HSS members were studied in this test series to investigate the difference in cyclic response of A1085 and A500 HSS. This was accomplished using a test frame capable of applying large axial deformations and forces to HSS test specimens. The design and construction of the test specimens selected for component testing is described in this chapter, along with the loading protocol applied during testing. This chapter also includes an overview of the test setup, as well as a discussion of the rationale behind the design of the test frame. The test frame was designed to be sufficiently flexible to test HSS members of varying sizes and lengths, while also making the process of preparing and testing specimens as efficient as possible. The instrumentation used to collect data during the tests is also discussed in this chapter.

3.2 TEST SPECIMEN DESIGN

3.2.1 *Overview*

A total of twenty square HSS specimens were tested in the first series of tests at the University of Washington Structural Research Lab (UW SRL). The steel tubes used in this research project were provided by four different steel producers, which will be referred to as Producers “Yellow”, “Red”, “Blue”, and “White” to maintain producer anonymity. Ten different HSS shapes were provided in both ASTM A500 Grade C and ASTM A1085 steel, and the sections provided by each of the producers are shown below in Table 3.1. The 35 cells shaded in green denote a section provided by each specific producer. The tubes were delivered in 40’ long sections to allow enough length to test multiple specimens from each tube while still leaving enough length for material testing. Duplicates of each of the 40’ sections were supplied, which

made it possible to quickly fabricate and test replacement specimens if errors were made in the fabrication or testing of the specimens.

Table 3.1. Available HSS Shapes

	ASTM A500				ASTM A1085			
HSS Shape	**YELLOW**	**RED**	**BLUE**	**WHITE**	**YELLOW**	**RED**	**BLUE**	**WHITE**
10x10x3/8								
8x8x1/2								
8x8x3/8								
7x7x1/2								
7x7x3/8								
7x7x5/16								
6x6x1/2								
6x6x3/8								
6x6x5/16								
5x5x3/8								

Table 3.2 below indicates the sections tested from each producer during test series 1. These sections were selected for testing based on their local compactness ratio, global slenderness ratio, predicted capacity, and availability from the various producers. Ten square HSS shapes were tested in both A500 and A1085 steel in this test series. A500 HSS from four different steel producers were tested, while all ten A1085 specimens in this test series were provided by producer Yellow. The other sections shown in Table 3.1 will be tested in future test series.

Table 3.2. Test Specimens – Test Series 1

	ASTM A500				ASTM A1085
HSS Shape	**YELLOW**	**RED**	**BLUE**	**WHITE**	**YELLOW**
10x10x3/8					
8x8x1/2					
8x8x3/8					
7x7x1/2					
7x7x3/8					
7x7x5/16					
6x6x1/2					
6x6x3/8					
6x6x5/16					

The expected yield and critical buckling loads of the specimens tested in this series are shown in Table 3.3 below. The expected yield force, $P_{y,e}$, is calculated as the nominal cross-sectional area of the specimen, A_g, multiplied by the expected yield strength, R_yF_y. The yield overstrength factor, R_y, is 1.3 for A500 Grade C HSS and 1.25 for A1085 HSS, as discussed in Chapter 2. Additionally, the nominal yield strength, F_y, is 50 ksi for both types of steel. The critical buckling force, $P_{cr,e}$, is calculated based on the material and geometric properties of each test specimen. The maximum test specimen size was constrained by the equipment available at the UW SRL. As described in detail later in this chapter, two large hydraulic actuators were used to push and pull on a steel sliding beam attached to the test specimens to apply tensile and compressive forces. These actuators were capable of applying axial forces up to 1000 kips in tension and 700 kips in compression to the test specimens.

Table 3.3. Expected Tensile and Compressive HSS Member Capacity

	Expected Yield Force, $P_{y,e}$ (kips)		**Expected Critical Buckling Force, $P_{cr,e}$ (kips)**	
HSS Shape	**A500**	**A1085**	**A500**	**A1085**
10x10x3/8	858	917	605	628
8x8x1/2	878	936	491	511
8x8x3/8	676	722	387	404
7x7x1/2	754	806	347	364
7x7x3/8	583	623	278	292
7x7x5/16	493	528	239	252
6x6x1/2	633	673	216	225
6x6x3/8	493	525	175	185
6x6x5/16	418	447	153	157
5x5x3/8	402	428	96	101

3.2.2 *Test Specimen Layout and Connections*

The test specimens studied in this test series were comprised of a 237.5” long square HSS member welded to a trapezoidal gusset plate at each end. The gusset plates were connected to steel connection plates at both the north and south ends of the test frame with twelve 1” diameter A490 bolts. Slots were cut in the HSS members using a plasma cutter so that the gusset plates could be welded to the tubes. Additionally, net section reinforcement plates were welded to the sides of the HSS members. This was done to prevent the sections from failing due to tensile rupture on the net section, since the slots in the member reduced the cross sectional area of the member. A description of the connection design is presented below in further detail. Figure 3.1 below shows the overall layout of the design of the test specimens.

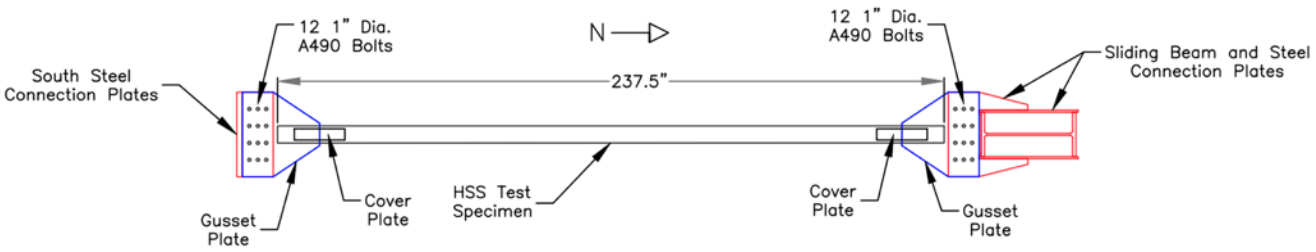

Figure 3.1. Test Specimen Layout

The exact length of the test specimens, 237.5”, was selected based on the as-built dimensions of the test frame as described in Section 3.6. After establishing the A500 and A1085 HSS shapes to be tested in this experimental program, it was necessary to design connections specific to each of the ten shapes. The dimensions of the gusset plates and fillet welds for each of the test specimens are shown below in Table 3.4. The height of each gusset plate was 30”, matching the dimension of the steel connection plates at the end reaction block and sliding beam. Through an iterative design process, this layout was found to be adequate for all of sections, and fit with the geometry of the test frame and bolt pattern. Since the thickness of the gusset plates was less than the horizontal gap between the steel connection plates (0.875”), shim plates were

used to fill this gap and provide a tight fit between the plates. These shim plates prevented the connection plates from being bent when the gusset plates were bolted into place.

The gusset plates were designed to provide pinned end conditions for the test specimens, allowing them to rotate as they buckled laterally under compressive displacements. A gap with a length of three times the gusset plate thickness was created between the steel connection plates and the end of the HSS member to accommodate this rotation. The gusset plates were sized to provide adequate length for the fillet welds, without requiring excessively large welds. Table 3.4 below shows the geometry of the gusset plates for each HSS shape tested, along with the dimensions of the fillet welds and slot eccentricities. The following limit states were evaluated for each of the ten gusset plate designs: yielding on the gross area, tensile rupture, block shear, bearing and tear out, and buckling. The Whitmore section was used to determine the effective width of the sections. Figure 3.2 below shows the common dimensions of the gusset plates, although the exact geometry varied between the different plates. Drawings of all 10 gusset plate designs are shown in Appendix 1. Calculations for the dimensions of the gusset plates and fillet welds connecting the gusset plates to the HSS members can be found in Appendix 2.

Table 3.4. Gusset Plate and Fillet Weld Design

	Gusset Plate		Fillet Weld		Slot
Section	**Length (in.)**	**Thickness (in.)**	**Length (in.)**	**Size (in.)**	**Slot Eccentricity (in.)**
10x10x3/8	38.25	0.75	25.0	0.5	0.375
8x8x1/2	32.25	0.75	19.0	0.625	0.3125
8x8x3/8	32.875	0.625	20.0	0.5	0.3125
7x7x1/2	29.875	0.625	17.0	0.5	0.25
7x7x3/8	29.5	0.5	17.0	0.5	0.25
7x7x5/16	30.5	0.5	18.0	0.5	0.25
6x6x1/2	26.875	0.625	14.0	0.5	0.25
6x6x3/8	27.5	0.5	15.0	0.4375	0.25
6x6x5/16	27.125	0.375	15.0	0.4375	0.25
5x5x3/8	24.125	0.375	12.0	0.375	0.1875

Twelve 1” diameter A490 bolts were used to connect the gusset plates to the steel connection plates at both ends. As shown in Figure 3.2, the bolt rows were spaced at 6” vertically

and 3” horizontally, and 2.5” from the vertical edge of the plate. This spacing was designed to prevent block shear and tear out from occurring in the sections. The bolts were pretensioned to a minimum of 64 kips each using a hydraulic torque wrench, which was verified through the use of load indicating washers. This was done to prevent the bolts from slipping during the tests, although due to the large axial forces and displacements, the bolts slipped during each of the tests. Calculations for the design of the bolts and bolt hole layout can be found in Appendix 2.

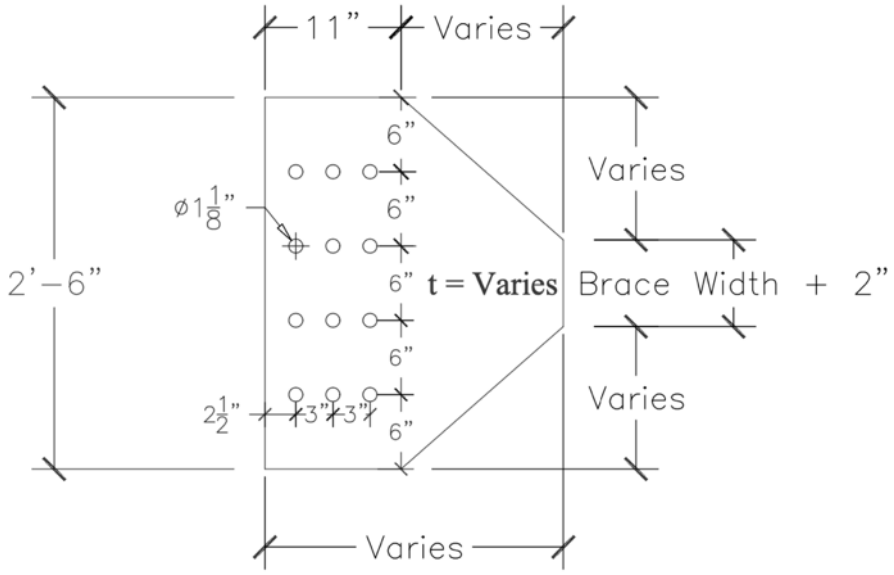

Figure 3.2. Gusset Plate Design - General

The gusset plates were intentionally welded slightly eccentrically to the center of the members, causing the specimens to consistently buckle towards the west side of the test frame. This was done because of the larger clearance between the actuator and test specimen on the west side of the test frame, preventing the braces from buckling into the actuator reaction blocks. Additionally, the eccentric slots made it easier to set up instrumentation to capture buckling displacements using a single set of string potentiometers along the east face of the specimen. Previous work at the UW SRL used a ratio of slot eccentricity to radius of gyration (*e/r*) to determine the amount of gusset plate eccentricity. In these previous projects, an *e/r* ratio of 0.1 was used to determine the slot eccentricity, and this ratio was used in this project as well. This

amount of applied eccentricity did not significantly reduce the compressive capacity of the sections, while also ensuring that the specimens behaved in a predictable manner.

Net section reinforcement was provided by welding rectangular steel plates along the east and west sides of the brace at both ends. These cover plates increased the effective area of the brace at the locations of the longitudinal slots, such that the effective area at these locations exceeded the gross area of the HSS member. This prevented tensile rupture from occurring at the end of the specimens, which could occur in an unreinforced section prior to local buckling and fracture at the center of the specimen. The welds on both sides of the reinforcing plates were designed to develop the expected strength of the cover plate on both sides of the slot. These plates ranged in size from 16" by 2.75" up to 24" by 5.25". All of the plates were 3/8" thick, and were welded to the specimens with a 1/4" fillet weld. Further calculations for the cover plates can be found in Appendix 2.

3.3 TEST SPECIMEN PROPERTIES

Previous research has shown that the inelastic response of HSS members is affected by the cross-sectional compactness and global slenderness ratios. The ductility of HSS members is highly dependent on brace local compactness and global slenderness, due to the potential for the development of significant localized strains at the center of bracing members undergoing low-cycle fatigue. (AISC, 2016) As braces buckle under compressive displacements, local deformations develop at the center plastic hinge location in the member. These substantial localized strains can cause the members to fracture in a non-ductile manner in tension, and therefore it is critical that bracing members in seismic force resisting systems are capable of withstanding significant inelastic buckling without fracturing. The limiting width-to-thickness ratios provided in Table 1.1 are designed to prevent bracing members from experiencing local buckling before the development of strain hardening in tension, which results in the bracing member performing in a ductile manner during seismic events.

Braces with varying width-to-thickness and global slenderness ratios were tested in this experimental program to investigate the differences between A1085 and A500 HSS across a wide range of local and global slenderness ratios.

Figure 3.3 below shows the range of global slenderness and local compactness ratios of the specimens tested in this series. The nominal width-to-thickness ratios of the specimens ranged from 9 to 25, and the global slenderness ratios ranged from about 60 to 127. This test series includes specimens that met the AISC limits for highly ductile and moderately ductile members, as well as a number of sections with b/t ratios exceeding the moderately ductile limits.

The color scheme shown in Figure 3.3 is maintained through the entire document for the A500 and A1085 HSS specimens. The A500 and A1085 specimens of the same section have the same color, but when shown in the same plot the A500 specimen is denoted by a hollow circle and the A1085 specimen is shown as a filled in circle. To maintain consistency, the plots in the results and analysis sections of this thesis follow the same color convention as above.

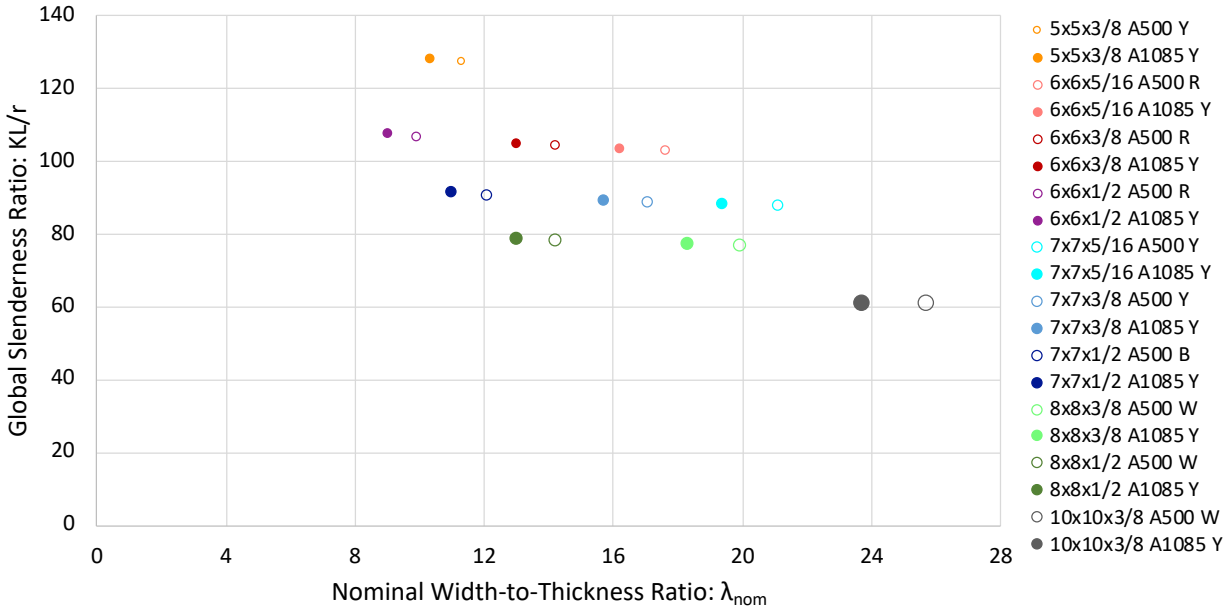

Figure 3.3. Range of Global Slenderness and Local Compactness Ratios

Table 3.5 below shows the nominal width-to-thickness ratio of each test specimen, with the shading of each cell based on the AISC width-to-thickness limits. Specimens meeting the AISC width-to-thickness criteria for highly ductile members are shaded in green, while those meeting the moderately ductile limits are shaded in orange. Specimens exceeding the AISC limits for moderately ductile members are shaded in red.

Table 3.5. Test Specimen Width-to-Thickness Ratios

	Nominal Width-to-Thickness Ratio	
HSS Shape	**A500 Gr. C**	**A1085**
10x10x3/8	*25.7*	23.7
8x8x1/2	14.2	13
8x8x3/8	19.9	18.3
7x7x1/2	12.1	11
7x7x3/8	17.1	15.7
7x7x5/16	21.1	19.4
6x6x1/2	9.9	9
6x6x3/8	14.2	13
6x6x5/16	17.6	16.2
5x5x3/8	11.3	10.3

The slenderness ratio of braces in SCBFs is limited by $Lc/r \leq 200$, which significantly exceeds the slenderness ratio of any of the specimens tested in this experimental program. The global slenderness ratios for each test specimen are shown in Table 3.6 below. This upper limit is intended to prevent undesirable dynamic effects caused by excessive brace slenderness. However, bracing members with larger slenderness ratios typically exhibit elastic buckling behavior under larger compressive axial deformations than stocky members, making them more ductile. When braces buckle inelastically, increased compressive deformations result in larger rotation at the mid-span plastic hinge, which leads to the development of local deformations at this location (Tremblay, 2002). Generally, the local strains that develop in the plastic hinge region of a buckling brace are larger for braces with lower global slenderness for the same compressive deformation. Therefore, braced frames designed with more slender braces provide larger inelastic deformation capacity under cyclic loading. Although ductility generally increases with greater global slenderness, the compressive axial force capacity is reduced in more globally slender braces. In design, it is often desired to have relatively similar tensile and compressive force capacities in braces, and thus it isn't feasible to use excessively slender braces. In practice, many braced frames use braces with a KL/r ratio of between 40 and 100 to attain adequate compressive force capacity while still maintaining sufficient ductility. (Sabelli et al., 2013).

Table 3.6. Test Specimen Global Slenderness Ratios

	Nominal Global Slenderness Ratio	
HSS Shape	**A500 Gr. C**	**A1085**
10x10x3/8	60.6	60.9
8x8x1/2	78.1	78.6
8x8x3/8	76.6	76.9
7x7x1/2	90.3	91.0
7x7x3/8	88.3	88.6
7x7x5/16	87.3	87.6
6x6x1/2	106.5	107.5
6x6x3/8	104.2	104.6
6x6x5/16	102.8	103.3
5x5x3/8	127.0	127.7

Notably, the global slenderness ratio for braces in ordinary concentrically braced frames (OCBFs) in a V or inverted-V configuration is more restrictive than that for SCBFs and is limited by the equation:

$$Lc/r \leq 4\sqrt{E/F_Y}$$

This limits the slenderness of A500 Grade C and A1085 braces in OCBFs to just under 100, which is intended to reduce the development of unbalanced forces within a braced frame after the bracing member has buckled in compression. (AISC, 2016).

3.3.1 *Geometric Properties*

Measurements of the geometric properties of the test specimens were taken to evaluate differences between the A500 and A1085 HSS. The wall thicknesses were measured using a micrometer, with two measurements taken at each of the four walls at both ends of the specimen, and the average of these values is denoted as t_m. These measurements, along with the nominal wall thickness, t_{nom}, are shown in Table 3.7 below. Additionally, this table shows the ratio of the measured-to-nominal wall thickness, as well as the ratio of the measured-to-required wall

thickness of the A1085 specification, $t_{req,A1085}$. The A1085 specification permits only a 5% reduction in wall thickness, compared with 10% tolerance of the A500 specification.

Table 3.7. Wall Thickness Measurements

Test Specimen	Nominal Wall Thickness, t_{nom} (in)	Measured Wall Thickness, t_m (in)	t_m / t_{nom}	$t_m / t_{req,A1085}$
5x5x3/8 A500 Y	0.349	0.360	1.032	1.01
5x5x3/8 A1085 Y	0.375	0.376	1.003	1.06
6x6x5/16 A500 R	0.291	0.305	1.048	1.03
6x6x5/16 A1085 Y	0.313	0.313	1.000	1.05
6x6x3/8 A500 R	0.349	0.367	1.052	1.03
6x6x3/8 A1085 Y	0.375	0.375	1.000	1.05
6x6x1/2 A500 R	0.465	0.479	1.030	1.01
6x6x1/2 A1085 Y	0.5	0.486	0.972	1.02
7x7x5/16 A500 Y	0.291	0.290	0.997	0.98
7x7x5/16 A1085 Y	0.313	0.305	0.974	1.03
7x7x3/8 A500 Y	0.349	0.342	0.980	0.96
7x7x3/8 A1085 Y	0.375	0.365	0.973	1.02
7x7x1/2 A500 B	0.465	0.464	0.998	0.98
7x7x1/2 A1085 Y	0.5	0.484	0.968	1.02
8x8x3/8 A500 W	0.349	0.350	1.003	0.98
8x8x3/8 A1085 Y	0.375	0.370	0.987	1.04
8x8x1/2 A500 W	0.465	0.461	0.991	0.97
8x8x1/2 A1085 Y	0.5	0.488	0.976	1.03
10x10x3/8 A500 W	0.349	0.347	0.994	0.97
10x10x3/8 A1085 Y	0.375	0.366	0.976	1.03

The ratio of the measured wall thickness to the wall thickness required by the A1085 specification is shown below in Figure 3.4 for all test specimens. The bars representing A500 HSS are hollow, while the A1085 HSS are shown as solid bars on the plot. The bar color indicates the steel producer. This figure shows all of the A1085 HSS met the 5% wall thickness tolerance, while only four of the ten A500 HSS met this requirement. However, most of the A500 tubes were within about 3% of this wall thickness requirement. The difference in wall thickness between the A500 and A1085 specimens was typically about 5% or less. This figure shows that while there was some difference in wall thickness between the two types of steel, the differences were relatively small.

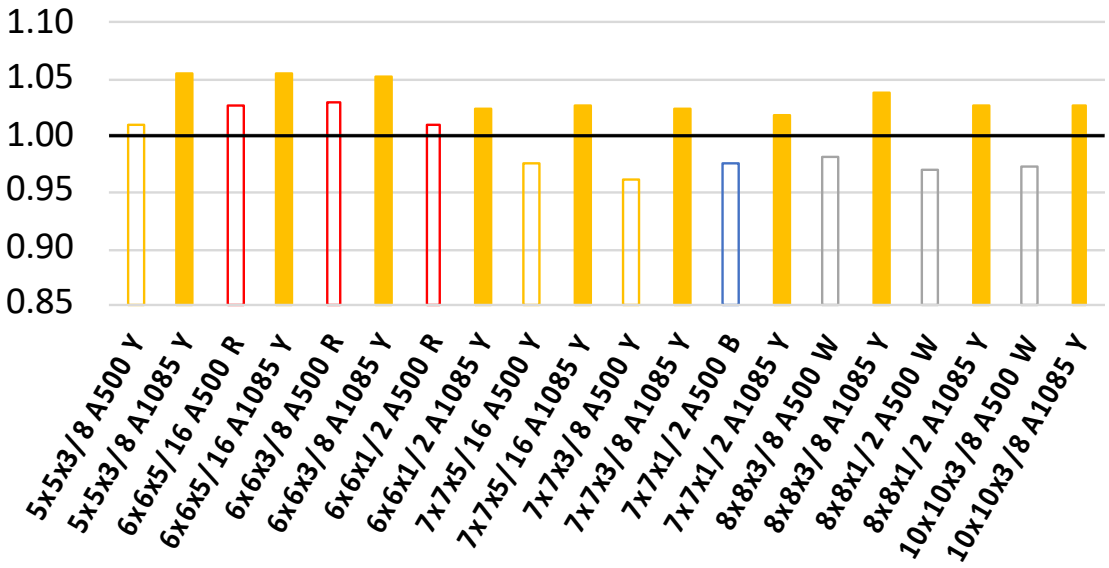

Figure 3.4. Ratio of Measured Wall Thickness to A1085 HSS Requirement

Table 3.8 shows the measured and nominal local slenderness ratios, λ_m and λ_{nom}, for each test specimen. The ratio of measured-to-nominal local slenderness is also shown for each specimen. The measured width-to-thickness ratio was calculated as the brace width minus two times the measured corner radius, divided by the measured wall thickness. Additional tables of the measured geometric properties are included in Appendix 2. This table shows that for all of the test specimens, λ_{nom} exceeded λ_m, indicating that the test specimen cross-sections were more compact than expected. Generally, the ratio of λ_m to λ_{nom} was between 0.85 and 0.95, meaning that the test were are typically 5% to 15% more cross-sectionally compact than assumed. Additional analysis of the geometry of the cross sections is presented in below.

Table 3.8. Measured and Nominal Local Slenderness Ratios

HSS Section	λ_m	λ_{nom}	$\lambda_m / \lambda_{nom}$	$\lambda_{nom} / \lambda_{HD}$	$\lambda_{nom} / \lambda_{MD}$
5x5x3/8 A500 Y	9.7	11.3	0.86	0.82	0.70
5x5x3/8 A1085 Y	9.4	10.3	0.91	0.74	0.63
6x6x5/16 A500 R	15.8	17.6	0.90	1.28	1.09
6x6x5/16 A1085 Y	14.9	16.2	0.92	1.16	0.99
6x6x3/8 A500 R	12.3	14.2	0.86	1.04	0.88
6x6x3/8 A1085 Y	12.2	13	0.94	0.93	0.79
6x6x1/2 A500 R	8.4	9.9	0.85	0.72	0.61
6x6x1/2 A1085 Y	8.9	9	0.99	0.64	0.55
7x7x5/16 A500 Y	19.6	21.1	0.93	1.54	1.31
7x7x5/16 A1085 Y	18.6	19.4	0.96	1.39	1.18
7x7x3/8 A500 Y	15.6	17.1	0.91	1.25	1.06
7x7x3/8 A1085 Y	14.2	15.7	0.91	1.12	0.96
7x7x1/2 A500 B	11.0	12.1	0.91	0.88	0.75
7x7x1/2 A1085 Y	10.1	11	0.92	0.79	0.67
8x8x3/8 A500 W	18.3	19.9	0.92	1.45	1.24
8x8x3/8 A1085 Y	15.9	18.3	0.87	1.31	1.12
8x8x1/2 A500 W	13.5	14.2	0.95	1.04	0.88
8x8x1/2 A1085 Y	11.7	13	0.90	0.93	0.79
10x10x3/8 A500 W	24.4	25.7	0.95	1.88	1.60
10x10x3/8 A1085 Y	23.1	23.7	0.98	1.69	1.45

A summary of the measured and nominal width-to-thickness ratios is shown below in Table 3.9. The data in this table is categorized based on steel type and steel producer. All of the A1085 specimens in this test series came from Producer Y, and the average ratio of λ_m to λ_{nom} for these specimens was 0.93. On average, the A1085 specimens were 7% more cross-sectionally compact than expected. The average ratio for the entire set of A500 specimens was 0.90, corresponding to a 10% reduction in actual cross-sectional slenderness. The average λ_m to λ_{nom} ratios for A500 specimens from all four producers were between 0.87 and 0.94. The sample size from each producer is small, and thus it is difficult to draw conclusions about the differences between the steel tubes manufactured by these producers. The data indicates that the difference between the measured and nominal width-to-thickness ratios was slightly larger for the A500 than the A1085 specimens. The A1085 HSS of a given shape have a slightly lower nominal

width-to-thickness ratio than the A500 HSS due the tighter geometric tolerances required by the A1085 specification. However, this data shows that the actual difference in cross-sectional compactness between the A500 and A1085 sections is less than the nominal value. Although in nine of the ten HSS shapes tested the measured b/t ratio of the A1085 section was less than that of the A500 section, the difference in cross-sectional compactness was less than expected.

Table 3.9. Summary of Local Slenderness Ratios

$\lambda_m / \lambda_{nom}$	**A1085 - Y**	**A500 - ALL**	**A500 - Y**	**A500 - R**	**A500 - W**	**A500 - B**
Average	0.93	0.90	0.90	0.87	0.94	0.91
Standard Deviation	0.037	0.037	0.038	0.025	0.018	-
# of HSS Specimens	10	10	3	3	3	1

3.3.2 *Material Properties*

The material properties of the test specimens were measured through tension coupon and Charpy V-Notch testing. Tube sections about 24" long were cut from each of the 35 HSS shapes provided by the various steel producers for material testing purposes. Flat plates were cut from the walls of each of these sections, and the tension coupons and Charpy V-Notch specimens were machined from these plates. The tension coupons were machined using a waterjet cutter, and tension tests were completed following ASTM Standard Test Methods and Definitions for Mechanical Testing of Steel Products (ASTM, 2017). Two tension coupons from each test specimen were machined and tested at the UW SRL. The measured material properties of the HSS members tested in Test Series 1 are shown in Table 3.10 below. This data shows that the measured yield and ultimate strengths, $F_{y,m}$ and $F_{u,m}$, of the A500 and A1085 test specimens were relatively similar across the entire test series. Additionally, this table shows the measured yield strength ratio, $R_{y,m}$, and tensile strength ratio, $R_{t,m}$, for each test specimen, along with the percent elongation of the specimens. Further evaluation of this data is presented below.

Table 3.10. Material Properties from Tension Coupon Testing

HSS Section	Measured Yield Strength, $F_{y,m}$ (ksi)	Measured Yield Strength Ratio, $R_{y,m}$	Measured Tensile Strength, $F_{u,m}$ (ksi)	Measured Tensile Strength Ratio, $R_{t,m}$	Percent Elongation (%)
5x5x3/8 A500 Y	65.38	1.31	71.9	1.16	30.79
5x5x3/8 A1085 Y	66.04	1.32	74.6	1.15	32.83
6x6x5/16 A500 R	57.37	1.15	72.8	1.17	34.65
6x6x5/16 A1085 Y	62.07	1.24	71.9	1.11	34.11
6x6x3/8 A500 R	61.19	1.22	76.4	1.23	35.36
6x6x3/8 A1085 Y	66.81	1.34	72.6	1.12	31.86
6x6x1/2 A500 R	62.84	1.26	67.1	1.08	33.48
6x6x1/2 A1085 Y	67.85	1.36	72.0	1.11	34.88
7x7x5/16 A500 Y	62.71	1.25	70.0	1.13	31.16
7x7x5/16 A1085 Y	57.70	1.15	64.1	0.99	33.12
7x7x3/8 A500 Y	61.35	1.23	72.2	1.16	30.76
7x7x3/8 A1085 Y	61.89	1.24	70.1	1.08	31.32
7x7x1/2 A500 B	57.82	1.16	69.1	1.11	29.6
7x7x1/2 A1085 Y	64.38	1.29	71.7	1.10	32.7
8x8x3/8 A500 W	66.19	1.32	76.5	1.23	34.44
8x8x3/8 A1085 Y	60.37	1.21	72.1	1.11	34.2
8x8x1/2 A500 W	65.47	1.31	72.0	1.16	34.27
8x8x1/2 A1085 Y	64.42	1.29	75.4	1.16	32.23
10x10x3/8 A500 W	59.02	1.18	69.5	1.12	34.2
10x10x3/8 A1085 Y	58.34	1.17	73.8	1.14	34.94

The measured yield strength ratios are shown in Figure 3.5. The horizontal lines at 1.25 and 1.3 indicate the nominal yield strength ratios for A1085 and A500 HSS, respectively. The nominal yield strength is 50 ksi for both A500 Grade C and A1085 HSS. Once again, the bar color indicates the steel producer, and the hollow bars represent A500 specimens while the solid bars represent A1085 specimens. This figure shows that the measured yield strengths of the specimens were relatively similar across the test series. The measured yield strength of all of the A500 and A1085 specimens significantly exceeded the minimum yield strength requirement of 50 ksi. Additionally, the measured yield strengths for all specimens were less than 70 ksi, which is the maximum yield strength permitted by the A1085 specification. Therefore, all of the A500 and A1085 specimens met the yield strength requirements for A1085 HSS.

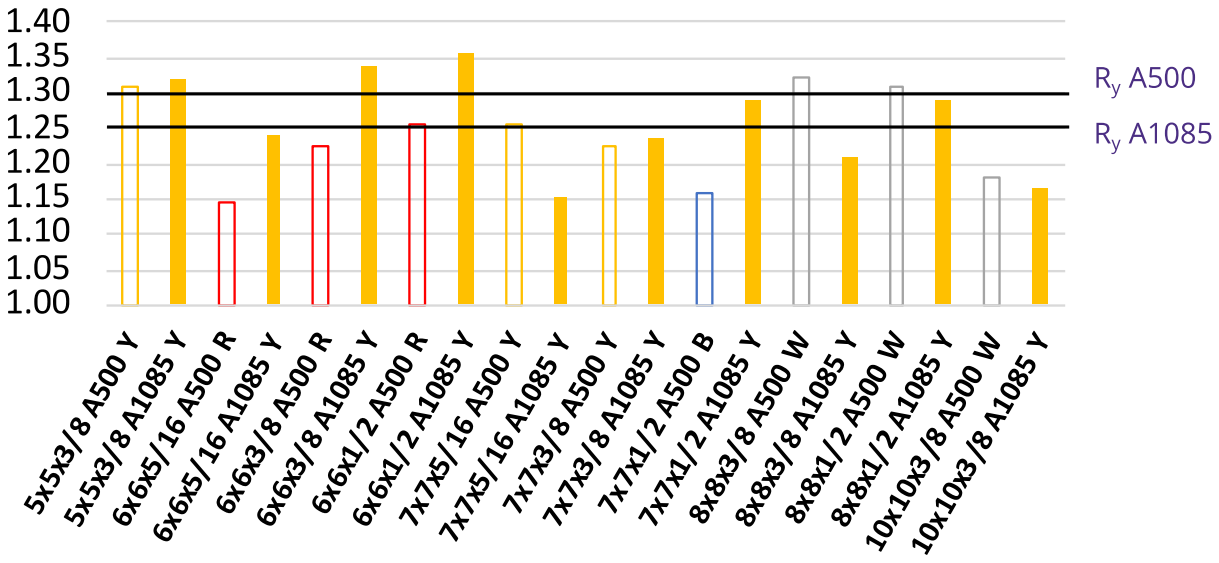

Figure 3.5. Measured Yield Strength Ratios

A summary of the yield strength data is presented below in Table 3.11. The average measured yield strength ratio, $R_{y,m}$, for the A1085 specimens was 1.26, which is slightly greater than the nominal value. The average value of $R_{y,m}$ for the A500 specimens was 1.24, which is slightly less than the nominal value for A500 Gr. C HSS. The average measured yield strength of the A1085 specimens was 62.98 ksi, compared with 61.93 ksi for the A500 specimens. The variability was similar for both types of steel, with standard deviations of 3.5 ksi for the A1085 HSS and 3.18 for the A500 HSS. Three A500 HSS specimens were tested from each of the Yellow, Red , and White steel producers, and the average $R_{y,m}$ values for these producers were 1.26, 1.21, and 1.27, respectively. Only one A500 specimen was tested from producer Blue, with an $R_{y,m}$ value of 1.16. The standard deviation of the $R_{y,m}$ values for A500 HSS from producer White was 0.08, compared with 0.04 and 0.06 for producers Yellow and Red. Despite these minor variations in yield strength across the different steel producers, the overall differences in yield strength between the A500 and A1085 specimens were minimal.

Table 3.11. Summary of Measured Yield Strengths

	# of HSS Specimens	Measured Yield Stress, $F_{y,m}$ (ksi)		Measured Yield Strength Ratio, $R_{y,m}$	
		Average	Standard Deviation	Average	Standard Deviation
All Specimens	20	62.46	3.30	1.25	0.07
A500 - ALL	10	61.93	3.18	1.24	0.06
A1085 - Y	10	62.98	3.50	1.26	0.07
A500 - Y	3	63.15	2.05	1.26	0.04
A500 - R	3	60.47	2.81	1.21	0.06
A500 - W	3	63.56	3.95	1.27	0.08
A500 - B	1	57.82	-	1.16	-

In Figure 3.6 below, the measured tensile strength of each test specimen is normalized by the minimum required tensile strength for A1085 HSS, 65 ksi. The minimum tensile strength required by the A500 specification is 62 ksi, but this figure clearly shows that all of the A500 and A1085 test specimens met the 65 ksi requirement for A1085 HSS. The nominal tensile strength ratios of A500 and A1085 HSS are 1.2 and 1.15, respectively, and thus the expected tensile strengths for both types of steel are just under 75 ksi. The measured tensile strengths were lower than the expected tensile strength for most of the A500 and A1085 test specimens.

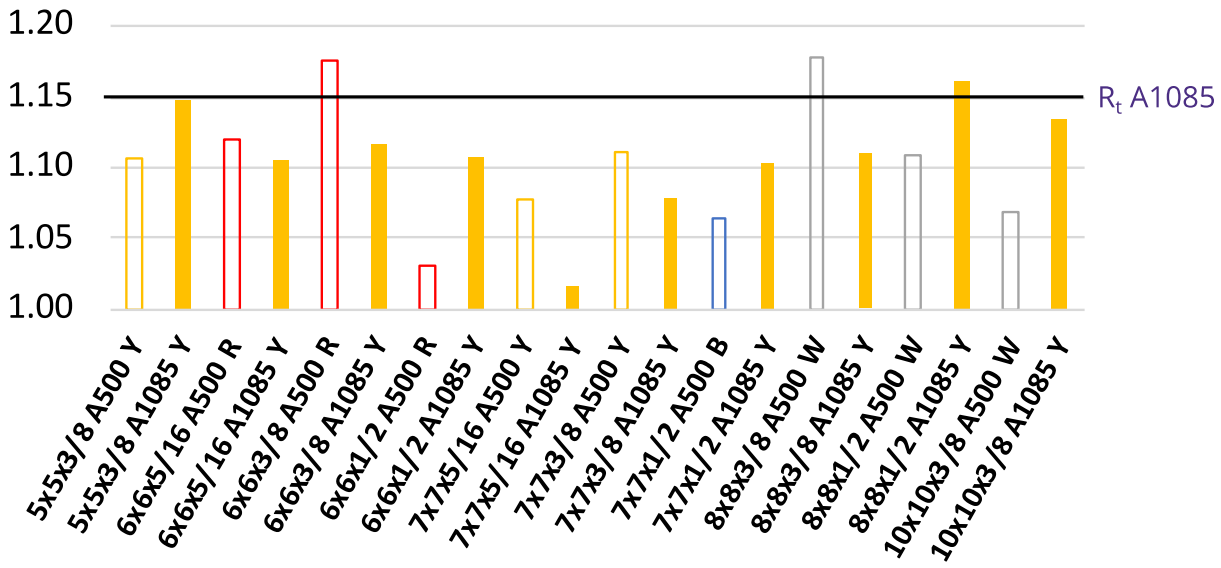

Figure 3.6. Ratio of Measured to Minimum Tensile Strength of A1085 HSS

Table 3.12 below shows a summary of the tensile strength data. This table shows that the tensile strength properties were nearly identical between the A500 and A1085 test specimens. The average measured tensile strength, $F_{y,m}$, was 71.83 ksi for the A1085 specimens and 71.75 ksi for the A500 specimens, with similar amounts of variation in the data. The average $R_{t,m}$ values for the A500 HSS from producers Yellow, Red, and White were 1.15, 1.16, and 1.17. The corresponding standard deviation values were 0.02, 0.08, and 0.06, respectively. The measured tensile strength ratios, were 1.11 for the A1085 specimens and 1.16 for the A500 specimens. In both cases, the nominal value of R_t exceeded the average measured value by 0.04. The tables and figures showing the yield and ultimate strength data indicate that the difference in strength between the A500 and A1085 specimens is relatively small. All of the A500 and A1085 specimens met the yield and ultimate strength criteria for A1085 HSS.

Table 3.12. Summary of Measured Tensile Strengths

		Measured Tensile Strength, $F_{u,m}$ (ksi)		**Measured Tensile Strength Ratio, $R_{t,m}$**	
	# of HSS Specimens	**Average**	**Standard Deviation**	**Average**	**Standard Deviation**
All Specimens	20	71.8	3.30	1.13	0.07
A500 - ALL	10	71.75	3.02	1.16	0.05
A1085 - Y	10	71.83	3.12	1.11	0.05
A500 - Y	3	71.37	1.19	1.15	0.02
A500 - R	3	72.10	4.69	1.16	0.08
A500 - W	3	72.67	3.55	1.17	0.06
A500 - B	1	69.1	-	1.11	-

Charpy V-Notch (CVN) specimens were tested using a Charpy Machine at the UW SRL to determine the toughness of the different A1085 and A500 HSS members. The results of the Charpy specimen tests are shown in Table 3.13 below. As mentioned previously, the A1085 specification introduced a Charpy V-Notch toughness requirement of 25 ft-lbs at 40° F, whereas the A500 specification does not require HSS sections to meet any minimum toughness requirement. These impact tests were performed to study the energy absorption capacity and toughness of A1085 and A500 HSS members.

The Charpy specimens were machined by Laboratory Testing, Inc to meet the requirements established by the ASTM Standard Test Methods for Notched Bar Impact Testing

of Metallic Materials (ASTM, 2007). Three Charpy specimens were machined from the flat wall sections of each of the test specimens, in addition to two sets of three Charpy specimens machined from the corners of two test specimens. The results of Charpy specimens taken from the corners of tubes are denoted with *C in the table below. The testing procedure followed the ASTM E23 standard for each of the tests. Standard-size Charpy specimens (55mm x 10mm x 10mm) were produced from all of the 1/2" thick tubes, but sub-size specimens had to be machined from the thinner tube sections. From the 3/8" thick HSS members, 55mm x 10mm x 7.5mm specimens were machined, while 55mm x 10mm x 5mm specimens were machined from the 5/16" thick sections.

The specimen size and average absorbed energy value is shown in Table 3.13 below for each test specimen. The Charpy machine was positioned in its high-energy setting prior to each test with an initial potential energy of 120 lb-ft. For some specimens, the hammer of the pendulum did not fully fracture the Charpy specimens. If at least two of the three specimens from a given set did not fracture, the absorbed energy is recorded as 120+ lb-ft. However, if only one of the three Charpy specimens did not fracture, the average value of the two Charpy specimens that fractured during testing is recorded in the table below. Additionally, the standardized absorbed energy is also shown in the table below for each specimen. These values were calculated by multiplying the measured toughness value by the ratio of standard CVN specimen width to the actual CVN specimen width. For 7.5 mm sub-size specimens, the measured toughness values were multiplied by 1.33, while the values for the 5 mm specimens were multiplied by 1.5. This data shows that all but two of the A1085 specimens had a standardized toughness value of at least 25 lb-ft, and in only one case was the standardized toughness value significantly below 25 lb-ft. This correlation between the energy absorbed by sub-size and standard size CVN specimens may not be entirely accurate since the relationship between the sub-size and standard size CVN specimens is not linear. However, this correlation is recommended by ASTM A370 for determining the toughness criteria for various sub-size specimens.

Table 3.13. Charpy V-Notch Test Results

Test Specimen	CVN Specimen Width (mm)	Absorbed Energy (ft-lbs)	Standardized Absorbed Energy (ft-lbs)
5x5x3/8 A500 Y	7.5	12.8	17.0
5x5x3/8 A1085 Y	7.5	18.8	25.0
6x6x5/16 A500 R	5	40.8	81.6
6x6x5/16 A1085 Y	5	23.0	46.0
6x6x3/8 A500 R	7.5	42.5	56.5
6x6x3/8 A1085 Y	7.5	18.8	25.0
6x6x1/2 A500 R	10	120 +	120 +
6x6x1/2 A1085 Y	10	27.8	27.8
7x7x5/16 A500 Y	5	15.7	23.6
7x7x5/16 A1085 Y	5	18.5	27.8
7x7x3/8 A500 Y	7.5	14.3	19.0
7x7x3/8 A1085 Y	7.5	17.3	23.0
7x7x1/2 A500 B	10	42.0	42.0
7x7x1/2 A1085 Y	10	28.7	28.7
8x8x3/8 A500 W	7.5	65.5	87.1
8x8x3/8 A1085 Y	7.5	8.5	11.3
8x8x1/2 A500 W	10	67.3	67.3
8x8x1/2 A1085 Y	10	40.3	40.3
10x10x3/8 A500 W	7.5	120 +	120 +
10x10x3/8 A1085 Y	7.5	20.7	27.5
8x8x1/2 A1085 Y *C	10	89.5	89.5
8x8x1/2 A500 W *C	10	120 +	120 +

Proper calibration of the Charpy machine at the UW SRL was verified through the NIST Charpy Verification program. A set of five full-size Charpy reference specimens were ordered from NIST to be used in the self-verification of the UW Charpy machine. These specimens were cooled to a temperature of -40° F using a calcium chloride and dry ice bath, and were tested within five seconds after being removed from the cooling bath. After testing the first two specimens it was clear that the Charpy machine was not operating correctly, as the measured impact energy of the Charpy reference specimens was significantly greater than the expected value for the reference specimens provided by NIST. Per NIST, the expected absorbed energy value of the reference specimens was 14.9 J at -40° F. The Charpy machine was taken apart and

cleaned thoroughly to reduce the amount of unwanted friction in the system. The next three reference specimens were then tested, and the measured impact energy was still slightly greater than the expected value provided by NIST. It is possible that the tested reference specimens were not exactly at a temperature of -40° F when tested, which may have caused these minor differences. The results of the calibration tests are shown below in Table 3.14, including the specimen temperature and time to impact after removal from the cooling bath.

Table 3.14. Charpy V-Notch Calibration Test Results

Charpy Specimen	Temperature (°C)	Time (s)	Energy Absorbed (ft-lbs)	Energy Absorbed (J)
1	-40.1	3.8	12.7	17.2
2	-39.4	3.6	13.5	18.3
3	-40.0	4.5	13.0	17.6
4	-39.4	5.0	13.3	18.0
5	-40.8	4.4	13.0	17.6

The measured toughness for each specimen is shown below in Figure 3.7, normalized by the 25 ft-lb requirement for standard size A1085 Charpy specimens. The color scheme and format of this figure is the same as that of the previous figures presented in this section. The data shows a significant amount of variation in toughness between the A500 and A1085 specimens. Additionally, this figure shows significant variation in toughness between the different producers of the A500 steel. It is evident that the A500 specimens from Producers Red and White were significantly tougher than both the A500 and A1085 specimens from Producer Yellow. Further analysis of this data will be presented below.

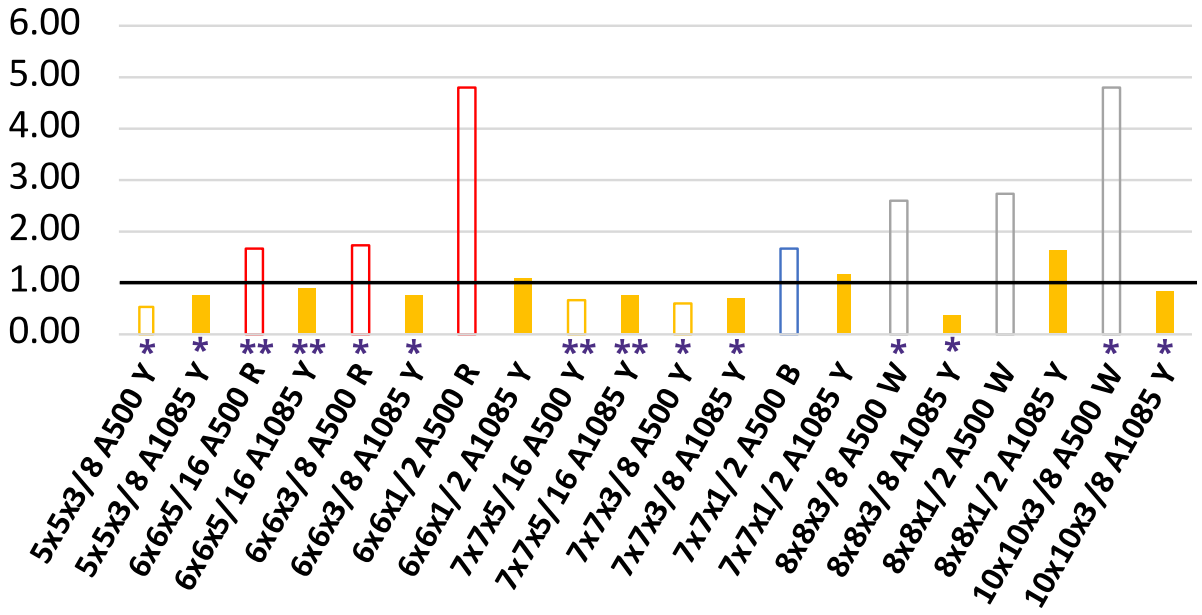

Figure 3.7. Measured CVN Toughness Normalized by A1085 Requirement

The standardized toughness values are shown below in Figure 3.8, normalized by the 25 ft-lb requirement for standard size A1085 Charpy specimens. The toughness values for the sub-size Charpy specimens were standardized following the approach discussed above. This makes it possible to compare the toughness values across the different size specimens. The standardized toughness values in the figure below also show a significant difference in toughness between the different producers. The standardized toughness values of the A1085 specimens were relatively similar across the test series, with most values slightly greater than the 25 ft-lb requirement for A1085 HSS. However, there were two cases in which the standardized toughness value was less than 25 ft-lbs. The 7x7x3/8 A1085 Y specimens had an average toughness of just under 25 ft-lbs, while the 8x8x3/8 A1085 Y specimens had an average toughness value less than half of the required toughness. However, the thickness corrections applied may not be entirely accurate, and the unmodified toughness values are discussed below.

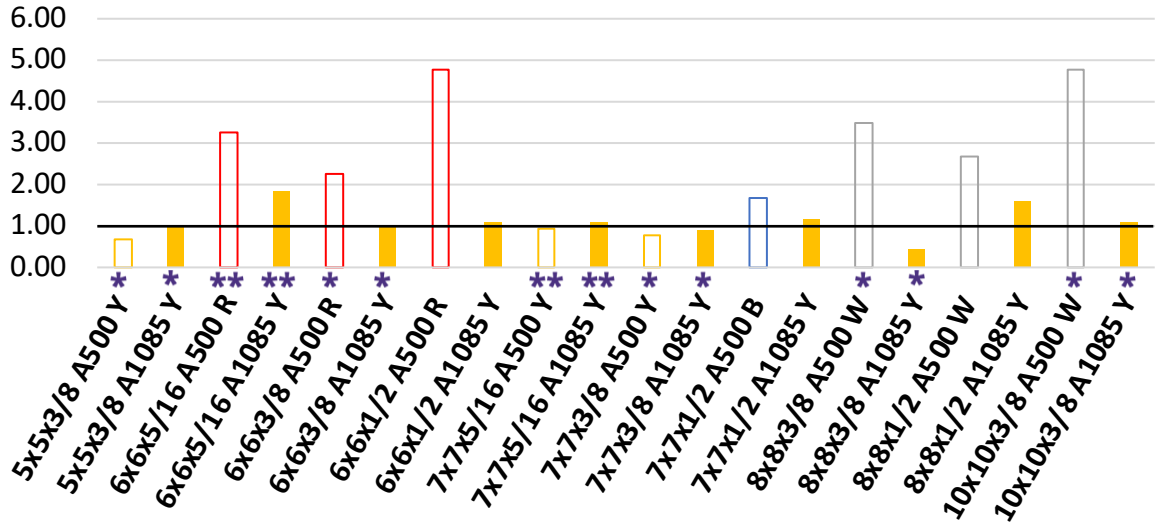

Figure 3.8. Standardized CVN Toughness Normalized by A1085 Requirement

A summary of the unmodified toughness data is shown below in Table 3.15. In this table, the data is separated by steel type, producer, and Charpy specimen size. Toughness comparisons can be made between Charpy specimens of the same size, but not between specimens of different sizes.

Table 3.15. Comparison of Charpy V-Notch Data - Unmodified

Specimen	Width (mm)	Average (ft-lbs)	Standard Deviation	# HSS Members
A1085	10	41.3	22.6	3
	7.5	16.8	4.8	5
	5	20.8	3.2	2
A500 - All	10	76.4	39.8	3
	7.5	33.8	25.2	4
	5	28.3	17.7	2
A500 Y	7.5	13.6	1.06	2
	5	15.7	-	1
A500 R	10	120+	-	1
	7.5	42.5	-	1
	5	40.8	-	1
A500 W	10	67.3	-	1
	7.5	92.8	38.5	2
A500 B	10	42.0	-	1
A500 W *C	10	120+	-	1
A1085 Y *C	10	89.5	-	1

All of the A1085 specimens in this test series were made by steel Producer Yellow. The standard size Charpy specimens from both the A500 and A1085 HSS members met the ASTM A1085 requirement of 25 ft-lbs at 40^{o} F. Producer Yellow also manufactured three of the A500 test specimens, and a set of 5 mm and two sets of 7.5 mm subsize specimens were machined from these specimens. The average toughness value of the subsize 7.5 mm A1085 Y Charpy specimens was 16.8 ft-lbs, compared with 13.6 ft-lbs for the similar A500 Y Charpy specimens. The subsize 5 mm Charpy specimens from the A1085 Y HSS had an average toughness value of 20.8 ft-lbs, compared with 15.7 ft-lbs for the similar A500 Y specimens. In both cases, the toughness values of the A1085 Charpy specimens were measured to be about 25% greater than the A500 specimens from Producer Yellow. This demonstrates a modest increase in toughness in the A1085 steel from Producer Yellow.

However, the overall average toughness values of the A500 specimens exceeded that of the A1085 specimens for the standard 10 mm, subsize 7.5 mm, and subsize 5 mm Charpy specimens. This is due to the increased toughness measured in the A500 specimens from Producers Red, White, and Blue. The overall average toughness value of the standard size A500 specimens is nearly double that of the A1085 specimens. Additionally, the measured toughness values of the 7.5 mm A500 specimens from producers Red and White were more than twice that of similar size A1085 specimens. Although the sample size of Charpy specimens from different steel producers is small, the data in Table 3.15 indicates that the A500 specimens from producers Red, White, and Blue have significantly greater toughness than the A500 and A1085 specimens from producer Yellow.

Additionally, the Charpy specimens machined from the corners of HSS members were found to have significantly greater toughness than specimens from the flat wall sections. Standard size Charpy specimens were machined from the corners of the 8x8x1/2 A500 W and 8x8x1/2 A1085 Y specimens. The average measured toughness values for these corner specimens were 120+ and 89.5 ft-lbs, respectively. The toughness values of the standard size Charpy specimens from the flat walls of the same members were found to be 67.3 ft-lbs and 40.3 ft-lbs, respectively. In both cases, the measured toughness values of the corner Charpy specimens were about twice that of the specimens from the flat wall sections.

3.3.3 *Summary of Test Specimen Properties*

The measured test specimen properties discussed in the previous sections indicate that the differences between the A500 and A1085 test specimens are relatively minor. Measurements of test specimen geometry showed that the walls of the A500 specimens were slightly thinner than the A1085 specimens, but were typically within about 5% of the thickness of walls of the A1085 tubes. Additionally, several of the A500 specimens met the wall thickness requirements for A1085 HSS, and most of the A500 specimens were within 3% of the tube thickness requirement. Further evaluation of the geometric properties showed that the measured width-to-thickness ratios of all of the specimens were less than their respective nominal b/t ratios. The difference between the measured and nominal width-to-thickness ratios was slightly greater for the A500 specimens, thereby reducing the actual difference in cross-sectional compactness between the A500 and A1085 specimens of the same size.

The results of the tensile tests indicated that the yield and ultimate strengths were nearly identical between the A500 and A1085 specimens, although there was some slight variation between the producers of the A500 specimens. Additionally, Charpy V-Notch testing showed that all of the standard size A500 and A1085 Charpy specimens met the toughness requirements of the A1085 specification. The A1085 specimens from Producer Yellow were found to be slightly tougher than the A500 specimens from the same producer. However, the A500 specimens from the other producers had significantly greater toughness than the A1085 specimens. In general, the measured geometric and material properties of the A500 and A1085 specimens were quite similar across the entire test series.

3.4 LOADING PROTOCOL

Quasi-Static cyclic displacements were applied to the test specimens using the two high capacity hydraulic actuators attached to the sliding beam. The full displacement profile applied to each test specimen is shown below in Figure 3.9. The actuators were controlled using MTS MultiPurpose Testware (MPT) Software, and were programmed to run under displacement control. The actuators applied identical displacements to the ends of the sliding beam, loading the test specimen evenly without applying any end rotation. Prior to running the full loading protocol, two cycles of ±1/16" displacements were applied to the test specimen. These small cycles were used to check that the instrumentation was functioning properly, and ensure that everything was in place to run the full procedure.

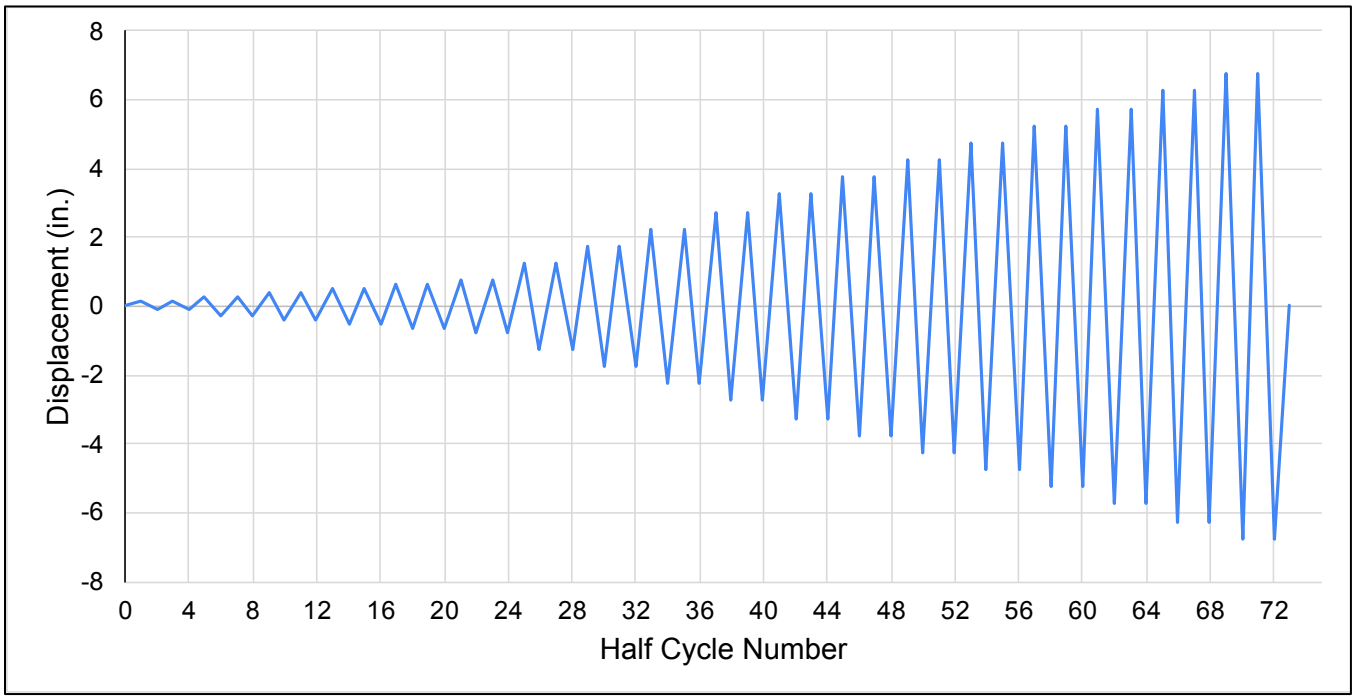

Figure 3.9. Applied Displacement Protocol

In the full displacement procedure, cyclic displacements of increasing magnitude were applied until the test specimen fractured. In each cycle, the test specimen was first pushed to a positive target displacement by using the actuators to push out onto the sliding beam, putting the specimen into tension. After the actuators reached their positive target displacement, the loading was reversed and the specimen was then put into compression. The actuators pulled the sliding

beam to reach the compressive target displacement of the same magnitude. The actuators applied two full cycles at each target displacement, which made it possible to observe the cyclic strength degradation in the specimens. In most cases the test specimens fractured prior to reaching the maximum displacement shown in the profile. The same displacement profile was applied to each of the test specimens up until the point of fracture.

For the first six target displacements, the targets were set to increase in 1/8" increments from 0.125" to 0.75". These relatively small target displacements and increments made it possible to capture the buckling and yielding behavior of the test specimens. The predicted buckling displacements were calculated for each of the test specimens based on the expected axial compressive strength, and ranged from 0.11" to 0.39". Additionally, the yield displacement, Δ_y, for each specimen was calculated to be around 0.5". Although the brace axial displacement was slightly different than the applied actuator displacement due to gusset plate deformation, bending in the sliding beam, and bolt slip, these first six target displacements were generally able to capture the initial buckling and yielding behavior of the test specimens. Beyond the 0.75" target displacement cycles, the target displacements were increased in increments of Δ_y (0.50"). These increasing cyclic displacements were applied up until the point of brace fracture. The design of the test displacement protocol was based on previous work at the UW SRL as well as other recommendations for cyclic testing of steel components. (ATC, 1992, Krawinkler, 2009)

3.5 PRE-TESTING PROCEDURE

An organized procedure was followed to efficiently prepare the specimens for testing. First, the 40' tube sections were cut down to 237.5" using a plasma cutter. The plasma cutter was then used to cut slots into both ends of the tube, to allow for the gusset plates to be attached. Next, the gusset and shim plates corresponding to the specimen were bolted into the steel connection plates at both ends of the test frame. The steel tube was then moved into the test frame using the overhead crane to lower the specimen into the correct position with the gusset plates through the slots. Wood blocks were used to keep the HSS member in the correct vertical position, centered on the gusset plates. The tube was shifted longitudinally using the crane and

other methods to provide the correct gusset plate clearance at the south end of the test frame (3 times the thickness of the gusset plate).

It was critical to have the test specimen in just the right position, since the gusset plates were designed with just a 1/8" tolerance in the connection plates. The test frame was used as a jig for the test specimen, making it possible to tack weld the HSS member and gusset plates to keep them in the right place before they could be fully welded. First, the south gusset plate was tack welded to the steel tube once the correct position was verified. Shim plates were used as necessary to keep the gusset plates centered on the slots. Next, the actuators were used to move the sliding beam and north gusset plate into the correct position at the north end of the test frame, sliding the gusset plate through the slot until the proper clearance was achieved. The north gusset plate was then tack welded to the tube, and the specimen was removed from the test frame. The tack welds held the gusset plates in the correct position for testing until a certified welder could fully weld the gusset plates to the steel tube. The net section reinforcement plates were also tack welded to the sides of the test specimens to hold them in position until they could be fully welded. Figure 3.10 below shows a test specimen in place before and after being welded.

Once the specimen was fully welded, strain gauges were attached to all four faces of the specimen at both quarter points as described in Section 3.7.3. The specimen was then moved back into place in the test frame. At both the north and south connection plates, twelve 1" diameter A490 bolts were used to connect the specimen to the test frame. These bolts were tightened using a hydraulic torque wrench until the load indicating washers showed that the correct bolt tension was achieved by squirting out orange epoxy. The strain gauges were connected to the data acquisition system, and all of the instruments described in Section 3.7 below were attached to the specimen and test frame. Four digital cameras were placed around the test frame to record the test from different angles. A camera was placed at both the north and south gusset plates, documenting the bending of the gusset plates as well as bolt slip. A vertical line was drawn on the gusset plate using white-out at the edge of the connection plate, which was useful for observing the magnitude of the bolt slippage. One camera was placed on the east actuator reaction block focused on the center of the test specimen to observe local buckling effects, tearing, and out of plane displacement. Another camera placed atop the end reaction block showed a view of the entire specimen throughout the test. Photographs were taken simultaneously on all four cameras set up around the test specimen by connecting each camera to

a remote trigger. During testing, pictures were generally taken every 5 seconds, with increased frequency towards the end of each test as the specimen began to tear and eventually fractured. A mobile camera was also used to capture different views of the specimen, such as close-up images of the local deformations.

(a) (b)

Figure 3.10. Test Specimen Prior to Welding (a) and Fully Welded (b)

3.6 TEST SETUP DESIGN

3.6.1 *Overall Layout*

This section will describe the layout of the setup used for the experiments, and will also provide details regarding each of the test frame components. The test frame shown below in Figure 3.11 and Figure 3.12 was designed to fit within the constraints of the strong floor of the UW SRL, while also being compatible with the available equipment and machinery in the lab.

The geometry and location of the test frame on the strong floor were carefully considered in order to develop a test setup that would maximize the use of space on the strong floor, and would also be flexible enough to test braces of varying lengths and sizes. Two hydraulic actuators were located on the east side of the strong floor, oriented in the north-south direction parallel to the test specimens. This configuration made it possible to test braces with varying lengths, while also providing adequate space for the specimens to buckle horizontally. It was necessary to develop a test frame compatible with a wide range of HSS shapes that could be modified to accommodate various brace lengths to study the effects of brace compactness and slenderness. Note that Figure 3.11 and Figure 3.12 below show the layout of the test frame on the strong floor for 237.5" and 165.5" test specimens, respectively.

The capacity of the test frame was designed based on the potential actuator force. The two large hydraulic actuators used in this setup were capable of applying forces up to 1000 kips in tension and 700 kips in compression, and thus all components of the test frame were designed to withstand the maximum applied force. The actuators operated under displacement control, and applied cyclic displacements to the test specimen by pushing and pulling on the sliding beam at the north end of the test frame. The brace test specimens were bolted to a connection plate on the sliding beam, which slides back and forth on PTFE sliding surfaces to apply displacements to the test specimens. The actuators were mounted to concrete reaction blocks that resisted the horizontal loads applied by the actuators. On the south end of the test frame, a steel connection plate was bolted to the other end of the specimens, holding the south end of the test specimen in place. These connection plates were anchored to a large reaction block fixed to the strong floor to resist the applied forces.

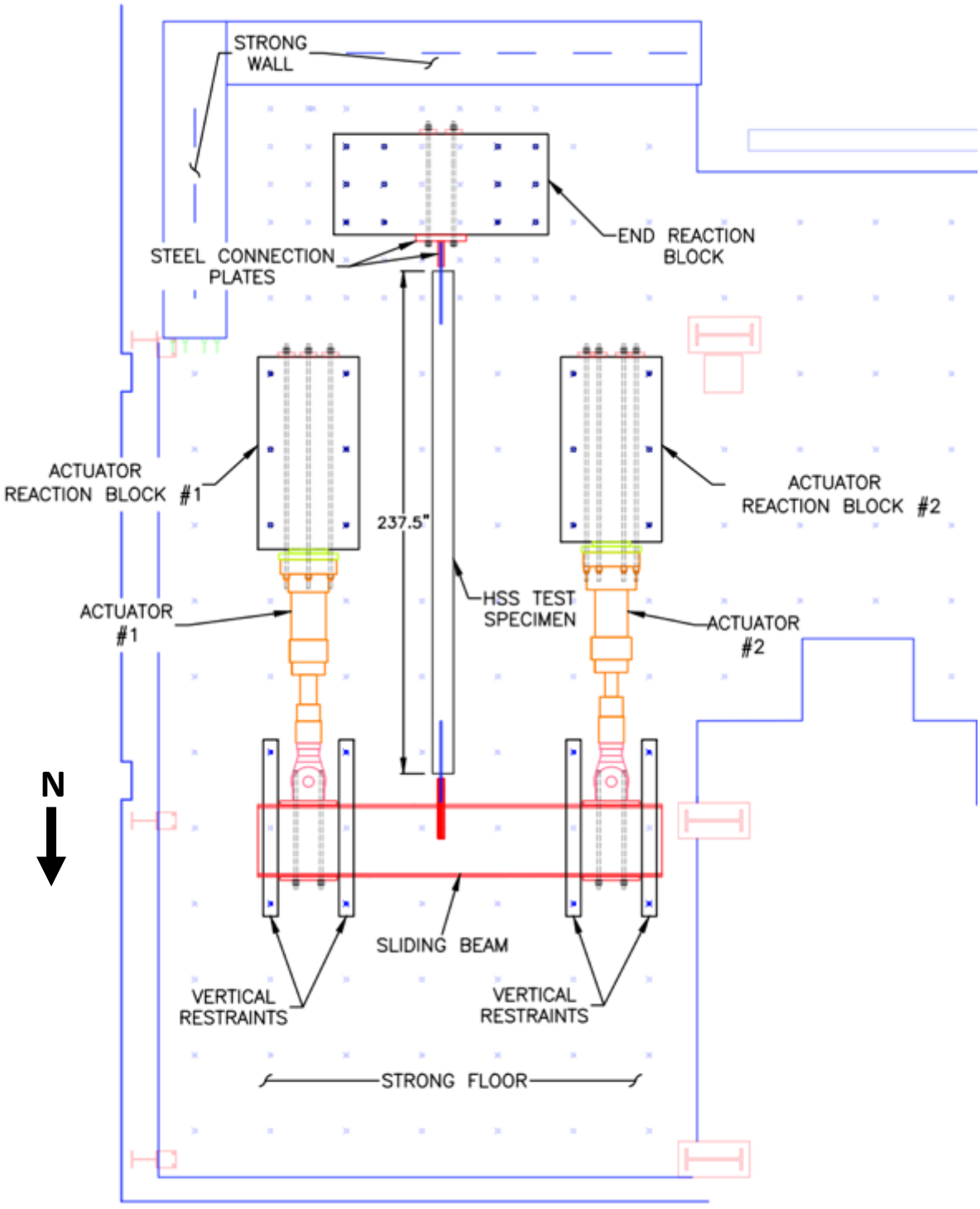

Figure 3.11. Overview of Test Frame for 237.5" Specimens

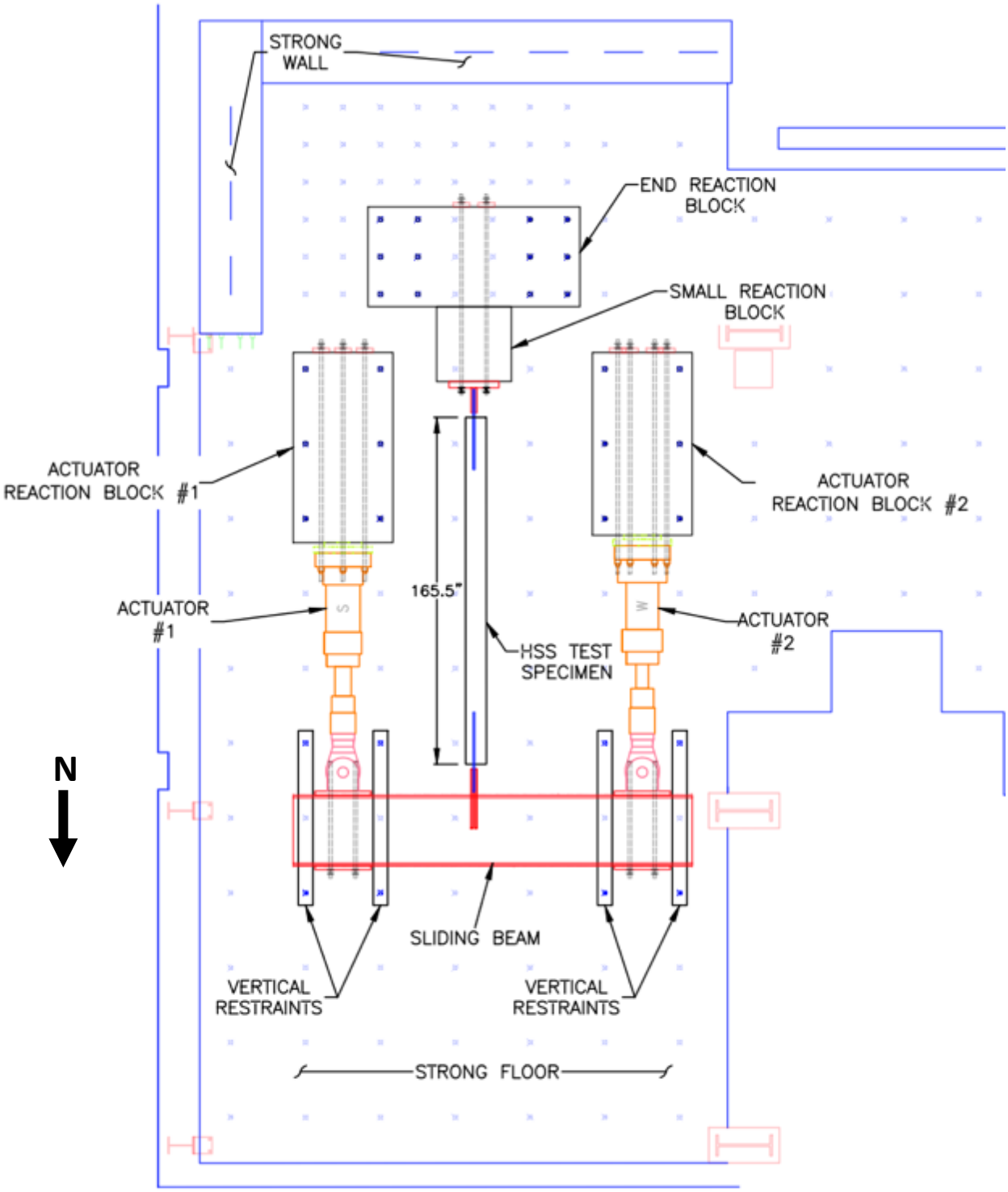

Figure 3.12. Overview of Test Frame for 165.5" Specimens

In this test series, the brace specimens were cut to 237.5” in length and varied in size from 5x5x3/8 to 10x10x3/8. This is the maximum brace length that can be tested in the test frame, due to the geometry of the strong floor, test frame, and actuator range of motion. The geometry of the test specimens in this series is shown in Figure 3.1. Only the results of specimens tested during test series 1 will be presented in this thesis. Other tests will be performed using alternative test frame configurations. The test frame accommodates specimens ranging in length from 165.5” to 237.5” by changing the position of the end reaction block and using an additional 36” long reaction block.

Additionally, the test frame was designed to accommodate the full range of motion of the actuators, allowing for displacements of 10” in both tension and compression. The adaptable design of the test frame made it possible to evaluate the effects of brace compactness and slenderness while also studying and comparing the results of the A500 and A1085 test specimens. The location and orientation of the test frame on the strong floor was constrained by the geometry of the vertical tie down locations, as well as the availability of materials and equipment in the lab. After considering several options, it was decided that the test specimens would be oriented in the north-south direction on the east side of the strong floor, as shown in Figure 3.13 below. This position maximized the length of components that could be tested in the frame, while also allowing for flexibility in the length of braces being tested.

Figure 3.13. Orientation of Test Frame and Specimen on Strong Floor

The end reaction block was placed on the south side of the strong floor to take advantage of the higher density of anchor locations, since this block was required to resist the combined horizontal forces of both hydraulic actuators, up to 1000 kips. The location of the block is shown in Figure 3.14 and Figure 3.15 below. This block was prestressed to the strong floor with twelve 1-3/4" diameter 150 ksi threaded bars to provide adequate frictional resistance. At the south side of the strong floor near the strong wall, the vertical tie down holes were spaced at 18", but were spaced at 36" elsewhere on the floor. Placing the end block at the south side of the floor allowed for greater flexibility in future tests, making it possible to move the blocks in increments of 18" rather than 36".

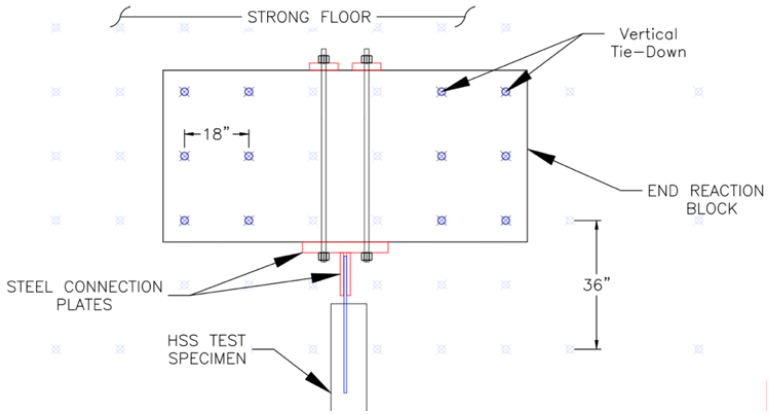

Figure 3.14. Layout of South End of Test Frame

(a) (b)

Figure 3.15. End Reaction Block – Before (a) and After (b) Being Moved Into Place

3.6.2 *Horizontal Loading System*

Two high capacity hydraulic actuators were used in parallel to apply a horizontal force of up to 1000 kips to the test specimens. The actuators and actuator reaction blocks were spaced 12' apart on center and oriented in the north-south direction. Figure 3.16 below shows the layout of the actuators and sliding beam. The actuator spacing was designed such that the actuator reaction blocks would be compatible with the vertical tie down holes, while also providing adequate clearance for the expected horizontal buckling of the test specimens. Early in the design process, it was decided that the buckling of the braces should be controlled so that they buckle horizontally to prevent them from buckling downwards into the strong floor.

Figure 3.16. Orientation of Actuators and Sliding Beam

At a pressure of 3000 psi, the larger of the two actuators had a capacity of about 450 kips in compression and 375 kips in tension, while the less powerful actuator had a capacity of about 350 kips in compression and 275 kips in tension. However, in order to test the largest test specimens, it was necessary to increase the hydraulic pump pressure above 3000 psi to achieve a total horizontal force of nearly 1000 kips. Figure 3.17 below shows the geometry of the actuators and sliding beam at the north end of the strong floor. Due to the difference in capacity between the two actuators, it was necessary to space the actuators asymmetrically about the test specimen to use the full capacity of each actuator. Therefore, the more powerful actuator was spaced 63"

horizontally away from the center of the specimen, while the weaker actuator was spaced 81" from the specimen. This spacing matches the 9:7 capacity ratio of the actuators, making it possible to use the full capacity of each actuator while applying identical displacements to both sides of the sliding beam. This ensured that the horizontal force was applied entirely in the longitudinal direction of the test specimen, preventing the sliding beam from rotating at the point of connection to the test specimen. A concrete-filled built up steel sliding beam at the north end of the test frame was connected to the actuators at its ends, and was bolted to the test specimens near its center. As the actuators pushed and pulled on the sliding beam, the forces were transferred to the test specimen. The sliding beam was supported by a series of four vertical constraints, which provided a sliding surface for the beam while also preventing vertical movement. The design of the test frame components will be discussed in further detail below.

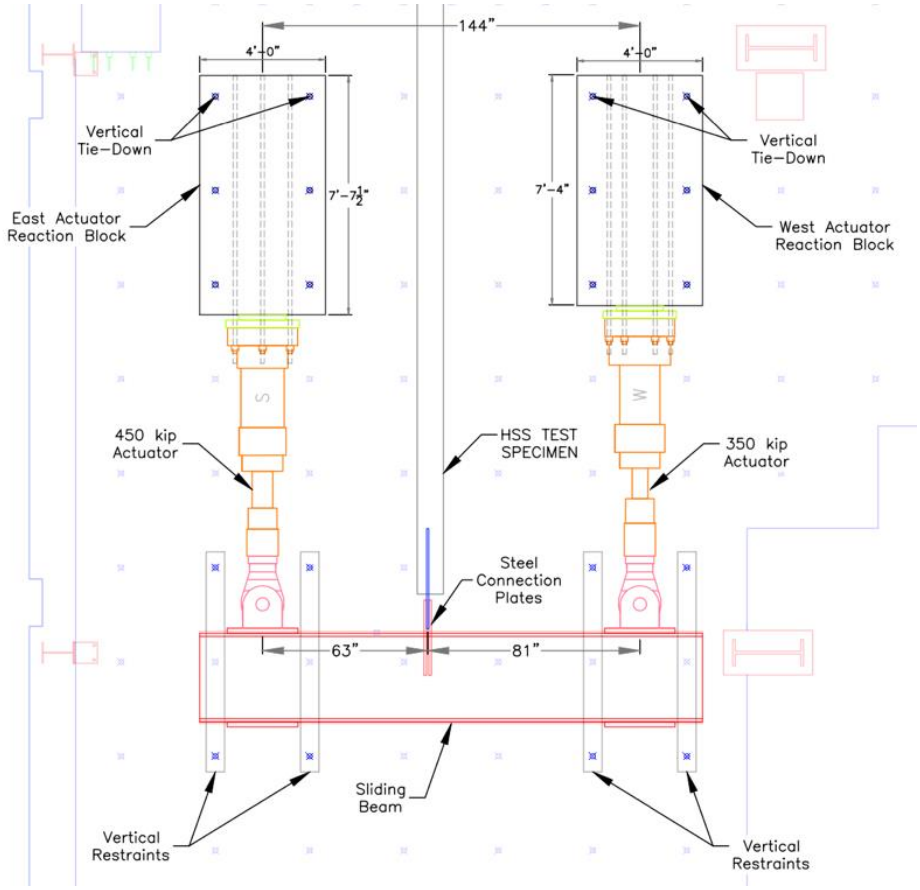

Figure 3.17. Layout of Actuators and Sliding Beam

The off-center positioning of the actuators on the sliding beam was designed so that the test specimens would be centered on the end reaction block. This prevented the reaction block from twisting or rotating when loaded. Each actuator was anchored to a concrete reaction block using six 1-1/4" diameter 150 ksi threaded bars post-tensioned to 100 kips each, for a total lateral prestressing force of 600 kips per actuator. The threaded bars were placed through open conduits at the bases of the actuators and through the reaction blocks, prestressed to the specified force, and bolted to both ends of the blocks. This prevented the actuators from moving or slipping off the reaction blocks when in tension and prevented fatigue loading of the threaded bars. The reaction block used for the actuator on the west side of the test frame was constructed prior to this project, and had been used in previous experiments. The center of the conduits and actuator on this existing reaction block was about 26" above the strong floor, and in order to reuse this block, it was decided that the rest of the test frame would be designed to match this height.

Two 3" thick steel actuator base plates were produced by Custom Steel Fabricators Inc., each with two different bolt hole patterns matching the openings of the adaptor plates at the base of each actuator. The dimensions of these base plates are shown below in Figure 3.18, while Figure 3.19 shows the layout of the actuator assembly. These base plates were designed to accommodate the 1-1/4" diameter 150 ksi threaded bars and provide a solid bearing surface behind each actuator. A circular 2" thick elastomeric cotton duct pad was placed behind each actuator between the base plate and reaction block to accommodate small actuator rotations relative to the reaction block. Additionally, the actuator swivel heads were oriented horizontally along the sliding beam in the east-west direction to allow for small rotations of the sliding beam when loaded by the actuators.

The actuator reaction blocks were anchored to the strong floor using six 1-3/4" diameter 150 ksi threaded bars. These bars were post-tensioned to 200 kips each, providing a total of 1200 kips of tie-down force to each block. Based on a coefficient of static friction of 0.40, these threaded bars provide the reaction blocks with nearly 500 kips of slip resistance each. Before post-tensioning the reaction blocks to the floor, the blocks were lifted and a layer of hydrostone was poured beneath. The hydrostone provides a smooth, flat contact surface beneath the reaction blocks to improve the connection between the blocks and strong floor. Drawings of the actuator reaction blocks can be found in Appendix 1.

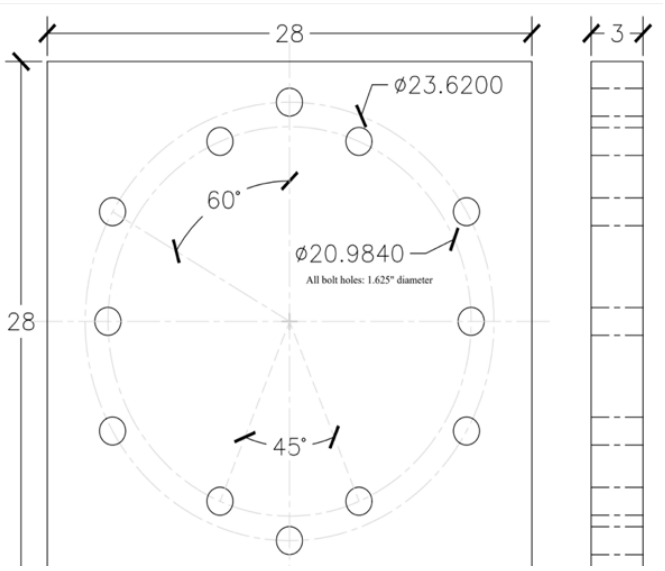

Figure 3.18. Actuator Base Plate Design

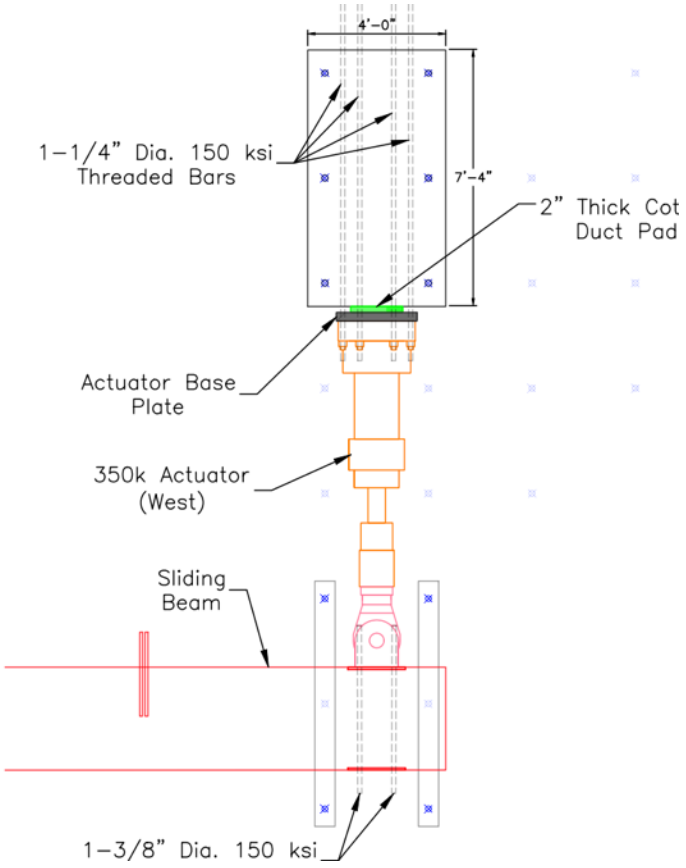

Figure 3.19. Actuator Assembly and Connections

3.6.3 *Sliding Beam Design*

The sliding beam was used to transfer the applied displacements from the actuators to the test specimen. Therefore, the sliding beam was required to be very stiff to prevent it from bending significantly under large forces, which would reduce the axial displacements ultimately transmitted to the test specimens. The design of the sliding beam was influenced by the geometry of the test frame and strong floor, as well as the requirements for the test specimens. The beam was comprised of a 16' long W33x201 beam with 3/4" thick steel plates welded to its flanges, creating a box section as shown in Figure 3.20 below.

Early in the design process, it was decided that it would be more efficient to fabricate a built-up sliding beam section rather than use a very large, singular I-beam. Designing a built-up section allowed for the use of a W33x201 beam rather than a significantly deeper and heavier beam, which would make it more difficult to accommodate the full actuator displacements. A built-up concrete filled steel beam was selected to maximize strength and stiffness while minimizing beam depth. This relatively stiff sliding beam ensured that the displacements applied by the actuators were nearly identical to the displacement of the test specimens, although there was some difference due to the bending of the beam, deformation of the connection plates, and slight movement of the reaction blocks.

Based on the 1000 kip maximum potential horizontal force applied by the actuators to the sliding beam, the maximum possible bending moment in the sliding beam was 2835 kip-ft. Additionally, the maximum shear force that can be applied using the actuators was 540 kips. The original, unmodified A992 W33x201 beam had a nominal yield moment M_n of 2858 kip-ft and a nominal shear strength V_n of 723 kips. With the addition of the A572 Gr. 50 3/4" thick steel plates, as well as filling the section with concrete, the shear and moment capacity of the sliding beam significantly exceeded the demands. The 3/4" thick steel plates were welded to the flanges of the W33x201 section along the entire length of the sliding beam with a 1/2" fillet weld. This weld was designed to withstand the shear flow resulting from a 1000 kip horizontal force. Detailed calculations for the sliding beam can be found in Appendix 2.

Prior to being moved into place, the beam was moved into a vertical position and filled with concrete to provide additional strength and stiffness. PVC pipes were placed through the holes in the flanges before the beam was filled with concrete to provide clear conduits for the threaded bars. Additionally, four 3/4" thick steel plates were welded to the north and south faces

of the sliding beam flanges where the actuators connect to the beam. These bearing plates reduced the stress concentrations in the sliding beam by spreading the prestressing forces over a larger area. The sliding beam was significantly over-designed for the maximum actuator force of 1000 kips to ensure that the beam would be durable, rigid, and capable of withstanding the large number of load cycles applied during the tests. Figure 3.21 provides detailed dimensions for the geometry of the sliding beam and connection plates, as well as the sizes and locations of the welds. The web of the beam and steel plates were oriented to be parallel with the strong floor, and were capable of resisting the bending moment and shear force created when the actuators push and pull on the test specimens. Four 1-9/16” diameter holes were drilled through both flanges on the east and west ends of the beam so that the actuators could be attached to the sliding beam using 1-3/8” diameter 150 ksi threaded bars.

(a) (b)

Figure 3.20. Sliding Beam - Original (a) and In Upright Position (b)

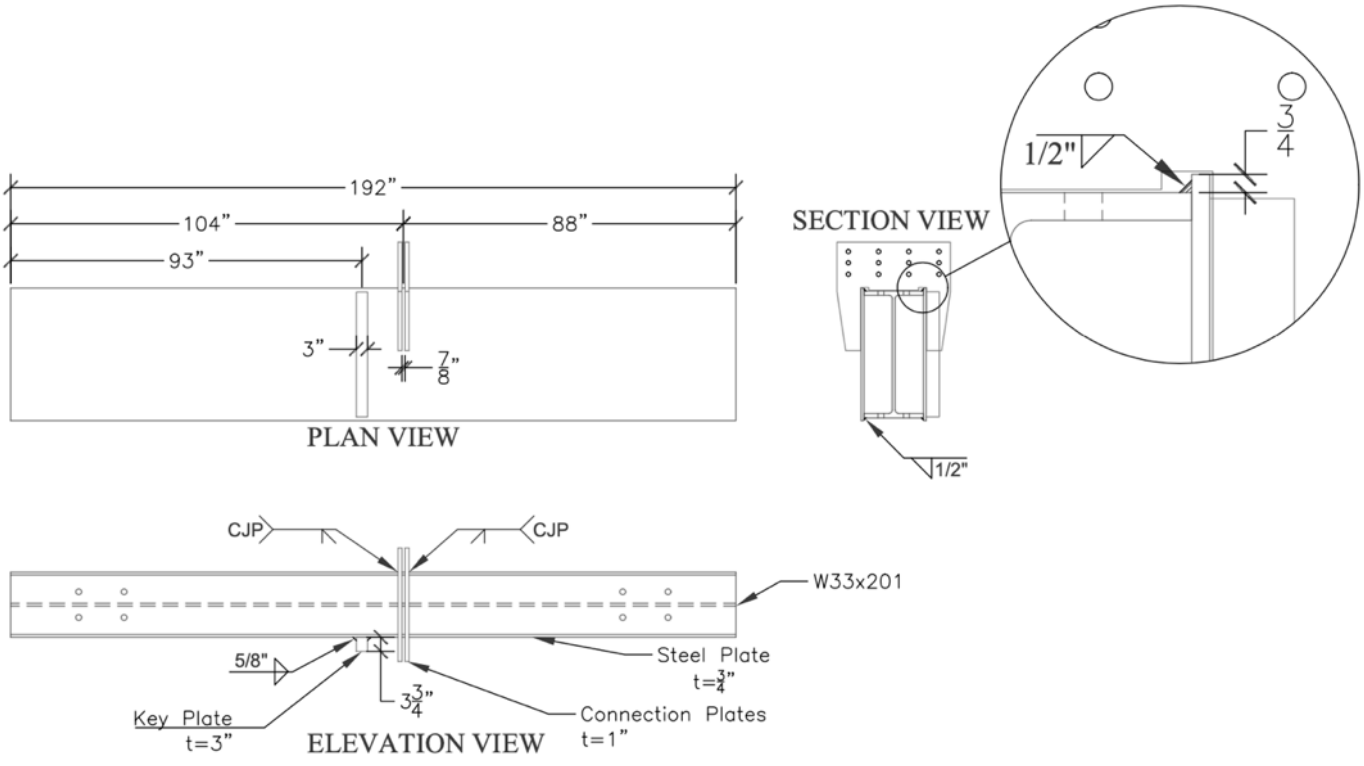

Figure 3.21. Sliding Beam Dimensions

The vertical movement of the sliding beam was resisted by a series of four vertical restraints, as shown below in Figure 3.22. These vertical restraints also functioned as sliding surfaces for both the top and bottom surfaces of the sliding beam. A 4x4x3/8 HSS provided the bottom sliding surface for the beam, and was welded to the top of a 14" deep I-Beam. The bottom supports were anchored to the strong floor using 1" diameter threaded rods. The bottom side of a 6x6x1/4 HSS provided the top sliding surface for the sliding beam. The top and bottom sliding surfaces were connected using 1" diameter threaded rods through 1-1/4" diameter holes cut through the top flange of the bottom I-beam, bottom HSS, and top HSS spaced 84" apart. This increased spacing ensured that the actuators could apply their full range of motion, and provided additional flexibility in the test frame.

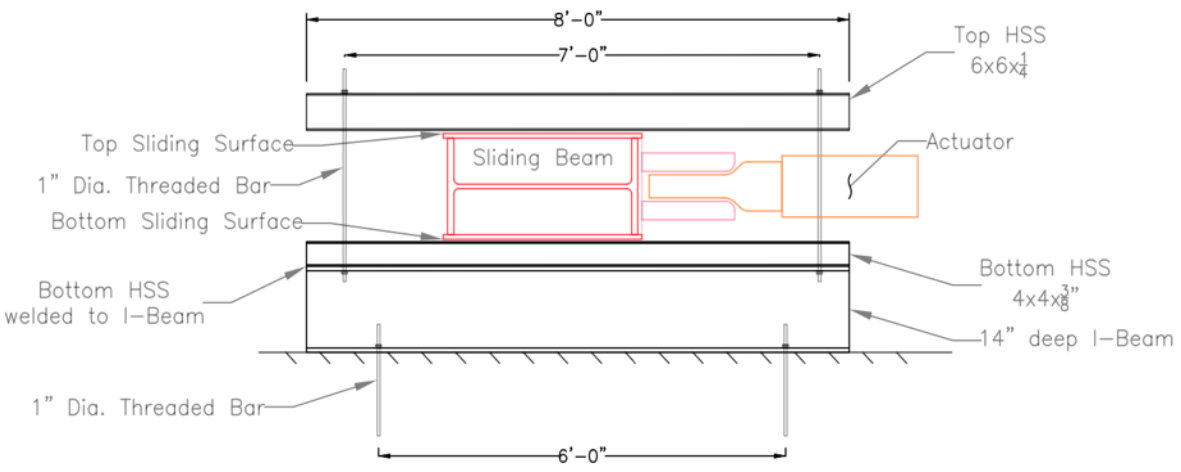

Figure 3.22. Cross-Sectional View of Sliding Beam and Vertical Restraint System

Polytetrafluoroethylene (PTFE), stainless steel, and grease were used to provide a nearly frictionless sliding surface in the locations where the sliding beam was in contact with the vertical restraints. PTFE strips were adhered to the top and bottom faces of the HSS at points of contact with the sliding beam. Strips of stainless steel were tack welded to the top and bottom surfaces of the sliding beam in contact with the HSS. The sliding surface design was based on previous experiments carried out in the UW Structural Research Lab. This sliding surface minimized the frictional resistance between the sliding beam and vertical restraints, making it possible to apply nearly all of the horizontal forces directly to the test specimens. By pushing and pulling on the sliding beam with no specimen in place, it was determined that the frictional resistance of the sliding surface was less than 1000 lbs.

The potential for unwanted lateral movement in the sliding beam was mitigated through the addition of a key and keyway system as shown in Figure 3.23 below. A 3" thick, 3.5" deep, and 33.375" long rectangular plate function as the "key" in the system. This plate was welded to the bottom cover plate of the sliding beam with a 1/2" fillet weld, and was oriented in the north-south direction. To form the keyway, a 4" thick Gr. A36 steel trapezoidal plate was welded to a 3" thick Gr. A36 steel floor plate. This plate was anchored to the strong floor using four 1-3/4"

diameter 150 ksi threaded bars prestressed to 200 kips each. The keyway plate was welded to the floor plate with a 5/16” fillet weld around the perimeter of the base of the keyway plate. As the sliding beam moved north and south, there was about 3/8” of clearance between the east and west sides of the key plate and keyway, preventing unwanted sliding resistance. However, if the sliding beam was subjected to significant lateral forces and moved in the east-west direction, the key plate would make contact with the keyway to prevent significant lateral displacements. The fillet weld around the base of the keyway plate was designed to resist the maximum expected lateral force applied by the actuators if unwanted lateral movement occurred in the sliding beam. Calculations for the design of the key and keyway system are included in Appendix 2.

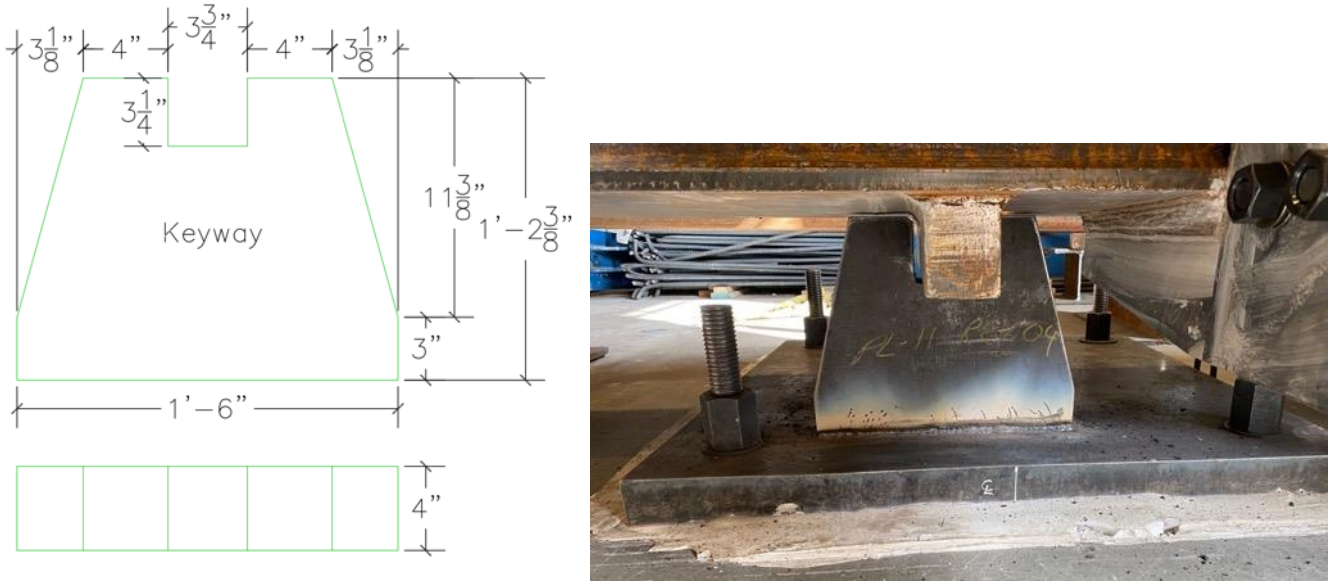

(a) (b)

Figure 3.23. Keyway Plate Dimensions (a) and Keyway Plate Welded in Place (b)

Two 1” thick steel plates welded to the sliding beam were used to connect the sliding beam to the test specimens at the north end of the test frame. Drawings of these connection plates are provided below in Figure 3.24. These plates were welded to the sliding beam with 1” CJP welds along the top and bottom plates and front face of the sliding beam. The connection plates extend 17” along the top and bottom plates of the sliding beam to provide additional connection strength and distribute the forces over a greater area. The connection plates were spaced with a 7/8” gap between the plates to allow the gusset plates of the test specimens to easily slide in between. A pattern of twelve 1-1/8” diameter bolt holes were drilled through each of the

connection plates, matching the bolt hole pattern of the gusset plates at the brace ends. These plates were designed to be significantly stronger than the gusset plates of the test specimens to prevent the connection plates from being damaged during testing. The maximum gusset plate thickness is 3/4", and thus any bearing deformations were isolated to the gusset plates rather than the connection plates. Instead of being centered on the sliding beam between the two actuators, the connection plates were offset from the center by 9" towards the east. This was done to account for the difference in the capacity of the actuators, allowing each actuator to push and pull at its full capacity without causing any twisting in the sliding beam or specimen.

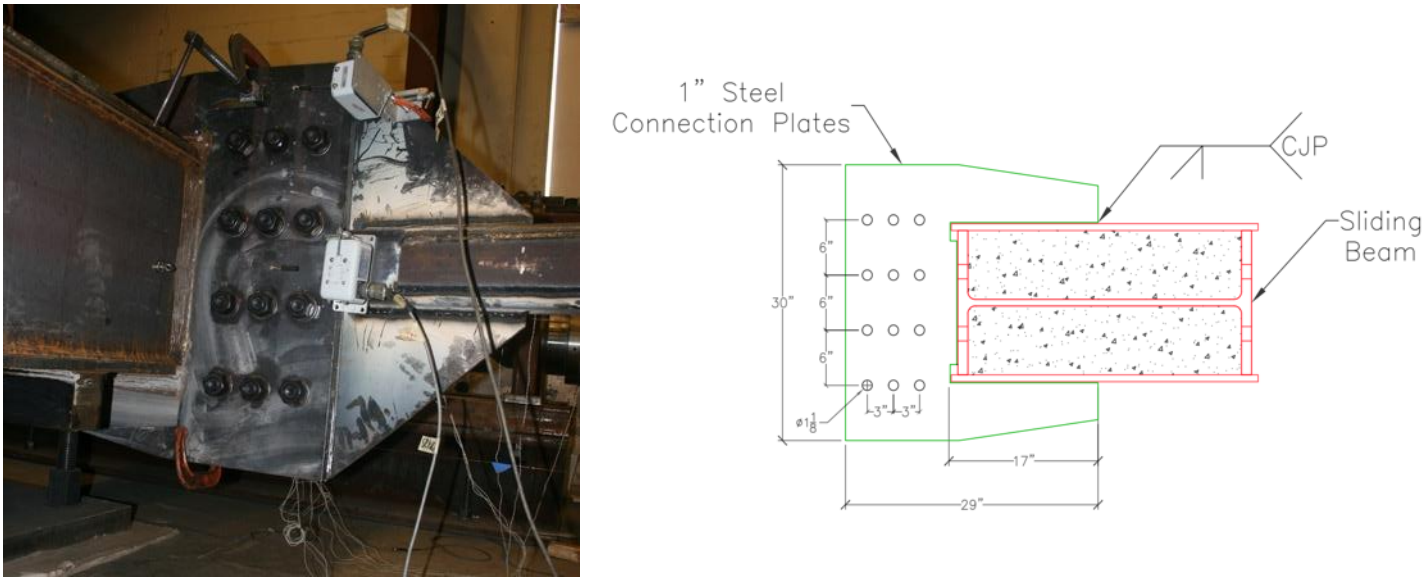

(a) (b)

Figure 3.24. Sliding Beam Connection Plate - During Testing (a) and Elevation (b)

3.6.4 *End Connection Plate and Reaction Block Design*

Two 1" thick steel connection plates were also used at the south end of the test frame to connect the test specimens to the end reaction block. These connection plates were also spaced with a 7/8" gap to allow the gusset plates of the test specimens to be bolted into place. The bolt hole pattern of the south connection plates was identical to the north connection plates and gusset

plates of the specimens. 1” CJP welds along the length of the connection plates were used to fasten the plates to a 3” thick, 24” by 30” plate attached to the north face of the end reaction block. This thick plate was used to distribute the forces over a larger area, and was anchored to the end reaction block using eight 1-3/8” diameter 150 ksi threaded bars. The hole pattern through the 3” steel plate was designed to make it easy to access and tighten the bolts connecting the gusset plates of the specimens to the connection plates. An Abaqus finite element model was created to analyze the stress distribution in the steel plate connected to the face of the end reaction block. The results of this Abaqus model are displayed in Figure 3.25. A linear load with a total tensile force of 1000 kips was applied along the vertical centerline of the plate, and it was determined that the stress in a 3” thick steel would be significantly less than the expected yield stress of the plate.

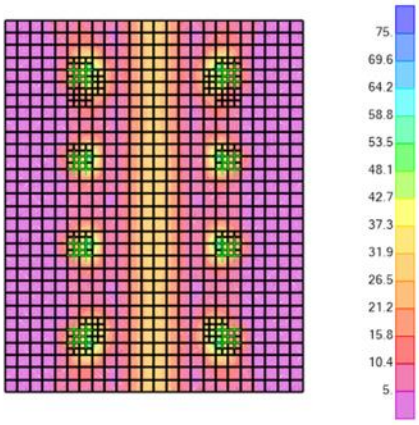

Figure 3.25. Abaqus Model of End Connection Plate

Anchoring the plate to the reaction block minimized the movement of the test specimens at the south end of the test frame, ensuring that the cyclic displacements were applied directly to the test specimens. The geometry of the end connection plate is shown in Figure 3.26. The threaded bars were prestressed to 180 kips each, for a total pre-tension force of 1440 kips. Prestressing the bars prevented the bars from becoming fatigued or yielding during testing, so that the same bars could be used in many tests before being replaced. The prestressing force of 1440 kips exceeded the maximum design lateral force of 1000 kips, preventing the south connection plates from shifting when the test specimens were put into tension.

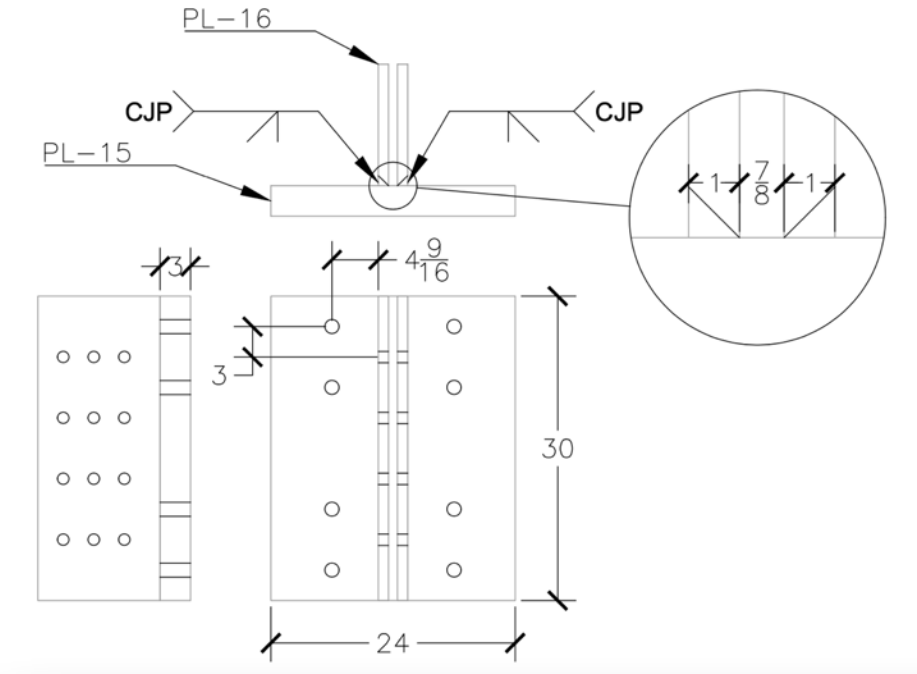

Figure 3.26. End Connection Plate Details

The concrete reaction block at the south end of the test frame was designed to resist the combined forces of the actuators, and was anchored to the strong floor using 12 1-3/4" diameter 150 ksi threaded bars. This block was oriented in the east-west direction, with the end connection plate fastened to the north face at the center of the block. The anchoring bars were prestressed to 200 kips each, and with a coefficient of friction of 0.4 provided nearly 1000 kips of slip resistance. The 12 vertical tie downs were located at the east and west ends of the block, in two rows of three tie downs at each end. Prior to being prestressed to the strong floor, this block was lifted and a layer of hydrostone was poured beneath the block to provide a uniform bearing surface to maximize its slip resistance. Due to the significant horizontal forces applied at the center of the reaction block, the design of the steel reinforcement was carefully considered to ensure that the block would not fail due to the high bending and shear stresses. Detailed drawings of the reaction blocks and rebar layout can be found in Appendix 1.

A smaller concrete reaction block was also designed and built in order to make the test frame flexible enough to test specimens with varying lengths. This smaller block was 36" wide by 36" long, with a height of 41", matching that of the larger end reaction block. Eight conduits

from the front to the back of the block were created using PVC pipes, and these ducts allowed the steel connection plate to be attached to the north face of the block using another set of 1-3/8" diameter 150 ksi threaded bars. When placed in front of the large end reaction block, this smaller block reduced the brace span by 3'. In order to achieve a 6' reduction in brace length, the large end block must be moved 36" north and anchored to the strong floor. The smaller block could then be placed directly in front of the end block. The steel connection plate could be attached to north face of the smaller block, with the blocks connected using a set of 1-3/8" diameter 150 ksi prestressed threaded bars.

The location and orientation of these blocks on the strong floor maximized the flexibility of the test frame by taking advantage of the higher density of anchor locations at the south end of the strong floor. Since the large end reaction block must remain on the section of the strong floor with the 18" tie down spacing, the smaller block is necessary to bridge the gap between the anchor locations and the shorter braces. In order to test 20', 17', or 14' long test specimens, the large end reaction block only needs to be moved once, and the small end reaction block can quickly be moved into place. This makes it relatively easy to modify the test frame to accommodate braces of varying lengths.

3.7 TEST INSTRUMENTATION

An assortment of instruments were utilized to capture the loads, strains, displacements, and deformations during the tests to accurately measure the behavior of the test specimens. LabVIEW software from National Instruments was used to collect data from the potentiometers and strain gauges. Sections 3.7.2 and 3.7.3 below describe the potentiometers and strain gauges used in the tests. Additionally, Optotrak sensors connected to NDI First Principles software provided accurate displacement readings throughout the experiments, which is described below in Section 3.7.4. The arrangement of instrumentation used to measure the performance of the test specimens was identical between the different specimens. All potentiometers and strain gauges were calibrated prior to testing.

3.7.1 *Actuators – Load Cell and LVDT*

The two hydraulic actuators that applied cyclic loads to the test specimens also provided force and displacement data through internal load cells and LVDTs. As described in previous sections, the actuators acted in parallel to apply equal displacements to both ends of the sliding beam to load the test specimens. The load cells were used to determine the total axial forces applied to the specimens throughout the tests. The load cell and LVDT data was also used to make sure the actuators were running properly, since it was easy to check to make sure that the actuator displacements were equal throughout the tests, and also that the actuator capacity ratio (9:7) was maintained during testing. The offset geometry of the actuators on the sliding beam allowed the actuators to apply forces relative to their individual capacities with equivalent displacements, allowing both actuators to utilize their full capacities when testing larger specimens.

3.7.2 *Potentiometers*

Potentiometers were used to measure displacements in both the test specimens and test frame during the experiments. Two types of potentiometers were used during the tests: UniMeasure P510 string potentiometers and BEI Duncan 600 Series linear conductive potentiometers. Typically, string potentiometers were used to measure displacements greater than about 2", or in cases where significant rotation was expected. The arrangement of string potentiometers around the test frame is shown below in Figure 3.28. Duncan potentiometers were used when displacements less than 2" were expected. The location of the Duncan potentiometers is shown in Figure 3.29.

(a) (b) (c)

Figure 3.27. String (a and b) and Duncan Potentiometers (c)

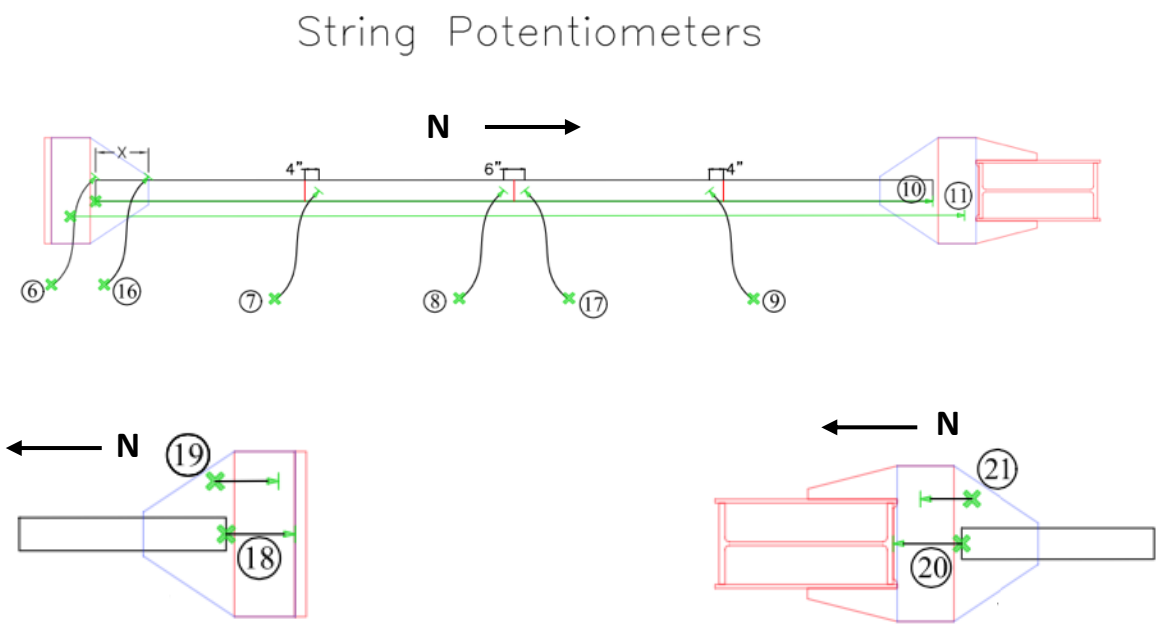

Figure 3.28. String Potentiometer Layout

The axial deformation of the test specimens was measured using potentiometers 10 and 11. String potentiometer 10 was placed directly on the south end of the test specimen using a C-clamp, and a string ran along the length of the specimen all the way to the north end of the brace. This potentiometer directly measured the axial displacement of the HSS member. Potentiometer 11 also measured axial displacement, although it was clamped to the end connection plates at both the south and north ends of the test frame, and thus captured the axial deformation of the HSS member as well as the axial deformation of the gusset and connection plates.

String potentiometers 6, 7, 8, 9, 16, and 17 were used to measure the lateral displacement of the test specimens. Potentiometers 6 and 16 were attached to the south gusset plate of the specimen, with 6 just above the end of the HSS member and 16 about 10" north along the gusset plate. These potentiometers were used to calculate the gusset plate rotation, which was useful for correcting the axial displacement data to account for rigid body rotation effects. Potentiometers 7 and 9 measured the out of plane displacement of the specimen at the quarter-points, while potentiometers 8 and 17 measured the lateral displacement at the center. Using multiple potentiometers to measure lateral displacement at various points along the specimen provided a significant level of redundancy for data collection.

String potentiometers 18, 19, 20, and 21 were used to measure the bolt slip and gusset plate elongation at both the north and south gusset plates. Potentiometers 18 and 20 were connected to the side of the HSS member at the ends with a C-clamp, and a wire attached to a magnet extended away from the specimen to capture the bolt slip and gusset plate elongation. Potentiometers 19 and 21 were clamped directly to the sides of the gusset plate, and a wire connected them to the steel connection plates at both ends. These potentiometers also measured the gusset plate elongation and bolt slip.

A Duncan Potentiometer was attached to the base of each concrete reaction block to measure the movement of the reaction blocks during the tests. This data was collected to monitor the blocks for signs of slippage before any significant block movement occurred. Potentiometers 12, 13, and 14 were attached to the bases of the east, west, and end reaction blocks, respectively. Potentiometer 22 was attached to the top of the 3" thick steel connection plate, measuring the relative movement between the connection plate and reaction block. This potentiometer was added after observing some signs of minor connection plate movement during testing. However, the connection plate was re-stressed to the face of the end reaction block, and this movement was no longer noticeable after increasing the prestressing force to its original level.

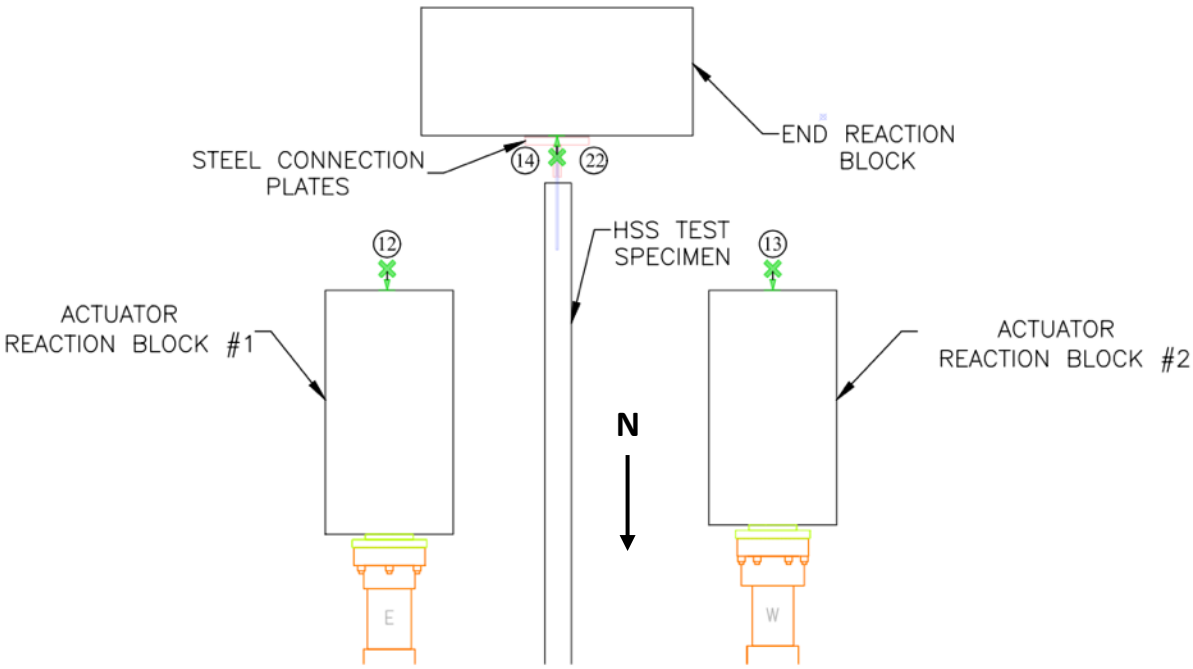

Figure 3.29. Duncan Potentiometer Layout

3.7.3 *Strain Gauges*

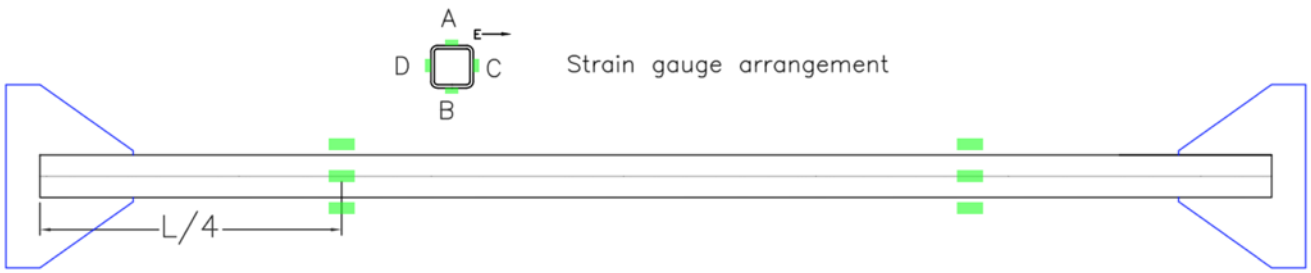

Figure 3.30. Strain Gauge Layout

Strain gauges were applied to all four faces of the HSS member at both quarter points to measure the axial strain in the test specimen. The strain gauges were placed along the centerline on each side of the brace and oriented in the longitudinal direction. The strains measured by the strain gauges were used to determine the axial force in the specimen and compare it to the axial force output from the internal actuator load cells. Additionally, the strain gauges were useful for determining the yield point in the test specimens. Having a total of eight strain gauges per specimen provided adequate redundancy, and the strain gauges were calibrated prior to each test. To connect the strain gauges at the north quarter point to the Data Acquisition System, the strain gauge wires were soldered to extension wires that connected to the DAQ. 3-wire gauges were used to compensate for temperature fluctuation throughout the test.

3.7.4 *Optotrak System*

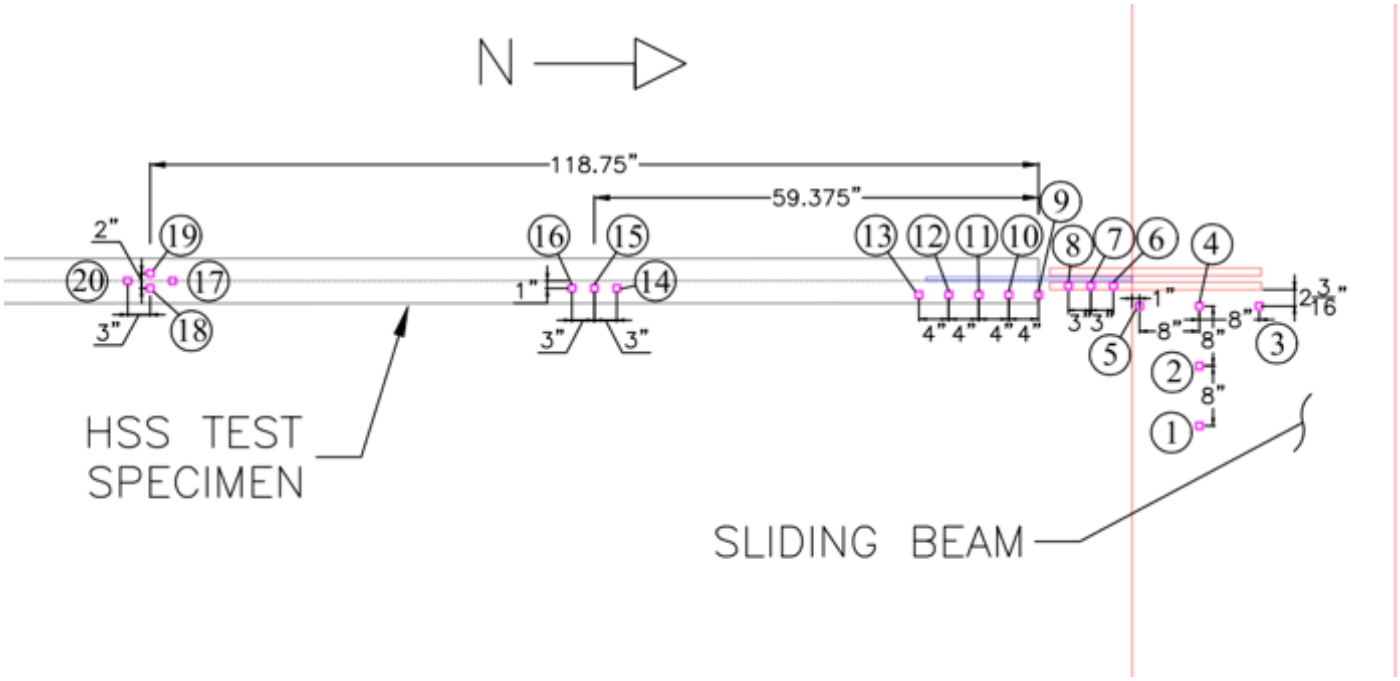

Figure 3.31. Optotrak LED Layout

Optotrak LED sensors were applied to the test specimen and frame to accurately capture the displacements of various components during the tests. Northern Digital Inc. (NDI) software was used to capture the 3-Dimensional displacement of each sensor. The Optotrak system uses a series of three cameras to determine the exact position of the LED sensors, and is accurate to within a millimeter. The system was placed at the northeast side of the test frame, with the cameras pointed southwest towards the sliding beam and test specimen. This high-resolution data could be used to determine the exact rotation of the gusset plates during the test, the out of plane movement of the HSS member, and the longitudinal and transverse movement of the sliding beam. There were a total of 20 LEDs placed on the specimen and frame, and the layout of these sensors is shown above in Figure 3.31. These sensors were applied using double sided tape once the test specimen was moved into position. Effort was made to place the LED sensors in the exact same position for each test for easy comparisons between specimens.

Chapter 4. TEST RESULTS AND OBSERVATIONS

4.1 INTRODUCTION

In this chapter, observations and results from each of the completed tests will be presented to describe the performance of the various test specimens. The behavior of the test specimens will be described based on the observed brace performance states, as well as the measured force and displacement data recorded during the tests.

For each of the twenty specimens, a brief test summary is provided to articulate the major events and outcomes of each test. Plots of the force-displacement responses for each of the test specimens are also shown. The applied axial forces were measured using the actuator load cells, and the axial displacements were measured using string potentiometers along the length of the specimen. Other strain and displacement measurements were collected using the instruments described in 3.7. Table 4.1 below defines the nomenclature used to describe the observations of brace behavior during testing. These performance states were adapted from a previous research project at the UW SRL. (Swatosh, 2016) As compressive axial forces are applied to the test specimens, they begin to buckle out of plane, shown as B1. The horizontal buckling displacement increases under greater compressive displacements, and a plastic hinge develops at the center of the specimen. Performance state B2 develops when the mid-span deflection exceeds twice the brace width. Eventually, local deformations begin to develop at the center plastic hinge region in the brace due to high localized strains. This behavior is often referred to as cupping and is labeled as B3-C. As the cyclic displacements continue, striations and tearing begin to develop under tensile displacements at the top and bottom corners at the center of the specimens, labeled as B3-T. Typically, the test specimens fractured (B4) under tensile displacements, although there were several cases in which the brace tore almost entirely through the cross section in tension, but did not fracture until the subsequent compressive displacement.

Table 4.1. Brace Performance States

Picture	Abbreviation	Performance State	Description
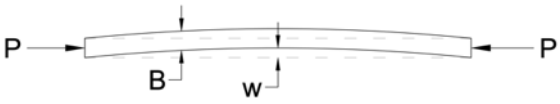	B1	Initial Global Buckling	Brace mid-span deflection, *w*, is visible but less than twice the brace depth, *B*. Begins when maximum compressive load is reached.
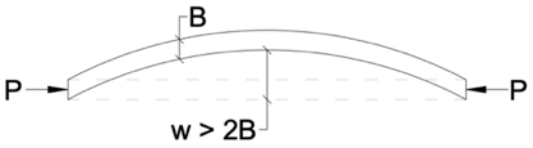	B2	Moderate Global Buckling	Brace mid-span deflection, *w*, exceeds twice the brace depth, *B*.
	B3 – C	Local Buckling Deformations	Visible local buckling deformations near midpoint of the brace.
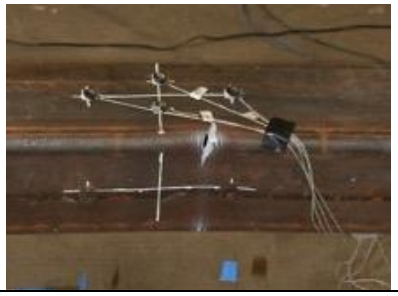	B3 – T	Striations and Tearing	Striation lines begin to separate in the plastic hinge region of the brace, and eventually tearing spreads through the cross section.
	B4	Brace Fracture	Brace fractures through the entire cross section.

The naming convention for each of the test specimens is based on the HSS shape, steel type (ASTM A1085 or A500), and producer (Y-Yellow, R-Red, B-Blue, and W-White). For example, a 7x7x1/2 test specimen made of A500 steel produced by the manufacturer designated as "Blue" would be named "7x7x1/2 A500 B". This convention is followed for all of the specimens to avoid any potential for confusion. Several tables are presented at the beginning of Section 4.2 to provide information regarding the properties and performance of the test specimens. Table 4.2 shows the geometric properties of the specimens, including the nominal and measured wall thickness (t_{nom} and t_{meas}) , brace compactness ratios (b/t_{nom} and b/t_{meas}), and nominal global slenderness ratios. The methods used to determine the measured wall thickness and width-to-thickness ratio are described in Chapter 3. The nominal b/t ratio is highlighted to show whether the specimen meets the AISC width-to-thickness limits for highly ductile (green) or moderately ductile (orange) members, or in red if the specimen does not meet either AISC width-to-thickness ratio requirement.

Next, Table 4.3 displays the measured material properties and expected yield and critical loads for each specimen. The measured yield and ultimate stress values were determined through coupon testing at the UW SRL as described in Section 3.5, and were used to determine the brace yield force. The yield force of each specimen was calculated by multiplying the actual cross sectional area of the HSS member by the measured yield strength. The actual cross sectional area was calculated by multiplying the nominal gross area, A_g, by the ratio of measured to nominal wall thickness, t_m and t_{nom}. The average energy absorbed by the Charpy V-Notch specimens from each section are also shown in this table, which was determined following the procedure described in Section 3.3.

Following this, Table 4.4 provides a summary of test specimen performance based on the performance states described in Table 4.1 and other observed events during testing. In addition to the five performance states, the other critical testing events shown in this table are brace yielding and maximum applied tensile load. In this table, the occurrence of brace yielding is defined as the point at which the applied tensile force first exceeds the predicted yield load, P_y, shown in Table 4.3. The measured brace axial displacements and approximate drift ratios are tabulated at the initiation of each performance state, as well as the other testing events described above. The

approximate drift ratio corresponding to the measured brace displacement is based on a brace in a chevron configuration with an assumed angle of 45°, as shown in Figure 4.1.

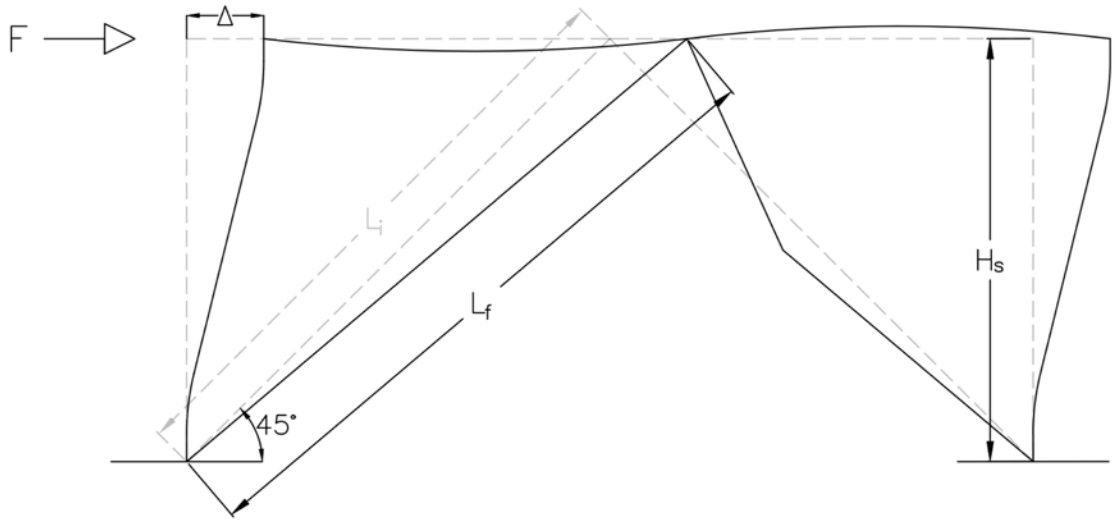

Figure 4.1. Assumed Braced Frame Configuration

Since all test specimens had an initial length, L_i, of 237.5", the corresponding story height, H_s, based on the above frame configuration is calculated as follows:

$$H_s = \sqrt{2 \cdot {L_i}^2} = 167.9"$$

The assumed story lateral displacement, Δ, can be calculated based on the axial deformation of the brace, L_f - L_i , and the assumed frame geometry.

$$\Delta = (L_f - L_i) \cdot 2 \cdot \cos(45°) = 1.41 \cdot (L_f - L_i)$$

The approximate drift ratio, expressed as a percentage of story height, is calculated as $\frac{\Delta}{H_s} \cdot 100$. All approximate drift ratios presented in this thesis are calculated following this approach.

The target displacement corresponding to the initiation of each performance state and event are also presented in Table 4.4. Underneath the target displacement, the number in parentheses indicates whether the test event occurred during the first or second cycle of the given target displacement. This information is especially useful when making comparisons between test specimens, since knowing just the axial deformation and force does not sufficiently characterize the behavior of the specimen during the test. Distinction is made between the target displacement, which is the peak applied actuator displacement in a given cycle, and the brace

axial displacement, which is the actual axial displacement of the brace measured using a string potentiometer. During testing, it was observed that the brace axial displacement was generally slightly different than the applied actuator displacement due to issues such as bolt slip, gusset plate elongation, and bolt bearing.

The axial force at the initiation of each test event is also shown in Table 4.4. The ratio of axial force to the measured yield load or critical buckling load is shown in parentheses, based on the calculated yield and critical buckling loads shown in Table 4.3. Under each performance state, it is indicated whether the axial force is shown as a ratio of the yield or critical buckling load. For the brace fracture performance state, there were several cases in which test specimens fractured in compression rather than tension. In these cases, the force at the point of brace fracture is represented as a ratio of the expected critical buckling load rather than the yield load. These cases are noted with an asterisk next to the ratio of axial load at fracture.

The maximum tensile and compressive axial brace displacements prior to fracture are tabulated in Table 4.5. The approximate drift ratios corresponding to these peak displacements are shown in this table, and are calculated following the approach presented above. The displacement and drift ranges are also shown in this table, and are calculated as the sum of the maximum compressive and tensile displacements or drifts prior to brace fracture.

As mentioned above, brief test summaries are provided for all of the test specimens. Unexpected behavior during testing is noted in these individual test summaries. At the start of each summary, an axial force-displacement hysteretic curve is presented. The development of each performance state during testing is indicated by a symbol on the hysteretic curve. In these plots, the applied axial force is normalized by the brace yield force, which is shown in Table 4.3.

The brace axial displacement is also normalized, and is shown as a percentage of brace length. In these summaries, the brace axial displacement is used to describe the condition of the brace at various test events, while the target displacement and cycle provides additional information about when these events occurred. Photographs are included in several summaries to explain the observed behavior and document damage to the brace throughout testing. A detailed test summary is provided for the 5x5x3/8 A500 Y test specimen, and more succinct summaries are provided for all other tests.

4.2 TEST RESULTS

Table 4.2. Summary of Geometric Properties

Test Specimen	Area, A_g (in.^{2})	Moment of Inertia, I (in.^{4})	Wall Thickness, t		Local Compactness, b/t		Global Slenderness, KL/r
			Nominal, t_{nom} (in.)	Measured, t_m (in.)	Nominal, b/t_{nom}	Measured, b/t_{meas}	
5x5x3/8 A500 Y	6.18	21.7	0.349	0.360	11.3	9.7	127.0
5x5x3/8 A1085 Y	6.58	22.8	0.375	0.376	10.3	9.4	127.7
6x6x5/16 A500 R	6.43	34.3	0.291	0.305	17.6	15.8	102.8
6x6x5/16 A1085 Y	6.87	36.3	0.313	0.313	16.2	14.8	103.3
6x6x3/8 A500 R	7.58	39.5	0.349	0.367	14.2	12.3	104.2
6x6x3/8 A1085 Y	8.08	41.6	0.375	0.375	13	12.2	104.6
6x6x1/2 A500 R	9.74	48.3	0.465	0.479	9.9	8.4	106.5
6x6x1/2 A1085 Y	10.36	50.5	0.5	0.486	9	8.9	107.5
7x7x5/16 A500 Y	7.59	56.1	0.291	0.290	21.1	19.6	87.3
7x7x5/16 A1085 Y	8.12	59.6	0.313	0.305	19.4	18.6	87.6
7x7x3/8 A500 Y	8.97	68.7	0.349	0.342	17.1	15.6	88.3
7x7x3/8 A1085 Y	9.58	68.7	0.375	0.365	15.7	14.2	88.6
7x7x1/2 A500 B	11.6	80.5	0.465	0.464	12.1	11.0	90.3
7x7x1/2 A1085 Y	12.4	84.7	0.5	0.484	11	10.1	91.0
8x8x3/8 A500 W	10.4	100	0.349	0.350	19.9	18.3	76.6
8x8x3/8 A1085 Y	11.1	106	0.375	0.370	18.3	15.9	76.9
8x8x1/2 A500 W	13.5	125	0.465	0.461	14.2	13.5	78.1
8x8x1/2 A1085 Y	14.4	131	0.5	0.488	13	11.7	78.6
10x10x3/8 A500 W	13.2	202	0.349	0.347	25.7	24.4	60.6
10x10x3/8 A1085 Y	14.1	214	0.375	0.366	23.7	23.1	60.9

Table 4.3. Summary of Material Properties and Expected Forces

Test Specimen	Measured Yield Strength, F_y (ksi)	Measured Ultimate Strength, F_u (ksi)	Yield Load, P_y (kips)	Critical Buckling Load, P_{cr} (kips)	CVN Absorbed Energy (ft-lbs)
5x5x3/8 A500 Y	65.38	71.86	416.8	96.2	12.8
5x5x3/8 A1085 Y	66.04	74.62	435.7	101.3	18.8
6x6x5/16 A500 R	57.37	72.77	386.6	152.7	40.8
6x6x5/16 A1085 Y	62.07	71.92	426.4	1110.2	23
6x6x3/8 A500 R	61.19	76.36	487.7	175.2	42.5
6x6x3/8 A1085 Y	66.81	72.64	539.8	185.4	18.7
6x6x1/2 A500 R	62.84	67.05	630.5	215.6	120+
6x6x1/2 A1085 Y	67.85	71.96	683.2	225.0	27.8
7x7x5/16 A500 Y	62.71	70.02	474.3	239.1	15.7
7x7x5/16 A1085 Y	57.7	64.13	456.5	251.7	18.5
7x7x3/8 A500 Y	61.35	72.19	539.3	277.9	14.3
7x7x3/8 A1085 Y	61.89	70.07	577.1	292.2	17.3
7x7x1/2 A500 B	57.82	69.14	669.3	347.3	42
7x7x1/2 A1085 Y	64.375	71.68	772.7	363.6	28.7
8x8x3/8 A500 W	66.19	76.52	690.3	387.0	65.5
8x8x3/8 A1085 Y	60.37	72.12	661.2	404.3	8.5
8x8x1/2 A500 W	65.47	72.01	876.2	491.2	67.3
8x8x1/2 A1085 Y	64.42	75.43	905.4	511.4	40.3
10x10x3/8 A500 W	59.02	69.45	774.6	605.3	120+
10x10x3/8 A1085 Y	58.34	73.76	802.9	627.9	20.7

Table 4.4. Summary of Test Specimen Performance

HSS Section	B1: Global Buckling			B2: Moderate Buckling		
	Displacement (in.) (*Approx. Drift (%)*)	Target (in.) (*Cycle*)	Force (k) ($P/P_{critical}$)	Displacement (in.) (*Approx. Drift (%)*)	Target (in.) (*Cycle*)	Force (k) ($P/P_{critical}$)
5x5x3/8 A500 Y	-0.18 *-(0.15)*	0.25 *(1)*	-95.3 *(0.99)*	-1.06 *-(0.88)*	1.25 *(1)*	-56.3 *(0.13)*
5x5x3/8 A1085 Y	-0.19 *-(0.15)*	0.25 *(1)*	-98.4 *(0.97)*	-1.26 *-(1.05)*	1.25 *(1)*	-57.5 *(0.57)*
6x6x5/16 A500 R	-0.22 *-(0.18)*	0.25 *(1)*	-125.8 *(0.82)*	-1.79 *-(1.49)*	1.75 *(1)*	-52.8 *(0.35)*
6x6x5/16 A1085 Y	-0.18 *-(0.15)*	0.25 *(1)*	-139.8 *(0.87)*	-1.63 *-(1.36)*	1.75 *(1)*	-64.0 *(0.40)*
6x6x3/8 A500 R	-0.19 *-(0.16)*	0.25 *(1)*	-168.7 *(0.96)*	-1.75 *-(1.46)*	1.75 *(1)*	-72.0 *(0.41)*
6x6x3/8 A1085 Y	-0.15 *-(0.13)*	0.25 *(1)*	-180.0 *(0.97)*	-1.63 *-(1.36)*	1.75 *(1)*	-81.0 *(0.44)*
6x6x1/2 A500 R	-0.18 *-(0.15)*	0.375 *(1)*	-218.7 *(1.01)*	-1.20 *-(1.00)*	1.25 *(1)*	-111.0 *(0.51)*
6x6x1/2 A1085 Y	-0.19 *-(0.16)*	0.375 *(1)*	-218.6 *(0.97)*	-1.75 *-(1.46)*	1.75 *(1)*	-109.2 *(0.49)*
7x7x5/16 A500 Y	-0.21 *-(0.18)*	0.375 *(1)*	-209.8 *(0.88)*	-1.65 *-(1.38)*	1.75 *(1)*	-58.6 *(0.25)*
7x7x5/16 A1085 Y	-0.21 *-(0.18)*	0.375 *(1)*	-201.5 *(0.80)*	-1.69 *-(1.41)*	1.75 *(1)*	-81.2 *(0.32)*
7x7x3/8 A500 Y	-0.26 *-(0.22)*	0.375 *(1)*	-231.8 *(0.83)*	-1.76 *-(1.46)*	1.75 *(1)*	-99.5 *(0.36)*
7x7x3/8 A1085 Y	-0.27 *-(0.23)*	0.375 *(1)*	-254.9 *(0.87)*	-1.82 *-(1.52)*	1.75 *(1)*	-106.0 *(0.36)*
7x7x1/2 A500 B	-0.22 *-(0.18)*	0.375 *(1)*	-278.8 *(0.80)*	-1.75 *-(1.46)*	1.75 *(1)*	-124.0 *(0.36)*
7x7x1/2 A1085 Y	-0.32 *-(0.27)*	0.375 *(1)*	-305.7 *(0.84)*	-1.87 *-(1.56)*	1.75 *(1)*	-141.9 *(0.39)*
8x8x3/8 A500 W	-0.31 *-(0.26)*	0.5 *(1)*	-328.8 *(0.81)*	-2.17 *-(1.81)*	1.75 *(1)*	-62.8 *(0.16)*
8x8x3/8 A1085 Y	-0.31 *-(0.26)*	0.5 *(1)*	-328.8 *(0.81)*	-2.17 *-(1.81)*	1.75 *(1)*	-62.8 *(0.16)*
8x8x1/2 A500 W	-0.32 *-(0.27)*	0.625 *(1)*	-418.2 *(0.82)*	-2.10 *-(1.75)*	2.25 *(1)*	-158.3 *(0.31)*
8x8x1/2 A1085 Y	-0.32 *-(0.27)*	0.625 *(1)*	-418.2 *(0.82)*	-2.10 *-(1.75)*	2.25 *(2)*	-158.3 *(0.31)*
10x10x3/8 A500 W	-0.45 *-(0.38)*	0.75 *(1)*	-507.6 *(0.81)*	- -	- -	- -
10x10x3/8 A1085 Y	-0.45 *-(0.38)*	0.75 *(1)*	-507.6 *(0.81)*	- -	- -	- -

Table 4.4 Continued

B3-C: Local Buckling			**B3-T: Striations/Tearing**			**B4: Fracture**		
Displacement (in.) (*Approx. Drift (%)*)	Target (in.) (*Cycle*)	Force (k) ($P/P_{critical}$)	Displacement (in.) (*Approx. Drift (%)*)	Target (in.) (*Cycle*)	Force (k) (P/P_{yield})	Displacement (in.) (*Approx. Drift (%)*)	Target (in.) (*Cycle*)	Force (k) (P/P_{yield})
-4.38	4.75	-19.5	4.92	5.25	399.0	5.13	5.75	116.0
-(3.65)	*(2)*	*(0.05)*	*(4.10)*	*(1)*	*(0.96)*	*(4.28)*	*(1)*	*(0.28)*
-5.01	5.25	-17.6	4.43	5.75	76.0	5.25	5.75	116.7
-(4.18)	*(1)*	*(0.17)*	*(3.69)*	*(1)*	*(0.17)*	*(4.38)*	*(1)*	*(0.27)*
-2.72	2.75	-30.1	2.45	3.25	252.0	2.93	3.75	99.6
-(2.27)	*(2)*	*(0.20)*	*(2.04)*	*(2)*	*(0.65)*	*(2.44)*	*(1)*	*(0.26)*
-2.56	2.75	-33.5	2.46	3.25	272.1	3.13	3.75	123.0
-(2.13)	*(2)*	*(0.21)*	*(2.05)*	*(2)*	*(0.64)*	*(2.61)*	*(1)*	*(0.29)*
-3.16	3.25	-43.5	3.27	3.75	457.0	3.74	4.25	190.0
-(2.63)	*(2)*	*(0.25)*	*(2.73)*	*(2)*	*(0.94)*	*(3.12)*	*(1)*	*(0.39)*
-3.06	3.25	-40.4	2.70	3.75	196.4	0.55	4.25	-25.2
-(2.55)	*(2)*	*(0.22)*	*(2.25)*	*(2)*	*(0.36)*	*(0.46)*	*(1)*	*(0.1*)*
-3.58	3.75	-44.0	3.78	4.25	492.0	0.20	4.75	-43.3
-(2.98)	*(2)*	*(0.20)*	*(3.15)*	*(1)*	*(0.78)*	*(0.17)*	*(1)*	*(0.2*)*
-4.13	4.25	-51.6	4.58	5.25	626.6	4.67	5.75	200.0
-(3.44)	*(2)*	*(0.23)*	*(3.81)*	*(1)*	*(0.92)*	*(3.89)*	*(1)*	*(0.29)*
-1.82	1.75	-54.5	1.04	2.25	323.3	1.73	2.25	193.0
-(1.52)	*(1)*	*(0.23)*	*(0.86)*	*(1)*	*(0.68)*	*(1.44)*	*(1)*	*(0.41)*
-1.74	1.75	-56.3	1.35	2.25	264.7	1.99	2.75	146.1
-(1.45)	*(2)*	*(0.22)*	*(1.13)*	*(2)*	*(0.58)*	*(1.66)*	*(1)*	*(0.32)*
-2.23	2.25	-60.7	1.65	2.75	237.8	-1.82	2.75	-5.39
-(1.86)	*(2)*	*(0.22)*	*(1.38)*	*(2)*	*(0.44)*	*-(1.52)*	*(2)*	*(0.02*)*
-2.27	2.25	-82.6	1.44	2.75	234.0	2.36	3.25	152.5
-(1.89)	*(1)*	*(0.28)*	*(1.20)*	*(2)*	*(0.41)*	*(1.97)*	*(1)*	*(0.26)*
-3.17	3.25	-77.2	3.27	4.25	594.0	3.59	4.25	186.0
-(2.65)	*(2)*	*(0.22)*	*(2.73)*	*(1)*	*(0.89)*	*(2.99)*	*(2)*	*(0.28)*
-3.38	3.25	-80.2	3.37	4.25	771.0	3.48	4.25	260.5
-(2.82)	*(2)*	*(0.22)*	*(2.81)*	*(1)*	*(1.00)*	*(2.90)*	*(2)*	*(0.34)*
-1.68	1.75	-110.8	1.68	2.25	526.0	2.18	2.75	180.0
-(1.40)	*(2)*	*(0.27)*	*(1.40)*	*(2)*	*(0.80)*	*(1.82)*	*(1)*	*(0.27)*
-1.68	1.75	-110.8	1.68	2.25	526.0	2.18	2.75	180.0
-(1.40)	*(2)*	*(0.27)*	*(1.40)*	*(2)*	*(0.80)*	*(1.82)*	*(1)*	*(0.27)*
-2.58	2.75	-131.4	2.41	3.25	850.8	2.96	3.75	309.8
-(2.15)	*(2)*	*(0.26)*	*(2.01)*	*(1)*	*(0.94)*	*(2.46)*	*(2)*	*(0.34)*
-2.58	2.75	-131.4	2.41	3.25	850.8	2.96	3.75	309.8
-(2.15)	*(1)*	*(0.26)*	*(2.01)*	*(2)*	*(0.94)*	*(2.46)*	*(2)*	*(0.34)*
-1.15	1.25	-214.0	1.03	1.75	812.5	1.60	2.25	280.0
-(0.96)	*(1)*	*(0.34)*	*(0.85)*	*(1)*	*(1.01)*	*(1.33)*	*(1)*	*(0.35)*
-1.15	1.25	-214.0	1.03	1.75	812.5	1.60	2.25	280.0
-(0.96)	*(1)*	*(0.34)*	*(0.85)*	*(1)*	*(1.01)*	*(1.33)*	*(1)*	*(0.35)*

Table 4.4 Continued

Brace Yielding			**Peak Tensile Force**		
Displacement (in.) (*Approx. Drift (%)*)	Target (in.) (*Cycle*)	Force (k)	Displacement (in.) (*Approx. Drift (%)*)	Target (in.) (*Cycle*)	Force (kips) (P/P_{yield})
1.20 *(1.00)*	1.25 *(1)*	416.8	1.92 *(1.60)*	2.25 *(1)*	432.5 *(1.04)*
1.27 *(1.06)*	1.25 *(1)*	435.7	1.83 *(1.53)*	2.25 *(1)*	443.6 *(1.02)*
0.90 *(0.75)*	1.25 *(1)*	386.6	1.85 *(1.54)*	2.25 *(1)*	409.7 *(1.06)*
0.89 *(0.74)*	1.25 *(1)*	426.4	1.90 *(1.58)*	2.25 *(1)*	456.4 *(1.07)*
1.13 *(0.94)*	1.75 *(1)*	487.7	1.78 *(1.48)*	2.25 *(1)*	511.0 *(1.05)*
1.18 *(0.99)*	1.75 *(1)*	539.8	1.76 *(1.47)*	2.25 *(1)*	547.9 *(1.01)*
1.10 *(0.92)*	1.75 *(1)*	630.5	1.24 *(1.03)*	2.25 *(1)*	646.2 *(1.02)*
0.99 *(0.82)*	1.75 *(1)*	683.2	1.61 *(1.34)*	2.25 *(1)*	727.2 *(1.06)*
0.96 *(0.80)*	1.75 *(1)*	474.3	1.23 *(1.03)*	1.75 *(1)*	496.6 *(1.05)*
0.73 *(0.61)*	1.25 *(1)*	456.5	1.72 *(1.43)*	2.25 *(1)*	478.1 *(1.05)*
0.76 *(0.64)*	1.25 *(1)*	539.3	1.70 *(1.42)*	2.25 *(1)*	570.9 *(1.06)*
0.82 *(0.68)*	1.75 *(1)*	577.1	1.53 *(1.28)*	1.75 *(1)*	615.9 *(1.07)*
0.90 *(0.75)*	1.75 *(1)*	669.3	1.64 *(1.37)*	1.75 *(1)*	710.4 *(1.06)*
0.92 *(0.77)*	1.75 *(1)*	772.7	1.44 *(1.20)*	2.25 *(1)*	805.1 *(1.04)*
1.10 *(0.91)*	1.75 *(1)*	661.2	1.29 *(1.08)*	1.75 *(1)*	672.6 *(1.02)*
1.10 *(0.91)*	1.75 *(1)*	661.2	1.29 *(1.08)*	1.75 *(1)*	672.6 *(1.02)*
0.92 *(0.76)*	1.75 *(1)*	876.2	1.17 *(0.97)*	1.75 *(1)*	906.0 *(1.03)*
0.91 *(0.76)*	1.75 *(1)*	905.4	1.43 *(1.19)*	2.25 *(1)*	921.9 *(1.02)*
0.80 *(0.67)*	1.75 *(1)*	774.6	0.94 *(0.78)*	1.75 *(1)*	785.4 *(1.01)*
0.89 *(0.74)*	1.75 *(1)*	802.9	1.03 *(0.86)*	1.75 *(1)*	812.8 *(1.01)*

Table 4.5. Summary of Measured Axial Deformation

Test Specimen	**Tension** Displacement (in.) *(Approx. Drift (%))*	**Compression** Displacement (in.) *(Approx. Drift (%))*	**Range** Displacement (in.) *(Approx. Drift (%))*
5x5x3/8 A500 Y	5.13 *(4.28)*	4.89 *(4.07)*	10.02 *(8.35)*
5x5x3/8 A1085 Y	5.25 *(4.38)*	5.50 *(4.59)*	10.75 *(8.96)*
6x6x5/16 A500 R	3.06 *(2.55)*	3.26 *(2.71)*	6.31 *(5.26)*
6x6x5/16 A1085 Y	3.13 *(2.61)*	3.12 *(2.60)*	6.25 *(5.21)*
6x6x3/8 A500 R	3.74 *(3.12)*	3.72 *(3.10)*	7.46 *(6.22)*
6x6x3/8 A1085 Y	3.52 *(2.93)*	3.52 *(2.93)*	7.04 *(5.87)*
6x6x1/2 A500 R	4.45 *(3.71)*	4.06 *(3.39)*	8.51 *(7.10)*
6x6x1/2 A1085 Y	4.67 *(3.89)*	5.12 *(4.27)*	9.79 *(8.16)*
7x7x5/16 A500 Y	1.73 *(1.44)*	1.83 *(1.53)*	3.56 *(2.97)*
7x7x5/16 A1085 Y	1.99 *(1.66)*	2.31 *(1.92)*	4.29 *(3.58)*
7x7x3/8 A500 Y	2.51 *(2.09)*	2.79 *(2.33)*	5.30 *(4.42)*
7x7x3/8 A1085 Y	2.36 *(1.97)*	2.85 *(2.38)*	5.21 *(4.35)*
7x7x1/2 A500 B	3.59 *(2.99)*	4.16 *(3.47)*	7.75 *(6.46)*
7x7x1/2 A1085 Y	3.48 *(2.90)*	4.41 *(3.68)*	7.89 *(6.58)*
8x8x3/8 A500 W	1.24 *(1.04)*	1.90 *(1.58)*	3.14 *(2.62)*
8x8x3/8 A1085 Y	2.18 *(1.82)*	2.18 *(1.82)*	4.36 *(3.63)*
8x8x1/2 A500 W	2.71 *(2.26)*	2.80 *(2.34)*	5.51 *(4.60)*
8x8x1/2 A1085 Y	2.96 *(2.46)*	3.32 *(2.77)*	6.28 *(5.23)*
10x10x3/8 A500 W	2.10 *(1.75)*	2.48 *(2.07)*	4.58 *(3.81)*
10x10x3/8 A1085 Y	1.60 *(1.33)*	1.84 *(1.53)*	3.44 *(2.87)*

4.2.1 *5x5x3/8 A500 Y*

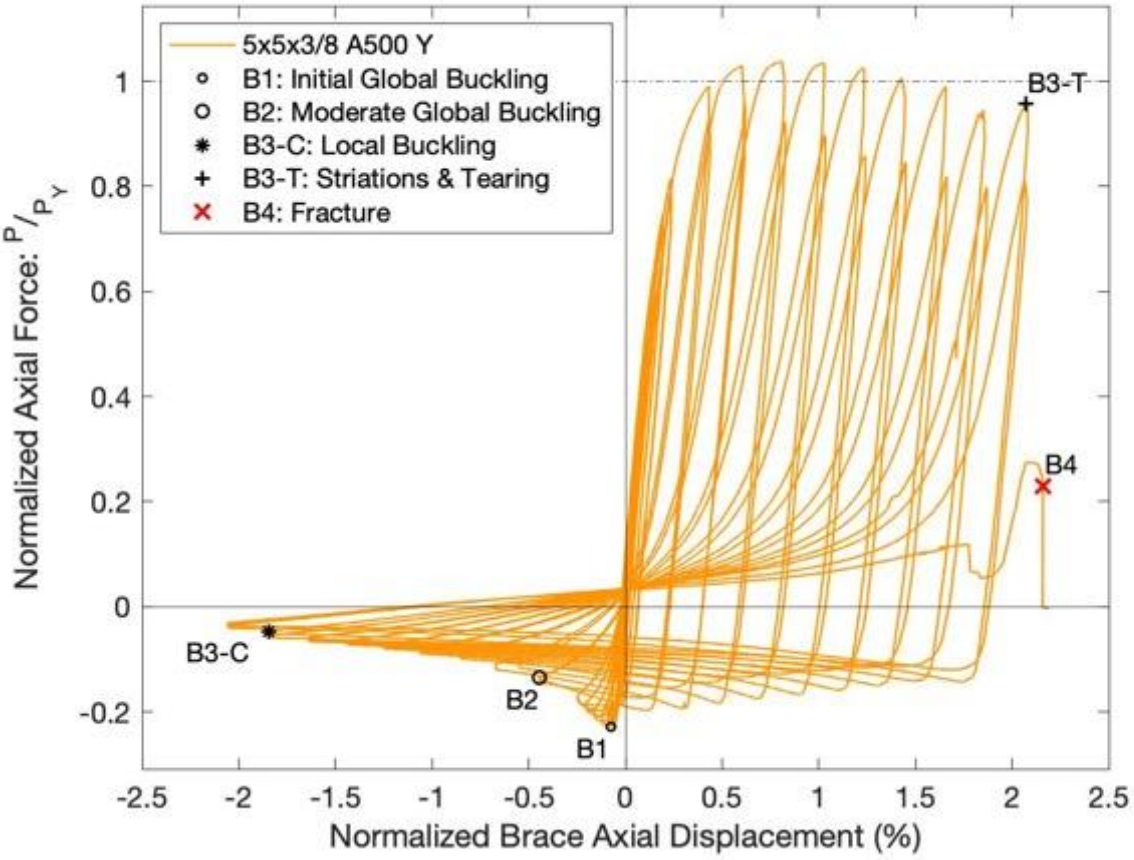

Figure 4.2. Brace Hysteretic Response: 5x5x3/8 A500 Y

For this first test specimen, a detailed review of the test procedure and observations will be presented. To begin the test, recordings for the LabVIEW and Optotrak data were started simultaneously. The actuator displacement procedure was then started, beginning with the 0.125" target displacements and progressing according to the loading protocol described in Section 3.7. In this first test, the actuators were stopped at nearly every peak and valley at each target displacement. During subsequent tests, the actuators were stopped less frequently, typically at larger cycles to check for cupping and tearing at the center of the specimen.

The specimen began to exhibit global buckling at a compressive displacement of about 0.18" during the first 0.25" target displacement cycle. A maximum compressive force of 98.4 kips was achieved at this axial displacement. During subsequent cycles, the lateral buckling displacement increased under the greater applied displacements. The specimen yielded in tension

at an axial displacement of 1.20” during the first 1.25” target displacement cycle. A peak tensile force of 443.6 kips was reached at an axial displacement of 1.92” during the first 2.25” target displacement cycle. The measured out-of-plane buckling displacement exceeded twice the brace width at compressive target displacements greater than 1.25”. As shown in Figure 4.2 above, after reaching this maximum axial force in tension, the applied forces slowly began to decrease in later cycles despite the increased displacements. Additionally, the maximum tensile force during the second cycle of each target displacement was significantly less than the applied force during the first cycle. This is evidence of strength degradation in the specimen, which is caused by the yielding and resulting plastic elongation of the member. This results in a reduction in the required tensile force during the second cycle at each level of displacement, which in most cases was about 15% lower than the force in the first cycle.

The bolts slipped at both the north and south gusset plates during the 1.75” target displacement cycles as the actuators pushed the specimen into tension. The magnitude of the bolt slip was measured to be about 1/8” at each end, and a loud banging sound was observed as the bolts slipped. Bolt slip was observed in all of the tests, although it occurred at different forces and displacements, and the magnitude of bolt slippage varied. Knocking sounds were observed when the brace was in tension during all future cycles as the bolts moved slightly. When the bolts slipped, the string potentiometer measuring the gusset plate elongation at the north gusset plate fell off, but was immediately put back in place.

Figure 4.3. Measured Bolt Slip at South Gusset Plate

As the magnitude of the lateral displacements continued to increase under the greater compressive axial displacements, it became apparent that the strings attached to the Optotrak sensors were getting caught on the string potentiometer wires running longitudinally along the length of the brace. This caused the string pot wires to be pulled slightly downwards, increasing the measured axial displacements. The axial displacement data was corrected after the test, and the Optotrak wires were moved beneath the string pot wires after the first cycle of the 2.75" target displacement. In all future tests, this issue was avoided by running the Optotrak wires underneath the string pot wires.

Local buckling at the center of the specimen was first observed at a compressive displacement of 4.35" during the second cycle of the 4.75" target displacement. This minor cupping was about 3/8" deep, and was centered about 3" south of the center of the test specimen. The 4.35" axial displacement corresponds to a story drift of about 3.65% for a brace in a chevron configuration at a 45^{o} angle. These local buckling deformations became increasingly severe under larger compressive displacements as shown in Figure 4.4 below.

(a) (b)

Figure 4.4. Initial Local Cupping (a) and Severe Local Cupping (b)

As the brace was cycled between compression and tension, striations eventually developed at the center of the specimen in tension. These striations were first observed in the top and bottom corners on the compressive face of the section at a tensile displacement of about 4.9" during the first 5.25" target displacement cycle. Increased cupping was observed at the

subsequent compressive displacement. Additional tearing through the top and bottom corners at the center of the specimen was observed in tension during the second cycle of the 5.25” target displacement.

The specimen ultimately fractured in tension during the first 5.75” target displacement cycle at an axial deformation of about 5.13”, corresponding to a peak story drift of about 4.11%. As the axial displacement increased during this final cycle, the tearing spread across the east, top, and bottom walls of the specimen. The west wall of the brace ultimately fractured at a tensile displacement of 5.13”. The overall deformation range was 9.82”, which corresponds to a story drift range of about 8.16% as defined in Section 4.1.

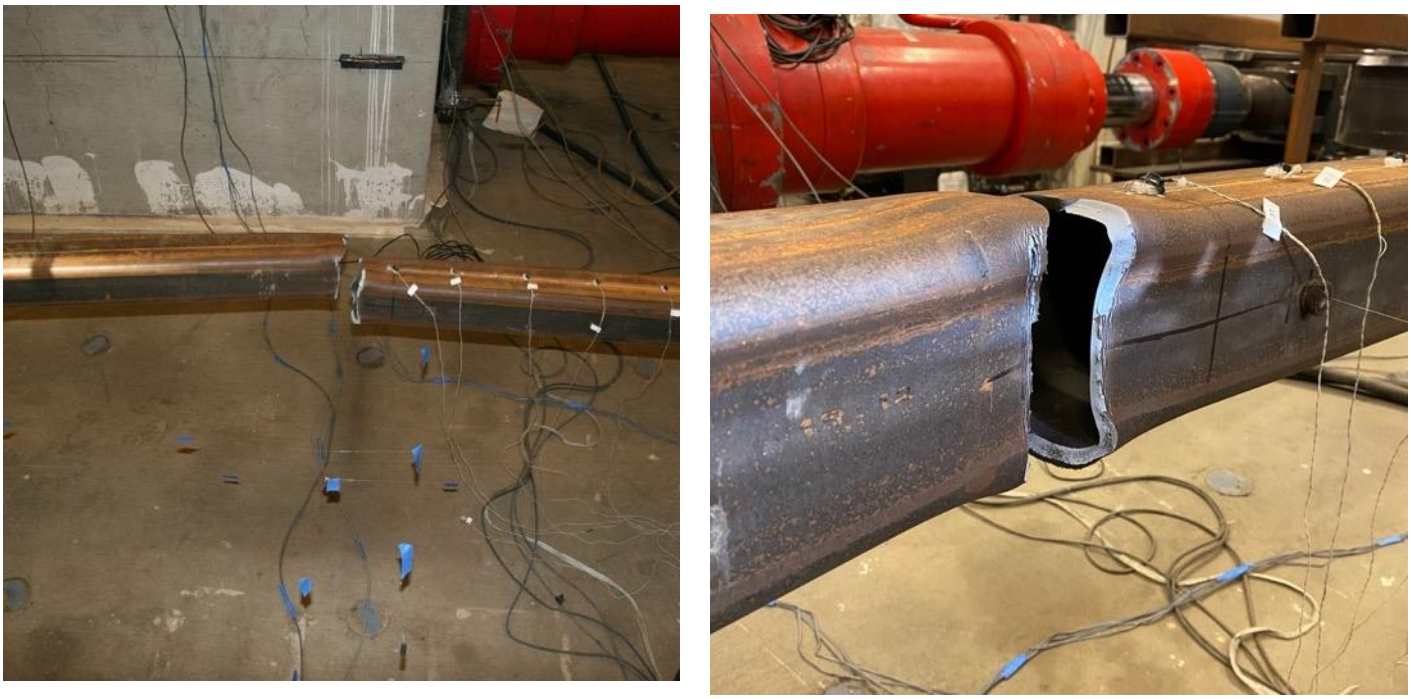

(a) (b)

Figure 4.5. Fractured Specimen – Top View (a) and Close-Up (b)

4.2.2 *5x5x3/8 A1085 Y*

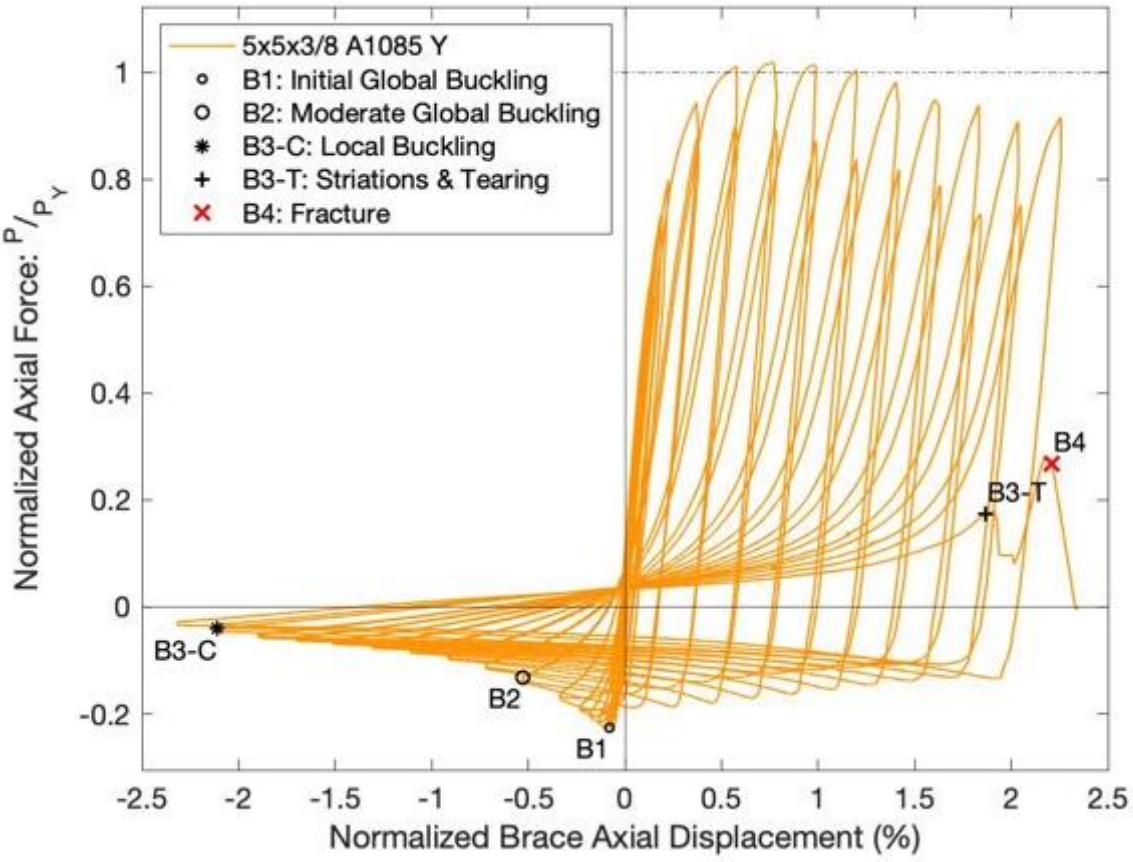

Figure 4.6 Brace Hysteretic Response: 5x5x3/8 A1085 Y

The 5x5x3/8 A1085 Y test specimen generally exhibited similar behavior as the 5x5x3/8 A500 Y specimen, and a brief summary of its performance is described below. Global buckling was observed at a compressive axial displacement of 0.19" during the 0.25" displacement cycles, and the specimen reached a maximum compressive load of 98.4 kips. The out-of-plane buckling exceeded twice the brace width at the peak compressive displacement of the 1.25" displacement cycles. The specimen reached a maximum tensile force of 443.6 kips at an axial displacement of 1.83", and the tensile forces slowly decreased during the following cycles. Local cupping at the center of the specimen was observed at a compressive axial displacement of just over 5" during the 5.25" displacement cycles. These local deformations became more severe during subsequent cycles, and eventually led to tearing and fracture of the specimen in tension. Tearing at the center of the specimen was initially observed during the second cycle of the 5.75" target displacement,

and the tearing quickly spread across the east, top, and bottom walls of the section. The brace fractured in tension during this same cycle, at an axial displacement of 5.25".

4.2.3 *6x6x5/16 A500 R*

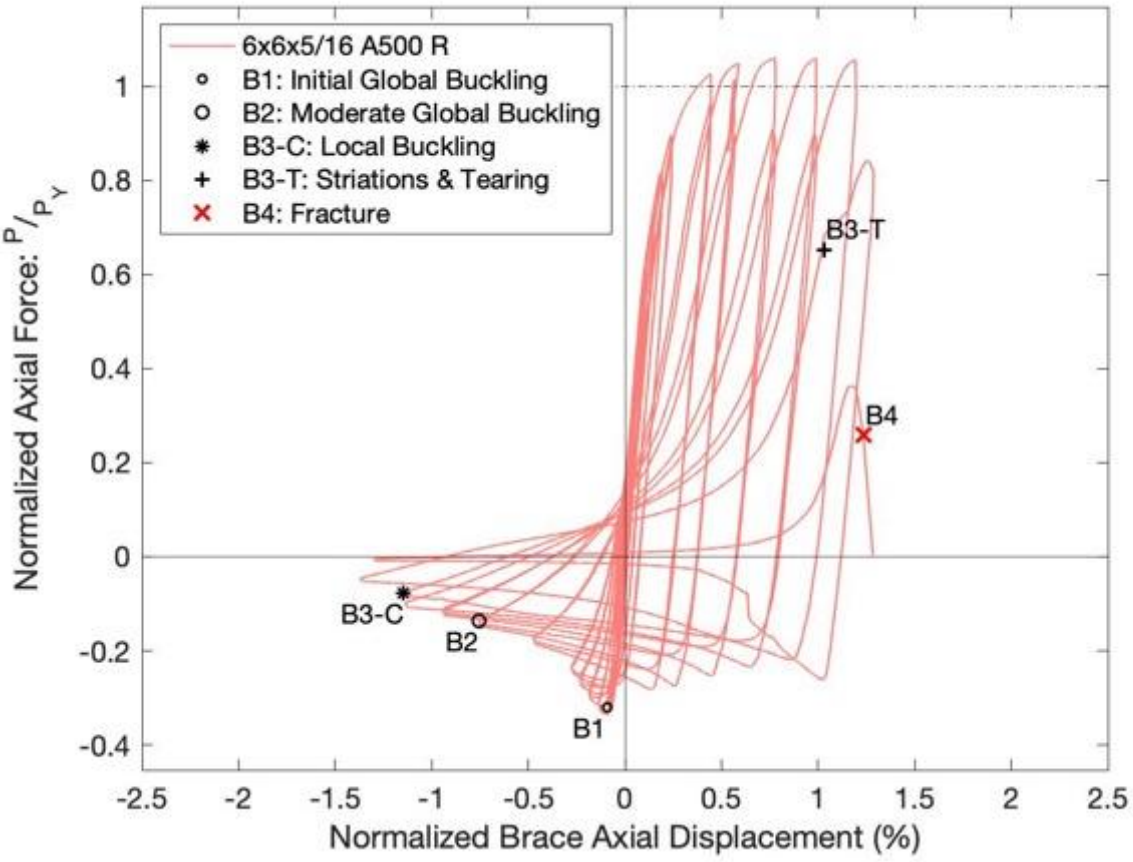

Figure 4.7. Brace Hysteretic Response: 6x6x5/16 A500 R

The 6x6x5/16 A500 R test specimen exhibited global buckling at a compressive displacement of 0.22" during the 0.25" target displacement cycles, at which point the specimen reached a peak compressive force of 129.7 kips. The lateral displacement of the specimen increased under larger compressive displacements, and exceeded twice the brace width at a compressive displacement of 1.79". The peak tensile force of 409.7 kips occurred at an axial displacement of 1.85". The tensile forces achieved at the target displacements from 1.25" to 2.75" remained relatively constant during the first cycle at each displacement, and only

significantly decreased once tearing began to develop in the specimen. Local buckling was observed at a compressive displacement of about 2.72” during the second 2.75” target displacement cycle. Striations and tearing developed at the center of the specimen in tension as the axial displacements approached the 3.25” target displacement during the second cycle. The tearing quickly spread across the cross section during this cycle, leaving only the west wall section remaining.

After the specimen reached this peak tensile displacement, the direction of buckling switched and the brace began to buckle towards the east as the specimen was pushed towards the target displacement of 3.25” in compression. This unexpected behavior was likely caused by the brace tearing through much of the cross section, which caused the specimen to open up at the center and push out towards the east side of the test frame. Figure 4.8 below shows this behavior, the image on the left shows the original buckling direction of the specimen during the cycles leading up to brace tearing. The photographs on the center and right show the brace buckling to the east after tearing. The out-of-plane buckling displacement was measured manually, since this behavior caused the string potentiometers at the center of the specimen to be out of range. The brace fractured in tension during the first cycle of the 3.75” target displacement prior to reaching the peak displacement.

Figure 4.8. Horizontal Buckling Behavior - 6x6x5/16 A500 HSS

4.2.4 *6x6x5/16 A1085 Y*

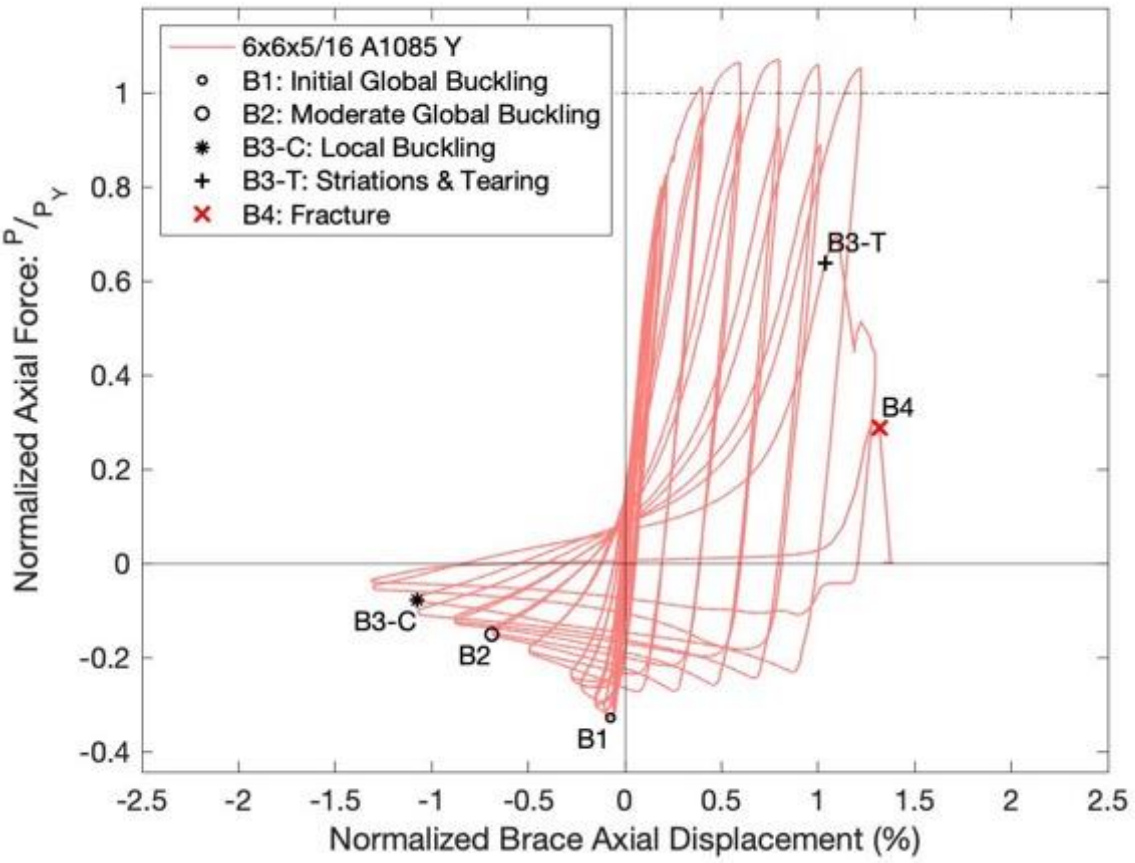

Figure 4.9. Brace Hysteretic Response: 6x6x5/16 A1085 Y

Global buckling was observed in the 6x6x5/16 A1085 Y specimen at a compressive displacement of 0.18", and reached a maximum compressive force of 139.6 kips. The buckling displacement exceeded twice the brace width during the 1.75" target cycles. The maximum tensile force of 456.4 kips was reached at a displacement of 1.9" during the first 2.25" target cycle. The peak tensile forces remained relatively constant prior to the development of striations and tearing. Local buckling deformations were observed at a compressive displacement of 2.56" during the second 2.75" target displacement cycle. Striations and tearing began to develop at the center of the specimen in tension during the second 3.25" target displacement cycle, which led to a significant reduction in peak tensile force. The brace fractured in tension during the subsequent cycle at an axial displacement of 3.13" prior to reaching the peak target displacement.

4.2.5 *6x6x3/8 A500 R*

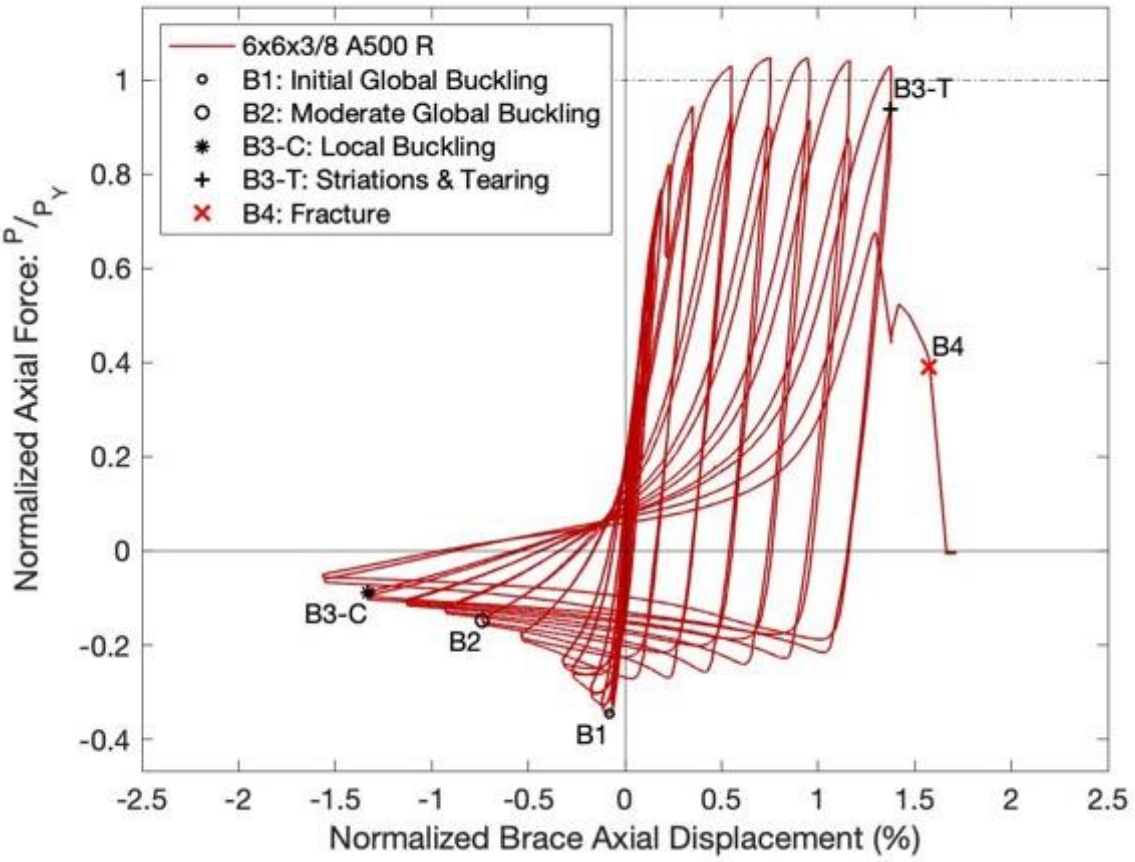

Figure 4.10. Brace Hysteretic Response: 6x6x3/8 A500 R

The 6x6x3/8 A500 R test specimen exhibited global buckling during the first 0.25” target displacement cycle at a compressive displacement of about 0.19” and reached a peak force of 168.7 kips. As the displacements increased, the horizontal buckling displacements continued to increase, and exceeded twice the brace width during the 1.75” target cycles. A maximum tensile force of 511 kips was reached at an axial displacement of 1.78”, and the peak tensile forces remained relatively constant until striations and tearing developed at the center of the specimen. Local buckling deformations were first observed at an axial compressive displacement of 3.16” during the second 3.25” target cycle. This cupping behavior became more severe under increased compressive displacements. Striations were observed at the center of the specimen during the second 3.75” target cycle. The tearing spread across the section in tension during the subsequent cycle, and the brace ultimately fractured at an axial displacement of 3.74” during this first 4.25” target cycle.

4.2.6 *6x6x3/8 A1085 Y*

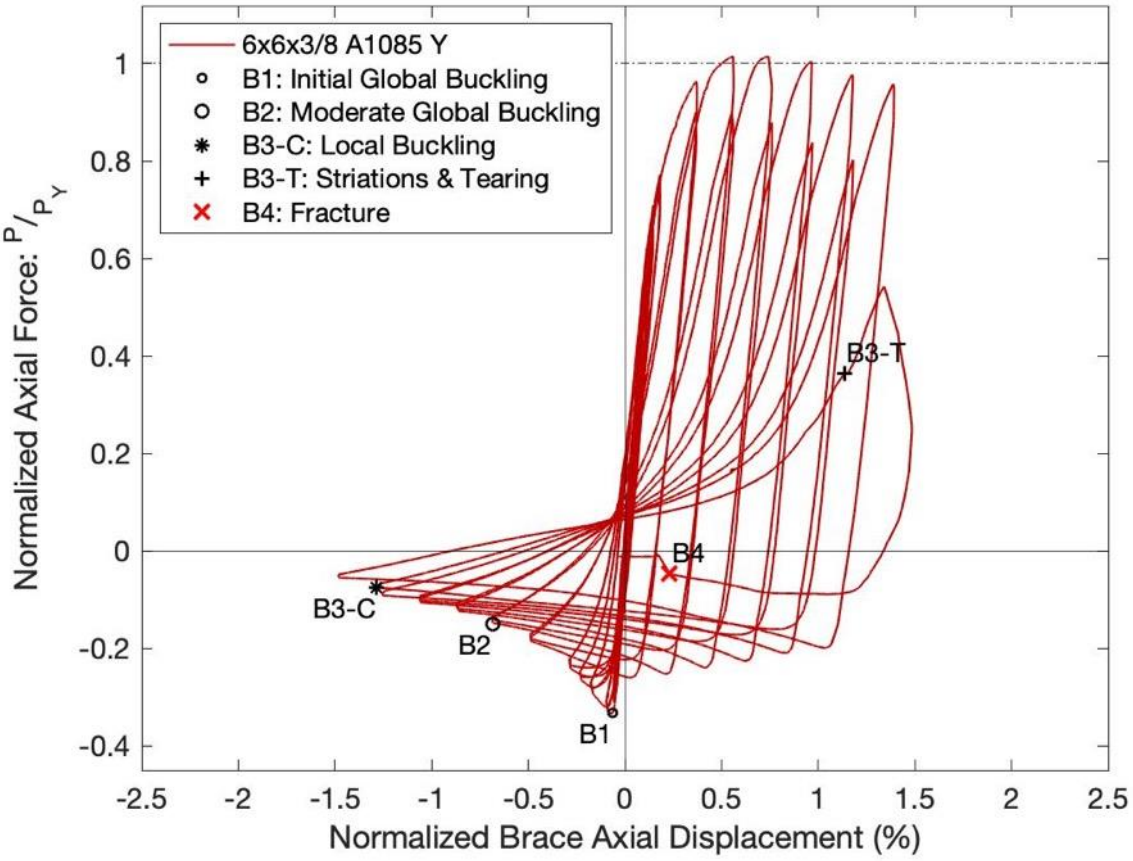

Figure 4.11. Brace Hysteretic Response: 6x6x3/8 A1085 Y

Global buckling was observed in the 6x6x3/8 A1085 Y specimen at a compressive displacement of about 0.15”, and reached a peak compressive force of 180 kips at this point. The horizontal buckling displacement at the center of the specimen exceeded twice the brace depth during the 1.75” target displacement cycles. This specimen reached a peak tensile force of 547.9 kips at an axial displacement of 1.76”, and the peak tensile forces decreased slightly in subsequent cycles at larger displacements. Local buckling deformations were initially observed during the second cycle of the 3.25” target displacement, at an axial displacement of about 3.06”. These deformations became more severe during the following cycles. Striations and tearing developed at the center of the brace during the second cycle of this 3.75” target displacement, but the brace did not fracture at the peak tensile displacement. Only the west wall of the specimen remained intact, and when the loading was reversed and the brace was put into compression it fractured at a displacement of 0.55” prior to reaching its neutral position.

4.2.7 *6x6x1/2 A500 R*

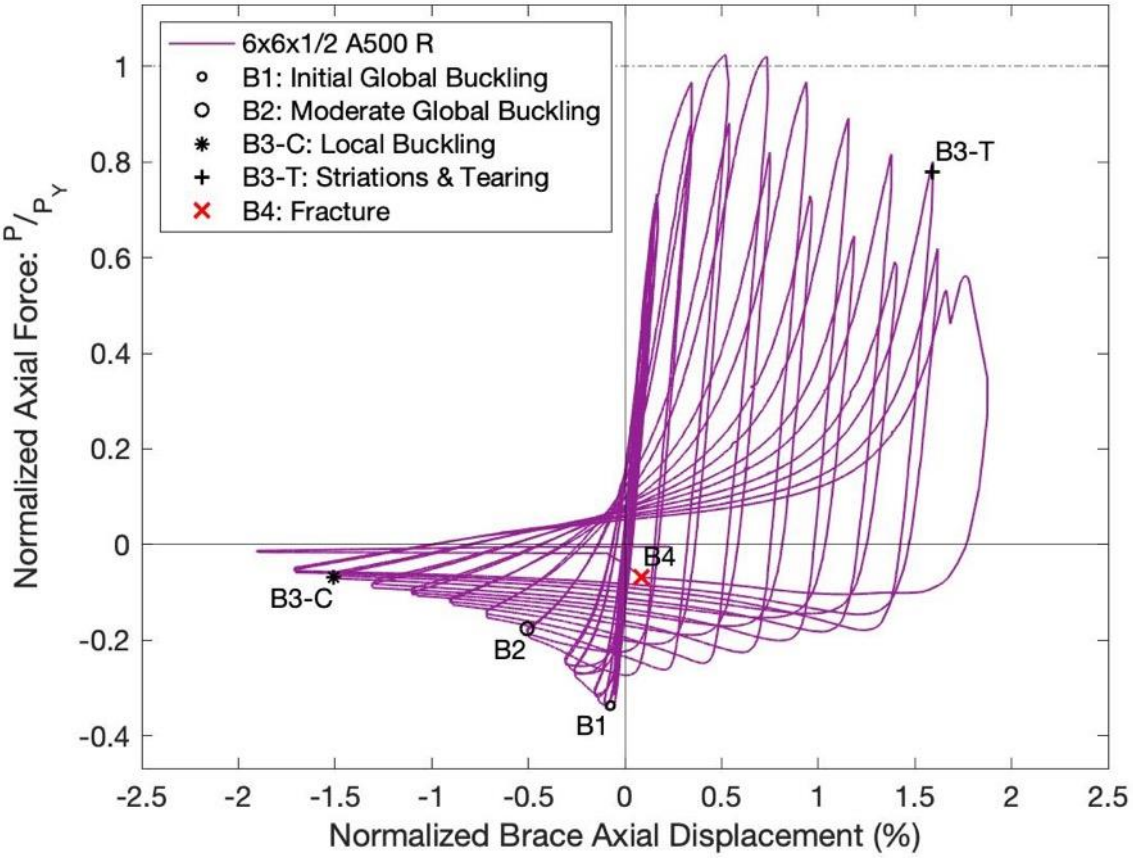

Figure 4.12. Brace Hysteretic Response: 6x6x1/2 A500 R

The 6x6x1/2 A500 R specimen experienced global buckling at a compressive axial displacement of 0.18”, and reached a maximum compressive force of 218.7 kips. The horizontal buckling displacement increased with larger axial displacements, and the global buckling exceeded twice the brace width during the 1.25” target cycles. A peak tensile force of 646.2 kips was developed at an axial displacement of 1.24”, and the peak tensile forces diminished relatively quickly in later cycles. Local cupping was initially observed during the 3.75” cycles at a compressive displacement of 3.58”. These local buckling deformations became more severe at larger compressive displacements, and minor striations developed when the brace was put into tension during the first 4.25” displacement cycle. Minor tearing was observed near the peak tensile displacement in the subsequent cycle, and the tearing spread across the cross section during the first 4.75” cycle. At the peak tensile displacement, only the west wall of the section

remained intact, and when the loading was reversed the brace ultimately fractured at a displacement of 0.2” before reaching the original neutral position.

4.2.8 *6x6x1/2 A1085 Y*

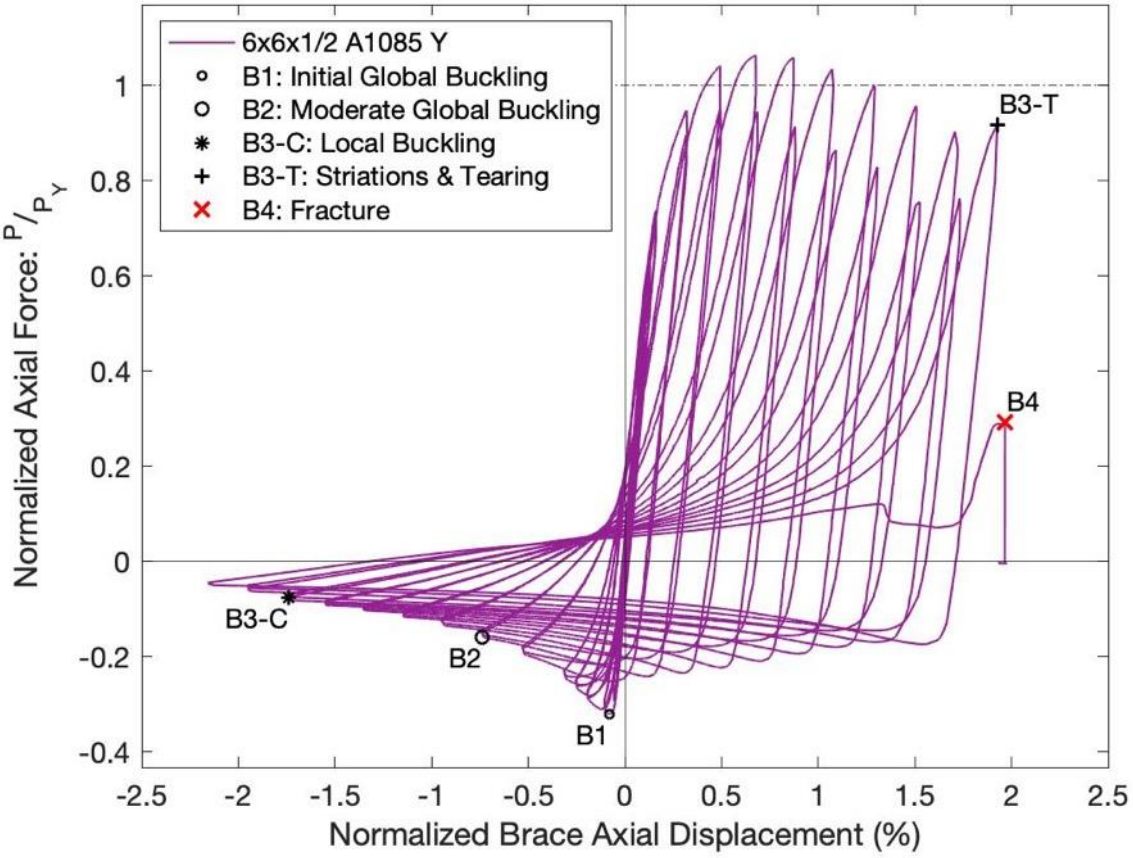

Figure 4.13. Brace Hysteretic Response: 6x6x1/2 A1085 Y

Global buckling was observed in the 6x6x1/2 A1085 Y specimen at a compressive displacement of 0.25”, and the maximum compressive force was 218.7 kips. The lateral displacement at the center of the specimen reached a magnitude of twice the brace width at a compressive displacement of about 1.75”. The maximum tensile force was 727.2 kips, which corresponded to an axial brace displacement of 1.61”. The applied tensile forces in the following cycles decreased beyond this point, as the applied displacements grew larger. Local buckling deformations were first observed during the second cycle of the 4.25” target cycles, at an axial displacement of about 4.13”. During the 4.75” cycles, this cupping became more severe, and striations were observed at the center of the specimen in tension during the first cycle of the

5.25” target displacement. During the second cycle, tearing spread throughout the cross section and eventually the brace fractured at an axial displacement of 4.67”.

4.2.9 *7x7x5/16 A500 Y*

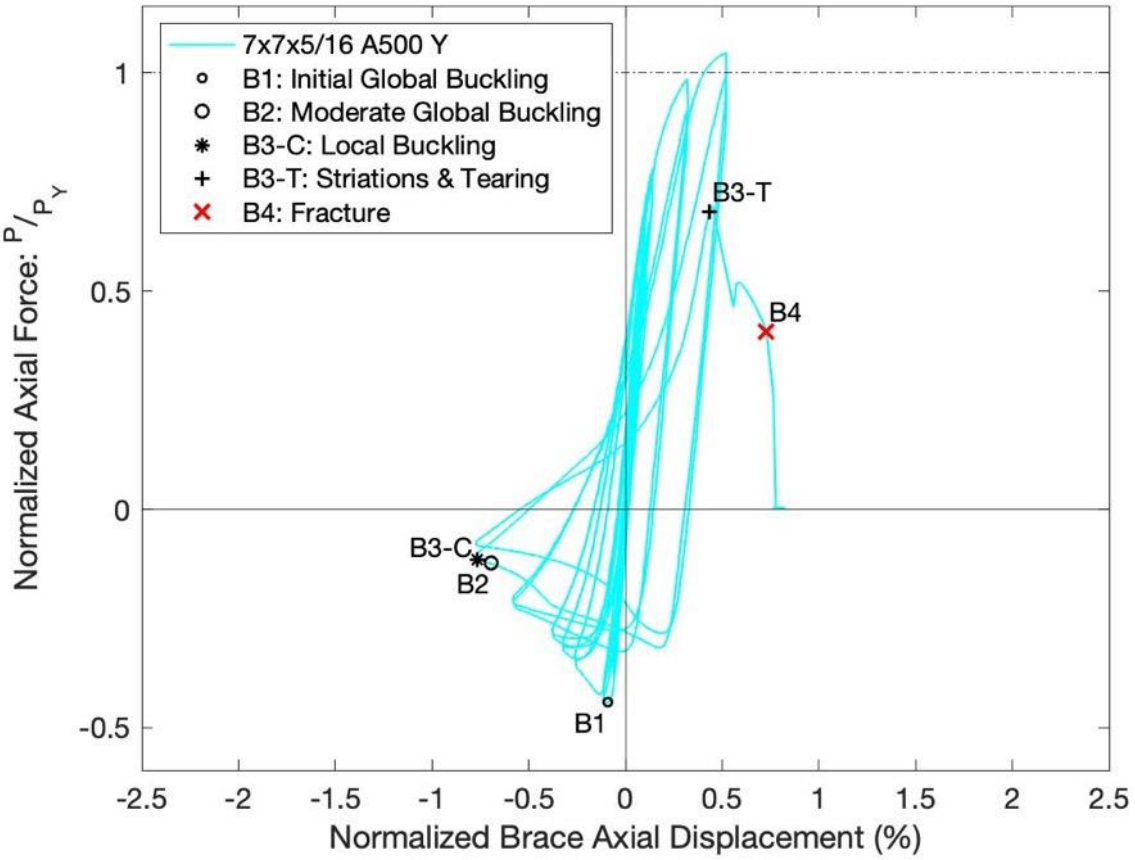

Figure 4.14. Brace Hysteretic Response: 7x7x5/16 A500 Y

The 7x7x5/16 A500 Y specimen exhibited global buckling at a compressive displacement of about 0.21”, where it reached a maximum compressive force of 209.8 kips. The lateral displacement at the center of the specimen did not exceed twice the brace width until it reached a compressive axial displacement of 1.65” during the 1.75” displacement cycles. Local buckling was observed at this same displacement level during the first cycle, at an axial displacement of 1.77”. A maximum tensile force of 496.6 kips was reached at an axial displacement of 1.23” during the first 1.75” target displacement cycle. After completing the 1.75” cycles, striations and tearing began to develop at the center of the specimen during the first 2.25” cycle. This tearing

quickly spread across the cross section, and the brace fractured in tension at an axial displacement of 1.73”.

4.2.10 *7x7x5/16 A1085 Y*

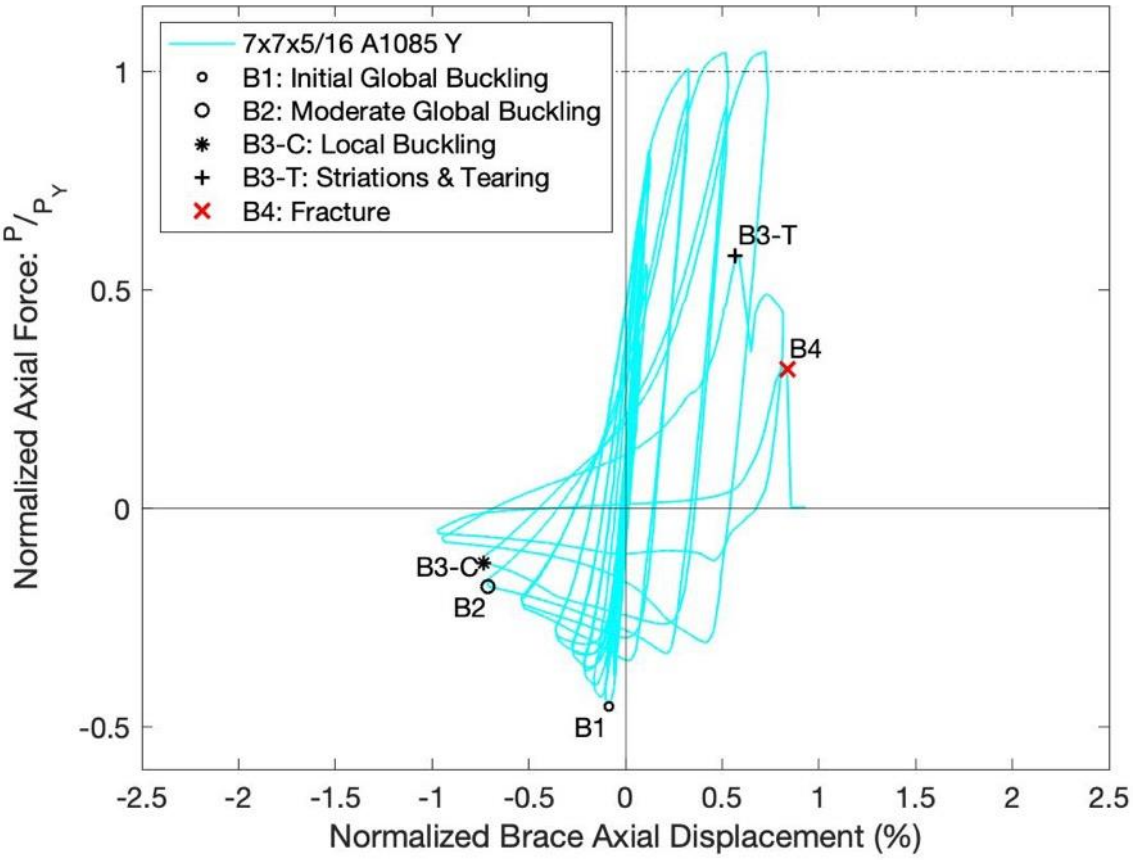

Figure 4.15. Brace Hysteretic Response: 7x7x5/16 A1085 Y

Global buckling was observed in the 7x7x5/16 A1085 Y specimen at an axial displacement of about 0.21”, and at this point the specimen experienced to a maximum compressive force of 201.5 kips. The buckling displacement exceeded twice the brace width at a compressive displacement of 1.69” during the first 1.75” displacement cycle. Local buckling was observed at the center of the specimen at an axial displacement of about 1.74” during the following cycle. The peak tensile force of 478.1 kips was reached at an axial displacement of 1.72” during the first cycle of the 2.25” target displacements. Striations and tearing developed in tension during the subsequent cycle resulting in a reduction in peak axial force, which was about

40% lower than the previous cycle. This tearing spread across the cross section, but the specimen did not fracture until it was put into tension during the first cycle at 2.75", at an axial displacement of about 1.93".

4.2.11 *7x7x3/8 A500 Y*

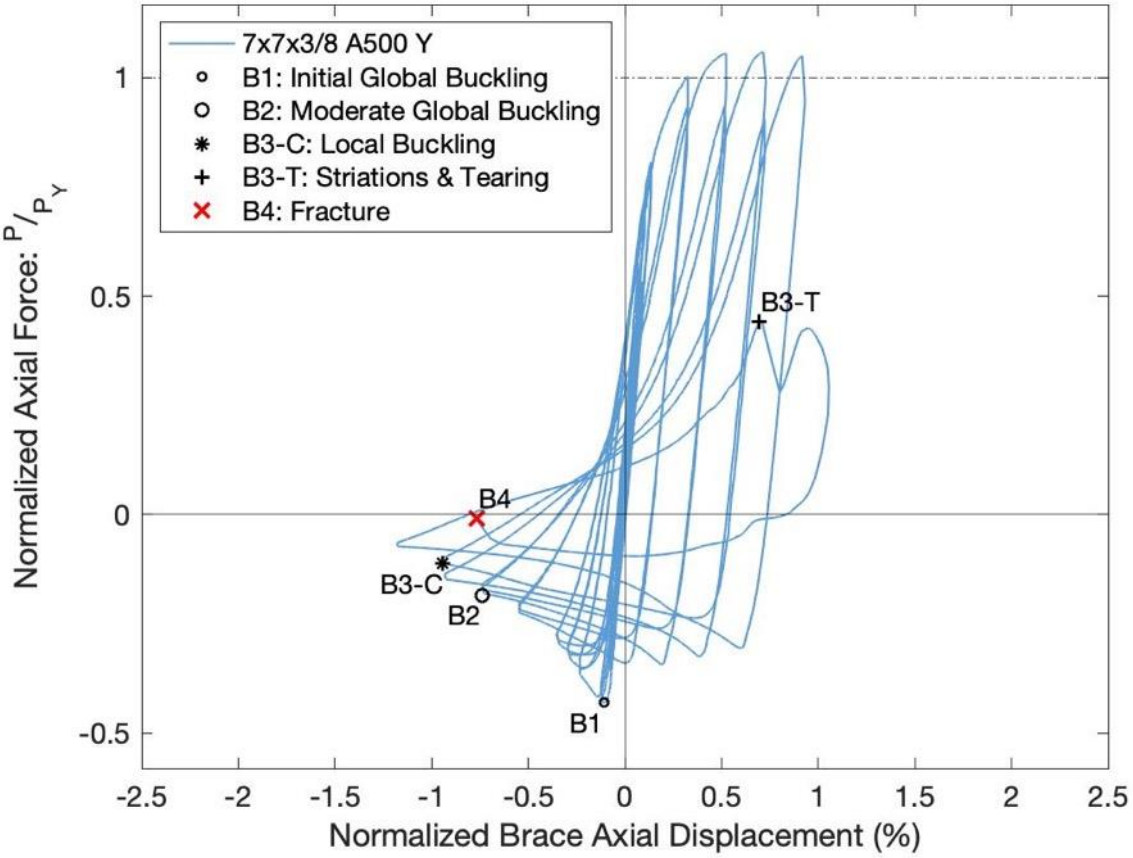

Figure 4.16. Brace Hysteretic Response: 7x7x3/8 A500 Y

Global buckling was observed in the 7x7x3/8 A500 Y specimen at an axial displacement of about 0.26", at which point the specimen reached a maximum compressive force of 231.8 kips. The horizontal displacement at the center of the specimen exceeded twice the brace width at a compressive axial displacement of 1.76". Local buckling deformations at the center of the specimen were first observed at a compressive axial displacement of about 2.23" during the second 2.25" target displacement cycle. A peak tensile force of 570.9 kips was reached at an axial displacement of about 1.7", and the peak forces during the first cycles of the 1.75", 2.25", and 2.75" were relatively constant. Striations and tearing were observed in tension during the

second 2.75” cycle, and the tearing spread across the east, top, and bottom sections of the cross section as the specimen reached its peak displacement. However, the brace did not fracture until it was put into compression, and ultimately fractured at a compressive displacement of about 1.82”.

4.2.12 *7x7x3/8 A1085 Y*

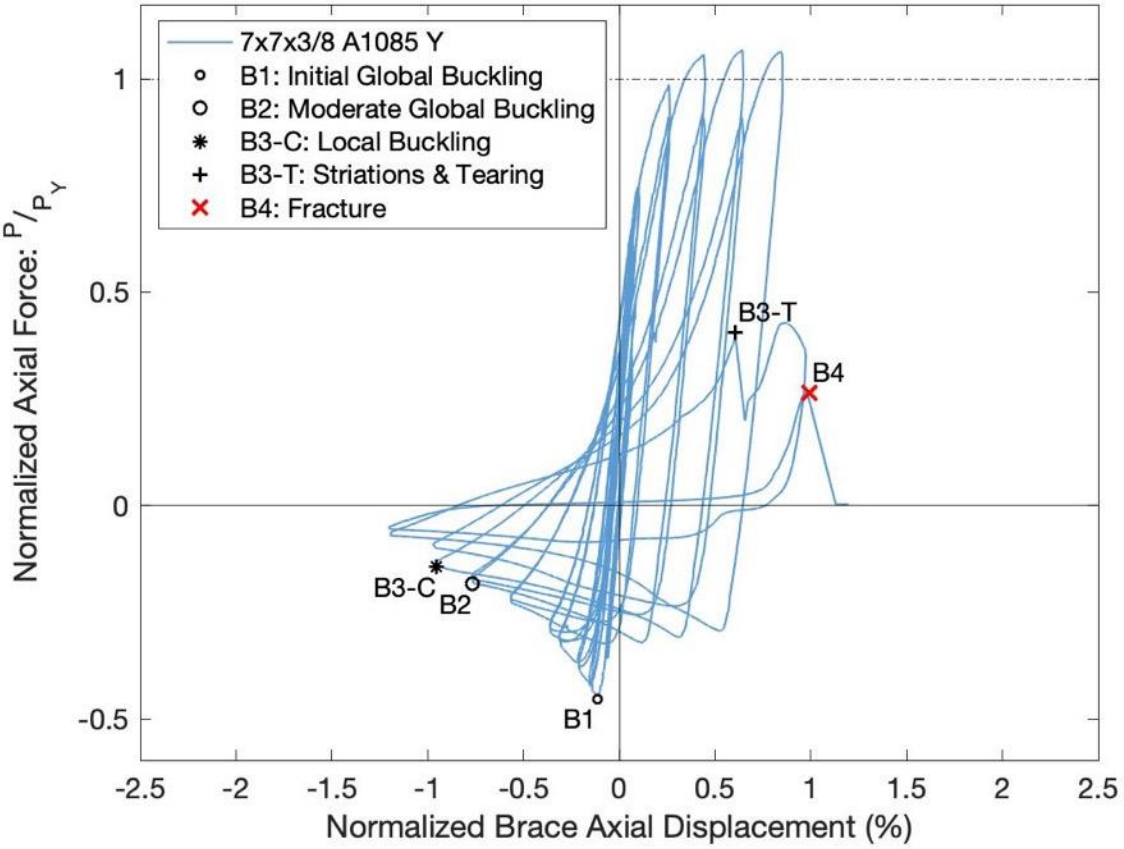

Figure 4.17. Brace Hysteretic Response: 7x7x3/8 A1085 Y

The 7x7x3/8 A1085 Y specimen buckled under a compressive displacement of 0.27” and reached a peak compressive force of 254.9 kips at this point. The horizontal displacement at the center of the specimen exceeded twice the brace width at an axial displacement of about 1.82”. Local buckling was observed at the center of the brace during the first 2.25” target displacement cycle at a compressive displacement of 2.27”. A maximum tensile force of 615.9 kips was reached at an axial displacement of 1.53” during the first 1.75” target displacement cycle. The tensile force applied during the first cycle of the 1.75”, 2.25” and 2.75” target displacements

remained relatively constant. Striations were observed at the center of the specimen at an axial displacement of about 1.44” during the second 2.75” target displacement cycle, and tearing spread across much of the cross section during this cycle. The brace didn’t fracture until it was put into tension during the subsequent cycle, the first 3.25” target displacement cycle. The brace fractured in tension at an axial displacement of 2.31”.

4.2.13 *7x7x1/2 A500 B*

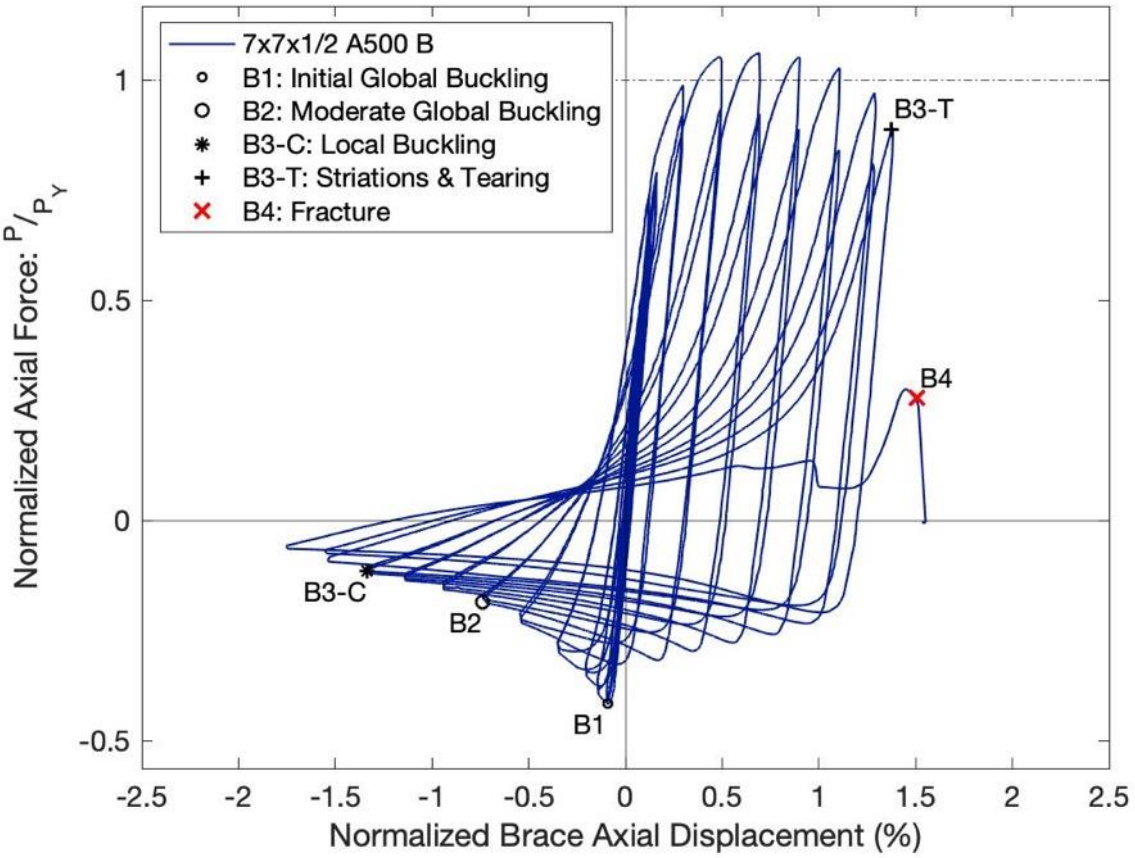

Figure 4.18. Brace Hysteretic Response: 7x7x1/2 A500 B

Global buckling was first observed in the 7x7x1/2 A500 B specimen at a compressive displacement of about 0.22”, at which point the brace reached a maximum compressive force of 278.8 kips. The horizontal buckling displacement exceeded twice the brace width in compression during the 1.75” target displacement cycles. A maximum tensile force of 710.4 kips was reached at an axial displacement of 1.64”, during the first 2.25” target displacement cycle. At larger target displacements, the peak tensile forces in the first cycle diminished slowly. Local cupping

was observed during the second cycle at the 3.25” target displacement. The cupping became more acute under greater compressive displacements. Due to this damage to the plastic hinge region of the brace, minor striations began to develop in tension during the first 4.25” displacement cycle. The brace ultimately fractured in tension during the subsequent cycle, at an axial displacement of about 3.45”.

4.2.14 *7x7x1/2 A1085 Y*

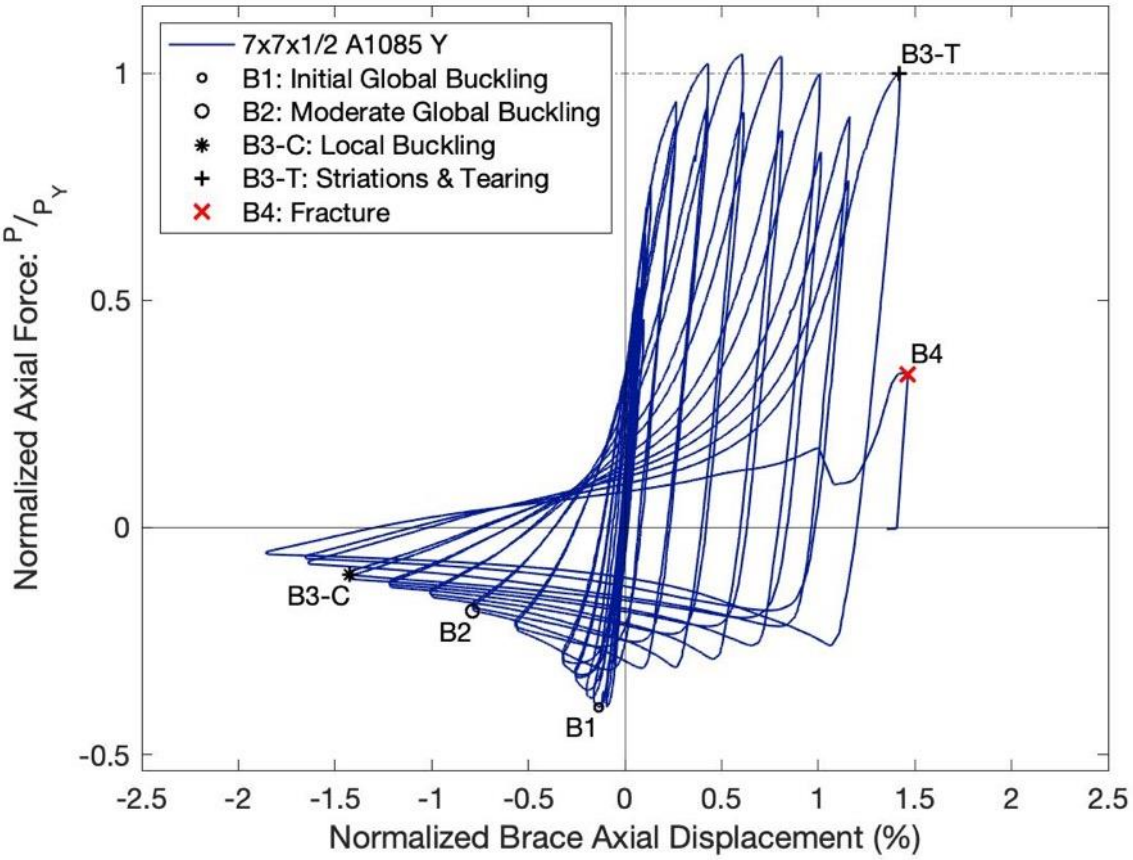

Figure 4.19. Brace Hysteretic Response: 7x7x1/2 A1085 Y

The 7x7x1/2 A1085 Y specimen experienced global buckling at a compressive axial displacement of about 0.32”, at which point it reached a maximum compressive force of 305.7 kips. The horizontal buckling displacement at the center of the specimen exceeded twice the brace width during the 1.75” target displacement cycles. A maximum tensile force of 805.1 kips was reached at an axial displacement of 1.44” during the first 2.25” target displacement cycle. The maximum tensile force achieved during the first cycle of the larger target displacements

diminished slowly, although at there was a significant increase in the axial force between the first 3.75” and 4.25” target displacement cycles. Local buckling was initially observed during the second 3.25” cycle, at an axial displacement of about 3.38”. Minor striations developed at the center of the specimen during the first 4.25” cycle, although significant tearing did not occur until the subsequent cycle. Tearing began to spread through the section during the second 4.25” cycle, an eventually the brace fractured at an axial displacement of about 3.42”.

4.2.15 *8x8x3/8 A500 W*

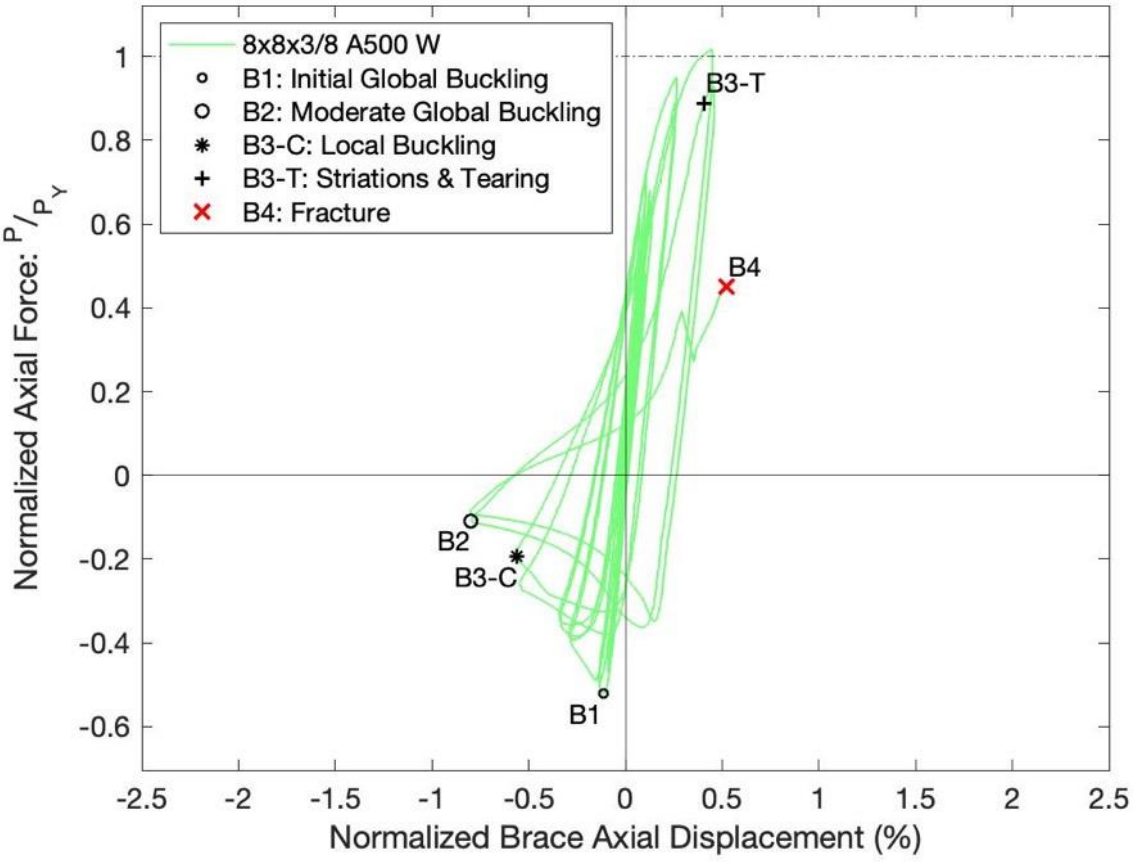

Figure 4.20. Brace Hysteretic Response: 8x8x3/8 A500 W

Global buckling was observed in the 8x8x3/8 A500 W specimen at a compressive axial displacement of about 0.33”, at which point the brace reached a peak compressive force of 360 kips. Local buckling at the center of the brace was first observed during the second 1.25” cycle at a compressive axial displacement of about 1.33”. A maximum tensile force of 702.7 kips was

reached at an axial displacement of 1.06” during the first 1.75” cycle. The local buckling deformations became more severe during the 1.75” target displacement cycles. Striations developed at the center of the brace at a tensile axial displacement of 0.96” during the second 1.75” target displacement cycle. The lateral displacement at the center of the brace exceeded twice the brace width during the 1.75” target cycles, after local buckling had already developed at the center. During the first 2.25” target cycle, the tearing propagated across the brace and the brace eventually fractured at an axial displacement of 1.25”.

4.2.16 *8x8x3/8 A1085 Y*

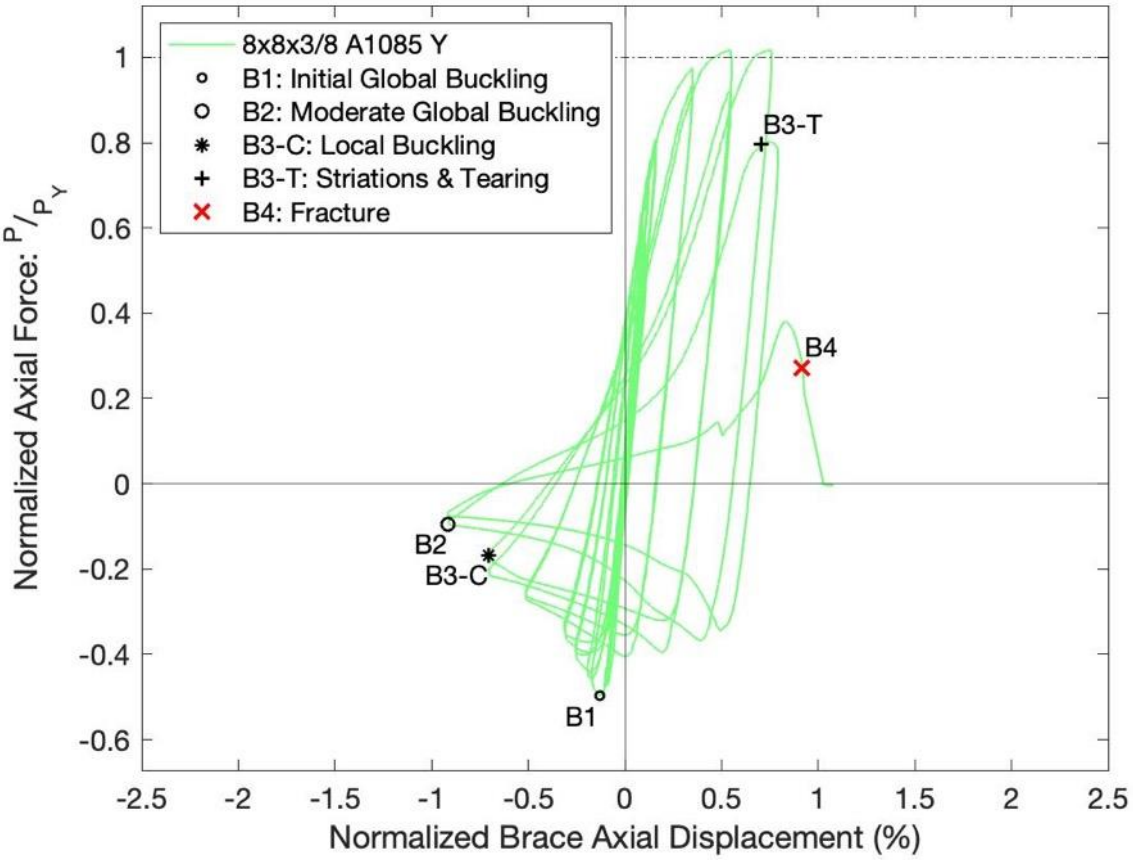

Figure 4.21. Brace Hysteretic Response: 8x8x3/8 A1085 Y

The 8x8x3/8 A1085 Y specimen exhibited global buckling at an axial displacement of about 0.31”, at which point a maximum compressive force of 328.8 kips was applied. The brace reached a peak tensile force of 672.6 kips at an axial displacement of 1.29” during the first 1.75” target displacement cycle. Local buckling was initially observed during the second 1.75” target

displacement cycle, at an axial displacement of 1.68". The horizontal buckling displacement at the center of the brace exceeded twice the brace width in compression during the 1.75" target cycles. As the brace was put into tension during the second 2.25" target displacement cycle, striations and tearing developed at the center of the brace. The tearing spread across the east and bottom walls of the tube, leaving the west wall and much of the top wall intact. The tearing propagated across the rest of the section during the subsequent cycle, the first 2.75" cycle. The brace ultimately fractured during this cycle at an axial displacement of about 2.18".

4.2.17 ***8x8x1/2 A500 W***

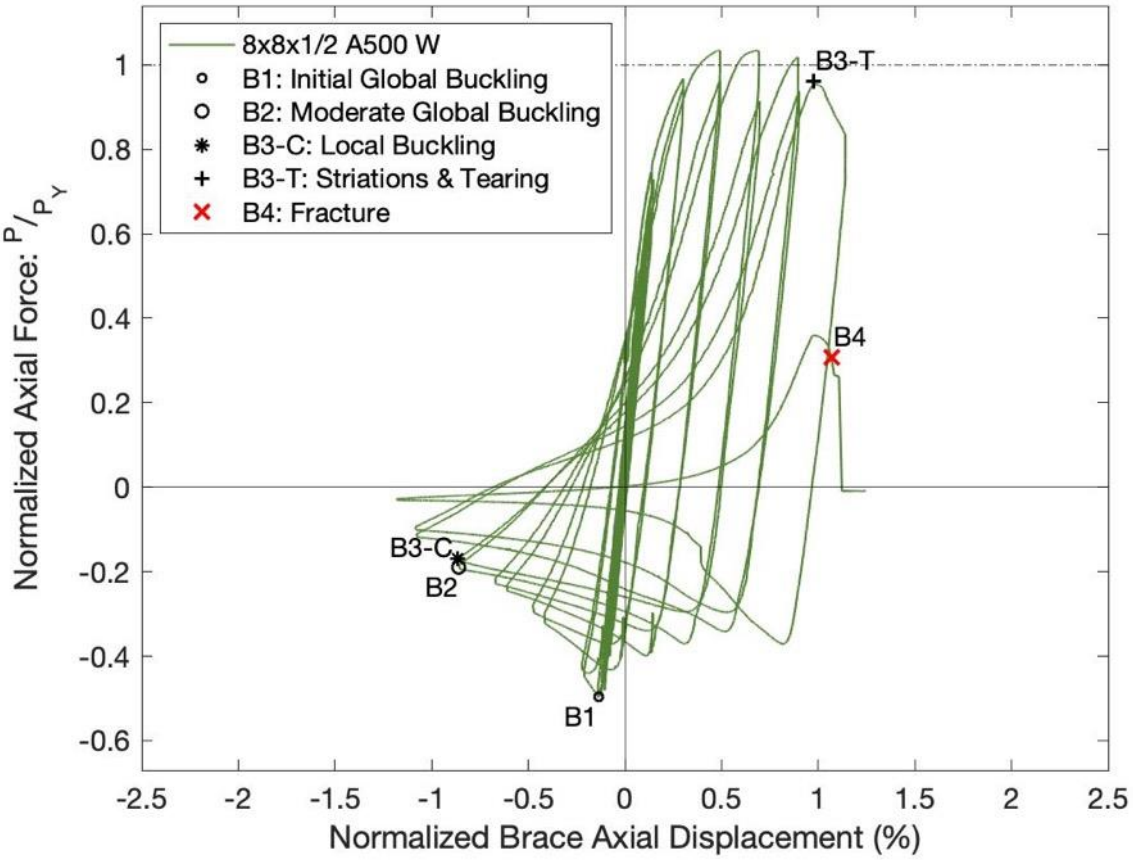

Figure 4.22. Brace Hysteretic Response: 8x8x1/2 A500 W

The 8x8x1/2 A500 W test specimen exhibited global buckling behavior at a compressive axial displacement of about 0.33", and reached a peak compressive force of 434.7 kips at this

point. The maximum axial force of 906.0 kips was reached at an axial displacement of 1.17” during the first 1.75” target displacement cycle. The lateral buckling displacement exceeded twice the brace width during the 2.25” target displacement cycles. Local buckling deformations were first observed at a compressive axial displacement of 2.05” during the second 2.25” target displacement cycle. Striations and tearing developed during the first 3.25” target displacement cycle at an axial displacement of 2.32”. During this cycle, the tearing propagated across much of the cross section, leaving only the west flange at the center intact. The direction of buckling flipped when the brace was put into compression, and the brace began to buckle towards the east. Figure 4.23 below shows this behavior, the image on the left shows the original buckling direction of the specimen during the cycles leading up to brace tearing. The photographs on the center and right show the brace buckling to the east after tearing. The out-of-plane buckling displacement was measured manually, since this behavior caused the string potentiometers at the center of the specimen to be out of range. The tearing spread throughout the rest of the cross section during the subsequent cycle in tension, and the brace ultimately fractured at an axial displacement of 2.54”.

Figure 4.23. Horizontal buckling behavior of the 8x8x1/2 A500 W Specimen

4.2.18 *8x8x1/2 A1085 Y*

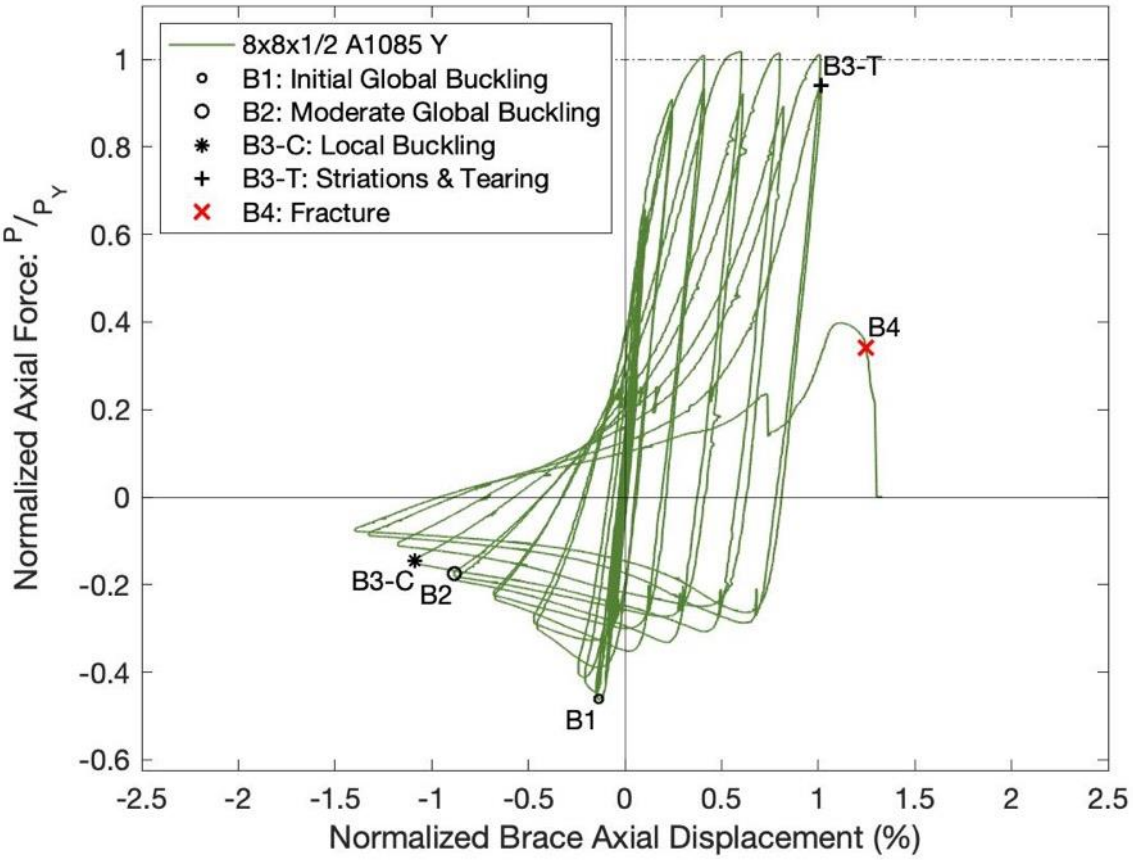

Figure 4.24. Brace Hysteretic Response: 8x8x1/2 A1085 Y

The 8x8x1/2 A1085 Y test specimen reached a maximum compressive force of 418.2 kips, and global buckling under this load was observed at an axial displacement of 0.32”. The horizontal buckling displacement exceeded twice the brace width at an axial displacement of 2.1” in compression during the 2.25” target displacement cycles. A maximum tensile force of 921.9 kips was reached during the first 2.25” target displacement cycle, at which point the brace axial displacement was 1.43”. Local buckling deformations at the center of the specimen were first observed during the first 2.75” target displacement cycle, at an axial displacement of 2.58”. Striations were initially observed at the corners of the specimen during the second 3.25” target displacement cycle, at a tensile axial displacement of 2.41”. Tearing propagated throughout the cross section during the first 3.25” target displacement cycle, and the brace ultimately fractured in tension at an axial displacement of 2.96”.

4.2.19 *10x10x3/8 A500 W*

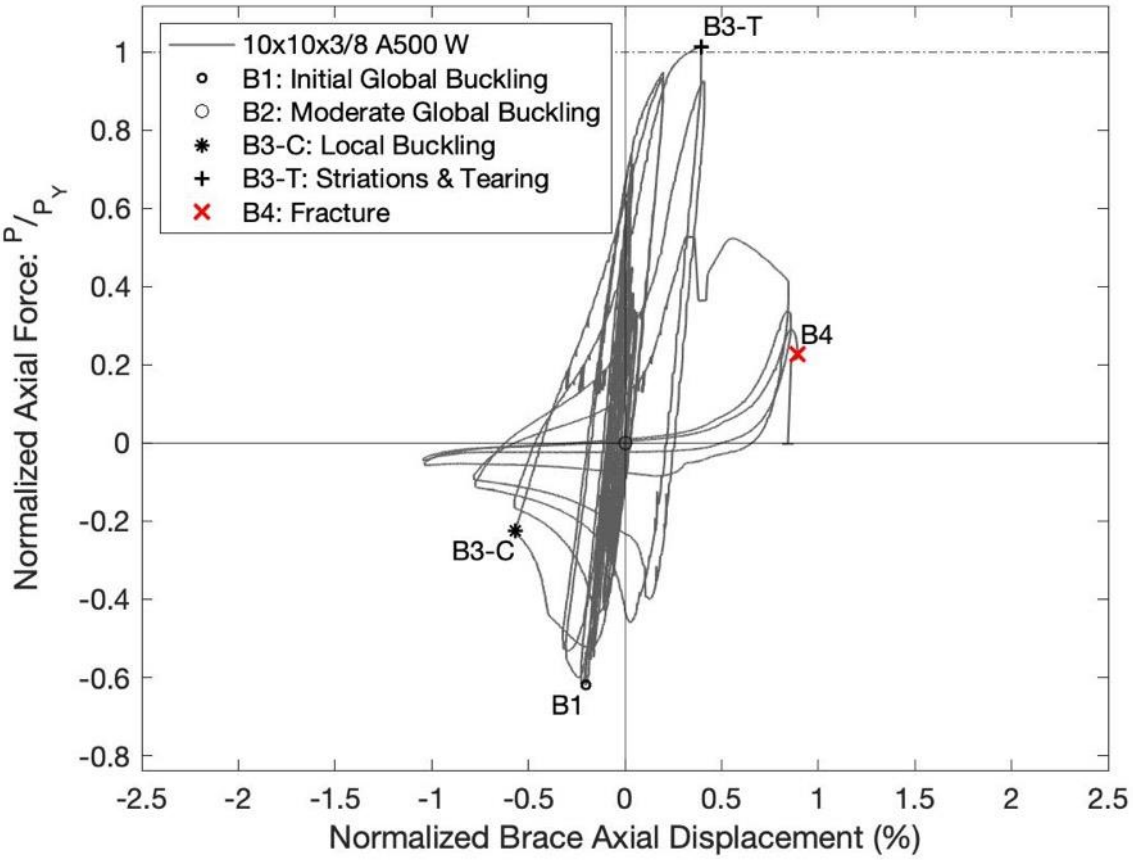

Figure 4.25. Brace Hysteretic Response: 10x10x3/8 A500 W

Global buckling was observed in the 10x10x3/8 A500 W test specimen at a compressive axial displacement of 0.48”, and the specimen reached a peak compressive force of 480.1 kips at this point. Unlike previous tests, the horizontal buckling displacement did not exceed twice the brace width prior to brace fracture. Local buckling deformations were first observed at a compressive axial displacement of 1.35” during the first 1.25” target displacement cycle. This was the earliest development of local buckling deformations of any of the previous test specimens. A maximum tensile force of 785.4 kips was reached at an axial displacement of 0.94” during the first 1.75” target displacement cycle. Striations were observed in the center of the specimen at the corners during this same cycle at the peak axial displacement of 0.94”. Tearing did not propagate across the cross section until the first 2.25” target displacement cycle, at which point the tearing spread across the east wall and halfway across the top and bottom walls. The local buckling deformations became more severe in these larger displacement cycles and the

tearing continued to spread across the cross section, but the brace survived both 2.25” target displacement cycles. The brace ultimately fractured in tension during the first 2.75” target displacement cycle, at an axial displacement of 2.12”.

4.2.20 *10x10x3/8 A1085 Y*

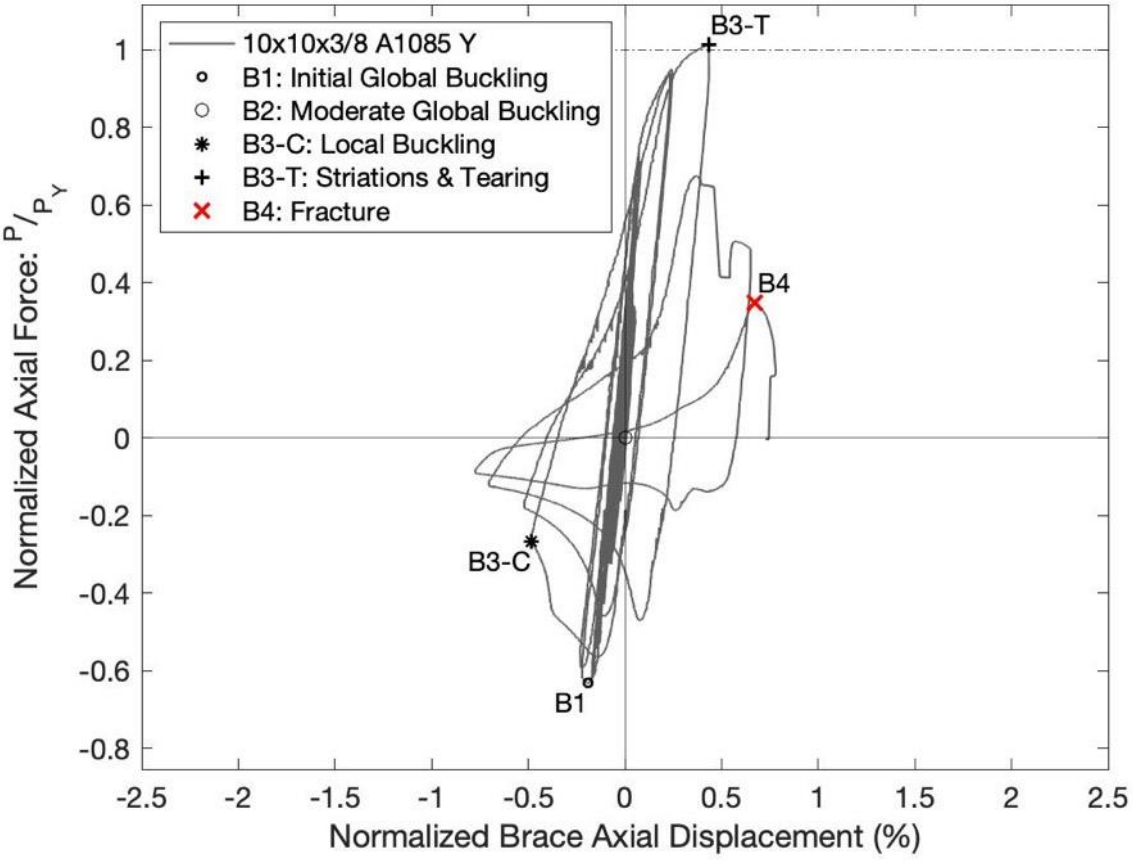

Figure 4.26. Brace Hysteretic Response: 10x10x3/8 A1085 Y

The 10x10x3/8 A1085 Y test specimen reached a maximum compressive force of 507.6 kips, at which point it experienced global buckling at an axial displacement of 0.45”. Similar to the 10x10x3/8 A500 W specimen, the horizontal buckling displacements did not exceed twice the brace width prior to brace fracture. A maximum tensile force of 812.8 kips was reached at an axial displacement of 1.03” during the first 1.75” target displacement cycle. Local buckling deformations at the center of the brace were first observed at a compressive axial displacement

of 1.15” during the first 1.25” target displacement cycle. Striations developed at the corners of the brace during the first 1.75” target displacement cycle at a tensile displacement of 1.03”. Tearing propagated halfway through the cross section during the subsequent cycle. The brace fractured in tension at an axial displacement of 1.6” during the first 2.25” target displacement cycle.

Chapter 5. DATA ANALYSIS

5.1 INTRODUCTION

The processing and analysis of the experimental results and observations discussed in Chapter 4 is presented in this chapter. The data analysis and interpretation of results makes it possible to compare aspects of test specimen performance that cannot be directly measured through observation. Test specimen response and behavior is quantified in this chapter using the analysis techniques discussed below. In this analysis, comparisons are made to investigate the impact of the study variables such as specimen local compactness, global slenderness, and steel type on the cyclic response of braces.

Section 5.2 describes the methods used to process the raw data collected during the tests. Next, comparisons of test specimen performance and behavior between the A500 and A1085 specimens from each of the ten HSS shapes are presented in Section 5.3. These comparisons are based on factors such as test specimen geometry, material properties, yield force, ultimate force, buckling force, deformation capacity, and energy dissipation capacity.

Comparisons across the entire data set are presented in Section 5.4. The effects of cross-sectional compactness, global slenderness, steel type, and steel producer are analyzed based on the ductility, energy dissipation capacity, and toughness of the specimens. Various data trends are discussed in this section, which are used to explain differences in behavior between the test specimens.

5.2 DATA PROCESSING

As described in Section 3.7, the displacement, strain, and force data were collected using LabVIEW software developed by National Instruments. Data points were collected at a frequency of 5 Hz throughout the entirety of each test, and data collection was only stopped upon the completion of a test when the brace fractured. Similarly, Optotrak data was collected using Northern Digital, Inc. First Principles software. Since data was recorded during the entire testing procedure, the data files were generally quite large. These files were processed to remove data collected during stops and holds, as well as unexpected spikes in the data.

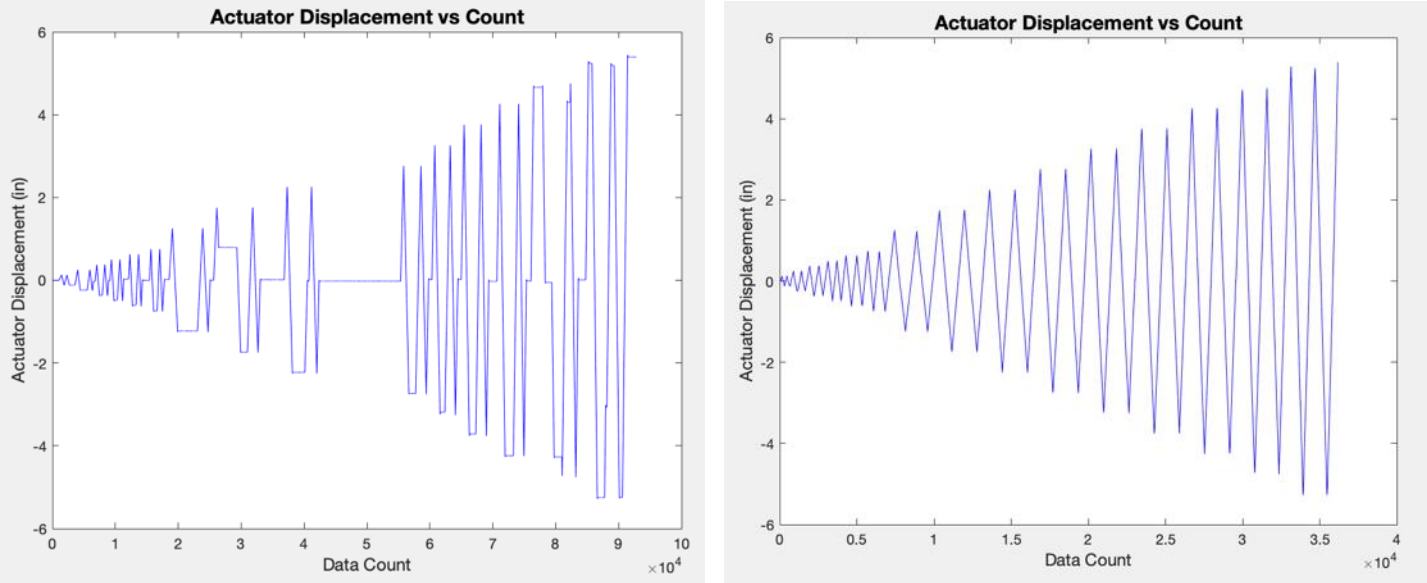

(a) (b)

Figure 5.1. Raw (a) and Processed (b) LabVIEW Data

Several Matlab scripts were developed to automatically process the test data, which are included in Appendix 4. The code to process the data was written to remove data points during pauses for which the actuators were not moving during test holds. Generally, the script removes rows of data if the difference in actuator position between two points is below a certain tolerance. Since the actuators were moved at a faster rate during larger displacement cycles, the code is flexible and uses different processing variables based on the target displacement. Figure 5.1 above shows the difference between the original, raw test data and the trimmed data with the holds removed. This reduced the size of the file significantly, making the data analysis process faster and easier.

After processing the raw data, corrections were applied to the brace axial displacement data to account for rotation of the instrument. In particular, the string potentiometer attached to the side of the brace measuring axial displacement rotated as the specimen buckled out of plane (horizontally) when the brace was in compression. This rotation amplified the measured compressive axial displacement, and needed to be corrected. In this script, the angle of rotation at the brace end was calculated based on the measured rotation of the gusset plates. String potentiometers measured the displacement at two locations along the gusset plates, which was used to calculate the end rotation of the plates throughout each test. The data from the

string potentiometers attached to the gusset plates and brace was processed to remove spikes in the data, which made it easier to determine and correct the rotations during the tests. This was accomplished by checking whether the difference in two adjacent data values exceeded a set tolerance. The tolerance was assigned manually.

Additionally, this script required several geometric inputs from the test specimen and instrumentation to accurately correct for the rigid body rotation of the axial brace string potentiometer. These inputs include the distance between gusset plate string potentiometers, the gusset plate width and eccentricity, the brace width, and exact location of the axial brace string pot relative to the north and south ends of the brace. Figure 5.2 (b) below shows the rigid body rotation at the ends of the test specimen which causes the amplification of the axial brace string potentiometer measurements. Corrections to the measured axial displacements are not necessary when the brace is straight (a).

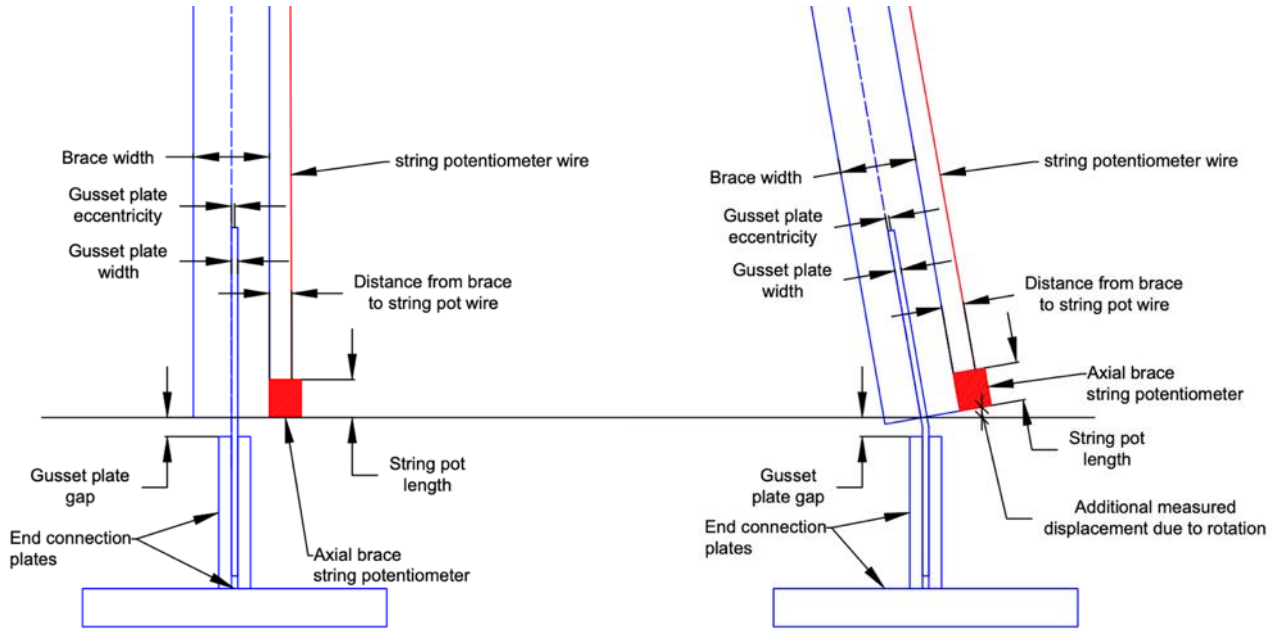

(a) (b)

Figure 5.2. Effects of string potentiometer rigid body rotation

As shown in Figure 5.3 below, these corrections were significant when the brace was subjected to large compressive displacements, due to the significant rotation of the gusset plates

as the brace buckled horizontally. The corrected axial displacements were compared to data from another string potentiometer measuring the total specimen axial displacement from the north to south connection plates. This was done to ensure that the corrected brace axial displacement data was accurate. After properly correcting the test data, it was saved as a final data file which was used to analyze the specimen behavior and performance. The plots and tables in the following sections were developed using these final data files for each test specimen.

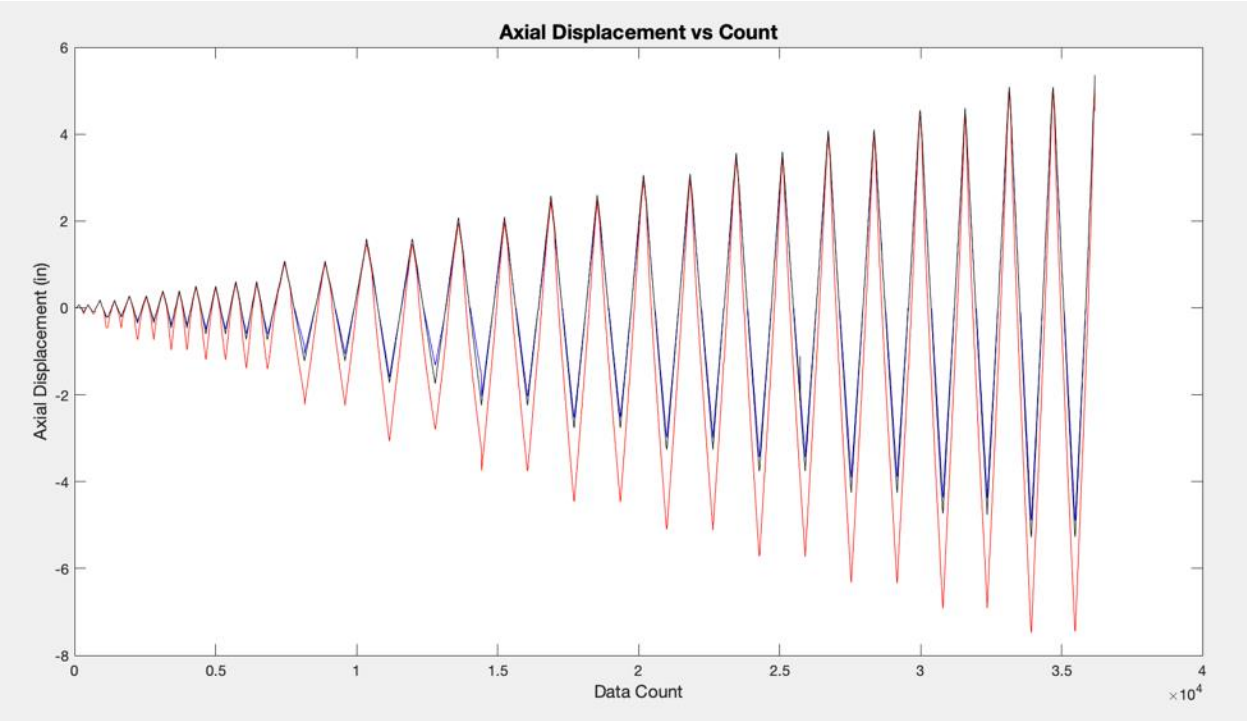

Figure 5.3. Original (Red), Corrected (Blue), and Total (Black) Axial Displacement

One of the comparisons presented in this analysis is based the normalized energy dissipation capacity for each of the test specimens. Energy dissipation capacity is a key component of the seismic performance of brace members in braced frames. To perform adequately in seismic events, braced frames must be able to dissipate seismic energy through the inelastic buckling and yielding of braces. Energy dissipation is based on the force-displacement behavior of a member, and is calculated following the general form of the equation shown below:

$$W = \int F \cdot \Delta d$$

The above integral can be used to determine the area under the force-displacement curve during each cycle of testing, which is the amount of energy dissipated during the cycle. The energy dissipation capacity of a member is the total amount of energy dissipated prior to fracture, and is the summation of energy dissipated in each cycle. The cumulative energy dissipated by each member was calculated using a Matlab script modified from a previous research project at the UW SRL. (Swatosh, 2016) In this script, a cumulative trapezoidal integration was performed across the entire force-displacement history for each test. This integration is described by the following equation:

$$W = \sum_{i=1}^{n} \frac{F_i + F_{i-1}}{2} (\Delta_i - \Delta_{i-1})$$

In the above equation, W represents the cumulative energy dissipated during a test, F is the applied actuator force, Δ is the axial brace displacement, and n is the number of data points during the test. This script calculated the cumulative energy dissipated for all of the completed cycles during each test, and a similar script was used to calculate the energy dissipated by the brace during the final cycle prior to fracture.

5.3 PAIRED HSS SECTIONS

In this section, comparisons will be presented between the A1085 and A500 specimens for each HSS shape included in this experimental program. In these comparisons, the differences in cross-sectional geometry and material properties will be evaluated between the A500 and A1085 sections. Additionally, comparisons of specimen performance will be discussed for each of the HSS shapes. These comparisons are presented to evaluate the relationship between steel type and brace performance. Table 5.1 below presents a summary of the observed performance for each of the twenty test specimens. The maximum tensile and compressive force, $P_{T,max}$ and $P_{C,max}$, for each of the specimens are presented, as well as the ratio of these peak forces to the predicted yield and critical buckling forces, P_Y and P_{Cr}. The maximum tensile and compressive brace axial displacements are presented in this table as $\Delta_{T,max}$ and $\Delta_{C,max}$, respectively. The overall displacement range is displayed in this table as Δ_{Range}, which is the sum of the peak tensile and compressive displacements. The accumulated brace displacement is also presented in

this table, which is computed as the summation of all brace axial displacements prior to the point of brace fracture, and is shown in the table as Δ_{Acc}. For each of these axial brace displacement measurements, the corresponding approximate drift ratio is shown below in parentheses. The approximate drift ratio is calculated following the approach presented in Section 4.1. The normalized energy dissipation capacity of each specimen is also shown in this table. The energy dissipation capacity, $\sum E_{Diss}$, calculated following the approach discussed above, is normalized by the measured cross-sectional area and yield strength of each specimen, $A_{g,m}$ and $F_{Y,m}$, respectively.

In the section comparisons presented below, the force-displacement hysteretic curves for both the A1085 and A500 specimens are presented on a single plot. These plots are shown for each individual specimen in Section 4.2, and in the following plots the hysteretic curve for the A500 section is shown in gray to distinguish between the A1085 and A500 sections. Additionally, the normalized cumulative energy dissipated at each target displacement and at the point of fracture is shown in a plot for each pair of test specimens, where once again the A500 curve is shown in gray. These plots show the energy dissipation capacity as well as the maximum axial displacement prior to fracture. In these plots, the energy dissipation capacity is again normalized by $A_{g,m}$ and $F_{Y,m}$ for each specimen. Additional information regarding the geometric and material properties of the test specimens can be found in Table 4.2 and Table 4.3. A brief comparison is presented for each pair of HSS shapes based on the observed ductility and energy dissipation capacity. Unexpected brace behavior is noted in these comparisons, and differences in specimen performance are explained based on data in the comparison tables and figures.

Table 5.1. Comparison of Test Specimen Performance

Test Specimen	$P_{T,max}$ (kips) ($P_{T,max}/P_Y$)	$P_{C,max}$ (kips) ($P_{C,max}/P_{Cr}$)	$\Delta_{T,max}$ (in.) (Drift %)	$\Delta_{C,max}$ (in.) (Drift %)	Δ_{Range} (in.) (Drift %)	Δ_{Acc} (in.) (Drift %)	$\frac{\sum E_{Diss}}{A_{g,m}F_{y,m}}$
5x5x3/8 A500 Y	432.50 *(1.04)*	-95.30 *(0.99)*	5.13 *(4.28)*	4.89 *(4.07)*	10.02 *(8.35)*	119.54 *(99.65)*	20.57
5x5x3/8 A1085 Y	443.60 *(1.02)*	-98.38 *(0.97)*	5.25 *(4.38)*	5.50 *(4.59)*	10.75 *(8.96)*	132.02 *(110.05)*	21.74
6x6x5/16 A500 R	409.70 *(1.06)*	-125.75 *(0.82)*	3.06 *(2.55)*	3.26 *(2.71)*	6.31 *(5.26)*	52.34 *(43.63)*	13.29
6x6x5/16 A1085 Y	456.40 *(1.07)*	139.80 *(0.87)*	3.13 *(2.61)*	3.12 *(2.60)*	6.25 *(5.21)*	51.33 *(42.79)*	12.57
6x6x3/8 A500 R	511.00 *(1.05)*	-168.70 *(0.96)*	3.74 *(3.12)*	3.72 *(3.10)*	7.46 *(6.22)*	65.80 *(54.85)*	16.45
6x6x3/8 A1085 Y	547.90 *(1.01)*	-180.00 *(0.97)*	3.52 *(2.93)*	3.52 *(2.93)*	7.04 *(5.87)*	56.61 *(47.19)*	13.63
6x6x1/2 A500 R	646.20 *(1.02)*	-218.70 *(1.01)*	4.45 *(3.71)*	4.06 *(3.39)*	8.51 *(7.10)*	80.64 *(67.22)*	17.25
6x6x1/2 A1085 Y	727.20 *(1.06)*	-218.60 *(0.97)*	4.67 *(3.89)*	5.12 *(4.27)*	9.79 *(8.16)*	97.41 *(81.21)*	22.36
7x7x5/16 A500 Y	496.60 *(1.05)*	-209.80 *(0.88)*	1.73 *(1.44)*	1.83 *(1.53)*	3.56 *(2.97)*	20.29 *(16.91)*	5.82
7x7x5/16 A1085 Y	478.10 *(1.05)*	-201.50 *(0.80)*	1.99 *(1.66)*	2.31 *(1.92)*	4.29 *(3.58)*	27.94 *(23.30)*	8.01
7x7x3/8 A500 Y	570.90 *(1.06)*	-231.80 *(0.83)*	2.51 *(2.09)*	2.79 *(2.33)*	5.30 *(4.42)*	35.26 *(29.40)*	10.49
7x7x3/8 A1085 Y	615.90 *(1.07)*	-254.90 *(0.87)*	2.36 *(1.97)*	2.85 *(2.38)*	5.21 *(4.35)*	37.42 *(31.20)*	9.76
7x7x1/2 A500 B	710.40 *(1.06)*	-278.80 *(0.80)*	3.59 *(2.99)*	4.16 *(3.47)*	7.75 *(6.46)*	70.86 *(59.08)*	19.31
7x7x1/2 A1085 Y	805.10 *(1.04)*	-305.70 *(0.84)*	3.48 *(2.90)*	4.41 *(3.68)*	7.89 *(6.58)*	70.13 *(58.46)*	18.21
8x8x3/8 A500 W	702.70 *(1.02)*	359.98 *-(0.93)*	1.24 *(1.04)*	1.90 *(1.58)*	3.14 *(2.62)*	18.10 *(15.09)*	4.97
8x8x3/8 A1085 Y	672.60 *(1.02)*	-328.80 *(0.81)*	2.18 *(1.82)*	2.18 *(1.82)*	4.36 *(3.63)*	27.43 *(22.87)*	9.18
8x8x1/2 A500 W	905.97 *(1.03)*	-434.72 *(0.88)*	2.71 *(2.26)*	2.80 *(2.34)*	5.51 *(4.60)*	38.25 *(31.89)*	12.66
8x8x1/2 A1085 Y	921.90 *(1.02)*	-418.20 *(0.82)*	2.96 *(2.46)*	3.32 *(2.77)*	6.28 *(5.23)*	44.07 *(36.74)*	13.29
10x10x3/8 A500 W	785.40 *(1.01)*	-480.10 *(0.79)*	2.10 *(1.75)*	2.48 *(2.07)*	4.58 *(3.81)*	25.71 *(21.43)*	5.96
10x10x3/8 A1085 Y	812.80 *(1.01)*	-507.60 *(0.81)*	1.60 *(1.33)*	1.84 *(1.53)*	3.44 *(2.87)*	15.66 *(13.05)*	4.67

5.3.1 *Section 1: 5x5x3/8 HSS*

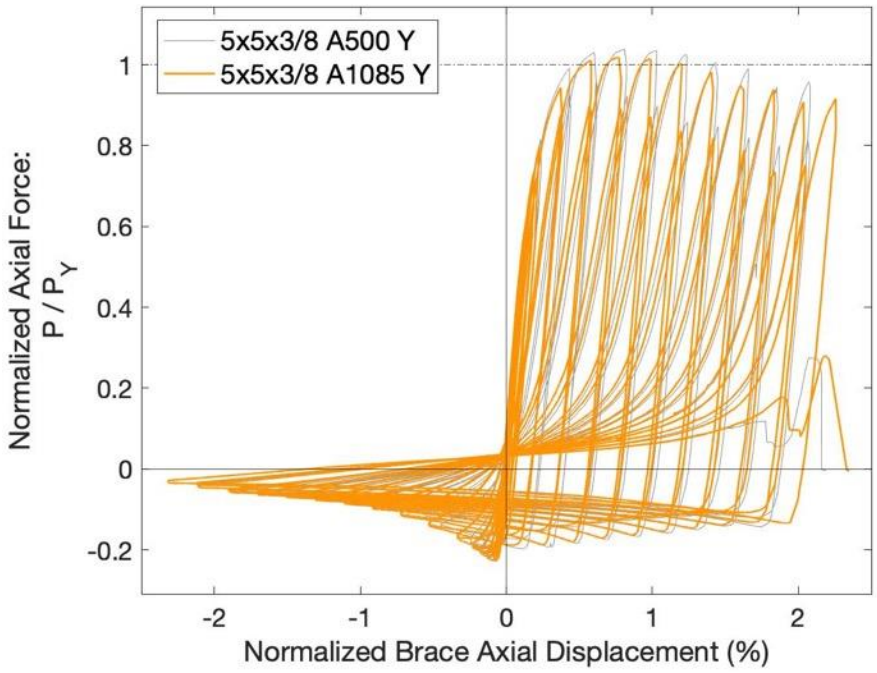

Figure 5.4. Force-Displacement Response - 5x5x3/8 HSS

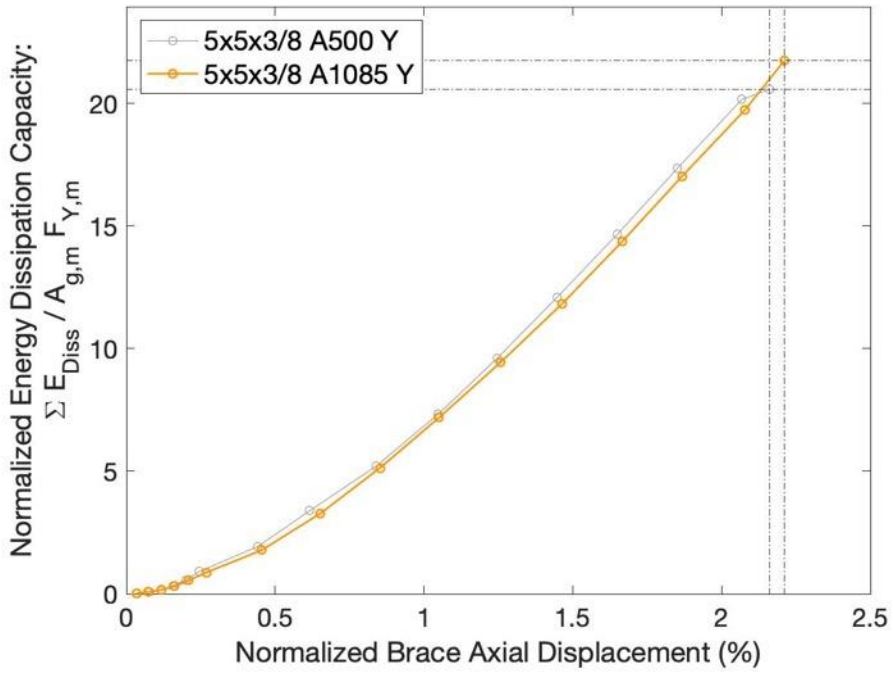

Figure 5.5. Energy Dissipation Capacity - 5x5x3/8 HSS

The 5x5x3/8 HSS specimens exhibited similar behavior throughout testing, although the 5x5x3/8 A1085 Y specimen demonstrated slightly greater ductility than the 5x5x3/8 A500 Y specimen. Both sections meet the AISC width-to-thickness limits for highly-ductile members. These specimens were the most globally slender members tested, with KL/r ratios of about 127. As shown in Table 4.3, the toughness of the A1085 specimen was slightly greater than that of the A500 specimen. The ratios of maximum measured tensile and compressive forces to the predicted yield and critical buckling loads were 1.04 and 0.99 for the A500 specimen, and 1.02 and 0.97 for the A1085 specimen, as shown in Table 5.1.

The force-displacement responses shown in Figure 5.4. are nearly identical until the final cycle for each specimen. The A500 specimen fractured during the first 5.75" target displacement cycle, while the A1085 section survived an additional cycle, and fractured in tension during the second 5.75" cycle. The A1085 specimen reached a displacement range of 10.75" (8.96% drift), compared with 10.02" (8.35% drift) for the A500 specimen. The axial displacements measured for these specimens are the largest and second largest of any test specimen included in this test series. The accumulated brace displacement prior to fracture of the A1085 specimen was 132.0" (110.1% drift), which was about 10% greater than that of the A500 specimen. Additionally, the A1085 specimen exhibited slightly greater energy dissipation capacity compared with the A500 specimen, which is shown in Figure 5.5. The normalized energy dissipation capacity of the A1085 specimen was about 6% greater than the A500 specimen.

5.3.2 *Section 2: 6x6x5/16 HSS*

The 6x6x5/16 HSS specimens performed similarly in most respects, with only minor differences in behavior and performance. The A1085 specimen just barely meets the AISC limit for moderately ductile members with a nominal b/t ratio of 16.2, while the A500 specimen does not meet the criteria for moderately ductile members. The A500 specimen was found to have significantly greater toughness through Charpy V-Notch testing, as shown in Table 4.3. The ratios of maximum measured tensile and compressive forces to the predicted yield and critical buckling loads were 1.06 and 0.82 for the A500 specimen, and 1.07 and 0.87 for the A1085 specimen, as shown in Table 5.1. These maximum compressive forces were relatively low compared to other test specimens, and may have been caused by extra eccentricity in the gusset

plates or initial member crookedness. The maximum tensile and compressive axial displacements were similar for both specimens. The A500 specimen reached a displacement range of 6.32" (5.26% drift), compared with 6.25" (5.21% drift) for the A1085 specimen. Brace fracture occurred in tension during the first 3.75" target displacement cycle in both specimens.

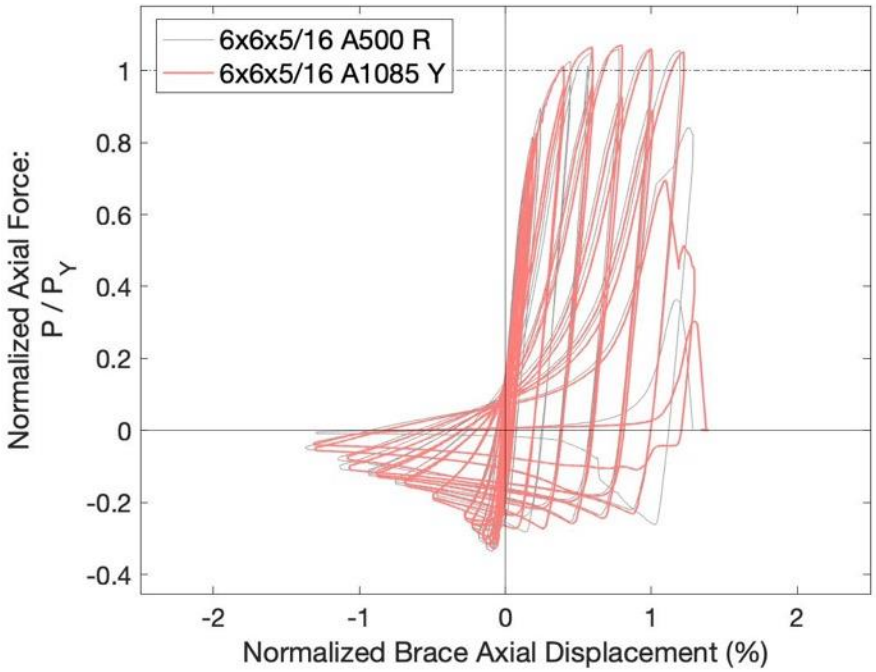

Figure 5.6. Force-Displacement Response – 6x6x5/16 HSS

The accumulated brace displacements and story drifts were nearly identical between the specimens, with the A500 specimen exhibiting less than a 2% increase compared with the A1085 specimen. The normalized energy dissipation capacity of the A500 specimen was about 6% greater than that of the A1085 specimen, as shown in Figure 5.7. Part of this difference may be due to the post-tearing behavior exhibited by the two specimens. After striations began to develop in the A500 specimen, the axial force continued to increase to about 80% of the maximum tensile force. In contrast, the development of striations in the A1085 specimen was quickly followed by the propagation of brace tearing, which led to a significant reduction in axial force during this penultimate cycle. This behavior can be seen in Figure 5.6, and may have been a factor in the lower energy dissipation capacity of the A1085 specimen.

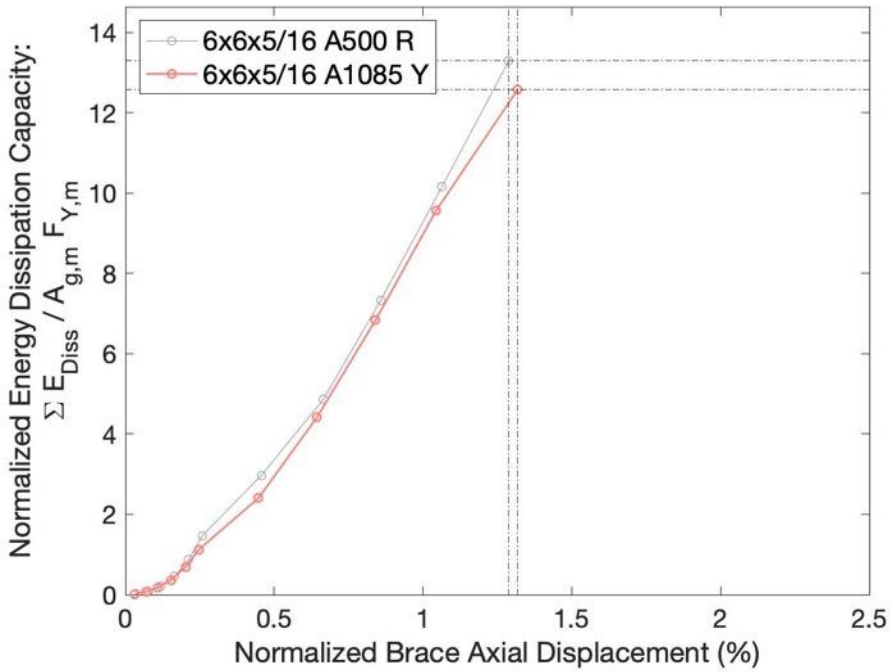

Figure 5.7. Energy Dissipation Capacity – 6x6x5/16 HSS

5.3.3 ***Section 3: 6x6x3/8 HSS***

The 6x6x3/8 A500 R test specimen exhibited slightly better performance than the 6x6x3/8 A1085 Y specimen in terms of ductility and energy dissipation capacity. The A1085 specimen meets AISC width-to-thickness limits for highly ductile members, while the A500 specimen meets the moderately ductile criteria. It was determined that the A500 specimen is significantly tougher than the A1085 specimen through Charpy V-Notch testing, as shown in Table 4.3. The ratios of maximum measured tensile and compressive forces to the predicted yield and critical buckling loads were 1.01 and 0.97 for the A1085 specimen, and 1.05 and 0.96 for the 6x6x3/8 A500 specimen. The A500 specimen exhibited slightly greater ductility prior to fracture than the A1085 specimen. The A500 specimen reached a displacement range of 7.46” (6.22% drift), compared with 7.04” (5.87% drift) for the A1085 specimen. The A1085 specimen fractured in compression during the second 3.75” target displacement cycle, while the A500 specimen fractured in tension during the first 4.25” target displacement.

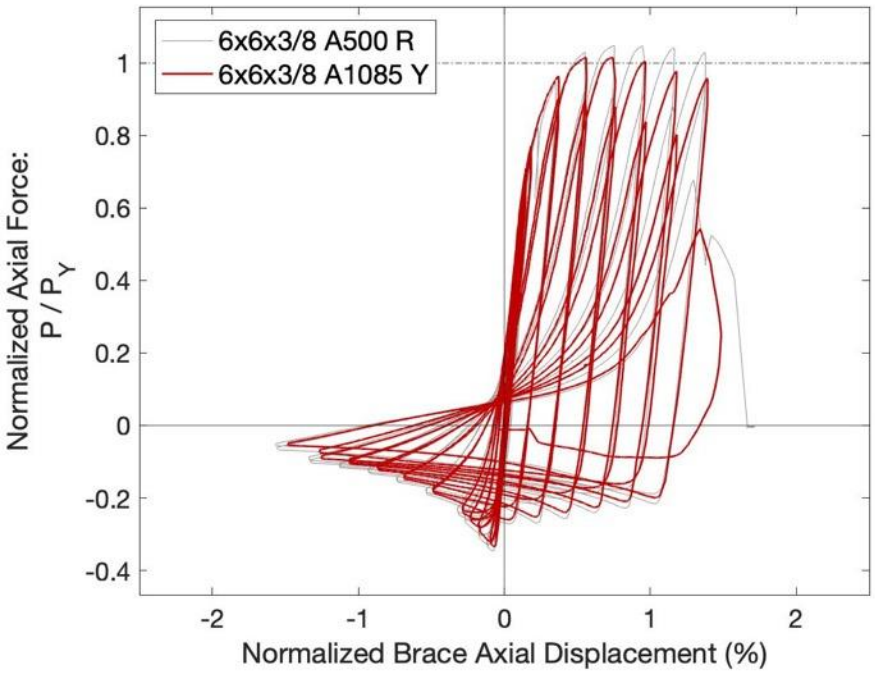

Figure 5.8. Force-Displacement Response– 6x6x3/8 HSS

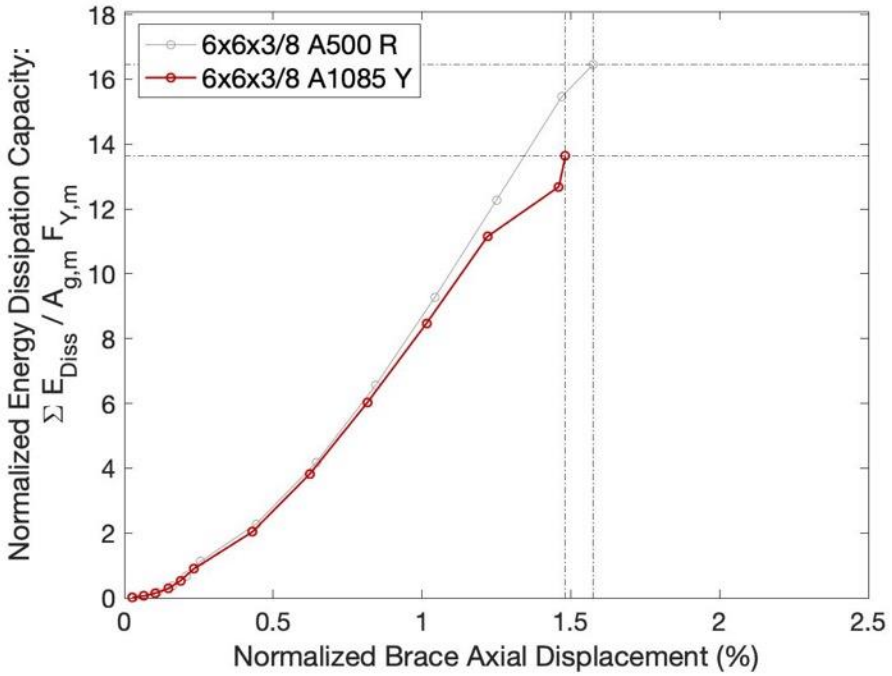

Figure 5.9. Energy Dissipation Capacity – 6x6x3/8 HSS

The accumulated axial brace displacement and story drift was about 16% greater in the A500 specimen. Some of this difference is a result of the A1085 specimen fracturing nearly a full cycle after the A500 specimen. The normalized energy dissipation capacity of the A500 specimen exceeds that of the A1085 specimen by 20.6%, as shown in Figure 5.9 above. It is clear from this plot that much of the increase in energy dissipation capacity occurs during the later cycles of testing. Figure 5.8 shows that in the A1085 specimen, the peak tensile forces decreased in later cycles after the maximum tensile force was reached. However, the peak tensile forces remained nearly constant in the A500 specimen during these larger displacement cycles. This behavior resulted in larger hysteretic loops for the A500 specimen, corresponding to an increased energy dissipation capacity.

5.3.4 *Section 4: 6x6x1/2 HSS*

The 6x6x1/2 A1085 Y specimen performed significantly better than the A500 specimen, exhibiting greater ductility as well as a higher energy dissipation capacity. Both sections meet AISC width-to-thickness requirements for highly ductile members. However, Charpy V-Notch tests demonstrated that the A500 specimen had significantly greater toughness than the A1085 specimen, as shown in Table 4.3. The ratios of maximum measured tensile and compressive forces to the predicted yield and critical buckling loads were 1.02 and 1.01 for the A500 specimen, and 1.06 and 0.97 for the A1085 specimen. The A1085 specimen displayed greater ductility prior to brace fracture compared to the A500 specimen. The A1085 specimen achieved an overall brace axial displacement range of 9.79” (8.16% drift), compared with 8.51” (7.10% drift) for the A500 specimen. The A1085 specimen fractured in tension during the first 5.75” target displacement cycle, while the A500 specimen fractured in tension during the first 4.75” cycle.

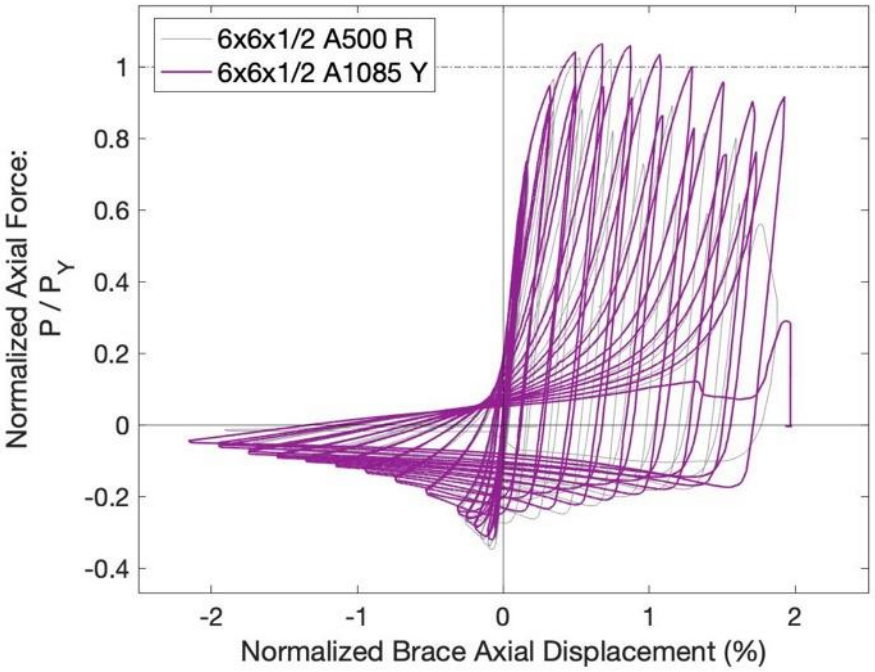

Figure 5.10. Force-Displacement Response – 6x6x1/2 HSS

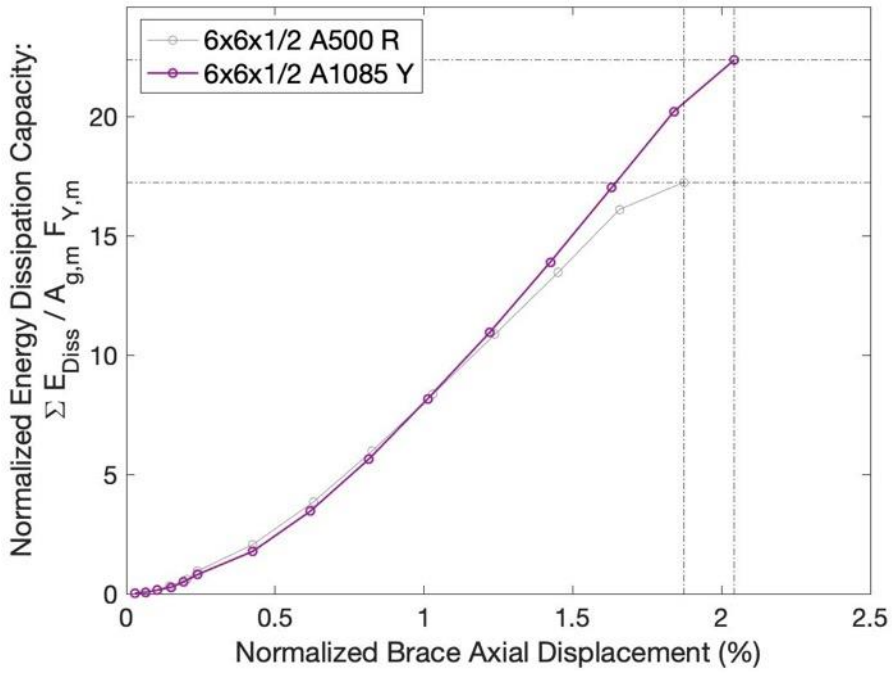

Figure 5.11. Energy Dissipation Capacity – 6x6x1/2 HSS

The accumulated axial brace displacement and story drift was about 21% greater in the A1085 specimen, further demonstrating the increase in brace ductility. The A1085 specimen survived several additional cycles beyond the point at which the A500 specimen fractured. The observed increased ductility in the A1085 specimen led to a nearly 30% increase in normalized energy dissipation capacity compared with the A500 specimen. Figure 5.11 clearly shows the elevated energy dissipation capacity and increased brace ductility in the A1085 specimen. Additionally, Figure 5.10 shows that the peak tensile forces of the A1085 specimen remained relatively high during the later cycles, but diminished quickly in the A500 specimen. This difference in peak tensile force behavior resulted in larger hysteretic loops for the A1085 specimen, corresponding to a greater energy dissipation capacity.

5.3.5 *Section 5: 7x7x5/16 HSS*

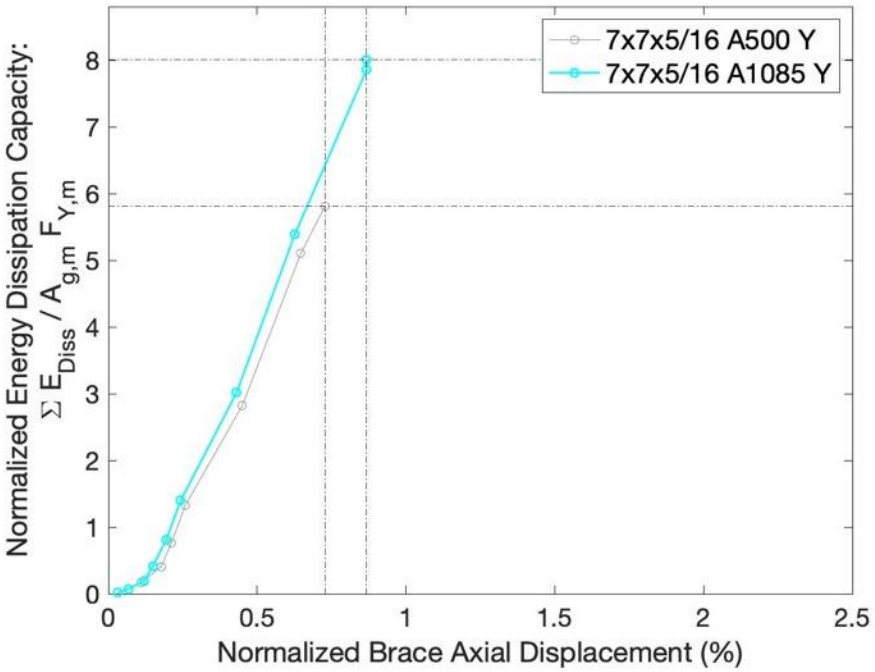

Figure 5.12. Force-Displacement Response – 7x7x5/16 HSS

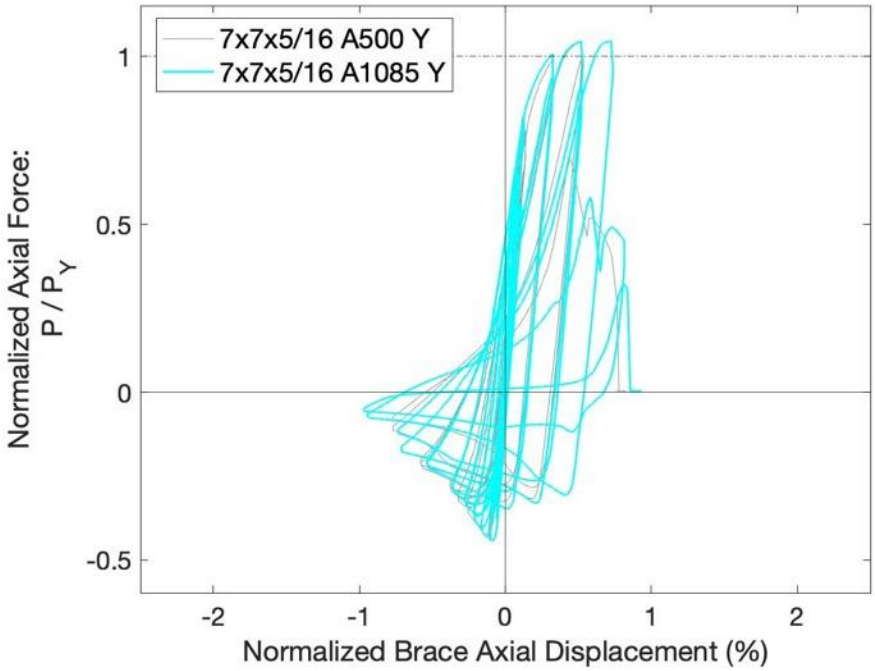

Figure 5.13. Energy Dissipation Capacity – 7x7x5/16 HSS

The 7x7x5/16 A1085 Y specimen exhibited greater ductility and energy dissipation capacity than the 7x7x5/16 A500 Y specimen, although neither specimen sustained the levels of axial displacement or drift observed in previous tests. These sections are considered non-seismically compact according the AISC width-to-thickness limits. Charpy V-Notch testing demonstrated only a minor difference in toughness between the specimens. The ratios of maximum measured tensile and compressive forces to the predicted yield and critical buckling loads were 1.05 and 0.88 for the A500 specimen, and 1.05 and 0.80 for the A1085 specimen.

The A1085 specimen displayed significantly greater ductility prior to brace fracture than the A500 specimen. The brace axial displacement range of the A1085 specimen was 4.29” (3.58% drift), compared with just 3.56” (2.97% drift) in the A500 specimen. The A1085 specimen fractured in tension during the first 2.75” target displacement cycle, while the A500 specimen fractured during the first 2.25” cycle. The accumulated axial brace displacement and story drift was 37.7% larger in the A1085 specimen, further showing the increase in brace ductility compared to the A500 specimen. The energy dissipation capacity of the A1085 specimen was found to be 37.6% greater than that of the A500 specimen. Figure 5.13 shows that the energy dissipated by the A1085 specimen slightly exceeded that of the A500 specimen

throughout the test, and continued to increase beyond the point at which the A500 specimen fractured. The A1085 specimen was able to dissipate significantly more energy as a result of surviving two additional full displacement cycles.

5.3.6 *Section 6: 7x7x3/8 HSS*

Both 7x7x3/8 HSS specimens sustained similar ductility prior to brace fracture, although the 7x7x3/8 A500 Y specimen displayed slightly greater energy dissipation capacity. The A1085 specimen meets the width-to-thickness requirements for moderately members, while the A500 specimen does not. Charpy V-Notch testing showed a slight increase in the toughness of the A1085 specimen compared with the A500 specimen. The ratios of maximum measured tensile and compressive forces to the predicted yield and critical buckling loads were 1.06 and 0.83 for the A500 specimen, and 1.07 and 0.87 for the A1085 specimen.

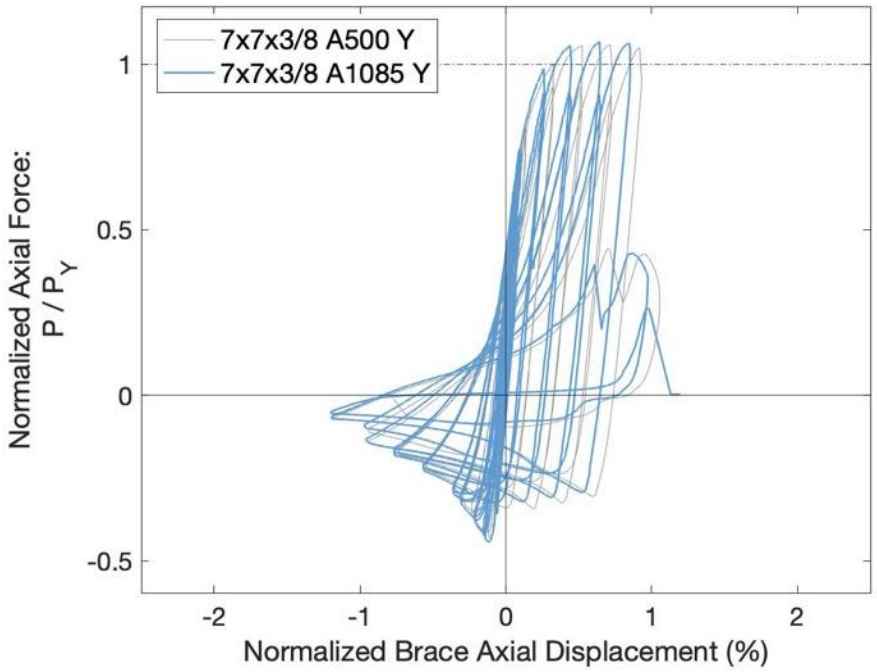

Figure 5.14. Force-Displacement Response – 7x7x3/8 HSS

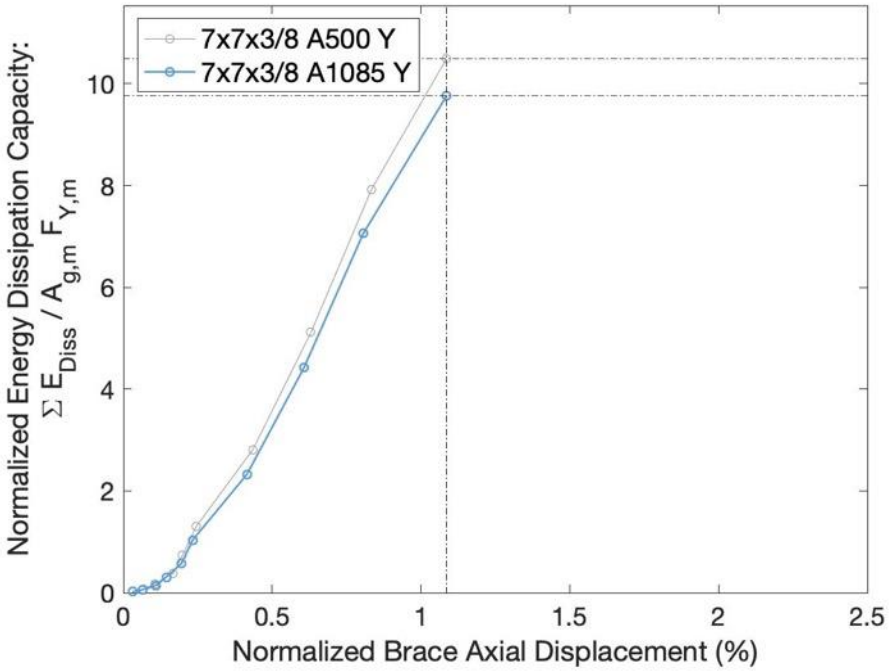

Figure 5.15. Energy Dissipation Capacity – 7x7x3/8 HSS

The measured axial displacement ranges were nearly identical, with the A500 specimen reaching a range of 5.30” (4.42% drift), compared with 5.21” (4.35% drift) for the A1085 specimen. The A500 specimen fractured in compression during the second 2.75” cycle, while the A1085 specimen fractured in tension during the subsequent cycle. As a result of surviving an additional half cycle, the accumulated axial brace displacement was about 6% greater in the A1085 specimen. The energy dissipation capacity of the A500 specimen was about 7.5% greater than that of the A1085 specimen. The difference in energy dissipation capacity is depicted in Figure 5.15, which shows a slight increase in the energy dissipated by the A500 specimen throughout the test. This may be attributed to minor differences in the force-displacement responses of the two specimens. It is evident from Figure 5.14 that the hysteretic loops of the A500 specimen are slightly larger, which is a result of this specimen reaching larger tensile displacements at each target displacement cycle. The cause of these differences is unclear, but it may be related to a difference in the magnitude of bolt slip between the two specimens. This may have an impact on the peak brace displacements, since increased bolt slip can cause a reduction in axial brace deformation.

5.3.7 *Section 7: 7x7x1/2 HSS*

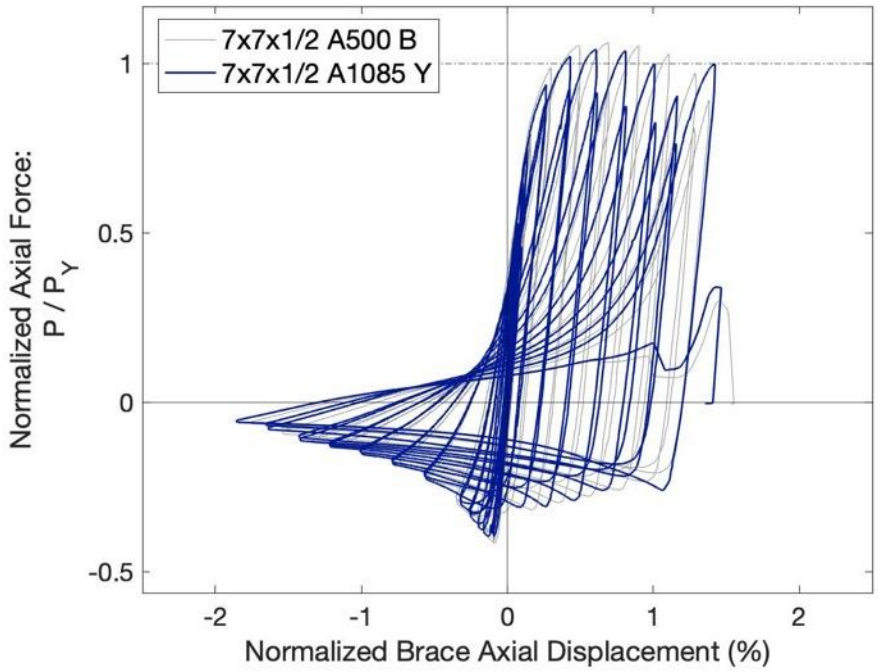

Figure 5.16. Force-Displacement Response – 7x7x1/2 HSS

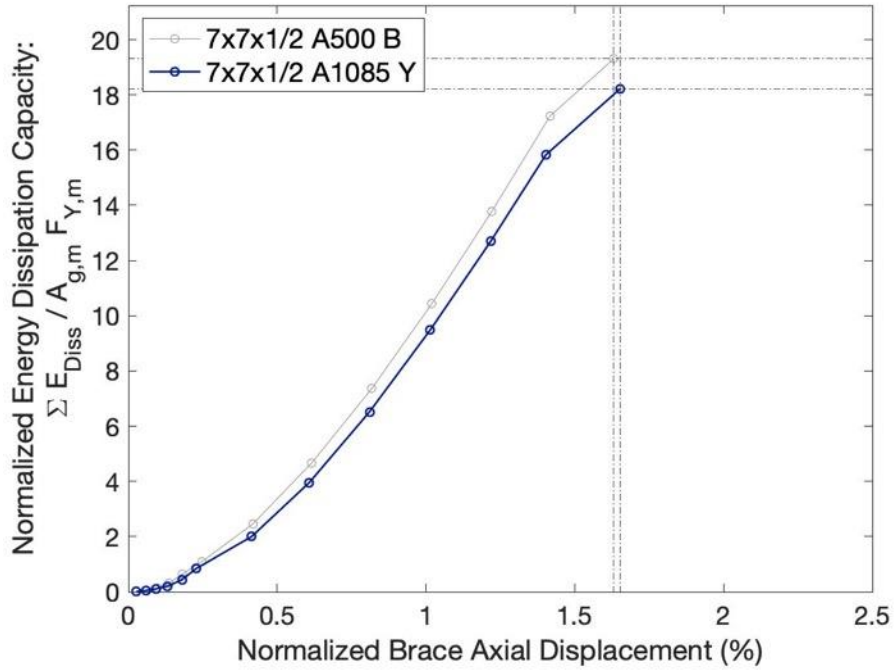

Figure 5.17. Energy Dissipation Capacity – 7x7x1/2 HSS

The 7x7x1/2 HSS specimens exhibited similar behavior and performance throughout testing, with some minor differences in ductility and energy dissipation capacity. Both of the specimens meet AISC width-to-thickness limits for highly ductile members. The 7x7x1/2 A500 B specimen was measured to have greater toughness than the 7x7x1/2 A1085 Y specimen through Charpy V-Notch testing. The ratios of maximum measured tensile and compressive forces to the predicted yield and critical buckling loads were 1.06 and 0.80 for the A500 specimen and 1.04 and 0.84 for the A1085 specimen.

The maximum tensile and compressive axial displacements prior to fracture were similar for both sections, which can be seen in in Table 5.1 above. The A500 specimen reached a displacement range of 7.75" (6.46% drift), compared with 7.89" (6.58% drift) for the A1085 specimen. Both specimens fractured in tension during the second 4.25" target displacement cycle. The difference in accumulated axial displacement and drift is negligible, only about 1%. This is to be expected, as both specimens fractured at nearly identical displacements during the same target displacement cycle. The normalized energy dissipation capacity of the A500 specimen was about 6% greater than that of the A1085 specimen. Figure 5.17above shows that the energy dissipation behavior of the two specimens begins to diverge at displacements greater than 0.25%, and it is evident that the normalized energy dissipation capacity of the A500 specimen is slightly greater at larger displacements. This increase in energy dissipation capacity may be attributed to the differences in force-displacement response during larger cyclic displacements. Figure 5.16 shows that at target displacements greater than 0.5%, the A500 specimen reached greater tensile forces and axial brace displacements. This behavior resulted in larger hysteretic loops, which may explain the 6% increase in normalized energy dissipation capacity despite similar levels of ductility.

5.3.8 ***Section 8: 8x8x3/8 HSS***

The 8x8x3/8 A1085 Y specimen exhibited significantly greater ductility and energy dissipation capacity than the 8x8x3/8 A500 W specimen. Both specimens exceed the AISC width-to-thickness requirements for both highly and moderately ductile members. Charpy V-

Notch testing showed that the A500 specimen was significantly tougher than the A1085 specimen, as shown in Table 4.3. The ratios of measured to predicted maximum tensile and compressive loads were 1.02 and 0.93 for the A500 specimen, and 1.02 and 0.81 for the A1085 specimen.

The A1085 specimen displayed greater ductility prior to brace fracture, which can be seen in Figure 5.18. The A1085 specimen achieved an axial displacement range of 4.36" (3.63% drift), which is nearly 40% greater than the A500 specimen. This specimen ultimately fractured in tension during the second 2.75" target displacement cycle, while the A500 specimen fractured a full three cycles earlier, during the first 2.25" target displacement cycle. The accumulated axial displacement prior to fracture was about 50% greater in the A1085 specimen, which makes sense given the increased fracture life of this specimen. The normalized energy dissipation capacity of the A1085 specimen was about 85% greater than that of the A500 specimen. Figure 5.19 below shows this increase in energy dissipation capacity and ductility. By withstanding an additional three cycles prior to fracture, the A500 specimen was able to dissipate significantly more energy through inelastic buckling and yielding. Figure 5.18 shows the force-displacement behavior and large hysteretic loops of the A1085 specimen during these later cycles beyond the point at which the A500 specimen fractured.

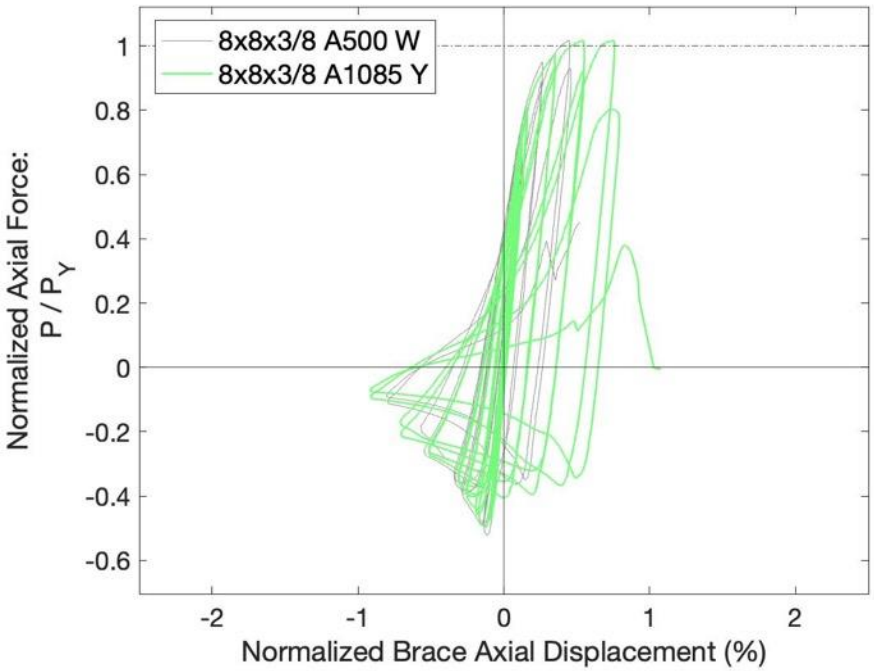

Figure 5.18. Force-Displacement Response – 8x8x3/8 HSS

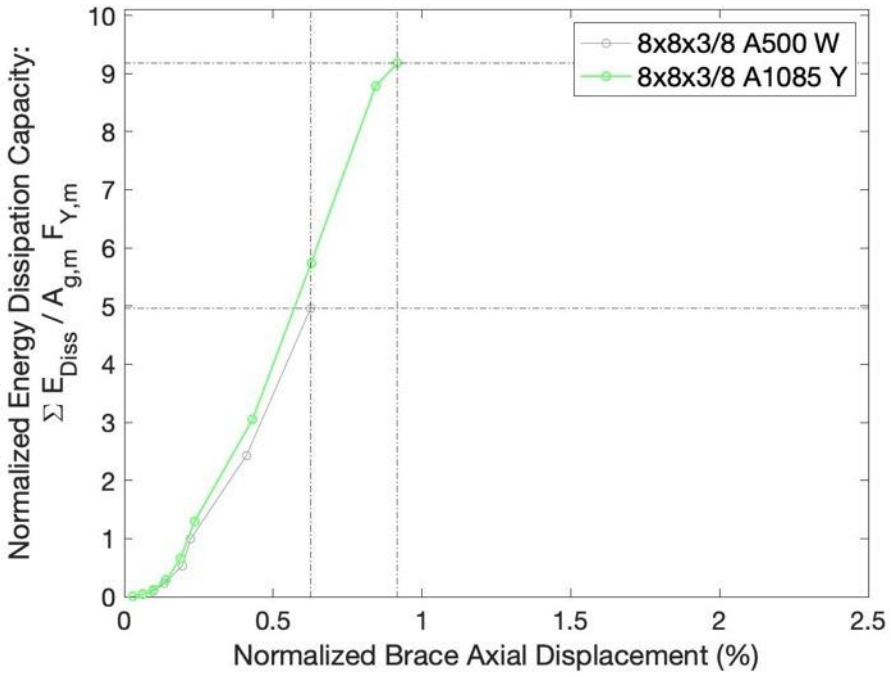

Figure 5.19. Energy Dissipation Capacity – 8x8x3/8 HSS

5.3.9 ***Section 9: 8x8x1/2 HSS***

The 8x8x1/2 A1085 Y specimen exhibited slightly more ductility and energy dissipation capacity than the 8x8x1/2 A500 W specimen. The A500 specimen meets the AISC width-to-thickness requirements for moderately ductile members, while the A1085 specimen meets the criteria for highly ductile members. Charpy V-Notch testing indicated that the A500 specimen was significantly tougher than the A1085 specimen, as shown in Table 4.3. The ratios of maximum measured tensile and compressive loads to the predicted yield and critical buckling loads were 1.03 and 0.88 for the A500 specimen, and 1.02 and 0.82 for the A1085 specimen. The brace axial displacement values tabulated in in Table 5.1 show that the A1085 specimen exhibited slightly more ductility prior to fracture. The displacement range of the A1085 specimen was 6.28” (5.23% drift), which was about 15% greater than that of the A500 specimen. Brace fracture ultimately occurred in the A1085 specimen during the first 3.75” target displacement cycle, while the A500 specimen fractured in tension during the second 3.25” target cycle. This delay in brace fracture resulted in a 15% increase in total accumulated axial displacement in the A1085 specimen.

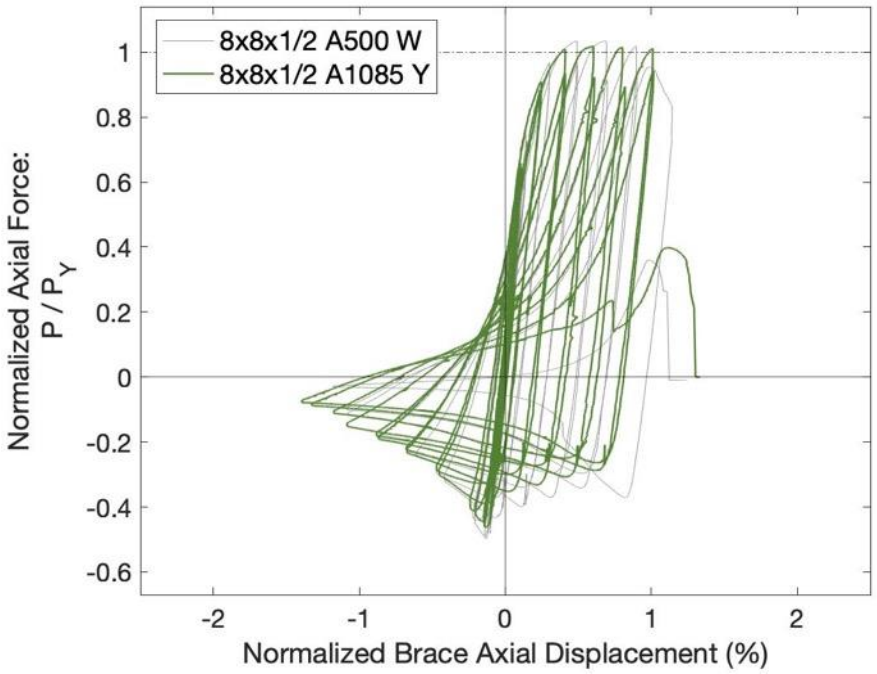

Figure 5.20. Force-Displacement Response – 8x8x1/2 HSS

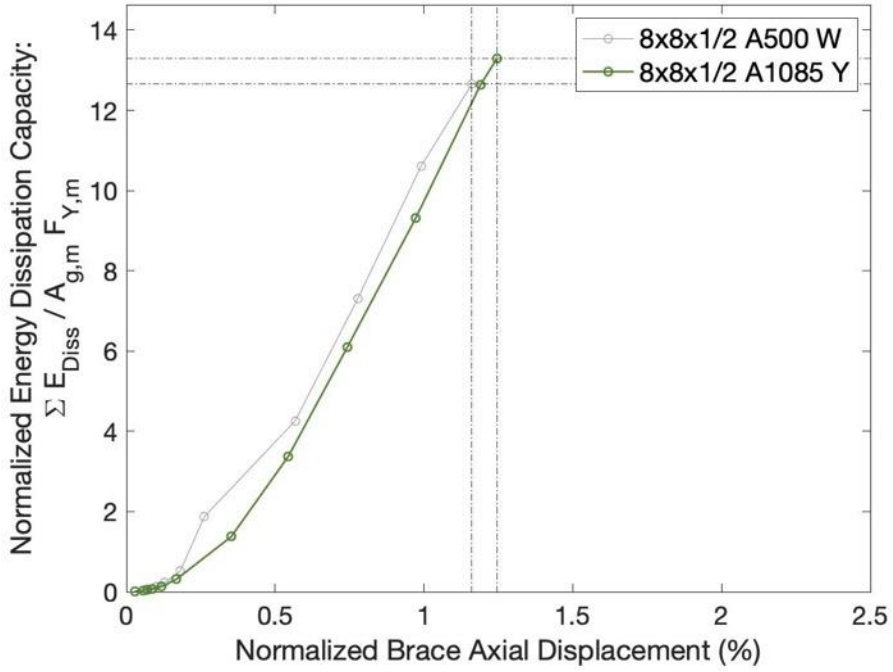

Figure 5.21. Energy Dissipation Capacity – 8x8x1/2 HSS

The normalized energy dissipation capacity of the A1085 specimen was about 5% greater than that of the A500 specimen. Figure 5.21 shows that the A500 specimen actually exhibits

slightly better energy dissipation behavior throughout much of the test. It can be seen in Figure 5.20 that the A500 specimen reached larger tensile displacements in cycles greater than 0.25%. This resulted in a slight increase in energy dissipation throughout the test for the A500 specimen. However, the overall normalized energy dissipation capacity of the A1085 specimen is slightly greater as a result of the energy dissipated during the final cycle, beyond the point at which the A500 specimen fractured.

5.3.10 ***Section 10: 10x10x3/8 HSS***

The 10x10x3/8 A500 W specimen exhibited significantly more ductility and energy dissipation capacity than the 10x10x3/8 A1085 Y specimen. Both specimens exceed the AISC width-to-thickness limits for moderately ductile members. These were the stockiest members tested during this test series, with a global slenderness ratio of just over 60. Charpy V-Notch testing showed that the A500 specimen was significantly tougher than the A1085 specimen. The ratios of maximum measured tensile and compressive forces to the predicted yield and critical buckling loads were 1.01 and 0.79 for the A500 specimen and 1.01 and 0.81 for the A1085 specimen.

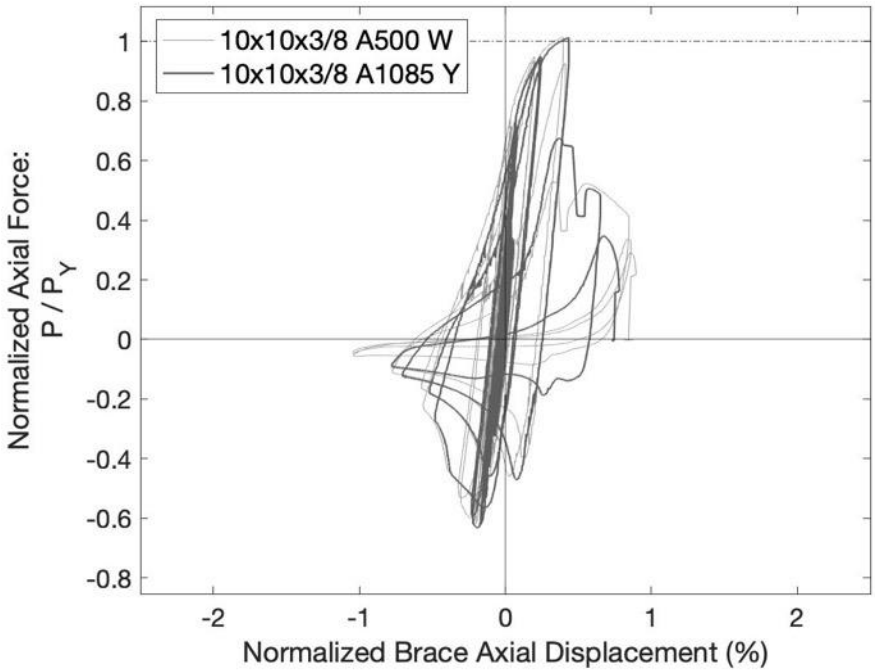

Figure 5.22. Force-Displacement Response – 10x10x3/8 HSS

The tabulated brace axial displacement values presented in in Table 5.1 clearly show that the A500 specimen exhibited significantly more ductility prior to fracture. The displacement range of the A500 specimen was 4.58" (3.81% drift), about 33% greater than that of the A1085 specimen. In both specimens, striations and tearing developed in tension during the first 1.75" cycle. However, the A500 specimen fractured in tension during the first 2.75" target displacement cycle, while the A1085 specimen fractured during the first 2.25" cycle. The A500 specimen exhibited significant post-tearing ductility, which was not observed in the A1085 specimen. The accumulated axial displacement prior to fracture was about 64% greater in the A500 specimen, which is a result of the post-tearing ductility observed in this specimen. This significant post-tearing ductility was not observed in any of the other test specimens included in this test series. The measured normalized energy dissipation capacity of the A500 specimen was about 28% greater than that of the A1085 specimen. This can be seen in Figure 5.23, which shows that the energy dissipation behavior was relatively similar until the A1085 specimen fractured.

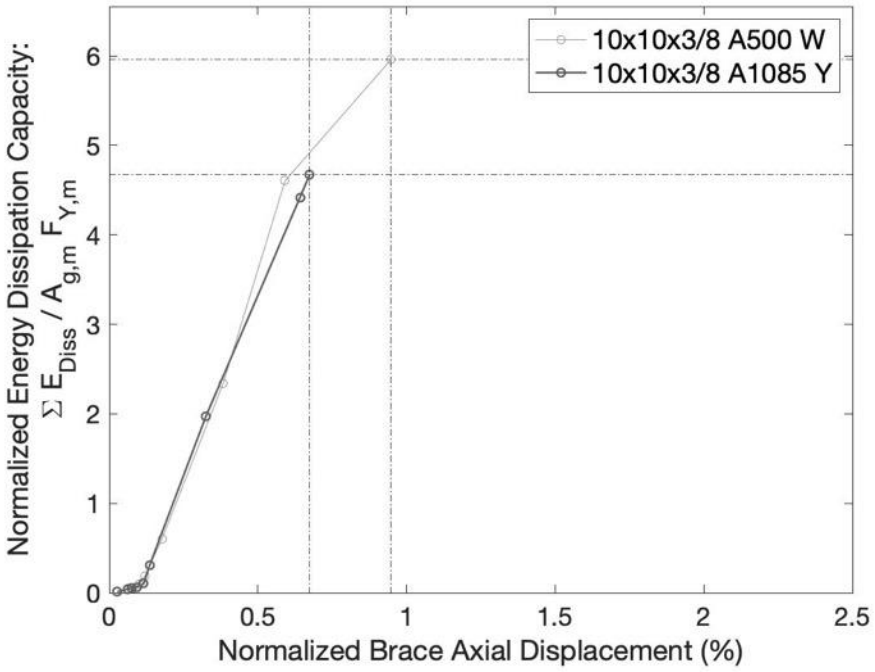

Figure 5.23. Energy Dissipation Capacity – 10x10x3/8 HSS

5.4 OVERALL TEST SERIES COMPARISONS

In this section, comparisons are presented to characterize the performance and behavior between all of the specimens in this test series. The effects of brace local compactness, global slenderness, steel producer and steel type are investigated in this section. These comparisons are based on structural response parameters such as deformability, energy dissipation capacity, and measured material properties. Various trends in the data are discussed based on the following analyses.

In the plots below, the color scheme developed in Chapter 3 is followed, such that the color of each marker is based on the corresponding HSS shape. Both the A500 and A1085 sections of the same size are shown by the same color. The A500 specimens are represented by hollow circles on the plots, and A1085 specimens are shown as solid circles. To provide extra clarity in these plots, the size of each marker corresponds to the specimen size, with the 5x5x3/8 HSS specimens represented by smaller markers, and the 10x10x3/8 HSS specimens by larger markers.

5.4.1 *Brace Local Slenderness*

The effects of brace local compactness on structural response parameters such as deformation capacity and energy dissipation capacity are investigated in this section. Different measurements of ductility are presented in this section, including brace axial displacement, peak story drift, and accumulated axial displacement, to characterize the deformability of test specimens and evaluate the effects of steel type on structural response. Brace local compactness has been shown to have a significant impact on brace performance, and these data trends will be examined in this section. Additionally, this analysis allows for comparisons to be made between the performance of the A500 and A1085 test specimens.

In the following plots, the width-to-thickness ratios of the specimens are normalized by the AISC width-to-thickness limits for highly ductile members, λ_{HD}, and moderately ductile members, λ_{MD}. These limits are shown in Table 1.1 for A500 and A1085 HSS. Additionally, the measured brace axial displacement is normalized by the brace length and is shown as a

percentage in the plots below. In other figures, approximate drifts are calculated following the approach shown in Section 4.1, and are shown as a percentage of assumed story height.

Figure 5.24 below plots the axial displacement range against the nominal brace compactness, λ_{nom}, normalized by λ_{HD} for each of the twenty test specimens. Specimens meeting the AISC criteria for highly ductile members are represented by markers to the left of the vertical line at 1.0, while non-seismically compact specimens are shown to the right of this line. It is evident from this plot that an increased nominal width-to-thickness ratio is associated with a decrease in axial displacement range. This fits with data from previous experimental programs discussed in Chapter 2, which showed that less cross-sectionally compact HSS members generally fracture at lower levels of axial displacement. The power regression curve below accounts for a significant amount of the variation in the data, with an R^2 value of 0.82.

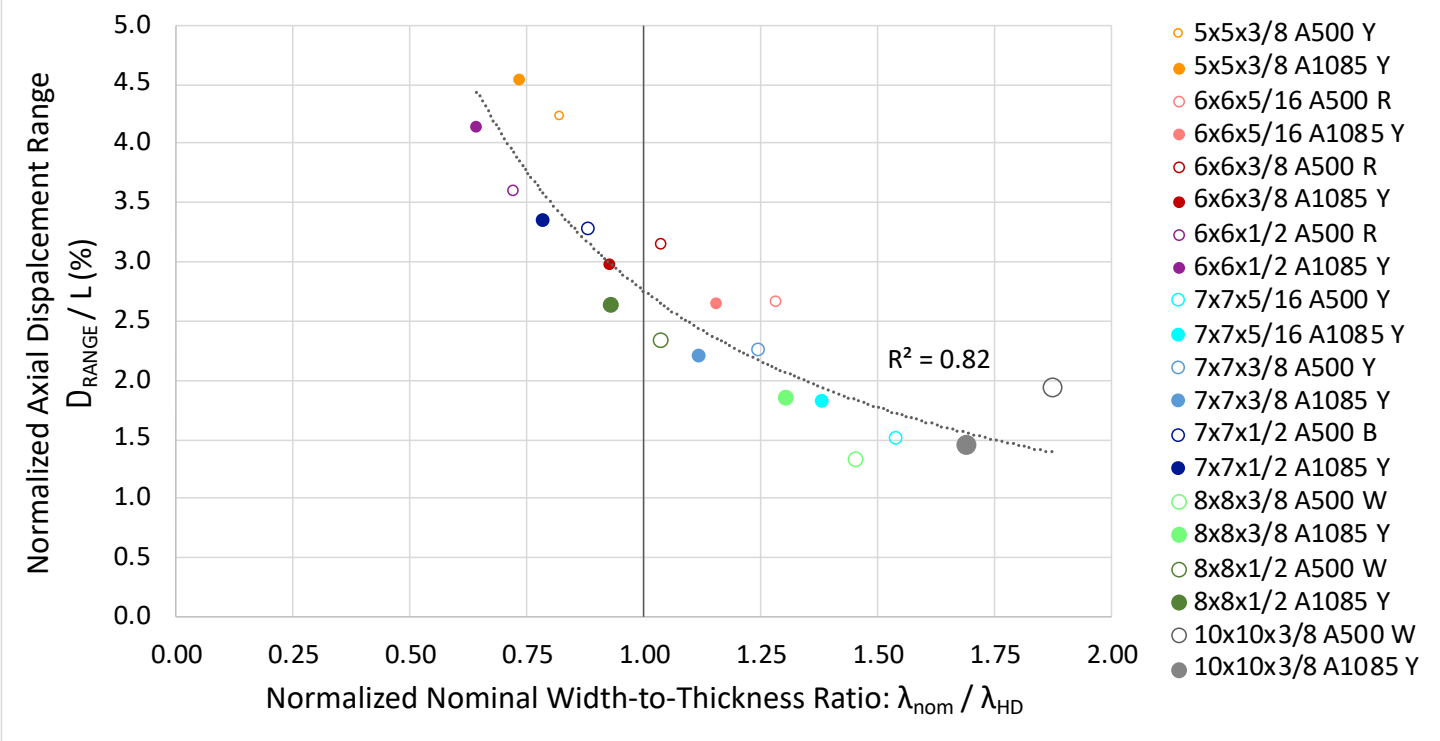

Figure 5.24. Axial Displacement Range vs. Local Compactness: λ_{HD}

Test specimens meeting AISC limits for highly ductile members reached axial displacement ranges of at least 2.5%, or about 6". Additionally, the most compact specimens, with λ_{nom} of less than about 12, reached axial displacement ranges of at least 3.25%, or about

7.75". All of the test specimens with λ_{nom} of less than 1.25 times the λ_{HD} limits reached axial displacement ranges of at least 2.2% prior to brace fracture. The 10x10x3/8 A500 W specimen is somewhat of an outlier in this data set, since it achieved an axial displacement range significantly larger than that of more compact sections, including the 8x8x3/8 A1085 Y and 7x7x5/16 A1085 Y test specimens. This was caused by post-tearing ductility observed in this specimen, which is described in detail in Section 5.3.10. λ_{nom} is slightly lower in the A1085 specimens than the A500 specimens of the same shape due to the tighter control over wall thickness required by the ASTM A1085 specification. Due to this minor increase in cross-sectional compactness, the A1085 specimens would be expected to perform slightly better than their A500 counterparts.

Figure 5.24 shows that an increase in ductility was not observed in all of the HSS shapes tested. In five of the ten sizes tested (5x5x3/8, 6x6x3/8, 7x7x5/16, 8x8x3/8, and 8x8x1/2 HSS) the A1085 specimen reached an axial displacement range of at least 0.25%, or about 0.6", greater than that of the A500 specimen. However, there were several cases in which the axial displacement range of the A500 specimen exceeded that of the A1085 specimen, including the 6x6x3/8 and 10x10x3/8 HSS members. Several other shapes displayed minimal difference between the measured axial displacement range of the A500 and A1085 HSS, despite the increase in local compactness associated with A1085 HSS. Therefore, this plot does not indicate a clear relationship between steel type and deformation capacity. This is not entirely unexpected, as the A500 and A1085 specimens were found to have very similar geometric and material properties as discussed in Chapter 3.

The axial displacement range is plotted against the nominal width-to-thickness ratio normalized by the AISC 341-16 limits for moderately ductile members, λ_{MD}. This plot is nearly identical to the previous, except that test specimens with λ_{nom} less than λ_{MD} rather than λ_{HD} are shown to the left of the vertical line at 1.0. This figure indicates that all specimens λ_{MD} requirements reached an axial displacement range of at least 2.0% prior to brace fracture. Additionally, the specimens with nominal width-to-thickness ratios less than 1.2 times the limits for moderately ductile members reached an axial displacement range of at least 1.8% prior to fracture.

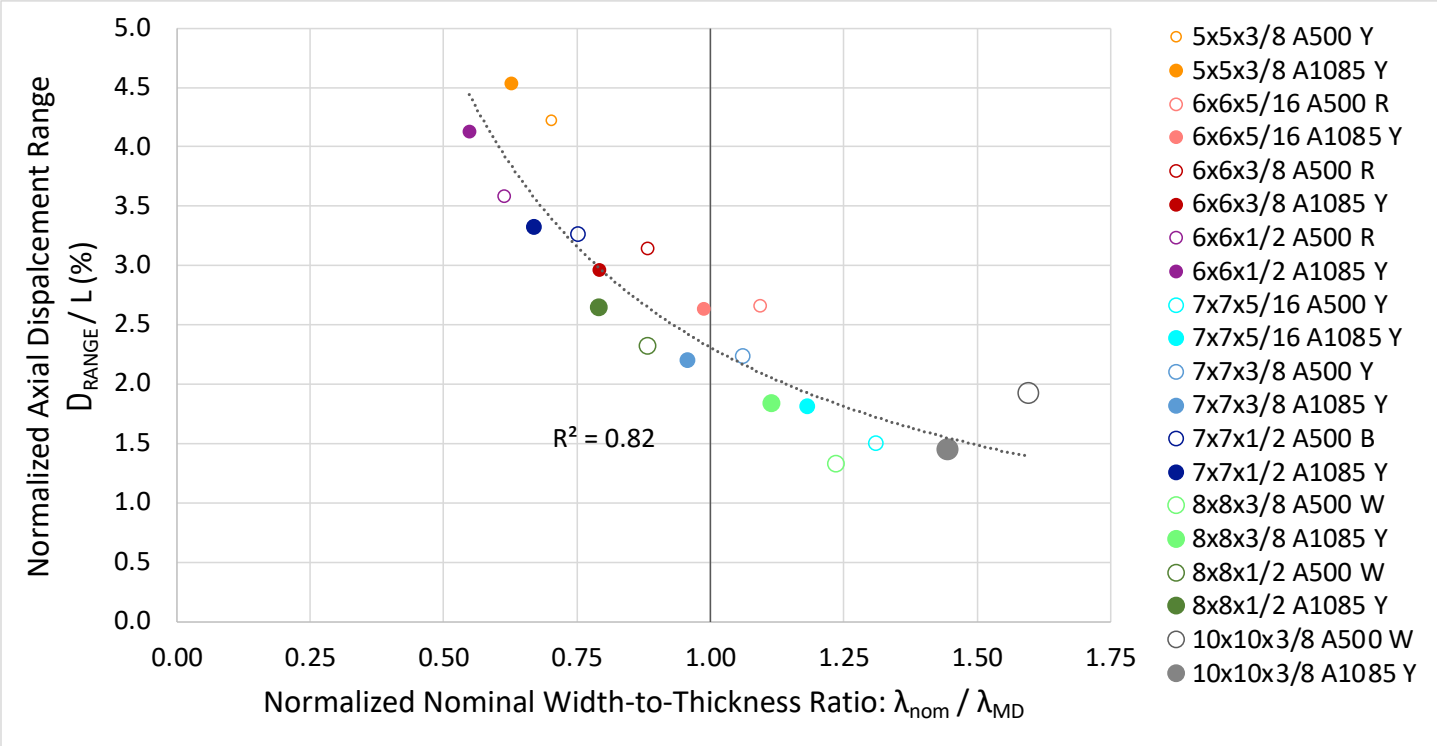

Figure 5.25. Axial Displacement Range vs. Local Compactness: λ_{MD}

In Figure 5.26, the measured width-to-thickness ratios, λ_m, are plotted against the axial displacement range. This figure displays a similar trend as the previous plot, showing that more cross-sectional compact sections reach greater displacement ranges prior to fracture. The measured width-to-thickness ratios were less than the nominal values for all twenty test specimens. The R^2 value of 0.84 corresponding the power curve below indicates that using λ_m rather than λ_{nom} results in a minor improvement in the fit of the regression line, but does not account for all of the variation in the data. In all but one of the test specimens, λ_m of the A500 specimen exceeded that of the A1085 specimen. Only in the 6x6x1/2 HSS was the A500 specimen found to be more cross-sectionally compact than the A1085 specimen. However, this increased measured local compactness was not associated with an increase in ductility, as the displacement range of the A1085 section was about 0.5% greater than that of the A500 specimen.

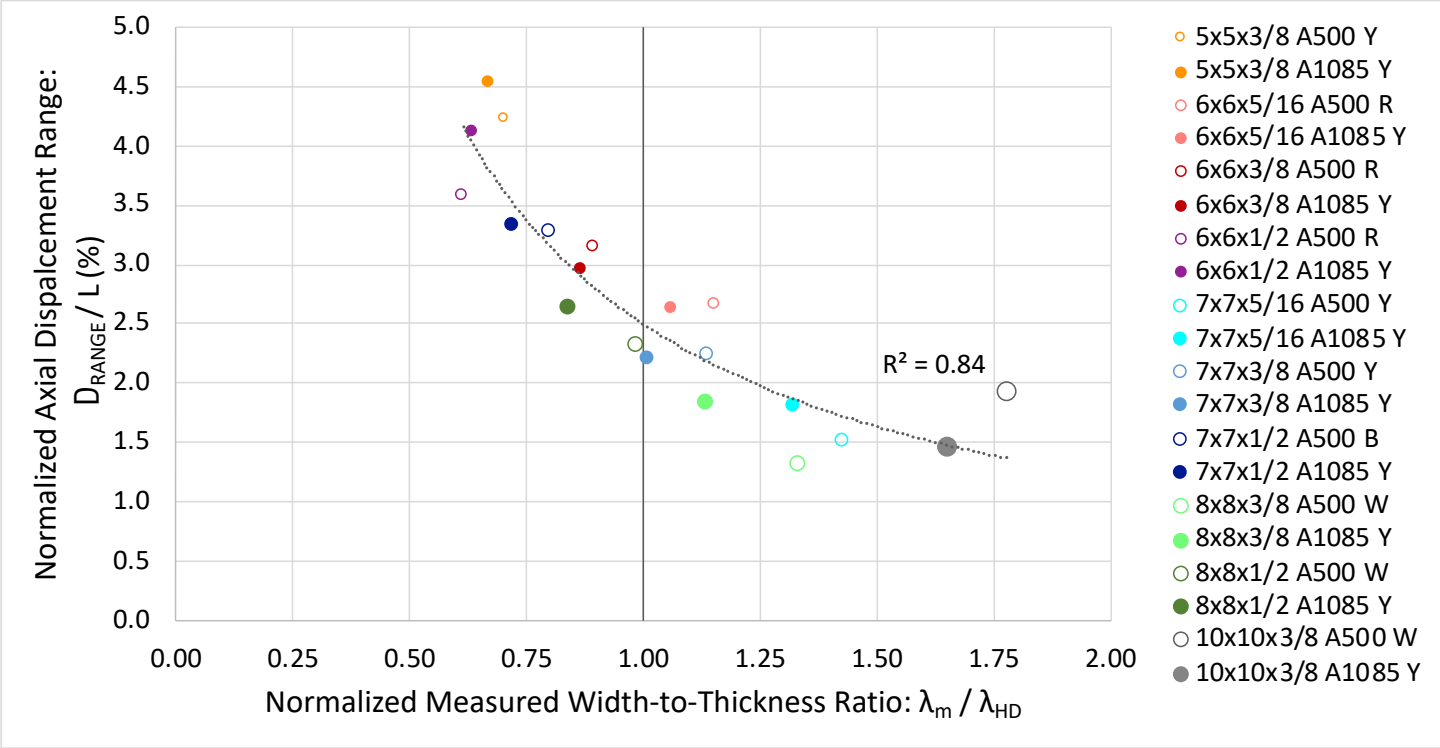

Figure 5.26. Axial Displacement Range vs. Measured Local Compactness: λ_{HD}

Figure 5.27 shows the axial displacement at the initiation of local buckling plotted against the normalized nominal width-to-thickness ratio. Local buckling deformations were observed in all test specimens prior to brace fracture. These deformations developed in the plastic hinge region of the brace when subjected to compressive displacements. This behavior develops as a result of high localized strains at the center of the brace as it buckles out of plane, which eventually results in the compressive wall of the brace folding inwards. Local buckling is a visible indication of damage to the brace, and braces typically fractured shortly after the development of these deformations. The plot below shows that the development of local buckling deformations is delayed in more cross-sectionally compact braces. This delay in damage to the brace leads to increase in fracture life, as shown in the previous figures. Similar to the previous plots discussed in this section, there is no clear relationship shown in this plot between specimen ductility and steel type. In five of the ten HSS shapes tested, local buckling was observed in the A1085 specimen at a larger compressive axial displacement than in the A500 specimen. However, there are also several cases in which local buckling deformations

developed later in A500 specimens, and other cases where there was no difference between the types of steel. This is likely a result of the similarities in material and geometric properties between the A500 and A1085 specimens.

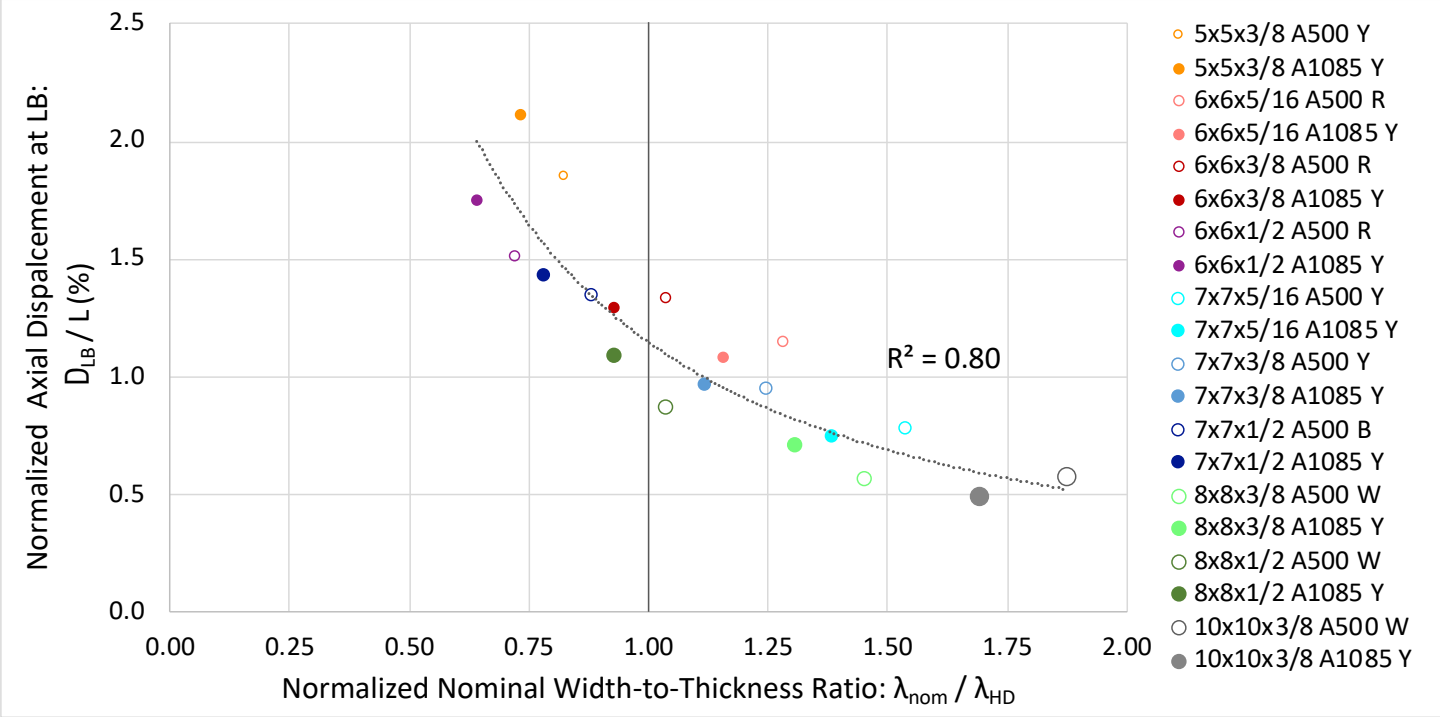

Figure 5.27. Axial Displacement at Local Buckling vs. Local Compactness: λ_{HD}

Another comparison between brace deformation capacity and cross-sectional compactness is presented in Figure 5.28, which shows the maximum story drift plotted against the normalized nominal width-to-thickness ratio. The approximate peak story drifts are based on the maximum tensile and compressive axial brace displacement prior to brace fracture. Similar to the previous comparisons, this plot does not show a distinct relationship between steel type and maximum story drift. In six of the ten shapes tested, the A1085 section achieved a peak story drift of at least 0.25% greater than that of the A500 specimen. However, this may partially be explained by the slight increase in cross-sectional compactness of the A1085 members. Additionally, there were several cases in which the A500 section reached a greater peak story drift than the A1085 specimen, and in other cases there was minimal difference in the measured ductility of the specimens.

However, this plot shows that all specimens classified as highly ductile members achieved story drifts of at least 2.5% prior to fracture. The target inelastic deformation for SCBFs prior to brace fracture is commonly assumed to be about 2.5% (Sabelli et al., 2013). The test specimens tested in this program that meet the criteria for seismically compact members achieve this target ductility level. Additionally, members with λ_{nom} ratios less than 90% of the AISC limits for highly ductile members reached peak story drifts of about 3.5% or higher. Several test specimens not meeting the AISC requirements for highly ductile members also reached peak story drifts of at least 2.5%, including the 6x6x3/8 A500 R, 6x6x5/16 A1085 Y, and 6x6x5/16 A500 R specimens. However, other specimens with similar λ_{nom} ratios did not achieve this level of ductility, such as the 8x8x1/2 A500 W, 7x7x3/8 A1085 Y, and 7x7x3/8 A500 Y specimens. Additionally, test specimens with nominal b/t ratios of less than 1.25 times AISC limits for highly ductile members achieved peak story drifts of at least 2.25%. The power regression line shown in the plot below accounts for much of the variation in the data, with an associated R^2 value of 0.85.

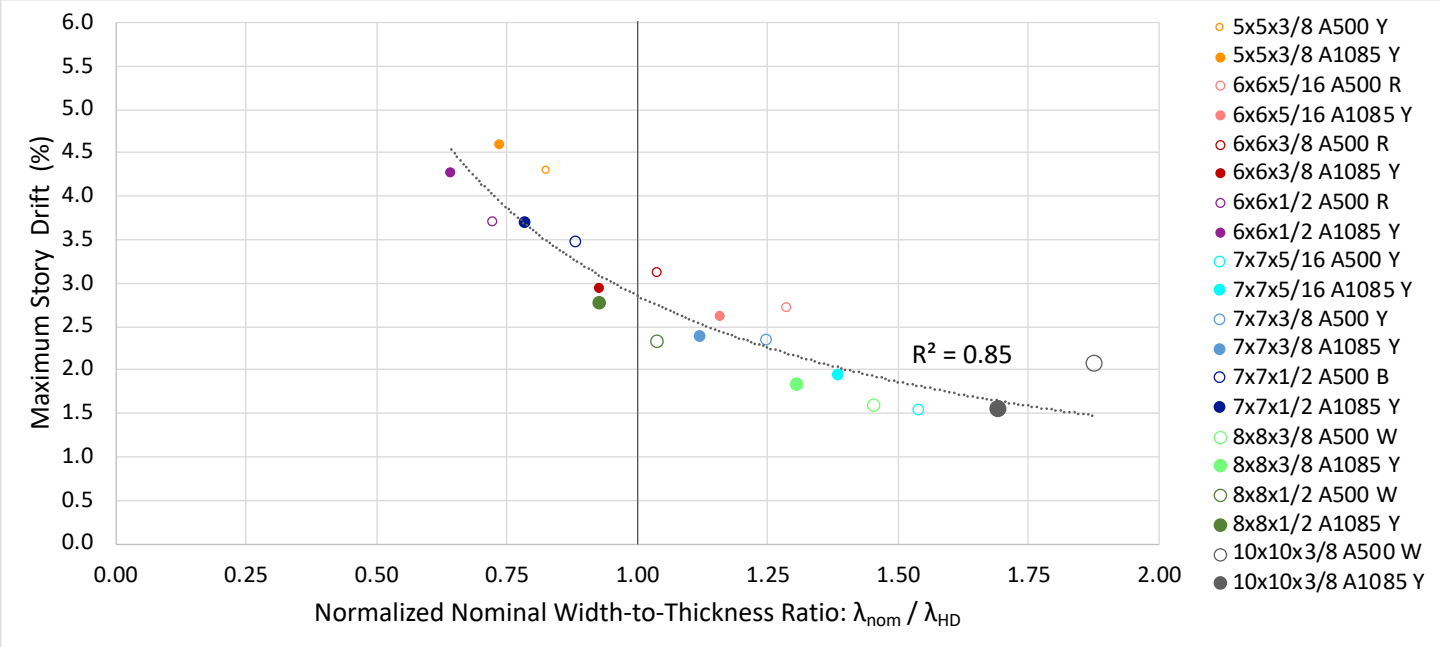

Figure 5.28. Approximate Peak Story Drift vs. Local Compactness: λ_{HD}

The maximum story drift prior to brace fracture is also shown in Figure 5.29, in which the nominal width-to-thickness ratio is normalized by the AISC 341-16 limits for moderately

ductile members. This figure shows that all test specimens with a nominal b/t ratio less than 1.25 times the moderately ductile limits achieved a maximum story drift of at least 1.5% prior to fracture. This indicates that braces with width-to-thickness ratios exceeding the moderately ductile limits may exhibit sufficient ductility in OCBFs.

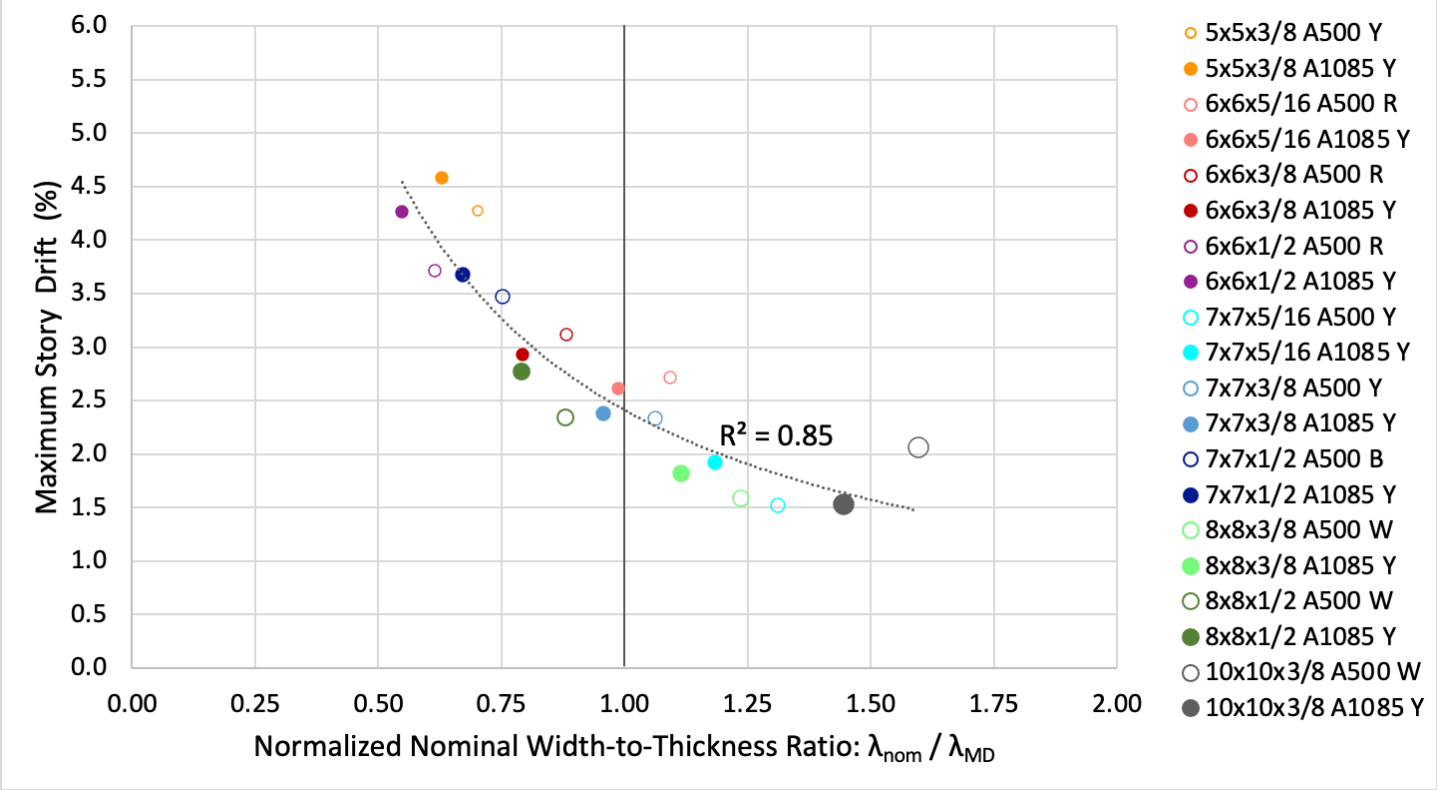

Figure 5.29. Approximate Peak Story Drift vs. Local Compactness: λ_{MD}

Test specimen ductility was also measured in the form of accumulated axial displacement prior to the point of fracture, which is shown in Figure 5.30. The calculation of accumulated brace displacement is described above in Section 5.3. Unlike the previous measurements of brace ductility discussed, the accumulated axial displacement takes into account whether the brace fractured during the first or second cycle of a given target displacement, providing a more refined measurement of deformation capacity. Once again, the relationship between increased cross-sectional compactness and brace ductility is displayed by this plot. The accumulated axial displacement was greatest in the 5x5x3/8 HSS specimens, with both sections reaching well over

100” of accumulated displacement prior to brace fracture. These members meet the AISC width-to-thickness requirements for highly ductile members, and were also the most globally slender of any of the test specimens. The accumulated brace axial displacement prior to fracture is highly dependent on the loading protocol used in testing, which has been shown to affect the structural response of HSS members. All test specimens in this test series were subjected to identical displacement histories, which makes it possible to compare the accumulated axial displacement between specimens.

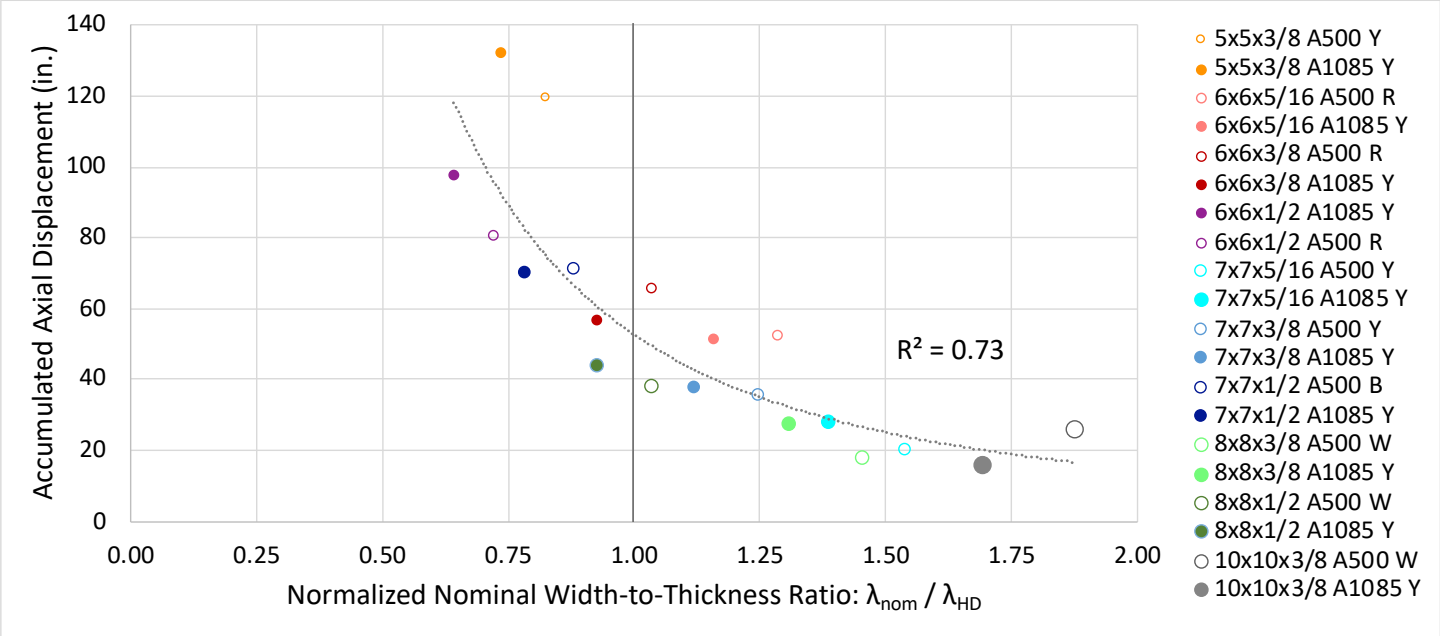

Figure 5.30. Accumulated Axial Displacement vs. Local Compactness: λ_{HD}

Based on the plot of accumulated axial displacement above, there is no clear relationship between steel type and ductility. There were six cases in which the accumulated axial displacement of the A1085 specimen exceeded that of the A500 specimen of the same shape. However, there were two cases in which the A500 specimen exhibited greater ductility, and two cases in which the difference was negligible. As discussed previously, some of the increase in accumulated axial displacement of the A1085 specimens may be attributed to their slightly more compact cross sections relative to the A500 specimens. In general, the trends observed in the plot

of accumulated axial displacement are in agreement with the measurements of brace ductility discussed above.

Another measurement of test specimen performance, the normalized energy dissipation capacity, is plotted in Figure 5.31 below against the nominal width-to-thickness ratio normalized by λ_{HD}. This plot shows a clear relationship between more cross-sectionally compact sections and an increase in energy dissipation capacity. The energy dissipation capacity is normalized by the measured area and yield strength of each test specimen to account for differences in geometric and material properties. The regression curve shown in the plot provides a fairly accurate fit to the data, with an R^2 value of 0.84. Specimens with a nominal width-to-thickness ratio less than about 85% of the AISC limits for highly ductile members exhibit the greatest energy dissipation capacity, as shown by the cluster of markers at the top left of the plot. Test specimens with nominal b/t ratios between 0.9 and 1.15 times the AISC limit for highly ductile members generally display a moderate energy dissipation capacity relative to other test specimens. The energy dissipation capacity is significantly lower in members with nominal b/t ratios greater than 1.4 times the AISC limit for highly ductile members. The reduced energy dissipation capacity in these less cross-sectionally compact sections is associated with the reduced ductility and fracture life observed in these test specimens. Specimens categorized as highly ductile members exhibited greater ductility, and thus were able to dissipate more energy through inelastic buckling and yielding prior to fracture.

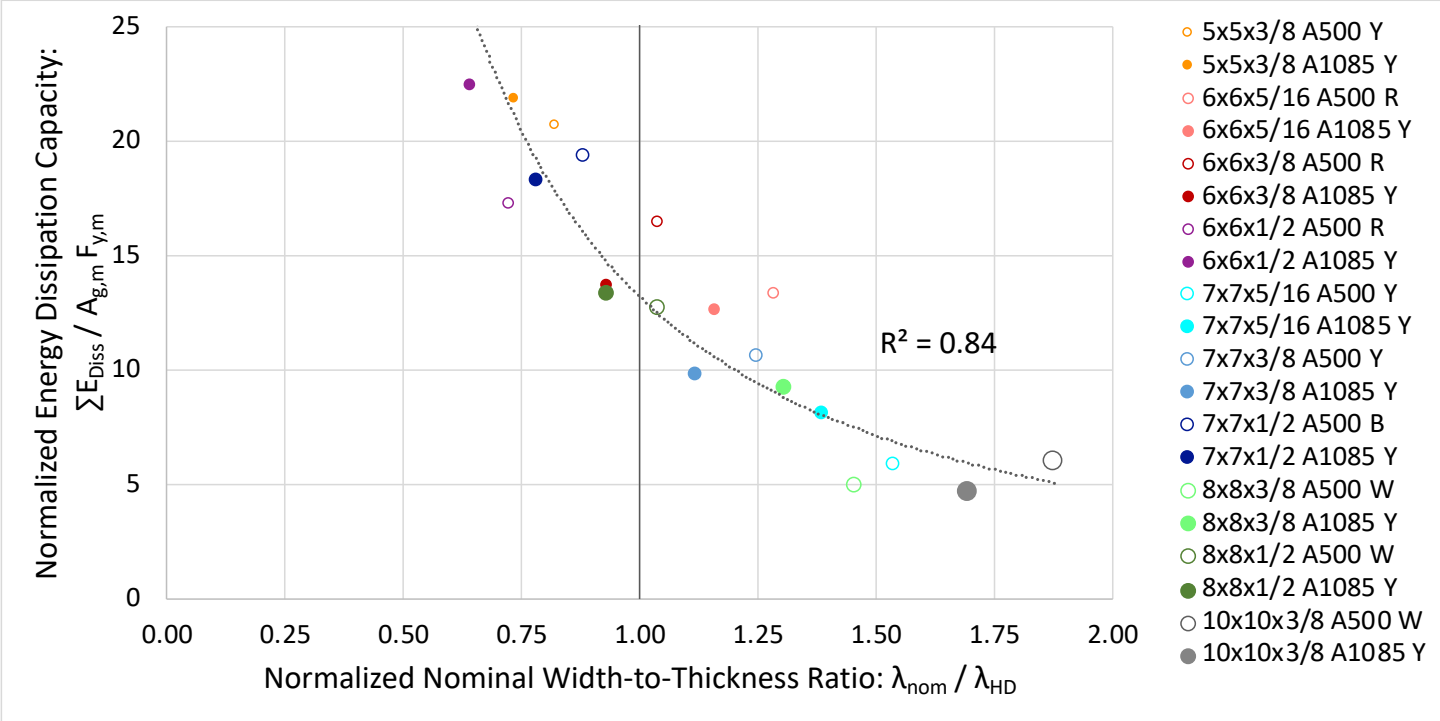

Figure 5.31. Energy Dissipation Capacity vs. Local Compactness: λ_{HD}

The normalized energy dissipation capacity is plotted against λ_{nom} normalized the AISC limits for moderately ductile members, λ_{MD}. This figure is nearly identical to the above plot, except that markers to the left of the vertical line at 1.0 represent specimens meeting the moderately ductile limits. This figure indicates that specimens with λ_{nom} less than 75% of the limits for moderately ductile members exhibit the greatest energy dissipation behavior. Additionally, specimens with λ_{nom} less than 1.2 times λ_{MD} are capable of dissipating a significant amount of energy prior to brace fracture compared to the specimens with λ_{nom} greater than 1.2 times λ_{MD}. Further analysis of the measured energy dissipation capacity is presented in Section 5.4.2.

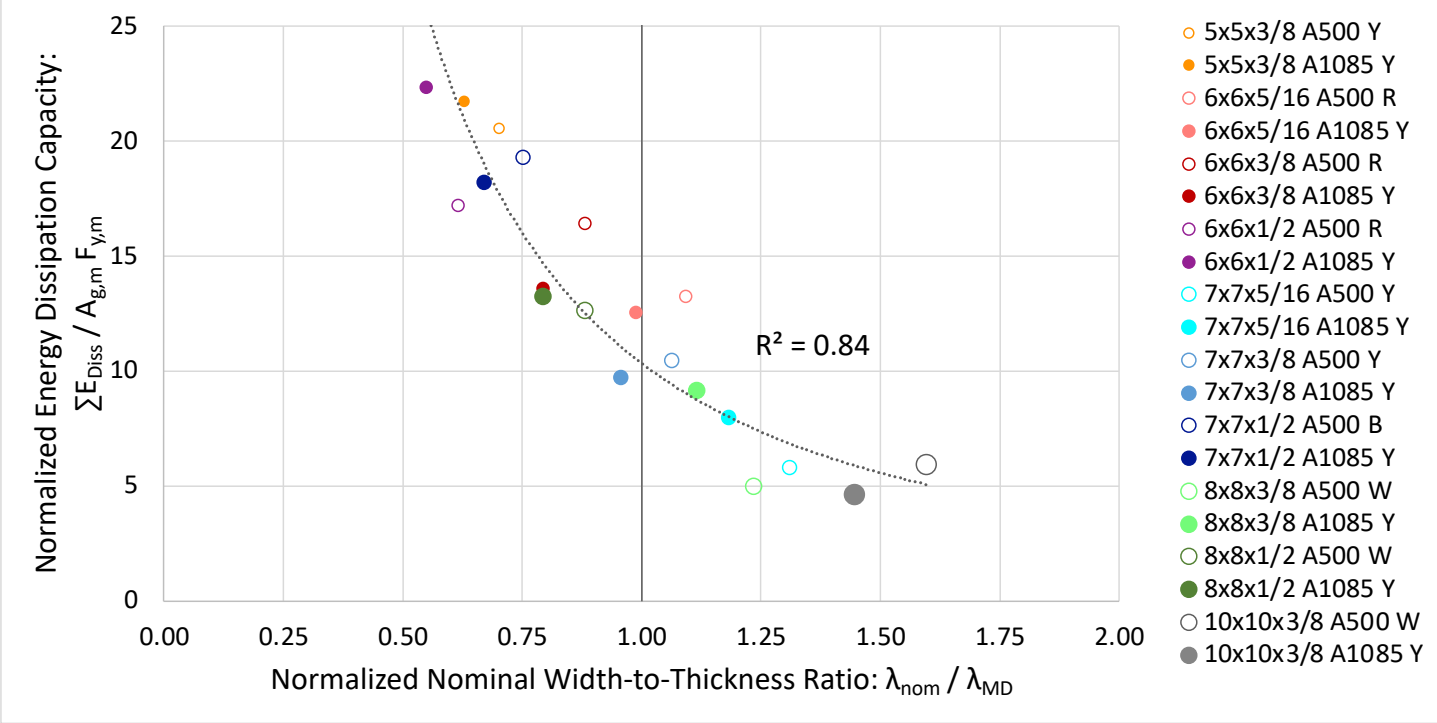

Figure 5.32. Energy Dissipation Capacity vs. Local Compactness: λ_{MD}

5.4.2 *Brace Global Slenderness*

In this section, the effects of brace global slenderness on test specimen performance are examined. Similar to Section 5.4.1, response parameters such as deformability and energy dissipation capacity are used to investigate these effects. Previous research has demonstrated a relationship between increased global slenderness and improved structural response of HSS members. These trends will be explored in this section, and further comparisons between the performance of A500 and A1085 test specimens will be developed.

Figure 5.33 below shows a plot of the axial brace displacement range versus the global slenderness ratio, KL/r, of the test specimens. There is a clear trend showing an increase in brace axial displacement range with greater global slenderness. This trend has been observed in previous research on the behavior of HSS members subjected to inelastic cyclic loading, which is discussed in Chapter 2. The global slenderness of the HSS members included in this test series ranges from about 60 to nearly 130. The global slenderness ratios for test specimens with the same width are relatively similar, which is shown by the five distinct groups circled on the plot.

Multiple HSS shapes were tested for three of these groups, the 6” sections shown in red and purple, the 7” sections shown in blue, and the 8” sections shown in green. For each group, the axial displacement range increased in the members with thicker walls, which are therefore more cross-sectionally compact. This is in line with the above observations that axial deformation range increases with greater cross-sectional compactness.

It is difficult to draw clear conclusions about the effect of steel type on brace ductility from Figure 5.33. As discussed above, it was expected that the A1085 members of a given shape would perform slightly better due to their increased cross-sectional compactness, which in previous research has been shown to correlate with improved ductility. This plot shows that the axial displacement range generally increased for members with the same wall thickness but smaller width. This was the case for all A1085 and A500 test specimens with nominal wall thicknesses of 5/16” and 1/2". Members with wall thicknesses of 3/8” generally followed this trend as well, although the 10x10x3/8 A500 W specimen exhibited a greater displacement range than both 8x8x3/8 members, despite being a more stocky specimen with a larger width-to-thickness ratio. Test specimens with the same wall thickness but smaller widths have greater global slenderness, but are also more cross-sectionally compact, making it difficult to associate the observed increase in ductility with either variable.

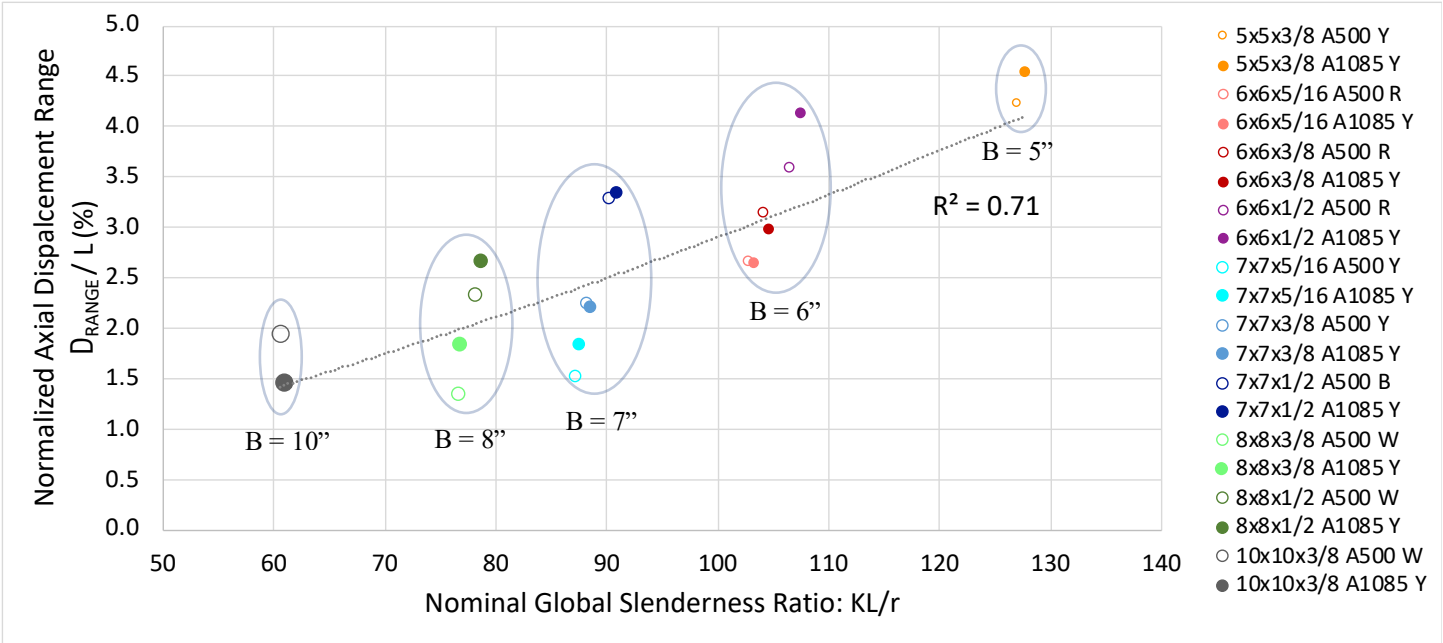

Figure 5.33. Axial Displacement Range vs. Global Slenderness

However, it is possible to evaluate the effects of brace slenderness based on the observed displacement range in members with similar nominal b/t ratios made of the same type of steel. The 6x6x3/8 A1085 Y and 8x8x1/2 A1085 Y specimens have identical nominal b/t ratios, but the 6x6x3/8 specimen is significantly more globally slender. The 6x6x3/8 A1085 Y specimen achieved a displacement range of 2.96%, about 12% greater than that of the 8x8x1/2 A1085 Y specimen. This trend is also observed in the 6x6x1/2 A500 R and 8x8x1/2 A500 W specimens. These specimens also have identical nominal b/t ratios, but the 6x6x1/2 specimen is more globally slender. The 6x6x1/2 A500 R specimen achieved a displacement range of 3.14%, which is about 35% greater than that of the 8x8x1/2 A500 W specimen. Additionally, the 6x6x5/16 A1085 Y specimen was slightly less cross-sectionally compact than the 7x7x3/8 A1085 Y specimen, but significantly more globally slender with a KL/r ratio of 103.3 compared with 88.6. The more slender 6x6x5/16 A1085 Y specimen reached a displacement range of 2.63%, about 20% greater than that of the 7x7x3/8 A1085 Y specimen. This trend was observed throughout the data set, showing an increase in ductility in more globally slender members with similar width-to-thickness ratios.

Figure 5.34 below shows the displacement at the initiation of local buckling deformations plotted against the nominal global slenderness of each test specimen. This plot shows that local buckling deformations develop at larger compressive axial displacements in more globally slender braces. This is associated with an increase in ductility in more globally slender test specimens, which is clearly displayed in Figure 5.33. The trends observed in both plots indicate delayed damage to the center of the brace is related to an increase in fracture life. Additionally, these plots do not show a relationship between steel type and brace deformability. As discussed in the previous sections, this is likely due to the similarities in the measured similarities in the geometric and material properties of the A500 and A1085 test specimens.

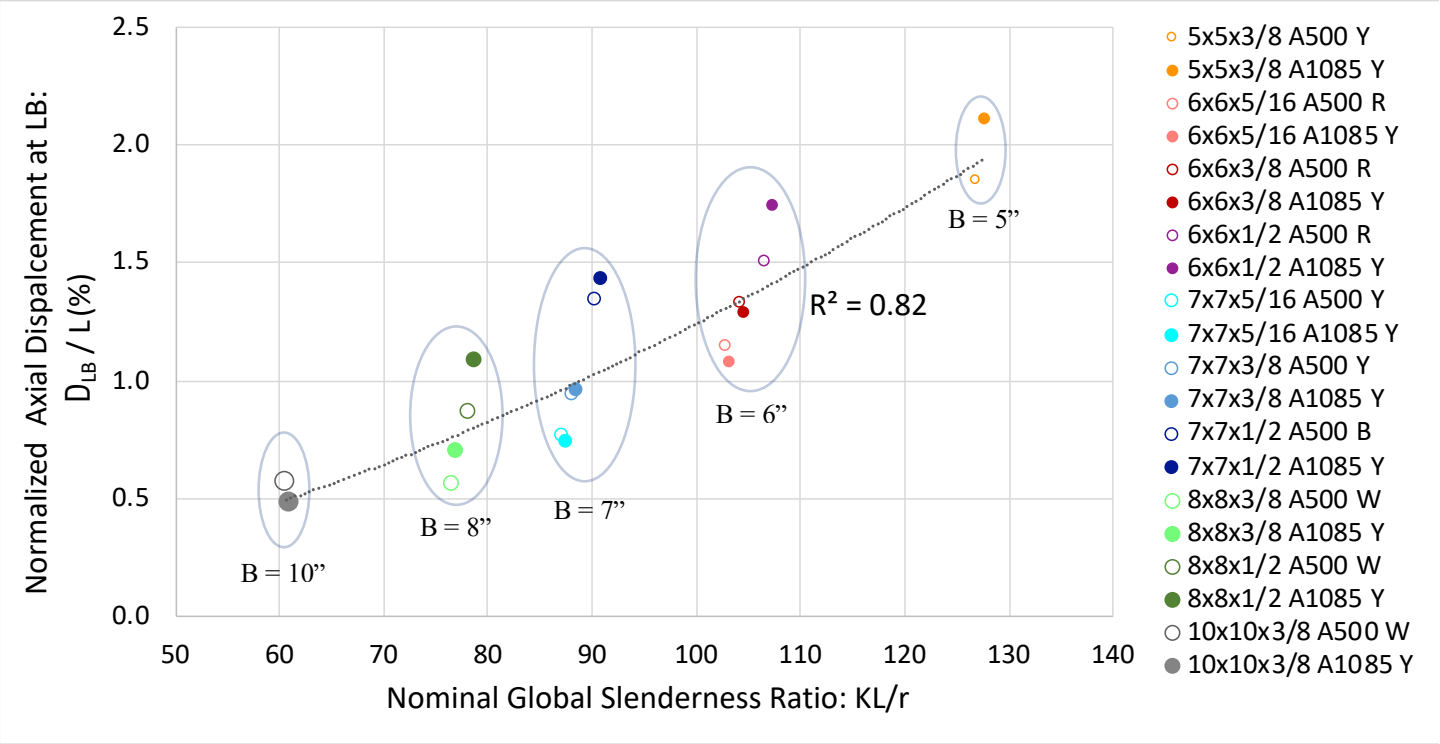

Figure 5.34. Axial Displacement at Local Buckling vs. Global Slenderness

Figure 5.35 below shows that all three non-highly ductile members that reached peak story drifts of at least 2.5% were relatively slender, with KL/r ratios of at least 100. The members with similar nominal width-to-thickness ratios that did not achieve this level of ductility were slightly stockier, with KL/r ratios of less than 90. This lower global slenderness may explain the difference in behavior between these non-highly ductile members. All test specimens reached a peak story drift of at least 1.50% prior to brace fracture. As shown by Figure 5.36 below, the accumulated axial displacement capacity also increases with greater global slenderness. It is difficult to draw conclusions regarding the relationship between steel type and deformation capacity from the figure below alone, since the width-to-thickness ratios of the specimens were shown to have a significant impact on ductility in the previous section. The figures in Section 5.4.1 did not indicate any significant relationship between steel type and brace deformation capacity.

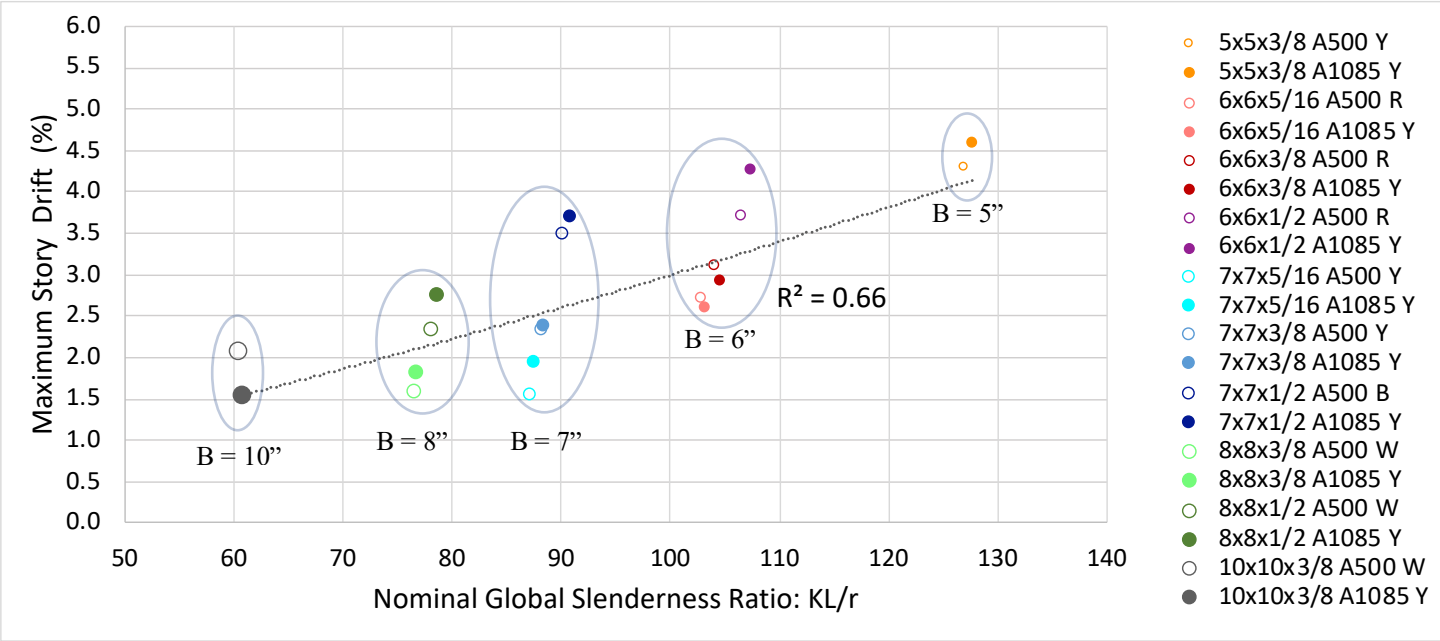

Figure 5.35. Approximate Peak Story Drift vs. Global Slenderness

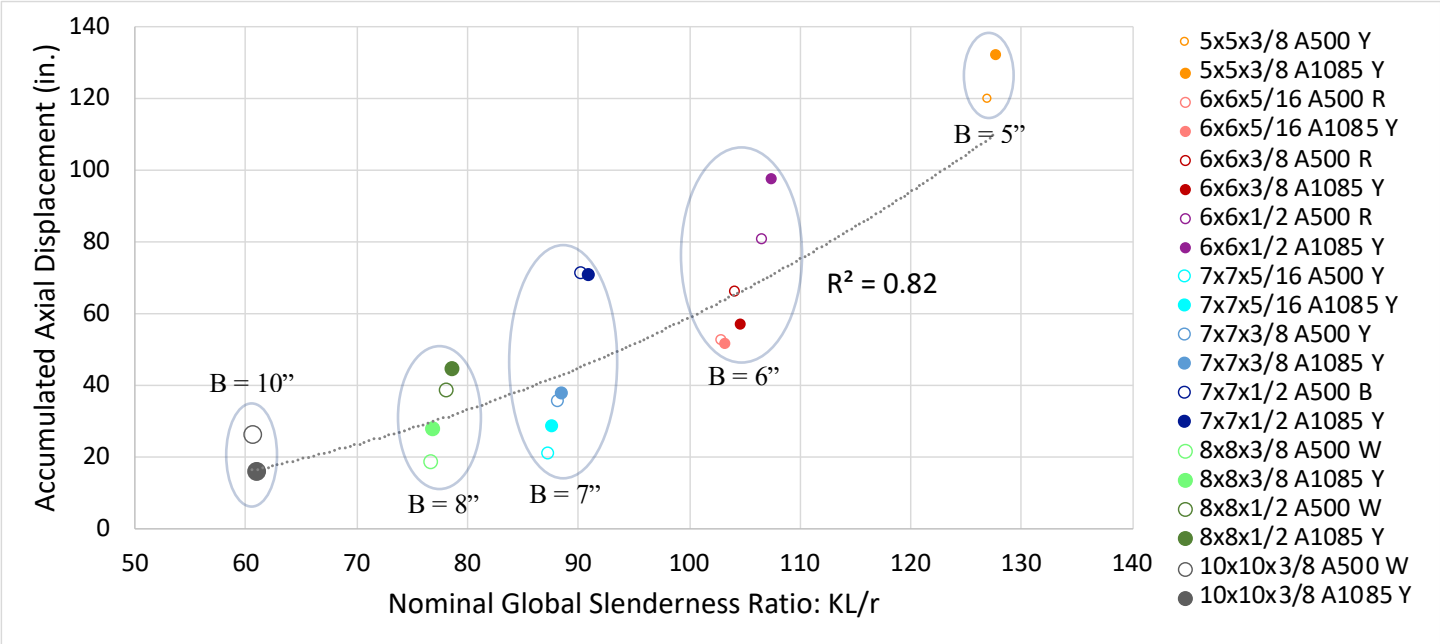

Figure 5.36. Accumulated Axial Displacement vs. Global Slenderness

Normalized energy dissipation capacity is plotted against brace global slenderness in Figure 5.37. This plot shows a relationship between energy dissipation capacity and global slenderness, indicating that energy dissipation capacity increases with greater global slenderness.

However, there significant variation between the energy dissipation capacity of sections with similar KL/r ratios. The normalized energy dissipation capacity of the 7x7x1/2 A500 B specimen is more than three times larger than that of the 7x7x5/16 A500 Y specimen, despite having a difference in slenderness ratio of about 3%. This variation in energy dissipation capacity is also observed in the test specimens with widths of 6" and 8", which shows that energy dissipation capacity relates strongly to other variables such as brace cross-sectional compactness.

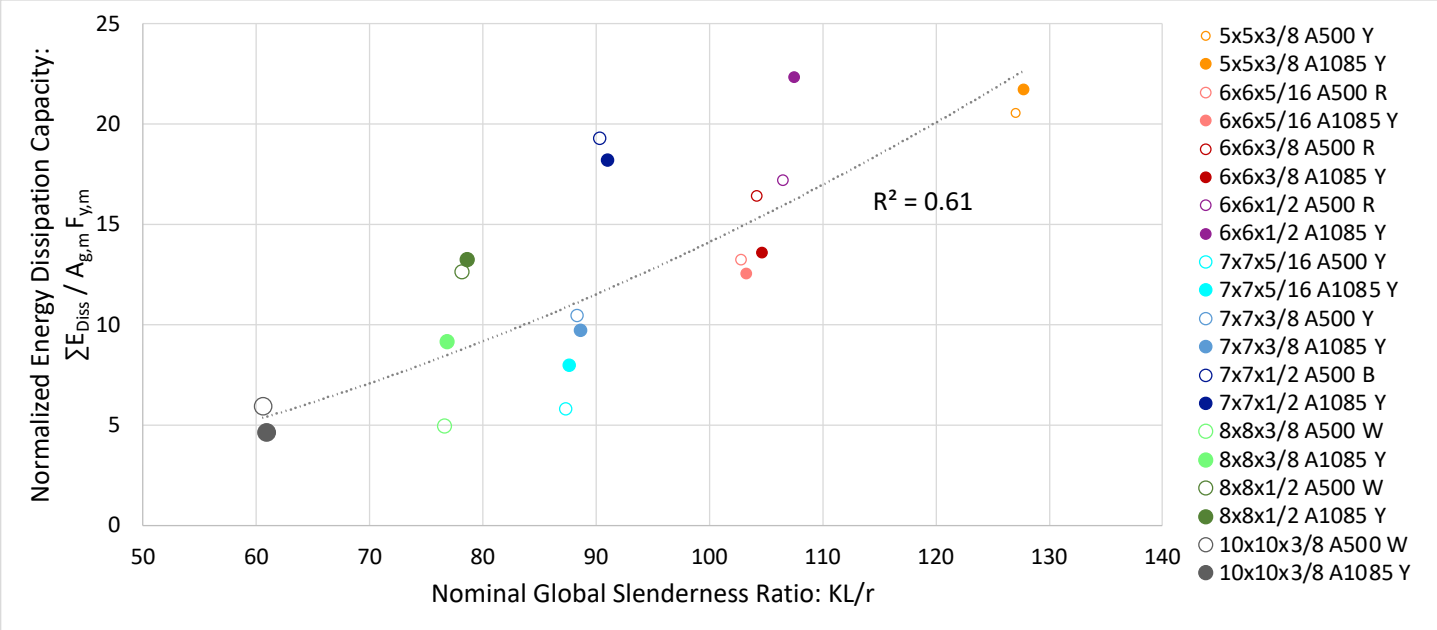

Figure 5.37. Energy Dissipation Capacity vs. Global Slenderness

Similar to the previous plots of test specimen deformation capacity, Figure 5.37 does not show a strong relationship between steel type and energy dissipation capacity. Of the ten HSS shapes tested, five of the A1085 sections exhibited greater energy dissipation capacity than their A500 counterpart, while in the other five cases the energy dissipation capacity was greater in the A500 section. The cases in which one type of steel performed better than the other do not seem to be related to cross-sectional compactness or global slenderness. Therefore, there is no observed relationship between steel type and energy dissipation capacity.

5.4.3 *Brace Toughness*

As discussed in Chapter 3, the toughness of each test specimen was evaluated through Charpy V-Notch testing. An analysis of the Charpy V-Notch test results, along with geometric and other material properties, is presented in Chapter 3. This analysis showed significant variation in test specimen toughness between the different types of steel and steel producers. The effects of measured toughness on brace deformability and energy dissipation capacity are also investigated in this section. Due to differences in Charpy specimen size, it is difficult to draw conclusions across the entire data set. Separate figures for each of the different size Charpy specimens are presented below. For each HSS shape tested, the Charpy specimens machined from the A1085 and A500 HSS shapes are the same size. This makes it possible to investigate the effects of toughness on ductility and energy dissipation capacity between the different test specimens.

The figures below follow the same color scheme as the previous plots, with A1085 specimens represented by solid circles and A500 specimens by hollow circles. The Charpy specimens taken from the corners of the HSS are represented by diamond shaped markers, and each plot is clearly labelled with the size of the Charpy specimens being compared. Several sets of Charpy specimens did not fracture during testing, and absorbed the entire 120 ft-lbs of energy applied. These specimens are represented in the figures below with an arrow indicating that the actual energy absorption capacity exceeded the capacity of the Charpy machine.

Figures 5.38, 5.39, and 5.40 below display the maximum story drift plotted against the measured toughness values for the standard size, subsize 7.5 mm, and subsize 5 mm Charpy specimens, respectively. These figures do not show a clear relationship between toughness and brace deformation capacity. In only about half of the HSS shapes tested did the specimen with greater measured toughness exhibit more ductility prior to fracture. In several cases, the tougher specimen displayed significantly less ductility. This can be seen in the 6x6x1/2 specimens in Figure 5.38 below. The measured toughness of the 6x6x1/2 A1085 Y specimen was 27.8 ft-lbs, significantly lower than the 120+ ft-lbs measured for the 6x6x1/2 A500 R specimen. However, the 6x6x1/2 A1085 Y specimen reached a maximum story drift 0.5% greater than the 6x6x1/2 A500 R specimen. In only about half of the HSS shapes tested did the tougher specimen exhibit greater ductility prior to fracture. The observed variability in the data set makes it difficult to draw conclusions regarding the effect of toughness on brace ductility.

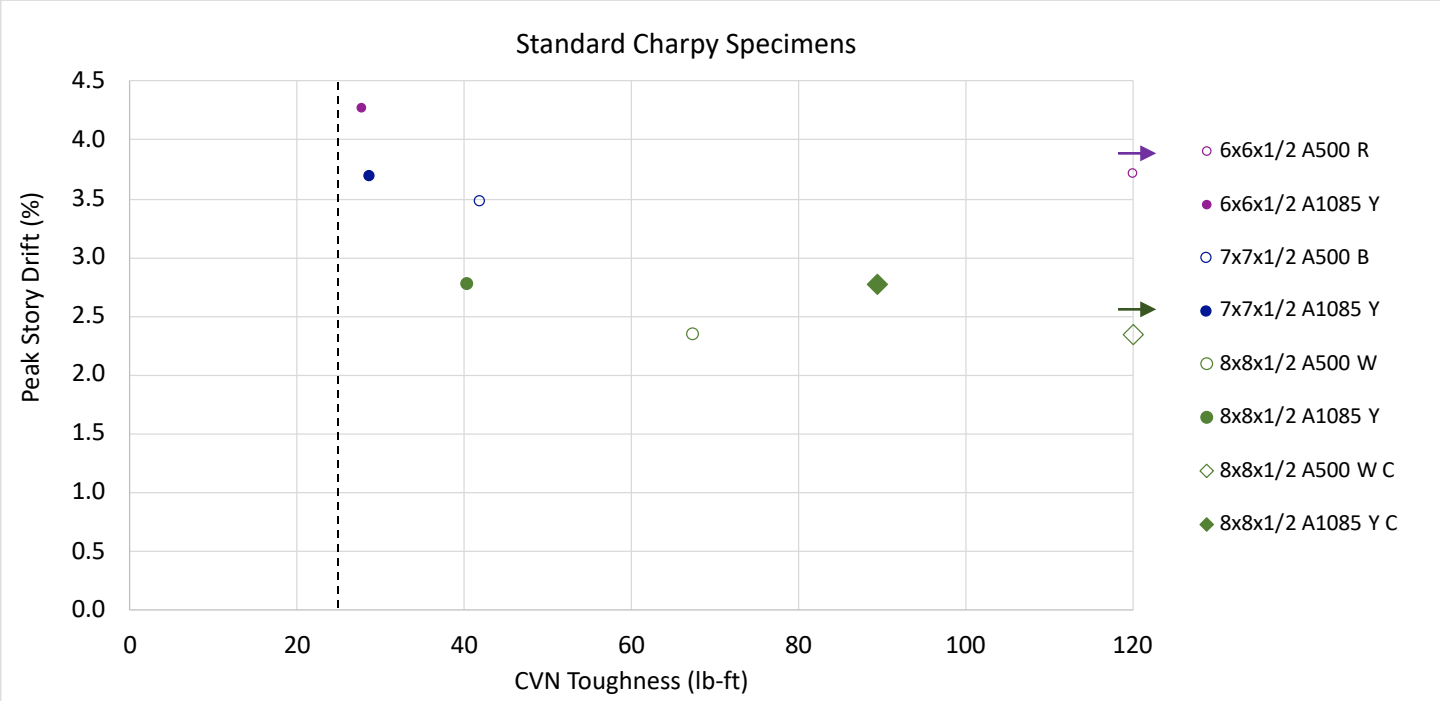

Figure 5.38. Peak Story Drift vs. Raw CVN Toughness: Standard Specimens

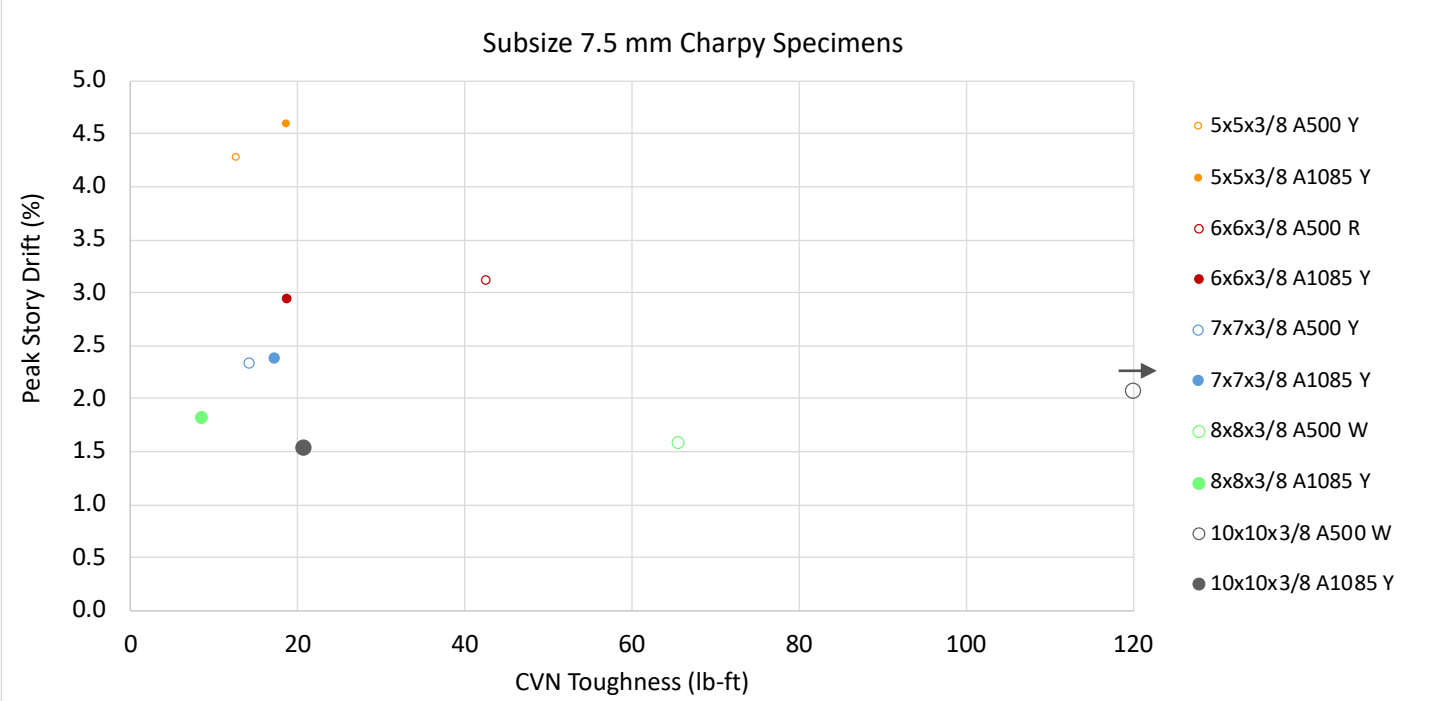

Figure 5.39. Peak Story Drift vs. Raw CVN Toughness: 7.5 mm Specimens

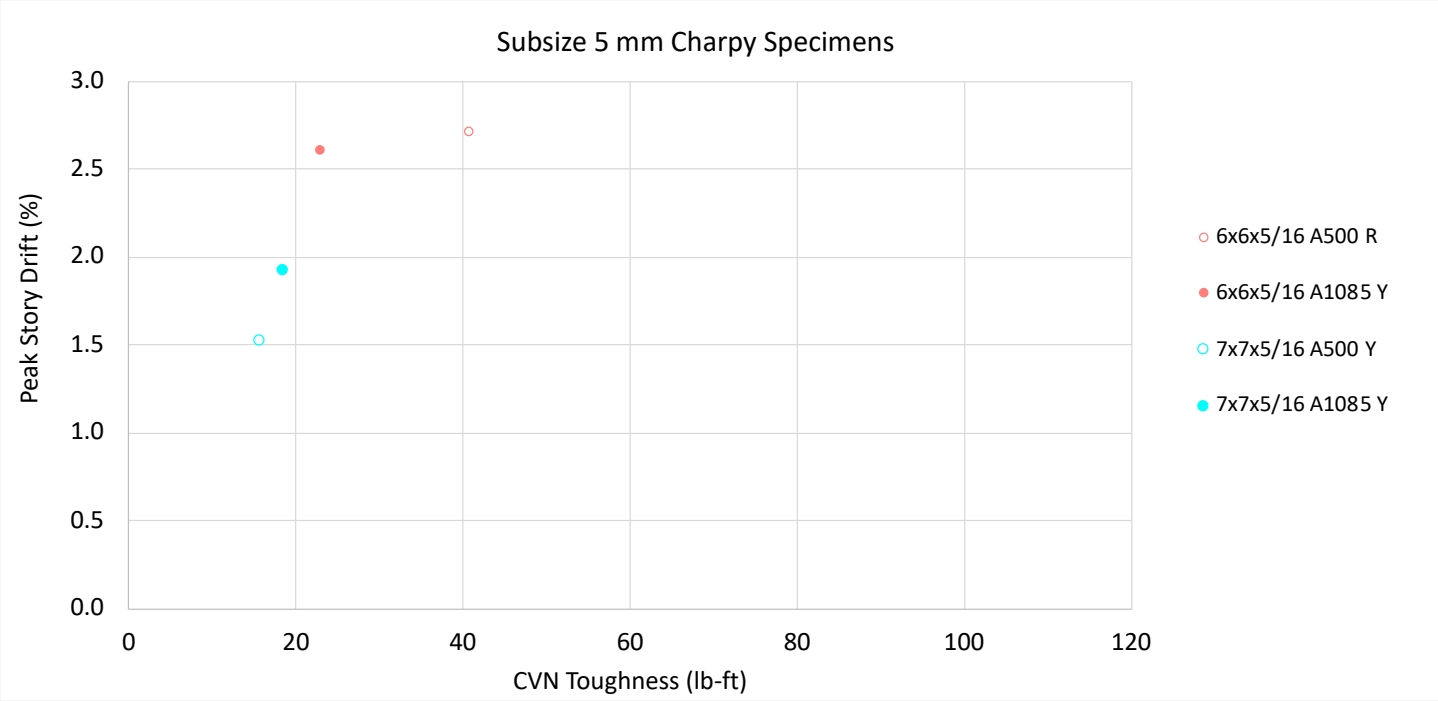

Figure 5.40. Peak Story Drift vs. Raw CVN Toughness: 5 mm Specimens

The standardized CVN toughness of all specimens plotted against the peak story drift is shown below in Figure 5.41. The measured toughness values were corrected based on the size of the Charpy specimen, as discussed in Section 3.3. The vertical line at 25 lb-ft represents the toughness required by the ASTM A1085 specification. The standardization of the toughness data makes it possible to compare the toughness values from different size Charpy specimens, although the thickness correction used may not fully capture the correlation between the energy absorbed by the different sized specimens. Similar to the figures discussed above, this data in does not show a clear relationship between specimen toughness and deformability. In half of the pairs of HSS shapes evaluated, the specimen with greater toughness exhibited less deformability prior to fracture. This indicates that increased toughness is not necessarily associated with increased deformability.

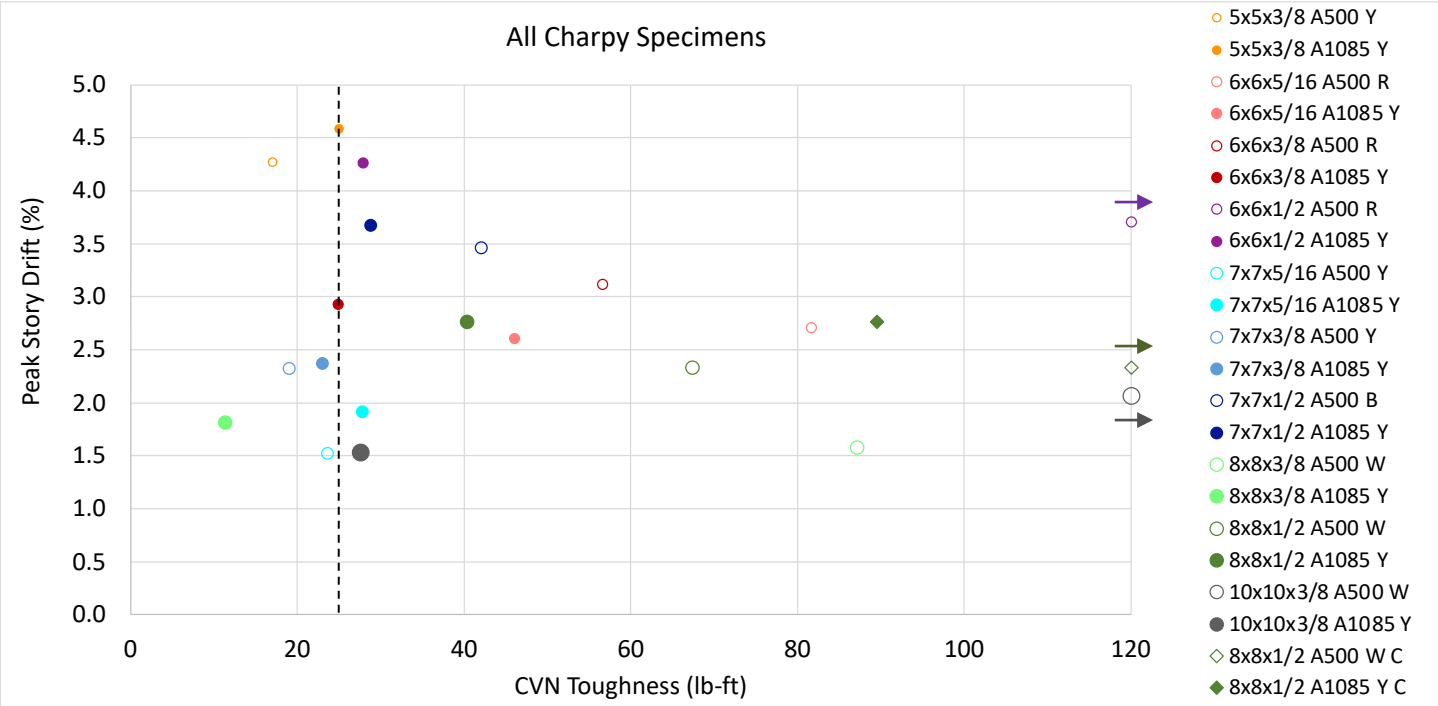

Figure 5.41. Peak Story Drift vs. Standardized CVN Toughness: All Specimens

The normalized energy dissipation capacity is plotted against the measured toughness values for each size of Charpy specimen in Figures 5.42, 5.43, and 5.44 below. Similar to the figures above, it is difficult to draw conclusions about the effect of toughness on energy dissipation capacity. In six of the ten HSS shapes tested, the specimen with greater toughness exhibited greater energy dissipation capacity. However, there are several cases shown in which specimens with significantly lower toughness displayed better energy dissipation behavior. The standardized toughness values of all test specimens are plotted against the normalized energy dissipation capacity in Figure 5.45. Based on the figures below, there is no clear link between toughness and energy dissipation capacity. Factors such as brace local compactness and global slenderness were shown to have a more significant impact on brace ductility and energy dissipation capacity than the measured toughness. The effect of toughness on specimen performance and behavior is not well-defined, and further investigation is required to fully characterize its impact on brace response.

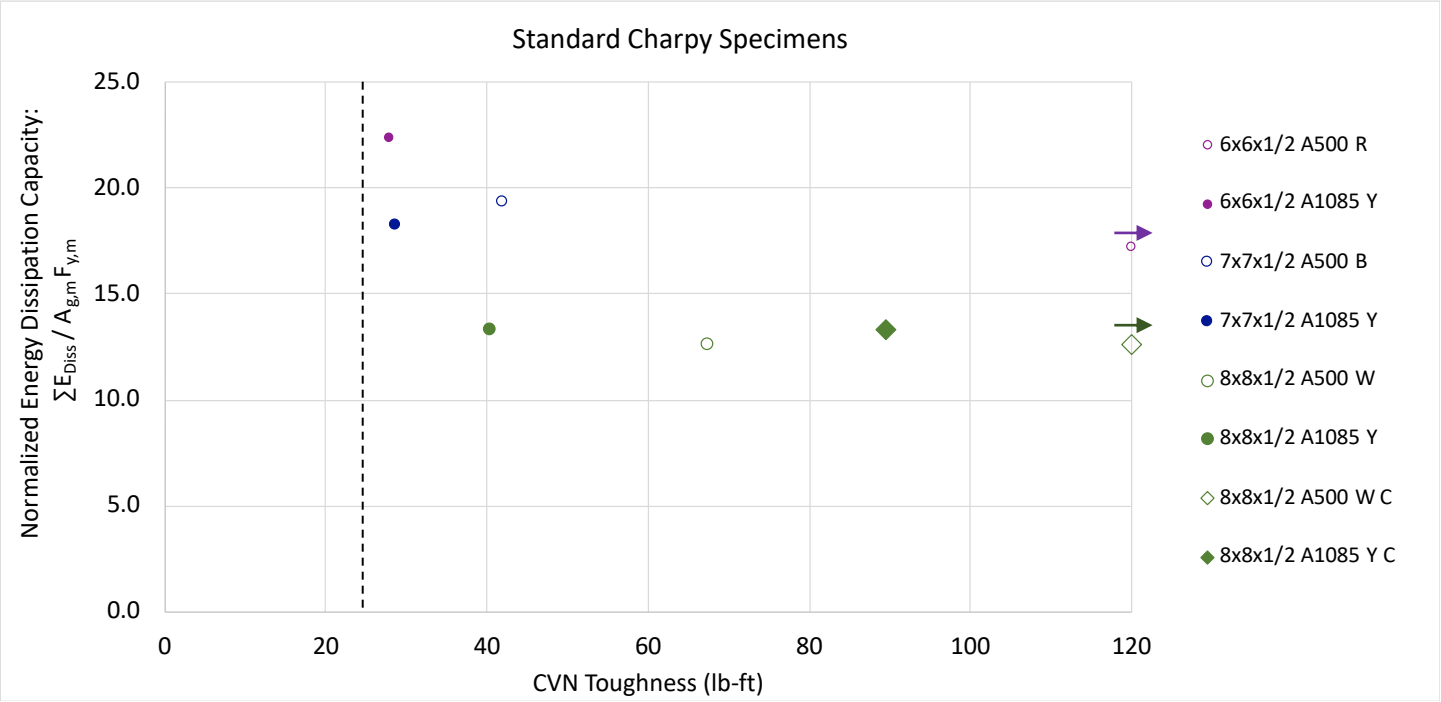

Figure 5.42. Energy Dissipation vs. Raw CVN Toughness: Standard Specimens

Figure 5.43. Energy Dissipation vs. Raw CVN Toughness: 7.5 mm Specimens

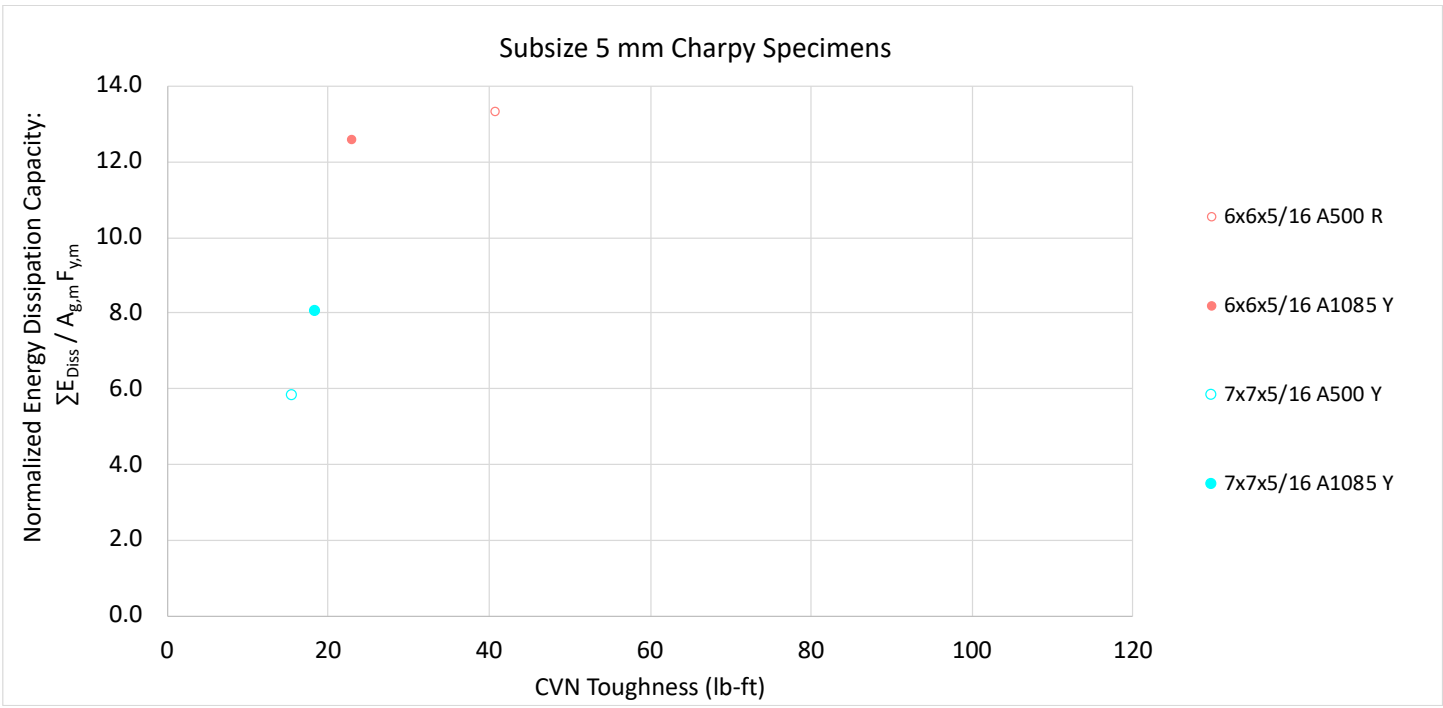

Figure 5.44. Energy Dissipation vs. Raw CVN Toughness: 5 mm Specimens

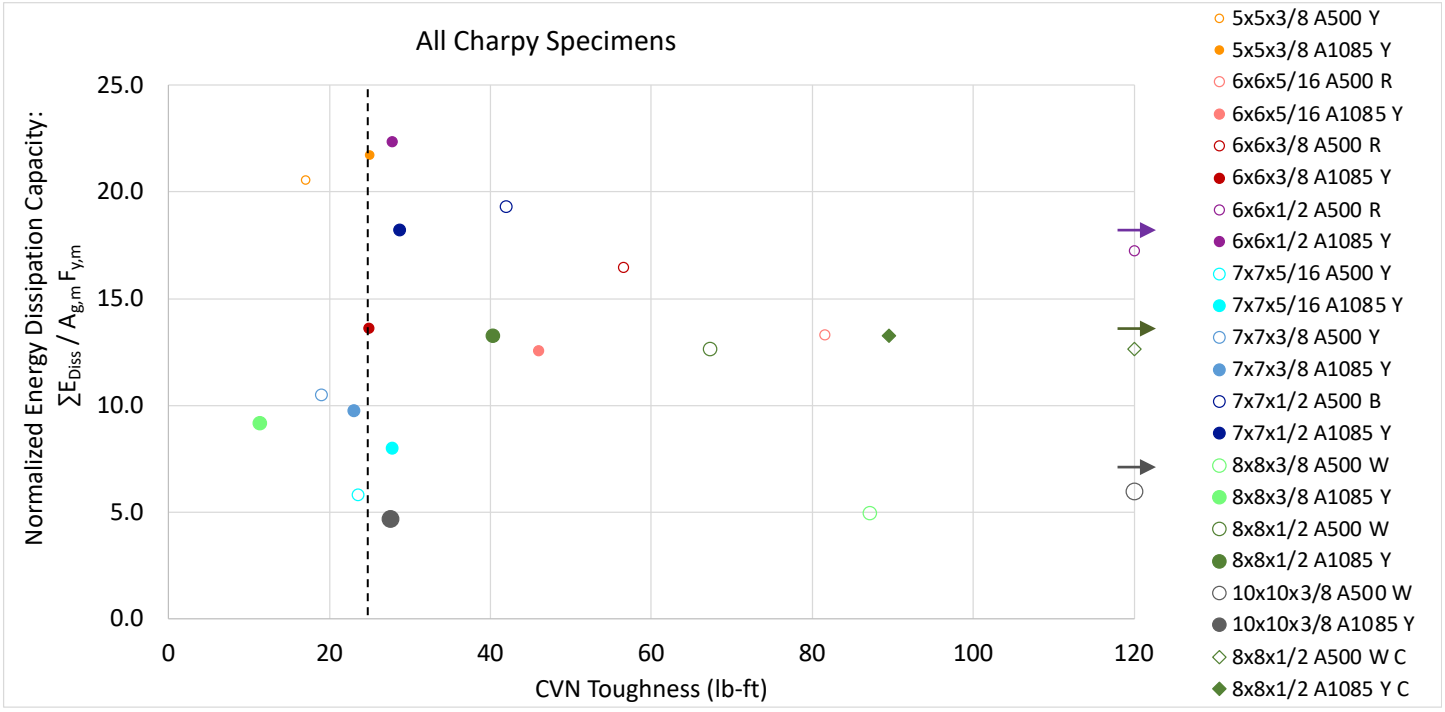

Figure 5.45. Energy Dissipation vs. Standardized CVN Toughness: All Specimens

5.5 SUMMARY OF FINDINGS

The results of the twenty component tests performed at the UW SRL showed relatively small differences between the A500 and A1085 specimens. Pairs of test specimens of the same shape were evaluated in Section 5.3. For some HSS shapes tested, the A1085 specimen demonstrated greater deformability and energy dissipation than the A500 specimen of the same shape, while in other cases the A500 specimen showed an improved structural response. The results across the entire test series were evaluated in Section 5.4. The figures presented in this series indicate that brace deformability and energy dissipation capacity are greater in specimens with more compact cross sections and increased global slenderness. Specimens both meeting and slightly exceeding the AISC 341-16 width-to-thickness limits for highly ductile members displayed ductile responses and large energy dissipation capacities prior to brace fracture. Additionally, no relationship was observed between brace toughness and structural response. It is evident that the brace performance is most influenced by brace local slenderness and global slenderness. Additionally, no significant relationship was established between steel type and structural response, as the A500 and A1085 specimens exhibited generally similar behavior across the entire test series. This may be a result of the similarities in geometric and material properties of the A500 and A1085 specimens presented in Chapter 3.

Chapter 6. EVALUATION OF PERFORMANCE-BASED ENGINEERING TOOLS

6.1 INTRODUCTION

In this chapter, an evaluation of performance-based engineering tools used to model the nonlinear behavior of rectangular and square HSS braces in braced frames subjected to seismic loading will be presented. The modeling parameters considered here are those used to predict the nonlinear response of rectangular HSS braces in braced frames. This procedure is described in AISC 342 (under development at time of writing), which governs the seismic evaluation and retrofit of structural steel buildings. (AISC, Draft 2021) This standard is designed to replace the provisions included in Chapter 9 of ASCE/SEI 41. (ASCE, 2017) The modeling parameters discussed in this section are relevant for Tier 3 systematic procedures for evaluation and retrofit. Both linear and nonlinear analysis procedures are presented in these standards, which are based on the modeling parameters described in this section. The nonlinear analysis procedures presented in Section C3 of AISC 342 will be analyzed in this chapter and compared with the measured force-displacement responses of the specimens tested in this experimental program. Backbone curves can be developed from the mechanical and geometric properties of a given brace and the predictive equations for tensile and compressive deformation capacity. The general format of the predicted inelastic response of braces in tension and compression is shown in Figure 6.1.

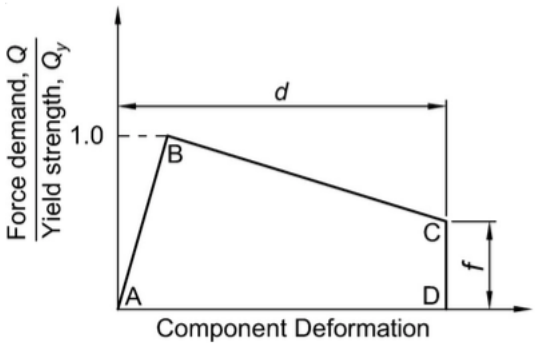

Figure 6.1. Generalized Brace Force-Deformation Response (AISC, Draft 2021)

6.2 NONLINEAR MODELING OF BRACING MEMBERS

For each of the twenty test specimens, backbone curves have been developed based on the nonlinear modeling procedure presented in Section C3 of AISC 342. A sample calculation of the predicted force-deformation behavior based on this procedure is presented in Appendix 2. The force-deformation relationship shown in Figure 6.1 is used to model the nonlinear response of braces subjected to seismic loading. Separate backbone curves are developed for tension and compression due to the differences in brace behavior under tensile and compressive loads. The nonlinear analysis procedure for rectangular HSS braces is presented in Section 3.4b of AISC 342, which includes modeling parameters for the predicted total axial deformation, *d*, and strength ratio at the maximum deformation, *f*. The strength ratio, *f,* is used to model the predicted strength degradation associated with greater brace deformations. Modeling parameters were calculated for each test specimen based on Table C3.4 of AISC 342. This table includes equations used to calculate *n*-factors for braces in tension and compression, which are used to predict brace deformation capacity. These equations take into account brace local and global slenderness, which have been shown have a significant impact on brace ductility.

For tension of a rectangular HSS brace:

$$n = 4.7 \cdot \left(\frac{\lambda}{\lambda_{hd}}\right)^{-0.99} \cdot \left(\frac{\left(\frac{L_c}{r}\right)}{\sqrt{\frac{E}{F_{ye}}}}\right)^{0.24}$$

For compression of a rectangular HSS brace:

$$n = 3.0 \cdot \left(\frac{\lambda}{\lambda_{hd}}\right)^{-0.96} \cdot \left(\frac{\left(\frac{L_c}{r}\right)}{\sqrt{\frac{E}{F_{ye}}}}\right)^{1.0}$$

These *n*-factors, along with the predicted tensile and compressive axial yield deformations, Δ_T and Δ_C, are used to determine the axial modeling parameters.

For tension of a rectangular HSS brace:

$$\Delta_T = \frac{(P_{ye} \cdot L_c)}{A_g \cdot E}$$

$$d = n \cdot \Delta_T$$

For compression of a rectangular HSS brace:

$$\Delta_C = \frac{(P_{ce} \cdot L_c)}{A_g \cdot E}$$

$$d = n \cdot \Delta_C$$

The computed modeling parameters for the test specimens are shown in Table 6.1. The total axial deformation, *d*, is shown for both the predicted tensile and compressive responses. The residual strength of each test specimen at the maximum tensile and compressive displacements is also presented in this table. The residual axial force is calculated as the strength ratio, *f*, multiplied by the expected tensile and compressive strengths of the member. In tension, the strength ratio is 1.0, indicating that strength degradation is not expected in tension prior to fracture. The strength ratio is 0.2 in compression, due to the expected strength degradation associated with brace buckling.

Table 6.1. Test Specimen Modeling Parameters

			n-factor		***d* (in.)**		***f* * P (k)**	
Test Specimen	**Δ_T (in.)**	**Δ_C (in.)**	**Tension**	**Compression**	**Tension**	**Compression**	**Tension**	**Compression**
5x5x3/8 A500 Y	0.53	0.127	8.77	21.75	4.67	2.77	401.7	19.2
5x5x3/8 A1085 Y	0.51	0.126	9.76	23.88	5.00	3.01	411.3	20.3
6x6x5/16 A500 R	0.53	0.195	5.37	11.51	2.86	2.24	418.0	30.5
6x6x5/16 A1085 Y	0.51	0.193	5.93	12.50	3.03	2.41	429.4	32.3
6x6x3/8 A500 R	0.53	0.189	6.67	14.32	3.55	2.71	492.7	35.0
6x6x3/8 A1085 Y	0.51	0.188	7.39	15.65	3.78	2.94	505.0	37.1
6x6x1/2 A500 R	0.53	0.181	9.58	20.71	5.10	3.75	633.1	43.1

			n-factor		*d* (in.)		*f* * P (k)	
Test Specimen	**Δ_T (in.)**	**Δ_C (in.)**	**Tension**	**Compression**	**Tension**	**Test Specimen**	**Δ_T (in.)**	**Δ_C (in.)**
6x6x1/2 A1085 Y	0.51	0.178	10.71	22.88	5.48	4.07	647.5	45.0
7x7x5/16 A500 Y	0.53	0.258	4.32	8.21	2.30	2.12	493.4	47.8
7x7x5/16 A1085 Y	0.51	0.254	4.77	8.92	2.44	2.27	507.5	50.3
7x7x3/8 A500 Y	0.53	0.254	5.33	10.16	2.84	2.58	583.1	55.6
7x7x3/8 A1085 Y	0.51	0.250	5.89	11.06	3.02	2.76	598.8	58.4
7x7x1/2 A500 B	0.53	0.245	7.55	14.48	4.02	3.55	754.0	69.5
7x7x1/2 A1085 Y	0.51	0.240	8.43	15.98	4.32	3.84	775.0	72.7
8x8x3/8 A500 W	0.53	0.305	4.43	7.62	2.36	2.32	676.0	77.4
8x8x3/8 A1085 Y	0.51	0.298	4.89	8.28	2.50	2.47	693.8	80.9
8x8x1/2 A500 W	0.53	0.298	6.22	10.74	3.31	3.20	877.5	98.2
8x8x1/2 A1085 Y	0.51	0.291	6.90	11.76	3.53	3.42	900.0	102.3
10x10x3/8 A500 W	0.53	0.376	3.25	4.71	1.73	1.77	858.0	121.1
10x10x3/8 A1085 Y	0.51	0.365	3.58	5.12	1.83	1.87	881.3	125.6

Additionally, the expected deformations corresponding to different component performance levels can be predicted from nonlinear analyses that utilize these modeling parameters. These performance levels, as defined in ASCE/SEI 41, are immediate occupancy (IO), life safety (LS), and collapse prevention (CP). The portion of Table C2.4 of ASCE/SEI 41 that is relevant to this thesis is shown below in Table 6.2.

Table 6.2. Brace Performance Levels (ASCE, 2017)

Seismic-Force Resisting System	**Type**	**Structural Performance Levels**		
		Immediate Occupancy (IO)	**Life Safety (LS)**	**Collapse Prevention (CP)**
Braced Steel Frames	Primary and Secondary Elements	Minor yielding or buckling of braces	Many braces yield or buckle but do not totally fail. Many connections might fail.	Extensive yielding and buckling of braces. Many braces and their connections might fail.

The predicted axial deformation at each performance level was calculated based on Table C3.4 in AISC 342, and is shown in Table 6.3 below. The axial deformation at the collapse prevention performance state limit represents the predicted maximum compressive and tensile deformations prior to brace fracture. Local buckling deformations are expected to develop in the center of the brace at the collapse prevention performance level. An evaluation of the predicted and measured axial deformation capacity will be presented in Section 6.3.

Table 6.3. Test Specimen Performance State Acceptance Criteria

	IO (in.)		LS (in.)		CP (in.)	
Test Specimen	**Tension**	**Compression**	**Tension**	**Compression**	**Tension**	**Compression**
5x5x3/8 A500 Y	0.80	0.19	3.27	1.94	4.67	2.77
5x5x3/8 A1085 Y	0.77	0.19	3.50	2.11	5.00	3.01
6x6x5/16 A500 R	0.80	0.29	2.00	1.57	2.86	2.24
6x6x5/16 A1085 Y	0.77	0.29	2.12	1.69	3.03	2.41
6x6x3/8 A500 R	0.80	0.28	2.48	1.90	3.55	2.71
6x6x3/8 A1085 Y	0.77	0.28	2.65	2.06	3.78	2.94
6x6x1/2 A500 R	0.80	0.27	3.57	2.63	5.10	3.75
6x6x1/2 A1085 Y	0.77	0.27	3.84	2.85	5.48	4.07
7x7x5/16 A500 Y	0.80	0.39	1.61	1.48	2.30	2.12
7x7x5/16 A1085 Y	0.77	0.38	1.71	1.59	2.44	2.27
7x7x3/8 A500 Y	0.80	0.38	1.99	1.80	2.84	2.58
7x7x3/8 A1085 Y	0.77	0.37	2.11	1.93	3.02	2.76
7x7x1/2 A500 B	0.80	0.37	2.81	2.49	4.02	3.55
7x7x1/2 A1085 Y	0.77	0.36	3.02	2.69	4.32	3.84
8x8x3/8 A500 W	0.80	0.46	1.65	1.63	2.36	2.32
8x8x3/8 A1085 Y	0.77	0.45	1.75	1.73	2.50	2.47
8x8x1/2 A500 W	0.80	0.45	2.32	2.24	3.31	3.20
8x8x1/2 A1085 Y	0.77	0.44	2.47	2.39	3.53	3.42
10x10x3/8 A500 W	0.80	0.56	1.21	1.24	1.73	1.77
10x10x3/8 A1085 Y	0.77	0.55	1.28	1.31	1.83	1.87

6.3 EVALUATION OF PREDICTED BRACE PERFORMANCE

In this section, the predicted tensile and compressive axial displacement capacity shown in Table 6.3 will be compared to the measured displacement behavior of each test specimen. In the figures below, the measured force-displacement responses and corresponding backbone curves are plotted together to display differences between the measured and predicted nonlinear behavior. The backbone curves shown in the figures below were developed based on the procedure discussed in Section 6.2. However, additional analysis is required to fully evaluate the nonlinear procedures presented in Section C3 of AISC 342. It is difficult to characterize the data trends based on the comparison figures below, and thus additional tables and figures are presented later in this section to examine any trends in the data. This makes it possible to evaluate the accuracy of the predicted nonlinear force-displacement behavior based on steel type, width-to-thickness ratio, and global slenderness.

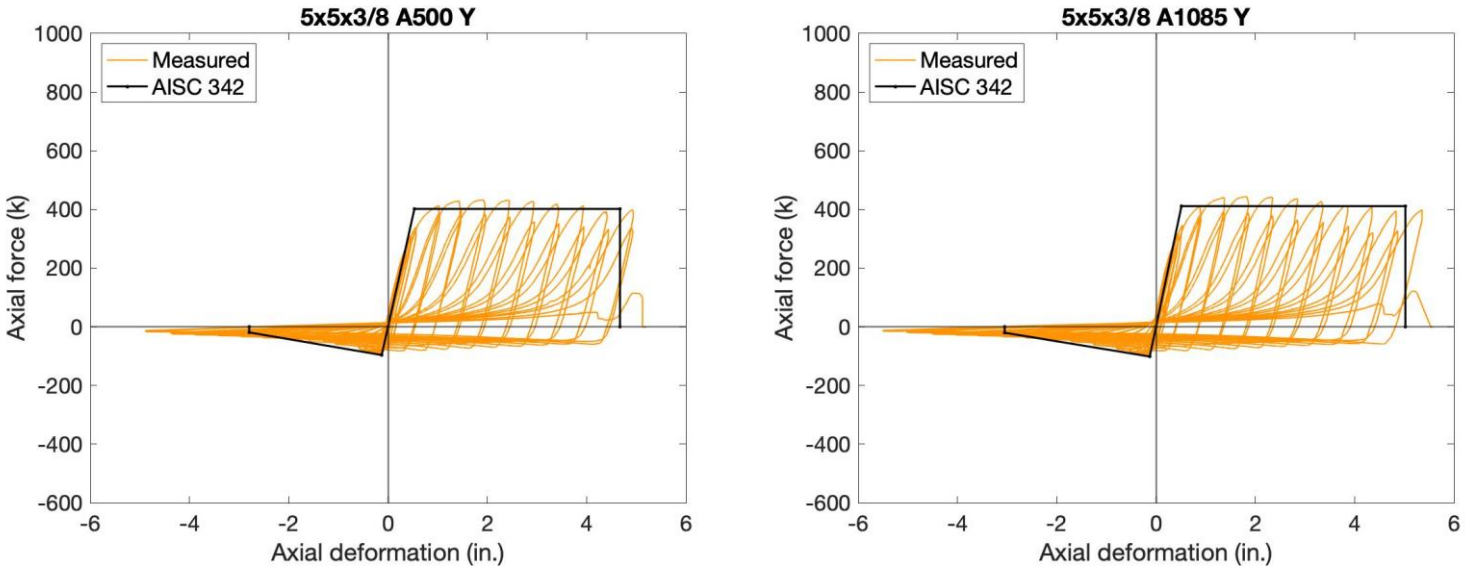

Figure 6.2. Backbone Curve Comparison – 5x5x3/8 HSS

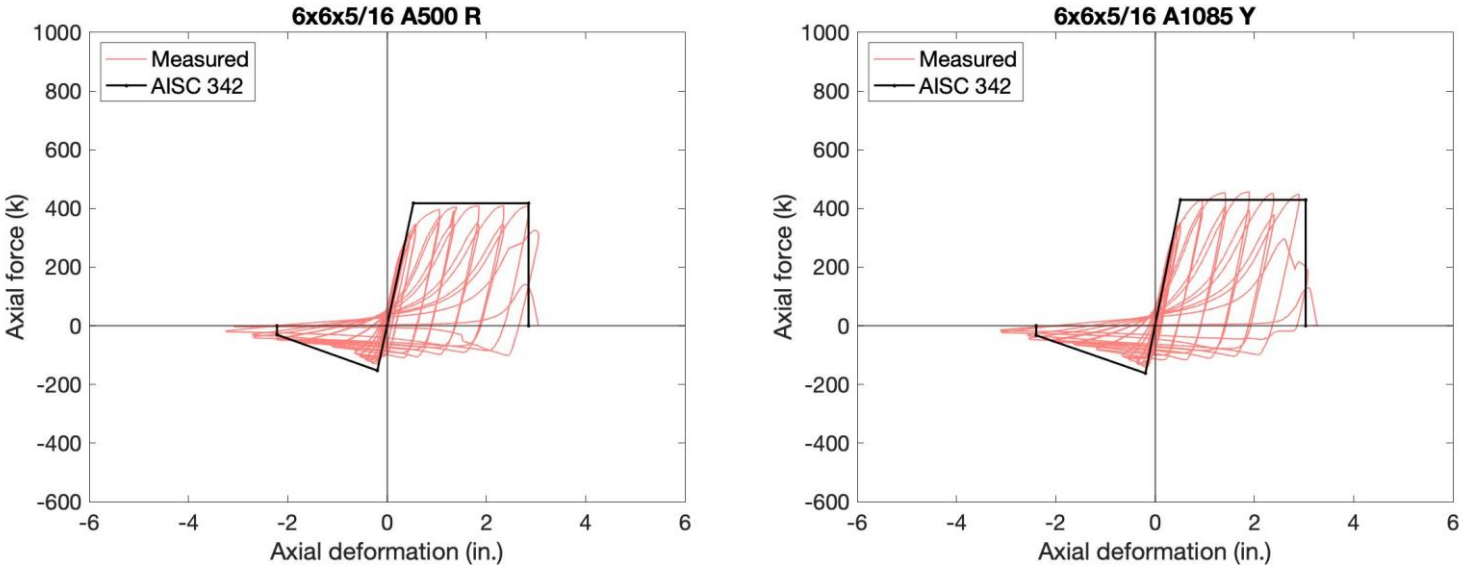

Figure 6.3. Backbone Curve Comparison – 6x6x5/16 HSS

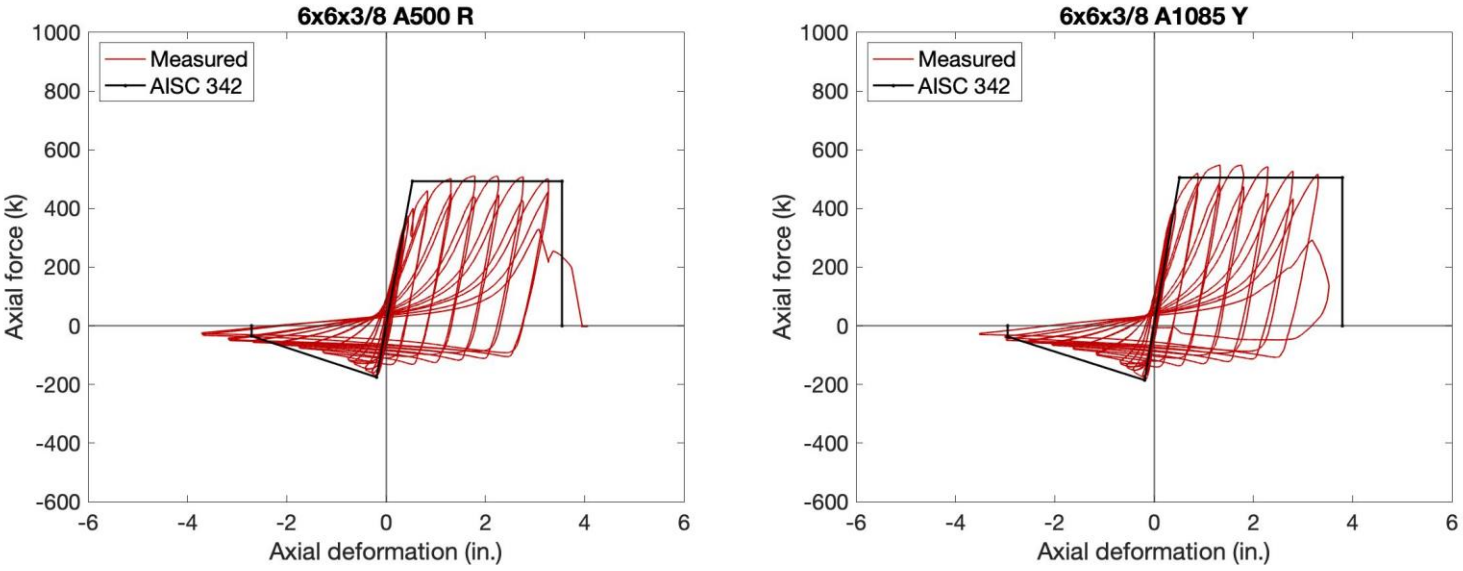

Figure 6.4. Backbone Curve Comparison – 6x6x3/8 HSS

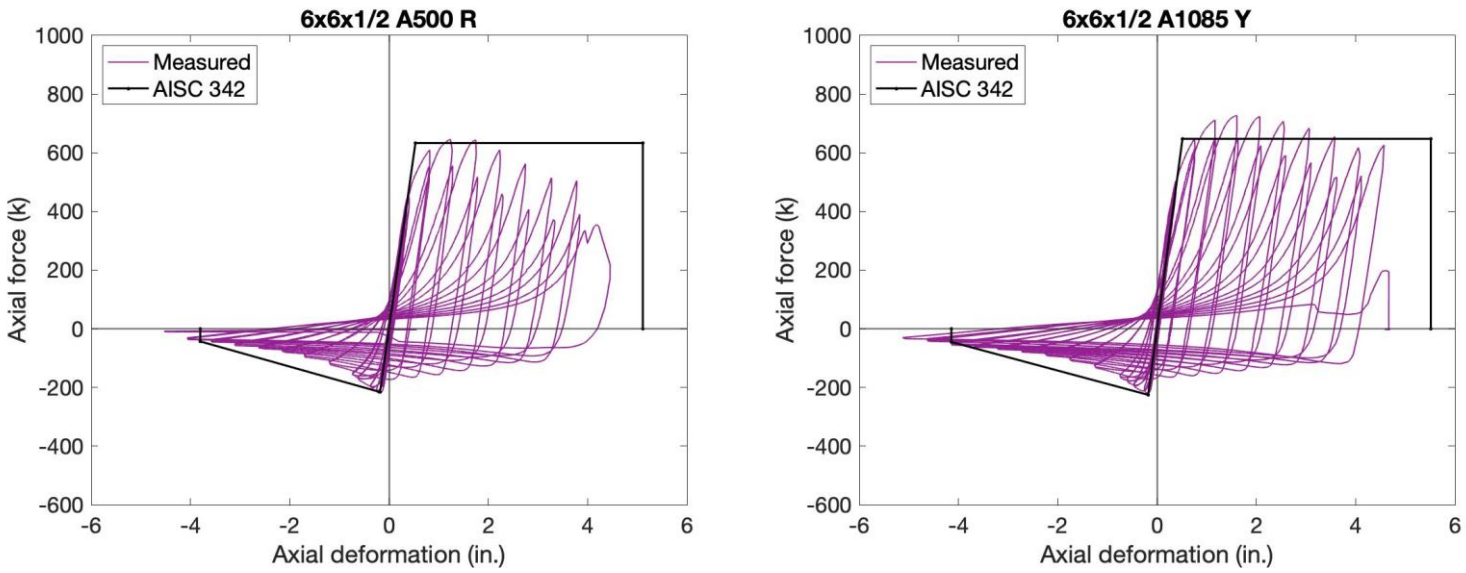

Figure 6.5. Backbone Curve Comparison – 6x6x1/2 HSS

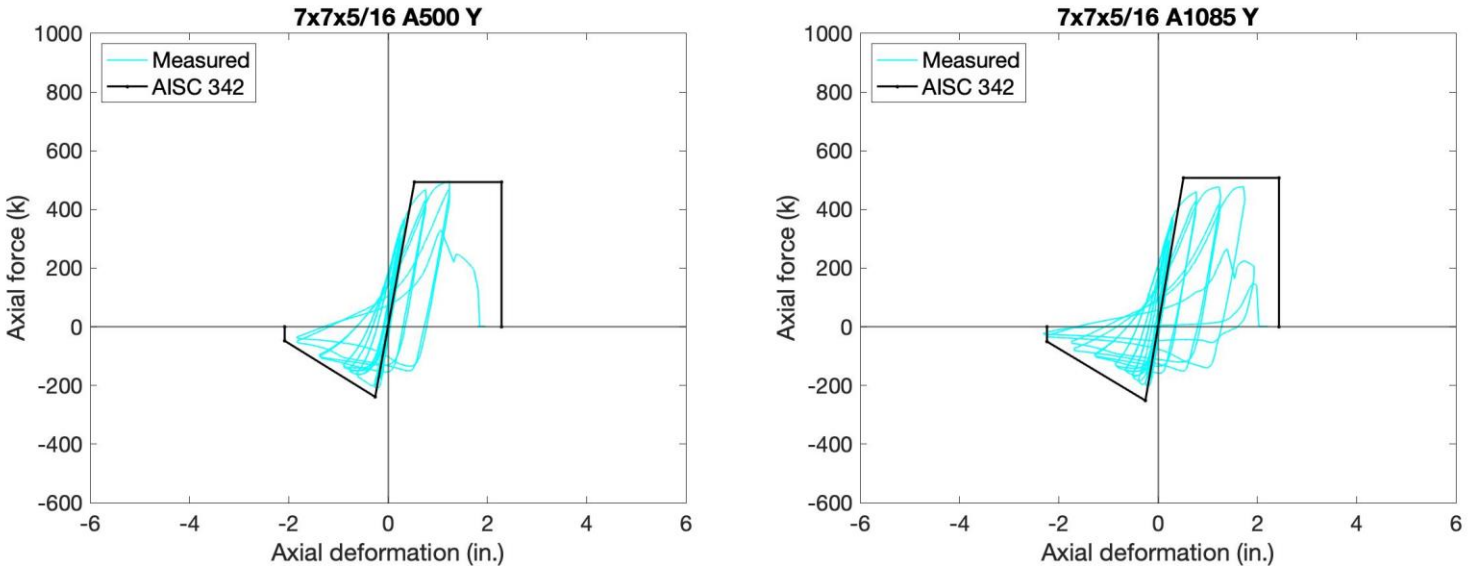

Figure 6.6. Backbone Curve Comparison – 7x7x5/16 HSS

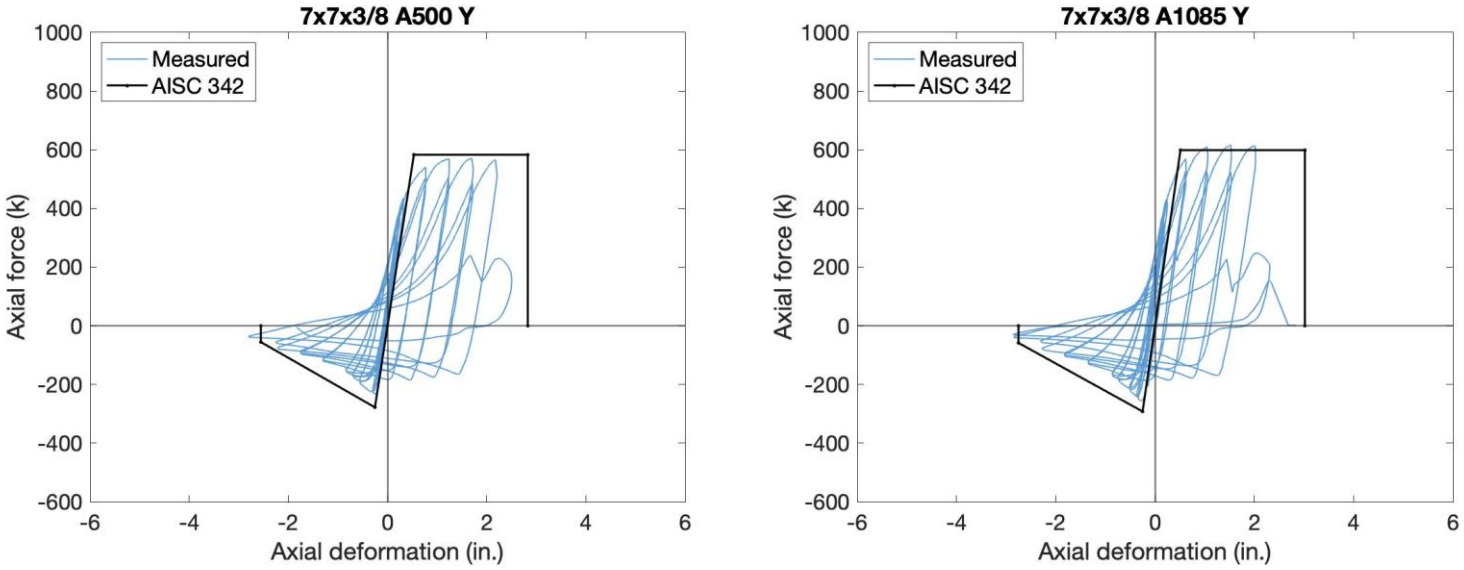

Figure 6.7. Backbone Curve Comparison – 7x7x3/8 HSS

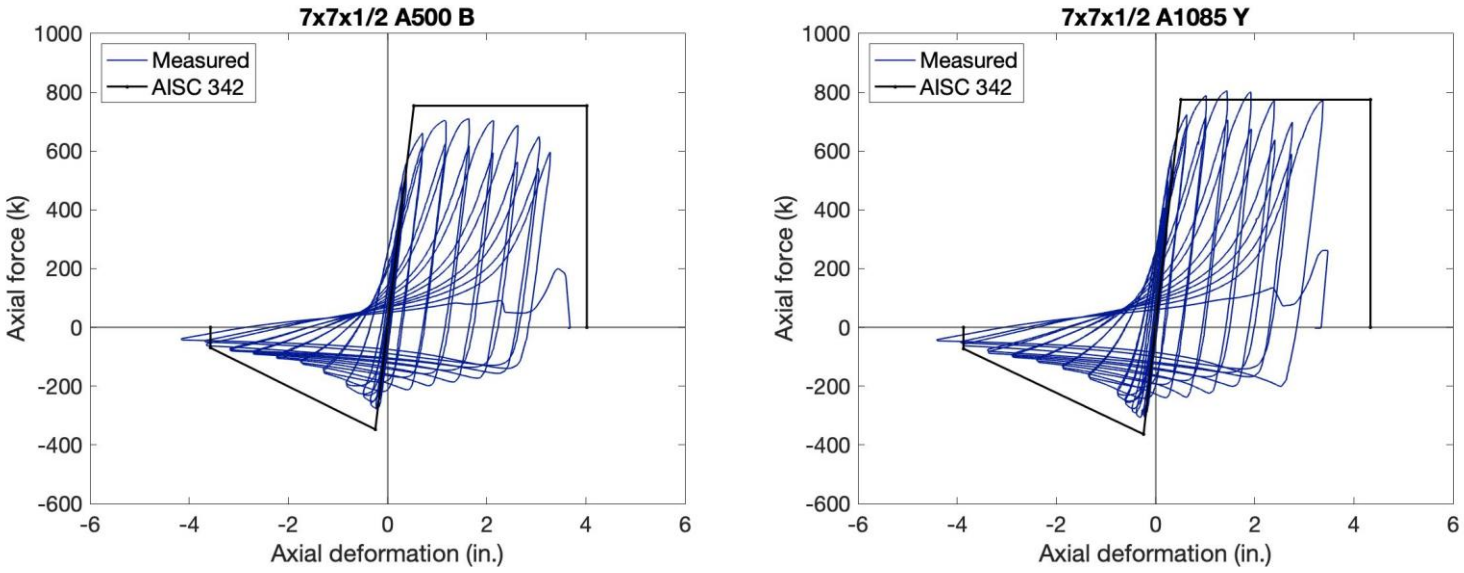

Figure 6.8. Backbone Curve Comparison – 7x7x1/2 HSS

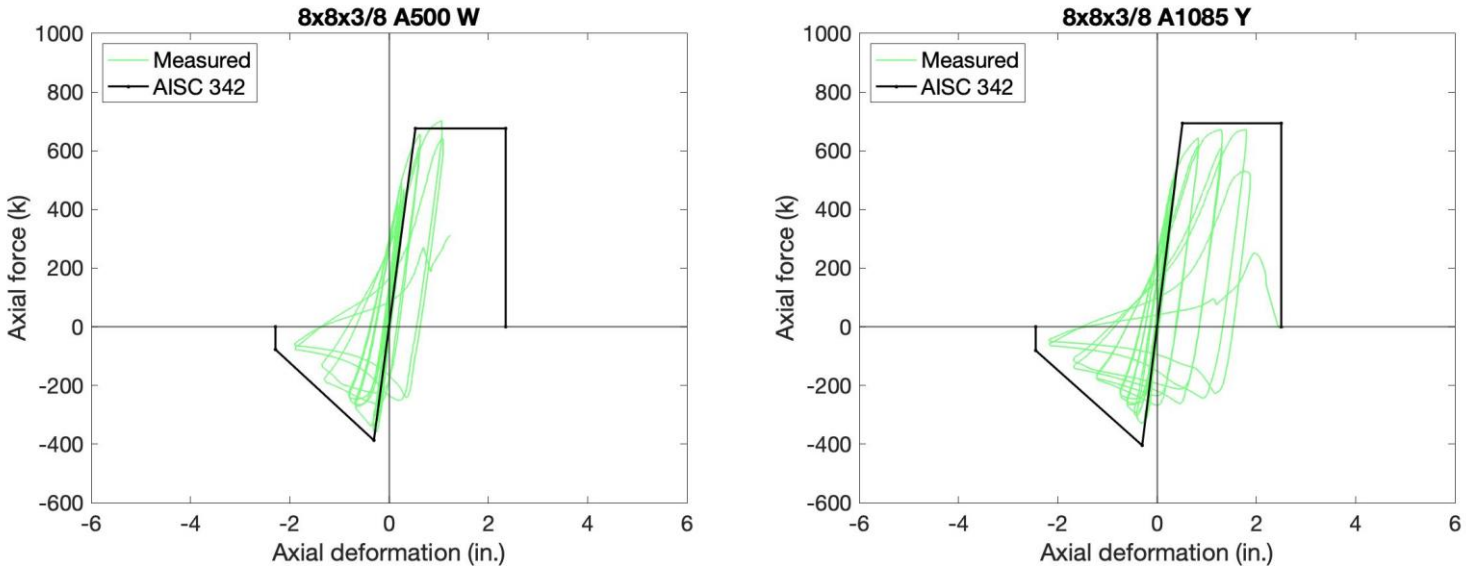

Figure 6.9. Backbone Curve Comparison – 8x8x3/8 HSS

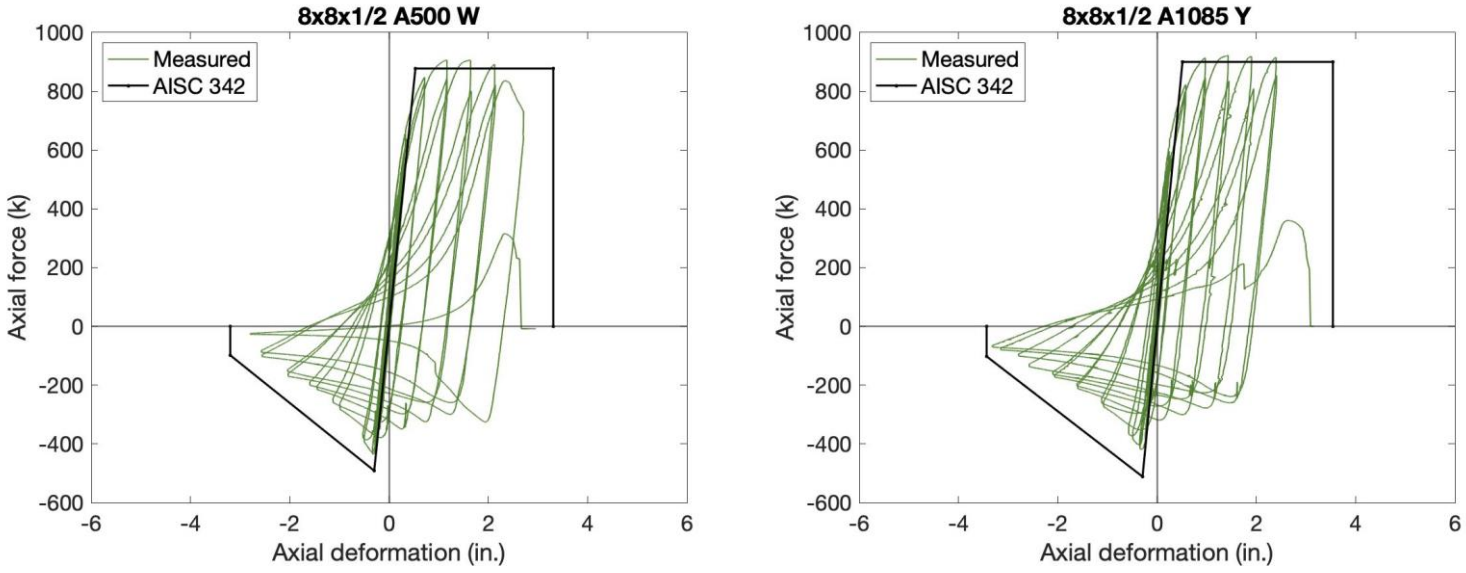

Figure 6.10. Backbone Curve Comparison – 8x8x1/2 HSS

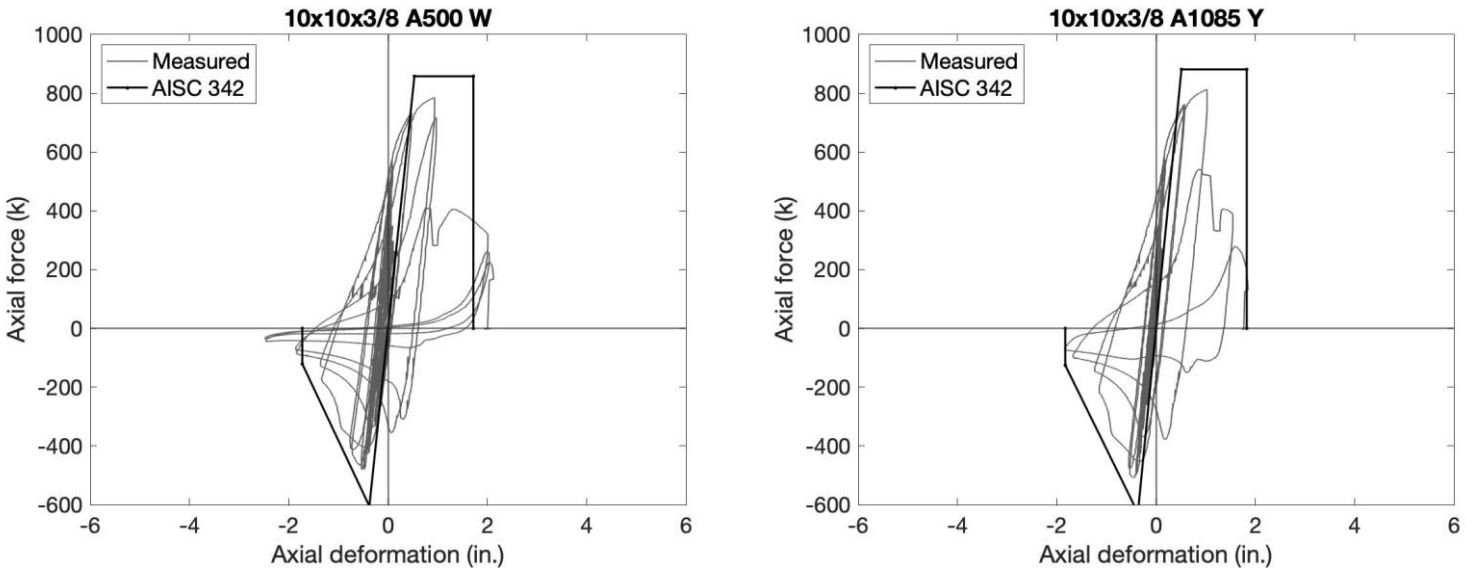

Figure 6.11. Backbone Curve Comparison – 10x10x3/8 HSS

In order to evaluate the accuracy of the AISC 342 backbone curves across the entire data set, the predicted and measured deformation capacities ($\Delta_{predicted}$ and $\Delta_{measured}$) are shown in Table 6.4 below. In this table, the ratio of measured-to-predicted tensile and compressive deformation capacity ($\Delta_{measured} : \Delta_{predicted}$) is also presented for each specimen. The data in this table makes it possible to investigate relationships and trends in the data. Table 6.5 presents a summary of the axial deformation capacity data, with specimens sorted by steel type and local slenderness. The data in the tables below makes it possible to evaluate the effects of variables such as brace local compactness, global slenderness, and steel type on the accuracy of the backbone curves.

Table 6.4. Comparison of Predicted and Measured Brace Axial Deformation

	Predicted Maximum Deformation (in.) $\Delta_{predicted}$		**Measured Maximum Deformation (in.) $\Delta_{measured}$**		**Ratio of Measured-to-Predicted Capacity $\Delta_{measured} : \Delta_{predicted}$**	
Test Specimen	**Tension**	**Compression**	**Tension**	**Compression**	**Tension**	**Compression**
5x5x3/8 A500 Y	4.67	2.77	5.13	4.89	1.10	1.76
5x5x3/8 A1085 Y	5.00	3.01	5.25	5.50	1.05	1.83
6x6x5/16 A500 R	2.86	2.24	3.06	3.26	1.07	1.45
6x6x5/16 A1085 Y	3.03	2.41	3.13	3.12	1.03	1.29
6x6x3/8 A500 R	3.55	2.71	3.74	3.72	1.05	1.37
6x6x3/8 A500 R	3.55	2.71	3.74	3.72	1.05	1.37
6x6x3/8 A1085 Y	3.78	2.94	3.52	3.52	0.93	1.20
6x6x1/2 A500 R	5.10	3.75	4.45	4.06	0.87	1.08
6x6x1/2 A1085 Y	5.48	4.07	4.67	5.12	0.85	1.26
7x7x5/16 A500 Y	2.30	2.12	1.73	1.83	0.75	0.86
7x7x5/16 A1085 Y	2.44	2.27	1.99	2.31	0.81	1.02
7x7x3/8 A500 Y	2.84	2.58	2.51	2.79	0.88	1.08
7x7x3/8 A1085 Y	3.02	2.76	2.36	2.85	0.78	1.03
7x7x1/2 A500 B	4.02	3.55	3.59	4.16	0.89	1.17
7x7x1/2 A1085 Y	4.32	3.84	3.48	4.41	0.81	1.15
8x8x3/8 A500 W	2.36	2.32	1.24	1.90	0.53	0.82
8x8x3/8 A1085 Y	2.50	2.47	2.18	2.18	0.87	0.88
8x8x1/2 A500 W	3.31	3.20	2.71	2.80	0.82	0.88
8x8x1/2 A1085 Y	3.53	3.42	2.96	3.32	0.84	0.97
10x10x3/8 A500 W	1.73	1.77	2.10	2.48	1.21	1.40
10x10x3/8 A1085 Y	1.83	1.87	1.60	1.84	0.87	0.99

Table 6.5. Summary of Measured and Predicted Behavior

	$\Delta_{measured} : \Delta_{predicted}$ Tension		$\Delta_{measured} : \Delta_{predicted}$ Compression	
	Average	**Standard Deviation**	**Average**	**Standard Deviation**
All Specimens	0.90	0.15	1.18	0.28
A500 HSS	0.92	0.20	1.19	0.31
A1085 HSS	0.88	0.09	1.16	0.27
$\lambda_{nom} < \lambda_{HD}$	0.92	0.10	1.30	0.32
$\lambda_{nom} > \lambda_{HD}$	0.89	0.18	1.09	0.23

Figure 6.12 and Figure 6.13 below provide a visual display of the quantitative data presented in the above tables. In both plots, markers shown above the black horizontal line at 1.0 represent test specimens that displayed a greater deformation capacity than predicted by the nonlinear modeling parameters presented above, while those below this line represent specimens that fractured at an axial deformation less than predicted. Additionally, the brace nominal width-to-thickness ratios, λ_{nom}, are normalized by the AISC compactness limits for highly ductile members, λ_{HD}. Markers to the left of the vertical line at 1.0 represent test specimens that are classified as highly ductile members, while those to the right of this line do not meet the highly ductile criteria. The accuracy of the nonlinear force-deformation models can be evaluated based on these plots, and the influence of variables such as steel type and cross-sectional compactness can be identified.

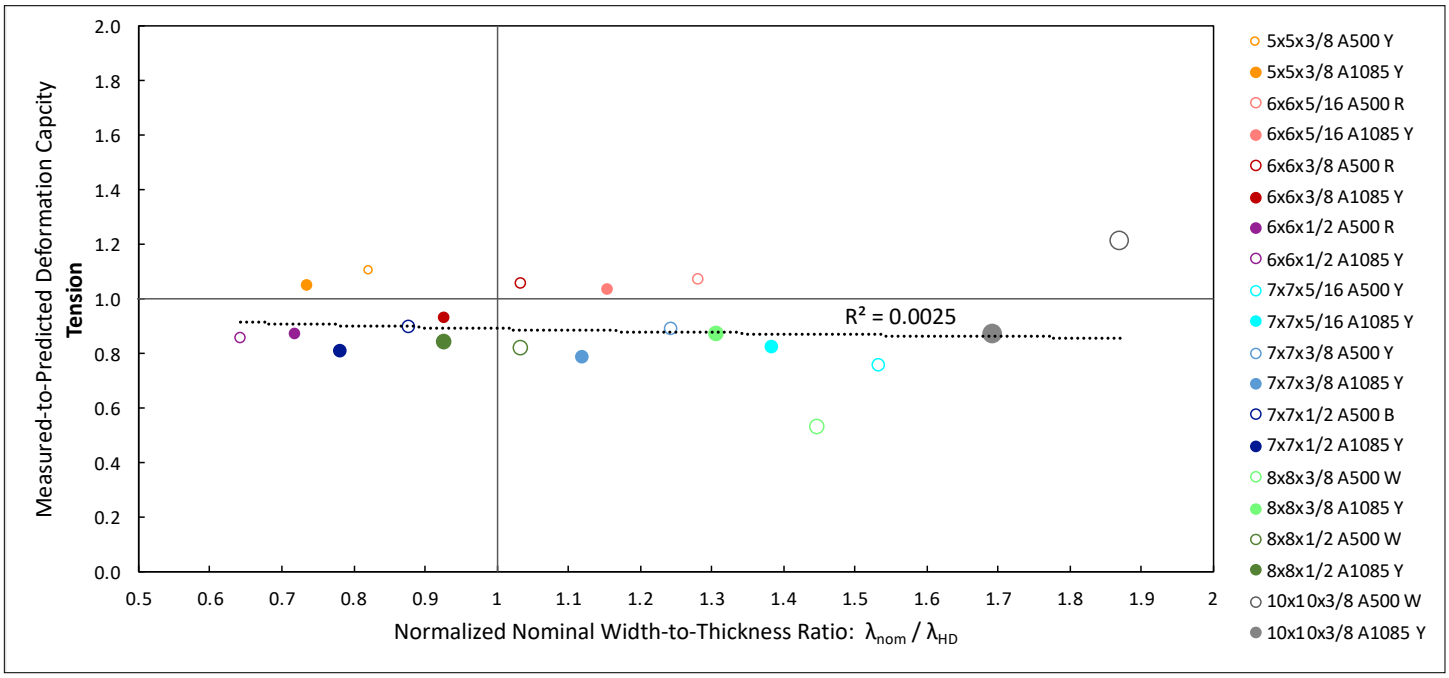

Figure 6.12. Evaluation of AISC 342 Predicted Tensile Deformation Capacity Based on Brace Local Slenderness Ratio

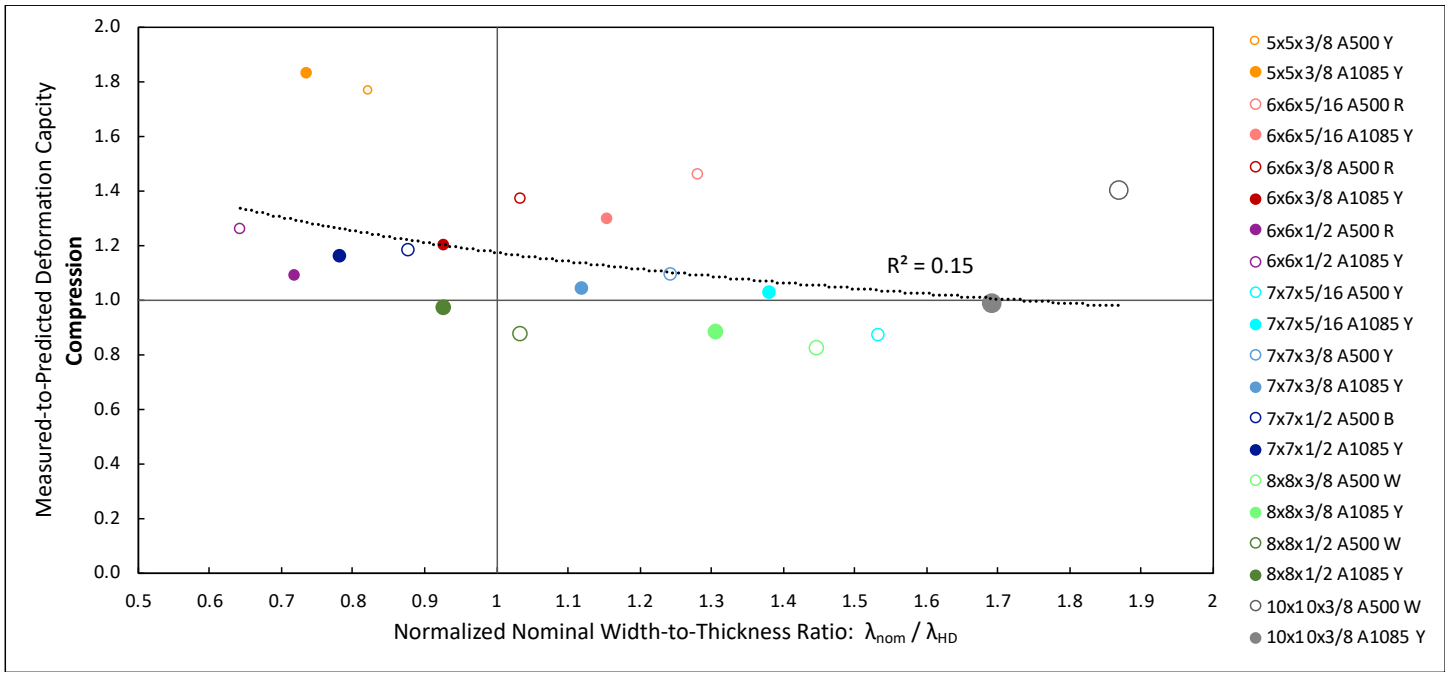

Figure 6.13. Evaluation of AISC 342 Predicted Compressive Deformation Capacity Based on Brace Local Slenderness Ratio

Figure 6.12 shows that in most cases, the predicted tensile deformation capacity exceeded the measured maximum tensile displacements. Of the twenty total test specimens, only six exhibited greater tensile deformation capacity than predicted. Four of these specimens were A500 members, while the other two were made of A1085 steel. Additionally, only two specimens with nominal b/t ratios meeting the AISC criteria for highly ductile members reached maximum tensile displacements greater than the predicted capacity.

There does not seem to be a strong relationship between steel type or brace compactness and the accuracy of predicted tensile deformation capacity, which is supported by the data in Table 6.5. On average, the measured maximum tensile displacements were 90% of the predicted capacity. The A500 specimens reached an average of 92% of predicted tensile deformation capacity, compared with 89% for the A1085 specimens. The variation in the measured-to-predicted tensile deformation ratio is greater in A500 HSS members, with a standard deviation of 0.20 compared with 0.09 for the A1085 specimens. The measured-to-predicted tensile deformation ratio of the A1085 specimens are all within 0.8 and 1.1, while this ratio ranges from 0.53 to 1.21 for the A500 specimens. Additionally, the predictions for specimens meeting the AISC width-to-thickness requirements for highly ductile members were slightly more accurate, with these specimens reaching an average of 92% of the predicted capacity compared with 89% for the non-seismically compact specimens. These differences are relatively minor, and may be a result of random variation in the data rather than any relationship between the accuracy of the predicted nonlinear behavior and steel type or brace compactness. However, it is evident from the data that the nonlinear force-deformation model tends to overestimate the tensile deformation capacity of HSS members.

Figure 6.13 shows that in general, the predicted compressive deformation capacity is slightly less than the measured capacity. Fourteen of the twenty test specimen reached compressive axial deformations greater than the predicted capacity, and all twenty specimens reached compressive displacements of at least 80% of the predicted capacity. The average measured-to-predicted compressive deformation ratio was 1.18 for the entire data set, and 1.19 for the A500 specimens compared with 1.16 for the A1085 specimens. These minor differences don’t indicate a significant relationship between the accuracy of the predicted compressive deformation capacity and steel type. The standard deviations related to compressive deformation

capacity are significantly greater than for the tensile deformation capacity, showing an increase in the variation between the predicted and measured compressive deformation behavior.

In all but one case, test specimens meeting the AISC width-to-thickness limits for highly ductile members exhibited greater than predicted compressive axial displacement behavior. The average ratio of measured-to-predicted compressive deformation capacity was 1.30 for seismically compact test specimens, compared with 1.09 for members exceeding these limits. The R-squared value of 0.15 shown in Figure 6.13 indicates that there is some correlation between tensile deformation capacity prediction accuracy and brace local slenderness, but this relationship does not explain all of the observed variation. The nonlinear force-deformation model seems to significantly underestimate the compressive axial deformation capacity of cross-sectionally compact square HSS members, and is slightly more accurate for members with less compact cross sections.

Figure 6.14 and Figure 6.15 below show the ratios of measured-to-predicted tensile and compressive axial deformation capacities plotted against brace global slenderness. Similar to the previous plots, the markers above the horizontal line at 1.0 represent test specimens that exhibited a measured axial deformation capacity greater than predicted based on the nonlinear force-deformation model. Markers below this line correspond to test specimens that exhibited less deformation capacity than predicted. The accuracy of the predicted deformation capacities can be evaluated based on these plots, as well as any data trends related to prediction accuracy and brace slenderness.

As discussed above, the maximum measured tensile displacement exceeded the predicted capacity in only six of the twenty test specimens. Figure 6.14 shows that in five of these specimens, the global slenderness ratio was greater than 100. The measured ductility of the 10x10x3/8 A500 W specimen, with a slenderness ratio of about 61, was somewhat of an outlier in the data set. As discussed in Section 5.2, the 10x10x3/8 A500 W specimen exhibited significant post-tearing ductility, which was not observed in other test specimens. This accounts for the large difference between the 10x10x3/8 A500 and A1085 markers in the figures above. Although the 10x10x3/8 A500 W specimen was measured to have significantly greater toughness than the A1085 specimen, an analysis of the relationship between toughness and ductility in Chapter 5 did not indicate a link between greater toughness and increased ductility. The measured material and geometric properties of the 10x10x3/8 A500 W specimen were

similar to other test specimens, with no unusual properties noted. The cause of the increased ductility in the 10x10x3/8 A500 W specimen is not clear.

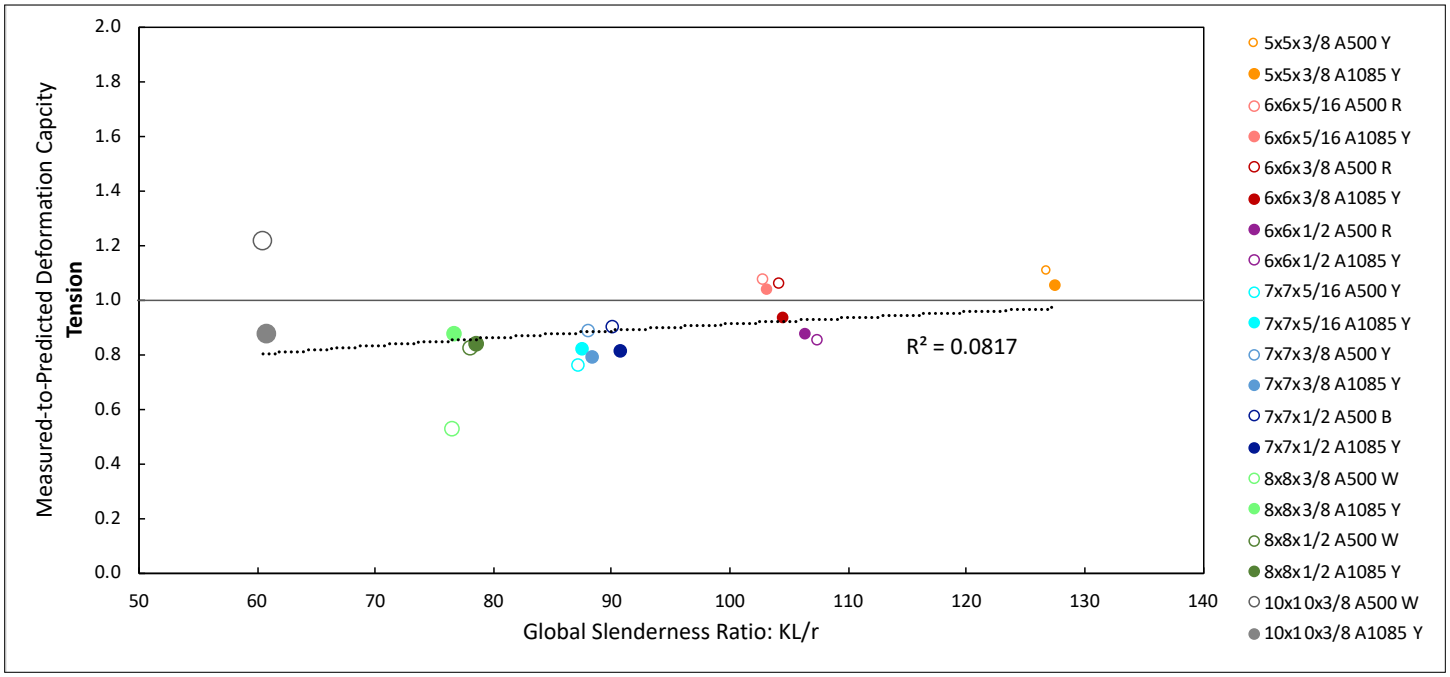

Figure 6.14. Evaluation of AISC 342 Predicted Tensile Deformation Capacity Based on Brace Global Slenderness Ratio

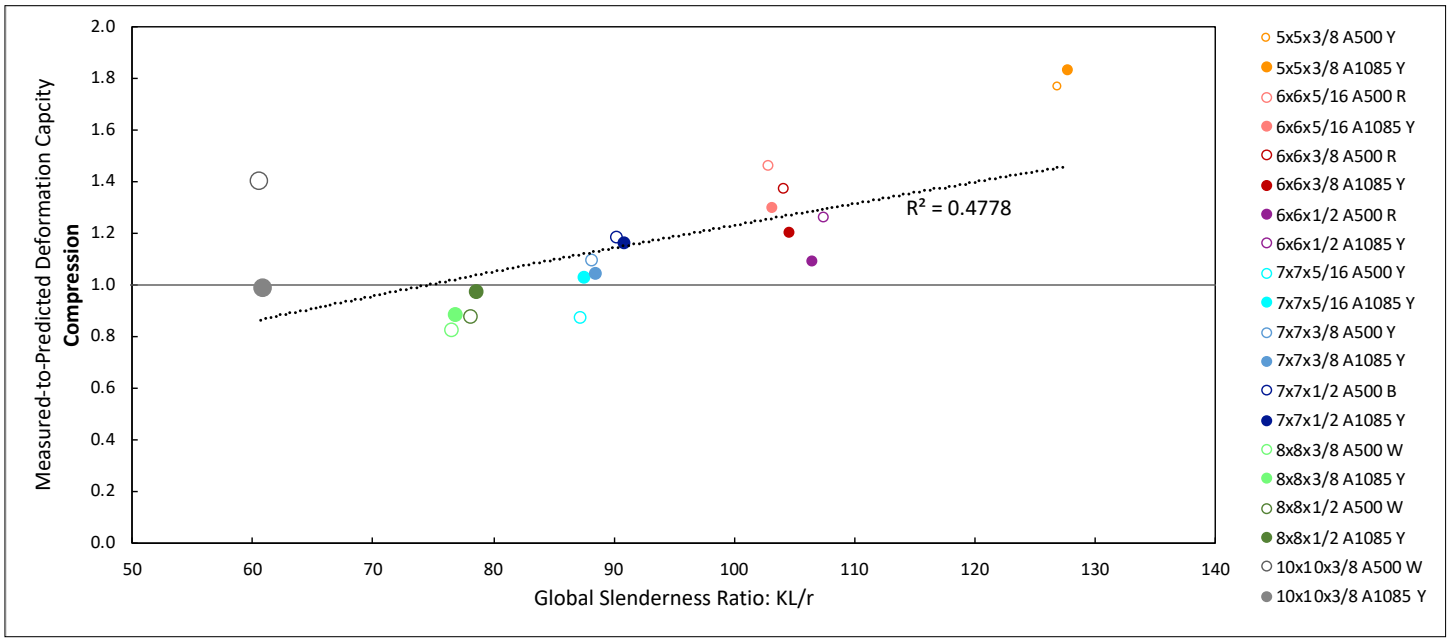

Figure 6.15. Evaluation of AISC 342 Predicted Compressive Deformation Capacity Based on Brace Global Slenderness Ratio

The data in Figure 6.14 indicates that there may be a relationship between the measured-to-predicted tensile deformation ratio and brace slenderness, and shows that the nonlinear model tends to overestimate the tensile deformation capacity of braces with KL/r ratios of less than 100. Based on the power curve fit to this data, the R-squared value is 0.0817, indicating that some of the variation in prediction accuracy is related to the brace global slenderness ratio. This model provides a fairly accurate prediction of tensile deformation capacity for HSS members with slenderness ratios above 100. All test specimens with KL/r ratios of at least 100 had measured-to-predicted tensile deformation capacity ratios between 0.85 and 1.1. Most specimens with KL/r ratios less than 100 had measured-to-predicted tensile deformation capacity ratios between 0.75 and 0.9, although there were two clear outliers in this group. Based on this data set, the nonlinear model provides a reasonable estimate of tensile deformation capacity for more slender braces, but tends to overestimate the tensile deformation capacity of more stocky members.

As displayed in Figure 6.15, there is also a clear relationship between greater brace slenderness and an increase in the measured-to-predicted compressive deformation capacity ratio. The R-squared value of 0.478 indicates that a significant amount of the variation in prediction accuracy is related to brace global slenderness. In test specimens with KL/r ratios greater than 80, the measured compressive deformation exceeded the predicted capacity in all but one case. Figure 6.15 clearly shows that this nonlinear model underestimates the compressive deformation capacity of slender HSS members, with KL/r ratios greater than 100. All but one specimen with a KL/r ratio greater than 100 exceeded the predicted compressive deformation capacity by at least 20%. This model provides a more accurate prediction of compressive deformation capacity for HSS members with KL/r ratios less than 100, as the measured-to-predicted compressive deformation ratio for these specimens ranged from 0.80 to 1.2, with the exception of one specimen. This model seems to overestimate the compressive deformation capacity of braces with KL/r ratios less than 80, since in all but one case the predicted capacity exceeded the maximum measured compressive deformation.

The 5x5x3/8 test specimens reached compressive deformations of nearly 1.8 times the predicted capacity, significantly greater than any other specimens. This level of compressive ductility does not seem to be related to the toughness or other material properties of these specimens. Both specimens were measured to absorb less than 20 ft-lbs through Charpy testing, which was fairly low relative to other test specimens. The measured yield strengths were slightly

above average, but were not significantly different than other specimens. As discussed above, it was observed that the AISC 342 models generally underestimate the compressive deformation capacity of specimens with low width-to-thickness ratios and high global slenderness ratios. Both of the 5x5x3/8 specimens met the AISC width-to-thickness limits for highly ductile members, and were the most globally slender specimens in this test series. Based on the observed trends in the accuracy of the compressive deformation capacity models, it makes sense that the 5x5x3/8 specimens exhibited significantly greater compressive ductility than predicted.

6.4 Evaluation of Local Buckling Behavior

As described in Table 6.2, extensive yielding and buckling is expected in braces at the collapse prevention (CP) limit state. Although it is not explicitly stated in AISC 342 or ASCE/SEI 41, local buckling deformations in the plastic hinge region of the brace typically develop under large compressive displacements associated with this extensive brace buckling. This local damage to the center of the brace was observed in all of the test specimens prior to brace fracture. In this section, the AISC 342 CP compressive deformation limits ($\Delta_{CP,predicted}$) are compared with the measured axial brace deformation at the development of local buckling ($\Delta_{LB,measured}$). These values are tabulated in Table 6.6 below, along with the ratio of $\Delta_{LB,measured}$ to $\Delta_{CP,predicted}$ for each specimen.

Table 6.6. Evaluation of Local Buckling and Collapse Prevention Deformations

Test Specimen	**$\Delta_{CP,predicted}$ (in.)**	**$\Delta_{LB,measured}$ (in.)**	**$\Delta_{LB,measured}$ / $\Delta_{CP,predicted}$**
5x5x3/8 A500 Y	2.77	4.38	1.58
5x5x3/8 A1085 Y	3.01	5.01	1.66
6x6x5/16 A500 R	2.24	2.72	1.22
6x6x5/16 A1085 Y	2.41	2.56	1.06
6x6x3/8 A500 R	2.71	3.16	1.17
6x6x3/8 A1085 Y	2.94	3.06	1.04
6x6x1/2 A500 R	3.75	3.58	0.95
6x6x1/2 A1085 Y	4.07	4.13	1.01

Test Specimen	$\Delta_{CP,predicted}$ (in.)	$\Delta_{LB,measured}$ (in.)	$\Delta_{LB,measured}$ / $\Delta_{CP,predicted}$
7x7x5/16 A500 Y	2.12	1.82	0.86
7x7x5/16 A1085 Y	2.27	1.74	0.77
7x7x3/8 A500 Y	2.58	2.23	0.87
7x7x3/8 A1085 Y	2.76	2.27	0.82
7x7x1/2 A500 B	3.55	3.17	0.89
7x7x1/2 A1085 Y	3.84	3.38	0.88
8x8x3/8 A500 W	2.32	1.33	0.57
8x8x3/8 A1085 Y	2.47	1.68	0.68
8x8x1/2 A500 W	3.20	2.05	0.64
8x8x1/2 A1085 Y	3.42	2.58	0.75
10x10x3/8 A500 W	1.77	1.35	0.76
10x10x3/8 A1085 Y	1.87	1.15	0.62

Figures 6.16 and 6.17 below show the ratios of $\Delta_{LB,measured}$ to $\Delta_{CP,predicted}$ for each specimen plotted against the width-to-thickness and global slenderness ratios. In these figures, markers above the horizontal line at 1.0 represent specimens that exhibited local buckling at a deformation greater than the predicted compressive CP deformation. Markers below the line represent specimens in which local buckling was observed at a deformation less than the compressive CP deformation.

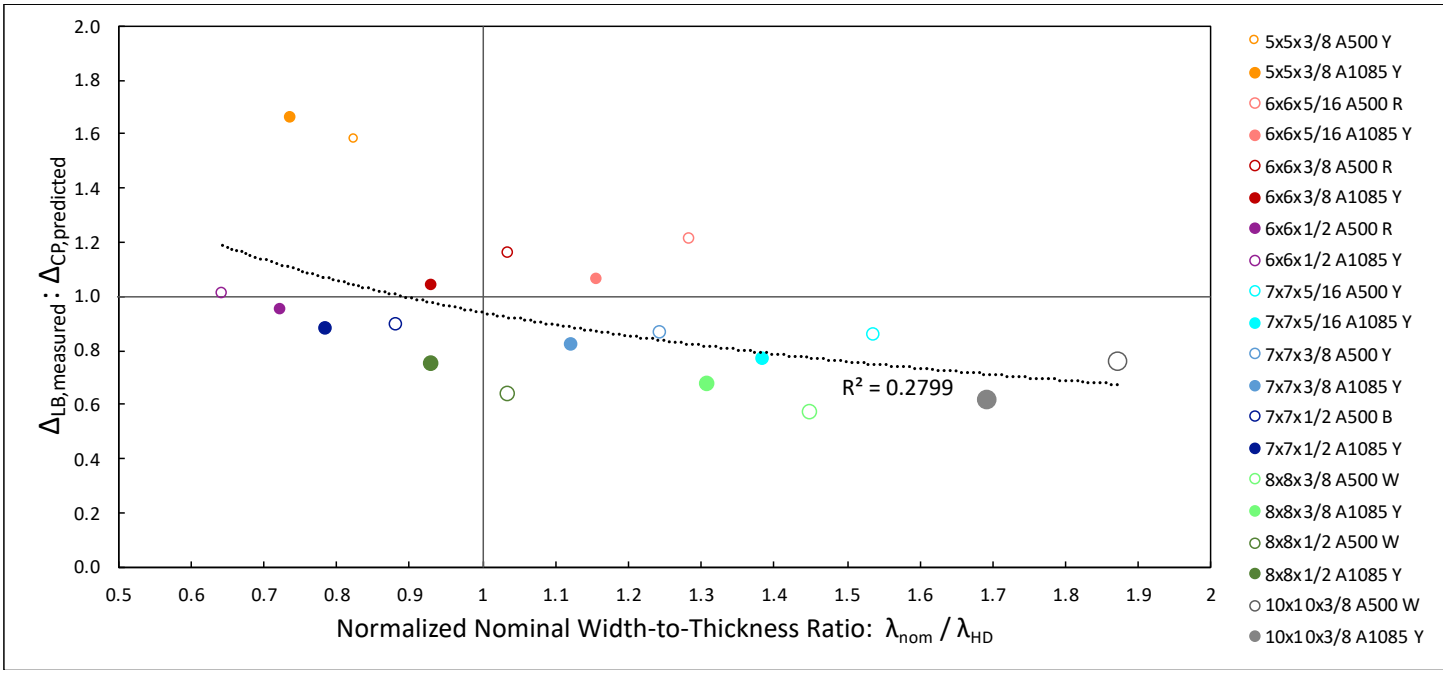

Figure 6.16. Evaluation of Local Buckling Behavior vs. Brace Compactness

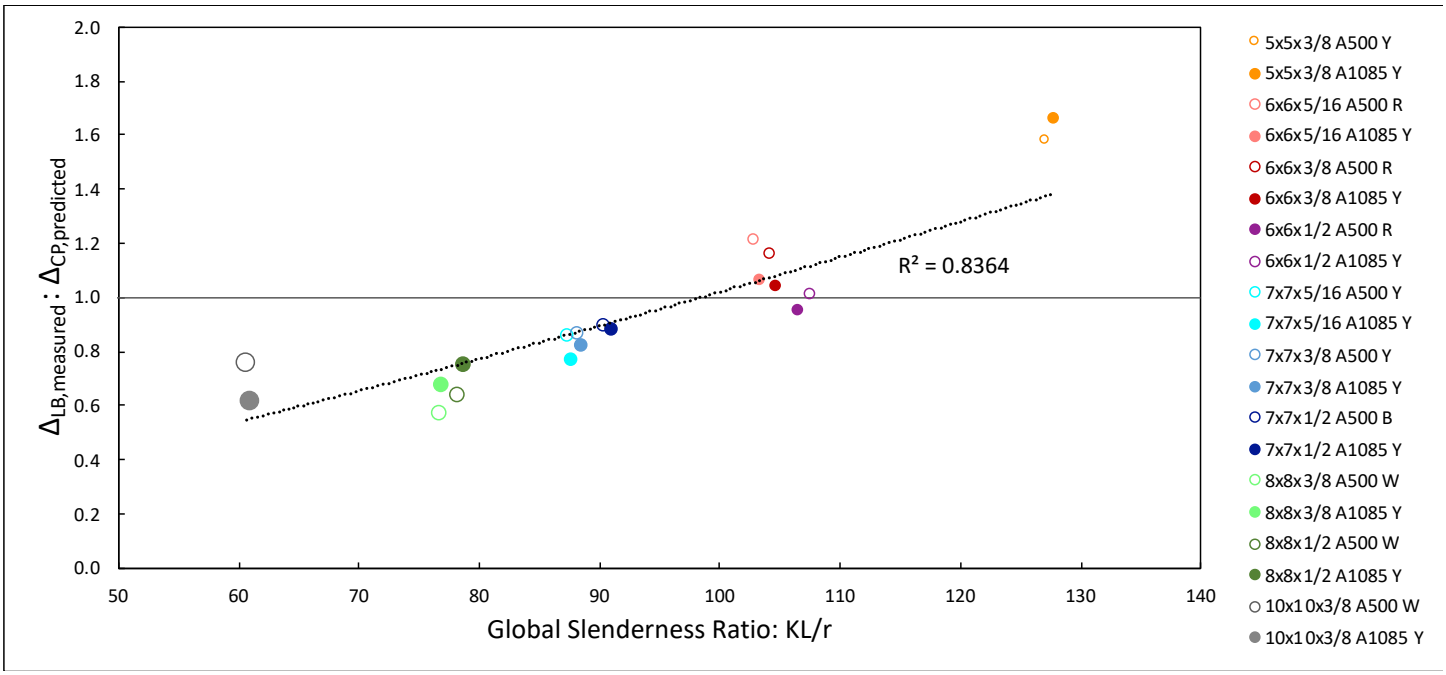

Figure 6.17. Evaluation of Local Buckling Behavior vs. Brace Slenderness

Power curves were fit to the data in each figure, and the resulting R-squared values are shown for each plot. The R-squared value of 0.836 in Figure 6.17 indicates that much of the variation in the data can be explained by differences in brace global slenderness. This correlation is significantly stronger than the relationship shown in Figures 6.16, which has an R-squared value of 0.28.

In seven of the twenty test specimens, local buckling developed at a compressive deformation greater than the predicted deformation capacity. In all of these cases, the braces were relatively slender, with KL/r ratios of at least 100. Local buckling is expected to develop in braces prior to fracture, and thus it is clear that the compressive deformation capacity of slender braces is underestimated by the AISC 342 nonlinear modeling procedure. The compressive deformation level at which local buckling is expected is not stated in AISC 342, but this behavior would be expected to develop prior to reaching the CP performance state. All of the test specimens with global slenderness ratios of less than 100 exhibited local buckling at compressive deformations less than the compressive deformation limit for CP. It was discussed in Section 6.3 that the models developed based on the AISC 342 procedure tend to underestimate the compressive deformation capacity of slender braces, and slightly overestimate the compressive

deformation capacity of stockier braces. These trends can be seen in Figure 6.17 as well, which shows that local buckling developed at compressive displacements larger than expected in more slender braces. In test specimens with KL/r ratios of less than 100, the ratios of $\Delta_{LB,measured}$ to $\Delta_{CP,predicted}$ ranged generally ranged from 0.6 to 0.9. Since AISC 342 does not state the expected deformation level associated with local buckling, it is difficult to evaluate the validity of the observed $\Delta_{LB,measured}$ to $\Delta_{CP,predicted}$ ratios for less slender braces.

Chapter 7. CONCLUSION

7.1 INTRODUCTION

Braced frames typically use HSS members as braces; the yielding and buckling of HSS sections is the primary yield mechanism in concentrically braced frames (SCBFs). As such, there is an interest in evaluating new HSS sections using ASTM 1085 HSS. Introduced in 2013, ASTM 1085 has more stringent geometric, strength and toughness requirements than conventional ASTM 500 (either C or dual B/C grade) HSS sections. As such, a research program was undertaken to compare ASTM 1085 and ASTM 500 HSS section with an eye towards understanding appropriate local slenderness limits for highly ductile and moderately ductile HSS sections.

Previous research has shown that braced frames with A1085 HSS braces exhibit greater ductility than those with A500 HSS braces. Additionally, research on the behavior of square HSS members has shown a relationship between seismic performance and brace local and global slenderness. In order to examine these relationships, test specimens were designed with a wide range of local and global slenderness ratios. The local slenderness ratios ranged from 9 to 25.7, while the global slenderness ratios ranged from 60 to 127. Test specimens were selected with b/t ratios both meeting and exceeding AISC requirements for highly and moderately ductile HSS members. The b/t ratios of the braces ranged from 0.64 to 1.88 times the AISC limits for highly ductile members, and 0.55 to 1.60 times the moderately ductile limits.

This research is the first phase of a multi-phase research program. The testing consisted of HSS sections subjected to cyclic axial demands. The primary study variables included: (1) type of HSS, i.e., A500C or A1085, (2) HSS producer, (3) KL/r and (4) b/t. For each specimen, the cyclic response was used to determine the deformability and energy dissipation capacity of the brace. Brace deformability was measured in several ways, including the axial displacement range (normalized to the initial brace length), and the story drift (assuming a 45-degree angle for the brace).

The results were compared to understand the benefits of A1085 sections and the b/t limits. A summary of the results from the twenty (20) HSS sections tested as part of this research project are presented in Section 7.2. This section will briefly describe the experimental program

and test results. In Section 7.3, conclusions will be presented based on the results of this test series. Finally, recommendations for further research regarding the seismic performance of ASTM A500 and A1085 square HSS members are presented in Section 7.4.

7.2 SUMMARY

The initial objective of the study was to compare nominally identical sections manufactured using A500 or A1058 sections. To this end, ten (10) different square HSS shapes in both ASTM A500 and A1085 steel were tested. These twenty specimens were used to study the effects of width-to-thickness ratio, global slenderness ratio, steel type, and steel producer on the cyclic axial response. The local and global slenderness ratios of the test specimens are shown in Table 7.1 below. One of the main goals of this project was to evaluate and compare the inelastic cyclic response of A500 and A1085 HSS members.

Each test specimen was subjected to the same quasi-static symmetric loading protocol, and all of the braces were the same length. Increasing cyclic displacements were applied until the test specimens fractured. In most cases, the braces fractured in tension. However, the 6x6x3/8 A1085 Y, 6x6x1/2 A500 R, and 7x7x3/8 A500 Y specimens fully fractured in compression following the development of tearing across much of the cross section in tension, prior to reaching the maximum compressive displacement.

Table 7.1. Test Specimen Local and Global Slenderness Ratios

HSS Section	b/t Ratio	KL/r Ratio
5x5x3/8 A500 Y	11.3	127.0
5x5x3/8 A1085 Y	10.3	127.7
6x6x5/16 A500 R	17.6	102.8
6x6x5/16 A1085 Y	16.2	103.3
6x6x3/8 A500 R	14.2	104.2
6x6x3/8 A1085 Y	13	104.6
6x6x1/2 A500 R	9.9	106.5
6x6x1/2 A1085 Y	9	107.5
7x7x5/16 A500 Y	21.1	87.3
7x7x5/16 A1085 Y	19.4	87.6

HSS Section	b/t Ratio	KL/r Ratio
7x7x3/8 A500 Y	17.1	88.3
7x7x3/8 A1085 Y	15.7	88.6
7x7x1/2 A500 B	12.1	90.3
7x7x1/2 A1085 Y	11	91.0
8x8x3/8 A500 W	19.9	76.6
8x8x3/8 A1085 Y	18.3	76.9
8x8x1/2 A500 W	14.2	78.1
8x8x1/2 A1085 Y	13	78.6
10x10x3/8 A500 W	25.7	60.6
10x10x3/8 A1085 Y	23.7	60.9

A summary of test specimen performance is provided in the figures below. The normalized axial displacement range is plotted against the nominal width-to-thickness ratio normalized by the AISC limits for highly ductile members in Figure 7.1. Another measurement of test specimen performance, the normalized energy dissipation capacity, is shown in Figure 7.2 plotted against the normalized nominal width-to-thickness ratio.

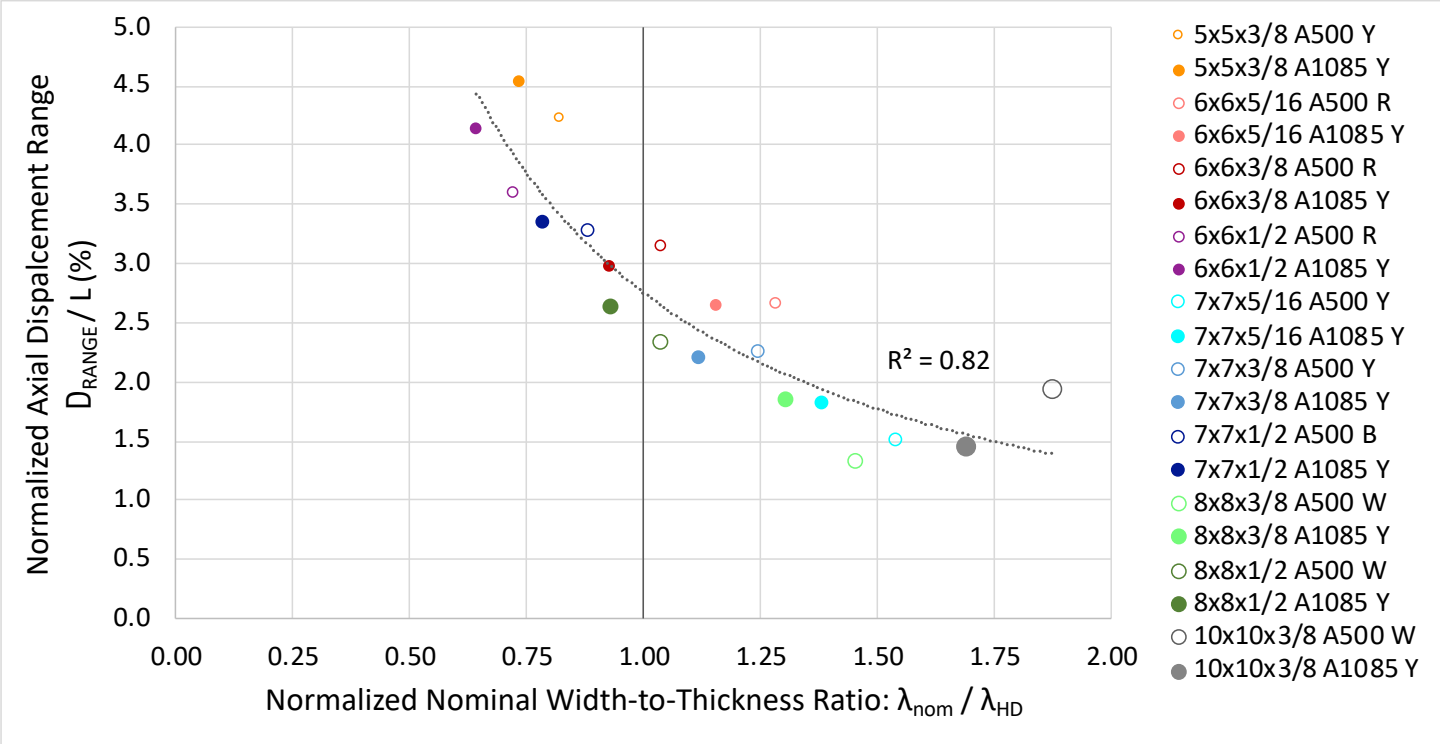

Figure 7.1. Axial Displacement Range vs. Local Compactness: λ_{HD}

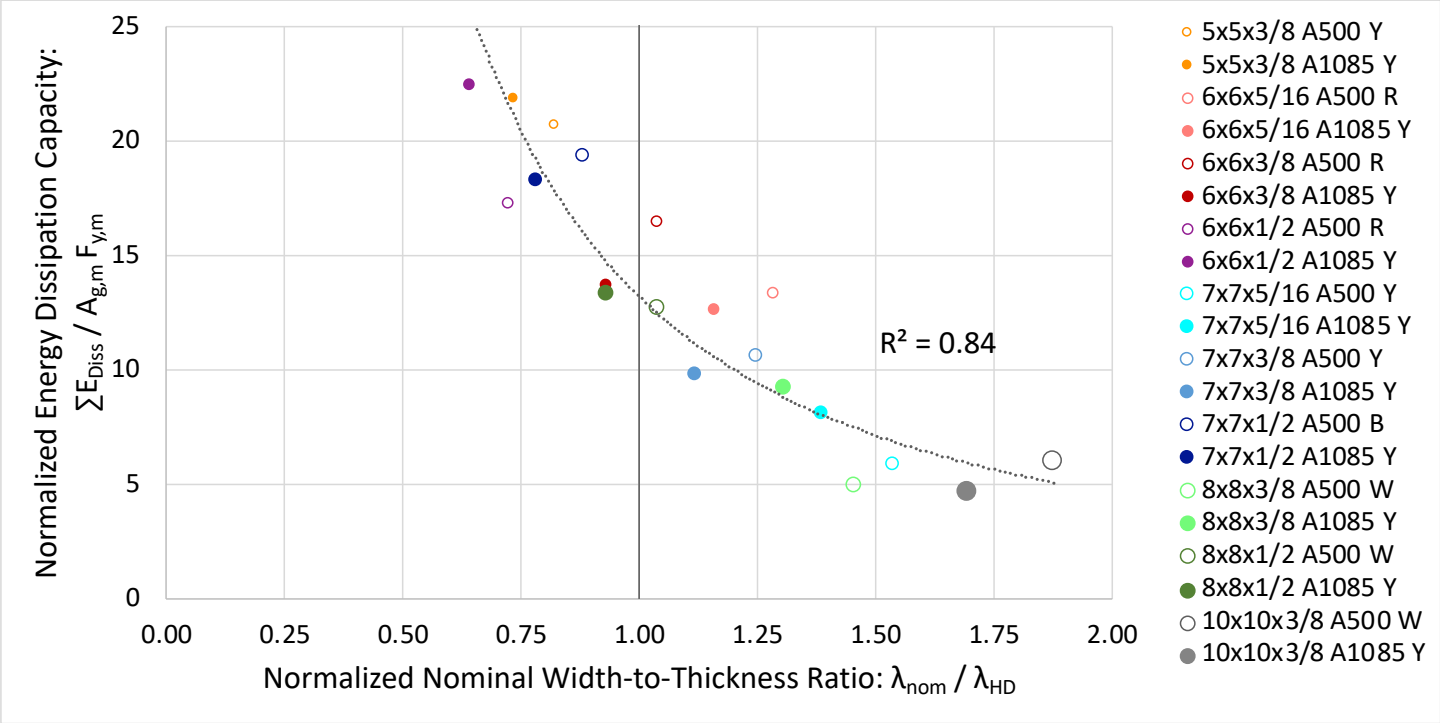

Figure 7.2. Energy Dissipation Capacity vs. Local Compactness: λ_{HD}

Similar plots are presented in Figures 7.3 and 7.4 below, except that in these figures the measurements of brace performance are plotted against the global slenderness ratio rather than the local slenderness ratio for each test specimen.

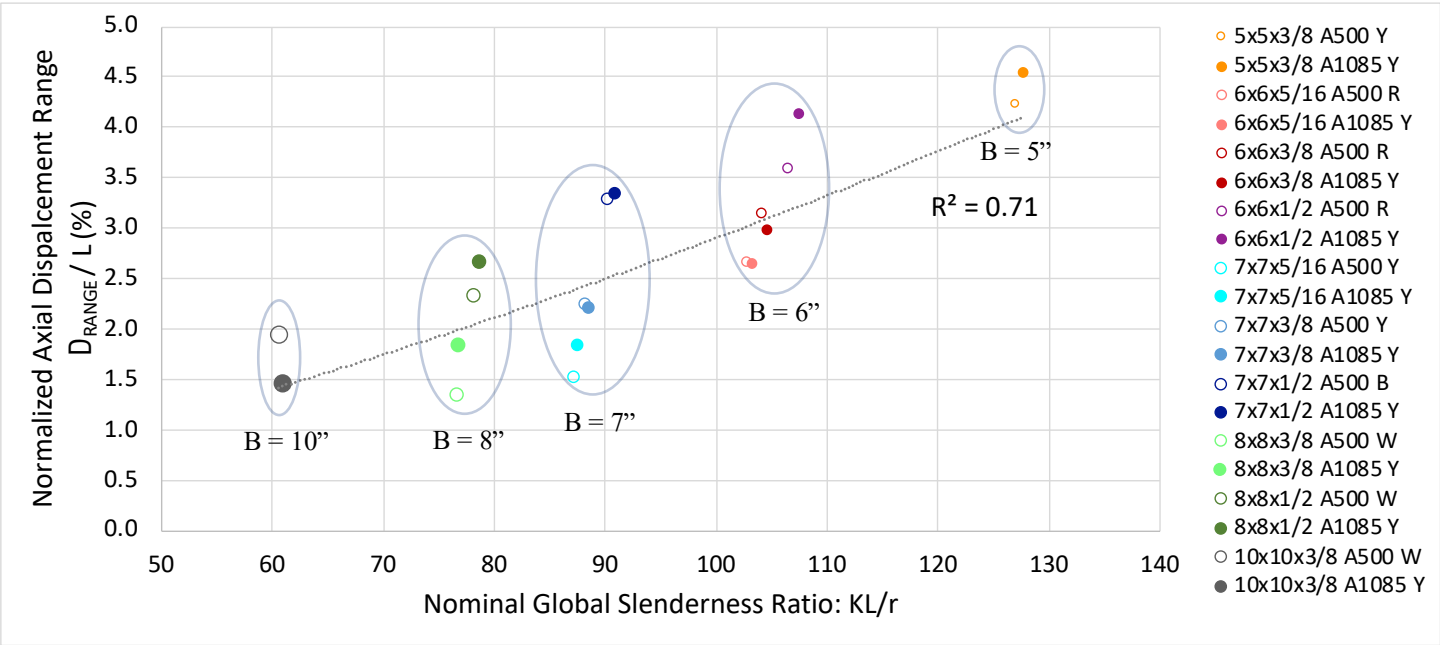

Figure 7.3. Axial Displacement Range vs. Global Slenderness

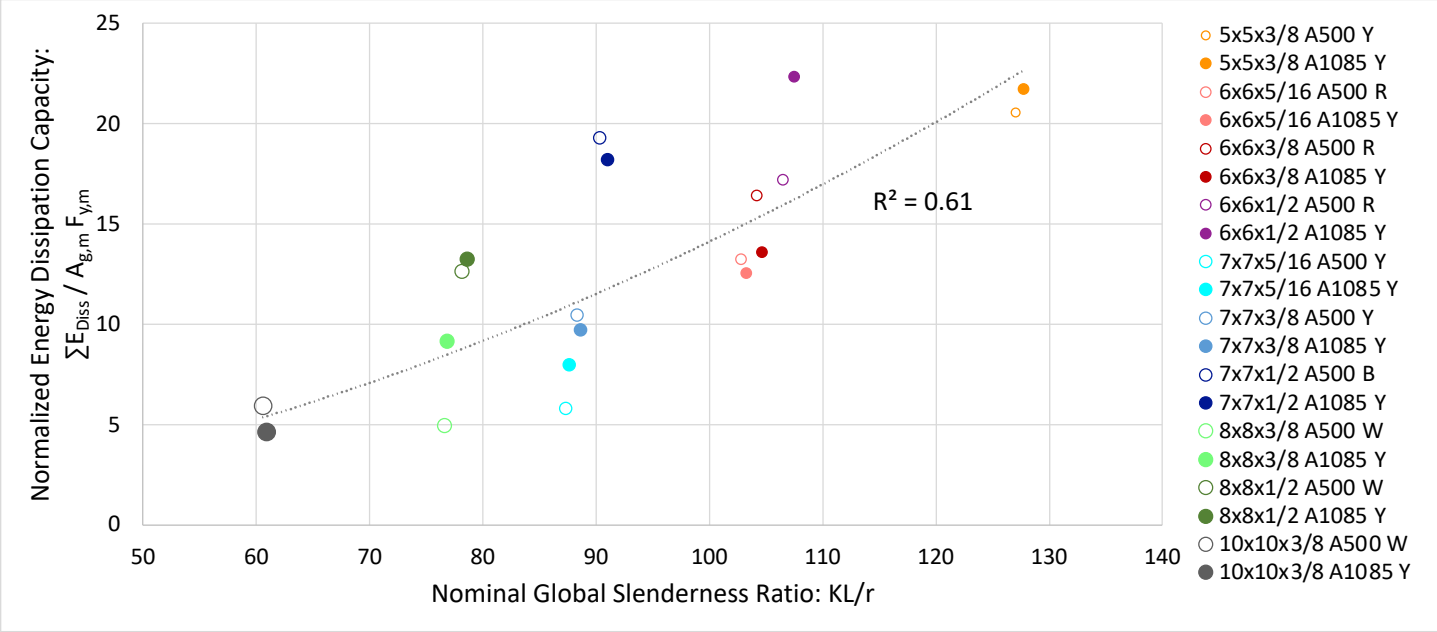

Figure 7.4. Energy Dissipation Capacity vs. Global Slenderness

7.3 CONCLUSIONS

The following provides a summary of the conclusions based on the test results and measured specimen properties.

- As expected, the cyclic response of HSS members depends significantly on brace local slenderness and global slenderness ratios, where the cyclic deformability increases with a decrease in b/t ratio and an increase in KL/r ratio. The most cross sectionally compact and globally slender test specimens exhibited the greatest deformability and energy dissipation capacity behavior prior to brace fracture. These trends were observed for both A500 and A1085 HSS test specimens.

- Braces with smaller b/t ratios, and thus more compact cross sections, exhibited greater deformability and energy dissipation capacity. These trends are shown in Figures 7.1 and 7.2 above. The data provides new information to understand the impact of the current b/t limits. The data indicates that all of the specimens meeting the current AISC width-to-

thickness limits for highly ductile members reached maximum story drifts of at least 2.5% prior to fracture. However, less cross sectionally compact HSS sections also provided a large degree of cyclic deformability, suggesting that the local slenderness ratio limits for highly and moderately ductile sections can be increased by up to 25%. However, further testing is needed to evaluate the impact of these increases. The normalized energy dissipation capacity was also found to be greater in more cross sectionally compact specimens. This increase in energy dissipation capacity is largely a result of the increased deformability observed in these specimens. The more cross sectionally compact specimens dissipated significant amounts of energy through inelastic buckling and yielding when subjected to larger axial displacements. Based on the results of this experimental program, it is evident that the AISC width-to-thickness limits for highly and moderately ductile members should be re-evaluated due to the substantial deformability and energy dissipation capacity of braces exceeding these current limits.

- Test specimens with larger global slenderness ratios were also shown to have greater deformability and improved energy dissipation behavior, as shown in Figures 7.3 and 7.4 above. However, the current AISC width-to-thickness limits for highly and moderately ductile members do not take into account the effects of global slenderness on brace performance. In this experimental program, several braces were tested with the same b/t ratios but different KL/r ratios. In each case, the more globally slender brace exhibited greater deformability and energy dissipation capacity. It is clear that the global slenderness ratio has a significant impact on brace performance, and therefore should be taken into account by the AISC limits for highly and moderately ductile members.

- For the braces provided, there was no discernable relationship between steel type and structural response, as both A500 and A1085 HSS specimens exhibited similar behavior across the entire test series. In six of the ten HSS shapes tested, the A1085 specimen exhibited more deformability than the corresponding A500 specimen. Some of this difference may be a result of the increased local compactness of the A1085 HSS members because of the geometric requirements. However there were several cases in which the A500 specimen exhibited a level of deformability greater than or equal to that

of the A1085 specimen. In five of the sizes tested, the A1085 specimen exhibited greater energy dissipation behavior, while in the other five shapes the normalized energy dissipation capacity was greater in the A500 specimen. However, comparing the A500 brace properties to the A1085 specification requirements indicates that some of the A500 braces met the requirements of the A1085 specification, and many of the A500 braces nearly met these requirements. It is expected that this is the reason that the test results do not show a significant difference in the two HSS specifications. All of the A1085 specimens met the requirements for A1085 HSS, while three of the ten A500 specimens met these requirements. Four of the A500 specimens met the 5% wall thickness tolerance of the A1085 specification, while the other six A500 braces were typically within 3% of meeting this requirement. Additionally, the measured yield and ultimate strengths between the A500 and A1085 HSS were nearly identical. The nominal yield strength for both types of steel is 50 ksi, and the nominal yield strength ratio, R_y, is 1.25 for A1085 HSS and 1.3 for A500 HSS. In this study, the average measured yield strength ratios for the A1085 braces were 1.26, compared with 1.24 for the A500 braces. Additionally, the average measured tensile strengths were 71.8 ksi for both types of steel. Charpy V-Notch testing showed that the A1085 specimens from steel producer Yellow had increased toughness compared with the A500 HSS from the same producer. However, the measured toughness values of the A500 HSS from other steel producers were significantly greater than that of the A1085 HSS. Additionally, analysis of the toughness data did not indicate a relationship between increased toughness and improved specimen performance.

- All of the A1085 HSS specimens in this test series were manufactured by one steel producer, and thus it is not possible to draw conclusions regarding the effect of steel producer on the performance of A1085 HSS. Additionally, the analysis of the data did not indicate a relationship between test specimen performance and producer of the A500 HSS. The A500 HSS specimens were manufactured by four different producers, but only one A500 specimen of each shape was tested. This made it difficult to compare the performance of the A500 HSS from different producers due to differences in local compactness and global slenderness ratios. There was some minor variation in the measured geometric and material properties of the A500 braces from different steel

producers, but the sample size was relatively small. As mentioned above, there were significant differences in the toughness of the A500 braces from different producers.

- As discussed in Chapter 6, the AISC 342 backbone curves tend to overestimate the tensile deformation capacity and underestimate the compressive deformation capacity of braces. Some of this may be due to the symmetric displacement protocol applied to the test specimens. The tensile displacements applied in this protocol may be greater than the typical demands on braces in braced frames, especially those in chevron configurations. Further, the accuracy of the backbone curves was found to depend significantly on the global slenderness ratio. The backbone curves tend to significantly overestimate the deformability of stockier braces, and underestimate the deformability of more globally slender braces.

7.4 Recommendations for Future Work

Based on the limitations of this research project, the following work is recommended to satisfy the current lack of information and other questions raised by this thesis.

- Investigation of the performance of relatively stocky test specimens. The global slenderness ratios of the HSS members included in this test series ranged from about 60 to nearly 130, while those used in braced frames typically range from about 40 to 100. Although previous research projects have investigated the behavior of stocky A500 square HSS components, the behavior of stocky A1085 HSS members requires additional research. In this program, only one test specimen meeting the AISC width-to-thickness limits for highly ductile members had a global slenderness ratio less than 90. Therefore, additional research is required to characterize the behavior of seismically compact A500 and A1085 HSS members with KL/r ratios between 40 and 90. This is especially important for A1085 HSS members, as there is a lack of data currently available regarding the performance of these components.

- Evaluation of the seismic performance of ASTM A1085 HSS specimens from different steel producers. All of the A1085 specimens in this test series were provided by a single steel producer, and A1085 HSS members from other producers may not exhibit the same structural response. It is possible that differences in material properties of the A1085 specimens from different producers could have an impact on brace performance.

- Study the effects of alternative displacement protocols on the performance of A500 and A1085 HSS members. In this test program, all test specimens were subjected to the same symmetric cyclic displacements. This displacement protocol was not representative of the expected axial displacements applied to bracing members in braced frames during earthquakes. Alternative displacement protocols should be applied in future component tests of A500 and A1085 HSS to examine differences in structural response.

- Refine the AISC 342 backbone curves used to model the nonlinear response of braces. As mentioned above, the backbone curves tend to overestimate the deformation capacity of stockier braces and underestimate the deformability of more globally slender braces. The modeling parameters used to develop these models should be re-assessed based on this data. The accuracy of the backbone curves may perhaps be improved by weighting the global slenderness ratio more highly in the computation of brace deformation capacity.

- Study the impact of b/t on system performance using multi-stripe analysis. This work is necessary to fully characterize the effects of brace width-to-thickness ratio on cyclic response. This will make it possible to evaluate the current width-to-thickness limits for highly and moderately ductile HSS braces.

- Investigate the effects of increasing the width-to-thickness ratio for braces in SCBFs and OCBFs on constructability. If it is shown that less cross sectionally compact braces exhibit adequate seismic performance in braced frames, it may be possible to increase the width-to-thickness limits for braces in SCBFs and OCBFs. Current width-to-thickness limits for highly and moderately ductile braces restrict the number of HSS members available for use in SCBFs and OCBFs. Increasing these limits would make it possible to

use larger and more locally slender braces, which may make SCBFs and OCBFs more practical seismic force resisting systems.

BIBLIOGRAPHY

AISC (2010). "Specification for Structural Steel Buildings." ANSI/AISC 360-10, American Institute of Steel Construction, Chicago, IL.

AISC (2016). "Seismic Provisions for Structural Steel Buildings." ANSI/AISC 341-16, American Institute of Steel Construction, Chicago, IL.

AISC (Draft - 2022). Seismic Provisions for Evaluation and Retrofit of Existing Steel Structural Buildings." AISC 342, American Institute of Steel Construction, Chicago, IL.

ASCE(2017). "Seismic Evaluation and Retrofit of Existing Buildings." ASCE/SEI-17, American Society of Civil Engineers, Reston, VA.

ASTM (2007). "Standard Methods for Notched Bar Impact Testing of Metallic Materials." ASTM E23-07a, ASTM International, West Conshohocken, PA.

ASTM (2017). "Standard Test Methods and Definitions for Mechanical Testing of Steel Products." ASTM A370-17, ASTM International, West Conshohocken, PA.

ATC (1992). "Guidelines for Cyclic Seismic Testing of Components of Steel Structures for Buildings." Report ATC-24, Applied Technology Council, Redwood City, CA.

Bradley, C. R., Fahnestock, L. A., Hines, E. M., and Sizemore, J. G. (2017). "Full-Scale Cyclic Testing of Low-Ductility Concentrically Braced Frames." Journal of Structural Engineering, 143(6), 04017029.

Fell, B. V., Kanvinde, A. M., Deierlein, G. G., and Myers, A. T. (2009). "Experimental Investigation of Inelastic Cyclic Buckling and Fracture of Steel Braces." Journal of Structural Engineering, 135(1), 19-32.

Gugerli, H. and Goel, S. C. (1982). "Inelastic Cyclic Behavior of Steel Bracing Members." Report UMCE 82R1, University of Michigan, Ann Arbor.

Hsiao, P.-C. (2012). "Seismic Performance Evaluation of Concentrically Braced Frames." Phd Dissertation, University of Washington, Seattle.

Ibarra, S. M. (2018). "Experimental Investigation of Chevron Special Concentrically Braced Frames with a Yielding Beam Plastic Mechanism." MS Thesis, University of Washington, Seattle.

ICBO (1988.) Uniform Building Code. International Conference of Building Officials, Whittier, CA.

Krawinkler, H. (2009). Loading Histories for Cyclic Tests in Support of Performance Assessment of Structural Components.

Lee, S. (1988.) "Seismic Behavior of Hollow and Concrete-Filled Square Tubular Bracing Members, Report UMCE 87-11, University of Michigan, Ann Arbor.

Liu, Z. and Goel, S. C. (1987). "Investigation of Concrete-Filled Steel Tubes under Cyclic Bending and Buckling." PhD Dissertation, University of Michigan, Ann Arbor.

Roeder, C., W., Sen, A. D., Asada, H., Ibarra, S. M., Lehman, D. E., Berman, J. W., Tsai, K. C., Tsai, C. Y., Wu, A. C., Wang, K. J., and Liu, R. (2020). "Inelastic Behavior and Seismic Design of Multistory Chevron-Braced Frames with Yielding Beams." Journal of Constructional Steel Research, v. 167, p. 105817.

Roeder, C., W., Sen, A. D., Terpstra, C., Ibarra, S. M., Liu, R., Lehman, D. E., and Berman, J. W. (2019). "Effect of Beam Yielding on Chevron Braced Frames." Journal of Constructional Steel Research, v. 159, p. 428-441.

Sabelli, R., Roeder, C. W., and Hajjar, J. R. (2013). "Seismic Design of Steel Concentrically Braced Frame Systems." NEHRP Seismic Design Technical Brief No. 8, National Institute of Standards and Technology Engineering Laboratory, Gaithersburg, MD.

Shaback, B., and Brown, T. (2003). "Behaviour of Square Hollow Structural Steel Braces with End Connections Under Reversed Cyclic Axial Loading." Canadian Journal of Civil Engineering, v. 30, p. 745-753.

Swatosh, M. A. (2016), "Seismic Evaluation and Retrofit of Concentrically Braced Frames." MS Thesis, University of Washington, Seattle.

Terpstra, C. (2017). "Impact of Beam Strength on Seismic Performance of Chevron Concentrically Braced Frames." MS Thesis, University of Washington, Seattle.

Tremblay, R. (2002). "Inelastic Seismic Response of Steel Bracing Members." Journal of Constructional Steel Research, v. 58, p. 665-701.

Tremblay, R. (2008). "Inelastic Cyclic Testing of Large Size Steel Bracing Members." The 14th World Conference on Earthquake Engineering, Beijing, China.

APPENDIX 1: TEST SETUP & SPECIMEN DRAWINGS

A1.1 – Reaction Block Design

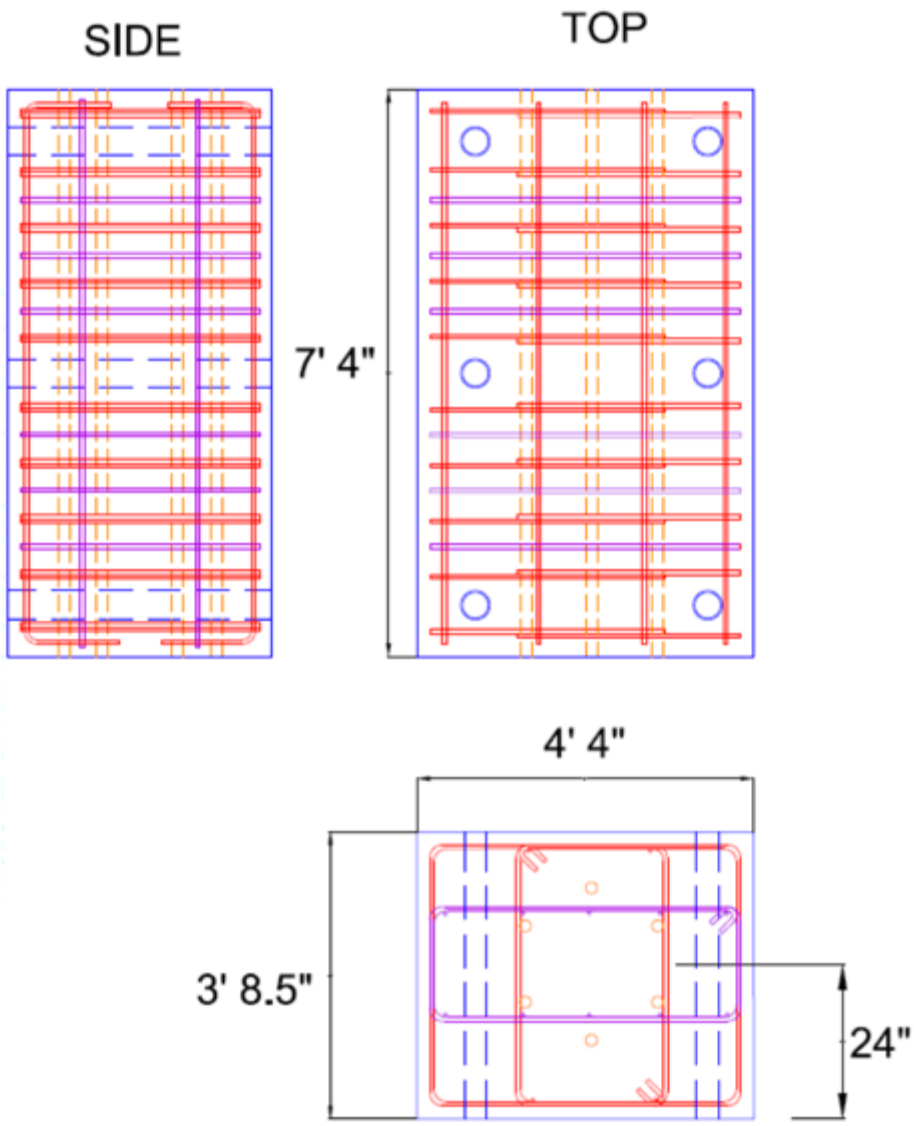

Figure A1.1: Existing Actuator Reaction Block and Rebar Layout – West Actuator

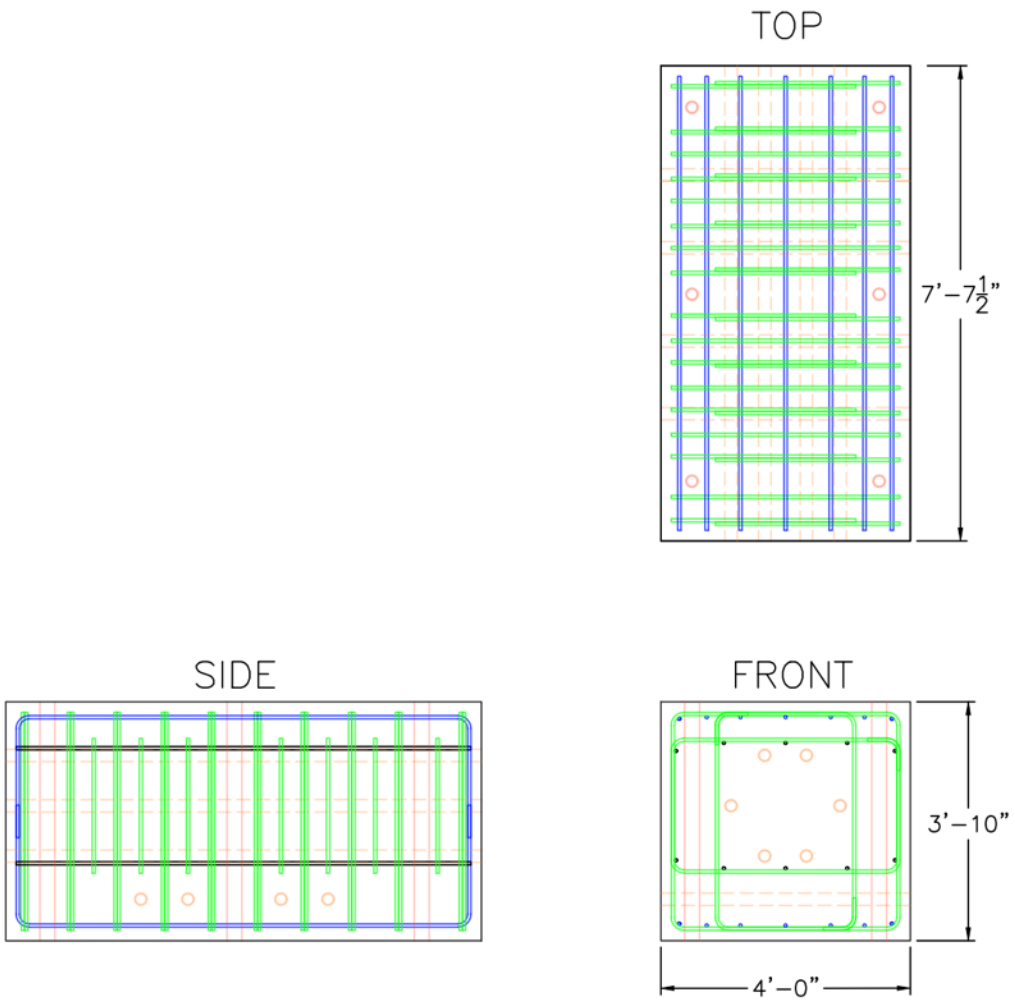

Figure A1.2: Actuator Reaction Block and Rebar Layout – East Actuator

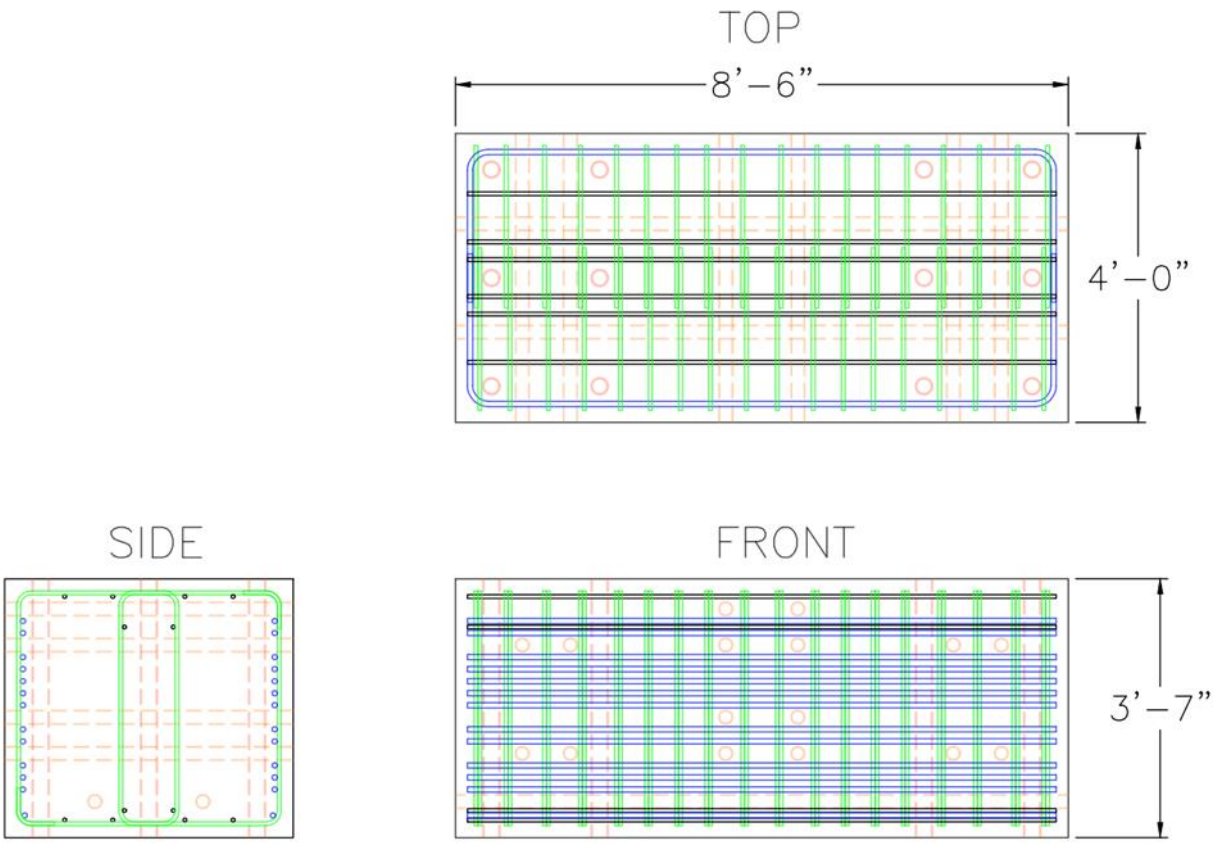

Figure A1.3: End Reaction Block and Rebar Layout

A1.2 – Sliding Beam & Connection Plate Design

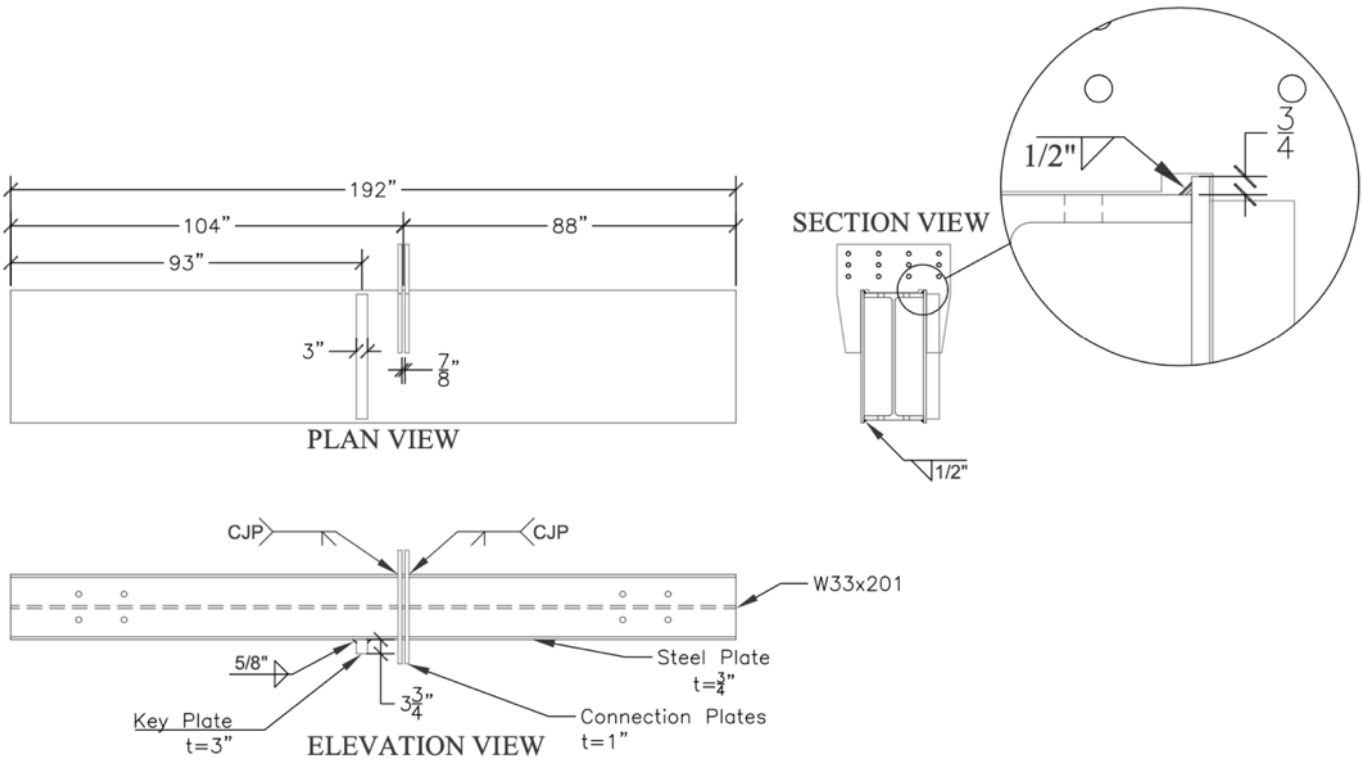

Figure A1.4: Sliding Beam Dimensions

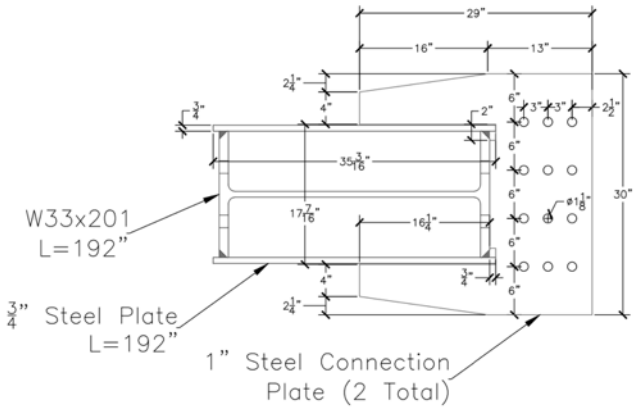

Figure A1.5: Sliding Beam and Connection Plate Cross Section

A1.3 – Actuator Backing Plate Design

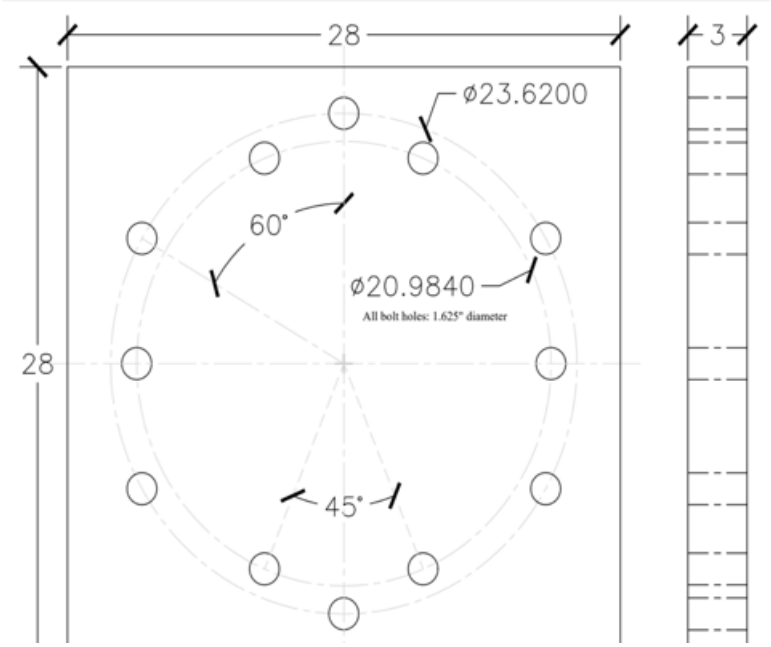

Figure A1.6: Actuator Backing Plate Dimensions

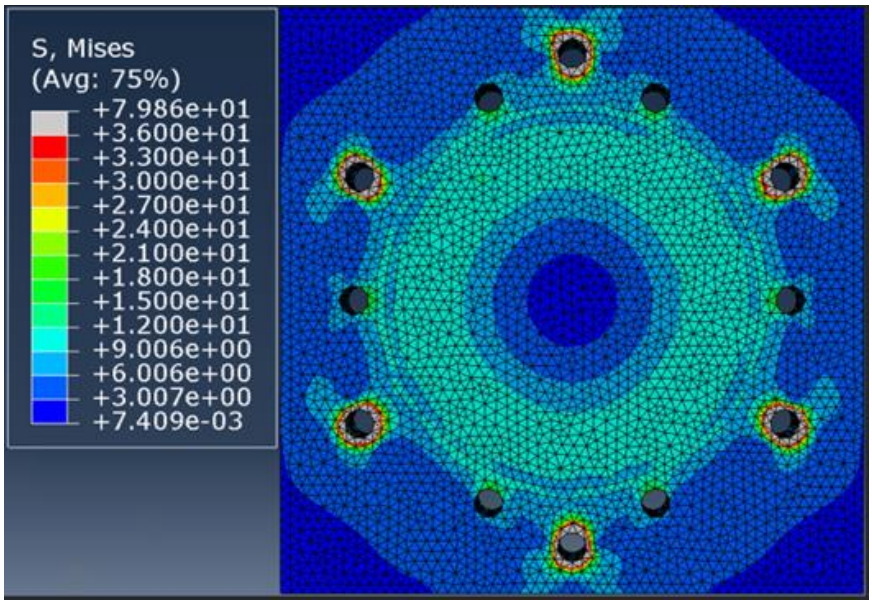

Figure A1.7: Actuator Backing ABAQUS Model

A1.4– Gusset Plate Design

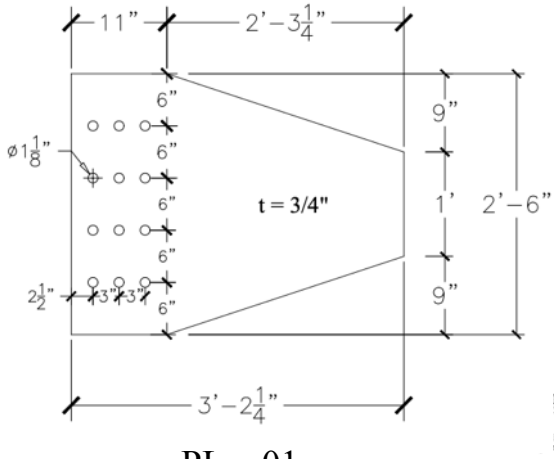

PL – 01

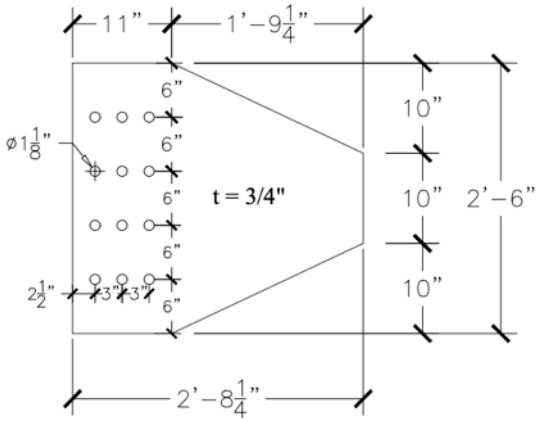

PL – 02

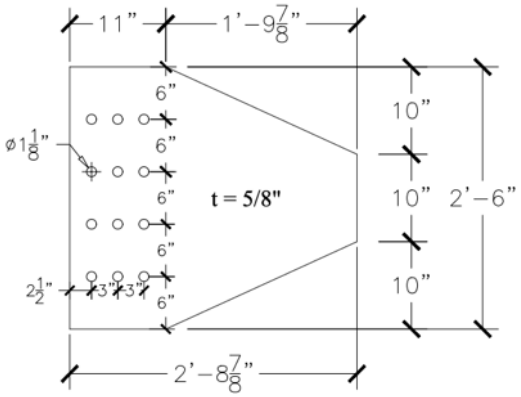

PL – 03

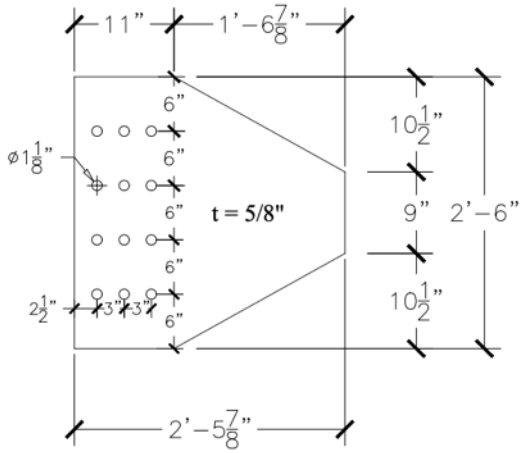

PL – 04

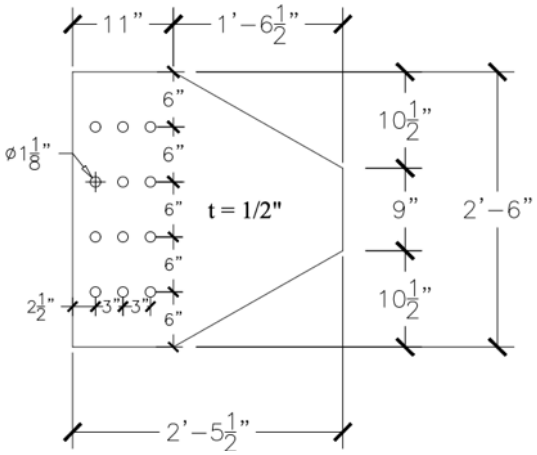

PL – 05

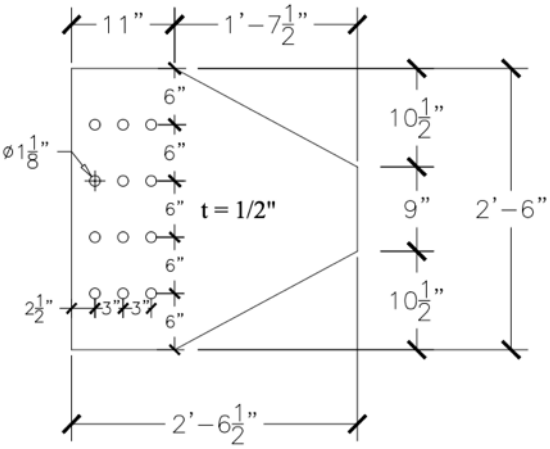

PL – 06

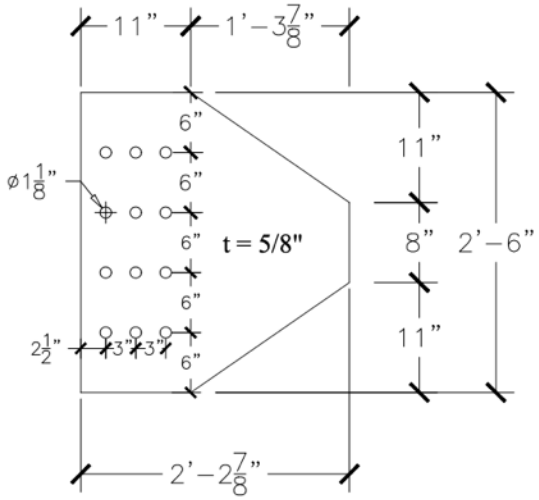

PL – 07

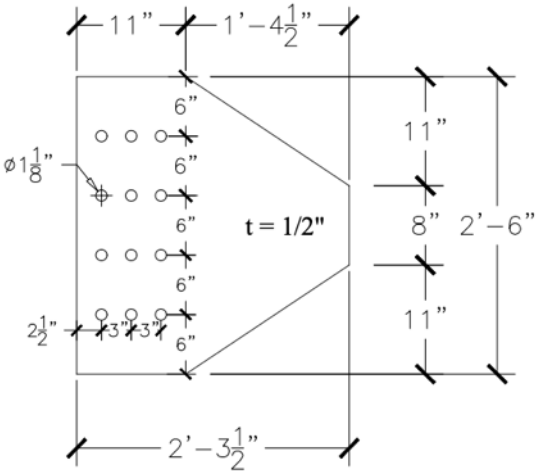

PL – 08

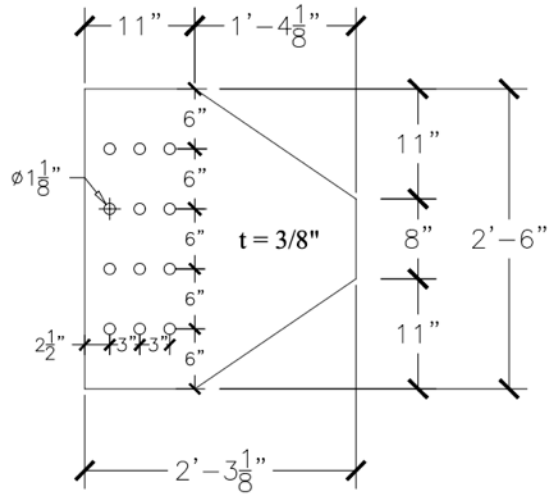

PL – 09

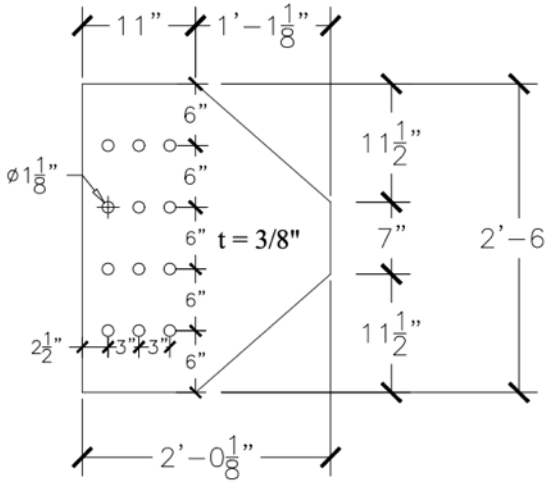

PL – 10

APPENDIX 2: SAMPLE CALCULATIONS

A2.1 – Sliding Beam Calculations

Sliding Beam Design

$L\_Act := 63\ in$ Distance from 450 kip actuator to center of test specimen

$P\_max := 550\ kip$ Maximum force applied by 450 kip actuator in compression

$M\_u := L\_Act \cdot P\_max = 2887.5\ kip\ ft$ Maximum applied bending moment in sliding beam

$FS := 1.2$

$phi := 0.9$

$$M\_req := \frac{FS \cdot M\_u}{phi} = 3850\ kip\ ft$$

$$V\_req := \frac{(FS \cdot P\_max)}{phi} = 733.3333\ kip$$

W33x201 Sliding Beam

$f\_y := 50\ ksi$

$d\_b := 33.7\ in$

$S\_xb := 686\ in\ in\ in$

$M\_b := S\_xb \cdot f\_y = 2858.3333\ kip\ ft$ Yielding moment capacity of W33x201 beam

$t\_p := \frac{3}{4}\ in$

$$S\_xp := \frac{t\_p \cdot d\_b^{\,2}}{6} = 141.9612\ in^3$$

$M\_p := S\_xp \cdot f\_y = 591.5052\ kip\ ft$ Yielding moment capacity of 0.75" thick steel plate

$M\_sb := M\_b + 2 \cdot M\_p = 4041.3438\ kip\ ft$

$M\_sb = 4041.3438\ kip\ ft$ Total yielding moment capacity of sliding beam

$$FS\_M := \frac{FS \cdot M\_sb}{M\_req} = 1.2596$$

Shear Capacity

$V\_p := 0.6 \cdot f\_y \cdot (t\_p \cdot d\_b) = 758.25\ kip$ Shear capacity of 0.75" thick steel plate

$V\_b := 723\ kip$ Shear capacity of W33x201 beam

$V\_sb := 2 \cdot 0.9 \cdot V\_p + V\_b = 2087.85\ kip$ Total shear capacity of sliding beam

$$FS\_V := \frac{(FS \cdot V\_sb)}{V\_req} = 3.4165$$

Weld Design

$I\_b := 11600\ in^4$

$t\_p := 0.75\ in$

$I\_p := \frac{1}{12} \cdot t\_p \cdot d\_b^3 = 2392.0471\ in^4$

$I\_tot := I\_b + 2 \cdot I\_p = 16384.0941\ in^4$

$t\_f := 1.15\ in$

$b\_f := 15.7\ in$

$Q := \left(\left(d\_b - \frac{t\_f}{2}\right) \cdot (t\_f \cdot b\_f)\right) = 598.0719\ in^3$

$V := 540\ kip$

$q\_tot := \frac{(V \cdot Q)}{I\_tot} = 19.7117\ \frac{kip}{in}$ Shear flow q - distributed to each fillet weld

$q\_i := \frac{q\_tot}{2} = 9.8559\ \frac{kip}{in}$ Shear flow per fillet weld

$phi\_2 := 0.75$

$F\_e := 70\ ksi$

$t\_e := \frac{q\_i}{phi\_2 \cdot 0.60 \cdot F\_e} = 0.3129\ in$ Required effective throat of weld

$w := \frac{t\_e}{\frac{1}{\sqrt{2}}} = 0.4425\ in$ Required length of fillet weld leg

A2.2 – Vertical Restraint Calculations

Stability Bracing Requirements

Treat brace specimen as a column: AISC Manual 16.1 Appendix 6

Section 6.2: Column Bracing

6.2.2: Nodal Bracing

$Pr := 1000\ kip$ Maximum axial force in column

$Pbr := 0.01 \cdot Pr = 10\ kip$ Required strength of point braces

$Nbr := 4$ Number of brace locations per end: 4 sets of vertical tie downs

$Nrod := 2$ Number of tie down rods per vertical tie down location

Required Strength

$P\_i := \frac{Pbr}{Nbr \cdot Nrod} = 1.25\ kip$ Minimum required clamping force/strength at each tie down

Using 1" 150 ksi Williams Bars: 0.6Pu = 76.5 kips

Required Stiffness

$phi := .75$

$Lbr := 21 \cdot 12\ in$ Unbraced Length (in) of test specimen

$Bbr := \frac{1}{phi} \cdot \left(8 \cdot \frac{Pr}{Lbr}\right) = 42.328\ \frac{kip}{in}$ Required stiffness of the point braces

Bracing at sliding beam end: Assume bottom sliding surface (HSS atop I-Beam connected to floor) is rigid relative to top constraint

$Ll := 84\ in$ Horizontal length between clamping bars

$Lsb := 33\ in$ Width of sliding beam

Treating top beam as simply supported - upward force of beam applied at mid-span (worst case)

$E := 29000\ ksi$

1) 6x6x1/4 HSS sections above sliding beam: 4 along length of beam

$I\_1 := 28.6\ in^4$ $A\_1 := 5.24\ in^2$

$I\_1tot := 4 \cdot I\_1 = 114.4\ in^4$ Total moment of inertia of top beams

$Dmax\_1 := \frac{\left(Pbr \cdot Ll^3\right)}{48 \cdot E \cdot I\_1tot} = 0.0372\ in$ Maximum deflection of top beams due to bending

$L\_r := 30\ in$ Length of 1" steel threaded rod connecting top and bottom HSS

$A\_r := 0.85\ in^2$ Area of 1" steel rod

$D2 := \frac{(Pbr \cdot L\_r)}{A\_r \cdot (2 \cdot Nbr) \cdot E} = 0.0015\ in$ Deflection due to axial elongation of 1" diamenter Williams rods

$B\_1 := \frac{Pbr}{Dmax\_1 + D2} = 258.1246\ \frac{kip}{in}$

$\frac{B\_1}{Bbr} = 6.0982$ Combined stiffness of top beams is adequate: Satisfies requirements

Section 6.3: Beam Bracing - Sliding Beam

6.3.1b: Nodal Bracing

Required Strength: EQ A-6-7

$Mr := 2835\ kip\ ft$ Required flexural strength per LRFD load combinations

$Mr = 34020\ kip\ in$

$Cd := 1.0$

$ho := 33.68\ in - 1.15\ in = 32.53\ in$ Distance between flange centroids

$Prb := \frac{0.02 \cdot Mr \cdot Cd}{ho} = 20.9161\ kip$ Required strength of sliding beam

Beam not subjected to double curvature bending

Required stiffness: EQ A-6-8

$B\_br := \frac{(10 \cdot Mr \cdot Cd)}{Lbr \cdot ho} = 41.5002\ \frac{kip}{in}$ Required stiffness of sliding beam

$L\_sb := 16\ ft = 192\ in$

$I\_sb := 16384\ in^4$ Total moment of inertia of sliding beam (including 3/4" plates but not concrete)

$D\_sb := \frac{\left(Pr \cdot L\_sb^3\right)}{48 \cdot E \cdot I\_sb} = 0.3103\ in$ Displacement of sliding beam from actuators' force

$B\_sb := \frac{Pr}{D\_sb} = 3222.2222\ \frac{kip}{in}$ Stiffness of sliding beam - OK - significantly exceeds required stiffness

A2.3 – Keyway Plate Design

Keyway Plate Design

$f_y := 36\ ksi$

$t := 3\ in$	Plate thickness
$w := 14\ in$	Plate width
$h := 14\ in$	Plate height
$h_1 := 2.5\ in$	Expected height of contact

$I := \frac{t \cdot w^3}{12} = 686\ in^4$

$W := \frac{t \cdot w^2}{6} = 98\ in^3$

$F := 80\ kip$	Predicted maximum horizontal load applied due to contact between key and keyway
$M := F \cdot h = 1120\ kip\ in$	Maximum bending moment due to applied force
$\sigma_{contact} := \frac{F}{h_1 \cdot t} = 10.6667\ ksi$	Bearing stress at point of contact
$\sigma_{moment} := \frac{M}{W} = 11.4286\ ksi$	Bending stress at base of keyway

Base Weld Design AISC SCM Table 8-4: Eccentrically Loaded Weld Groups Special Case - load not in plane of weld group

$e\_x := 14.375$	Maximum eccentricity of lateral force on keyway (in)
$P := 80$	Potential lateral force (kips)
$C\_1 := 1$	Electrode coefficient strength (E70XX electrodes)
$l\_w := 18$	Weld length (in - base of keyway)

$a := \frac{e\_x}{l\_w} = 0.7986$

$d\_w := 4\ in$	Lateral distance between welds
$k := 0$	Loads not in plane of weld
$C := 1.57$	Coefficient from Table 8-4

$phi := 1$

$D\_min := \frac{P}{phi \cdot C \cdot C\_1 \cdot l\_w} = 2.8309$ Required weld size

(Sixteenths of an inch)

$D := 0.4375$ Try 5/8" weld

$R\_n := C \cdot C\_1 \cdot D \cdot 16 \cdot l\_w = 197.82$ Nominal weld strength (kips)

A2.4 – Connection Design

Connection Design												
Required force	*Pc*	k	858.0	936.0	676.0	754.0	583.1	493.4	633.1	492.7	418.0	401.7
Yield stress	*Fy*	ksi	50	50	50	50	50	50	50	50	50	50
Tensile strength	*Fu*	ksi	62	62	62	62	62	62	62	62	62	62
Elastic modulus	*E*	ksi	29000	29000	29000	29000	29000	29000	29000	29000	29000	29000
Section	-	-	**HSS10x10x3/8**	**HSS8x8x1/2**	**HSS8x8x3/8**	**HSS7x7x1/2**	**HSS7x7x3/8**	**HSS7x7x5/16**	**HSS6x6x1/2**	**HSS6x6x3/8**	**HSS6x6x5/16**	**HSS5x5x3/8**
Effective length factor	*K*	-	1.0	1.0	1.0	1.0	1.0	1.0	1.0	1.0	1.0	1.0
Length	*L*	in	237.5	237.5	237.5	237.5	237.5	237.5	237.5	237.5	237.5	237.5
Radius of gyration	*r*	in	3.92	3.04	3.1	2.63	2.69	2.72	2.23	2.28	2.31	1.87
Global slenderness ratio	*lambda_g*	-	60.6	78.1	76.6	90.3	88.3	87.3	106.5	104.2	102.8	127.0
Local slenderness ratio	*lambda_l*	-	25.6	14.2	19.9	12	17	21.1	9.91	14.2	17.6	11.3
Highly Ductile b/t limit	*lambda_l_limit*	-	13.7	13.7	13.7	13.7	13.7	13.7	13.7	13.7	13.7	13.7
Elastic buckling stress	*Fe*	ksi	78.0	46.9	48.8	35.1	36.7	37.5	25.2	26.4	27.1	17.7
Critical stress	*Fcr*	ksi	38.2	32.0	32.6	27.5	28.3	28.6	21.8	22.6	23.1	15.6
Gross area	*Ag*	in2	13.2	14.4	10.4	11.6	8.97	7.59	9.74	7.58	6.43	6.18
Critical buckling force	*Pcr*	k	505	461	339	320	254	217	212	171	148	96
Yield force	*Py*	k	660	720	520	580	449	380	487	379	322	309
Compression-tension force ratio	*beta*	-	0.76	0.64	0.65	0.55	0.57	0.57	0.44	0.45	0.46	0.31
Design overstrength			**1.70**	**2.03**	**2.00**	**2.36**	**2.30**	**2.27**	**2.98**	**2.87**	**2.82**	**4.18**
Brace width	*b*	in	10.000	8.000	8.000	7.000	7.000	7.000	6.000	6.000	6.000	5.000
Brace wall thickness	*t*	in	0.349	0.465	0.349	0.465	0.349	0.291	0.465	0.349	0.291	0.349
Brace splice connection length	*Lc,temp*	in	**22.0**	**18.0**	**17.4**	**14.5**	**15.0**	**15.2**	**12.2**	**12.7**	**12.9**	**10.3**
Design connection length	*Lc,des1*	in	25.0	19.0	20.0	17.0	17.0	18.0	16.0	15.0	15.0	12.0
Gusset plate width	*Bw*		38.868	29.939	31.094	26.630	26.630	27.785	24.475	23.321	23.321	18.856
Gusset plate thickness	*tp*	in	0.40	0.57	0.40	0.51	0.40	0.32	0.47	0.38	0.33	0.39
	tp,des	**in**	**0.750**	**0.750**	**0.625**	**0.625**	**0.500**	**0.500**	**0.625**	**0.500**	**0.375**	**0.375**
Controlling material thickness	*tmin*	in	0.349	0.465	0.349	0.465	0.349	0.291	0.465	0.349	0.291	0.349
Minimum weld size	*wmin*	in	0.19	0.19	0.19	0.19	0.19	0.19	0.19	0.19	0.19	0.19
Design weld size	*w*	in	0.375	0.625	0.500	0.500	0.500	0.500	0.500	0.438	0.438	0.375
Required weld length	*Lc,weld*	in	25.68	16.81	15.18	16.93	13.09	11.08	14.21	12.64	10.72	12.02
	RyFy	ksi	65	65	65	65	65	65	65	65	65	65
Brace end-to-end length	*L*	in	237.5	237.5	237.5	237.5	237.5	237.5	237.5	237.5	237.5	237.5
Global slenderness ratio	*lambda_g*		60.6	78.1	76.6	90.3	88.3	87.3	106.5	104.2	102.8	127.0
Euler buckling stress	*Fe*	ksi	78.0	46.9	48.8	35.1	36.7	37.5	25.2	26.4	27.1	17.7
Critical buckling stress	*Fcr*	ksi	45.9	36.4	37.2	29.9	31.0	31.5	22.1	23.1	23.7	15.6
Expected tensile capacity	***Pt***		**858**	**936**	**676**	**754**	**583**	**493**	**633**	**493**	**418**	**402**
Expected compressive capacity	***Pc***		**690.2**	**597.5**	**441.2**	**396.0**	**316.9**	**272.5**	**245.8**	**199.9**	**174.1**	**109.7**
Weld filler metal capacity		k	1114	1410	1188	1010	1010	1069	950	779	779	534
Weld base metal capacity		k	1483	1502	1187	1344	1009	891	1265	890	742	712
Weld filler metal DCR		-	0.77	0.66	0.57	0.75	0.58	0.46	0.67	0.63	0.54	0.75
Weld base metal DCR		-	0.58	0.62	0.57	0.56	0.58	0.55	0.50	0.55	0.56	0.56

Section	-	-	HSS10x10x3/8	HSS8x8x1/2	HSS8x8x3/8	HSS7x7x1/2	HSS7x7x3/8	HSS7x7x5/16	HSS6x6x1/2	HSS6x6x3/8	HSS6x6x5/16	HSS5x5x3/8
Bolt limit states												
Bolt type	*Bolt type*	-	A490	A490	A490	A490	A490	A490	A490	A490	A490	A490
Bolt size	*Bolt size*	-	1	1	1	1	1	1	1	1	1	1
Shear location			Shaft	Shaft	Shaft	Shaft	Shaft	Shaft	Shaft	Shaft	Shaft	Shaft
Number of shear planes			2	2	2	2	2	2	2	2	2	2
Surface class		-	Class B	Class B	Class B	Class B	Class B	Class B	Class B	Class B	Class B	Class B
Number of slip planes	*ns*	-	2	2	2	2	2	2	2	2	2	2
Number of fillers		-	1	1	1	1	1	1	1	1	1	1
Mean installed bolt pretension to the specified minimum	*Du*		1.13	1.13	1.13	1.13	1.13	1.13	1.13	1.13	1.13	1.13
Number of bolts		#	12	12	12	12	12	12	12	12	12	12
Number of bolt rows		#	3	3	3	3	3	3	3	3	3	3
Gross bolt area		in^2	0.785	0.785	0.785	0.785	0.785	0.785	0.785	0.785	0.785	0.785
Net tensile area		in^2	0.606	0.606	0.606	0.606	0.606	0.606	0.606	0.606	0.606	0.606
Minimum bolt pretension		kip	64	64	64	64	64	64	64	64	64	64
Nominal tensile strength		kip	113	113	113	113	113	113	113	113	113	113
Nominal shear strength		kip	84	84	84	84	84	84	84	84	84	84
Mean slip coefficient		-	0.5	0.5	0.5	0.5	0.5	0.5	0.5	0.5	0.5	0.5
Factor for fillers	*hf*	-	1	1	1	1	1	1	1	1	1	1
Slip resistance		kip	**867.84**	**867.84**	**867.84**	**867.84**	**867.84**	**867.84**	**867.84**	**867.84**	**867.84**	**867.84**
Utilization (brace/connection)			*99%*	*108%*	*78%*	*87%*	*67%*	*57%*	*73%*	*57%*	*48%*	*46%*
Bolt shear resistance		kip	**1186.92**	**1186.92**	**1186.92**	**1186.92**	**1186.92**	**1186.92**	**1186.92**	**1186.92**	**1186.92**	**1186.92**
Utilization (brace/connection)			*72%*	*79%*	*57%*	*64%*	*49%*	*42%*	*53%*	*42%*	*35%*	*34%*
Gusset plate calculations												
Steel type		-	A572-50	A572-55	A572-55	A572-55	A572-55	A572-55	A572-55	A572-55	A572-55	A572-55
Width min			38.868	29.939	31.094	26.630	26.630	27.785	24.475	23.321	23.321	18.856
Thickness min			0.401	0.568	0.395	0.515	0.398	0.323	0.470	0.384	0.326	0.387
Width		in	**30.000**	**30.000**	**30.000**	**30.000**	**30.000**	**30.000**	**30.000**	**30.000**	**30.000**	**30.000**
Thickness		in	0.750	0.750	0.625	0.625	0.500	0.500	0.625	0.500	0.375	0.375
Unsupported length		in	2.250	2.250	1.875	1.875	1.500	1.500	1.875	1.500	1.125	1.125
Effective length factor	*K*	-	2.000	2.000	2.000	2.000	2.000	2.000	2.000	2.000	2.000	2.000
Effective length	*Lc*		4.500	4.500	3.750	3.750	3.000	3.000	3.750	3.000	2.250	2.250
Second moment of area		in^4	1.055	1.055	0.610	0.610	0.313	0.313	0.610	0.313	0.132	0.132
Radius of gyration		in	0.217	0.217	0.180	0.180	0.144	0.144	0.180	0.144	0.108	0.108
Edge distance parallel		in	2.500	2.500	2.500	2.500	2.500	2.500	2.500	2.500	2.500	2.500
Edge distance perpendicular		in	6.000	6.000	6.000	6.000	6.000	6.000	6.000	6.000	6.000	6.000
Bolt spacing parallel		in	3.000	3.000	3.000	3.000	3.000	3.000	3.000	3.000	3.000	3.000
Bolt spacing perpendicular		in	6.000	6.000	6.000	6.000	6.000	6.000	6.000	6.000	6.000	6.000
Tension stress distribution factor		-	1.000	1.000	1.000	1.000	1.000	1.000	1.000	1.000	1.000	1.000

Section	-	-	HSS10x10x3/8	HSS8x8x1/2	HSS8x8x3/8	HSS7x7x1/2	HSS7x7x3/8	HSS7x7x5/16	HSS6x6x1/2	HSS6x6x3/8	HSS6x6x5/16	HSS5x5x3/8
Block shear - shear plane gross	*Agv*	in^2	11.906	11.906	9.922	9.922	7.938	7.938	9.922	7.938	5.953	5.953
Block shear - shear plane net	*Anv*	in^2	8.531	8.531	7.109	7.109	5.688	5.688	7.109	5.688	4.266	4.266
Block shear tension plane	*Ant*	in^2	10.97	10.97	9.14	9.14	7.31	7.31	9.14	7.31	5.48	5.48
Bolt hole size		in	1.125	1.125	1.125	1.125	1.125	1.125	1.125	1.125	1.125	1.125
Gross area		in^2	22.50	22.50	18.75	18.75	15.00	15.00	18.75	15.00	11.25	11.25
Effective area		in^2	19.13	19.13	15.94	15.94	12.75	12.75	15.94	12.75	9.56	9.56
Yield strength		ksi	50	55	55	55	55	55	55	55	55	55
Tensile strength		ksi	65	70	70	70	70	70	70	70	70	70
Elastic modulus	*E*	ksi	29000	29000	29000	29000	29000	29000	29000	29000	29000	29000
Latteral stiffness (12E*I/L^3)			32,222	32,222	32,222	32,222	32,222	32,222	32,222	32,222	32,222	32,222
Gross yield resistance		kip	**1012.5**	**1113.8**	**928.1**	**928.1**	**742.5**	**742.5**	**928.1**	**742.5**	**556.9**	**556.9**
Utilization (brace/gusset)			*85%*	*84%*	*73%*	*81%*	*79%*	*66%*	*68%*	*66%*	*75%*	*72%*
Tensile rupture (net section)		kip	**932.3**	**1004.1**	**836.7**	**836.7**	**669.4**	**669.4**	**836.7**	**669.4**	**502.0**	**502.0**
Utilization (brace/gusset)			*92%*	*93%*	*81%*	*90%*	*87%*	*74%*	*76%*	*74%*	*83%*	*80%*
Bearing		kip	**810**	**891**	**742.5**	**742.5**	**594**	**594**	**742.5**	**594**	**445.5**	**445.5**
Utilization (brace/gusset)			*106%*	*105%*	*91%*	*102%*	*98%*	*83%*	*85%*	*83%*	*94%*	*90%*
Gusset plate block shear		kip	**784.3**	**844.6**	**703.8**	**703.8**	**563.1**	**563.1**	**703.8**	**563.1**	**422.3**	**422.3**
Utilization (brace/gusset)			*109%*	*111%*	*96%*	*107%*	*104%*	*88%*	*90%*	*88%*	*99%*	*95%*
Failure in net shear			1045.7	1126.1	938.4	938.4	750.8	750.8	938.4	750.8	563.1	563.1
Failure in gross shear			1070.2	1160.7	967.3	967.3	773.8	773.8	967.3	773.8	580.4	580.4
Tearout		kip	**998.2**	**1074.9**	**895.8**	**895.8**	**716.6**	**716.6**	**895.8**	**716.6**	**537.5**	**537.5**
Utilization (brace/gusset)			*86%*	*87%*	*75%*	*84%*	*81%*	*69%*	*71%*	*69%*	*78%*	*75%*
Clear distance, edge		in	1.9375	1.9375	1.9375	1.9375	1.9375	1.9375	1.9375	1.9375	1.9375	1.9375
Clear distance, bolt hole		in	1.875	1.875	1.875	1.875	1.875	1.875	1.875	1.875	1.875	1.875
Gusset plate buckling			**981.0**	**1075.7**	**896.4**	**896.4**	**717.1**	**717.1**	**896.4**	**717.1**	**537.9**	**537.9**
Utilization (brace/gusset)			*70%*	*56%*	*49%*	*44%*	*44%*	*38%*	*27%*	*28%*	*32%*	*20%*
Global slenderness ratio	*lambda_g*		20.8	20.8	20.8	20.8	20.8	20.8	20.8	20.8	20.8	20.8
Elastic buckling sterss	*Fe*	ksi	662.5	662.5	662.5	662.5	662.5	662.5	662.5	662.5	662.5	662.5
Critical buckling stress	*Fcr*	ksi	48.4	53.1	53.1	53.1	53.1	53.1	53.1	53.1	53.1	53.1

SAMPLE CONNECTION CALCULATION:

6x6x1/2 A500 HSS

Section Properties

Yield stress	F_y	ksi	50
Tensile strength	F_u	ksi	62
Yield Strength Factor	R_y		1.3
Ultimate Strength Factor	R_t		1.2
Elastic modulus	E	ksi	29000
Effective length factor	K	-	1.0
Length	L	in.	237.5
Radius of gyration	r	in.	2.23
Global slenderness ratio	λ_g	-	106.5
Local slenderness ratio	λ_l	-	9.9
Gross area	A_g	in^2	9.74
Brace width	B	in.	6
Wall thickness	t_{des}	in.	0.465

Expected Forces

$P_y = R_y \cdot F_y \cdot A_y = 1.3 \cdot 50 \cdot 9.74 = 633\ kips$ [Expected Yield Force]

$$4.71 \cdot \sqrt{\frac{E}{R_y F_y}} = 4.71 \cdot \sqrt{\frac{29000}{1.3 \cdot 50}} = 113.4$$

$\frac{KL}{r} = 106.5 < 113.4$

$F_e = \frac{(\pi^2 \cdot E)}{\frac{KL}{r}} = 25.23\ \boldsymbol{ksi}$ [Elastic Critical Stress]

$F_{cr} = 0.658^{\frac{R_y \cdot F_y}{F_e}} \cdot R_y \cdot F_y = 22.13\ \boldsymbol{ksi}$ [Critical Buckling Stress]

$P_{cr} = F_{cr} \cdot A_g = 215.6\ kips$ [Critical Buckling Force]

Weld Design

$L_{c,min} = \frac{P_y}{0.75 \cdot 0.6 \cdot F_u \cdot 4 \cdot t_{des}} = 12.2\ in.$ [Minimum brace connection length]

$L_{c,des} = 15.875\ in.$ [Design brace connection length]

$w_{GP,min} = 2 \cdot B \cdot \tan(30) + L_{c,des} = 22.17\ in.$ [Minimum gusset plate width]

$w_{GP,des} = 30\ in.$ [Design gusset plate width]

$t_{GP,min} = \frac{P_y}{55 \cdot 2 \cdot L_{c,des} \cdot \tan(30) + B} = 0.52\ in.$ [Minimum gusset plate thickness]

$t_{GP,des} = 0.625\ in.$ [Design gusset plate thickness]

$t_{min} = min(t_{GP,des}, t_{des}) = 0.465\ in.$ [Controlling material thickness]

$w_{min} = \frac{3}{16}\ in.$ [Minimum weld size]

$w_{des} = 0.50\ in.$ [Design fillet weld size]

$n_w = 4$ [Number of fillet welds]

$L_{c,w} = \frac{P_y}{n_w \cdot \Phi \cdot 0.6 \cdot F_{EXX} \cdot 0.707 \cdot w_{des}}$ [Required weld length]

$= \frac{633\ kips}{4 \cdot 0.75 \cdot 0.6 \cdot 70\ ksi \cdot 0.707 \cdot 0.5\ in.} = 14.1\ in.$

$R_f = 0.6 \cdot F_{EXX} \cdot 0.707 \cdot w_{des} \cdot n_w \cdot L_{c,des}$ [Weld filler metal capacity]

$= 0.6 \cdot 70\ ksi \cdot 0.707 \cdot 0.5" \cdot 15.875" = 943\ kips$

$DCR_{Filler\ Metal} = \frac{P_y}{R_f} = \frac{633\ kips}{943\ kips} = 0.67$ [OK]

$R_b = 0.6 \cdot 1.1 \cdot R_y F_y \cdot n_w \cdot w_{des} \cdot L_{c,des}$ [Weld base metal capacity]

$= 0.6 \cdot 1.1 \cdot 1.3 \cdot 50\ ksi \cdot 4 \cdot 0.5" \cdot 15.875" = 1255\ kips$

$DCR_{Base\ Metal} = \frac{P_y}{R_b} = \frac{633\ kips}{11255\ kips} = 0.50$ [OK]

Bolt Design

Bolt Properties

Bolt Type			A490
Shear Location			Shaft
Surface Class			Class B
Number of Bolts	n_b		12
Number of Shear Planes	n_v		2
Number of Slip Planes	n_s		2
Mean Slip Coefficient	c_s		0.5
Number of Fillers	n_f		1
Filler Factor	h_f		1.0
Mean Bolt Pretension Ratio	D_u		1.13
Bolt Size	d_b	in.	1
Minimum Bolt Pretension	$F_{t,b}$	kips	64
Gross Bolt Area	$A_{g,b}$	in^2	0.785
Net Tensile Area	$A_{n,b}$	in^2	0.606
Nominal Tensile Strength	F_{nt}	kips	113
Nominal Shear Strength	F_{nv}	kips	84

$\Phi R_{n,s} = c_s \cdot D_u \cdot h_f \cdot F_{nt} \cdot n_s \cdot n_b$ [Slip Resistance]

$= 0.5 \cdot 1.13 \cdot 1.0 \cdot 64\ kips \cdot 2 \cdot 12 = 868\ kips$

$DCR_{slip} = \frac{P_y}{\Phi R_s} = \frac{633\ kips}{868\ kips} = 0.72$ [OK]

$\Phi R_{n,v} = \Phi \cdot A_{n,b} \cdot F_{nv} \cdot n_v \cdot n_b$ [Bolt Shear Resistance]

$= 0.75 \cdot 0.606\ in^2 \cdot 113\ kips \cdot 2 \cdot 12 = 1187\ kips$

$DCR_{shear} = \frac{P_y}{\Phi R_n} = \frac{633\ kips}{1187\ kips} = 0.53$ [OK]

Gusset Plate Design

Gusset Plate Properties

Width	w_{GP}	in.	30
Thickness	t_{GP}	in.	0.625
Yield Strength	$F_{y,GP}$	ksi	55
Tensile Strength	$F_{u,GP}$	ksi	70
Unsupported Length	$L_{u,GP}$	in.	1.875
Effective Length Factor	K_{GP}	-	2
Effective Length	$L_{c,GP}$	in.	3.75
Moment of Inertia	$I_{GP,y}$	in^4	0.61
Radius of Gyration	$r_{GP,y}$	in.	0.18
Bolt Hole Diameter	d_{bh}	in.	1.125
Number of Bolts	n_b		12
Number of Bolt Rows	n_{br}		3
Number of Bolt Columns	n_{bc}		4
Edge Distance - Horizontal	l_{eh}	in.	2.5
Edge Distance - Vertical	l_{ev}	in.	6
Bolt Spacing – Horizontal	l_{bh}	in.	3
Bolt Spacing - Vertical	l_{bv}	in.	6

$$A_{gv} = 2\left(l_{eh} + (n_{br} - 1) \cdot l_{bh} - \frac{d_{bh}}{2}\right) \cdot t_{GP}$$ [Block Shear Plane – Gross Area]

$$= 2 \cdot \left(2.5" + (3 - 1) \cdot 3" - \frac{1.25"}{2}\right) \cdot 0.625" = 9.92\ in^2$$

$$A_{nv} = 2 \cdot \left(\left(l_{eh} - \frac{d_{bh}}{2}\right) + (n_{br} - 1) \cdot (l_{bh} - d_{bh})\right) \cdot t_{GP}$$ [Block Shear Plane – Net Area]

$$= 2 \cdot \left(\left(2.5" - \frac{1.25"}{2}\right) + (3 - 1) \cdot (3" - 1.25")\right) \cdot 0.625 = 7.11\ in^2$$

$$A_{nt} = (l_{bv} - d_{bh}) \cdot \left(\frac{n_b}{n_{br}} - 1\right) \cdot t_{GP}$$ [Block Shear Tension Plane]

$$= (6" - 1.25") \cdot \left(\frac{12}{3} - 1\right) \cdot 0.625" = 9.14\ in^2$$

$A_{g,GP} = w_{GP} \cdot t_{GP} = 30" \cdot 0.625" = 18.75\ in^2$ [Gusset Plate Gross Area]

$A_{e,GP} = \left(w_{GP} - (d_{bh} \cdot n_{bc})\right) \cdot t_{GP}$ [Gusset Plate Net Area]

$= \left(30" - (1.25" \cdot 4)\right) \cdot 0.625" = 15.94\ in^2$

$K_{GP} = \frac{(12 \cdot E \cdot I_{GP,y})}{L_{u,GP}{}^3} = \frac{(12 \cdot 29000\ ksi \cdot 0.61\ in^4)}{(1.875\ in)^3} = 32200 \frac{k}{in}$ [Gusset Plate Lateral Stiffness]

$\Phi R_{n,y} = \Phi \cdot F_{y,GP} \cdot A_{g,GP}$ [Gross Yield Strength]

$= 0.9 \cdot 55\ ksi \cdot 18.75\ in^2 = 928.1\ kips$

$DCR_y = \frac{P_y}{\Phi R_{n,y}} = \frac{633\ kips}{928.1\ kips} = 0.68$ [OK]

$\Phi R_{n,t} = \Phi \cdot F_{u,GP} \cdot A_{n,GP}$ [Tensile Rupture Strength]

$= 0.75 \cdot 70\ ksi \cdot 15.94\ in^2 = 836.7\ kips$

$DCR_t = \frac{P_y}{\Phi R_{n,t}} = \frac{633\ kips}{836.7\ kips} = 0.75$ [OK]

$\Phi R_{n,b} = 1.2 \cdot l_{eh} \cdot t_{GP} \cdot F_u \leq 2.4 \cdot d_b \cdot t_{GP} \cdot F_u$

$= 1.2 \cdot 2.5" \cdot 0.625" \cdot 70\ ksi = 131\ kips > 2.4 \cdot 1" \cdot 0.625" \cdot 70\ \text{ksi} = 105\ \text{kips}$

$\Phi R_{n,b} = \Phi \cdot 2.4 \cdot t_{GP} \cdot d_b \cdot F_{y,GP} \cdot n_b$ [Bearing Strength]

$= 0.75 \cdot 2.4 \cdot 0.625" \cdot 1" \cdot 55\ ksi \cdot 12 = 742.5\ kips$

$DCR_b = \frac{P_y}{\Phi R_{n,b}} = \frac{633\ kips}{742.5\ kips} = 0.84$ [OK]

$R_{n,bsn} = 0.6 \cdot F_{u,GP} \cdot A_{nv} + 1.0 \cdot F_{u,GP} \cdot A_{nt}$ [Block Shear – Net Section]

$= 0.6 \cdot 70\ ksi \cdot 7.11\ in^2 + 1.0 \cdot 70\ ksi \cdot 9.14\ in^2 = 938.4\ kips$

$R_{n,bsg} = 0.6 \cdot F_{y,GP} \cdot A_{gv} + 1.0 \cdot F_{u,GP} \cdot A_{nt}$ [Block Shear – Gross Section]

$= 0.6 \cdot 55\ ksi \cdot 9.92\ in^2 + 1.0 \cdot 70\ ksi \cdot 9.14\ in^2 = 967.3\ kips$

$\Phi R_{n,bs} = 0.75 \cdot min\left(R_{n,bsn}, R_{n,bsg}\right)$ [Block Shear Strength]

$= 0.75 \cdot 938.4\ kips = 703.8\ kips$

$DCR_{bs} = \frac{P_y}{\Phi R_{n,bs}} = \frac{633\ kips}{703.8\ kips} = 0.89$ [OK]

$l_{c,bh} = l_{bh} - d_{bh} = 3" - 1.25" = 1.875"$ [Clear Distance – Bolt Hole]

$l_{c,e} = l_{eh} - \frac{d_{bh}}{2} = 2.5" - \frac{1.125"}{2} = 1.94"$ [Clear Distance – Edge]

$\Phi R_{n,to} = \Phi 1.2 \cdot F_{u,GP} \cdot t_{GP} \left(l_{c,e} \left(\frac{n_b}{n_{br}} \right) + l_{c,bh} \left(\frac{n_b}{n_{br}} \right) (n_{br} - 1) \right)$ [Tearout Strength]

$= 0.75 \cdot 1.2 \cdot 70\ ksi \cdot 0.625" \left(1.94" \left(\frac{12}{3} \right) + 1.875" \left(\frac{n_b}{n_{br}} \right) (3 - 1) \right) = 895.8\ kips$

$DCR_{to} = \frac{P_y}{\Phi R_{n,to}} = \frac{633\ kips}{895.8\ kips} = 0.70$ [OK]

$\lambda_g = \frac{l_{c,GP}}{r_{GP,y}} = \frac{3.75"}{0.18"} = 20.8$ [Global Slenderness Ratio]

$F_{e,GP} = \frac{(\pi^2 \cdot E)}{\lambda_g{}^2} = \frac{(\pi^2 \cdot 29000\ ksi)}{20.8^2} = 662.5\ ksi$ [Elastic Critical Stress]

$4.71 \sqrt{\frac{E}{F_{y,GP}}} = 4.71 \sqrt{\frac{29000\ ksi}{55\ ksi}} = 108.2$ $\lambda_g < 108.2$

$F_{cr,GP} = 0.658^{\left(\frac{E}{F_{y,GP}} \right)} \cdot F_{y,GP}$ [Critical Buckling Stress]

$= 0.658^{\left(\frac{29000\ ksi}{55\ ksi} \right)} \cdot 55\ ksi = 53.1\ ksi$

$\Phi R_{n,bk} = \Phi \cdot A_{g,GP} \cdot F_{cr,GP}$ [Gusset Plate Buckling Strength]

$= 0.9 \cdot 18.75\ in^2 \cdot 53.1\ ksi = 896.4\ kips$

$DCR_{bk} = \frac{P_{cr}}{\Phi R_{n,bk}} = \frac{215.6\ kips}{896.4\ kips} = 0.27$ [OK]

A2.5– Net Section Reinforcement Design

Net Section Reinforcement Plate Design

HSS Shape	Thickness (in.)	Width (in.)	Length (in.)	Weld Size (in.)
10x10x3/8	3/8	5.25	24	1/4
8x8x1/2	3/8	5.25	24	1/4
8x8x3/8	3/8	4.25	20	1/4
7x7x1/2	3/8	4.25	20	1/4
7x7x3/8	3/8	4.25	20	1/4
7x7x5/16	3/8	3.25	18	1/4
6x6x1/2	3/8	3.25	18	1/4
6x6x3/8	3/8	3.25	18	1/4
6x6x5/16	3/8	3.25	18	1/4
5x5x3/8	3/8	2.75	16	1/4

SAMPLE NET SECTION REINFORCEMENT CALCULATION:

6x6x1/2 A500 HSS

Section Properties

Yield stress	F_y	ksi	50
Tensile strength	F_u	ksi	62
Yield Strength Factor	R_y		1.3
Ultimate Strength Factor	R_t		1.2
Elastic modulus	E	ksi	29000
Gross area	A_g	in^2	9.74
Brace width	B	in.	6
Wall thickness	t_{des}	in.	0.465
Gusset Plate Width	w_{GP}	in.	0.625
Workable Flat Width	w_f	in.	3.75

$w_s = w_{GP} + 0.125" = 0.625" + 0.125" = 0.75"$ [Slot Width]

$A_{nb} = A_g - 2 \cdot t_{des} \cdot w_s$ [Net Area at Slot]

$= 9.74\ in^2 - 2 \cdot 0.465" \cdot 0.75" = 9.04\ in^2$

$w_{f,a} = w_f - 2 \cdot \frac{w_{des}}{16} = 3.75" - 2 \cdot \frac{4}{16} = 3.25"$ [Available Flat Width]

$b_{cp} = 3.25"$ [Design Cover Plate Width]

$t_{cp} = 0.375"$ [Design Cover Plate Thickness]

$A_{cp} = b_{cp} \cdot t_{cp} = 1.22\ in^2$ [Cover Plate Area]

$L_{cp} = 18"$ [Design Cover Plate Length]

$\overline{x} = \frac{(B^2+2B^2)}{4(2B)} = \frac{(3\cdot(6\ in.)^2)}{4\cdot(2\cdot 6\ in)} = 2.25"$ [Connection Eccentricity]

$U = 1 - \frac{\overline{x}}{L_{cp}} = 1 - \frac{2.25"}{18"} = 0.875"$ [Shear Lag Factor]

Net Section Rupture Limit State

$A_e = U(A_{nb} + 2 \cdot A_{cp})$ [Section Effective Net Area]

$= 0.875(9.04\ in^2 + 2 \cdot 1.22\ in^2) = 10.1\ in^2$

$\frac{A_g}{A_e} = \frac{9.74\ in^2}{10.1\ in^2} = 0.97$ [OK: $A_e > A_g$]

Longitudinal Weld Design

Cover Plate & Fillet Weld Properties

Yield stress	$F_{y,cp}$	ksi	50
Yield Strength Factor	$R_{y,cp}$		1.1
Cover Plate Width	b_{cp}	in.	3.25
Cover Plate Thickness	t_{cp}	in.	0.375
Cover Plate Area	A_{cp}	in^2	1.22
Cover Plate Length	L_{cp}	in.	18
Weld Size	D	16ths of an in.	4
Weld Length	L_w	in.	16
Weld Electrode Strength	F_{EXX}	ksi	70
Number of Welds per Plate	n_w		2

$P_{y,cp} = R_{y,cp} \cdot F_{y,cp} \cdot A_{cp}$ [Expected Cover Plate Yield Force]

$= 1.1 \cdot 50\ ksi \cdot 1.22\ in^2 = 67\ kips$

$\Phi R_{n,w} = 1.392 \cdot D \cdot \frac{L_w}{2} \cdot n_w$ [Cover Plate Weld Strength]

$= 1.392 \cdot 4 \cdot \frac{18"}{2} \cdot 2 = 100.2\ kips$

$DCR_w = \frac{P_{y,cp}}{\Phi R_{n,w}} = \frac{67\ kips}{100.2\ kips} = 0.67$ [OK: $\Phi R_{n,w} > P_{y,cp}$]

Net Section Reinforcement Plate Design

Test Specimen	Thickness (in.)	Width (in.)	Length (in.)	Weld Size (in.)
6x6x1/2 A500 R	3/8	3.25	18	1/4

A2.6 – AISC 342 Nonlinear Analysis Procedure – 5x5x3/8 A1085 Y HSS

Material and Geometric Properties

$$E = 29000\ ksi$$

$$A_g = 6.58\ in^2$$

$$F_{ye} = R_y F_y = 1.25 \cdot 50\ ksi = 62.5\ ksi$$

$$L_c = K \cdot L_b = 1.0 \cdot 237.5\ in = 237.5\ in.$$

$$r = 1.86\ in.$$

$$F_e = \frac{\pi^2 E}{\left(\frac{L_c}{r}\right)^2} = 17.55\ ksi$$

$$F_{cre} = \left(0.658^{\left(\frac{F_{ye}}{F_e}\right)}\right) \cdot F_{ye} = 15.39\ ksi$$

$$\lambda = \frac{b}{t} = 10.3$$

$$\lambda_{hd} = 0.65 \cdot \sqrt{\frac{E}{F_{ye}}} = 0.65 \cdot \sqrt{\frac{29000\ ksi}{62.5\ ksi}} = 14.0$$

Expected strengths and yield deformations

$$P_{ye} = F_{ye} \cdot A_g = 62.5\ ksi \cdot 6.58\ in^2 = 411.3\ k$$

$$P_{ce} = F_{cre} \cdot A_g = 15.39\ ksi \cdot 6.58\ in^2 = 101.3\ k$$

$$\Delta_T = \frac{(P_{ye} \cdot L_c)}{A_g \cdot E} = \frac{(411.3\ k \cdot 237.5\ in.)}{6.58\ in^2 \cdot 29000\ ksi} = 0.51\ in.$$

$$\Delta_C = \frac{(P_{ce} \cdot L_c)}{A_g \cdot E} = \frac{(101.3\ k \cdot 237.5\ in.)}{6.58\ in^2 \cdot 29000\ ksi} = 0.13\ in$$

Nonlinear Analysis

For tension of a rectangular HSS brace:

$$n = 4.7 \cdot \left(\frac{\lambda}{\lambda_{hd}}\right)^{-0.99} \cdot \left(\frac{\left(\frac{L_c}{r}\right)}{\sqrt{\frac{E}{F_{ye}}}}\right)^{0.24} = 4.7 \cdot \left(\frac{10.3}{14.0}\right)^{-0.99} \left(\frac{\left(\frac{237.5\ in.}{1.86\ in.}\right)}{\sqrt{\frac{29000\ ksi}{62.5\ ksi}}}\right)^{0.24} = 9.76$$

For compression of a rectangular HSS brace:

$$n = 3.0 \cdot \left(\frac{\lambda}{\lambda_{hd}}\right)^{-0.96} \cdot \left(\frac{\left(\frac{L_c}{r}\right)}{\sqrt{\frac{E}{F_{ye}}}}\right)^{1.0} = 3.0 \cdot \left(\frac{10.3}{14.0}\right)^{-0.96} \cdot \left(\frac{\left(\frac{237.5\ in.}{1.86\ in.}\right)}{\sqrt{\frac{29000\ ksi}{62.5\ ksi}}}\right)^{1.0} = 23.88$$

For tension of a rectangular HSS brace:

$d = n \cdot \Delta_T = 9.76 \cdot 0.53\ in. = 5.00\ in.$

$f = 1.0$

$f \cdot P_{ye} = 1.0 \cdot P_{ye} = 1.0 \cdot 411.3\ k = 411.3\ k$

Acceptance Criteria:

IO: $1.5 \cdot \Delta_T = 1.5 \cdot 0.51\ in. = 0.77\ in.$

LS: $0.7 \cdot n \cdot \Delta_T = 0.7 \cdot 9.76 \cdot 0.51\ in. = 3.50\ in$

CP: $n \cdot \Delta_T = 9.76 \cdot 0.51\ in. = 5.00\ in.$

For compression of a rectangular HSS brace:

$d = n \cdot \Delta_C = 23.88 \cdot 0.13\ in. = 3.01\ in.$

$f = 0.2$

$f \cdot P_{ce} = 0.2 \cdot P_{ce} = 0.2 \cdot 101.3\ k = 20.3\ k$

Acceptance Criteria:

IO: $1.5 \cdot \Delta_C = 1.5 \cdot 0.13\ in. = 0.19\ in.$

LS: $0.7 \cdot n \cdot \Delta_C = 0.7 \cdot 23.88 \cdot 0.13\ in. = 2.11\ in.$

CP: $n \cdot \Delta_C = 23.88 \cdot 0.13\ in. = 3.10\ in.$

Modelling Parameters and Predicted Performance

Action	Modeling Parameters		Performance Level Criteria		
	d (in.)	$f \cdot P\ (k)$	IO (in.)	LS (in.)	CP (in.)
Tension	5.00	411.3	0.77	3.50	5.00
Compression	3.01	20.3	0.19	2.11	3.01

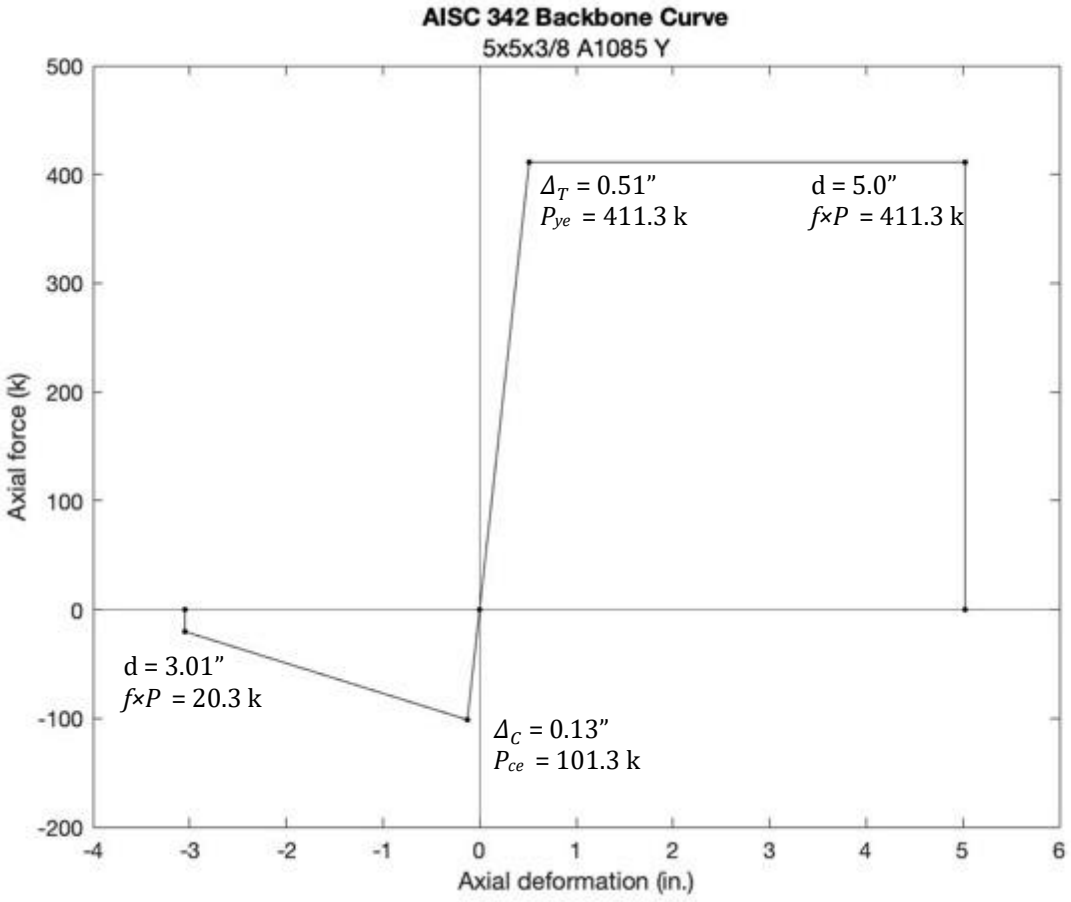
AISC 342 Backbone Curve
5x5x3/8 A1085 Y
Axial force (k)
Axial deformation (in.)
500
400
300
200
100
0
-100
-200
-4
-3
-2
-1
0
1
2
3
4
5
6
Δ_T = 0.51"
P_{ye} = 411.3 k
d = 5.0"
$f \times P$ = 411.3 k
d = 3.01"
$f \times P$ = 20.3 k
Δ_C = 0.13"
P_{ce} = 101.3 k

APPENDIX 3: MATERIAL PROPERTIES

A3.1 – Tension Coupon Information and Results

			Thickness				Width				Cross Sectional Area (in^2)	Yield		Ultimate		Elongation			Average
Producer	Material	Shape	Thickness 1 (in.)	Thickness 2 (in.)	Thickness 3 (in.)	Avg Thickness (in.)	Width 1 (in.)	Width 2 (in.)	Width 3 (in.)	Avg Width (in.)		Stress (ksi)	Average (ksi)	Stress (ksi)	Average (ksi)	Initial Gauge Length (in.)	Final Gauge Length (in.)	Percent Elongation	Percent Elongation
YELLOW	A500	5x5x3/8	0.344	0.344	0.344	0.344	1.497	1.498	1.497	1.497	0.515	65.07	65.38	72.48	71.86	2.07	2.71	30.95	30.79
			0.344	0.343	0.342	0.343	1.499	1.496	1.497	1.497	0.514	65.69		71.23		2.10	2.74	30.63	
YELLOW	A1085	5x5x3/8	0.366	0.362	0.358	0.359	1.502	1.502	1.5	1.501	0.539	65.34	66.04	74.84	74.62	1.79	2.37	32.18	32.83
			0.363	0.361	0.362	0.362	1.496	1.496	1.495	1.496	0.541	66.74		74.40		1.85	2.47	33.48	
RED	A500	6x6x5/16	0.29	0.29	0.289	0.290	1.498	1.497	1.498	1.498	0.434	60.2	57.37	74.23	72.77	2.06	2.78	34.77	34.65
			0.289	0.289	0.289	0.289	1.492	1.492	1.491	1.492	0.431	54.54		71.32		2.08	2.80	34.52	
YELLOW	A1085	6x6x5/16	0.309	0.309	0.308	0.309	1.505	1.504	1.504	1.504	0.464	62.62	62.07	71.72	71.93	2.05	2.77	35.07	34.11
			0.306	0.305	0.306	0.306	1.492	1.493	1.492	1.492	0.456	61.52		72.14		2.07	2.75	33.15	
RED	A500	6x6x3/8	0.353	0.353	0.354	0.353	1.496	1.496	1.495	1.496	0.528	62.43	61.19	76.46	76.36	2.06	2.78	35.42	35.36
			0.352	0.354	0.355	0.354	1.494	1.494	1.494	1.494	0.528	59.95		76.27		2.04	2.76	35.31	
YELLOW	A1085	6x6x3/8	0.369	0.367	0.368	0.368	1.496	1.497	1.497	1.497	0.551	66.9	66.81	72.85	72.64	2.05	2.68	31.08	31.86
			0.37	0.371	0.368	0.370	1.498	1.498	1.498	1.498	0.554	66.72		72.43		2.06	2.73	32.64	
RED	A500	6x6x1/2	0.466	0.462	0.459	0.462	1.495	1.495	1.494	1.495	0.691	63.59	62.84	68.30	67.05	2.06	2.71	31.46	33.48
			0.457	0.46	0.461	0.459	1.493	1.494	1.495	1.494	0.686	62.09		65.81		2.07	2.81	35.49	
YELLOW	A1085	6x6x1/2	0.487	0.484	0.483	0.485	1.504	1.502	1.503	1.503	0.728	67.6	67.85	71.61	71.96	2.07	-	-	34.88
			0.486	0.485	0.487	0.486	1.52	1.522	1.521	1.521	0.739	68.1		72.31		2.06	2.78	34.88	
YELLOW	A500	7x7x5/16	0.29	0.293	0.289	0.291	1.496	1.497	1.498	1.497	0.435	61.76	62.71	70.14	70.02	2.06	2.64	28.53	31.16
			0.294	0.292	0.292	0.293	1.497	1.497	1.498	1.497	0.438	63.66		69.89		2.07	2.76	33.79	
YELLOW	A1085	7x7x5/16	0.303	0.304	0.304	0.304	1.495	1.496	1.495	1.495	0.454	57.14	57.695	64.08	64.13	LASER EXT ISSUE			33.12
			0.302	0.302	0.302	0.302	1.498	1.502	1.502	1.501	0.453	58.25		64.18		2.08	2.77	33.12	
YELLOW	A500	7x7x3/8	0.341	0.341	0.342	0.341	1.495	1.496	1.495	1.495	0.510	62.03	61.35	71.80	72.19	2.10	2.74	30.59	30.76
			0.342	0.342	0.341	0.342	1.493	1.494	1.493	1.493	0.510	60.67		72.57		2.07	2.71	30.93	
YELLOW	A1085	7x7x3/8	0.366	0.365	0.369	0.367	1.497	1.498	1.498	1.498	0.549	62.19	61.89	70.19	70.07	2.12	2.79	31.32	31.32
			0.362	0.363	0.365	0.363	1.491	1.492	1.491	1.491	0.542	61.58		69.94		LASER EXT ISSUE			
BLUE	A500	7x7x1/2	0.457	0.457	0.457	0.457	1.496	1.496	1.496	1.496	0.684	58.09	57.82	69.14	69.14	2.10	2.73	29.90	29.60
			0.457	0.455	0.455	0.456	1.495	1.496	1.497	1.496	0.682	57.54		69.14		2.09	2.71	29.30	
YELLOW	A1085	7x7x1/2	0.48	0.483	0.478	0.480	1.495	1.496	1.495	1.495	0.718	63.74	64.38	71.98	71.68	2.06	2.75	33.25	32.70
			0.486	0.486	0.486	0.486	1.495	1.496	1.497	1.496	0.727	65.01		71.37		2.08	2.75	32.15	
WHITE	A500	8x8x3/8	0.345	0.345	0.345	0.345	1.5	1.499	1.499	1.499	0.517	66.02	66.19	75.67	76.52	2.03	2.75	35.18	34.44
			0.348	0.348	0.346	0.347	1.49	1.492	1.492	1.491	0.518	66.36		77.36		2.06	2.75	33.69	
YELLOW	A1085	8x8x3/8	0.341	0.342	0.341	0.341	1.497	1.496	1.499	1.497	0.511	60.61	60.37	73.69	72.12	2.04	2.75	35.08	34.20
			0.342	0.344	0.343	0.343	1.494	1.495	1.495	1.495	0.513	60.12		70.55		2.08	2.77	33.33	
WHITE	A500	8x8x1/2	0.46	0.462	0.46	0.461	1.498	1.499	1.499	1.499	0.690	65.92	65.47	72.04	72.01	2.09	2.78	33.12	34.27
			0.457	0.457	0.457	0.457	1.495	1.495	1.494	1.495	0.683	65.02		71.98		2.08	2.82	35.43	
YELLOW	A1085	8x8x1/2	0.481	0.484	0.482	0.482	1.492	1.493	1.493	1.493	0.720	62.26	64.42	74.53	75.43	2.11	2.80	32.83	32.23
			0.485	0.484	0.484	0.484	1.498	1.495	1.495	1.496	0.725	66.57		76.33		2.08	2.74	31.64	
WHITE	A500	10x10x3/8	0.349	0.349	0.35	0.349	1.494	1.494	1.495	1.494	0.522	60.93	59.02	70.61	69.45	2.11	2.75	30.11	34.20
			0.349	0.349	0.349	0.349	1.494	1.494	1.494	1.494	0.521	57.11		68.30		2.07	2.86	38.29	
YELLOW	A1085	10x10x3/8	0.362	0.363	0.371	0.365	1.498	1.498	1.499	1.498	0.547	58.07	58.34	70.47	73.76	2.06	2.77	34.22	34.94
			0.36	0.362	0.364	0.362	1.495	1.497	1.495	1.496	0.541	58.61		77.05		2.08	2.83	35.66	

A3.2 – Yield Strength Properties

HSS Section	Measured Yield Stress $F_{y,m}$ (ksi)	Measured Yield Strength Ratio $R_{y,meas}$	Expected Yield Stress $F_{y,nom}R_{y,nom}$ (ksi)
5x5x3/8 A500 Y	65.38	1.31	65
5x5x3/8 A1085 Y	66.04	1.32	62.5
6x6x5/16 A500 R	57.37	1.15	65
6x6x5/16 A1085 Y	62.07	1.24	62.5
6x6x3/8 A500 R	61.19	1.22	65
6x6x3/8 A1085 Y	66.81	1.34	62.5
6x6x1/2 A500 R	62.84	1.26	65
6x6x1/2 A1085 Y	67.85	1.36	62.5
7x7x5/16 A500 Y	62.71	1.25	65
7x7x5/16 A1085 Y	57.70	1.15	62.5
7x7x3/8 A500 Y	61.35	1.23	65
7x7x3/8 A1085 Y	61.89	1.24	62.5
7x7x1/2 A500 B	57.82	1.16	65
7x7x1/2 A1085 Y	64.38	1.29	62.5
8x8x3/8 A500 W	66.19	1.32	65
8x8x3/8 A1085 Y	60.37	1.21	62.5
8x8x1/2 A500 W	65.47	1.31	65
8x8x1/2 A1085 Y	64.42	1.29	62.5
10x10x3/8 A500 W	59.02	1.18	65
10x10x3/8 A1085 Y	58.34	1.17	62.5

		Measured Yield Stress (ksi)		Measured Yield Strength Ratio	
	# of Specimens	Average	Standard Deviation	Average	Standard Deviation
All Specimens	20	62.46	3.30	1.25	0.07
A500 - ALL	10	61.93	3.18	1.24	0.06
A1085 - Y	10	62.98	3.50	1.26	0.07
A500 - Y	3	63.15	2.05	1.26	0.04
A500 - R	3	60.47	2.81	1.21	0.06
A500 - W	3	63.56	3.95	1.27	0.08
A500 - B	1	57.82	-	1.16	-

A3.3 – Charpy V-Notch Test Results

Temperature	40 deg F				Sub-Size: 7.5 mm
Setting	High Energy				Sub-Size: 5 mm
			TEST SERIES 1		
			CVN Specimen Size	Absorbed Energy (ft-lbs)	
Producer	Material	Shape	Thickness (mm)	Individual	Average
YELLOW	A500	5x5x3/8	7.5	11.5 12.5 14.5	12.8
YELLOW	A1085	5x5x3/8	7.5	19.5 20.5 16.5	18.8
RED	A500	6x6x5/16	5	42 41 39.5	40.8
YELLOW	A1085	6x6x5/16	5	21 22.5 25.5	23.0
RED	A500	6x6x3/8	7.5	40 47 40.5	42.5
YELLOW	A1085	6x6x3/8	7.5	11 23 22	18.7
RED	A500	6x6x1/2	10	113.5* 117.5* 119*	120+
YELLOW	A1085	6x6x1/2	10	27 24.5 32	27.8
YELLOW	A500	7x7x5/16	5	17.5 17.5 12	15.7
YELLOW	A1085	7x7x5/16	5	21 22 12.5	18.5
YELLOW	A500	7x7x3/8	7.5	13.5 15.5 14	14.3
YELLOW	A1085	7x7x3/8	7.5	18.5 16.5 17	17.3
BLUE	A500	7x7x1/2	10	45.5 42.5 38	42.0
YELLOW	A1085	7x7x1/2	10	29 29 28	28.7
WHITE	A500	8x8x3/8	7.5	73 62 61.5	65.5
YELLOW	A1085	8x8x3/8	7.5	8.5 7 10	8.5
WHITE	A500	8x8x1/2	10	49.5 81 71.5	67.3
YELLOW	A1085	8x8x1/2	10	45 38 38	40.3
WHITE	A500	10x10x3/8	7.5	112.5* 113.5* 115.4*	120+
YELLOW	A1085	10x10x3/8	7.5	20 20.5 21.5	20.7
Yellow	A1085 - CORNER	8x8x1/2	10	98.5 102 68	89.5
White	A500 - CORNER	8x8x1/2	10	112.5* 115* 70	120+

A3.4 – Wall Thickness Measurements

Wall Thickness Measurements (in.)

Test Specimen	S Top 1	S Top 2	S Bot 1	S Bot 2	S W 1	S W 2	S E 1	S E 2	N Top 1	N Top 2	N Bot 1	N Bot 2	N W 1	N W 2	N E 1	N E 2	Avg Thickness	Nominal
10x10x3/8 A500 W	0.349	0.351	0.351	0.352	0.35	0.349	0.348	0.349	0.344	0.346	0.342	0.344	0.342	0.343	0.345	0.346	**0.347**	**0.349**
10x10x3/8 A1085 Y	0.367	0.369	0.365	0.366	0.367	0.366	0.365	0.366			Plasma Cut - Inaccurate Measurements						**0.366**	**0.375**
8x8x1/2 A500 W	0.464	0.462	0.461	0.46	0.46	0.461	0.463	0.459			Plasma Cut - Inaccurate Measurements						**0.461**	**0.465**
8x8x1/2 A1085 Y	0.488	0.491	0.491	0.489	0.487	0.485	0.484	0.487			Plasma Cut - Inaccurate Measurements						**0.488**	**0.5**
8x8x3/8 A500 W	0.3507	0.3503	0.3501	0.347	0.348	0.349	0.348	0.3501	0.3505	0.3504	0.3503	0.3506	0.3503	0.3508	0.3501	0.3502	**0.350**	**0.349**
8x8x3/8 A1085 Y	0.373	0.369	0.372	0.369	0.37	0.368	0.367	0.369			Plasma Cut - Inaccurate Measurements						**0.370**	**0.375**
7x7x1/2 A500 B	0.468	0.469	0.471	0.472	0.46	0.457	0.457	0.46	0.471	0.47	0.469	0.471	0.455	0.46	0.454	0.457	**0.464**	**0.465**
7x7x1/2 A1085 Y	0.484	0.485	0.486	0.48	0.485	0.486	0.483	0.485	0.482	0.483	0.481	0.485	0.484	0.483	0.483	0.484	**0.484**	**0.5**
7x7x3/8 A500 Y	0.342	0.34	0.343	0.341	0.34	0.342	0.342	0.341	0.34	0.342	0.343	0.34	0.343	0.343	0.346	0.343	**0.342**	**0.349**
7x7x3/8 A1085 Y	0.365	0.367	0.364	0.364	0.366	0.364	0.361	0.362	0.367	0.365	0.363	0.363	0.37	0.369	0.364	0.364	**0.365**	**0.375**
7x7x5/16 A500 Y	0.285	0.283	0.293	0.295	0.29	0.286	0.29	0.292	0.289	0.29	0.29	0.292	0.294	0.294	0.294	0.288	**0.290**	**0.291**
7x7x5/16 A1085 Y	0.298	0.296	0.302	0.304	0.307	0.302	0.307	0.311	0.303	0.303	0.312	0.306	0.307	0.306	0.31	0.31	**0.305**	**0.313**
6x6x1/2 A500 R			Plasma Cut - Inaccurate Measurements						0.481		0.477		0.48		0.479		**0.479**	**0.465**
6x6x1/2 A1085 Y			Plasma Cut - Inaccurate Measurements						0.491		0.495		0.492		0.486		**0.491**	**0.5**
6x6x3/8 A500 R			Plasma Cut - Inaccurate Measurements						0.369		0.364		0.366		0.368		**0.367**	**0.349**
6x6x3/8 A1085 Y			Plasma Cut - Inaccurate Measurements						0.3715		0.373		0.3745		0.3735		**0.373**	**0.375**
6x6x5/16 A500 R	0.303		0.3035		0.3045		0.307				Plasma Cut - Inaccurate Measurements						**0.305**	**0.291**
6x6x5/16 A1085 Y	0.312		0.314		0.315		0.309				Plasma Cut - Inaccurate Measurements						**0.313**	**0.313**
5x5x3/8 A500 Y			Plasma Cut - Inaccurate Measurements						0.362		0.36		0.358		0.358		**0.360**	**0.349**
5x5x3/8 A1085 Y			Plasma Cut - Inaccurate Measurements						0.379		0.38		0.371		0.375		**0.376**	**0.375**

A3.5 – Corner Radius Measurements

Test Specimen	Corner Radius Measurments (in.)								Average Radius (in.)	Radius / Thickness
10x10x3/8 A500 W	0.69	0.72	0.69	0.72	0.81	0.81	0.84	0.84	**0.77**	**2.19**
10x10x3/8 A1085 Y	0.88	0.88	0.88	0.88	0.94	0.88	0.91	0.90	**0.89**	**2.37**
8x8x1/2 A500 W	0.88	0.84	0.91	0.88	0.88	0.91	0.91	0.91	**0.89**	**1.91**
8x8x1/2 A1085 Y	1.13	1.16	1.16	1.16	1.13	1.13	1.16	1.13	**1.14**	**2.28**
8x8x3/8 A500 W	0.66	0.69	0.81	0.78	0.78	0.81	0.97	0.91	**0.80**	**2.29**
8x8x3/8 A1085 Y	1.06	1.09	1.13	1.09	1.00	1.03	1.06	1.03	**1.06**	**2.83**
7x7x1/2 A500 B	0.84	0.81	0.84	0.88	1.00	1.03	1.06	1.09	**0.95**	**2.03**
7x7x1/2 A1085 Y	1.03	1.03	1.09	1.13	0.97	1.00	1.06	1.06	**1.05**	**2.09**
7x7x3/8 A500 Y	0.78	0.81	0.81	0.78	0.84	0.88	0.88	0.88	**0.83**	**2.38**
7x7x3/8 A1085 Y	0.84	0.84	0.88	0.94	0.97	0.97			**0.91**	**2.42**
7x7x5/16 A500 Y	0.72	0.75	0.66	0.69	0.63	0.66	0.594	0.594	**0.66**	**2.27**
7x7x5/16 A1085 Y	0.69	0.72	0.72	0.63	0.63	0.63			**0.67**	**2.13**
6x6x1/2 A500 R	1.09	1.13	1.13	1.09	0.84	0.88	0.88	0.84	**0.98**	**2.12**
6x6x1/2 A1085 Y	0.84	0.84	0.88	0.81	0.81	0.81			**0.83**	**1.67**
6x6x3/8 A500 R	0.66	0.63	0.81	0.84	0.66	0.66	0.88	0.88	**0.75**	**2.15**
6x6x3/8 A1085 Y	0.75	0.75	0.69	0.66	0.75	0.75	0.69	0.69	**0.71**	**1.91**
6x6x5/16 A500 R	0.56	0.59	0.63	0.63	0.56	0.56	0.59	0.59	**0.59**	**2.03**
6x6x5/16 A1085 Y	0.56	0.59	0.66	0.69	0.75	0.72	0.72	0.72	**0.68**	**2.16**
5x5x3/8 A500 Y	0.72	0.72	0.75	0.78	0.81	0.78			**0.76**	**2.18**
5x5x3/8 A1085 Y	0.69	0.72	0.69	0.78	0.75	0.75			**0.73**	**1.94**

APPENDIX 4: MATLAB SCRIPTS

A4.1 – Data Trimming Script

```
%% INPUT INFORMATION %%
%Raw Data File Name
raw_data = 'Output Data.txt';  %enter raw data file name

%Brace Info
fy = 50;                %Approx yield stress of specimen
Ry = 1.3;               %Ry_A500 = 1.3  Ry_A1085 = 1.25
A_s = 13.2;             %Area of steel

%Trimming Tolerances
tol1 = 0.00000;          %For targets 1-3
tol2 = 0.00000;          %For targets 4-6
tol3 = 0.00000;          %For targets > 6

%New Data File name
new_data_file_name = '10x10x3_8_A1085_Y_Trim.txt';

%%%%%% END DATA INPUT %%%%%%%%%%%%%%%%%%%%%%%%%%%%%%%%%%%%%%%%%%%%%%%%%%%%


%% Load data
data = readmatrix(raw_data);

n = size(data,1);                %number of rows
m = size(data,2);                %number of columns


%% Find Peaks
small_Act_Disp = -1*data(:,9);   % 350k actuator displacement
point = data(:,6);               % Data count

[pks,loc] =
findpeaks(small_Act_Disp,point,'MinPeakProminence',.1,'MinPeakDistance',500);
peaks = [pks, loc];              % Find peaks and corresponding data count

t = size(peaks,1);               % Number of rows in peaks table

for i = 1:t                      % Formatting of data in table
    count(i) = [i]';
end
idx = count.';

for i = 1:t                      % Format target displacements in table
    target(i) = ceil(idx(i)/2);
end
target = target.';
peaks = [idx, pks, loc, target];

%% Add column for target displacement to data matrix
```

```
for i = 1:n-1
    for j = 1:t-1
        if data(i,6) > loc(j)
           data(i,40) = target(j);
        end
    end
end

for i = 1:n-1
    if data(i,6) < loc(1)
       data(i,40) = 1;
    end
end

%% Remove unwanted data during holds
delete = zeros(n,1);
j = 1;

% Assign tolerances 1,2,3 manually to delete data during holds
for e = 1:n-1
    if  data(e,40) <= 3                          % Trimming  first 3 targets
        diff = abs(data(e,9) - data(e-1,9));
        if diff < tol1
            delete(j,1) = e;
            j = j+1;
        end

    elseif (4 <= data(e,40)) && (data(e,40) <= 6)   %Trimming next targets
        diff = abs(data(e,9) - data(e-1,9));
        if diff < tol2
            delete(j,1) = e;
            j = j+1;
        end
    else
        diff = abs(data(e,9) - data(e-1,9));       % Trimming other targets
        if diff < tol3
            delete(j,1) = e;
            j = j+1;
        end
    end
end
delete = delete(1:j-1,1);
data([delete],:)= [];                    % Delete rows of data during holds



%% Write trimmed data to a new file, use for corrections
%     Make sure trimming parameters are working properly before exporting
%     trimmed data
%         Modify  tolerances, cycle numbers, etc if necessary
%
%           Format: 'SizexSizexThick_ness_Material_Trim'

writematrix(data, new_data_file_name)  %Write trimmed data to new text file
```

A4.2 – Data Correction Script

```
%% INPUT INFORMATION %%%%%%%%%%%%%%%%%%%%%%%%%%%%%%%%%%%%%%%%%%%%%%%%%%%%

%Trimmed Data File Name
input_data = '10x10x3_8_A1085_Y_Trim.txt';  %enter raw data file name

%Instrument Location Info
Dist_SP_SGPs = 10;    %Distance between gusset plate transverse string pots
GP_t = 0.75;               %Gusset plate width (in)
GP_Gap = 3*GP_t;           %Gap between gusset and connection plates
GP_ecc = 0.375;            %Gusset plate eccentricity (in)

NGP_SP_distx = 2;       %Horizontal distance from east face of brace to
string pot - North
NGP_SP_disty = 2.875;   %Longitudinal distance from end of brace to string
pot end - North

SGP_SP_distx = 2;       %Horizontal distance from east face of brace to
string pot - South
SGP_SP_disty = 2.875;   %Longitudinal distance from end of brace to string
pot end - South

brace_width = 10;       %Width of test specimen (in)

%Trimming Tolerances
tol1 = 0.0025;        % South Gusset Plate 1
tol2 = 0.0025;        % South Gusset Plate 2
tol3 = 0.01;          % Axial Displacement
tol4 = 0.1;           % Out of Plane Displacement

%New Data File name
new_data_file_name = '10x10x3_8_A1085_Y_Trim_Corr.txt';

%%%%%% END DATA INPUT %%%%%%%%%%%%%%%%%%%%%%%%%%%%%%%%%%%%%%%%%%%%%%%%%%%%

%% Load data
data = readmatrix(input_data);

n = size(data,1);            % Number of rows
m = size(data,2);            % Number of columns

for i = 1:n                  % Set up indexing
    data(i,6) = i;
end

%% Trim Gusset Plate Data
% Makes processing data easier
% South Gusset Plate 1
j = 1;
delete = zeros(n,1);
for i = 1:n-1
    diff = abs(data(i,13)-data(i+1,13));    % Trim spikes in data
    if diff > tol1                          % Assign tolerance 1 manually
        delete(j,1) = i;
```

```
        j = j+1;
    end
end
delete = delete(1:j-1,1);
data([delete],:)= [];

%South Gusset Plate 2
n = size(data,1);
j = 1;
delete2 = zeros(n,1);
diff = zeros(n,1);
for i = 1:n-1
    diff = abs(data(i,23)-data(i+1,23));    % Trim spikes in data
    if diff > tol2                          % Assign tolerance 2 manually
        delete2(j,1) = i;
        j = j+1;
    end
end
delete2 = delete2(1:j-1,1);
data([delete2],:)= [];


%% Correct for Rigid Body Rotation

count = data(:,6);                  % Data count - used for indexing
small_Act_Disp = -1*data(:,9);      % 350k actuator displacement
small_Act_Load = -1*data(:,8);      % 350k actuator load

SP_Trans_SGP1 = data(:,13);         % Gusset plate displacement - base
SP_Trans_C1 = data(:,15);           % Brace OOP displacement - center 1
SP_Long_Brace = data(:,17);         % Brace axial displacement
SP_Long_Tot = data(:,18);           % Total axial dispalcement
SP_Trans_SGP2 = data(:,23);         % Gusset plate displacement - end
SP_Trans_C2 = data(:,24);           % Brace OOP displacement - center 2
Target = data(:,40);                % Target displacement number

n = size(data,1);                   % Create indexing vector
for i = 1:n
    count(i) = [i]';
end
idx = count.';


for i = 1:n

    if SP_Trans_SGP1(i) > SP_Trans_SGP2(i)   % Correct axial displacement
data if gusset plate is rotated
        data(i,41) = SP_Long_Brace(i);

    else
        SGP_Trans_Mvmt(i) = SP_Trans_SGP2(i) - SP_Trans_SGP1(i);
%Difference between transverse movement of gusset plate string pots

        SGP_Rotation(i) = atand(SGP_Trans_Mvmt(i) / Dist_SP_SGPs);
%Calculate rotation angle of south gusset plate
```

```
        SGP_CCW_Rot(i) = 360 - SGP_Rotation(i);       %CCW rotation to new SP
location

        % Assuming CR at mid-point of GP gap
        NGP_dist_CRx = brace_width/2 - GP_ecc + NGP_SP_distx; %Horiz distance
from center of rot. - North
        NGP_dist_CRy = GP_Gap/2 + NGP_SP_disty; %Longitudinal distance from
center of rot to SP - North

        SGP_dist_CRx = brace_width/2 - GP_ecc + SGP_SP_distx; %Horiz distance
from center of rot. - South
        SGP_dist_CRy = GP_Gap/2 + SGP_SP_disty; %Longitudinal distance from
center of rot to SP - South

        NewDist_N_CRtoSP_y(i) = NGP_dist_CRx * sind(SGP_CCW_Rot(i)) +
NGP_dist_CRy * cosd(SGP_CCW_Rot(i));
                    %Calculate new longitudinal distance from CR to string
pot-North

        RB_Mvmt_N(i) = NewDist_N_CRtoSP_y(i) - NGP_dist_CRy;
                    %Change in longitudinal distance between CR and SP - North

        NewDist_S_CRtoSP_y(i) = SGP_dist_CRx * sind(SGP_CCW_Rot(i)) +
SGP_dist_CRy * cosd(SGP_CCW_Rot(i));
                    %Calculate new longitudinal distance from CR to string
pot-South

        RB_Mvmt_S(i) = NewDist_S_CRtoSP_y(i) - SGP_dist_CRy;
                    %Change in longitudinal distance between CR and SP - South

        Total_RB_AxialEff(i) = RB_Mvmt_N(i) + RB_Mvmt_S(i);

        data(i,41) = SP_Long_Brace(i) - Total_RB_AxialEff(i);
    end

end


%% Trim Axial Displacement Data
%Redefine Data Vectors
Corrected_Long_Brace = data(:,41);
small_Act_Load = -1*data(:,8);
small_Act_Disp = -1*data(:,9);

j = 1;
delete3 = zeros(n,1);
diff = zeros(n,1);
for i = 1:n-4
    diff(i) = abs(Corrected_Long_Brace(i) - Corrected_Long_Brace(i+1));
    if diff(i) > tol3           % Remove spikes in axial disp. data
        delete3(j,1) = i;       % Set tolerance manually
        j = j+1;
    end
end
delete3 = delete3(1:j-1,1);
data([delete3],:)= [];
```

```
%% Trim OOP Displacement Data
SP_Trans_C1 = data(:,15);
SP_Trans_C2 = data(:,24);
SP_Trans_SGP1 = data(:,13);
Brace_OOP_Disp = (SP_Trans_C1 + SP_Trans_C2)/2 - SP_Trans_SGP1;
            % Calculate brace OOP displacement at center
j = 1;
n = size(data,1);
delete4 = zeros(n,1);
diff = zeros(n,1);
for i = 2:n             % Trim data to remove spikes in OOP disp. data
    diff(i) = abs(Brace_OOP_Disp(i) - Brace_OOP_Disp(i-1));
    if diff(i) > tol4 && i < n-6 %Keep Last few data points!
        delete4(j,1) = i;
        j = j+1;
        Brace_OOP_Disp(i) = (SP_Trans_C1(i)+SP_Trans_C2(i))/2;
    end

end
delete4 = delete4(1:j-1,1);
data([delete4],:)= [];


%% Axial Displacement Corrections
%Recreate idx vector
n = size(data,1);
count = data(:,6);
for i = 1:n
    count(i) = [i]';
end
idx = count;

%Calculate the corrections made
Corrected_Long_Brace = data(:,41);
SP_Long_Brace = data(:,17);
Corrections = Corrected_Long_Brace - SP_Long_Brace;

SP_Long_Brace = data(:,17);
SP_Long_Tot = data(:,18);

%% Write corrected data to a new file, use for test summary
% %% Write trimmed + corrected data to a new file, use for data analysis
%     % Make sure corrections  are working properly before exporting
%         % Modify  brace, gusset, eccentricity, string pot locations, etc
%
%           % Format: 'SizexSizexThick_ness_Material_Trim_Corr'
%
% writematrix(data,new_data_file_name)  %Write corrected data to new text
file
```

APPENDIX 5: TEST REPORTS

5x5x3/8 A500 Y Brace Test Summary

Test Name: 5x5x3/8 A500 Y
Test Date: 3/17/21

Brace Properties

Measured Yield Stress (ksi)	65.38	**Area (in²)**	6.18
Measured Ultimate Stress (ksi)	71.86	**Moment of Inertia (in⁴)**	21.7
Yield Load (kips)	416.8	**Corner Radius (in.)**	0.76
Critical Buckling Load (kips)	96.2	**Thickness - Nominal (in.)**	0.349
Percent Elongation - 2" (%)	30.79	**Thickness - Measured (in.)**	0.36
CVN Width (mm)	7.5	**Brace Compactness Ratio (b/t) - Nominal ***	11.3
CVN Absorbed Energy (ft-lbs)	12.8	**Brace Compactness Ratio (b/t) - Measured**	9.67
Brace Length (in.)	237.5	**Global Slenderness ratio (KL/r)**	127

Specimen Performance

Test Event	Axial Brace Displacement (in.)	Target Displacement (in.) (Cycle)	Force (kips)	$P / P_{Yield/Critical}$	
Peak Tension Load	1.92	2.25 (1)	432.5	1.04	Y
B1: Initial Global Buckling	-0.18	0.25 (1)	-95.3	-0.99	C
B2: Moderate Global Buckling	-1.0553	1.25 (1)	-56.3	-0.13	C
B3-T: Local Buckling	-4.38	4.75 (2)	-19.5	-0.05	C
B3-C: Striations & Tearing	4.89	5.25 (1)	386.0	0.93	Y
B4: Brace Fracture	5.13	5.75 (1)	116.0	0.28	Y

Key Observations

Cycle #	Displacement	Observations
15-16	1.75”	Bolt slip at first tension cycle - loud bang. SP_SGP_E fell off specimen, replaced immediately.
17-18	2.25”	Banging sounds observed during tension cycles, near peak tension Comp. cycle 1 - SP_L_Br caught on Optotrak string, fixed, use hold data for brace axial displacement here!
27-28	4.75”	Minor cupping observed at peak compressive cycles
29-30	5.25”	Cupping at peak compressive cycles, major cupping at cycle 30. Striations observed at peak tensile displacements.
31-32	5.75”	Fractured in tension during first cycle!

Test Results

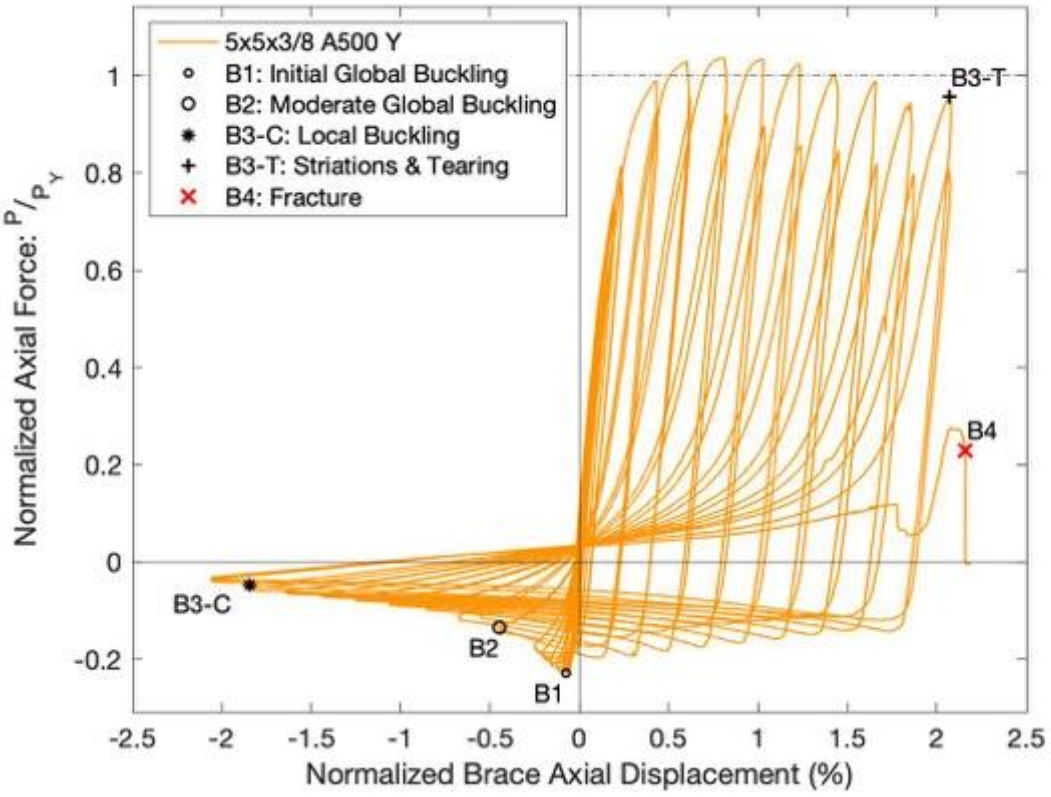

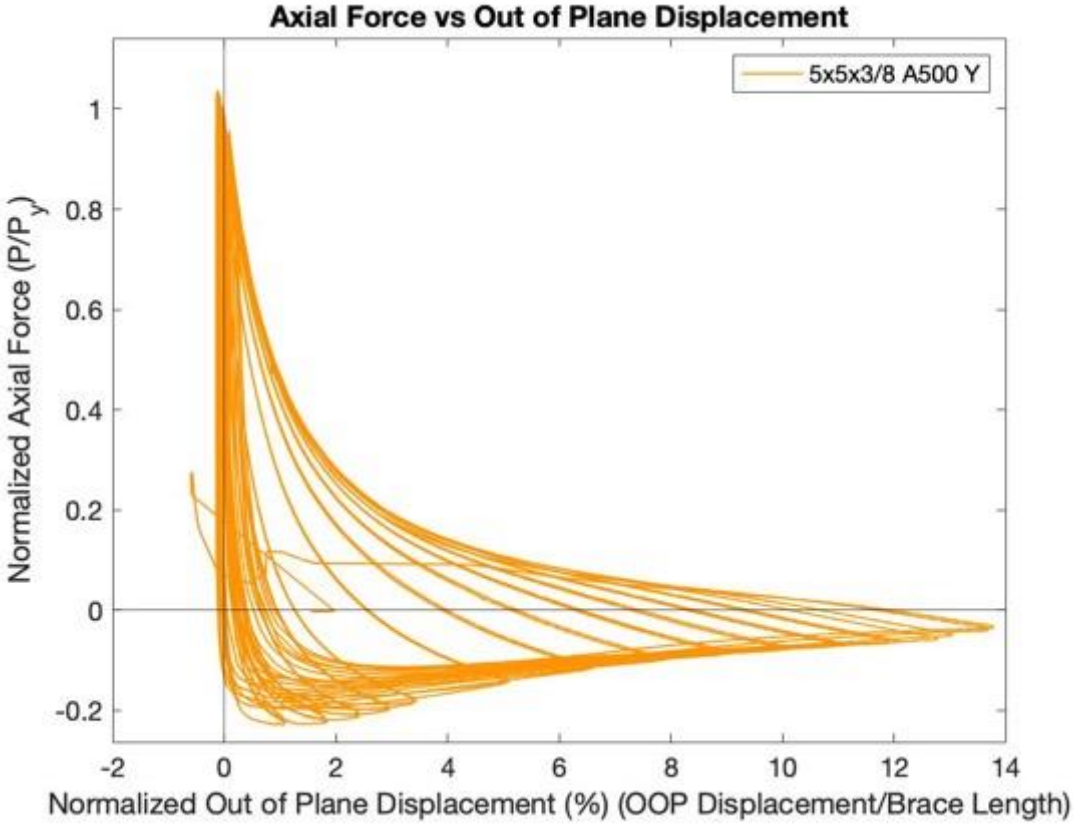
Axial Force vs Out of Plane Displacement
5x5x3/8 A500 Y
Normalized Axial Force (P/P_y)
1
0.8
0.6
0.4
0.2
0
-0.2
-2
0
2
4
6
8
10
12
14
Normalized Out of Plane Displacement (%) (OOP Displacement/Brace Length)

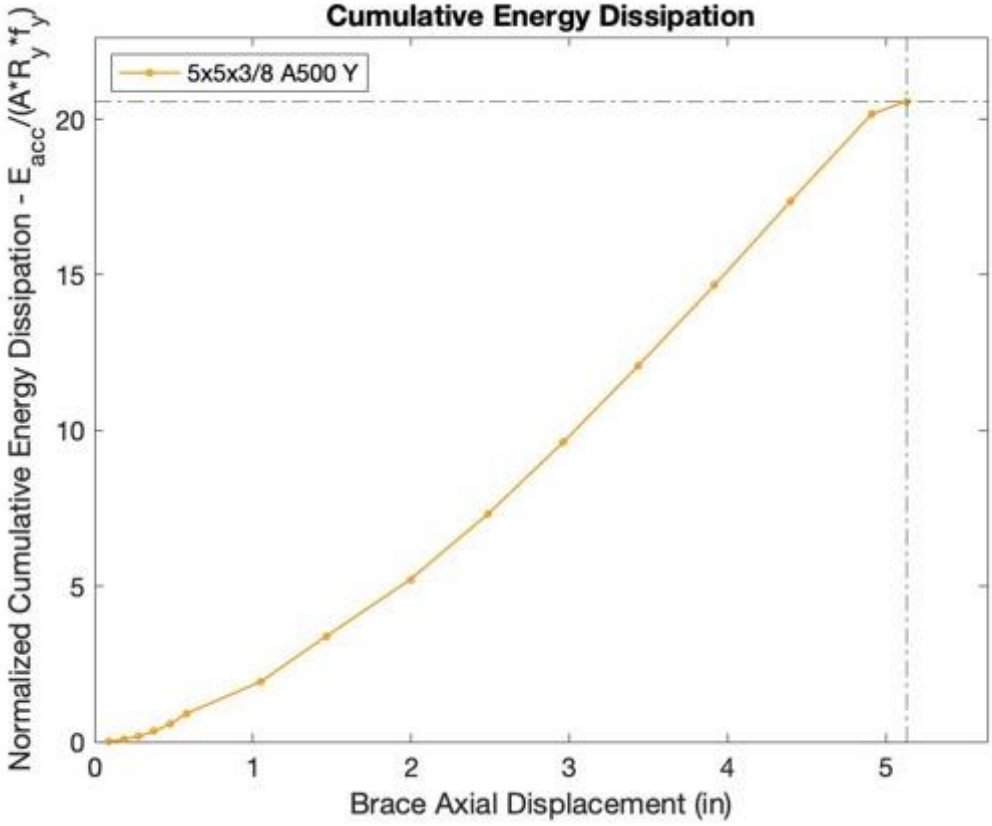
Cumulative Energy Dissipation
5x5x3/8 A500 Y
Normalized Cumulative Energy Dissipation - E_acc/(A*R_y*f_y)
20
15
10
5
0
0
1
2
3
4
5
Brace Axial Displacement (in)

Photos

Moderate cupping at center of brace: 5.25” cycles

Peak out of plane displacement: 5.25” cycles

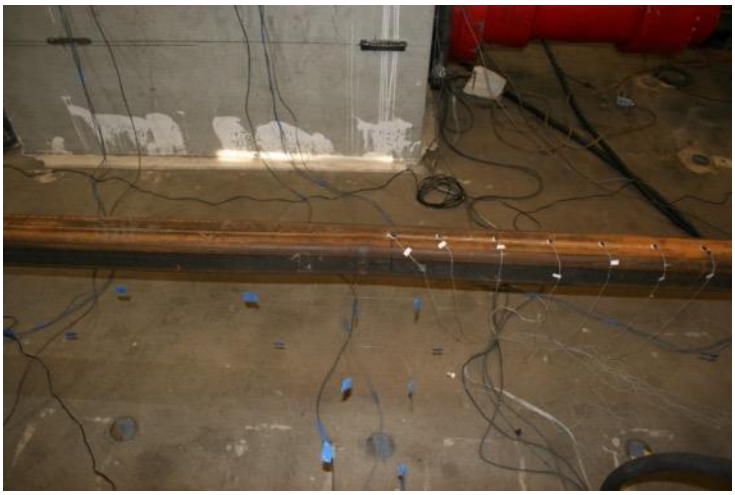

Striations beginning to develop at center of brace: 5.25” cycles

Specimen fractured in tension during first 5.75” cycle

5x5x3/8 A1085 Y Brace Test Summary

Test Name: 5x5x3/8 A1085 Y
Test Date: 4/2/21

Brace Properties

Measured Yield Stress (ksi)	66.04
Measured Ultimate Stress (ksi)	74.62
Yield Load (kips)	435.7
Critical Buckling Load (kips)	101.3
Percent Elongation - 2" (%)	32.83
CVN Width (mm)	7.5
CVN Absorbed Energy (ft-lbs)	18.8
Brace Length (in.)	237.5

Area (in²)	6.58
Moment of Inertia (in⁴)	22.8
Corner Radius (in.)	0.729
Thickness - Nominal (in.)	0.375
Thickness - Measured (in.)	0.376
Brace Compactness Ratio (b/t) - Nominal *	10.3
Brace Compactness Ratio (b/t) - Measured	9.42
Global Slenderness ratio (KL/r)	127.7

Specimen Performance

Test Event	Axial Brace Displacement (in.)	Target Displacement (in.) (Cycle)	Force (kips)	$P / P_{Yield/Critical}$	
Peak Tension Load	1.83	2.25 (1)	443.6	1.02	Y
B1: Initial Global Buckling	-0.19	0.25 (1)	-98.4	0.97	C
B2: Moderate Global Buckling	-1.26	1.25 (1)	-57.5	0.57	C
B3-T: Local Buckling	-5.01	5.25 (1)	-17.6	0.17	C
B3-C: Striations & Tearing	4.43	5.75 (2)	76.0	0.17	Y
B4: Brace Fracture	5.25	5.75 (2)	116.7	0.27	Y

Test Results

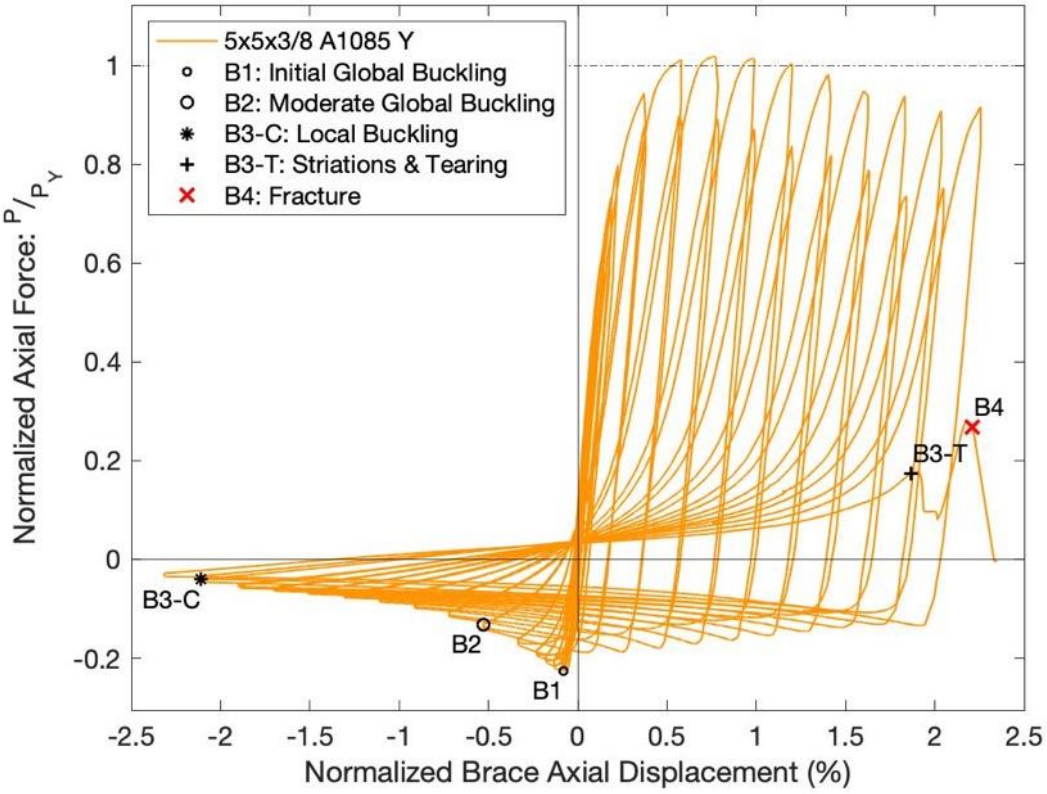

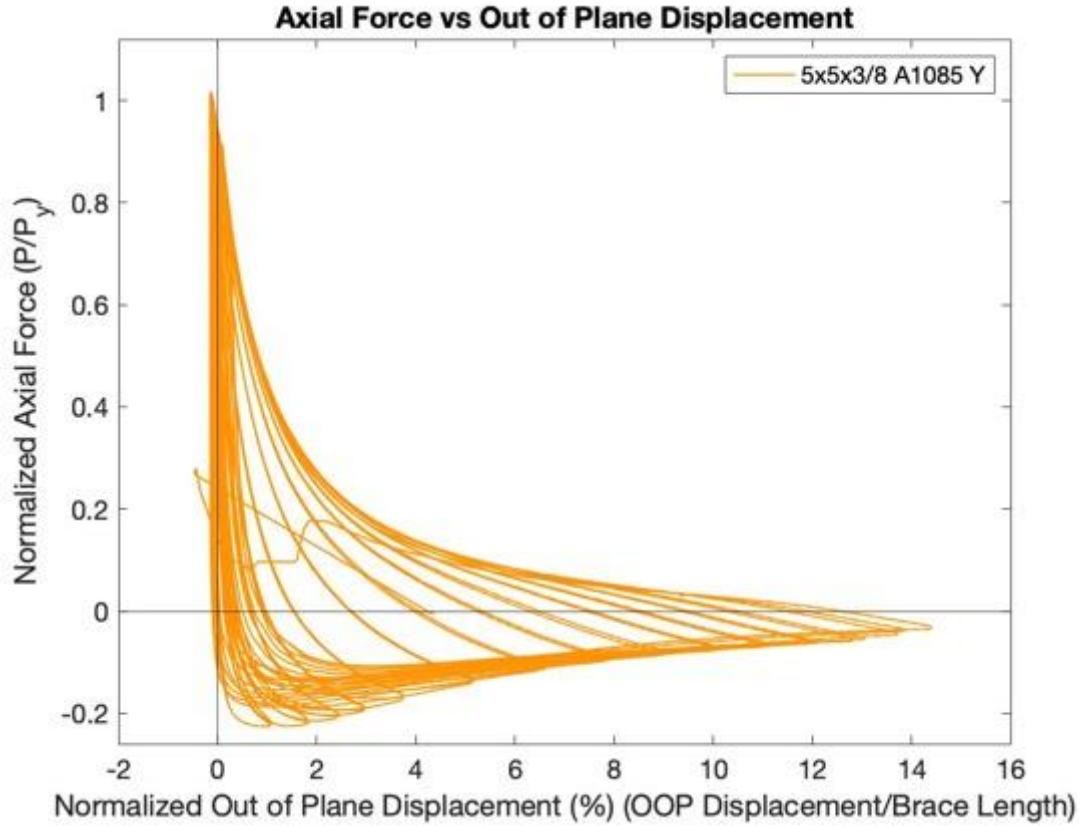

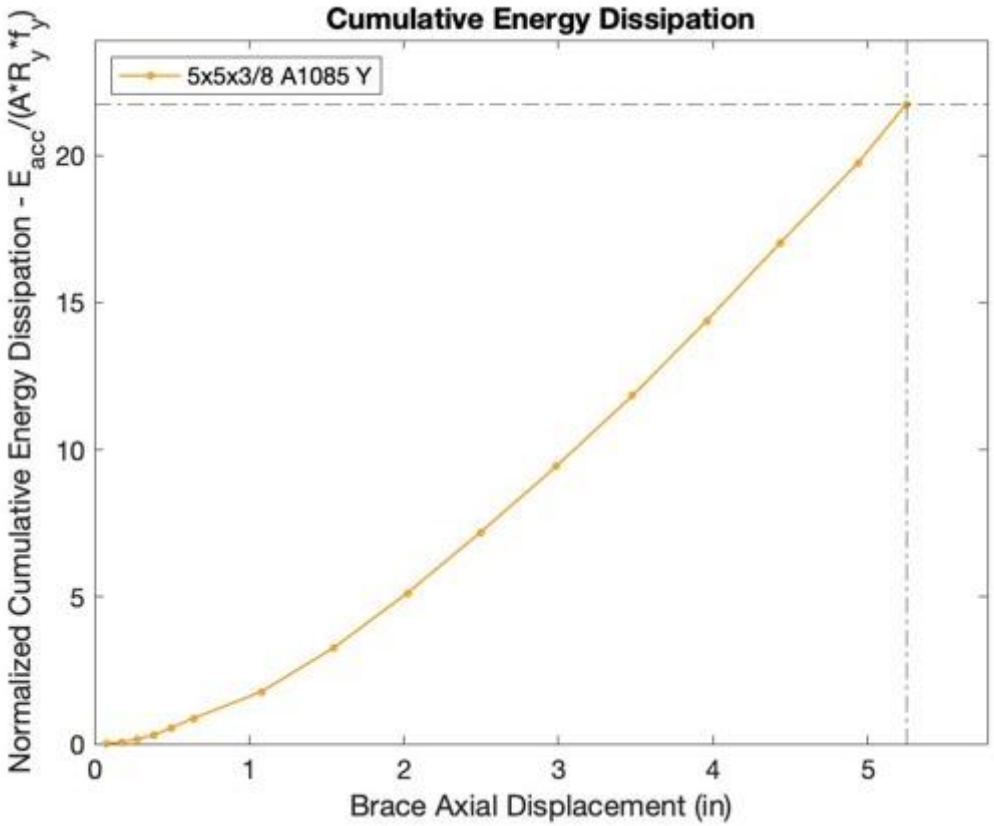

Key Observations

Cycle #	Displacement	Observations
11-12	0.75	Bolt slip first tension cycle - North gusset plate. Knocking/banging sounds when specimen in tension occurred during this cycle and beyond
15-16	1.75	Bolt slip first tension cycle - South gusset plate
27-28	4.75	Minor cupping observed at peak compressive displacements at the center of the specimen - east face
29-30	5.25	Moderate cupping observed at first peak compressive displacement Major cupping observed at second peak compressive displacement - cycle 30
31-32	5.75	Brace survived first tensile displacement - cycle 31 Major cupping observed at first peak compressive displacement - cycle 31 Brace tearing and fracture - second tensile displacement - cycle 32

Photos

Development of Tearing in Tension - 2nd cycle at 5.75”

Brace Fracture: 2nd Cycle at 5.75”

Peak Out of Plane Displacement: 5.75” Cycles

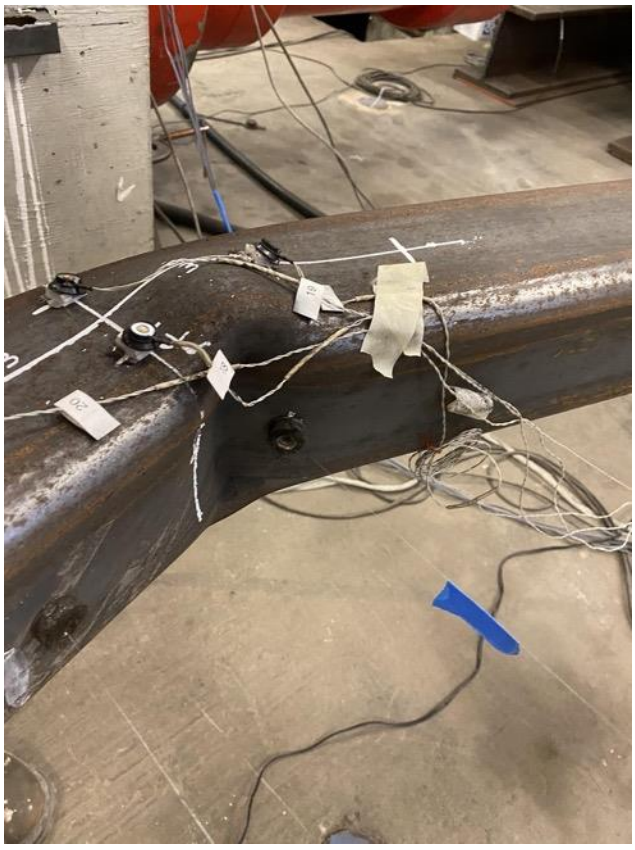

Cupping at Center of Specimen: 5.25” Cycles

6x6x5/16 A500 R Brace Test Summary

Test Name: 6x6x5/16 A500 R
Test Date: 4/7/2021

Brace Properties

Measured Yield Stress (ksi)	57.37
Measured Ultimate Stress (ksi)	72.77
Yield Load (kips)	386.6
Critical Buckling Load (kips)	152.7
Percent Elongation - 2" (%)	34.65
CVN Width (mm)	5
CVN Absorbed Energy (ft-lbs)	40.8
Brace Length (in.)	237.5

Area (in²)	6.43
Moment of Inertia (in⁴)	34.3
Corner Radius (in.)	0.59
Thickness - Nominal (in.)	0.291
Thickness - Measured (in.)	0.305
Brace Compactness Ratio (b/t) - Nominal *	17.6
Brace Compactness Ratio (b/t) - Measured	15.80
Global Slenderness ratio (KL/r)	102.8

Specimen Performance

Test Event	Axial Brace Displacement (in.)	Target Displacement (in.) (Cycle)	Force (kips)	$P / P_{Yield/Critical}$	
Peak Tension Load	1.85	2.25 (1)	409.7	1.06	Y
B1: Initial Global Buckling	-0.22	0.25 (1)	-125.8	0.82	C
B2: Moderate Global Buckling	-1.79	1.75 (1)	-52.8	0.35	C
B3-T: Local Buckling	-2.72	2.75 (2)	-30.1	0.20	C
B3-C: Striations & Tearing	2.45	3.25 (2)	252.0	0.65	Y
B4: Brace Fracture	2.93	3.75 (1)	99.6	0.26	Y

Observations

Cycle #	Displacement	Observations
15-16	1.75	Bolt slip at first tension cycle (15): ~⅛" Bolt slip at north and south gusset plates Knocking/banging sounds in tension - observed in all future cycles
19-20	2.75	Minor cupping observed at first compressive displacement - minimal at East/West faces Local cupping observed at second compressive displacement - center of cupping: 4.5" north of brace center

21-22	3.25	Major cupping at first and second peak compressive displacements Tearing began to occur when specimen in tension during second cycle (22) After tearing in specimen - buckling direction switched to east due to tearing initiating on the east face of the specimen. Out of plane string pots at quarter points and center of specimen out of range - manually measured out of plane buckling displacement at peak compressive displacement (cycle 22)
23-24	3.75	Specimen fractured in tension during first cycle (23)

Test Results

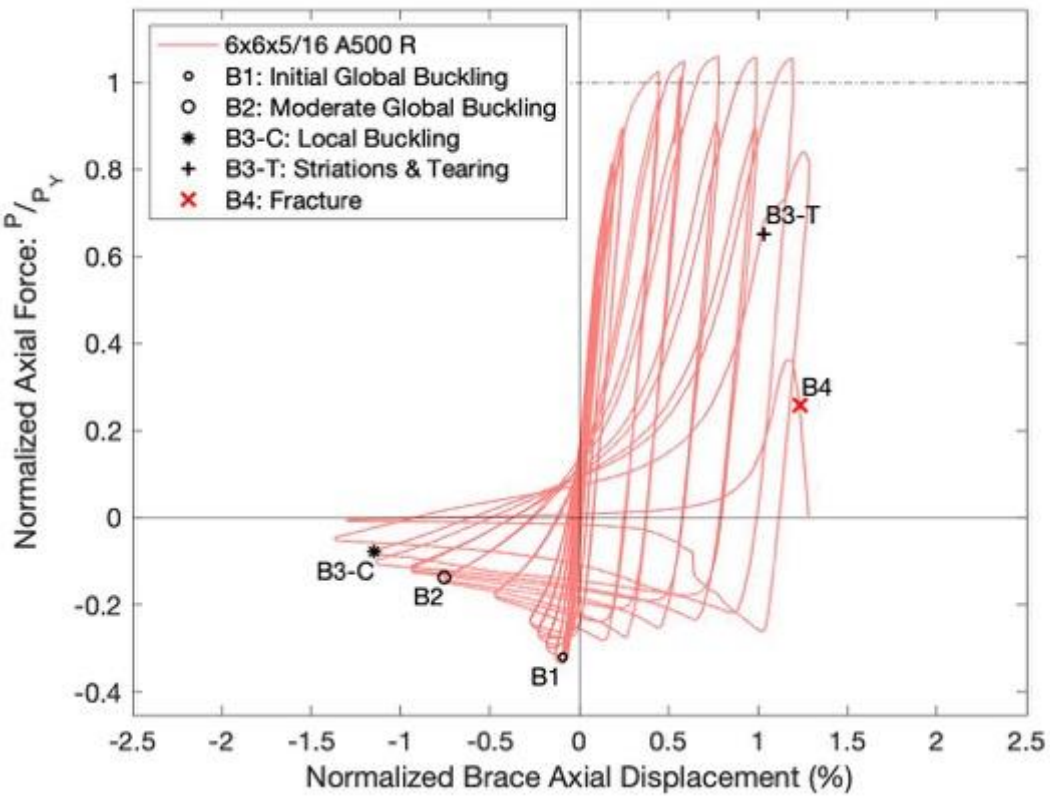

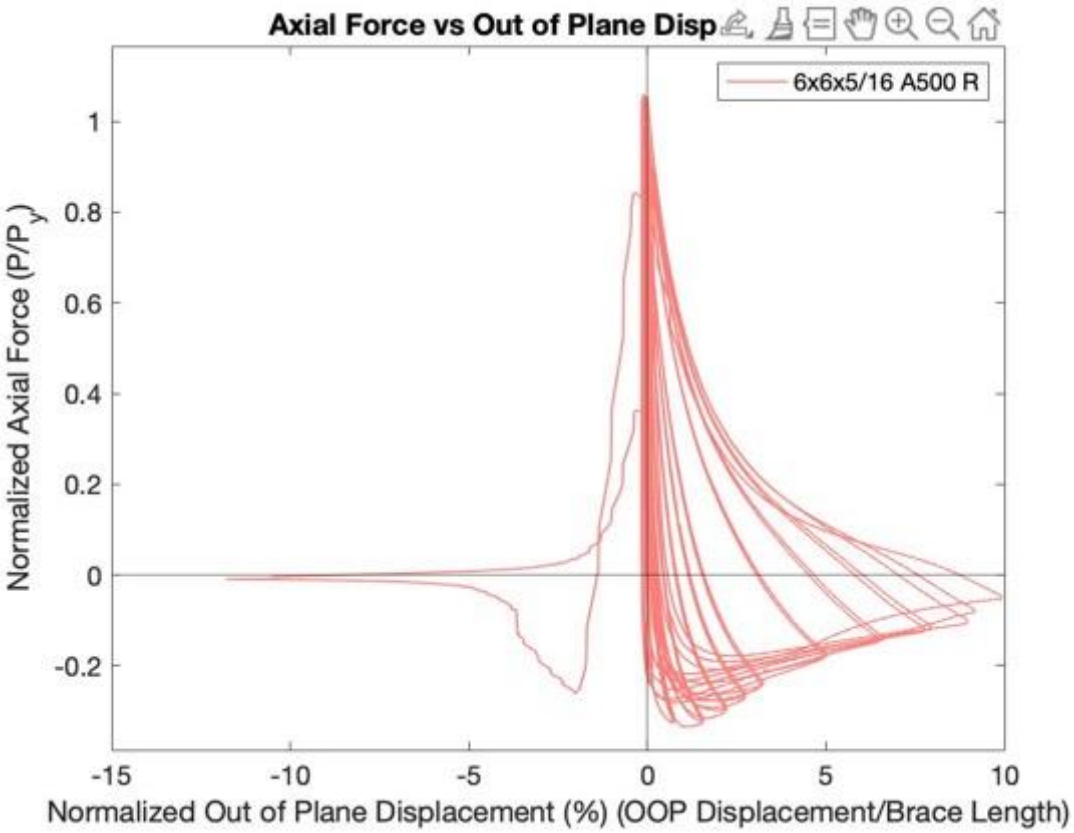
Axial Force vs Out of Plane Disp
6x6x5/16 A500 R
Normalized Axial Force (P/P_y)
1
0.8
0.6
0.4
0.2
0
-0.2
-15
-10
-5
0
5
10
Normalized Out of Plane Displacement (%) (OOP Displacement/Brace Length)

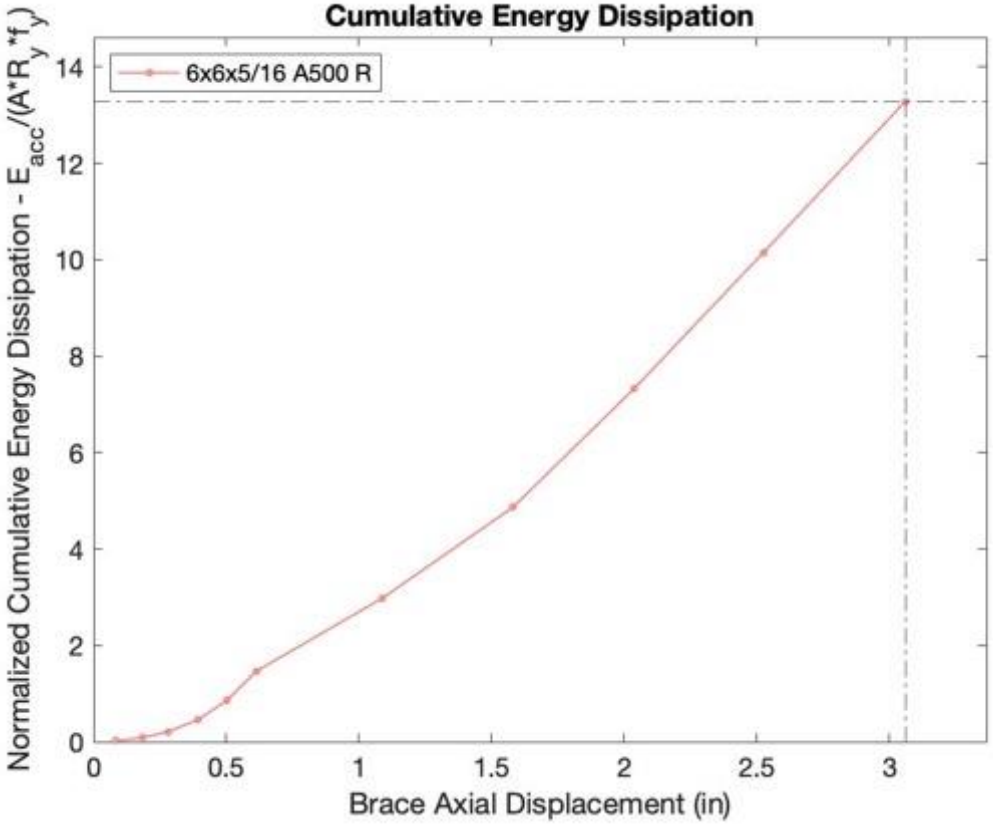
Cumulative Energy Dissipation
6x6x5/16 A500 R
Normalized Cumulative Energy Dissipation - E_acc/(A*R_y*f_y)
14
12
10
8
6
4
2
0
0
0.5
1
1.5
2
2.5
3
Brace Axial Displacement (in)

Photos

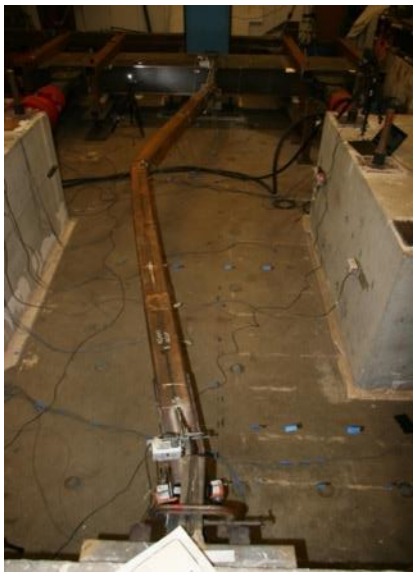

Peak Out of Plane Displacement (West): 3.25” Cycle 1

Peak Out of Plane Displacement (East): 3.25” Cycle 2

Fractured Specimen: 3.75” Displacement Cycle 1 - Tension

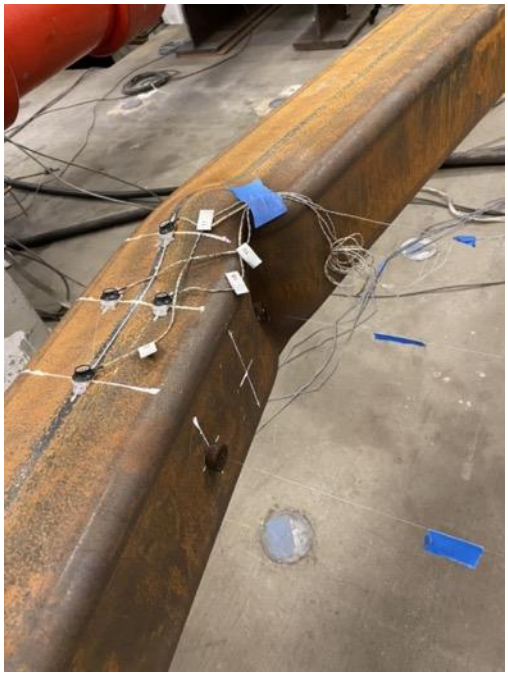

Cupping at Center of Specimen: 3.25” Cycles

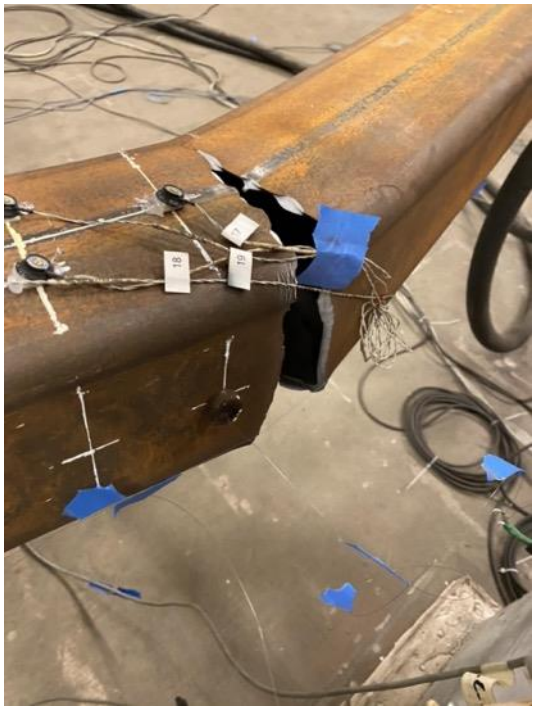

Tearing in Specimen: Cycle 2 at 3.25” Displacement

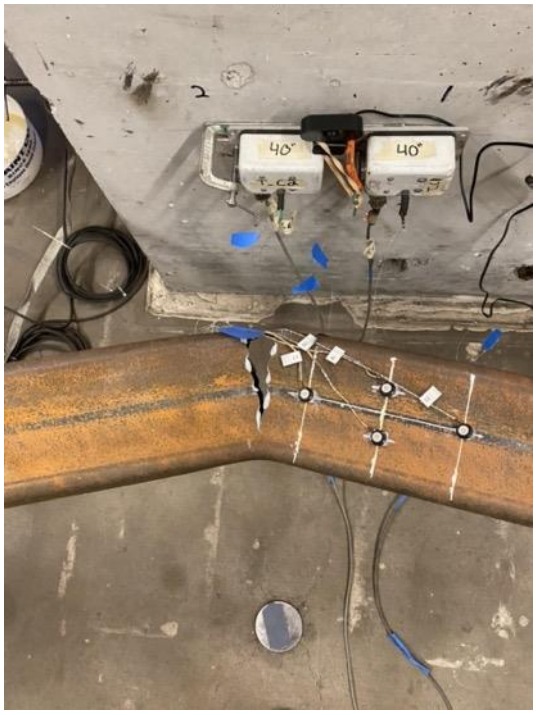

Top View of Tearing in Specimen: Cycle 2 at 3.25” Displacement

6x6x5/16 A1085 Y Brace Test Summary

Test Name: 6x6x5/16 A1085 Y
Test Date: 4/28/2021

Brace Properties

Measured Yield Stress (ksi)	62.07
Measured Ultimate Stress (ksi)	71.92
Yield Load (kips)	426.4
Critical Buckling Load (kips)	1110.2
Percent Elongation - 2" (%)	34.11
CVN Width (mm)	5
CVN Absorbed Energy (ft-lbs)	23
Brace Length (in.)	237.5

Area (in²)	6.87
Moment of Inertia (in⁴)	36.3
Corner Radius (in.)	0.676
Thickness - Nominal (in.)	0.313
Thickness - Measured (in.)	0.313
Brace Compactness Ratio (b/t) - Nominal *	16.2
Brace Compactness Ratio (b/t) - Measured	14.85
Global Slenderness ratio (KL/r)	103.3

Specimen Performance

Test Event	Axial Brace Displacement (in.)	Target Displacement (in.) (Cycle)	Force (kips)	$P / P_{Yield/Critical}$	
Peak Tension Load	1.90	2.25 (1)	456.4	1.07	Y
B1: Initial Global Buckling	-0.18	0.25 (1)	-139.8	0.13	C
B2: Moderate Global Buckling	-1.63	1.75 (1)	-64.0	0.06	C
B3-T: Local Buckling	-2.56	2.75 (2)	-33.5	0.03	C
B3-C: Striations & Tearing	2.46	3.25 (2)	272.0	0.64	Y
B4: Brace Fracture	3.13	3.75 (1)	123.0	0.29	Y

Key Observations

Cycle #	Displacement (in.)	Observations
9-10	0.625	Bolt slip - T1 - north and south gusset plates Knocking/racking sounds observed in tension - future cycles too Similar to previous cycles otherwise
17-18	2.25	Minimal / barely visible local cupping observed at C2 peak compressive displacement (~1/16”)

19-20	2.75	Minor local cupping (~¼") at C1 peak Moderate cupping at C2 peak - centered 1.5" north of center
21-22	3.25	Major cupping at C1 Tearing observed at T2 near peak tensile displacement Major cupping at C2 post-tearing
23-24	3.75	Fracture at T1!

Test Results

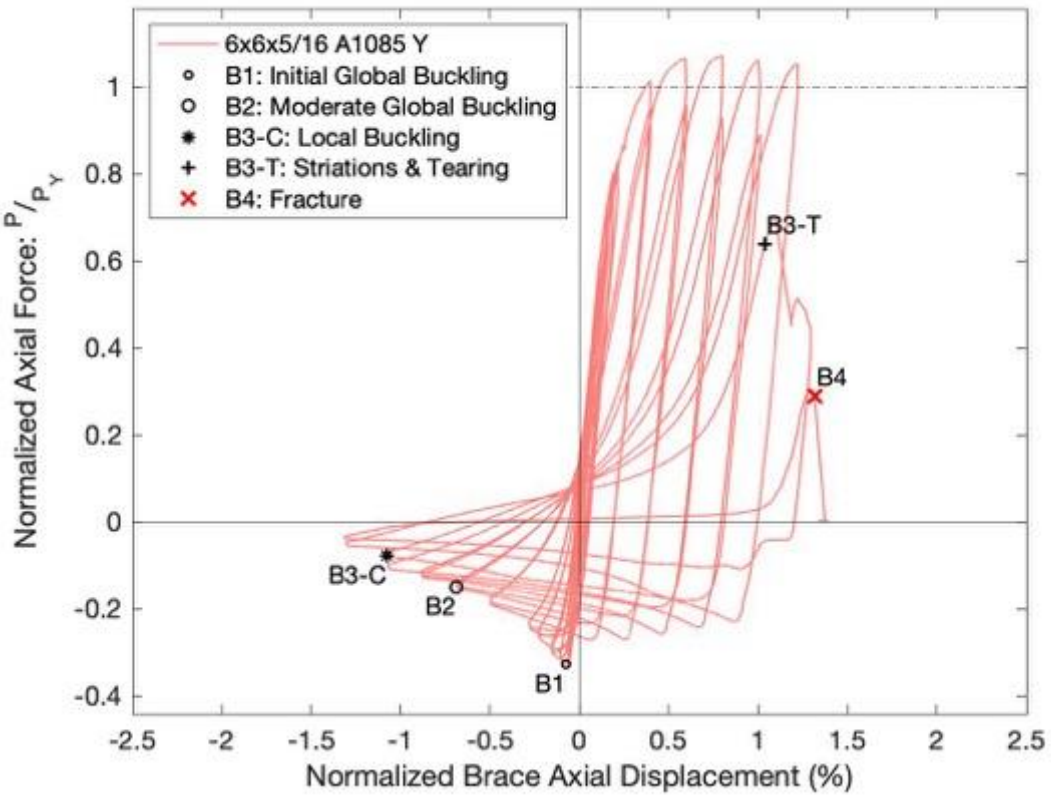

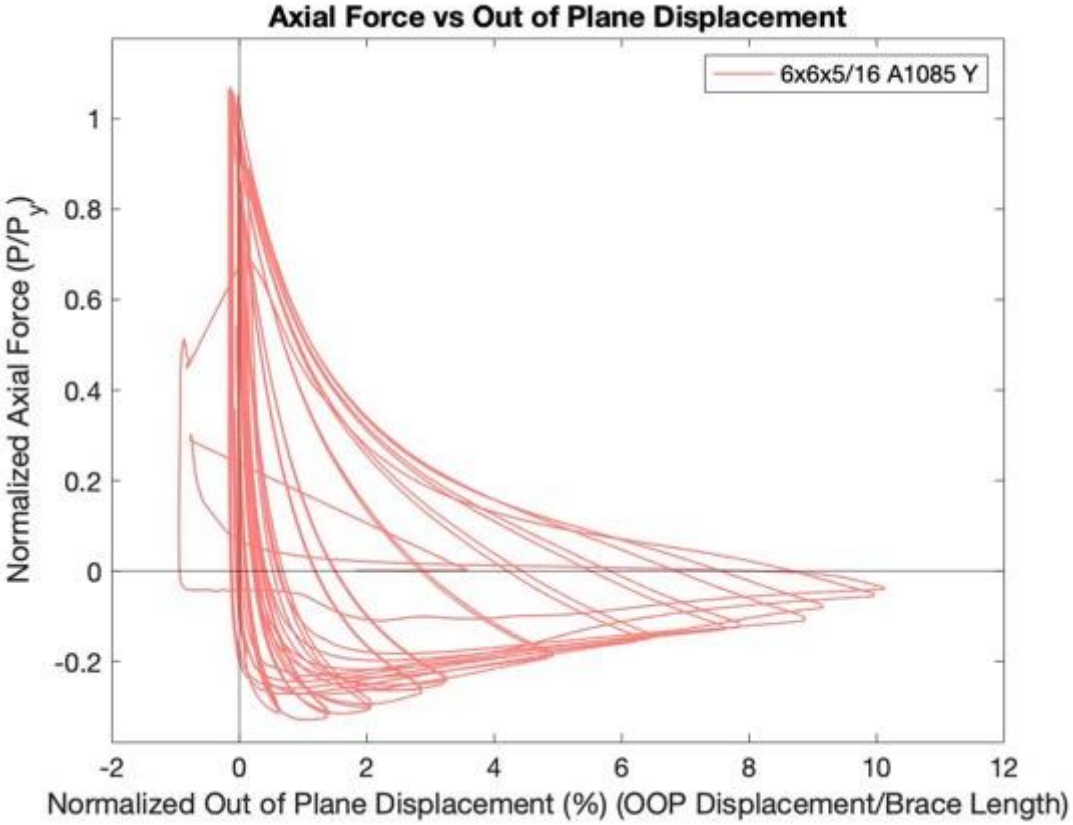
Axial Force vs Out of Plane Displacement
6x6x5/16 A1085 Y
Normalized Axial Force (P/P_y)
1
0.8
0.6
0.4
0.2
0
-0.2
-2
0
2
4
6
8
10
12
Normalized Out of Plane Displacement (%) (OOP Displacement/Brace Length)

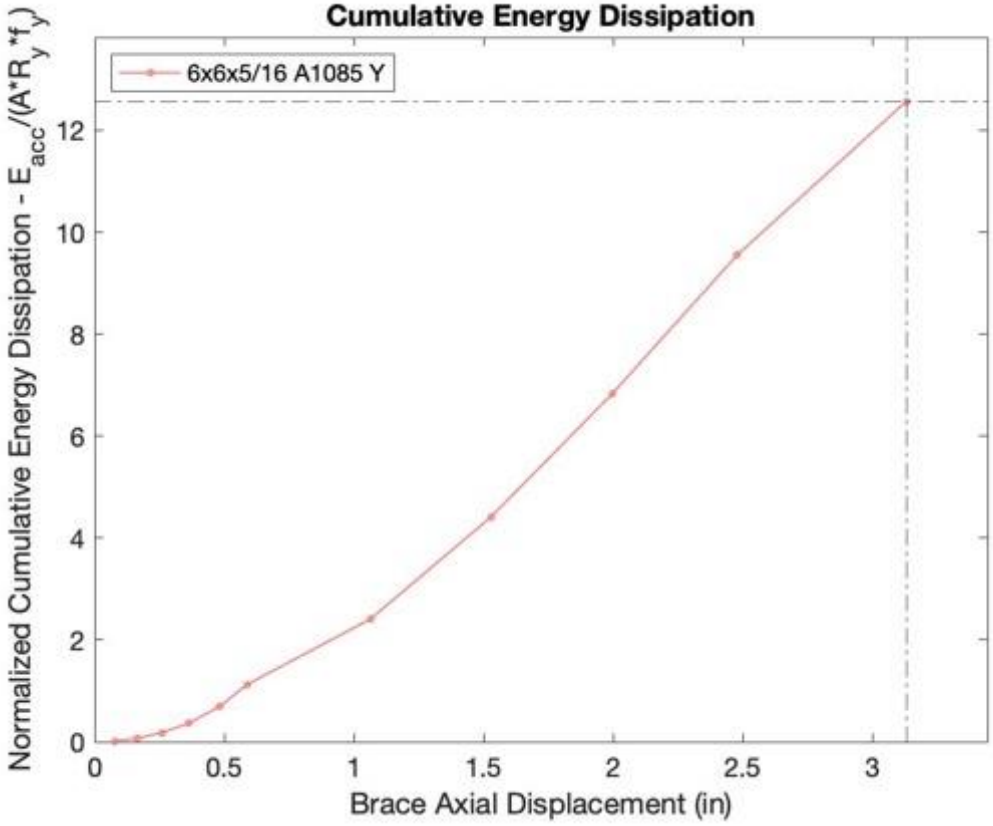
Cumulative Energy Dissipation
6x6x5/16 A1085 Y
Normalized Cumulative Energy Dissipation - E_acc/(A*R_y*f_y)
12
10
8
6
4
2
0
0
0.5
1
1.5
2
2.5
3
Brace Axial Displacement (in)

Photos

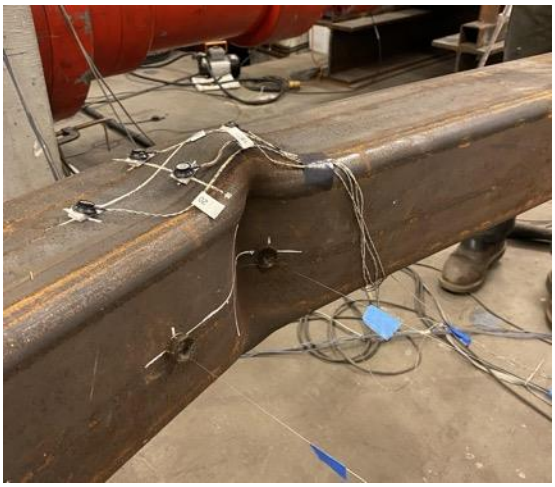

Cupping at Center of Specimen: 3.25” Cycle 1 C

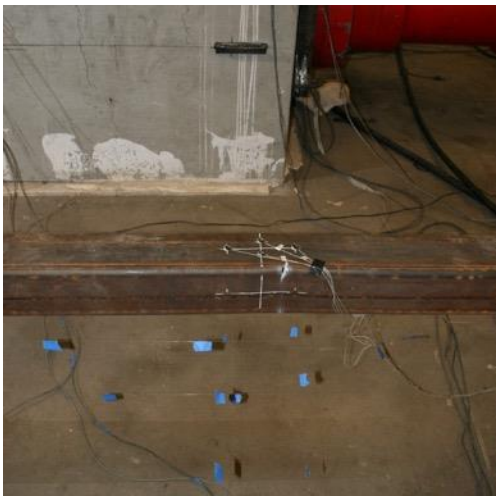

Initiation of Tearing: 3.25” Cycle 2 T

Cupping at Center of Specimen: 3.25” Cycle 2 C

Peak Out of Plane Displacement: 3.25” Cycles

Tearing Prior to Fracture: 3.75” Cycle 1 T

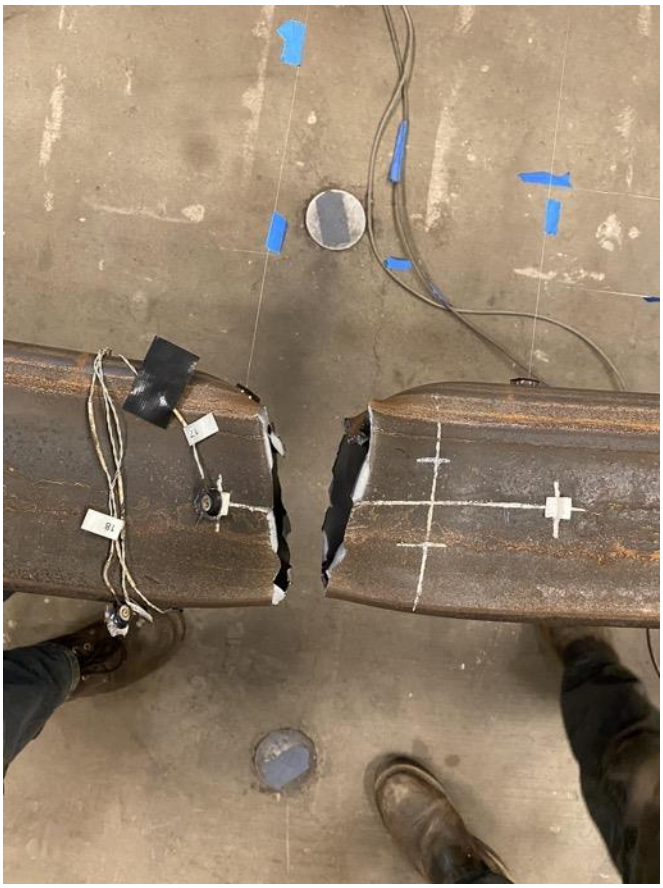

Fractured Specimen: 3.75” Cycle 1 T

6x6x3/8 A500 R Brace Test Summary

Test Name: 6x6x3/8 A500 R
Test Date: 4/22/2021

Brace Properties

Measured Yield Stress (ksi)	61.19
Measured Ultimate Stress (ksi)	76.36
Yield Load (kips)	487.7
Critical Buckling Load (kips)	175.2
Percent Elongation - 2" (%)	35.36
CVN Width (mm)	7.5
CVN Absorbed Energy (ft-lbs)	42.5
Brace Length (in.)	237.5

Area (in²)	7.58
Moment of Inertia (in⁴)	39.5
Corner Radius (in.)	0.75
Thickness - Nominal (in.)	0.349
Thickness - Measured (in.)	0.367
Brace Compactness Ratio (b/t) - Nominal *	14.2
Brace Compactness Ratio (b/t) - Measured	12.26
Global Slenderness ratio (KL/r)	104.2

Specimen Performance

Test Event	Axial Brace Displacement (in.)	Target Displacement (in.) (Cycle)	Force (kips)	$P / P_{Yield/Critical}$	
Peak Tension Load	1.78	2.25 (1)	511.0	1.05	Y
B1: Initial Global Buckling	-0.19	0.25 (1)	-168.7	0.96	C
B2: Moderate Global Buckling	-1.75	1.75 (1)	-72.0	0.41	C
B3-T: Local Buckling	-3.16	3.25 (2)	-43.5	0.25	C
B3-C: Striations & Tearing	3.23	3.75 (2)	428.0	0.88	Y
B4: Brace Fracture	3.74	4.25 (1)	190.0	0.39	Y

Key Observations

Cycle #	Displacement	Observations
9-10	0.625	Bolt slip South Gusset Plate, T1
13-14	1.25	Bolt slip North Gusset Plate, T1 Cracking/racking noises in tension
21-22	3.25	Minor cupping observed (~⅛") - C1

		Much warmer at center of brace Increased cupping observed (~⅜") - C2
23-24	3.75	Major cupping ~1.5" north of center - C1 Small striations in top East corner at the center of brace - T2 Major cupping observed - C2
25-26	4.25	Tearing & Fracture - T1 Two distinct loud bangs observed during fracture

Test Results

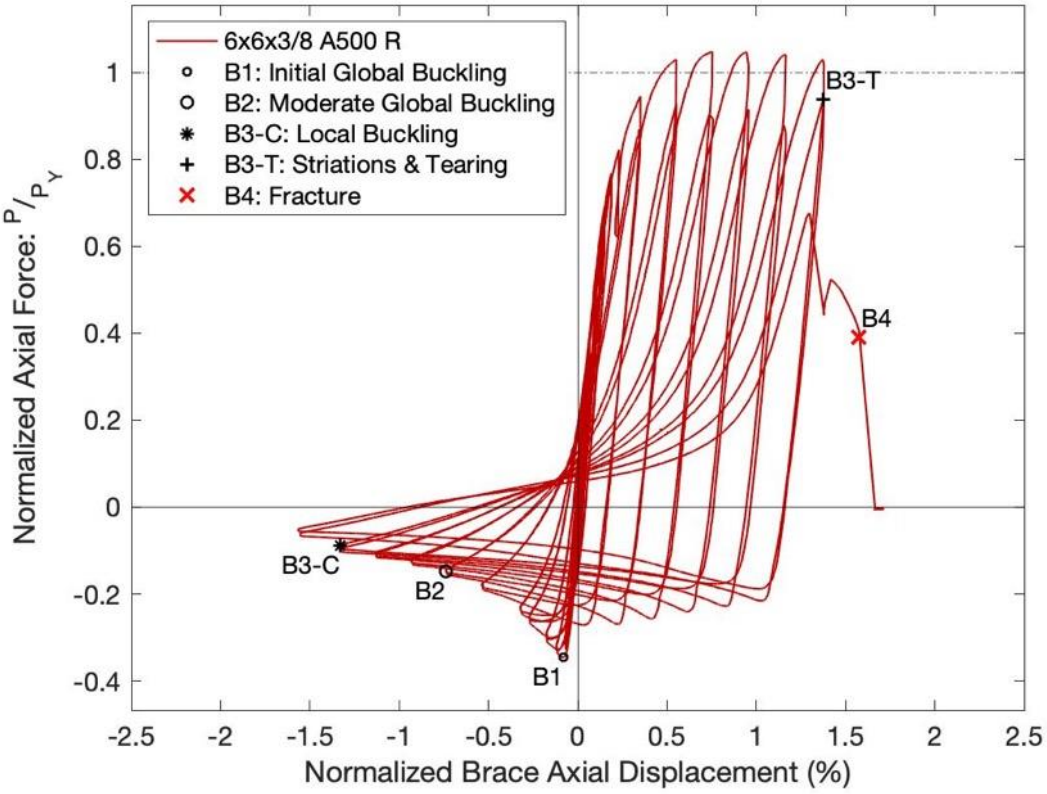

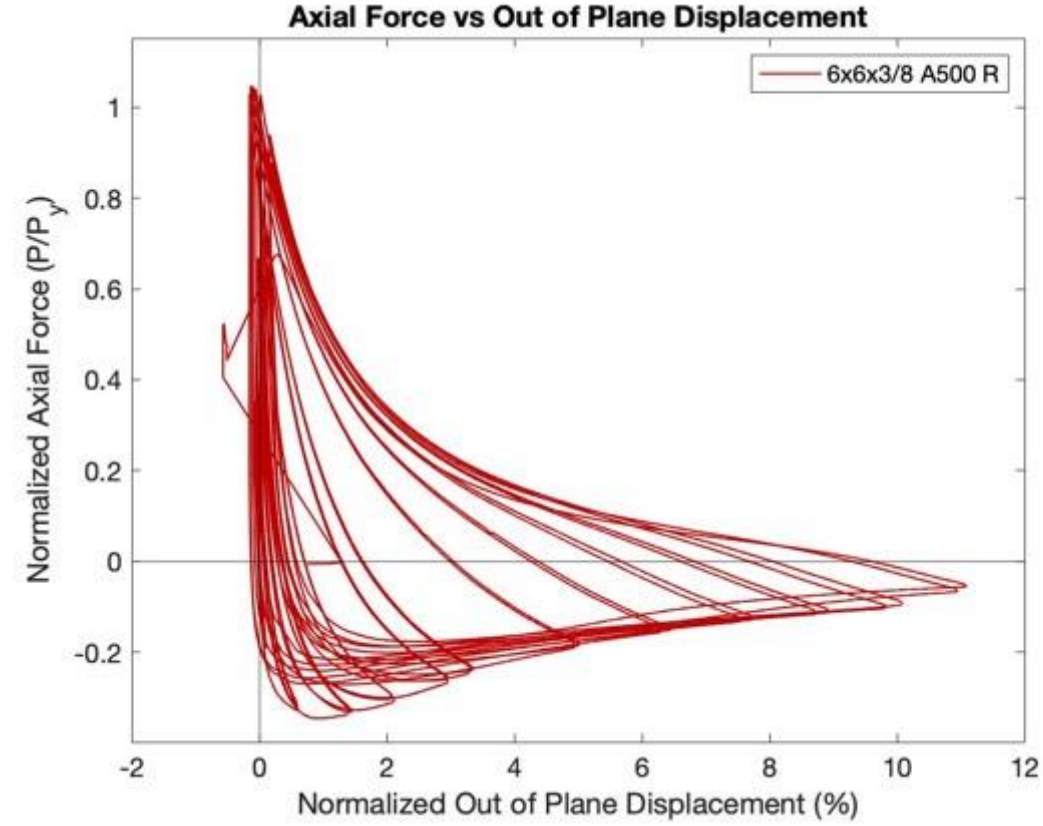
Axial Force vs Out of Plane Displacement
6x6x3/8 A500 R
Normalized Axial Force (P/P$_y$)
Normalized Out of Plane Displacement (%)
1
0.8
0.6
0.4
0.2
0
-0.2
-2
0
2
4
6
8
10
12

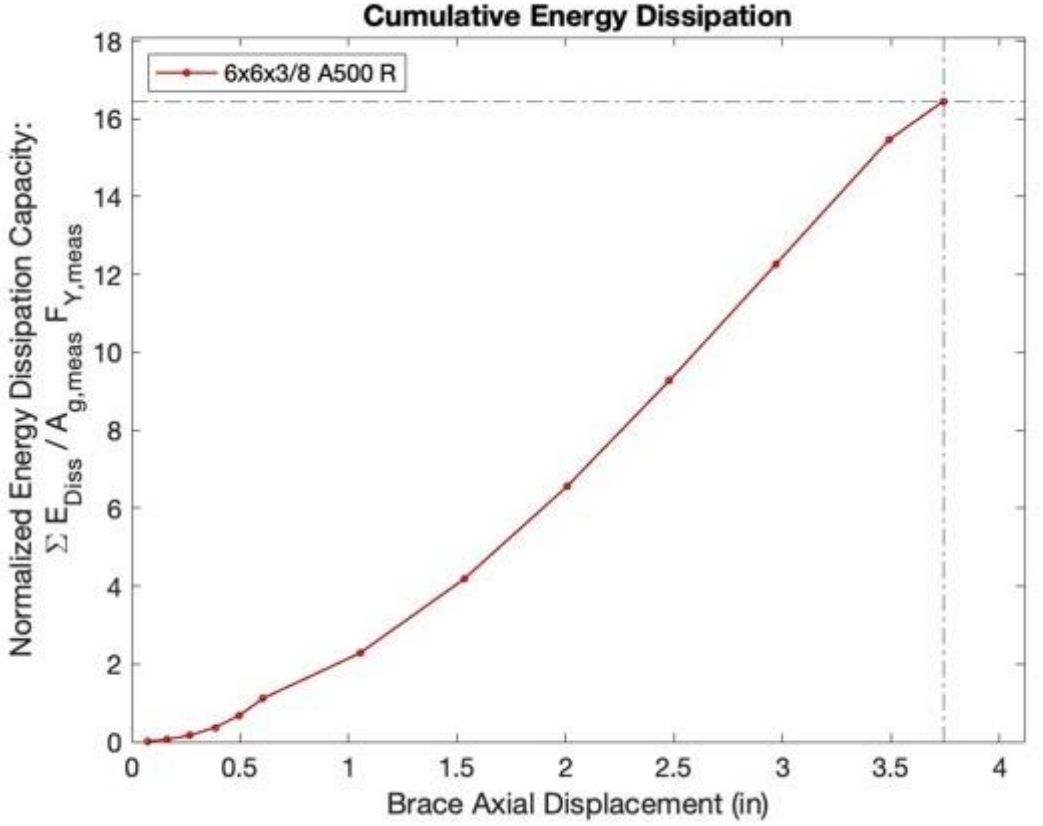
Cumulative Energy Dissipation
6x6x3/8 A500 R
Normalized Energy Dissipation Capacity:
$\Sigma E_{Diss} / A_{g,meas} F_{Y,meas}$
Brace Axial Displacement (in)
18
16
14
12
10
8
6
4
2
0
0
0.5
1
1.5
2
2.5
3
3.5
4

Photos

Peak Out of Plane Displacement: 3.75” Cycles

Initial Striations at Center of Specimen: 2nd Cycle at 3.75”

Cupping at Center of Specimen: 3.75” Cycle

Fractured Specimen: First Cycle at 4.25”

6x6x3/8 A1085 Y Brace Test Summary

Test Name: 6x6x3/8 A1085 Y
Test Date: 4/23/2021

Brace Properties

Measured Yield Stress (ksi)	66.81
Measured Ultimate Stress (ksi)	72.64
Yield Load (kips)	539.8
Critical Buckling Load (kips)	185.4
Percent Elongation - 2" (%)	31.86
CVN Width (mm)	7.5
CVN Absorbed Energy (ft-lbs)	18.7
Brace Length (in.)	237.5

Area (in²)	8.08
Moment of Inertia (in⁴)	41.6
Corner Radius (in.)	0.715
Thickness - Nominal (in.)	0.375
Thickness - Measured (in.)	0.375
Brace Compactness Ratio (b/t) - Nominal *	13
Brace Compactness Ratio (b/t) - Measured	12.19
Global Slenderness ratio (KL/r)	104.6

Specimen Performance

Test Event	Axial Brace Displacement (in.)	Target Displacement (in.) (Cycle)	Force (kips)	$P / P_{Yield/Critical}$	
Peak Tension Load	1.76	2.25 (1)	547.9	1.01	Y
B1: Initial Global Buckling	-0.15	0.25 (1)	-180.0	0.97	C
B2: Moderate Global Buckling	-1.63	1.75 (1)	-81.0	0.44	C
B3-T: Local Buckling	-3.06	3.25 (2)	-40.4	0.22	C
B3-C: Striations & Tearing	2.70	3.75 (2)	196.4	0.36	Y
B4: Brace Fracture	0.55	3.75 (2)	-25.2	0.14	C

Key Observations

Cycle #	Displacement (in.)	
7-8	0.5	Bolt slip: N & S gusset plates - Cycle T1 Similar OOP displacement as previous cycles
21-22	3.25	Minor cupping at C1 peak compressive displacement (~¼") Moderate cupping at C2 peak Center of cupping ~1" south of center

23-24	3.75	Major cupping at C1 peak Tearing at T2 - did not fracture! Tearing in east/top/bottom faces Specimen fractured as it was put into compression - C2 Ductile tearing of west face - fractured

Test Results

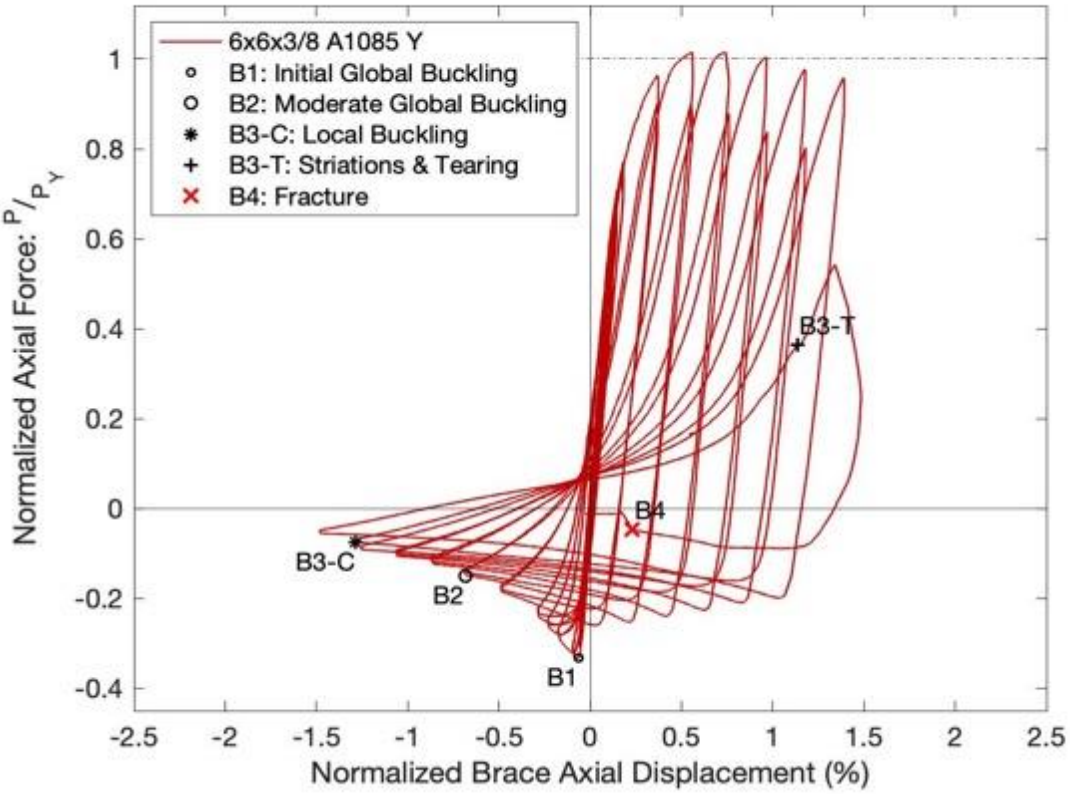

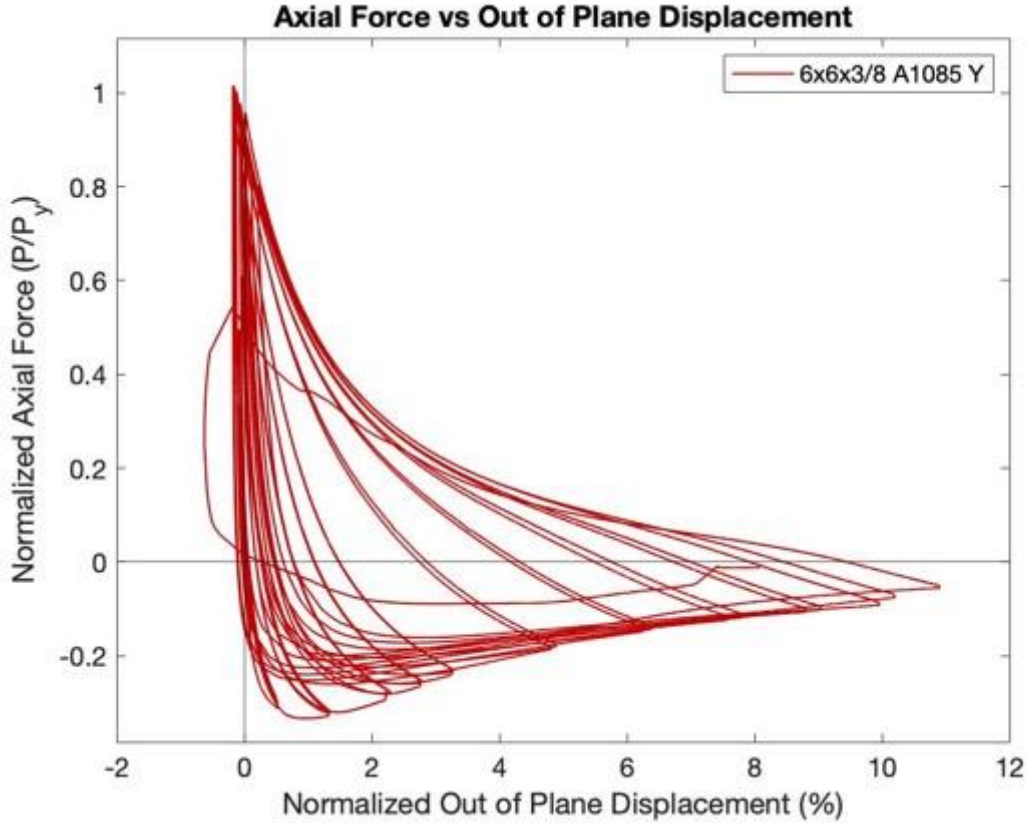
Axial Force vs Out of Plane Displacement
6x6x3/8 A1085 Y
Normalized Axial Force (P/P_y)
Normalized Out of Plane Displacement (%)
1
0.8
0.6
0.4
0.2
0
-0.2
-2
0
2
4
6
8
10
12

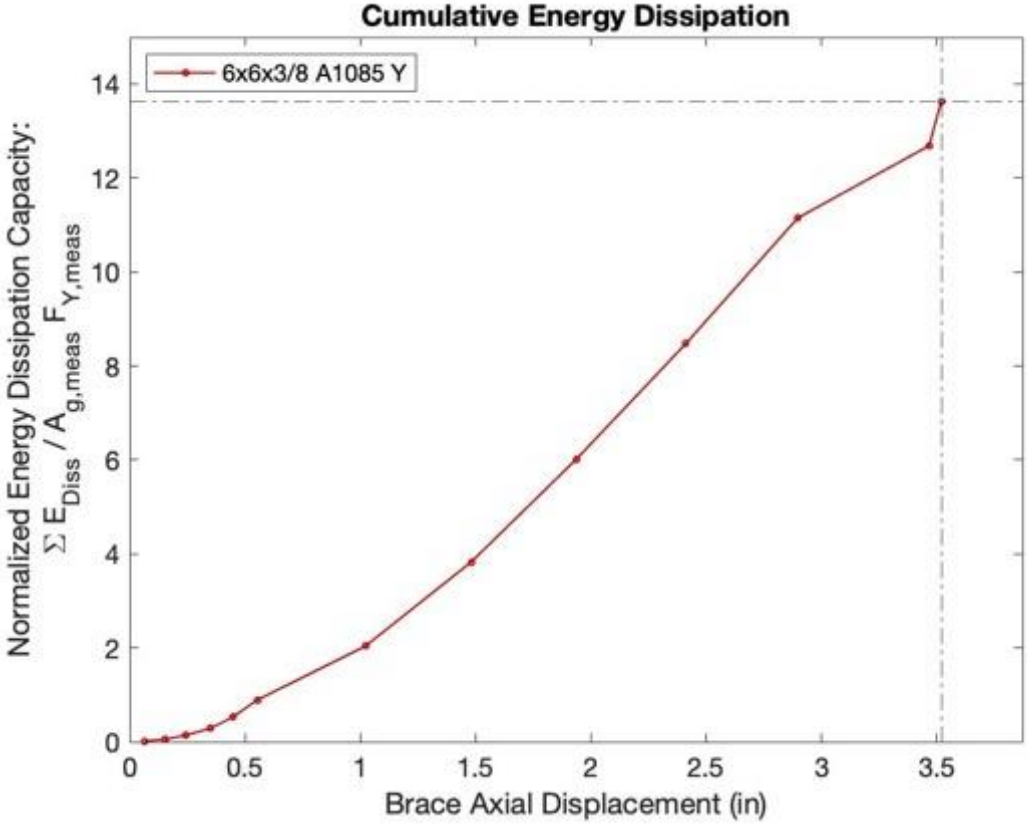
Cumulative Energy Dissipation
6x6x3/8 A1085 Y
Normalized Energy Dissipation Capacity:
Σ E_Diss / A_g,meas F_Y,meas
Brace Axial Displacement (in)
14
12
10
8
6
4
2
0
0
0.5
1
1.5
2
2.5
3
3.5

Photos

Tearing at Center of Specimen: First Cycle at 3.75”

Ductile Fracture of Specimen in Compression at 3.75”

Cupping at Center of Specimen: 3.75” Cycle 1

Fractured Specimen

6x6x1/2 A500 R Brace Test Summary

Test Name: 6x6x1/2 A500 R
Test Date: 4/30/2021

Brace Properties

Measured Yield Stress (ksi)	62.84
Measured Ultimate Stress (ksi)	67.05
Yield Load (kips)	630.5
Critical Buckling Load (kips)	215.6
Percent Elongation - 2" (%)	33.48
CVN Width (mm)	10
CVN Absorbed Energy (ft-lbs)	120+
Brace Length (in.)	237.5

Area (in²)	9.74
Moment of Inertia (in⁴)	48.3
Corner Radius (in.)	0.984
Thickness - Nominal (in.)	0.465
Thickness - Measured (in.)	0.479
Brace Compactness Ratio (b/t) - Nominal *	9.9
Brace Compactness Ratio (b/t) - Measured	8.42
Global Slenderness ratio (KL/r)	106.5

Specimen Performance

Test Event	Axial Brace Displacement (in.)	Target Displacement (in.) (Cycle)	Force (kips)	$P / P_{Yield/Critical}$	
Peak Tension Load	1.24	2.25 (1)	646.2	1.02	Y
B1: Initial Global Buckling	-0.18	0.375 (1)	-218.7	1.01	C
B2: Moderate Global Buckling	-1.20	1.25 (1)	-111.0	0.51	C
B3-T: Local Buckling	-3.58	3.75 (2)	-44.0	0.20	C
B3-C: Striations & Tearing	3.78	4.25 (1)	492.0	0.78	Y
B4: Brace Fracture	0.20	4.75 (1)	-43.3	0.20	C

Key Observations

Cycle #	Displacement (in.)	Observations
9-10	0.625	Bolt slip - T1 - north and south gusset plates Knocking/racking of bolts in tension - observed in future cycles
21-22	3.25	Minor cupping at C1 & C2 peak (~1/4”)
23-24	3.75	Cupping at C1 peak (~⅝”)

		Cupping at C2 peak (~¾") VERY hot to touch at center - C2 - significantly warmer than observed in previous tests
25-26	4.25	Striations observed at T1: East side corners Major cupping at C1 & C2 peak Glue on optotrak sensors melting at midspan - taped down at C1 Minor tearing observed at T2
27-28	4.75	Tearing at T1: Tore through half of the brace (East side) Complete fracture in C1 at before reaching peak displacement!

Test Results

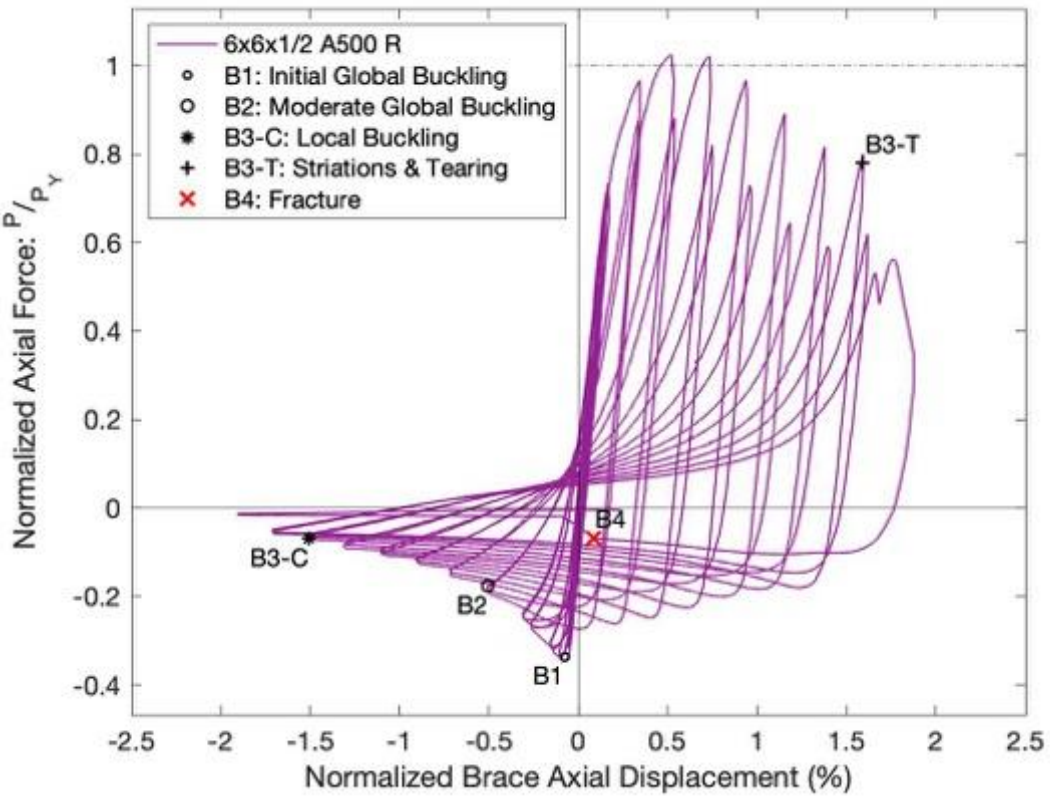

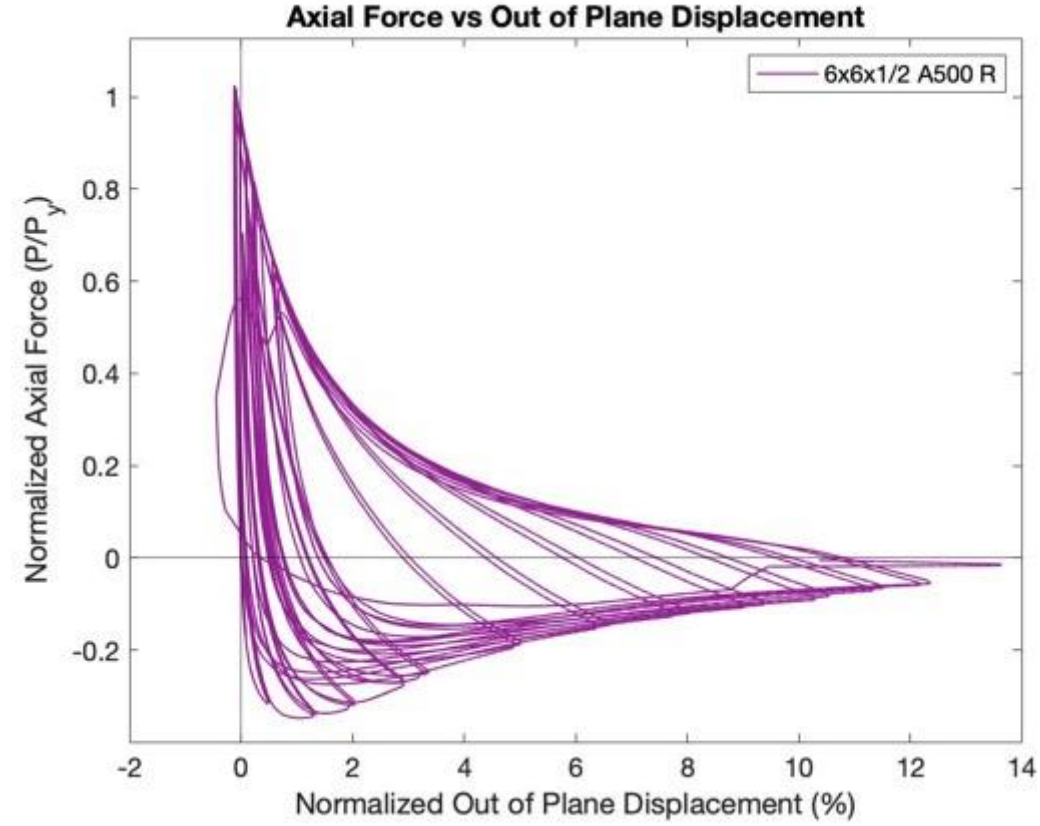
Axial Force vs Out of Plane Displacement
6x6x1/2 A500 R
Normalized Axial Force (P/P_y)
Normalized Out of Plane Displacement (%)
1
0.8
0.6
0.4
0.2
0
-0.2
-2
0
2
4
6
8
10
12
14

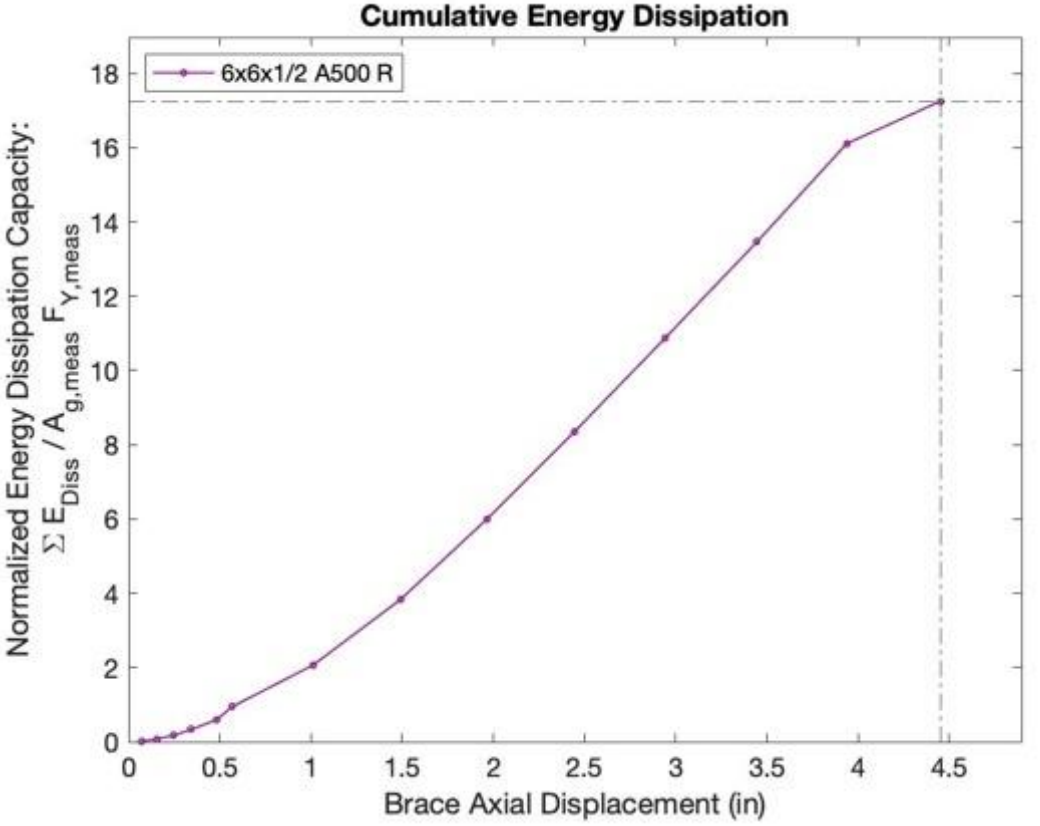
Cumulative Energy Dissipation
6x6x1/2 A500 R
Normalized Energy Dissipation Capacity:
Σ E_Diss / A_g,meas F_Y,meas
Brace Axial Displacement (in)
18
16
14
12
10
8
6
4
2
0
0
0.5
1
1.5
2
2.5
3
3.5
4
4.5

Photos

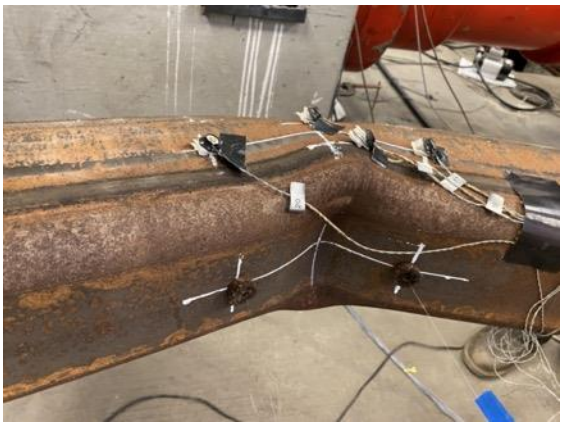

Cupping at Center of Brace: 3.75” Cycles

Initiation of Brace Tearing: 4.25” Cycle 2

Brace Tearing: 4.75” Cycle 1

Peak Out of Plane Displacement: 4.25” Cycles

Fractured Specimen: After Cycle 1 at 4.75”

6x6x1/2 A1085 Y Brace Test Summary

Test Name: 6x6x1/2 A1085 Y
Test Date: 5/6/2021

Brace Properties

Measured Yield Stress (ksi)	67.85
Measured Ultimate Stress (ksi)	71.96
Yield Load (kips)	683.2
Critical Buckling Load (kips)	225.0
Percent Elongation - 2" (%)	34.48
CVN Width (mm)	10
CVN Absorbed Energy (ft-lbs)	27.8
Brace Length (in.)	237.5

Area (in²)	10.36
Moment of Inertia (in⁴)	50.5
Corner Radius (in.)	0.833
Thickness - Nominal (in.)	0.5
Thickness - Measured (in.)	0.486
Brace Compactness Ratio (b/t) - Nominal *	9
Brace Compactness Ratio (b/t) - Measured	8.92
Global Slenderness ratio (KL/r)	107.5

Specimen Performance

Test Event	Axial Brace Displacement (in.)	Target Displacement (in.) (Cycle)	Force (kips)	$P / P_{Yield/Critical}$	
Peak Tension Load	1.61	2.25 (1)	727.2	1.06	Y
1: Initial Global Buckling	-0.19	0.375 (1)	-218.6	0.97	C
2: Moderate Global Buckling	-1.75	1.75 (1)	-109.2	0.49	C
3-T: Local Buckling	-4.13	4.25 (2)	-51.6	0.23	C
3-C: Striations & Tearing	4.49	5.25 (1)	626.6	0.92	Y
4: Brace Fracture	4.67	5.75 (1)	200.0	0.29	Y

Key Observations

Cycle #	Displacement	Observations
7-8	0.5	Bolt slip N & S gusset plates- T1 Similar to previous cycles
23-24	3.75	Minor cupping - C2 (~⅛")
25-26	4.25	Minor cupping - C1 (~¼")

		Moderate cupping - C2 (~½") Center of cupping: ½" north of center Very hot at center - LEDs coming off, taped down to hold in place
27-28	4.75	Cupping at C1 peak: ~1" Major Cupping at C2 peak Difficult to measure cupping at C1 and C2 due to significant local deformations at the top and bottom corners - fold in and up
29-30	5.25	Striations at center - T1 peak displacement Major cupping at C1 peak - very deep Fractured at T2 before reaching peak tensile displacement

Test Results

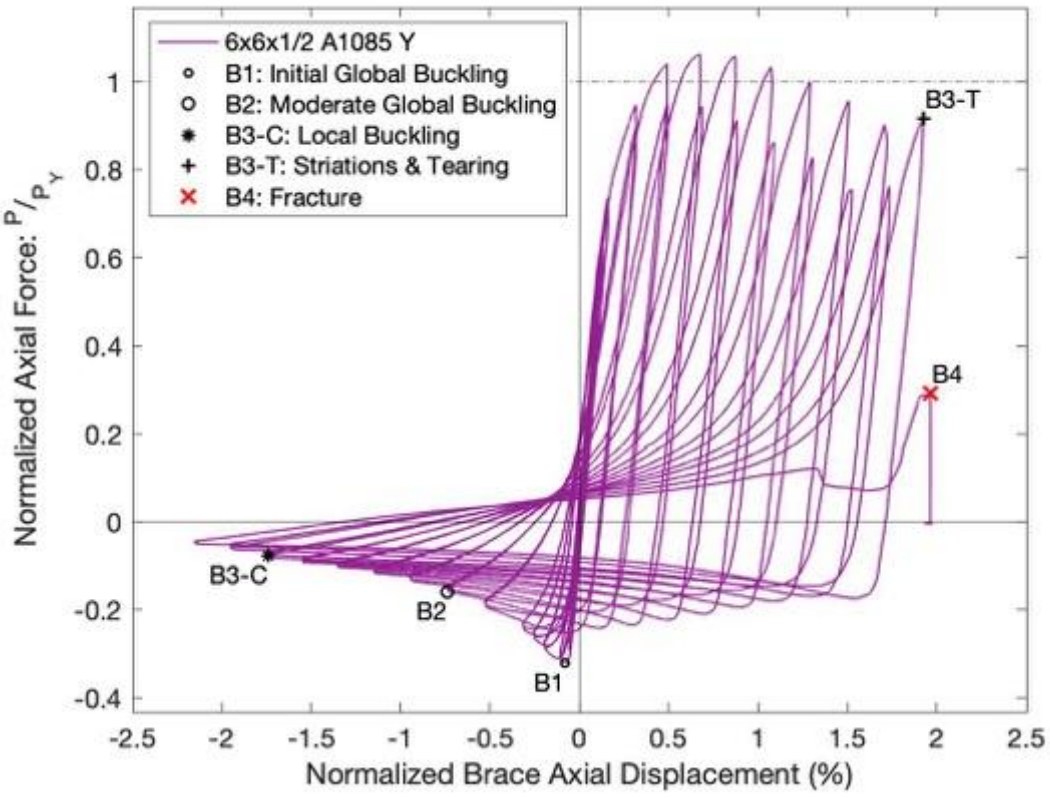

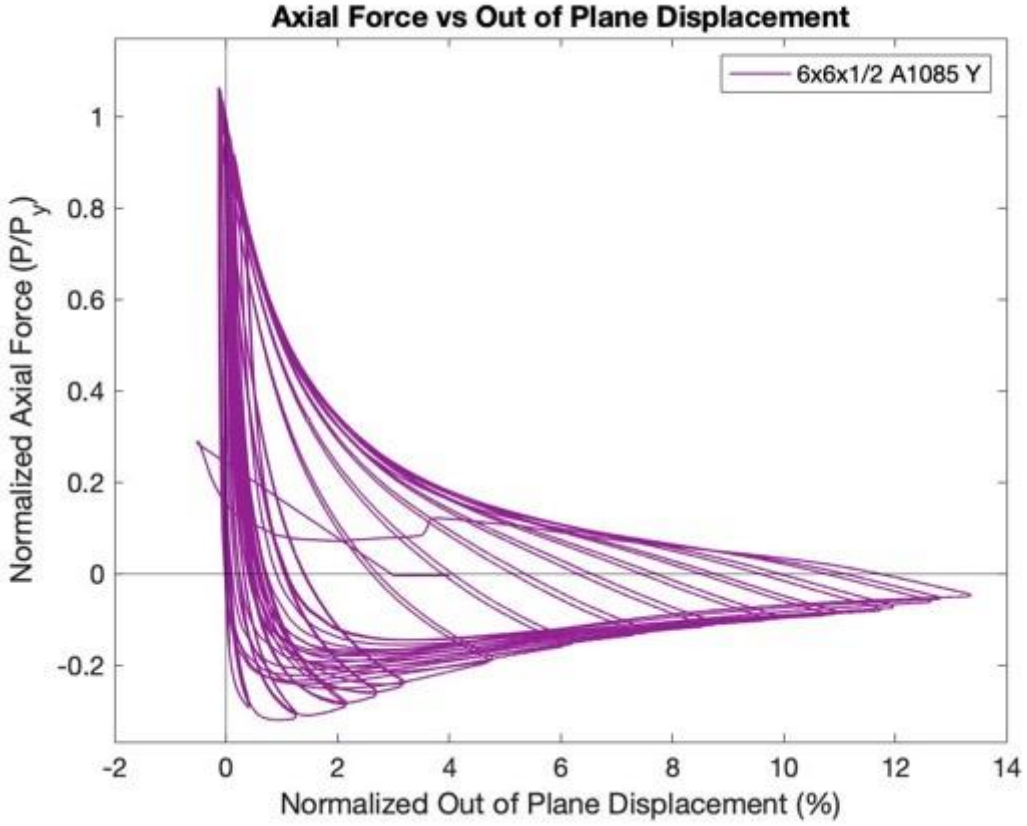
Axial Force vs Out of Plane Displacement
6x6x1/2 A1085 Y
Normalized Axial Force (P/P_y)
Normalized Out of Plane Displacement (%)
1
0.8
0.6
0.4
0.2
0
-0.2
-2
0
2
4
6
8
10
12
14

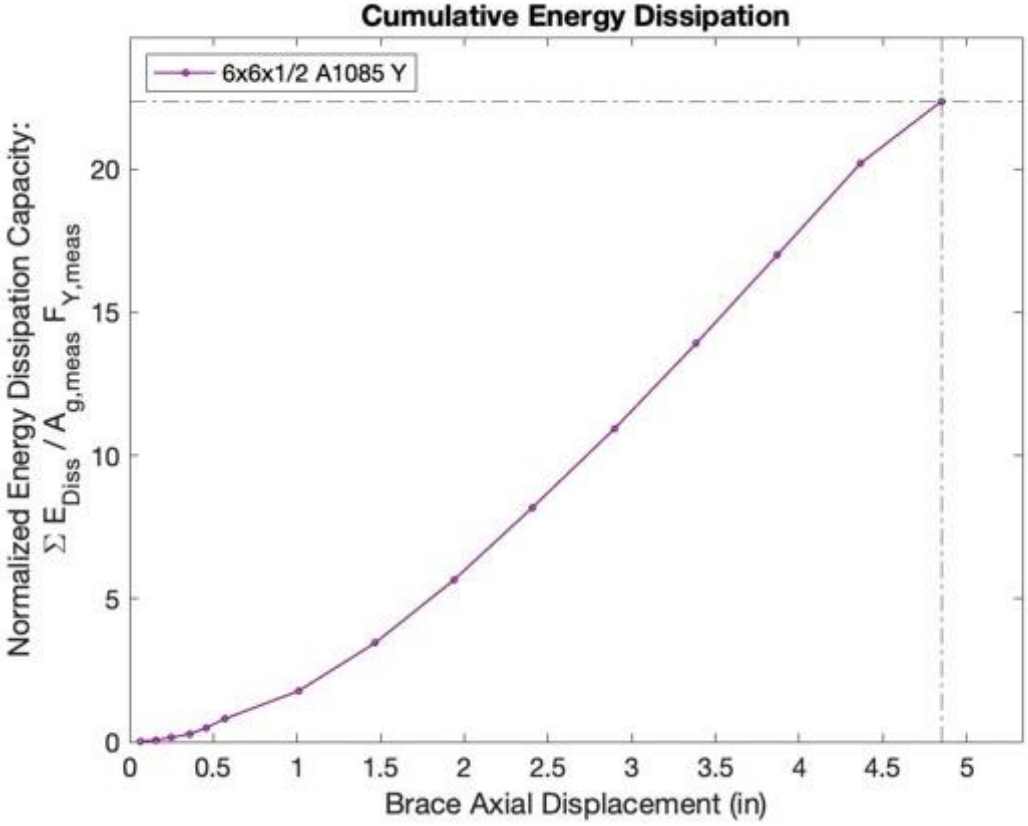
Cumulative Energy Dissipation
6x6x1/2 A1085 Y
Normalized Energy Dissipation Capacity:
Σ E_Diss / A_g,meas F_Y,meas
Brace Axial Displacement (in)
0
5
10
15
20
0
0.5
1
1.5
2
2.5
3
3.5
4
4.5
5

Photos

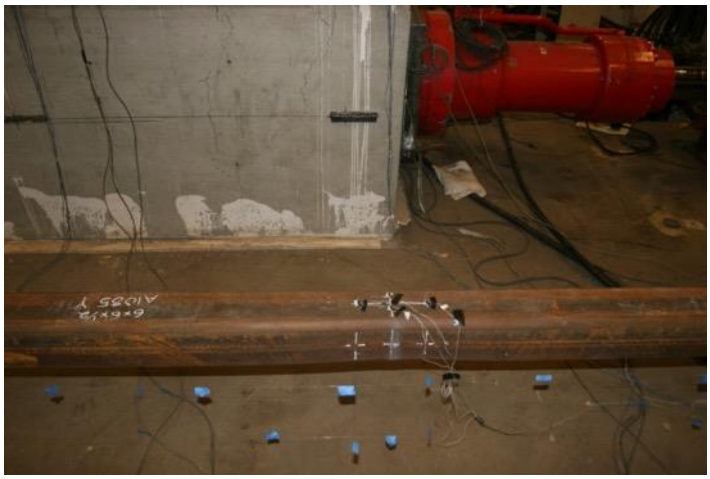

Development of Striations in Tension: First 5.25” Cycle

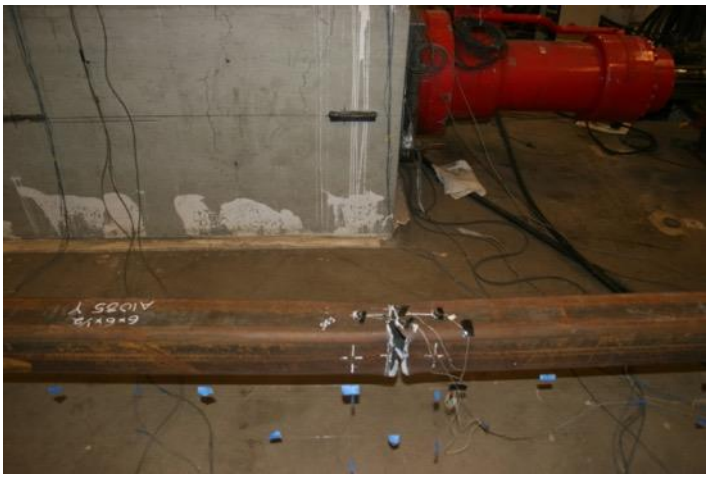

Tearing at Center of Specimen: Second 5.25” Cycle

Cupping at Center of Specimen: 4.75” Cycles

Fractured Specimen: Second Cycle at 5.25”

Peak Out of Plane Displacement: 5.25” Cycle

7x7x5/16 A500 Y Brace Test Summary

Test Name: 7x7x5/16 A500 Y
Test Date: 5/19/2021 - 11:00 AM

Brace Properties

Measured Yield Stress (ksi)	62.71
Measured Ultimate Stress (ksi)	70.02
Yield Load (kips)	474.3
Critical Buckling Load (kips)	239.1
Percent Elongation - 2" (%)	31.16
CVN Width (mm)	5
CVN Absorbed Energy (ft-lbs)	15.7
Brace Length (in.)	237.5

Area (in²)	7.59
Moment of Inertia (in⁴)	56.1
Corner Radius (in.)	0.66
Thickness - Nominal (in.)	0.291
Thickness - Measured (in.)	0.29
Brace Compactness Ratio (b/t) - Nominal *	21.1
Brace Compactness Ratio (b/t) - Measured	19.59
Global Slenderness ratio (KL/r)	87.3

Specimen Performance

Test Event	Axial Brace Displacement (in.)	Target Displacement (in.) (Cycle)	Force (kips)	$P / P_{Yield/Critical}$	
Peak Tension Load	1.23	1.75 (1)	496.6	1.05	Y
B1: Initial Global Buckling	-0.21	0.375 (1)	-209.8	0.88	C
B2: Moderate Global Buckling	-1.65	1.75 (1)	-58.6	0.25	C
B3-T: Local Buckling	-1.82	1.75 (1)	-54.5	0.23	C
B3-C: Striations & Tearing	1.04	2.25 (1)	323.3	0.68	Y
B4: Brace Fracture	1.73	2.25 (1)	193.0	0.41	Y

Key Observations

Cycle #	Displacement	Observations
7-8	0.5	Bolt slip T1 - N & S gusset plates Minor OOP buckling displacement
13-14	1.25	Similar to previous cycles No visible cupping observed & still cold at center

15-16	1.75	Moderate cupping observed - C1 peak compressive displacement. No minor cupping observed in previous cycles, the initial cupping in this specimen was relatively large (~1" deep) at C1. Cupping centered about 6" south of center Major cupping observed at C2 peak compressive displacement (1.75" deep) with significant vertical bending of top and bottom sides of tube at the location of cupping Specimen slightly warm at center. No striations observed at center at T1 or T2
17-18	2.25	Fractured in tension prior to reaching T1 peak displacement

Test Results

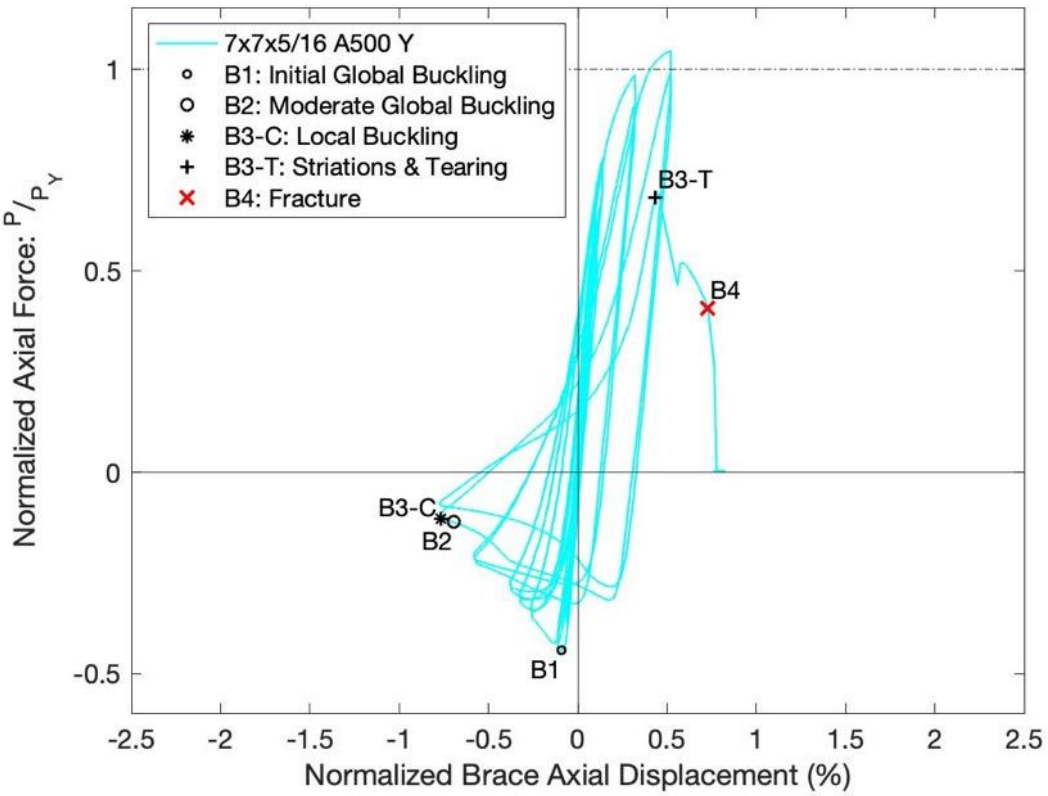

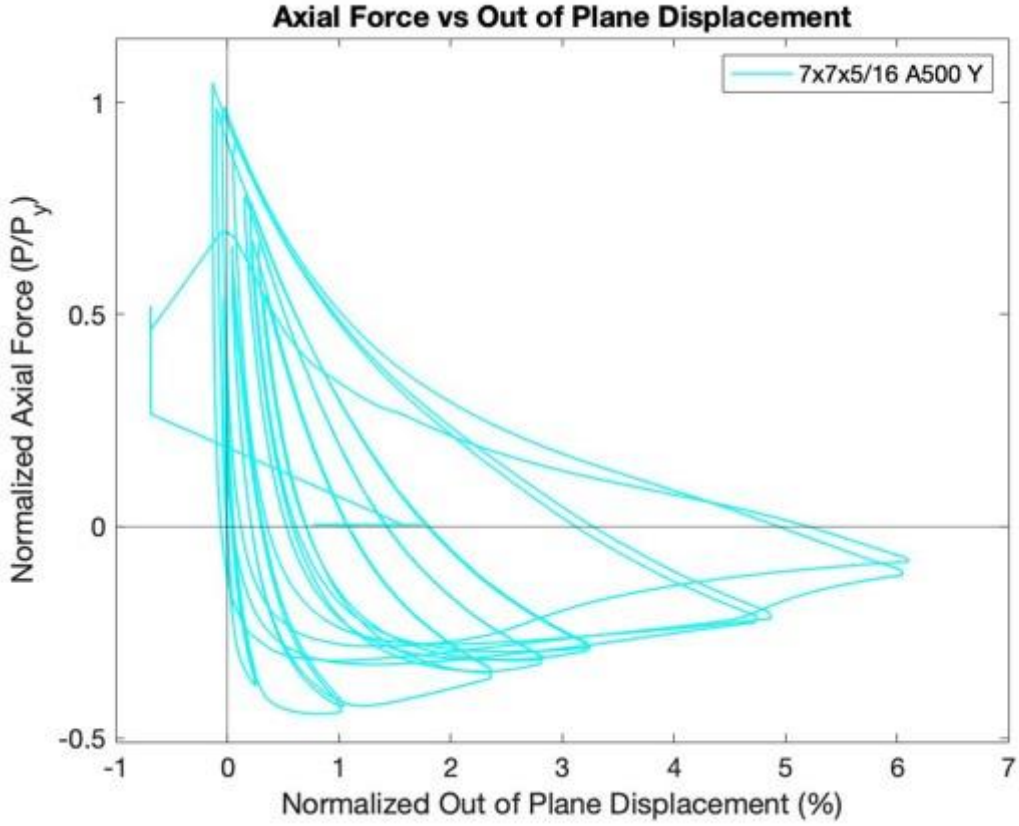
Axial Force vs Out of Plane Displacement
7x7x5/16 A500 Y
Normalized Axial Force (P/P_y)
Normalized Out of Plane Displacement (%)
1
0.5
0
-0.5
-1
0
1
2
3
4
5
6
7

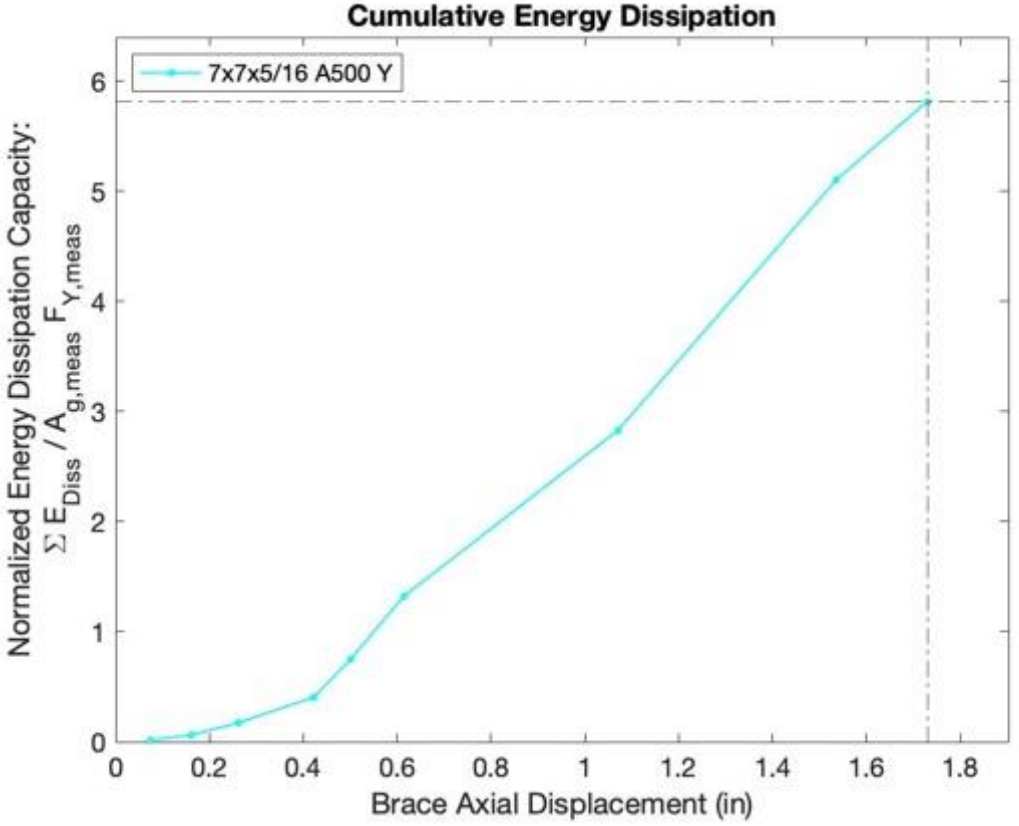
Cumulative Energy Dissipation
7x7x5/16 A500 Y
Normalized Energy Dissipation Capacity:
Σ E_Diss / A_g,meas F_Y,meas
Brace Axial Displacement (in)
0
1
2
3
4
5
6
0
0.2
0.4
0.6
0.8
1
1.2
1.4
1.6
1.8

Photos

Cupping at Center of Specimen: 1.75” Cycle 1 & 2 C

Fractured Specimen: 2.25” Cycle 1 T

Initial Striations at Center of Specimen: 2.25” Cycle 1 T

Tearing at Center of Specimen: 2.25” Cycle 1 T

Peak Out of Plane Displacement: 1.75” Cycle 1 & 2

7x7x5/16 A1085 Y Brace Test Summary

Test Name: 7x7x5/16 A1085 Y
Test Date: 5/20/2021 - 2:30 PM

Brace Properties

Measured Yield Stress (ksi)	57.7
Measured Ultimate Stress (ksi)	64.13
Yield Load (kips)	456.5
Critical Buckling Load (kips)	251.7
Percent Elongation - 2" (%)	33.12
CVN Width (mm)	5
CVN Absorbed Energy (ft-lbs)	18.5
Brace Length (in.)	237.5

Area (in²)	8.12
Moment of Inertia (in⁴)	59.6
Corner Radius (in.)	0.667
Thickness - Nominal (in.)	0.313
Thickness - Measured (in.)	0.305
Brace Compactness Ratio (b/t) - Nominal *	19.4
Brace Compactness Ratio (b/t) - Measured	18.58
Global Slenderness ratio (KL/r)	87.6

Specimen Performance

Test Event	Axial Brace Displacement (in.)	Target Displacement (in.) (Cycle)	Force (kips)	$P / P_{Yield/Critical}$	
Peak Tension Load	1.72	2.25 (1)	478.1	1.05	Y
B1: Initial Global Buckling	-0.21	0.375 (1)	-201.5	0.80	C
B2: Moderate Global Buckling	-1.69	1.75 (1)	-81.2	0.32	C
B3-T: Local Buckling	-1.74	1.75 (2)	-56.3	0.22	C
B3-C: Striations & Tearing	1.35	2.25 (2)	264.7	0.58	Y
B4: Brace Fracture	1.99	2.75 (1)	146.1	0.32	Y

Key Observations

Cycle #	Displacement (in.)	Observations
5-6	0.375	Minor OOP buckling displacement Bolt Slip - South Gusset Plate T2
11-12	0.75	Bolt Slip - North Gusset Plate T1 Similar to previous cycles
15-16	1.75	Minor cupping observed C1 peak displacement (~⅛") Moderate cupping observed C2 peak displacement (~1")

		Center of cupping: 4” North of center
17-18	2.25	No striations observed T1 peak displacement Major cupping observed C1 peak displacement (~2”) Striations and tearing at T2 peak displacement - tore through east, top, and bottom faces of specimen at cupping location Major cupping observed C2 peak displacement (~2”)
19-20	2.75	Fractured in first tension cycle before reaching peak displacement

Test Results

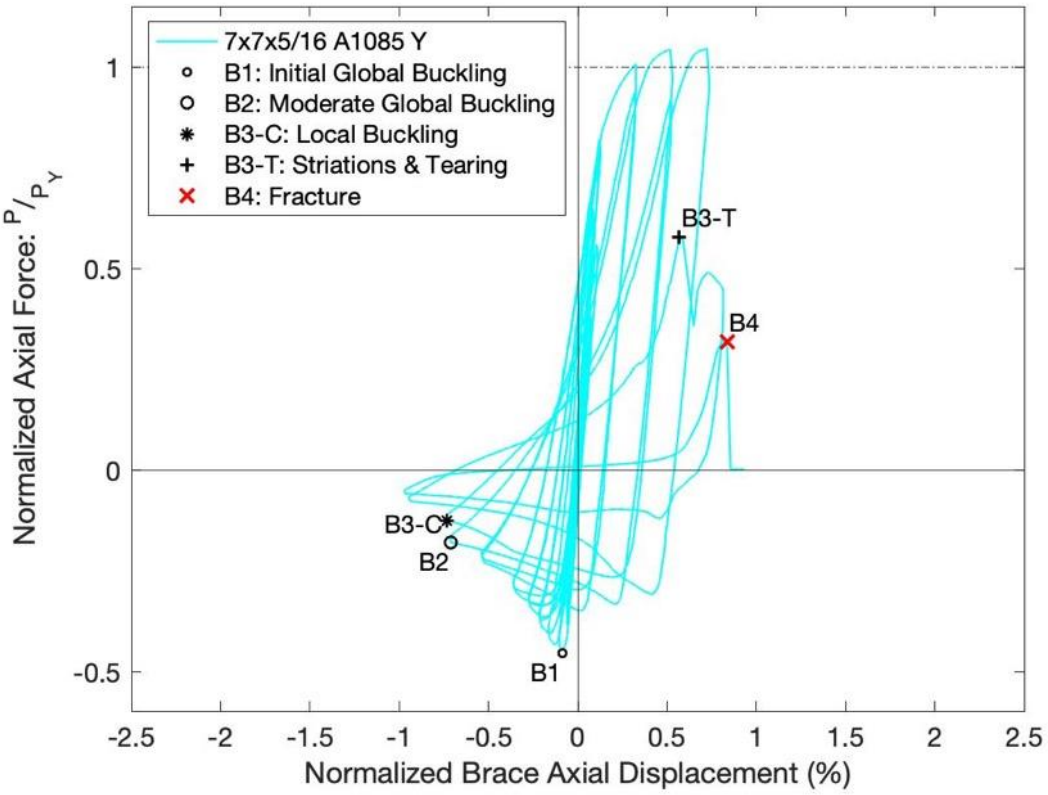

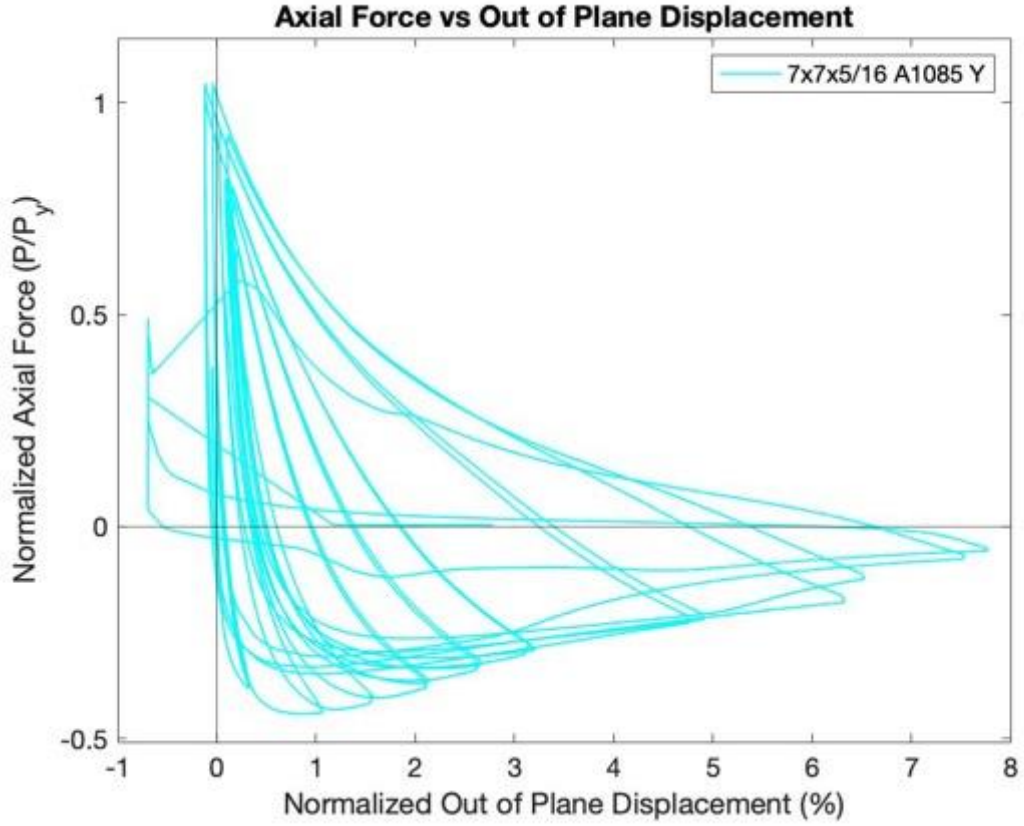
Axial Force vs Out of Plane Displacement
7x7x5/16 A1085 Y
Normalized Axial Force (P/P_y)
Normalized Out of Plane Displacement (%)
1
0.5
0
-0.5
-1
0
1
2
3
4
5
6
7
8

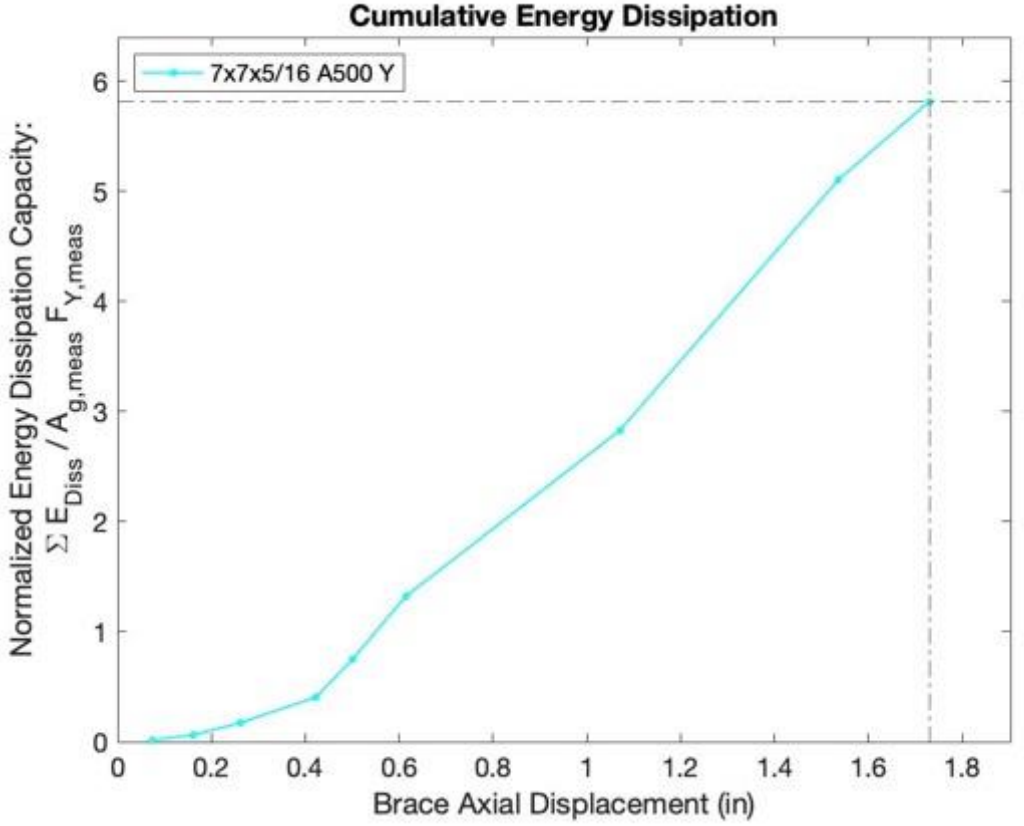
Cumulative Energy Dissipation
7x7x5/16 A500 Y
Normalized Energy Dissipation Capacity:
Σ E_Diss / A_g,meas F_Y,meas
Brace Axial Displacement (in)
6
5
4
3
2
1
0
0
0.2
0.4
0.6
0.8
1
1.2
1.4
1.6
1.8

Photos

Cupping at Center of Specimen: 2.25”
Cycles 1 and 2 C

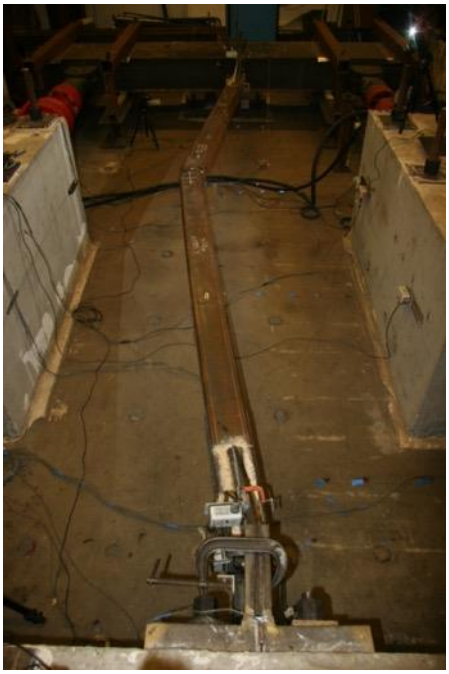

Peak out of Plane Displacement: 2.25”
Cycles 1 & 2 C

Fractured Specimen: 2.75” Cycle 1 T

Development of Striations at Center of Specimen:
2.25” Cycle 2 T

Tearing Through Specimen: 2.25” Cycle 2 T

7x7x3/8 A500 Y Brace Test Summary

Test Name: 7x7x3/8 A500 Y
Test Date: 5/25/2021 - 2:00 PM

Brace Properties

Measured Yield Stress (ksi)	61.35
Measured Ultimate Stress (ksi)	72.19
Yield Load (kips)	539.3
Critical Buckling Load (kips)	277.9
Percent Elongation - 2" (%)	30.76
CVN Width (mm)	7.5
CVN Absorbed Energy (ft-lbs)	14.3
Brace Length (in.)	237.5

Area (in²)	8.97
Moment of Inertia (in⁴)	68.7
Corner Radius (in.)	0.832
Thickness - Nominal (in.)	0.349
Thickness - Measured (in.)	0.342
Brace Compactness Ratio (b/t) - Nominal *	17.1
Brace Compactness Ratio (b/t) - Measured	15.60
Global Slenderness ratio (KL/r)	88.3

Specimen Performance

Test Event	Axial Brace Displacement (in.)	Target Displacement (in.) (Cycle)	Force (kips)	P / $P_{Yield/Critical}$	
Peak Tension Load	1.70	2.25 (1)	570.9	1.06	Y
B1: Initial Global Buckling	-0.26	0.375 (1)	-231.8	0.83	C
B2: Moderate Global Buckling	-1.76	1.75 (1)	-99.5	0.36	C
B3-T: Local Buckling	-2.23	2.25 (2)	-60.7	0.22	C
B3-C: Striations & Tearing	1.65	2.75 (2)	237.8	0.44	Y
B4: Brace Fracture	-1.82	2.75 (2)	-5.4	0.02	C

Key Observations

Cycle #	Displacement (in.)	Observations
7-8	0.5	Bolt slip T1 - North and South Gusset Plates Similar out of plane buckling displacement as previous cycles
17-18	2.25	Minor cupping observed at C1 peak displacement (~3/16” deep) Cupping observed at C2 peak displacement (~¾”) Center of cupping: 3” north of center

19-20	2.75	Major cupping observed at C1 peak displacement (~2+") Tearing observed at T2 peak displacement - through east, top, and bottom faces of specimen Brace fractured in compression in cycle 2, at about 1.5" displacement

Test Results

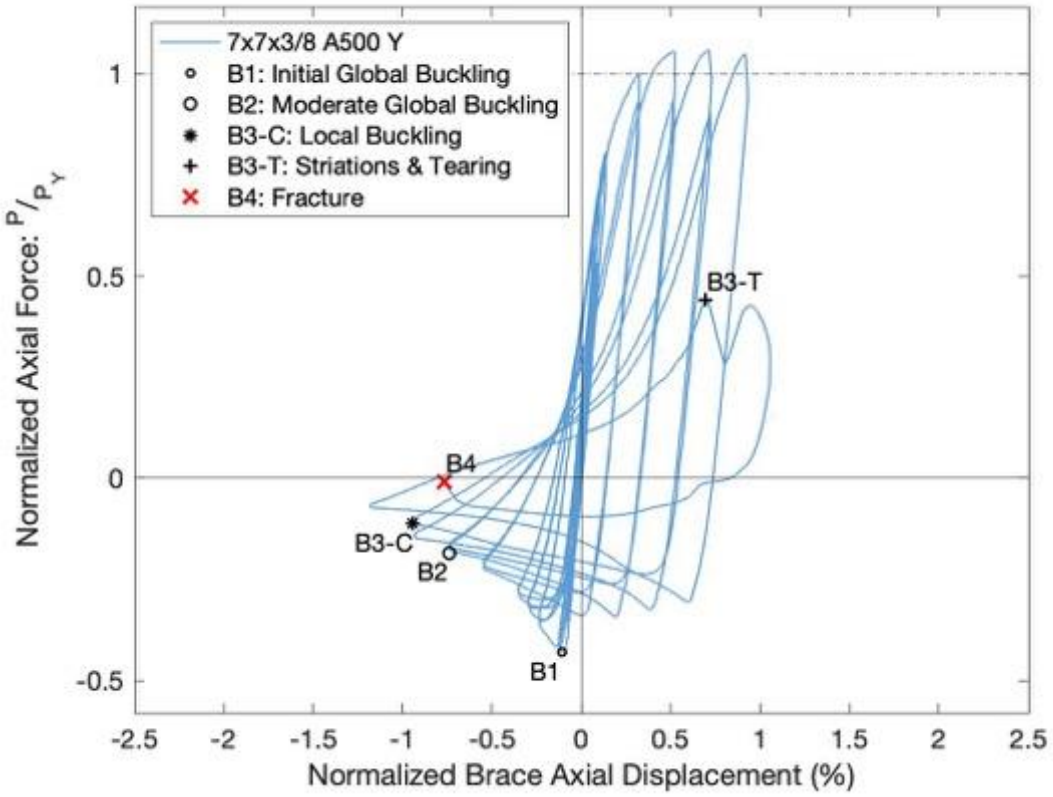

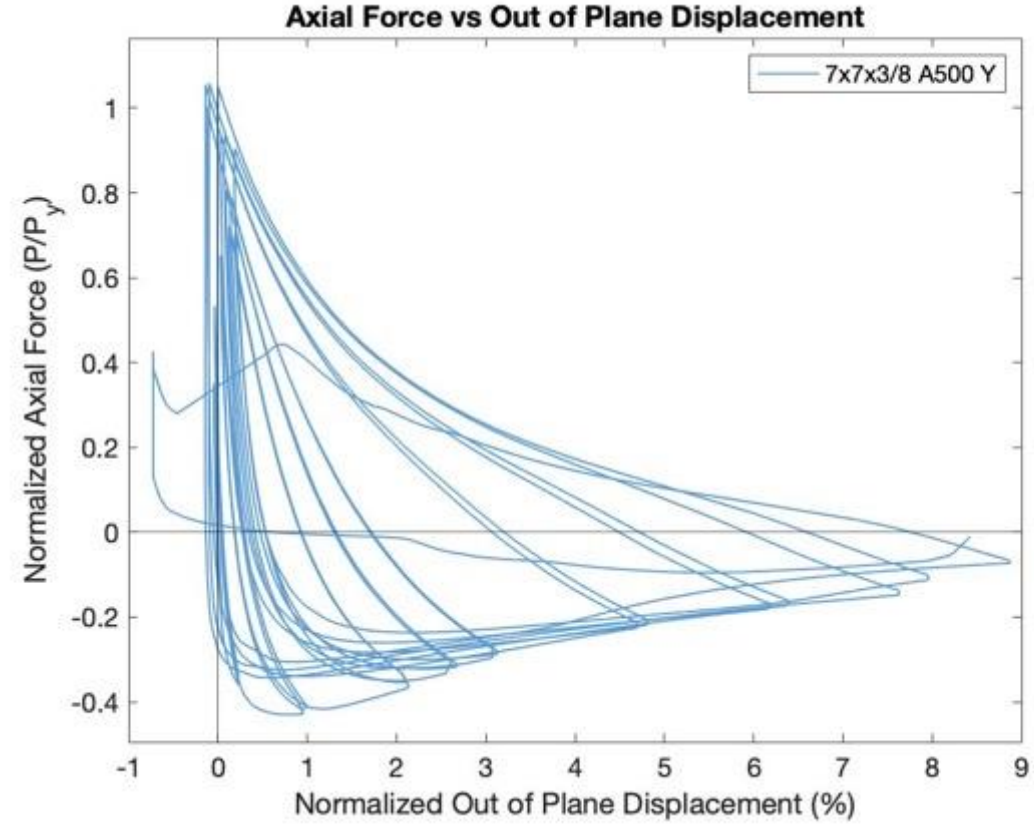
Axial Force vs Out of Plane Displacement
7x7x3/8 A500 Y
Normalized Axial Force (P/P_y)
Normalized Out of Plane Displacement (%)
1
0.8
0.6
0.4
0.2
0
-0.2
-0.4
-1
0
1
2
3
4
5
6
7
8
9

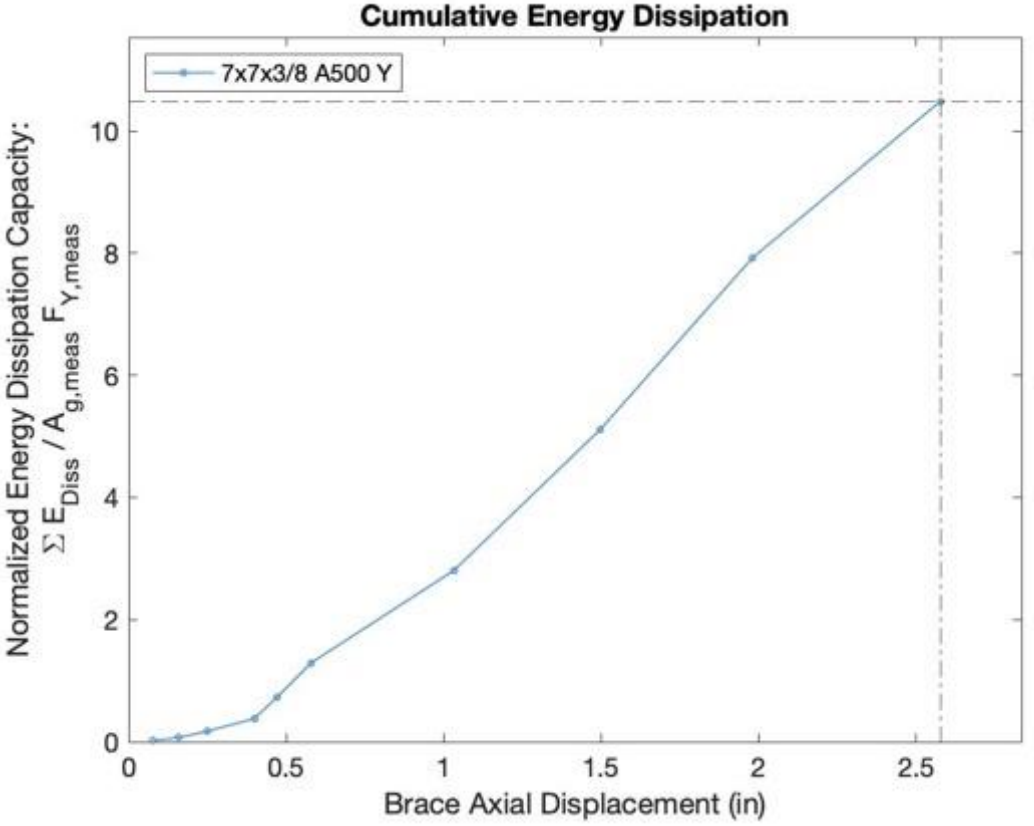
Cumulative Energy Dissipation
7x7x3/8 A500 Y
Normalized Energy Dissipation Capacity:
Σ E_Diss / A_g,meas F_Y,meas
Brace Axial Displacement (in)
10
8
6
4
2
0
0
0.5
1
1.5
2
2.5

Photos

Cupping at Center of Specimen: 2.75” Cycle 1 C

Initiation of Tearing at Center of Specimen: 2.75” Cycle 2 T

Tearing Through Center of Specimen: 2.75” Cycle 2 T

Fractured Specimen: 2.75” Cycle 2 C

7x7x3/8 A1085 Y Brace Test Summary

Test Name: 7x7x3/8 A1085 Y
Test Date: 5/27/2021 - 2:15 PM

Brace Properties

Measured Yield Stress (ksi)	61.89
Measured Ultimate Stress (ksi)	70.07
Yield Load (kips)	577.1
Critical Buckling Load (kips)	292.2
Percent Elongation - 2" (%)	31.32
CVN Width (mm)	7.5
CVN Absorbed Energy (ft-lbs)	17.3
Brace Length (in.)	237.5

Area (in²)	9.58
Moment of Inertia (in⁴)	68.7
Corner Radius (in.)	0.906
Thickness - Nominal (in.)	0.375
Thickness - Measured (in.)	0.365
Brace Compactness Ratio (b/t) - Nominal *	15.7
Brace Compactness Ratio (b/t) - Measured	14.21
Global Slenderness ratio (KL/r)	88.6

Specimen Performance

Test Event	Axial Brace Displacement (in.)	Target Displacement (in.) (Cycle)	Force (kips)	$P / P_{Yield/Critical}$	
Peak Tension Load	1.53	1.75 (1)	615.9	1.07	Y
B1: Initial Global Buckling	-0.27	0.375 (1)	-254.9	0.87	C
B2: Moderate Global Buckling	-1.82	1.75 (1)	-106.0	0.36	C
B3-T: Local Buckling	-2.27	2.25 (1)	-82.6	0.28	C
B3-C: Striations & Tearing	1.44	2.75 (2)	234.0	0.41	Y
B4: Brace Fracture	2.36	3.25 (1)	152.5	0.26	Y

Key Observations

Cycle #	Displacement (in.)	Observations
5-6	0.375	Minor bolt slip T1: North and South gusset plates Knocking and racking sounds when in tension Minor OOP buckling displacement
9-10	0.625	Major bolt slip T1: North and South gusset plates Similar to previous cycles

17-18	2.25	Minor cupping observed C1 peak displacement (~⅜" deep) Moderate/Major cupping observed C2 peak displacement (1.5") Cupping centered 2" North of center
19-20	2.75	Major cupping C1 peak displacement (2") Significant vertical deformation at top and bottom of brace at location of cupping Tearing through east, top, and bottom faces of brace at T2 peak displacement Major cupping at C2 peak displacement - similar to C1
21-22	3.25	Brace fracture in cycle T1 before reaching target displacement

Test Results

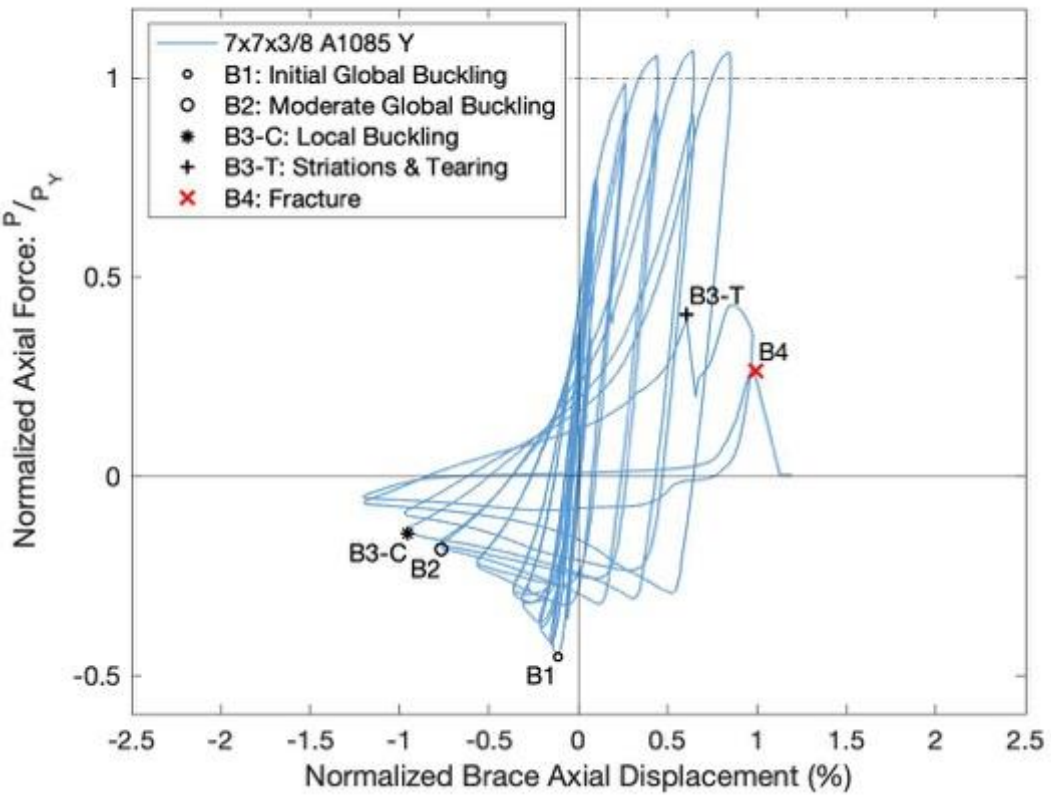

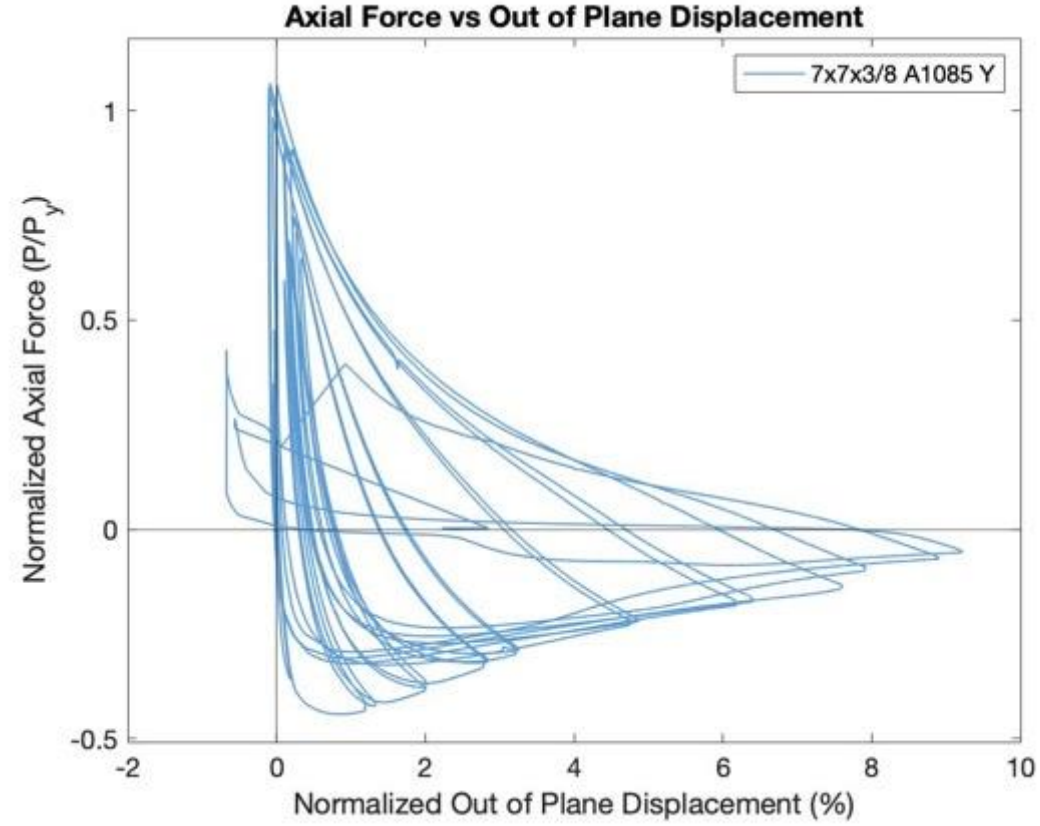
Axial Force vs Out of Plane Displacement
7x7x3/8 A1085 Y
Normalized Axial Force (P/P_y)
Normalized Out of Plane Displacement (%)
1
0.5
0
-0.5
-2
0
2
4
6
8
10

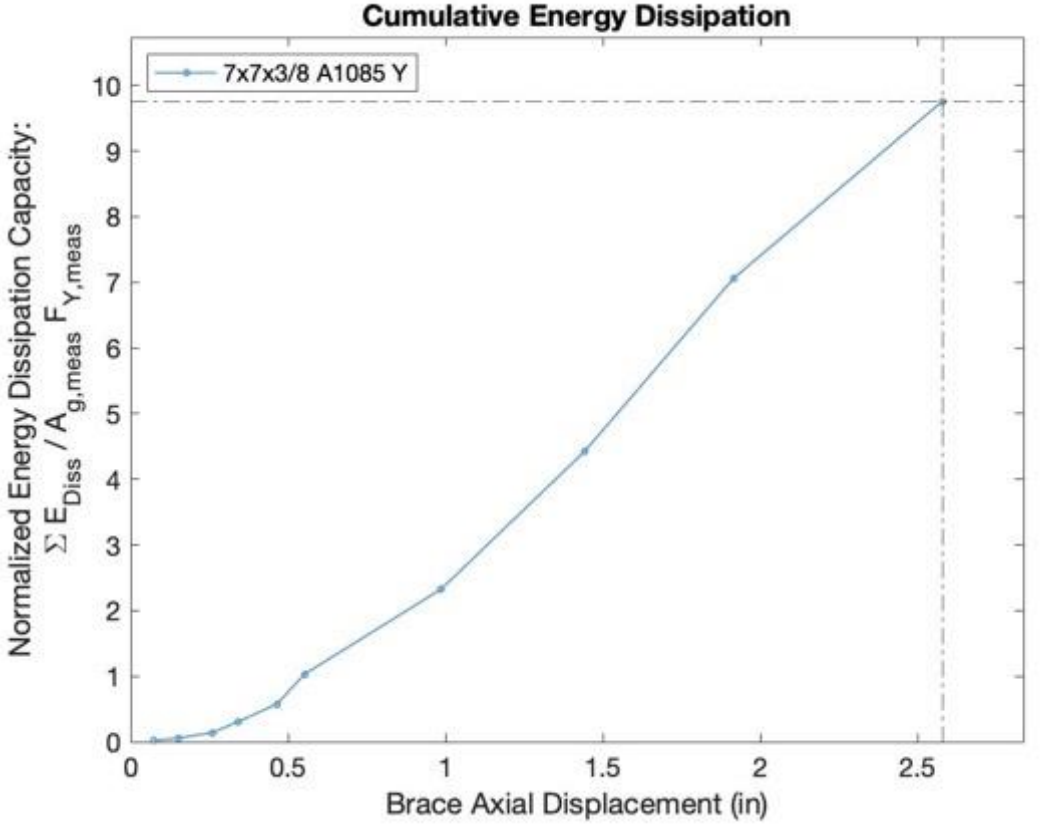
Cumulative Energy Dissipation
7x7x3/8 A1085 Y
Normalized Energy Dissipation Capacity:
Σ E_Diss / A_g,meas F_Y,meas
Brace Axial Displacement (in)
0
1
2
3
4
5
6
7
8
9
10
0
0.5
1
1.5
2
2.5

Photos

Cupping at Center of Specimen: 2.75” Cycles 1 & 2 C

Tearing Through Specimen: 2.75” Cycle 2 T

Initiation of Tearing at Center of Specimen: 2.75” Cycle 2 T

Fractured Specimen after 3.25” Displacement - Cycle 1 T

7x7x1/2 A500 B Brace Test Summary

Test Name: 7x7x1/2 A500 B
Test Date: 6/9/2021 - 1:00 PM

Brace Properties

Measured Yield Stress (ksi)	57.82
Measured Ultimate Stress (ksi)	69.14
Yield Load (kips)	669.3
Critical Buckling Load (kips)	347.3
Percent Elongation - 2" (%)	29.6
CVN Width (mm)	10
CVN Absorbed Energy (ft-lbs)	42
Brace Length (in.)	237.5

Area (in²)	11.6
Moment of Inertia (in⁴)	80.5
Corner Radius (in.)	0.945
Thickness - Nominal (in.)	0.465
Thickness - Measured (in.)	0.464
Brace Compactness Ratio (b/t) - Nominal *	12.1
Brace Compactness Ratio (b/t) - Measured	11.01
Global Slenderness ratio (KL/r)	90.3

Specimen Performance

Test Event	Axial Brace Displacement (in.)	Target Displacement (in.) (Cycle)	Force (kips)	P / $P_{Yield/Critical}$	
Peak Tension Load	1.64	1.75 (1)	710.4	1.06	Y
B1: Initial Global Buckling	-0.22	0.375 (1)	-278.8	0.80	C
B2: Moderate Global Buckling	-1.75	1.75 (1)	-124.0	0.36	C
B3-T: Local Buckling	-3.17	3.25 (2)	-77.2	0.22	C
B3-C: Striations & Tearing	3.27	4.25 (1)	594.0	0.89	Y
B4: Brace Fracture	3.59	4.25 (2)	186.0	0.28	Y

Key Observations

Cycle #	Displacement (in.)	Observations
11-12	0.75	Bolt slip T1 - North & South gusset plates Adjusted the string pot measuring the North gusset plate elongation - fell off when bolts slipped
21-22	3.25	Minor cupping at C1 peak displacement - (~⅛") Minor cupping at C2 peak displacement - (¼") Cupping more localized during second cycle

23-24	3.75	Cupping at C1 peak displacement - (¾") Location of cupping: ~1" North of center Major cupping at C2 peak displacement - (½") Unpredicted actuator behavior near peak tensile displacements - actuators not in sync, about a 1" difference in displacement near target peak
25-26	4.25	Same unpredicted actuator behavior near peak tensile displacement Striations observed near peak displacement – T1 Major cupping at C1 peak displacement - (2.5") Fractured during T2 near peak displacement

Test Results

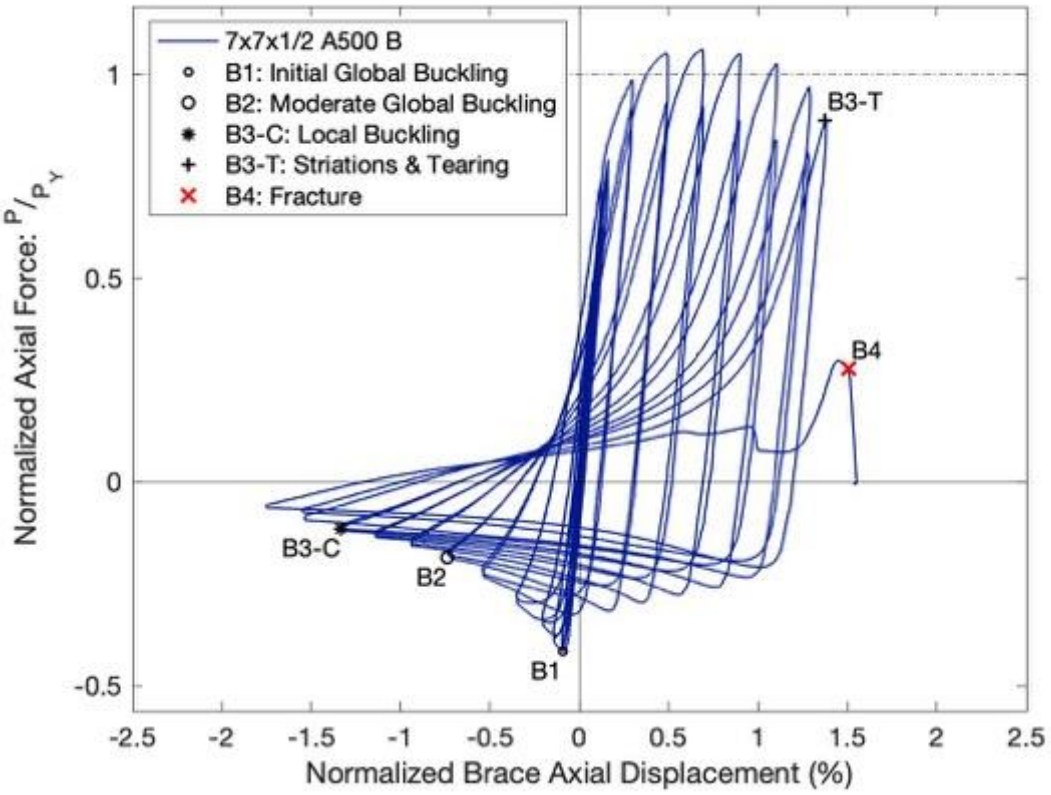

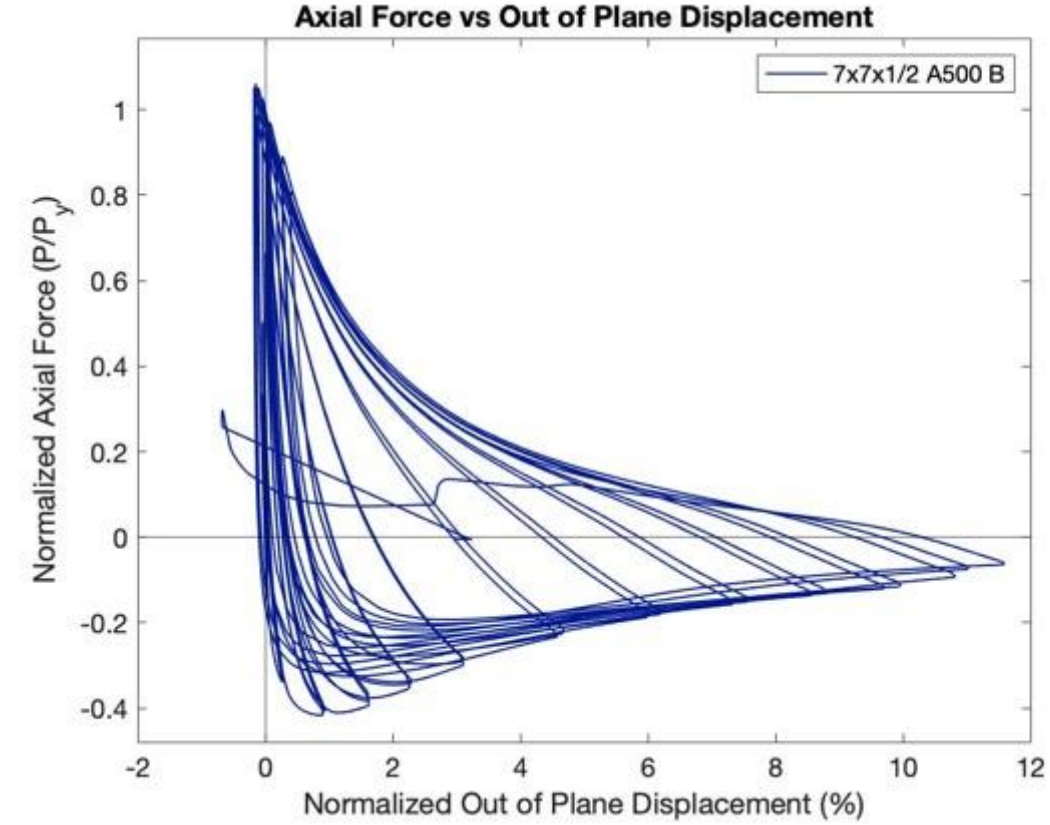
Axial Force vs Out of Plane Displacement
7x7x1/2 A500 B
Normalized Axial Force (P/P$_y$)
Normalized Out of Plane Displacement (%)
1
0.8
0.6
0.4
0.2
0
-0.2
-0.4
-2
0
2
4
6
8
10
12

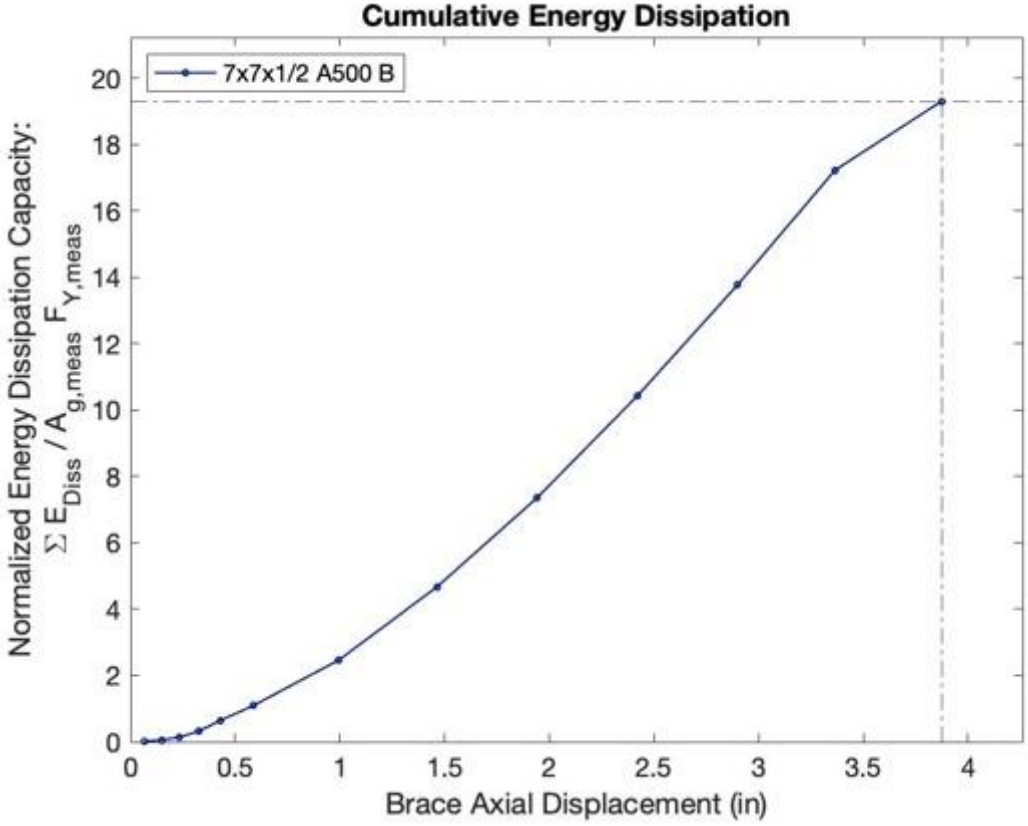
Cumulative Energy Dissipation
7x7x1/2 A500 B
Normalized Energy Dissipation Capacity:
$\Sigma E_{Diss} / A_{g,meas} F_{Y,meas}$
Brace Axial Displacement (in)
20
18
16
14
12
10
8
6
4
2
0
0
0.5
1
1.5
2
2.5
3
3.5
4

Photos

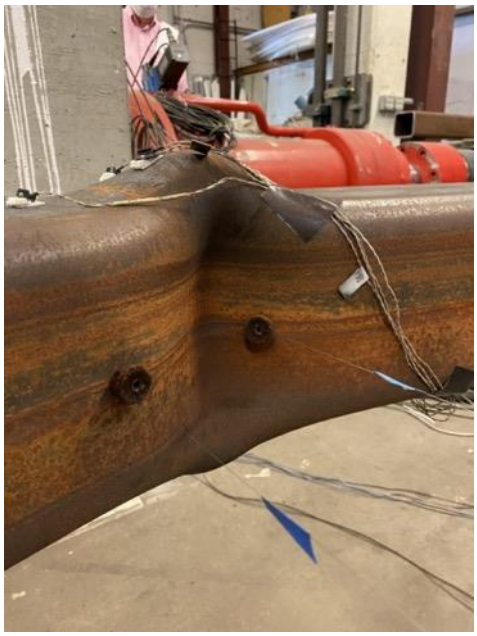

Cupping at Center of Brace: 3.75” Cycles

Development of Striations at Center of Brace: 4.25” Cycle 1 T

Tearing at Center of Specimen: 4.25” Cycles

Fractured Specimen

7x7x1/2 A1085 Y Brace Test Summary

Test Name: 7x7x1/2 A1085 Y
Test Date: 6/4/2021 - 11:30 AM

Brace Properties

Measured Yield Stress (ksi)	64.375
Measured Ultimate Stress (ksi)	71.68
Yield Load (kips)	772.7
Critical Buckling Load (kips)	363.6
Percent Elongation - 2" (%)	32.7
CVN Width (mm)	10
CVN Absorbed Energy (ft-lbs)	28.7
Brace Length (in.)	237.5

Area (in²)	12.4
Moment of Inertia (in⁴)	84.7
Corner Radius (in.)	1.047
Thickness - Nominal (in.)	0.5
Thickness - Measured (in.)	0.484
Brace Compactness Ratio (b/t) - Nominal *	11
Brace Compactness Ratio (b/t) - Measured	10.14
Global Slenderness ratio (KL/r)	91

Specimen Performance

Test Event	Axial Brace Displacement (in.)	Target Displacement (in.) (Cycle)	Force (kips)	$P / P_{Yield/Critical}$	
Peak Tension Load	1.44	2.25 (1)	805.1	1.04	Y
B1: Initial Global Buckling	-0.32	0.375 (1)	-305.7	0.84	C
B2: Moderate Global Buckling	-1.87	1.75 (1)	-141.9	0.39	C
B3-T: Local Buckling	-3.38	3.25 (2)	-80.2	0.22	C
B3-C: Striations & Tearing	3.19	4.25 (1)	760.0	0.98	Y
B4: Brace Fracture	3.48	4.25 (2)	270.0	0.35	Y

Key Observations

Cycle #	Displacement (in.)	Observations
7-8	0.5	Bolt slip T1: North and South gusset plates
21-22	3.25	Minor cupping at C1 peak displacement (~3/16”) Cupping at C2 peak displacement (~⅜”) Cupping location: 2” North of brace center

23-24	3.75	Cupping at C1 peak displacement (1”) Cupping at C2 peak displacement (1.25”) Very hot at center of specimen
25-26	4.25	Striations observed at T1 peak displacement Major cupping at C1 peak displacement (~1.75”) Fracture at T2 near peak displacement

Test Results

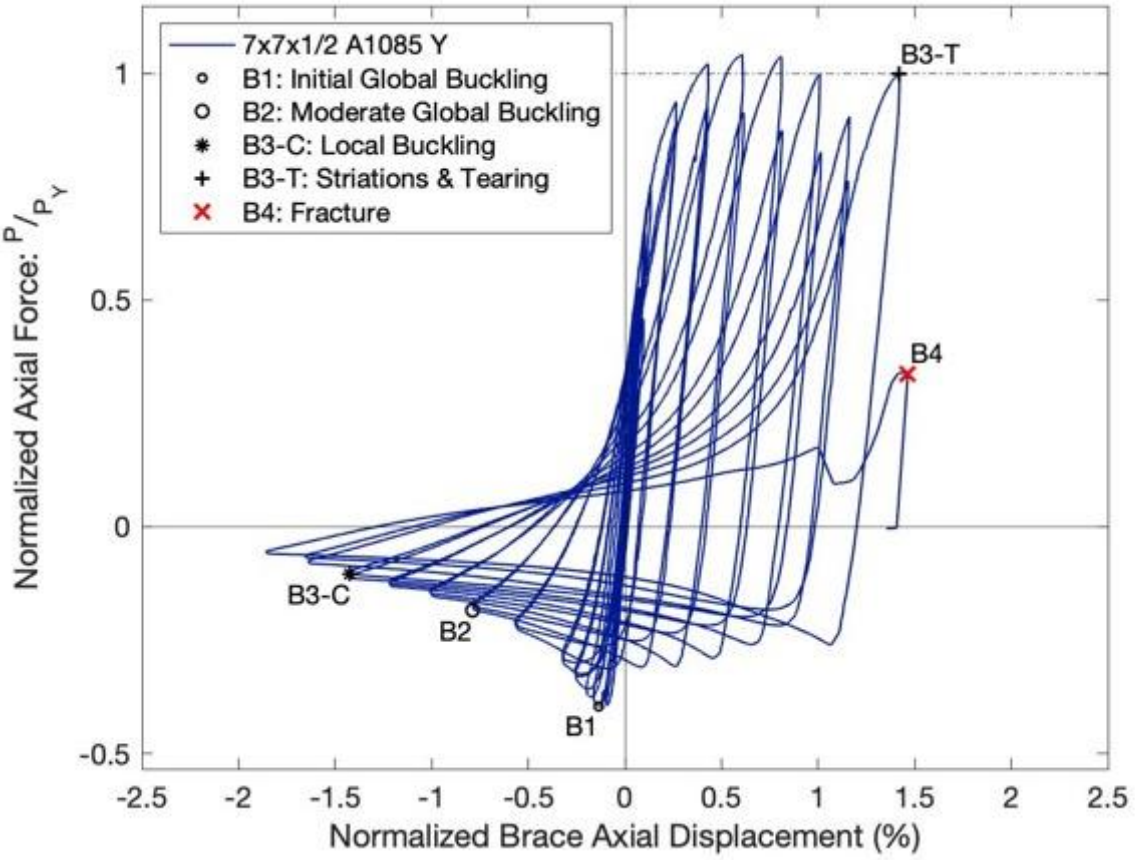

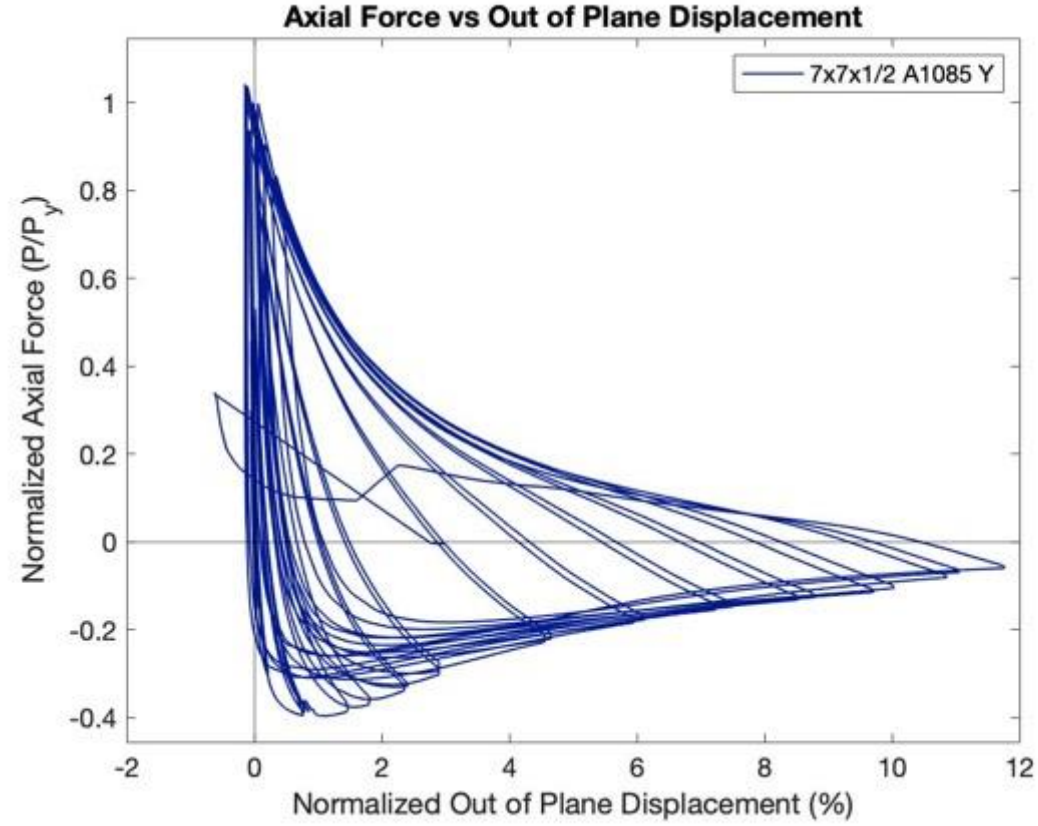
Axial Force vs Out of Plane Displacement
7x7x1/2 A1085 Y
Normalized Axial Force (P/P$_y$)
Normalized Out of Plane Displacement (%)
1
0.8
0.6
0.4
0.2
0
-0.2
-0.4
-2
0
2
4
6
8
10
12

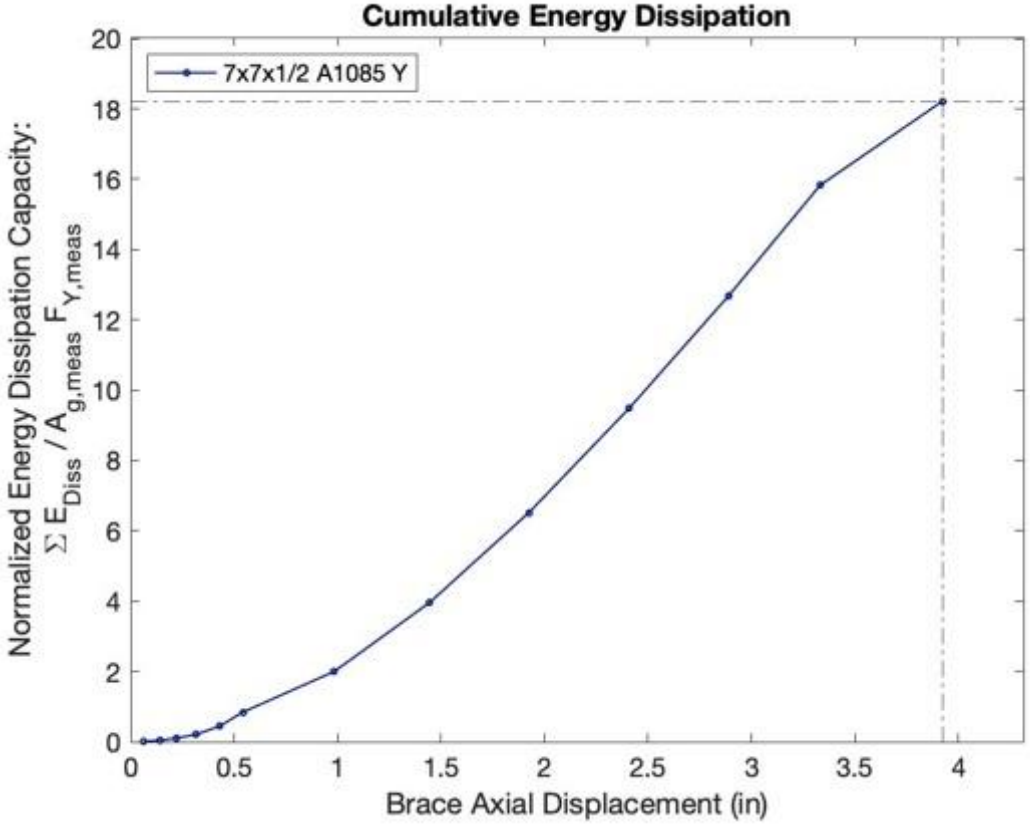
Cumulative Energy Dissipation
7x7x1/2 A1085 Y
Normalized Energy Dissipation Capacity:
$\Sigma E_{Diss} / A_{g,meas} F_{Y,meas}$
Brace Axial Displacement (in)
20
18
16
14
12
10
8
6
4
2
0
0
0.5
1
1.5
2
2.5
3
3.5
4

Photos

Cupping at Center of Specimen: 3.75”
Cycles 1 & 2 C

Closeup of Cupping: 4.25” Cycle 1 C

Development of Striations at Center of Specimen: 4.25”
Cycle 1 T

Fractured Specimen after 4.25”
Displacement - Cycle 2 T

8x8x3/8 A500 W Brace Test Summary

Test Name: 8x8x3/8 A500 W
Test Date: 6/11/2021 - 1:00 PM

Brace Properties

Measured Yield Stress (ksi)	66.19
Measured Ultimate Stress (ksi)	76.52
Yield Load (kips)	690.3
Critical Buckling Load (kips)	387.0
Percent Elongation - 2" (%)	34.44
CVN Width (mm)	7.5
CVN Absorbed Energy (ft-lbs)	65.5
Brace Length (in.)	237.5

Area (in²)	10.4
Moment of Inertia (in⁴)	100
Corner Radius (in.)	0.801
Thickness - Nominal (in.)	0.349
Thickness - Measured (in.)	0.35
Brace Compactness Ratio (b/t) - Nominal *	19.9
Brace Compactness Ratio (b/t) - Measured	18.28
Global Slenderness ratio (KL/r)	76.6

Specimen Performance

Test Event	Axial Brace Displacement (in.)	Target Displacement (in.) (Cycle)	Force (kips)	P / $P_{Yield/Critical}$	
Peak Tension Load	1.06	1.75 (1)	702.7	1.02	Y
B1: Initial Global Buckling	-0.28	0.5 (1)	360.0	-0.93	C
B2: Moderate Global Buckling	-1.89	1.75 (1)	-75.0	0.19	C
B3-T: Local Buckling	-1.33	1.25 (2)	-134.0	0.35	C
B3-C: Striations & Tearing	0.96	1.75 (2)	614.0	0.89	Y
B4: Brace Fracture	1.24	2.25 (1)	310.6	0.45	Y

Key Observations

Cycle #	Displacement (in.)	Observations
9-10	0.625	Bolt slip at North and South gusset plates - T1 String pot measuring total longitudinal displacement fell off during bolt slip, replaced immediately
13-14	1.25	No observed cupping at C1 peak displacement Cupping observed at C2 peak displacement - (¾")

15-16	1.75	Major cupping at C1 peak displacement (1.75”) Striations and minor tearing at top and bottom corners on east face of specimen at T2 peak displacement Major cupping at C2 peak displacement (2”)
17-18	2.25	Specimen fractured near T1 peak displacement

Test Results

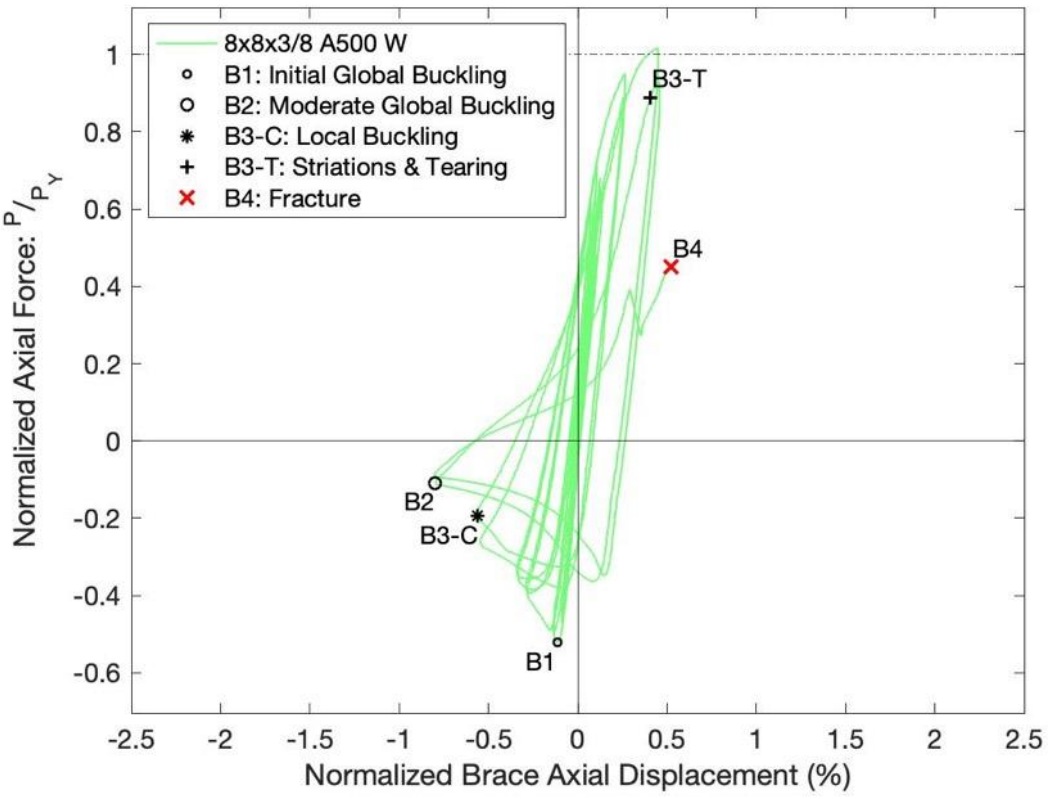

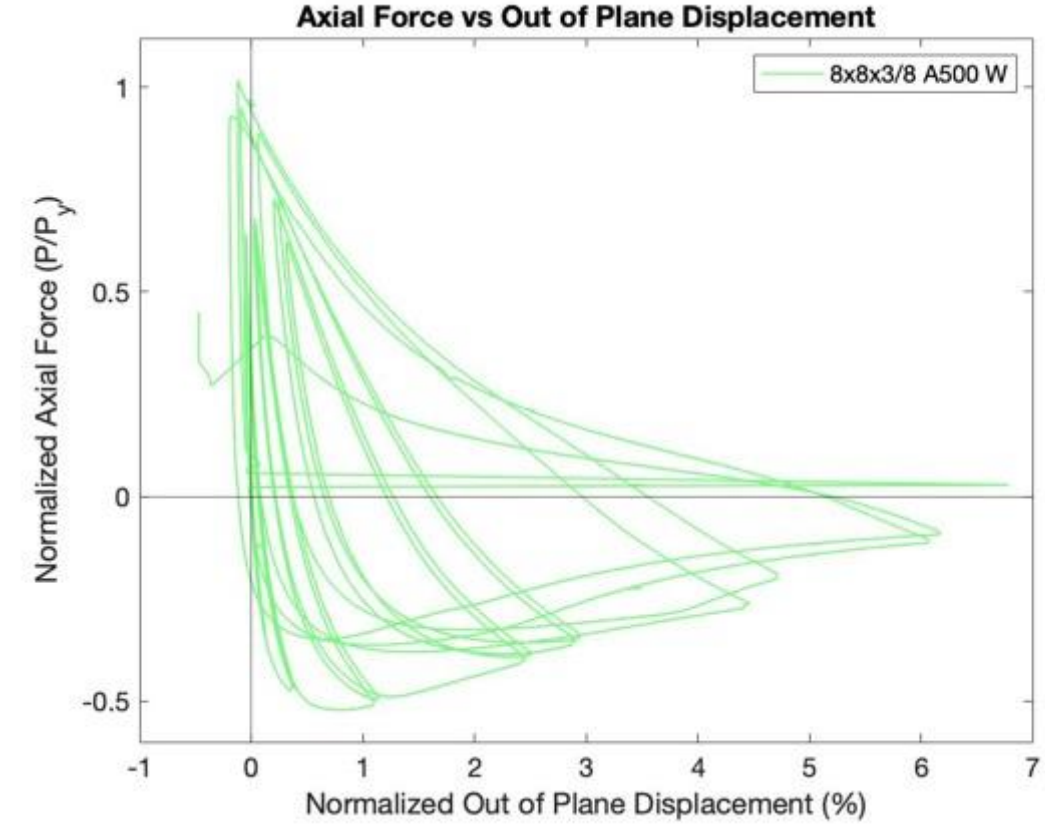
Axial Force vs Out of Plane Displacement
8x8x3/8 A500 W
Normalized Axial Force (P/P$_y$)
Normalized Out of Plane Displacement (%)
1
0.5
0
-0.5
-1
0
1
2
3
4
5
6
7

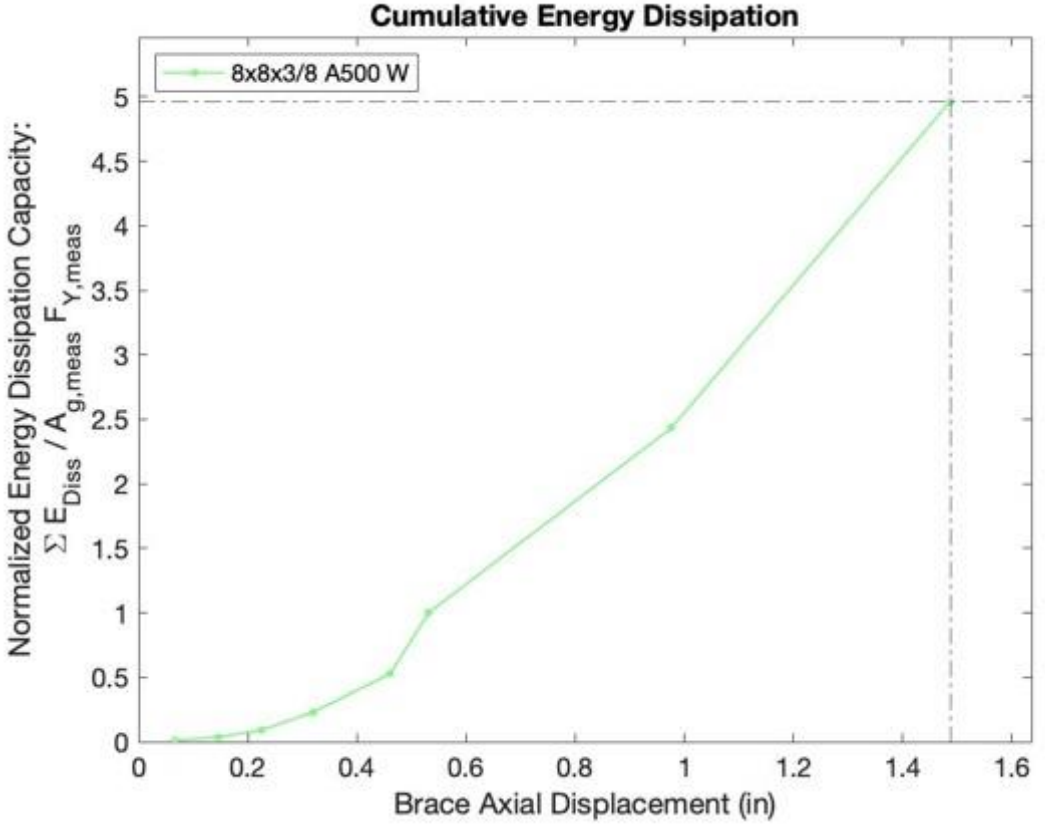
Cumulative Energy Dissipation
8x8x3/8 A500 W
Normalized Energy Dissipation Capacity:
$\Sigma E_{Diss} / A_{g,meas} F_{Y,meas}$
Brace Axial Displacement (in)
5
4.5
4
3.5
3
2.5
2
1.5
1
0.5
0
0
0.2
0.4
0.6
0.8
1
1.2
1.4
1.6

Photo

Cupping at Center of Specimen: 1.75” Cycle 1 C

Initiation of Striations and Tearing: 1.75” Cycle 2 T

Cupping after Initial Tearing: 1.75” Cycle 2 C

Tearing at Center Immediately Prior to Fracture: 2.25” Cycle 1 T

Peak OOP Displacement: 1.75”
Cycles 1 & 2 C

Fractured Specimen: 2.25” Cycle 1 T

8x8x3/8 A1085 Y Brace Test Summary

Test Name: 8x8x3/8 A1085 Y
Test Date: 6/15/2021 - 1:00 PM

Brace Properties

Measured Yield Stress (ksi)	60.37
Measured Ultimate Stress (ksi)	72.12
Yield Load (kips)	661.2
Critical Buckling Load (kips)	404.3
Percent Elongation - 2" (%)	34.2
CVN Width (mm)	7.5
CVN Absorbed Energy (ft-lbs)	8.5
Brace Length (in.)	237.5

Area (in²)	11.1
Moment of Inertia (in⁴)	106
Corner Radius (in.)	1.06
Thickness - Nominal (in.)	0.375
Thickness - Measured (in.)	0.37
Brace Compactness Ratio (b/t) - Nominal *	18.3
Brace Compactness Ratio (b/t) - Measured	15.89
Global Slenderness ratio (KL/r)	76.86

Specimen Performance

Test Event	Axial Brace Displacement (in.)	Target Displacement (in.) (Cycle)	Force (kips)	$P / P_{Yield/Critical}$	
Peak Tension Load	1.29	1.75 (1)	672.6	1.02	Y
B1: Initial Global Buckling	-0.31	0.5 (1)	-328.8	0.81	C
B2: Moderate Global Buckling	-2.17	1.75 (1)	-62.8	0.16	C
B3-T: Local Buckling	-1.68	1.75 (2)	-110.8	0.27	C
B3-C: Striations & Tearing	1.68	2.25 (2)	534.0	0.81	Y
B4: Brace Fracture	2.18	2.75 (1)	180.0	0.27	Y

Key Observations

Cycle #	Displacement (in.)	Observations
7-8	0.5	Minor bolt slip T1: North and South gusset plates Minor out of plane buckling displacement observed in compression
15-16	1.75	Minor cupping at C1 peak displacement (~⅛" deep) Slightly warm at center of specimen Cupping at C2 peak displacement (¾") Center of local cupping - 3.5" North of center

17-18	2.25	Major cupping at C1 peak displacement (2") Tearing through east/bottom faces - T2 peak displacement Major cupping at C2 peak displacement (2.25")
19-20	2.75	Fracture at T1 prior to peak displacement (~2.25" displacement)

Test Results

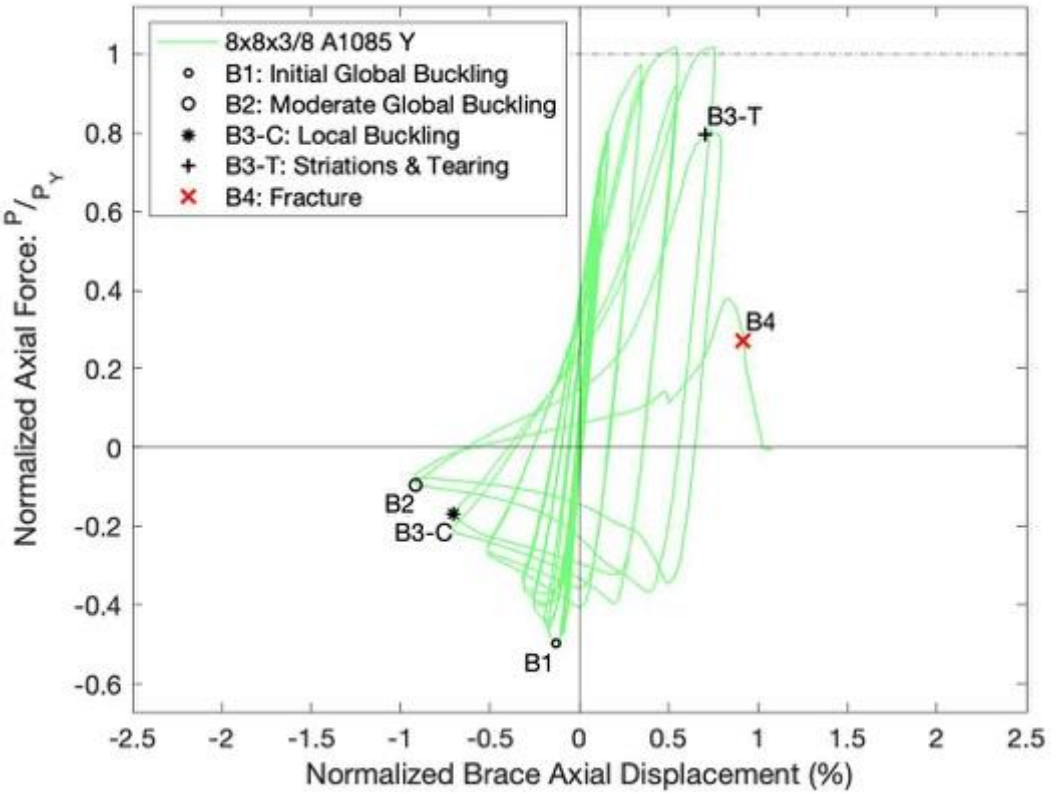

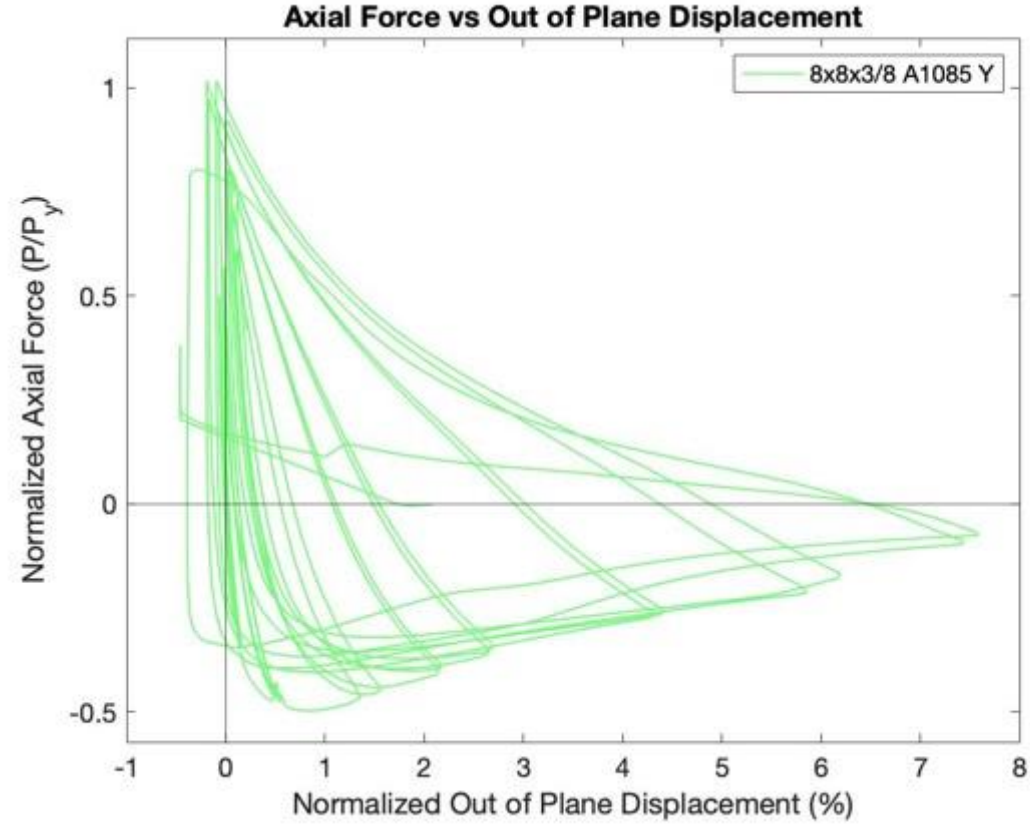
Axial Force vs Out of Plane Displacement
8x8x3/8 A1085 Y
Normalized Axial Force (P/P_y)
Normalized Out of Plane Displacement (%)
1
0.5
0
-0.5
-1
0
1
2
3
4
5
6
7
8

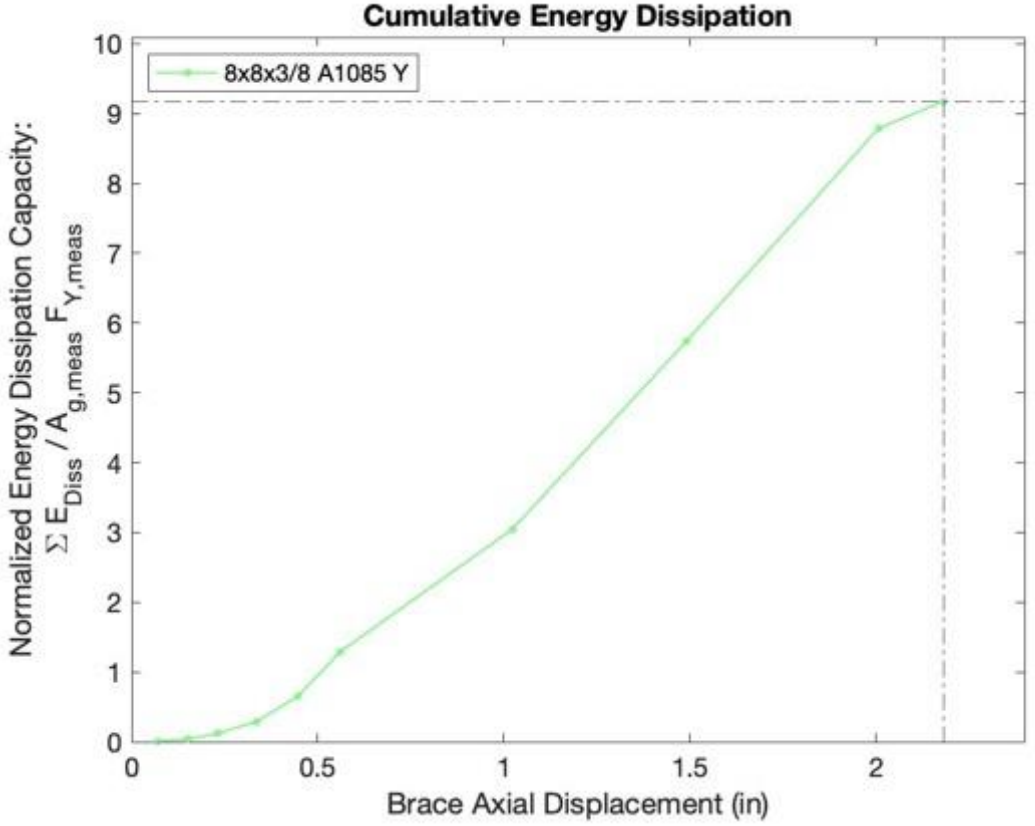
Cumulative Energy Dissipation
8x8x3/8 A1085 Y
Normalized Energy Dissipation Capacity:
Σ E_Diss / A_g,meas F_Y,meas
Brace Axial Displacement (in)
10
9
8
7
6
5
4
3
2
1
0
0
0.5
1
1.5
2

Photos

Cupping at Center of Specimen: 2.25” Cycle 1 C

Development of Striations and Tearing: 2.25” Cycle 2 T

Post-Tearing cupping at Center of Specimen: 2.25” Cycle 2 C

Fractured Specimen during 2.75” Cycle 1 T

8x8x1/2 A500 W Brace Test Summary

Test Name: 8x8x1/2 A500 W
Test Date: 6/23/21 & 7/2/21

Brace Properties

Measured Yield Stress (ksi)	65.47
Measured Ultimate Stress (ksi)	72.01
Yield Load (kips)	876.2
Critical Buckling Load (kips)	491.2
Percent Elongation - 2" (%)	33.12
CVN Width (mm)	10
CVN Absorbed Energy (ft-lbs)	67.3
Brace Length (in.)	237.5

Area (in²)	13.5
Moment of Inertia (in⁴)	125
Corner Radius (in.)	0.887
Thickness - Nominal (in.)	0.465
Thickness - Measured (in.)	0.461
Brace Compactness Ratio (b/t) - Nominal *	14.2
Brace Compactness Ratio (b/t) - Measured	13.51
Global Slenderness ratio (KL/r)	78.125

Specimen Performance

Test Event	Axial Brace Displacement (in.)	Target Displacement (in.) (Cycle)	Force (kips)	$P / P_{Yield/Critical}$	
Peak Tension Load	1.17	1.75 (1)	906.0	1.03	Y
B1: Initial Global Buckling	-0.33	0.625 (1)	-434.7	0.88	C
B2: Moderate Global Buckling	-2.04	2.25 (1)	-165.4	0.34	C
B3-T: Local Buckling	-2.05	2.25 (2)	-148.7	0.30	C
B3-C: Striations & Tearing	2.32	3.25 (1)	842.4	0.96	Y
B4: Brace Fracture	2.54	3.25 (2)	270.0	0.31	Y

Key Observations

Cycle #	Displacement (in.)	Observations
5-6	0.375	Stopped test after completing 1 full cycle due to unexpected actuator behavior Re-started test on 7/2/21 - Start with 0.375" Cycle 2 - Initial brace tensile force = 88 kip (From end of cycle 1) Bolt slip T2 - N & S GP
17-18	2.25	Very minor cupping (~⅛" deep, global) at peak compressive displacement C1 Local Cupping observed at peak displacement C2 (½" deep)
19-20	2.75	Cupping at C1 peak displacement ~1.75" deep No striations observed at T1 or T2 peak displacements

		Major cupping at C2 peak displacement ~2.75" deep
21-22	3.25	Striations and tearing at peak displacement T1 - Tore halfway through cross section, didn't fracture Direction of buckling switched to East in compression, tearing continued to develop through cross section Brace fractured in tension - T1 at about 3" displacement

Test Results

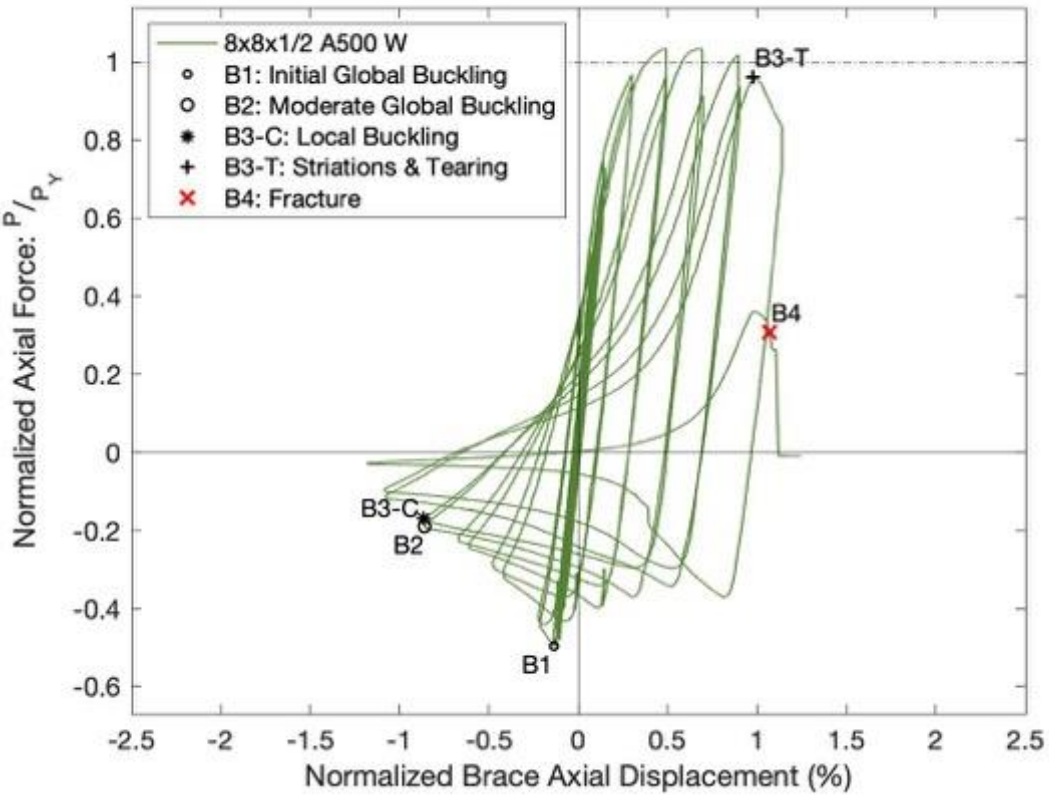

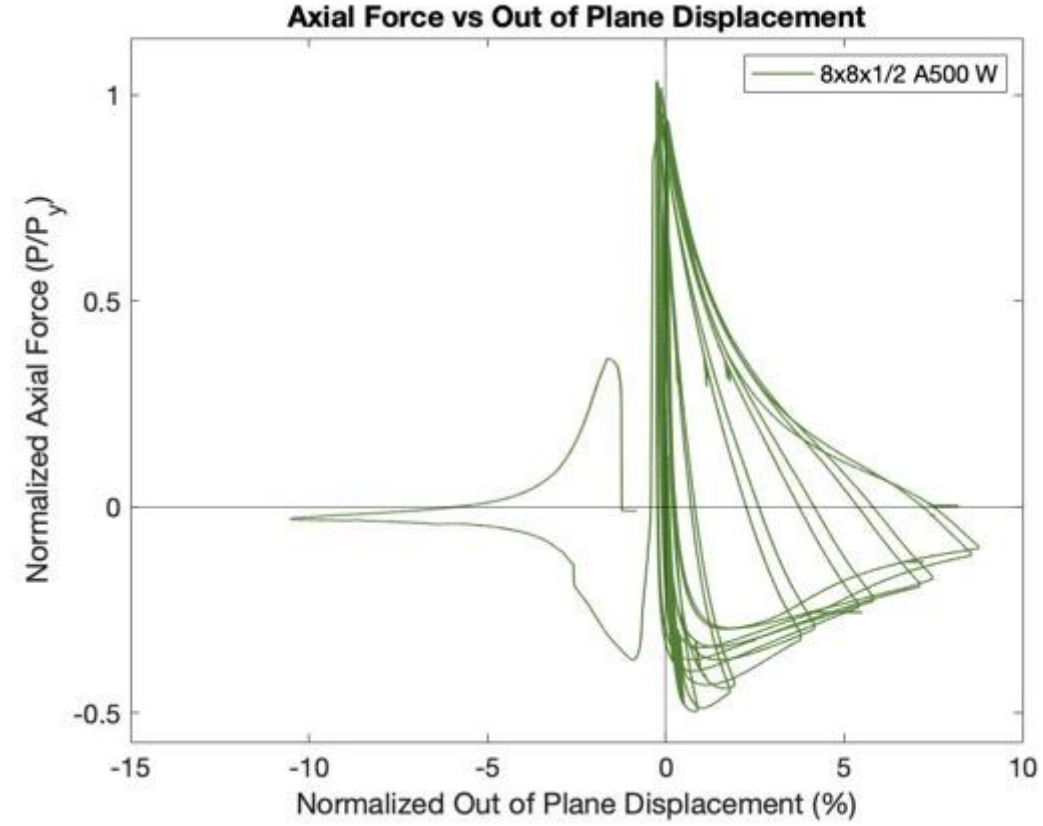
Axial Force vs Out of Plane Displacement
8x8x1/2 A500 W
Normalized Axial Force (P/P_y)
Normalized Out of Plane Displacement (%)
1
0.5
0
-0.5
-15
-10
-5
0
5
10

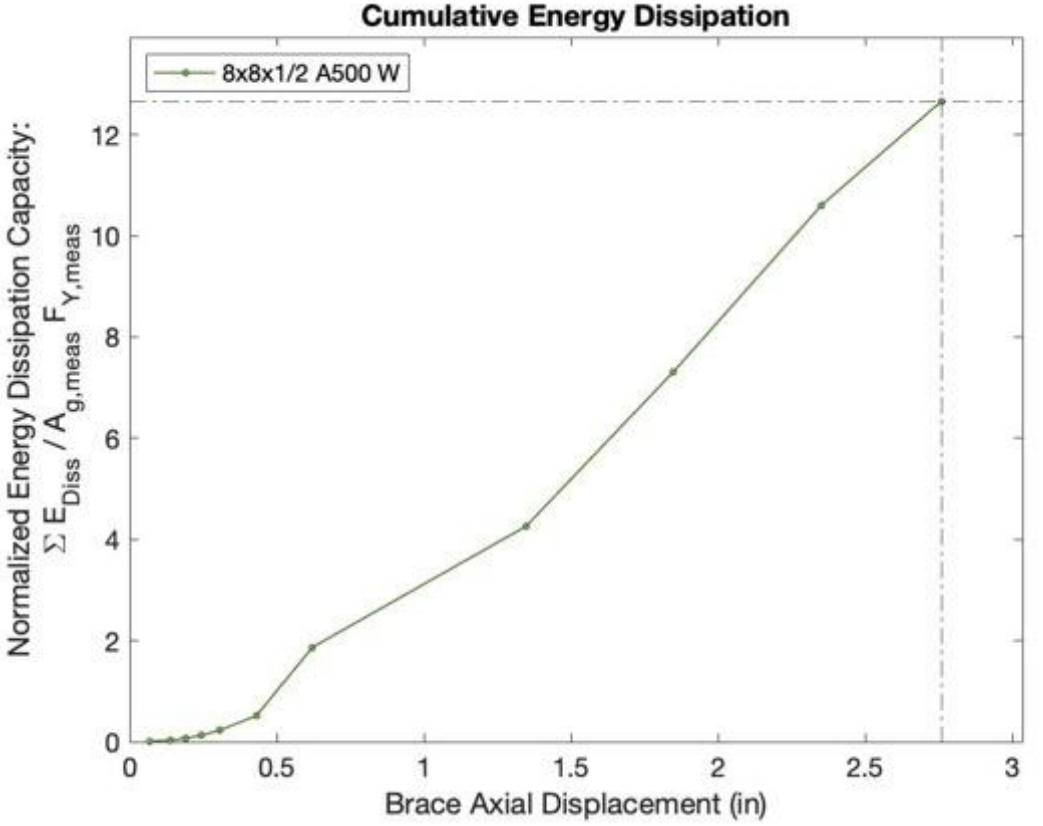
Cumulative Energy Dissipation
8x8x1/2 A500 W
Normalized Energy Dissipation Capacity:
Σ E_Diss / A_g,meas F_Y,meas
Brace Axial Displacement (in)
0
2
4
6
8
10
12
0
0.5
1
1.5
2
2.5
3

Photos

Cupping at Center of Specimen:
2.25” Cycle 2 C

Initiation of Striations and Tearing: 3.25” Cycle 1 T

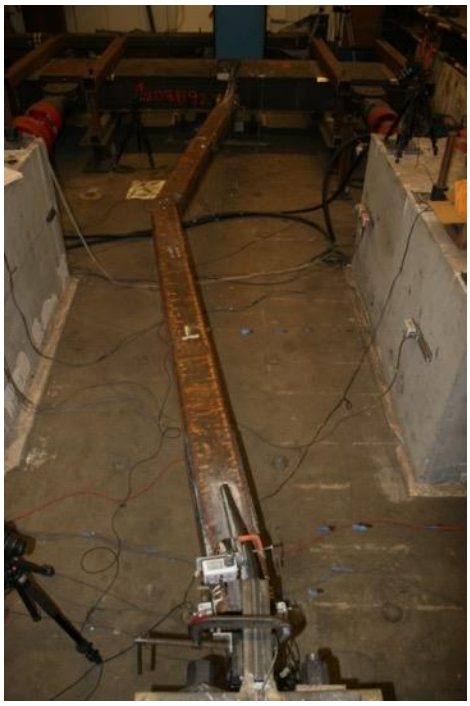

Peak Lateral Displacement: West
2.75” Cycles 1 & 2 C

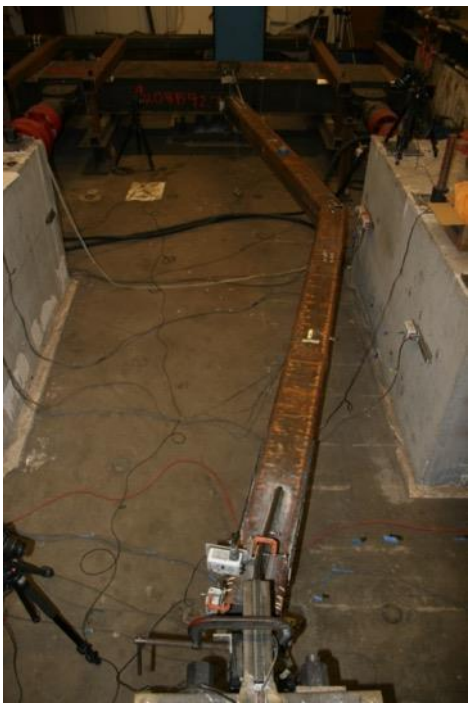

Peak Lateral Displacement: East
3.25” Cycle 1 C

Fractured Specimen: 3.25” Cycle 1 T

Tearing at Center of Specimen: 3.25” Cycle 1 C

8x8x1/2 A1085 Y Brace Test Summary

Test Name: 8x8x1/2 A1085 Y
Test Date: 7/8/21 - 10:00 AM

Brace Properties

Measured Yield Stress (ksi)	64.42
Measured Ultimate Stress (ksi)	75.43
Yield Load (kips)	905.4
Critical Buckling Load (kips)	511.4
Percent Elongation - 2" (%)	32.23
CVN Width (mm)	10
CVN Absorbed Energy (ft-lbs)	40.3
Brace Length (in.)	237.5

Area (in²)	14.4
Moment of Inertia (in⁴)	131
Corner Radius (in.)	1.141
Thickness - Nominal (in.)	0.5
Thickness - Measured (in.)	0.488
Brace Compactness Ratio (b/t) - Nominal *	13
Brace Compactness Ratio (b/t) - Measured	11.72
Global Slenderness ratio (KL/r)	78.64

Specimen Performance

Test Event	Axial Brace Deformation (in.)	Target Displacement (in.) (Cycle)	Force (kips)	$P / P_{Yield\|Critical}$	
Peak Tension Load	1.43	2.25 (1)	921.9	1.02	Y
1: Initial Global Buckling	-0.32	0.625 (1)	-418.2	0.82	C
2: Moderate Global Buckling	-2.10	2.25 (2)	-158.3	0.31	C
3-T: Local Buckling	-2.58	2.75 (1)	-131.4	0.26	C
3-C: Striations & Tearing	2.41	3.25 (2)	875.0	0.97	Y
4: Brace Fracture	2.96	3.75 (1)	309.8	0.34	Y

Key Observations

Cycle #	Displacement (in.)	Observations
3-4	0.25	Bolt Slip - NGP T1
5-6	0.375	Bolt Slip - SGP T1
9-10	0.625	Global Buckling observed - C1

19-20	2.75	Minor cupping observed at C1 peak displacement (~⅝" deep) Cupping observed at C2 peak displacement (~1.5" deep) Location of cupping: Center of specimen
21-22	3.25	Cupping observed at C1 peak displacement (~2" deep) Development of striations at corners - T2 peak Cupping observed at C2 peak displacement (~2.25" deep)
23-24	3.75	Specimen fractured at ~3.4" actuator displacement - T1

Test Results

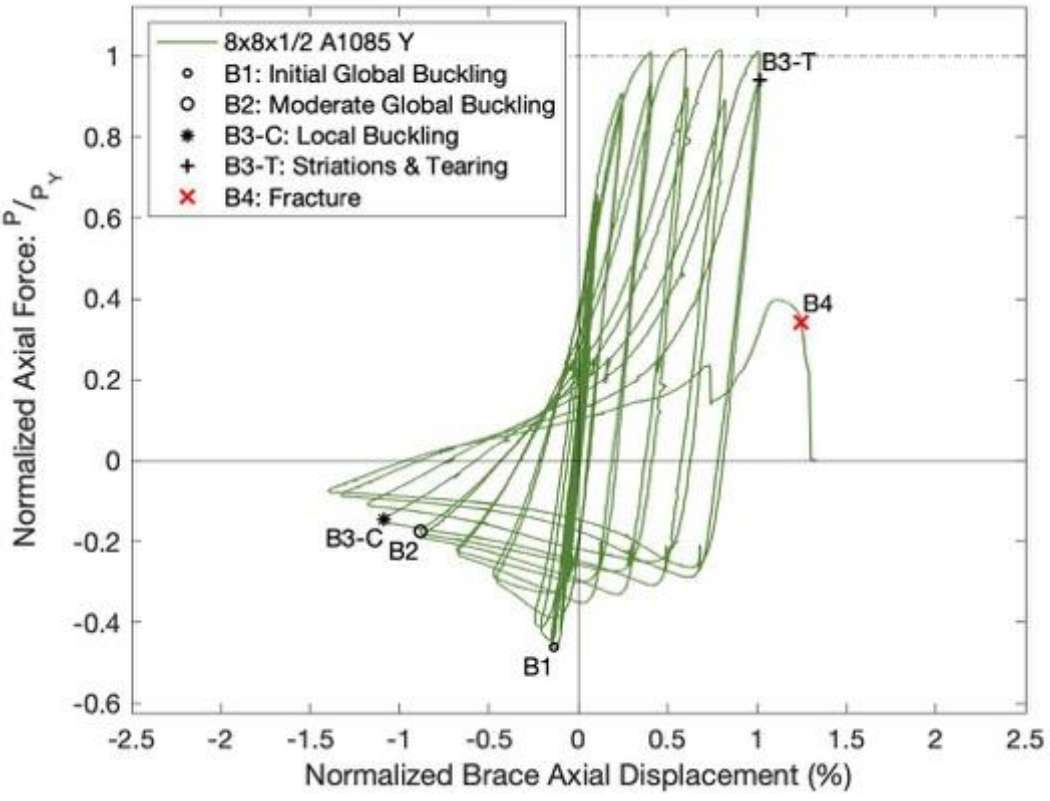

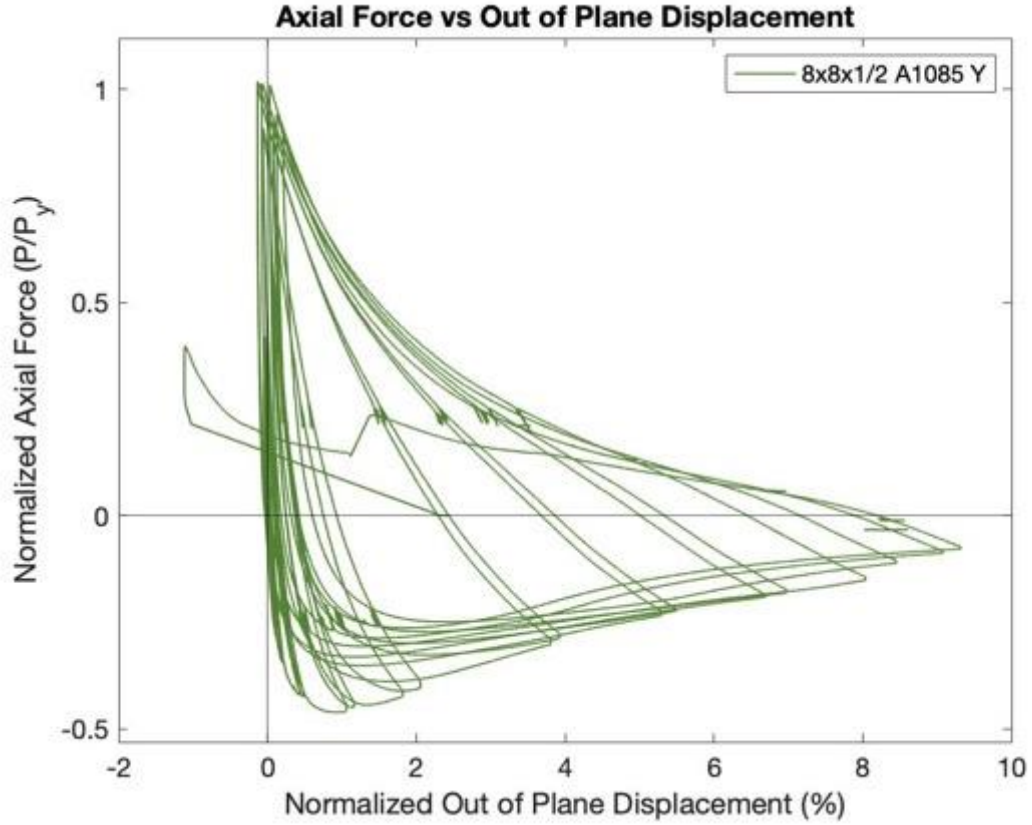
Axial Force vs Out of Plane Displacement
8x8x1/2 A1085 Y
Normalized Axial Force (P/P$_y$)
Normalized Out of Plane Displacement (%)
1
0.5
0
-0.5
-2
0
2
4
6
8
10

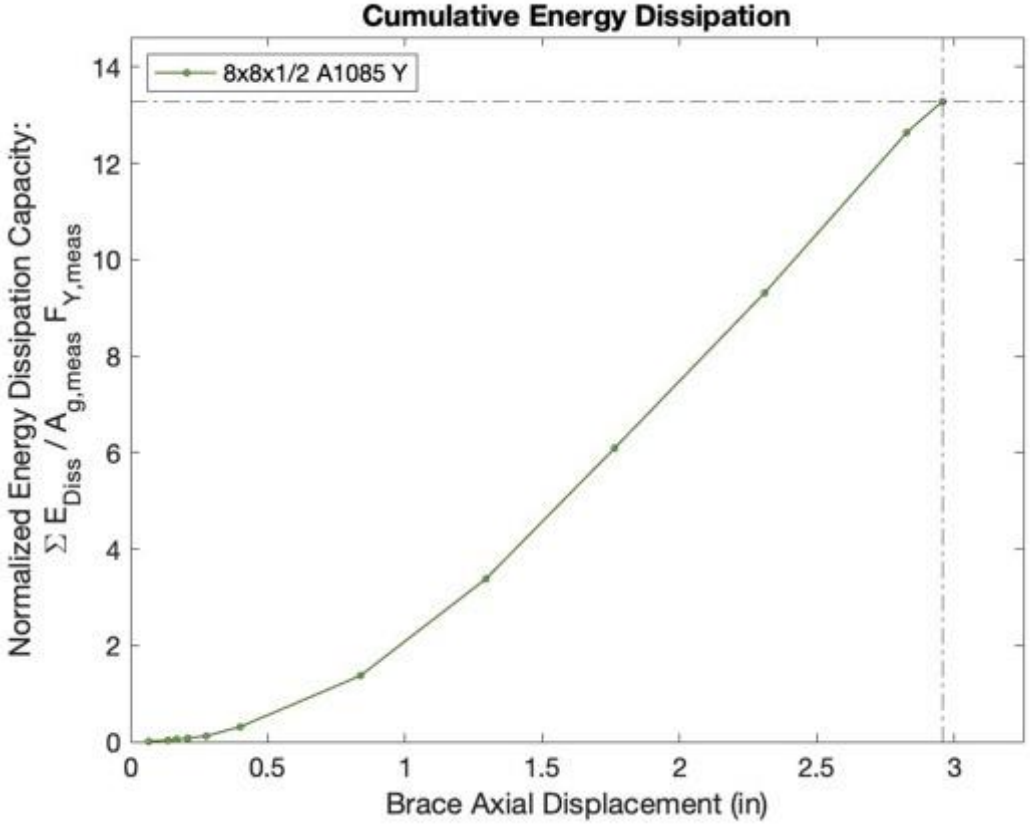
Cumulative Energy Dissipation
8x8x1/2 A1085 Y
Normalized Energy Dissipation Capacity:
$\Sigma E_{Diss} / A_{g,meas} F_{Y,meas}$
Brace Axial Displacement (in)
14
12
10
8
6
4
2
0
0
0.5
1
1.5
2
2.5
3

Photos

Cupping at Center of Specimen: 3.25” Cycles 1 & 2

Initiation of Striations and Tearing: 3.25” Cycle 1 T

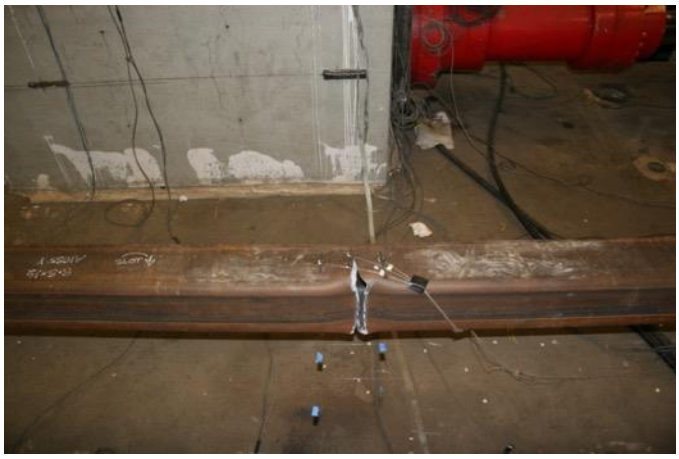

Tearing at Center of Specimen: 3.25” Cycle 1 T

Fractured Specimen: 3.75 Cycle 1 T

10x10x3/8 A500 W Brace Test Summary

Test Name: 10x10x3/8 A500 W
Test Date: 7/6/2021 - 11:00 AM

Brace Properties

Measured Yield Stress (ksi)	59.02
Measured Ultimate Stress (ksi)	69.45
Yield Load (kips)	774.6
Critical Buckling Load (kips)	605.3
Percent Elongation - 2" (%)	34.2
CVN Width (mm)	7.5
CVN Absorbed Energy (ft-lbs)	120+
Brace Length (in.)	237.5

Area (in²)	13.2
Moment of Inertia (in⁴)	202
Corner Radius (in.)	0.766
Thickness - Nominal (in.)	0.349
Thickness - Measured (in.)	0.347
Brace Compactness Ratio (b/t) - Nominal *	25.7
Brace Compactness Ratio (b/t) - Measured	24.40
Global Slenderness ratio (KL/r)	60.6

Specimen Performance

Test Event	Axial Brace Displacement (in.)	Target Displacement (in.) (Cycle)	Force (kips)	P / $P_{Yield/Critical}$	
Peak Tension Load	0.94	1.75 (1)	785.4	1.01	Y
B1: Initial Global Buckling	-0.48	0.75 (1)	-480.1	0.79	C
B2: Moderate Global Buckling	N/A	N/A	N/A	N/A	C
B3-T: Local Buckling	-1.35	1.25 (1)	-174.0	0.29	C
B3-C: Striations & Tearing	0.94	1.75 (1)	785.4	1.01	Y
B4: Brace Fracture	2.12	2.75 (1)	176.5	0.23	Y

Key Observations

Cycle #	Displacement (in.)	Observations
3-4	0.25	Bolt slip NGP - T2
7-8	0.5	Bolt slip SGP - T1
9-10	0.625	Global buckling observed
13-14	1.25	Cupping observed at C1 peak displacement (1.25” Deep) Location of cupping: 2.5” South of Center Cupping observed at C2 peak displacement (1-⅞” Deep)

15-16	1.75	Minor striations observed at corners - T1 peak Cupping observed at C1 peak displacement (2.5" deep) Tearing at top and bottom corners of east wall at T2 peak Cupping observed at C2 peak displacement (2.5" deep)
17-18	2.25	Tearing propagated across east, top, and bottom walls at T1 peak Cupping observed at C1 peak displacement (2.75" deep) Tearing continued to propagate during T2, but specimen did not fracture - only west flange remained intact Similar cupping behavior observed during C2 peak displacement
19-20	2.75	Specimen fractured during T1 cycle at an actuator displacement of about 2.5"

Test Results

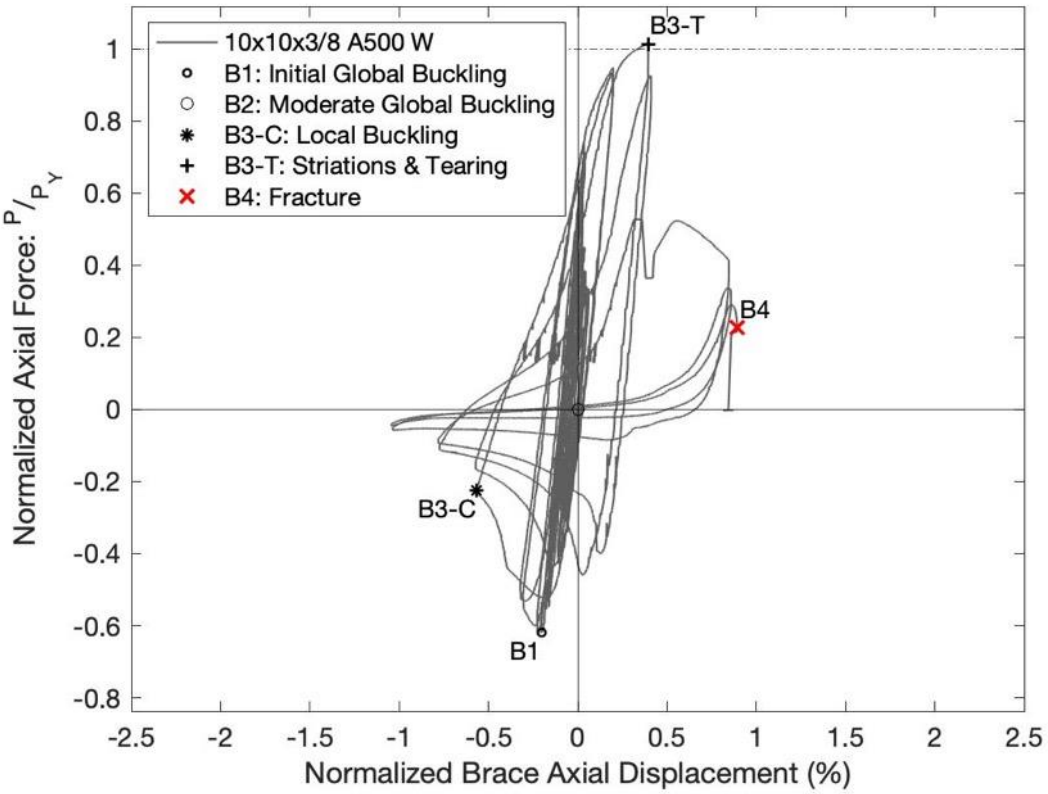

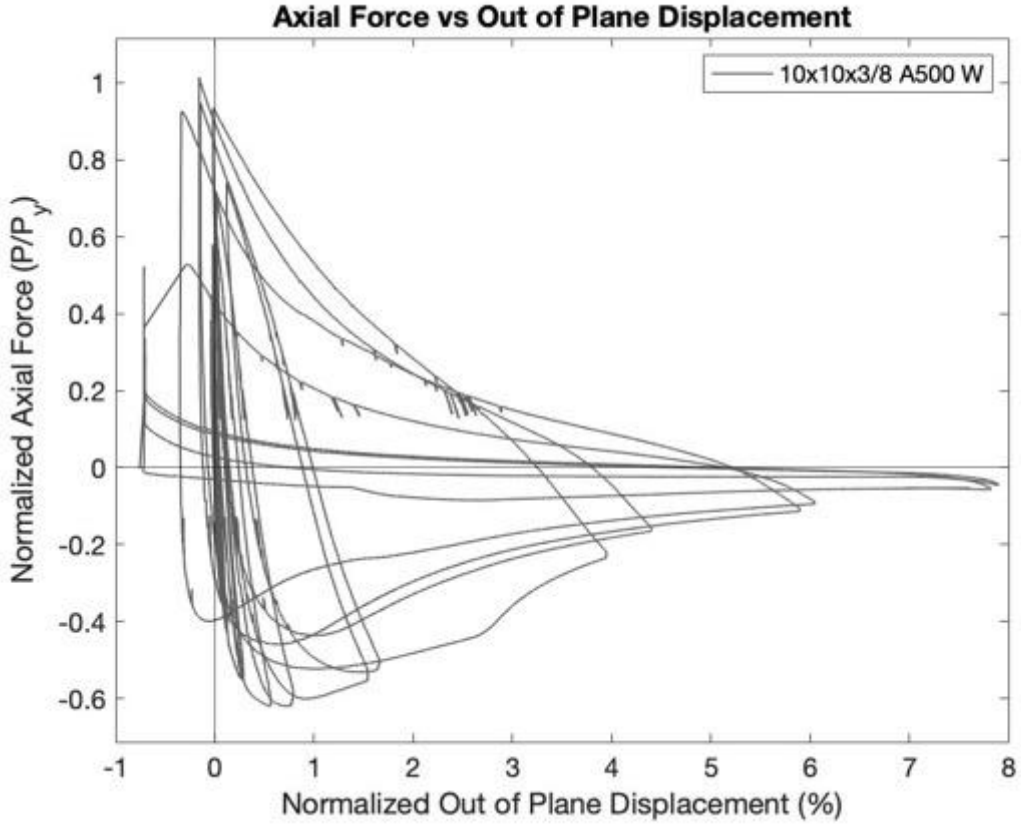
Axial Force vs Out of Plane Displacement
10x10x3/8 A500 W
Normalized Axial Force (P/P$_y$)
Normalized Out of Plane Displacement (%)
1
0.8
0.6
0.4
0.2
0
-0.2
-0.4
-0.6
-1
0
1
2
3
4
5
6
7
8

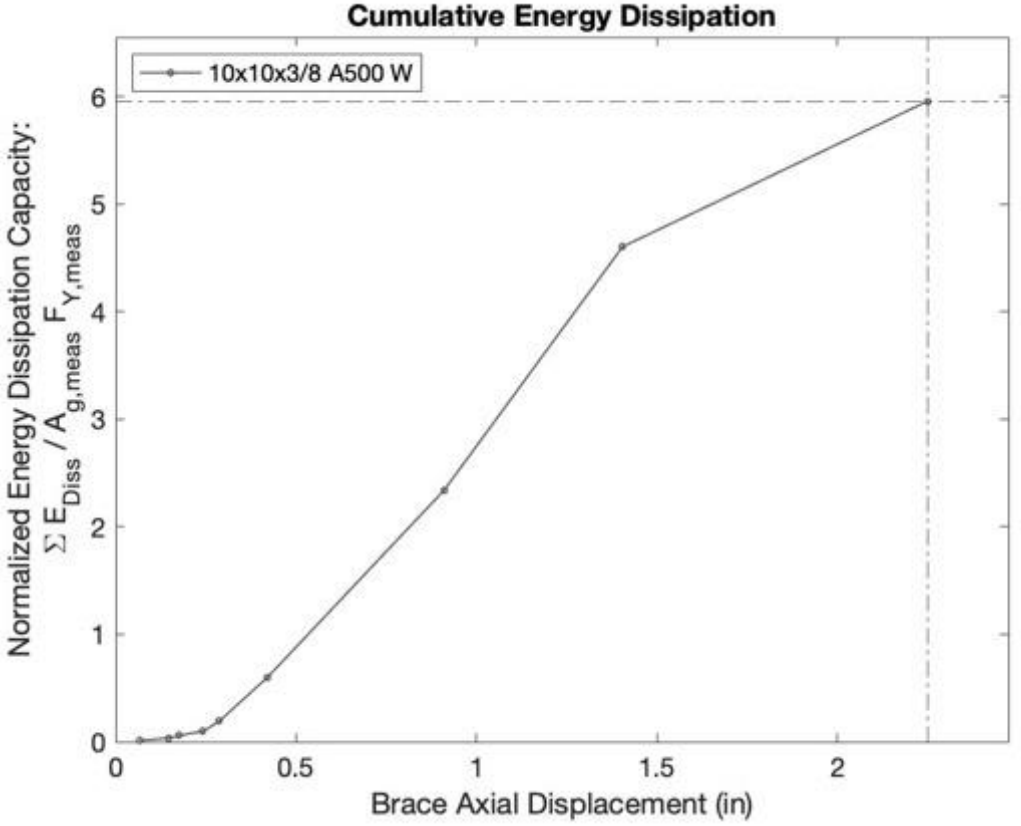
Cumulative Energy Dissipation
10x10x3/8 A500 W
Normalized Energy Dissipation Capacity:
$\Sigma E_{Diss} / A_{g,meas} F_{Y,meas}$
Brace Axial Displacement (in)
6
5
4
3
2
1
0
0
0.5
1
1.5
2

Photos

Cupping at Center of Specimen: 1.25” Cycle 1 C

Initiation of Striations and Tearing: 1.75” Cycle 1 T

Cupping after Initial Tearing at Corners: 1.75” Cycle 2 C

Propagation of Tearing at Center: 2.25” Cycle 1 T

Cupping After Tearing Through Cross Section: 2.25 Cycles 1 & 2 C

Specimen Immediately Before Fracture: 2.75” Cycle 1 T

10x10x3/8 A1085 Y Brace Test Summary

Test Name: 10x10x3/8 A1085 Y
Test Date: 7/7/21 - 11:00 AM

Brace Properties

Measured Yield Stress (ksi)	58.34
Measured Ultimate Stress (ksi)	73.76
Yield Load (kips)	802.9
Critical Buckling Load (kips)	627.9
Percent Elongation - 2" (%)	34.94
CVN Width (mm)	7.5
CVN Absorbed Energy (ft-lbs)	20.7
Brace Length (in.)	237.5

Area (in²)	14.1
Moment of Inertia (in⁴)	214
Corner Radius (in.)	0.766
Thickness - Nominal (in.)	0.375
Thickness - Measured (in.)	0.366
Brace Compactness Ratio (b/t) - Nominal *	23.7
Brace Compactness Ratio (b/t) - Measured	23.14
Global Slenderness ratio (KL/r)	60.90

Specimen Performance

Test Event	Axial Brace Displacement (in.)	Target Displacement (in.) (Cycle)	Force (kips)	$P / P_{Yield/Critical}$	
Peak Tension Load	1.03	1.75 (1)	812.8	1.01	Y
B1: Initial Global Buckling	-0.45	0.75 (1)	-507.6	0.81	C
B2: Moderate Global Buckling	N/A	N/A	N/A	N/A	C
B3-T: Local Buckling	-1.15	1.25 (1)	-214.0	0.34	C
B3-C: Striations & Tearing	1.03	1.75 (1)	812.5	1.01	Y
B4: Brace Fracture	1.60	2.25 (1)	280.0	0.35	Y

Key Observations

Cycle #	Displacement (in.)	Observations
5-6	0.375	Bolt Slip - North and South GPs - T1
11-12	0.75	Initial global buckling observed - C1
13-14	1.25	Cupping observed at C1 peak displacement (1” Deep) Location of cupping - 10” south of center Cupping observed at C2 peak displacement (1.75” Deep)

15-16	1.75	Striations observed at T1 peak displacement Cupping observed at C1 peak displacement (2.5" deep) Tearing propagated halfway through cross section at T2 Cupping observed at C2 peak displacement (2.5" deep)
17-18	2.25	Fracture during T1 at an actuator displacement of about 1.95"

Test Results

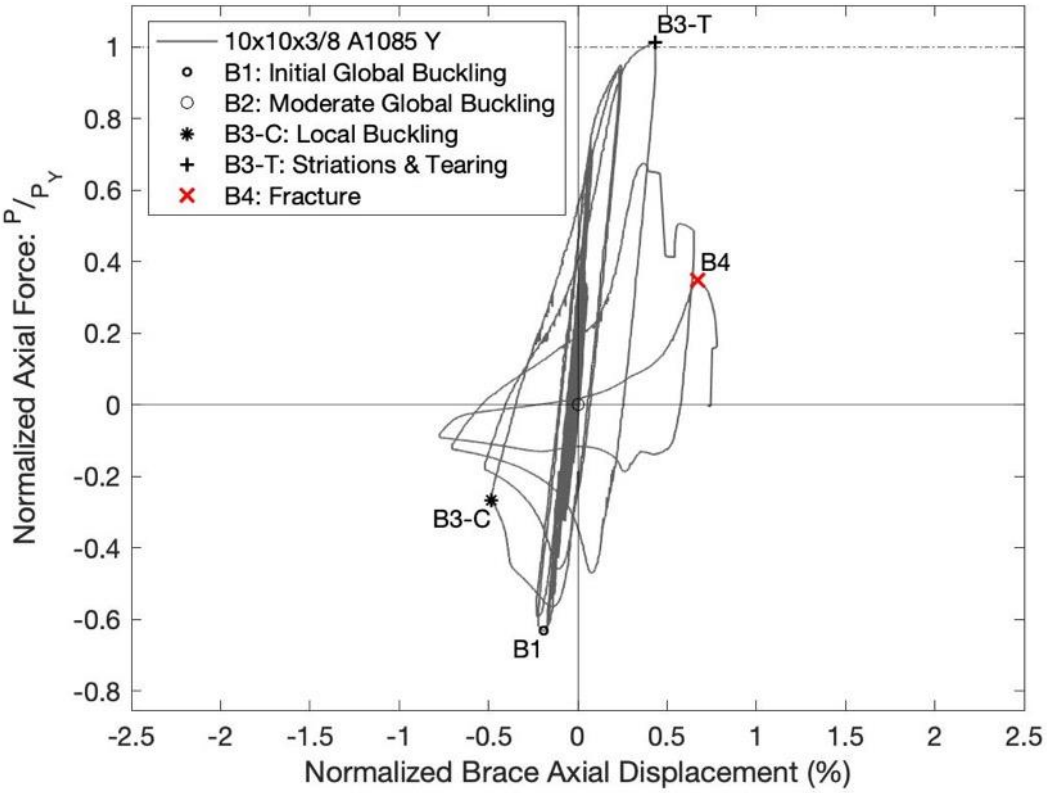

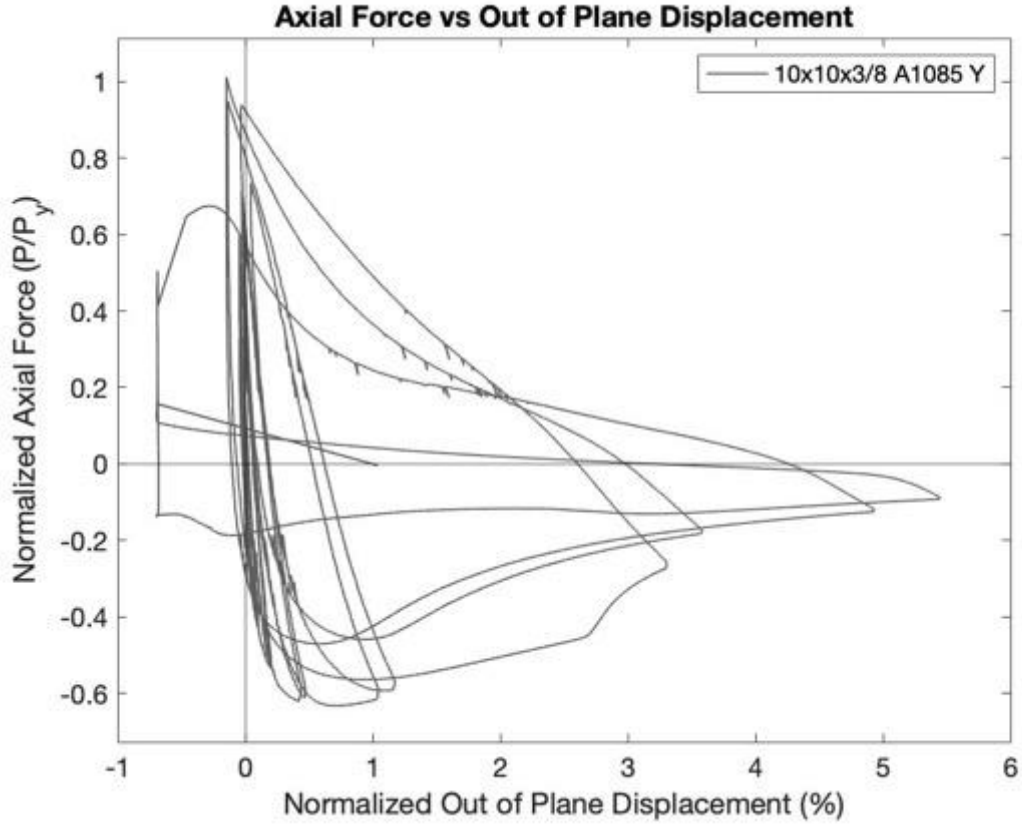
Axial Force vs Out of Plane Displacement
10x10x3/8 A1085 Y
Normalized Axial Force (P/P$_y$)
Normalized Out of Plane Displacement (%)
1
0.8
0.6
0.4
0.2
0
-0.2
-0.4
-0.6
-1
0
1
2
3
4
5
6

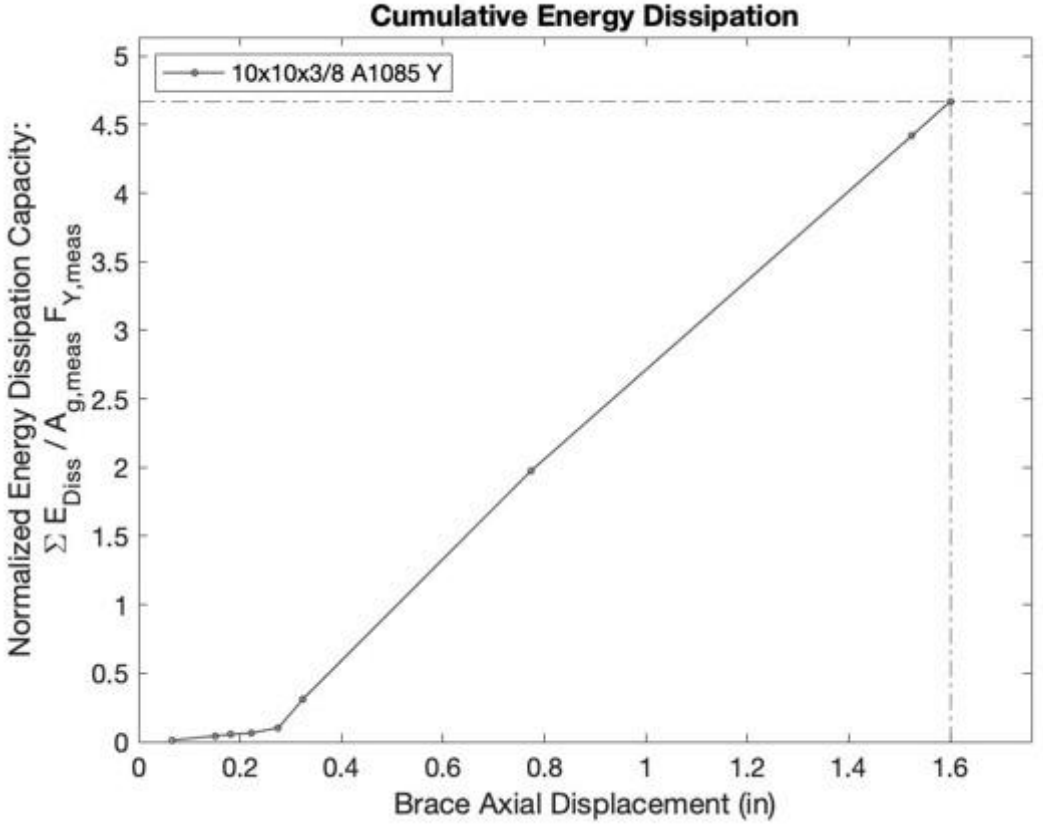
Cumulative Energy Dissipation
10x10x3/8 A1085 Y
Normalized Energy Dissipation Capacity:
$\Sigma E_{Diss} / A_{g,meas} F_{Y,meas}$
Brace Axial Displacement (in)
5
4.5
4
3.5
3
2.5
2
1.5
1
0.5
0
0
0.2
0.4
0.6
0.8
1
1.2
1.4
1.6

Photos

Cupping at Center of Specimen: 1.25” Cycle 1 C

Development of Striations at Corners: 1.75” Cycle 1 T

Cupping at Center of Specimen After Tearing: 2.25” Cycle 2 C

Tearing Across East Wall: 1.75” Cycle 2 T

Fractured Specimen: 3.75 Cycle 1 T

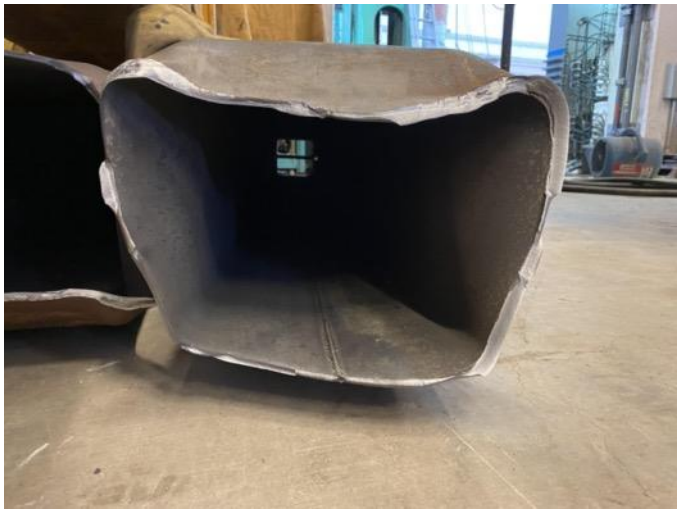

Cross Section of Fractured Specimen After Testing